NASA CR-187638

1990 RESEARCH REPORTS

NASA/ASEE SUMMER FACULTY FELLOWSHIP PROGRAM

JOHN F. KENNEDY SPACE CENTER
AND
UNIVERSITY OF CENTRAL FLORIDA

(NASA-CR-187638) RESEARCH REPORTS: 1990 NASA/ASEE SUMMER FACULTY FELLOWSHIP PROGRAM Final Report, Jun. - Aug. 1990 (NASA) 526 p

CSCL 05I

G3/99

N91-20022
--THRU--
N91-20038
Unclas
0001774

NASA
National Aeronautics and
Space Administration

1990 RESEARCH REPORTS

NASA/ASEE SUMMER FACULTY FELLOWSHIP PROGRAM

JOHN F. KENNEDY SPACE CENTER

UNIVERSITY OF CENTRAL FLORIDA

EDITORS:

Dr. Loren A. Anderson
Associate Professor of Engineering
University of Central Florida

Dr. Mark A. Beymer
Systems Training and Employee Development Branch
Kennedy Space Center

PREPARED FOR:

John F. Kennedy Space Center
Merritt Island, Florida

NASA Grant NGT-60002 Supplement: 4

Contractor Report No. CR-187638

September 1990

PREFACE

This document is a collection of technical reports on research conducted by the participants in the 1990 NASA/ASEE Summer Faculty Fellowship Program at Kennedy Space Center (KSC). This was the sixth year that a NASA/ASEE program has been conducted at KSC. The 1990 program was administered by the University of Central Florida in cooperation with KSC. The program was operated under the auspices of the American Society for Engineering Education (ASEE) with sponsorship and funding from the Office of Educational Affairs, NASA Headquarters, Washington, D.C. The KSC program was one of nine such Aeronautics and Space Research Programs funded by NASA Headquarters in 1990. The basic common objectives of the NASA/ASEE Summer Faculty Fellowship Program are:

a. To further the professional knowledge of qualified engineering and science faculty members;

b. To stimulate an exchange of ideas between participants and NASA;

c. To enrich and refresh the research and teaching activities of participants' institutions; and,

d. To contribute to the research objectives of the NASA centers.

The KSC Faculty Fellows spent ten weeks (June 4 through August 10, 1990) working with NASA scientists and engineers on research of mutual interest to the University faculty member and the NASA colleague. The editors of this document were responsible for selecting appropriately qualified faculty to address some of the many problems of current interest to NASA/KSC. A separate document reports on the administration aspects of the 1990 program. The NASA/ASEE program is basically a two-year program to allow in-depth research by the University faculty member. In most cases a faculty member has developed a close working relationship with a particular NASA group that has provided funding beyond the two-year limit.

TABLE OF CONTENTS

1990 NASA/ASEE SUMMER FACULTY FELLOWSHIP PROGRAM

JOHN F. KENNEDY SPACE CENTER
UNIVERSITY OF CENTRAL FLORIDA

FORMAL SPECIFICATION OF HUMAN-COMPUTER INTERFACES

PREPARED BY:	Dr. Brent Auernheimer
ACADEMIC RANK:	Associate Professor
UNIVERSITY AND DEPARTMENT:	California State University - Fresno Department of Computer Science
NASA/KSC	
DIVISION:	Data Systems
BRANCH:	Real Time Systems
NASA COLLEAGUE:	Mr. Les Rostosky
DATE:	August 10, 1990
CONTRACT NUMBER:	University of Central Florida NASA-NGT-60002 Supplement: 4

Acknowledgements

The support of my NASA colleagues Oscar Brooks, Steve Bryan, Bill Drozdick, Linda Koch, Les Rostosky, Bill Sloan, Lynn Svedin, and Larry Wilhelm is gratefully acknowledged. Thanks also to Steve Eckmann and Richard Kemmerer of the University of California, Santa Barbara for providing helpful comments and ideas.

Abstract

This report describes a high-level formal specification of a human-computer interface. A typical window manager is modeled. Previous work is reviewed and the ASLAN specification language is described. Top-level specifications written in ASLAN for a library and a multiwindow interface are discussed.

Table of Contents

I. Introduction

I.1 Organization of the Paper

This paper documents an attempt to formally specify a multiwindow user interface. The paper is organized as follows:

Section I briefly reviews the foundation laid in last summer's work and discusses motivations and expected results of using formal specification techniques on user interfaces. Section II[1] introduces the ASLAN formal specification language through the example in Appendix A. Section III is a detailed look at an abstract specification of a typical multiwindow interface. The formal specification discussed in Section III is in Appendix B. Finally, Section IV contains concluding remarks and recommendations.

I.2 Specification and Verification Terminology

Specifications are statements about the functionality of a system. Specifications express what is a system is to accomplish, not how it is to do it. In this paper, *formal specifications* are assertions about the behavior of a system. *Critical correctness criteria* are assertions that the specification and all refinements and implementations are to satisfy. *Formal verification* techniques demonstrate that implementations satisfy their specifications. In addition, it is useful to show that specifications meet their critical correctness criteria. This is sometimes called *design verification*. Neumann explains [12]:

> Formal verification has often been talked about as a technique for demonstrating consistency between code and assertions about that code, in some cases between code and specifications. Somewhat less popular has been the easier notion of using formal verification to demonstrate that a set of formal specifications is consistent with its formally axiomatized requirements, i.e., carrying out *design verification.*

I.3 Previous Work

This report describes a continuation of work on formalisms for user interface specification and design described in [1]. That work examined several recent research results in human-computer interaction (HCI) that may be applicable to NASA applications. One of the results examined was the formal specification of direct manipulation user interfaces for a secure military message system [7, 8].

[1] also contains an introduction to formal specification and verification including objections to the approach and reasonable expectations. It was recommended that a pilot study using formal techniques on a small, well-defined piece of a user interface be done. The subsystem to be specified should have clear, high-level correctness properties that must be met. The specification given in Appendix B of this paper is the portion of a user interface that manipulates windows. The correctness property that must be maintained is that users are not allowed to

[1]The information in II.2 and Appendix A is based on a portion of a paper by the author and Daniel Stearns, "Using the ASLAN specification language in undergraduate software engineering courses," submitted to *Computer Science Education*, July 1990

move, close, or resize certain windows. This correctness property was derived from current interface prototypes developed at NASA KSC.

Using formal specification techniques is costly. Benefits are realized when there are readily identifiable, critical correctness properties that must hold. This is the case for portions of proposed interfaces to shuttle and space station software.

Further, it is not necessary to carry out formal specification and verification to their full extent to realize benefits. Finding an appropriate level of formality and analysis can result in systems that users can have a high degree of confidence in. To summarize [1, section IV.2.2]:

> The general goal is to lower expectations for formal specification – the goal isn't necessarily provably correct software – but to specify important functionality and correctness criteria in a way that is reviewable by software engineers and integrates usefully in other software development efforts.

I.4 Formal Techniques and the Development of User Interfaces

As noted in [1], there is some controversy about the usefulness of formal specification and verification techniques in general. Because modern interfaces are visually complex and becoming more aural, some HCI researchers believe that prototyping and user interface management system (UIMS) are the correct approach to interface specification and development. Fischer is a critic of formal specification of interfaces [6, p. 50,51]:

> Static specification languages have little use in HCI software design. First, detailed specifications do not exist. Second, the interaction between a system and its user is highly dynamic and aesthetic, aspects that are difficult, if not impossible, to describe with a static language. ...A prototype makes it much easier and productive for designers and users to cooperate because users do not have to rely on written specifications, which do not indicate an interface's qualities. ...Validation and verification methods from other software domains have limited use in HCI. Formal correctness is crucial, but it is by no means a sufficient measure of the effectiveness and success of an HCI system.

Fischer's statements are true for most interface development efforts. Formal techniques aimed at low level or aesthetic portions of user interfaces may not be productive.

However, for critical aspects of NASA interfaces, such as alarm areas, critical correctness requirements are apparent and easily expressed. By using techniques employed in the specification of secure systems, formal specification becomes a valuable approach.

Further, it is possible to combine formal specifications of functionality with usability specifications. Carrol and Rosson have studied the design process and recommend an iterative approach of developing and integrating functionality and usability specifications [5, p. 1]:

> Much has been said about this "usability" problem regarding current interface designs. Less has been said about how to solve the problem. ...we develop an approach to the problem based on *usability specifications:* precise, testable statements

of performance goals for typical users carrying out tasks typical of their projected use of the system.

I.5 Two Views of Specifications

Most specification efforts target one of two goals: an executable specification (prototype system), or a proof that a specification meets critical correctness requirements ("design verification"). HCI specification are usually developed with the intent of having a prototype system that can be "checked for certain undesirable properties" [8, p. 211]. Because these specifications are to result in realistic prototypes, it is necessary to specify low-level events such as mouse clicks and beeps. Not surprisingly, it is not feasible to combine a huge quantity of implementation details with design verification of the specification.

The approach explored in this paper is to write abstract specifications and critical correctness requirements for a portion of a user interface without getting bogged down in implementation details. High-level specifications have been very successful in the field of secure systems. The formal specifications for these systems are shown to be consistent with their critical correctness criteria without becoming bogged down in implementation details. For example, in a short, high-level specification, Kemmerer shows fundamental flaws in a cryptosystem [10].

Although Jacob focuses on executable specifications and prototyping, he briefly discusses extensions to his techniques [8, p. 237]:

> In designing a secure message system, it is desirable to prove assertions about the security of the system formally. Such proofs are usually based on a formal specification of the system (with the proviso that the final software and hardware correctly implement the specification). This approach has not generally been used at the user interface level, but, if one had a formal specification of the user interface, it would be possible to provide proofs about the user interface.

I.6 Testing vs. Proving Specifications

A common and persistent criticism of formal specification and verification is that the quantity of proofs that must be done is overwhelming. a formal specification and statement of correctness, it is possible to gain insights into the system and confidence in the specification without performing proofs. The informal analysis of a formal specification can be a valuable technique for communication between software engineers.

More formally, symbolic execution tools have been developed [11]. Specifications can then be tested against correctness requirements. Testing specifications allows software engineers to play what-if games with the specification and may result in the discovery of system states that do not satisfy the correctness requirements.

These tools have been successfully used in the development of secure systems. Kemmerer explains the use of the Inatest tool on a cryptosystem specification [10, p. 453]:

> With the Inatest tool, it is possible to introduce assumptions about the system interactively, execute sequences of transforms, and check the results of these execu-

tions. This provides the user with a rapid prototype for testing properties of the cryptographic facilities ...

II. Formal Specification

II.1 The Aslan Specification Language

Software engineers' lack of exposure to formal specification systems is particularly disturbing in light of increasing dependence on critical software systems. Neumann describes examples of problems with specifications in four application areas: human safety, reliability, security, and user interfaces [12]. Neumann concludes (emphasis added):

> There are many contributions that good software engineering practice could have made to the prevention or minimization of these and many other problems. In particular, the sound use of system structuring, *specification languages capable of meaningful abstraction, and rigorous analysis of specifications* could all have had significant effects.

The ASLAN formal specification language is a partial solution to the above problem. Software engineers can use ASLAN to formally specify complex systems and develop their specifications through arbitrary levels of abstraction. When a specification is passed through the ASLAN Language Processor (ALP), software engineers receive a set of correctness conjectures.

The following sections describe features of ASLAN using a specification of a library as an example. The library example has been used in many formal specification workshops. A library specification written in the InaJo language appears in [11].

II.2 The ASLAN Approach

The ASLAN language is built on first order predicate calculus. Systems being specified are thought of as being in *states*, defined by the values of the system variables. Logical assertions are used to define the critical correctness requirements that must hold in every state and those that must hold between two consecutive states. The former are *state invariants*, while the latter are *constraints* on state transitions.

To prove that a specification satisfies its invariant and constraints, the ALP generates *correctness conjectures*. Correctness conjectures are logical statements whose proof ensures the correctness of the specification with respect to the invariant and constraint.

Appendix A contains a high-level specification of a library. Although the library could be further specified through more detailed levels of specification, only the top-level specification will be examined here.

The state variables for this system appear in the `VARIABLE` section of the specification. `Library` is a variable whose type is a collection of `Book`. At this level, `Book` is left as an unspecified type. A state variable `Checked_Out` maps each book into the boolean domain, while `Number_Out` maps library users to the the number of books they have checked out.

The specification contains an initial assertion defining possible starting states of the library. This assertion states that the library is initially empty, that no users have books out, and that, indeed, no books are checked out.

The library specification contains an invariant assertion to specify the essential properties that the system must have. The invariant states that

- when a book is checked out, it cannot be available. Similarly, an available book cannot simultaneously be checked out.
- the limit on the number of books checked out by any user is enforced
- no user has more than one copy of the same book checked out

Clearly, we want the initial state of the system to fulfill the invariant. The ALP will generate a logical implication that

$$\text{initial} \rightarrow \text{invariant}$$

The particular correctness conjecture generated is

```
    Library = EMPTY
  & FORALL u: User (Number_Books(u) = 0)
  & FORALL b: Book (~Checked_Out(B))
->
    FORALL b:Book( b ISIN Library ->
                     Checked_Out(b) & ~Available(b)
                   | ~Checked_Out(b) & Available(b))
  & FORALL u:User (Number_Books(u) <= Book_Limit)
  & FORALL u:User,b1, b2:Book(
                     Checked_Out_To(u, b1)
                   & Checked_Out_To(u, b2)
                   & Copy_Of(b1, b2)
                   -> b1 = b2)
```

It is up to the specifier, possibly with the help of a theorem prover, to prove the above correctness conjecture.

An empty library is not very interesting. The specification must define how the library can expand; that is, how the library can change from a current ('old') state to a new state in which more books are present.

Allowable state changes are specified as `transitions`. An ASLAN transition consists of a precondition (ENTRY) and a postcondition (EXIT). Transitions in the library example have only postconditions. The ALP assumes that omitted preconditions are true.

The Add_A_Book transition allows the library to expand. Because Add_A_Book does not have an entry assertion, it can be applied at any time. The exit assertion states the effect the application of the transition has on the state variables. It asserts that

- the user adding the book must be a member of the library staff,
- and assuming the user is a staff person and the book isn't already in the library (the apostrophe is the ASLAN notation for 'old value'),
- the book is added to the library
- the book is not checked out
- and in particular, this book has *never* been checked out

How can the specifier be assured that the Add_A_Book transition meets the correctness requirements embodied in the invariant? It must be proved that if the invariant holds in the current (old) state, and the transition is applied, then the invariant will hold in the new state. That is,

$$\text{invariant' \& entry' \& exit} \rightarrow \text{invariant}$$

Note that in the antecedent, the invariant and the entry assertion are evaluated in the old state. The exit assertion and the consequent are evaluated in the new state.

ASLAN specifications can be made up of several levels of abstraction. Given a multilevel specification, the ALP generates additional correctness conjectures that ensure that types, variables, and transitions are properly refined, and that the correctness requirements are met at every level of abstraction. Details are found in [4].

Ideally, ASLAN should be used to specify increasingly concrete levels of abstraction. The resulting specification would be a high level specification defining the system as an abstract data type, followed by intermediate levels leading to a low level specification close to code level. In this most detailed specification level, the transitions' entry and exit assertions become the the pre- and postconditions of programming language level procedures which implement them.

II.3 A Specifier-friendly Feature

Expressions in ASLAN look like first order logic assertions for a simple reason: the techniques and expressive power of first order logic can be used to prove correctness conjectures.

Unfortunately for specifiers with a programming background, the semantics of first order logic are not the same as those of procedural programming languages such as Pascal and C. Consider an alternate version of the Return transition:

```
TRANSITION Return(B: Book)
 EXIT
    Checked_Out'(B) ->  Checked_Out(B) = FALSE
                      & Number_Books(Responsible'(B)) =
                          Number_Books(Responsible'(B) - 1)   ,
```

The above exit assertion is written in a purely 'logical' form. Recall that the ALP will construct a correctness conjecture whose proof ensures the invariant holds after the application of Return:

```
    FORALL b:Book (b ISIN Library' ->
                     Checked_Out'(b) & ~Available'(b)
                   | ~Checked_Out'(b) & Available'(b))
  & FORALL u:User (Number_Books'(u) <= Book_Limit)
  & FORALL u:User,b1, b2:Book(
                     Checked_Out_To'(u, b1)
                   & Checked_Out_To'(u, b2)
                   & Copy_Of(b1, b2)
                   -> b1 = b2)
&
    Checked_Out'(B) ->  Checked_Out(B) = FALSE
                      & Number_Books(Responsible'(B)) =
                            Number_Books(Responsible'(B) - 1)
->
    FORALL b:Book (b ISIN Library ->
                     Checked_Out(b) & ~Available(b)
                   | ~Checked_Out(b) & Available(b))
  & FORALL u:User (Number_Books(u) <= Book_Limit)
  & FORALL u:User,b1, b2:Book(
                     Checked_Out_To(u, b1)
                   & Checked_Out_To(u, b2)
                   & Copy_Of(b1, b2)
                   -> b1 = b2)
```

It is a simple paper and pencil exercise to show that the conjecture generated cannot be proved. In particular,

- The new values of **Available** and **Checked_Out_To** are mentioned in the consequent invariant. Nothing can be proved about the new values of **Available** and **Checked_Out_To**. Neither variable was mentioned in the exit assertion of **Return**, and the antecedent invariant only relates old values of the state variables.
- Because the exit assertion was written as a logical implication, we have not specified what will happen when **Checked_Out'(B)** is false. In particular, if the book B was not checked out, the new value of **Checked_Out(B)** could be true or false. Also, the values of **Checked_Out** for books other than B are unspecified!

- Similarly, we have not specified the new values of Number_Books for all users *not* responsible for the particular book B being returned. In particular, the new value of Number_Books for such users could be any integer.

These differences between the semantics of logic and those of programming languages have caught professional specification writers by surprise [14].

The ASLAN language provides constructs that operate like programmers tend to think logical operations *should* operate. Corresponding to logical implication is the ASLAN IF-THEN-ELSE-FI, corresponding to disjunction is the ALT (alternative) statement, and corresponding to equality is the BECOMES statement. Details are found in [3, 4].

In addition, ASLAN supplies the implicit 'no changes' for variables mentioned in the invariant and constraint, but not mentioned in a particular transition.

These language features allow specifiers to write specifications in a more natural way. Readers should compare the Return transition above with the version in the appendix.

Preliminary work on extending ASLAN to facilitate specification of real-time systems is documented in [2].

III. Specification of a Multiwindow User Interface

III.1 Overview

Appendix B contains an ASLAN specification of an interface commonly provided by window managers running on the X window system [9, 13, 15]. Windows can be created, deleted, opened, closed, resized, moved, brought to the foreground, and be made the target of user input.

The specification has one feature not usually found in multiwindow interfaces: dedicated, reserved ("special") windows that cannot be moved, closed, or covered. Displays proposed for shuttle ground support software will have such areas.

This specification was written to be an abstract description of the operations provided by a window manager to a user. Note that pixels and mice, usually associated with such interfaces, are not mentioned. It is sometimes hard to determine an appropriate level of abstraction for a top-level specification. A guideline is that the most abstract specification be such that critical functionality and correctness requirements can be expressed in a form that is readily understandable and easily manipulable. In addition, top-level specifications should not restrict possible implementations and refinements.

Although only a top-level specification of the interface is provided, it is clear that more detailed levels of refinement could introduce implementation details such as pixels and mice.

Each major syntactic unit of the specification will be discussed in turn. Sections III.2 through III.8.8 refer directly to Appendix B. The following lexical convention is used: constants and ASLAN keywords are uppercase, type identifiers begin with uppercase, variables and definitions are lower case.

III.2 Types

Six unspecified types are declared to represent classes of system objects that require no elaboration at this level. For example, `Processes` can be associated with `Windows`, however at this level of abstraction it is not important how either is implemented. Further, how windows look on the screen (their `Representations`, `Sizes`, and `Locations`) are deferred.

The `Display_Levels` type represents the stacking level of windows on the screen. It is tempting to define `Display_Levels` as a synonym for integer. This would restrict possible implementations. As discussed in III.3, it is only necessary that `Display_Levels` have a less-than-or-equal ordering.

The state of a window is a simple enumerated type. The layout of a window is a structure of three fields: a location, size, and a representation. As discussed in section III.4, windows have a layout for when they are open, and another layout (an icon) for when they are closed. Finally, the contents of the current screen is of type `Displays` – a set of window layouts. The current display along with current stacking levels for the active windows defines the look of the screen.

III.3 Constants

Constants are unchanging mappings. For example, `INITIAL_OPEN_LAYOUT` associates a de-

fault look for windows opened for processes. With INITIAL_CLOSED_LAYOUT and INITIAL_STATE, the window manager determines the look of a window when it is created for a process.

OVERLAPS is an important relation that maps two layouts to true or false. The intent is that refinements of OVERLAPS will check to see if any of the first layout overlaps the second. This constant relation is useful in determining if windows are on the screen (overlap the BACKGROUND) and if they would obscure a restricted window.

LESS_OR_EQUAL is similar to OVERLAPS. This boolean constant maps window stacking levels. If Display_Levels is subsequently refined to be the integers, this constant may turn into nothing more than $\leq$.

SPECIAL is a boolean function that determines if a window is restricted. It is made a constant in this specification so that the mechanisms for making windows restricted or not can be omitted. It is reasonable that SPECIAL could be changed to be a state variable and state transitions for its manipulation be added.

III.4 State Variables

The value of the state variables determine the state of the interface. These values are changed by the application of the state transitions discussed in section III.8.

Windows are created for processes. The mapping of processes to windows is represented in process. When a process is bound to a window, the window will inherit the initial open and closed layouts from the process. These layouts (open_layout, closed_layout) can be changed by the resize and move state transitions. Associated with each window is also a stacking level display_level.

The layouts currently active on the screen are in display. The window selected to receive input is determined by the value of input_focus.

III.5 Definitions (Macros)

ASLAN definitions are macros used to make state transitions more understandable. Eight definitions are given to represent mundane events such updating the display and changing layout fields.

to_top_level is interesting because it specifies that the stacking level of its argument is to be less than all other windows, and that the relationship between other windows should remain as it was before the argument was made uppermost window.

There are two things to note. First, to_top_level may be restricting future implementations. It is not necessary for the argument's stacking level to be strictly less than that of all other windows, just that it be less than the level of all windows in its stack. That is, the topmost windows of independent stacks on the screen could have the same display_level. It is an interesting exercise to rewrite the definition to allow this.

Second, although it is specified that the relationships of other windows remains as they were before the state transition, it is possible that the value of display_level for each window has changed! This allows refinements and eventual implementations flexibility in assigning display levels - any implementation that has the argument window ending up on top, and doesn't

rearrange the other windows meets this specification.

`set_location` and `set_size` manipulate one field of a particular window's current layout. Care is taken that other fields for this window, and layouts for other windows are unchanged.

The `update_display` definitions specify the addition and deletion of layouts to the current display.

III.6 Initial Conditions

The `INITIAL` assertion describes the state of the interface when the system is first brought up. An informal reading of the assertion is "nothing is on the screen, and all windows are inactive, and windows that are created for processes will be on somewhere on the screen."

III.7 Critical Correctness Requirements

The critical correctness requirements are expressed in the `INVARIANT`. This assertion is to be true when the system is started, and continue to hold in every state the system can reach starting at the initial state and using the state transitions described in III.8. The assertion consists of three conjuncts. The first says that every layout on the screen has to be associated with an active window. The second asserts that every current layout must be at least partially on the screen. The third states that restricted windows are not covered.

III.8 State Transitions

The following subsections describe the eight state transitions. Since none of the transitions have explicitly stated `ENTRY` assertions, there are no restrictions on when the transitions can be applied. This corresponds to typical window managers – it is possible, for example, to attempt to close windows at any time.

Although there are no restrictions on when the transitions can be applied, it is not always the case that applying them has any effect on the state of the system. For example, most window managers will allow a user to close an already closed window. From the user's view, there is no change in the state of the display.

The specifications for the state transitions are written with this in mind. The style used is as follows: an exit assertion is a disjunct of two clauses joined by the ASLAN `ALT` operator. The first clause specifies the effect of the state transition when variables are changed (the closing of an open window, for example) and the second clause specifies that no variables change.

The `ALT` operator is logical disjunction augmented by statements specifying that unmentioned state variables do not change. These statements are generated automatically by the ALP [3, 4].

When reading the transitions it is important to pay careful attention to the use of the old-value operator (apostrophe). The following sections will focus on the first disjunct of each transition's exit assertion.

III.8.1 Window Closing (Iconifying)

To close a window `w`, it is necessary that `w` be open, that it is not a restricted window, that `w`'s new state is closed (and that the states of other windows are unchanged), that `w`'s open

layout is taken off the screen and replaced by its icon, and that the icon not be hidden.

III.8.2 Window Opening

`open_window` is symmetric to `close_window`.

III.8.3 Window Destruction

To destroy a window `w`, it is necessary that `w` active before the state transition and unused afterwards, that `w` is not a restricted window, and that the layout of `w` be removed from the screen.

III.8.4 Window Creation

Windows are created for and associated with processes. To create a window for process p it is necessary that there exists a window `w` that was inactive before the state transition and will become active. This window will inherit its initial state and layouts from p. `w` will be associated with p, and `w`'s current layout will be added to the display uncovered by other windows or icons.

III.8.5 Shifting Input Focus

This transition assumes that only one window at a time can be the target of user input. It is a simple transition that checks that only active windows can receive input.

III.8.6 Moving Windows

The `move` transition looks more complicated than it is. There are two symmetric cases for when the window to be moved, `w`, is open and closed. In either case, `w` cannot be a restricted window and the current display is modified. If `w`'s state is open then its location is changed, `w` must still be on the screen, and `w` cannot overlap any special windows. The case when `w` is closed is symmetric.

III.8.7 Window Resizing

This transition states that only ordinary, open windows can be resized. In addition, a window cannot be resized to overlap a restricted window.

III.8.8 Window Restacking

To bring an active window `w` to the foreground, the display must be changed, and the act of bringing `w` to the foreground must not overlap a restricted window.

IV. Concluding remarks

This paper has discussed formal specification of user interfaces. The particular approach taken was to construct an abstract, state-machine model of the interface using the ASLAN specification language. Emphasis was placed on defining essential functionality and critical correctness requirements without introducing implementation details.

The resulting specification defines the functionality of a typical window manager (Appendix B). The specification can be the foundation of several further activities:

- The correctness conjectures generated by the ASLAN language processor could be proved. Successful proofs would show that the specification satisfies its critical correctness criteria.

  Failed attempts to prove correctness conjectures have lead to new insights into the system being specified. Failed proofs can show misunderstandings in functionality, inconsistency, and incompleteness. These insights can be especially valuable to software engineers as they work toward defining essential functionality and correctness of a system.

- The specification can be expanded. It would be useful to refine the top-level specification into lower, more detailed specifications. A challenge is to refine the specification down to an implementation level at which objects such as pixels, mouse clicks, and scroll-bars are used. New techniques would have to be developed to maintain readability and understandability while handling the amount of detail at low levels.

- The specification could serve as inspiration for a specification of a particular part of the proposed shuttle/space station ground software. This is a promising area for further research. After informal requirements for, say, protected alarm areas on screens are developed, an effort should be made to formally specify their actions and correctness requirements.

- The specification could be tested. A symbolic execution tool for ASLAN specifications should be constructed.

Formal specification of user interfaces is not cost effective for most projects. However, for highly structured interfaces whose performance is critical (such as the NASA interfaces being developed) formal specification can play a valuable role in unambiguously defining functionality and providing confidence in meeting correctness requirements. There is considerable interest in formal techniques and proofs of correctness among developers of critical interfaces.

References

[1] B. Auernheimer. Formalisms for user interface specification and design. In NASA CR-166837, NASA Kennedy Space Center (October 1989).

[2] B. Auernheimer and R. A. Kemmerer. RT-ASLAN: a specification language for real-time systems. *IEEE Transactions on Software Engineering*, SE-12, 9 (September 1986).

[3] B. Auernheimer and R. A. Kemmerer. Procedural and nonprocedural semantics of the ASLAN formal specification language. *Proceedings of the nineteenth annual Hawaii international conference on system sciences* (January 1986).

[4] B. Auernheimer and R. A. Kemmerer. ASLAN users manual. Technical report TRCS84-10. Department of Computer Science, University of California, Santa Barbara (March 1985).

[5] J. Carroll and M. Rosson. Usability specifications as a tool in iterative development. In *Advances in human-computer interaction*, vol. 1. H. Hartson, ed. (1985).

[6] G. Fischer. Human-computer interaction software: lessons learned, challenges ahead. *IEEE Software* 6, 1 (January 1989).

[7] R. J. K. Jacob. A specification language for direct-manipulation user interfaces. *ACM Transactions on Graphics* 5, 4 (October 1986).

[8] R. J. K. Jacob. An executable specification technique for describing human-computer interaction. In *Advances in human-computer interaction*, vol. 1. H. Hartson, ed. (1985).

[9] O. Jones. *Introduction to the X window system.* Prentice-Hall (1989).

[10] R. A. Kemmerer. Analyzing encryption protocols using formal verification techniques. *IEEE Journal on Selected Areas in Communications*, 7, 4 (May 1989).

[11] R. A. Kemmerer. Testing formal specifications to detect design errors. *IEEE Transactions on Software Engineering*, SE-11, 1 (January 1985).

[12] P. G. Neumann. Flaws in specification and what to do about them. *ACM SIGSOFT Engineering Notes*, 14, 3 (May 1989).

[13] O' Reilly & Associates, Inc. *X Window System Series*, vols. 0-7.

[14] R. Platek and D. Sutherland. The semantics of the Freiertag MLS information flow tool and its impact on design verification: some SCOMP examples. Unpublished report, Odyssey Research Associates, Inc., Ithaca (December 1983).

[15] R. W. Scheifler and J. Gettys. The X window system. *ACM Transactions on Graphics* 5, 2, (April 1986).

Appendix A
Specification of A Library

```
SPECIFICATION Library
LEVEL Top_Level

TYPE
    User,
    Book,
    Book_Title,
    Book_Author,
    Book_Collection IS SET OF Book,
    Titles IS SET OF Book_Title,
    Pos_Integer  IS TYPEDEF i:INTEGER (i>0)

CONSTANT
    Title(Book):Book_Title,
    Author(Book):Book_Author,
    Library_Staff(User):BOOLEAN,
    Book_Limit:Pos_Integer

DEFINE
    Copy_Of(B1,B2:Book) : BOOLEAN ==
             Author(B1) = Author(B2)
          & Title(B1) = Title(B2)

VARIABLE
    Library:Book_Collection,
    Checked_Out(Book):BOOLEAN,
    Responsible(Book):User,
    Number_Books(User):INTEGER,
    Never_Out(Book):BOOLEAN,


DEFINE
    Available(B:Book):BOOLEAN ==
         B ISIN Library & ~Checked_Out(B),
    Checked_Out_To(U:User,B:Book):BOOLEAN ==
            Checked_Out(B)
         & Responsible(B)=U
```

```
INITIAL
       Library = EMPTY
    & FORALL u:User (Number_Books(u) = 0)
    & FORALL b:Book (~Checked_Out(b))

INVARIANT
      FORALL b:Book(b ISIN Library ->
                        Checked_Out(b) & ~Available(b)
                      | ~Checked_Out(b) &  Available(b))
    & FORALL u:User(Number_Books(u) <= Book_Limit)
    & FORALL u:User,b1,b2:Book(
            Checked_Out_To(u,b1)
         & Checked_Out_To(u,b2)
         & Copy_Of(b1,b2)
              -> b1=b2)

TRANSITION Check_Out(U:User,B:Book)
  EXIT
        Available'(B)
      & Number_Books'(U) < Book_Limit
      &  IF FORALL B1:Book (Checked_Out_To'(U,B1) -> ~Copy_Of(B,B1))
         THEN
          Number_Books(U) BECOMES (Number_Books'(U) + 1)
            &  (Checked_Out(B) BECOMES TRUE)
            &  (Responsible(B) BECOMES U)
            &  (Never_Out(B) BECOMES FALSE)
         FI

TRANSITION Return(B:Book)
  EXIT
    ( IF Checked_Out'(B)
        THEN Checked_Out(B) BECOMES FALSE
             & Number_Books(Responsible'(B))
                 BECOMES (Number_Books(Responsible'(B)) - 1)
      FI)

TRANSITION Add_A_Book(U:User,B:Book)
  EXIT
    ( IF Library_Staff(U)
      & B ~ISIN Library'
        THEN Library = Library'  UNION  {B}
             &  Checked_Out(B) BECOMES FALSE
             &  Never_Out(B)  BECOMES TRUE
```

```
      FI)


TRANSITION Remove_A_Book(U:User,B:Book)
  EXIT
    (IF Library_Staff(U)
       & Available'(B)
             THEN Library = Library' SET_DIFF {B}
    FI)


END Top_Level
END Library
```

Appendix B
Specification of a Multiwindow Interface

```
SPECIFICATION window_interface
INHIBIT /* do not produce correctness conjectures */
LEVEL Top_Level

/* Brent Auernheimer -- July 1990

   This is a high-level specification written using the Aslan
   specification language of a window-based
   user interface. Mice are not explicitly mentioned.

   Note that a ' ('prime') is the old-value operator.  That is,
   is x is a variable, then x' represents its value before the
   application of a transition. An unprimed x represents the
   new-value of x.

   This user interface is typical of window managers running
   on X. One added feature is SPECIAL windows
   which cannot be closed (iconified), moved, or covered by
   other windows or icons.

   Notational conventions --  alphanumeric tokens are lowercase
   except for the following:

      * Keywords and constants are uppercase.
      * Type identifiers begin with uppercase.

*/

TYPE
    Windows, Processes, Locations, Sizes, Representations, Display_Levels,
    States IS (OPEN, CLOSED, UNUSED),
    Layouts IS STRUCTURE OF
      (location: Locations, size: Sizes, rep: Representations),
    Displays IS SET OF Layouts

CONSTANT
    NULL_PROCESS: Processes,
    INITIAL_OPEN_LAYOUT(Processes): Layouts,
```

```
    INITIAL_CLOSED_LAYOUT(Processes): Layouts,
    INITIAL_STATE(Processes): States,

    /* OVERLAPS is to be  true if first argument overlaps the second */
    OVERLAPS(Layouts, Layouts): BOOLEAN,
    BACKGROUND: Layouts, /* windows must overlap the background */
    SPECIAL(Windows): BOOLEAN, /* some windows cannot be covered */

    /* the smallest display_level is the window closest to the top,
       the largest is the window buried the deepest */
    LESS_OR_EQUAL(Display_Levels, Display_Levels): BOOLEAN

VARIABLE
    process(Windows): Processes,
    open_layout(Windows): Layouts,
    closed_layout(Windows): Layouts,
    state(Windows): states,
    input_focus(Windows): BOOLEAN,
    display: Displays,
    display_level(Windows): Display_Levels

DEFINE
   /* DEFINitions are macros used to make state transitions easier to read */

   to_top_level(w: Windows): BOOLEAN ==
      /* w becomes the topmost window ... */
      FORALL w2: Windows (
         (w ~= w2)
             -> LESS_OR_EQUAL(display_level(w), display_level(w2))
              & display_level(w) ~= display_level(w2))

      /* all other windows maintain their previous relationship */
    & FORALL w1, w2: Windows (
         (w1 ~= w & w2 ~= w) -> (
               (LESS_OR_EQUAL(display_level'(w1), display_level'(w2))
                   -> LESS_OR_EQUAL(display_level(w1), display_level(w2)))
             & (LESS_OR_EQUAL(display_level'(w2), display_level'(w1))
                   -> LESS_OR_EQUAL(display_level(w2), display_level(w1))))),

    /* note that square brackets are used to select fields from
       structure typed variables */

    set_location(w: Windows, s: States, l: Locations): BOOLEAN ==
```

```
  ((s = OPEN)
     -> FORALL w1: Windows (
           (w = w1 -> open_layout(w)[location] = l
                    & open_layout(w)[size] = open_layout'(w)[size]
                    & open_layout(w)[rep] = open_layout'(w)[rep])
         & (w ~= w1 -> open_layout(w1) = open_layout'(w1)))
      & NoChange(closed_layout))

& ((s = CLOSED)
     -> FORALL w1: Windows (
           (w = w1 -> closed_layout(w)[location] = l
                    & closed_layout(w)[size] = closed_layout'(w)[size]
                    & closed_layout(w)[rep] = closed_layout'(w)[rep])
         & (w ~= w1 -> closed_layout(w1) = closed_layout'(w1)))
      & NoChange(open_layout)),

set_size(w: Windows, s: States, s1: Sizes): BOOLEAN ==
  ((s = OPEN)
     -> FORALL w1: Windows (
           (w = w1 -> open_layout(w)[size] = s1
                    & open_layout(w)[location] = open_layout'(w)[location]
                    & open_layout(w)[rep] = open_layout'(w)[rep])
         & (w ~= w1 -> open_layout(w1) = open_layout'(w1)))
     & NoChange(closed_layout))

& ((s = CLOSED)
     -> FORALL w1: Windows (
          (w = w1 -> closed_layout(w)[size] = s1
                   & closed_layout(w)[location] = closed_layout'(w)[location]
                   & closed_layout(w)[rep] = closed_layout'(w)[rep])
         & (w ~= w1 -> closed_layout(w1) = closed_layout'(w1)))
     & NoChange(open_layout)),

update_display_close(w: Windows): BOOLEAN ==
  (display = display'
         SET_DIFF {SETDEF l: Layouts (l = open_layout'(w))}
         UNION    {SETDEF l: Layouts (l = closed_layout'(w))}),

update_display_open(w: Windows): BOOLEAN ==
  display = display'
         SET_DIFF {SETDEF l: Layouts (l = closed_layout'(w))}
         UNION {SETDEF l: Layouts (l= open_layout'(w))},
```

```
  update_display_create(w: Windows): BOOLEAN ==
     (state(w) = OPEN & (display = display'
                         UNION {SETDEF 1: Layouts (1 = open_layout(w))}))
    | (state(w) = CLOSED & (display = display'
                         UNION {SETDEF 1: Layouts (1 = closed_layout(w))})),

  update_display_destroy(w: Windows): BOOLEAN ==
     (state(w) = OPEN & (display = display'
                        SET_DIFF {SETDEF 1: Layouts (1 = open_layout'(w))}))
    | (state(w) = CLOSED & (display = display'
                        SET_DIFF {SETDEF 1: Layouts (1 = closed_layout'(w))})),

  update_display_move (w: Windows): BOOLEAN ==
     (state'(w) = OPEN & (display = display'
           SET_DIFF {SETDEF 1: Layouts (1 = open_layout'(w))}
           UNION    {SETDEF 1: Layouts (1 = open_layout(w))}))
    | (state'(w) = CLOSED & (display = display'
           SET_DIFF {SETDEF 1: Layouts (1 = closed_layout'(w))}
           UNION    {SETDEF 1: Layouts (1 = closed_layout(w))}))


INITIAL /* the following assertion defines the initial state of the system */
  display = EMPTY
& FORALL w: Windows (
     state(w) = UNUSED
   & process(w) = NULL_PROCESS
   & input_focus(w) = false)
& FORALL p: Processes (
     OVERLAPS(INITIAL_OPEN_LAYOUT(p), BACKGROUND)
   & OVERLAPS(INITIAL_CLOSED_LAYOUT(p), BACKGROUND))

INVARIANT
/* the following assertion is the critical correctness requirements
   that must hold in every state (including the initial state */

  FORALL 1: Layouts (
     1 ISIN display ->
      EXISTS w: Windows (
            (state(w) = OPEN &  1 = open_layout(w))
            | (state(w) = CLOSED & 1 = closed_layout(w))))
 & FORALL 1: Layouts (
       1 ISIN display -> OVERLAPS(1, BACKGROUND))
 & FORALL w: Windows (
```

```
        SPECIAL(w) & state(w) ~= UNUSED
      -> EXISTS l: Layouts ((l ISIN display
                & (l = open_layout(w) | l = closed_layout(w)))
                   & FORALL l1: Layouts ((l ~= l1) & (l1 ISIN display)
                                         -> ~OVERLAPS(l1, l))))

/* the transitions are written to have NoChange to the state variables
   if they shouldn't be applied. These NoChange clauses could be
   rewritten to specify error notification and processing */

TRANSITION close_window(w: Windows) /* iconify */
  EXIT
    state'(w) = OPEN
  & ~SPECIAL(w)
  & state(w) BECOMES CLOSED
  & update_display_close(w)
  & to_top_level(w)

ALT NoChange

TRANSITION open_window(w: Windows)
  EXIT
    state'(w) = CLOSED
  & state(w) BECOMES OPEN
  & update_display_open(w)
  & to_top_level(w)

ALT NoChange

TRANSITION destroy_window(w: Windows)
  EXIT
    (state'(w) = OPEN | state'(w) = CLOSED)
  & state(w) BECOMES UNUSED
  & ~SPECIAL(w)
  & update_display_destroy(w)

ALT NoChange

TRANSITION create(p: Processes)
  EXIT
    EXISTS w: Windows (
      state'(w) = UNUSED
    & state(w) BECOMES INITIAL_STATE(p)
```

```
    & open_layout(w) BECOMES INITIAL_CLOSED_LAYOUT(p)
    & closed_layout(w) BECOMES INITIAL_OPEN_LAYOUT(p)
    & process(w) BECOMES p
    & update_display_create(w)
    & to_top_level(w))

 ALT NoChange

TRANSITION shift_focus(w: Windows)
/* assumes that only one window at a time has input focus and
   that closed windows can have input_focus */
  EXIT
     (state'(w) = OPEN | state'(w) = CLOSED)
   & FORALL w1: Windows (input_focus(w1) = (w1 = w))

ALT NoChange

TRANSITION move(w: Windows, l: Locations)
  EXIT
   (~SPECIAL(w)
 & update_display_move(w)
 & (((state'(w) = OPEN)
   & set_location(w, state'(w), l)
   & OVERLAPS(open_layout(w), BACKGROUND)
   & ~EXISTS w1: Windows (
        SPECIAL(w1) & state'(w1) ~= UNUSED
      & OVERLAPS(open_layout(w), open_layout'(w1))))

 |  ((state'(w) = CLOSED)
   & set_location(w, state'(w), l)
   & OVERLAPS(closed_layout(w), BACKGROUND)
   & ~EXISTS w1: Windows (
        SPECIAL(w1) & state'(w1) ~= UNUSED
      & OVERLAPS(closed_layout(w), open_layout'(w1))))))

 ALT NoChange


 TRANSITION resize(w: Windows, s: Sizes)
   EXIT
         (state'(w) = OPEN) & ~SPECIAL(w)
        & ~EXISTS w1: Windows(SPECIAL(w1) & (state'(w1) ~= UNUSED)
                    & OVERLAPS(open_layout(w), open_layout'(w1)))
```

```
        & set_size(w, state'(w), s)

ALT NoChange

TRANSITION to_foreground(w: Windows)
  EXIT
   to_top_level(w)
 & state'(w) ~= UNUSED
 & ~EXISTS w1: Windows(SPECIAL(w1) & (state'(w1) ~= UNUSED)
      & ((state'(w) = OPEN) & (OVERLAPS(open_layout'(w), open_layout'(w1)))
       | (state'(w) = CLOSED) & OVERLAPS(closed_layout'(w), open_layout'(w1))))

ALT NoChange

END Top_Level
END window_interface
```

1990 NASA/ASEE SUMMER FACULTY FELLOWSHIP PROGRAM

JOHN F. KENNEDY SPACE CENTER
UNIVERSITY OF CENTRAL FLORIDA

STUDY OF WAVELENGTH DIVISION MULTIPLEXING AS A MEANS OF INCREASING THE NUMBER OF CHANNELS IN MULTIMODE FIBER OPTIC COMMUNICATION LINKS

PREPARED BY: Dr. Harry Bates

ACADEMIC RANK: Professor

UNIVERSITY AND DEPARTMENT: Towson State University
Department of Physics

NASA/KSC

DIVISION: Electronic Systems

BRANCH: Communications

NASA COLLEAGUE: Mr. Po Huang

DATE: August 10, 1990

CONTRACT NUMBER: University of Central Florida
NASA-NGT-60002 Supplement: 4

ACKNOWLEDGEMENTS

This research effort would not have been possible with out the assistance, cooperation and careful planning of a number of people. Larry Hand and Po T. Huang suggested the program and provided valuable support along the way. Po T. Huang was always available to answer questions provide literature references and a lot of material from his personal library. He also gave guidance and support in more ways than can be described here. All levels of Engineering management above Po and Larry beginning with Perry Rodgers provided valuable assistance and showed genuine interest in the project. Everyone was willing to listen and suggest solutions to problems. Special thanks to Fred McKenzie for helping to provide computers and software to use at Headquarters Building and introductions to people who could help with other problems. Mark Nurge was also especially helpful in assisting with ideas and equipment needed to interface the Macintosh in the laboratory to the optical spectrum analyzer. Boeing Aerospace personnel were also most helpful in the laboratory. Special thanks to F. Houston Galloway and Bob Swindle who worked closely in all phases of this project including, but not limited to, design and acquisition of necessary equipment, shop work, and data collection. Thanks to Dr. Bob Youngquist who was willing to provide optical parts, filters and most of all ideas and approaches to technical problems. Last but not least I would like to thank Dr Loren Anderson of UCF who managed the Summer Faculty Program and provided a great deal of support and assistance.

ABSTRACT

A number of optical communication lines are now in use at the Kennedy Space Center (KSC) for the transmission of voice, computer data and video signals. At the present time all of these channels utilize a single carrier wavelength centered near 1300 nm. The theoretical bandwidth of the fiber far exceeds the utilized capacity. Yet practical considerations limit the usable bandwidth. The fibers have the capability of transmitting a multiplicity of signals simultaneously in each of two separate bands (1300nm and 1550 nm). Thus, in principle, the number of transmission channels can be increased without installing new cable if some means of wavelength division multiplexing (WDM) can be utilized. The main goal of these experiments was to demonstrate that a factor of 2 increase in bandwidth utilization can be achieved by proving that video and data signals can share the same fiber in both a unidirectional configuration and a bidirectional mode of operation. Both single and multimode fiber is installed at the Space Center. The great majority is multimode. Therefore this effort concentrated on multimode systems.

SUMMARY

Many optical communication links are now in use at the Kennedy Space Center (KSC) for the transmission of voice, computer data and video signals. At the present time all of these channels utilize a single carrier wavelength centered near 1300 nm. The theoretical bandwidth of the fiber far exceeds the utilized capacity. Yet practical considerations limit the usable bandwidth.

The main goal of this experimental program was to demonstrate that a factor of 2 increase in bandwidth utilization can be achieved by proving that video/digital data and digital data/digital data signals can share the same fiber in both a unidirectional configuration and a bidirectional mode of operation. This effort concentrated on multimode fiber systems.

During the project, a spectroscopic system was interfaced to a Macintosh computer. The system was used to characterize a number of WDM systems as well as a small number of components of the fiber optics communications systems at KSC.

A demonstration WDM 1300 nm /1550 nm link was demonstrated to work successfully with both video and digital data signals.

An experiment was performed to determine the susceptibility of the PCO receivers to crosstalk.

No tests were performed to establish nonlinearity limits in fibers nor were sufficient observations made to fully characterize the installed fiber optic system at KSC.

TABLE OF CONTENTS

LIST OF ILLUSTRATIONS

LIST OF TABLES

ABBREVIATIONS AND ACRONYMS LIST

CDSC	Communications Distribution and Switching Center
OSA	Optical Spectrum Analyzer
LED	Light Emitting Diode
KSC	Kennedy Space Center
WDM	Wavelength Division Multiplexer or Demultiplexer
TX	Transmitter
RX	Receiver
LID	Laser Diode

I. INTRODUCTION

A number of optical communication lines are now in use at the Kennedy Space Center (KSC) for the transmission of voice, computer data and video signals. At the present time all of these channels utilize a single carrier wavelength centered near 1300 nm. The theoretical bandwidth of the fiber far exceeds its capacity. The 1300 nm window has about 10,000 GHz of available bandwidth and only 0.01 GHz is utilized.

Practical considerations such as multimode dispersion, material dispersion, detector rise time, modulation limits of the receiver...etc. limit the usable bandwidth.[1] The fibers have the capability of transmitting a multiplicity of signals simultaneously in each of two separate bands (1300nm and 1550 nm)[2,3]. Thus, in principle, the number of transmission channels can be increased without installing new cable if wavelength division multiplexing (WDM) can be utilized. The main goal of these experiments was to demonstrate that at least a factor of 2 increase in bandwidth utilization can be achieved by proving that video and data signals can share the same fiber in both a unidirectional configuration and a bidirectional mode of operation. Both single and multimode fiber is installed at the Space Center. The great majority is multimode. Therefore this effort concentrated on multimode systems.

This experimental effort has not only been aimed at a demonstration of the WDM concept within the constraints of the KSC system, but also to understand the parameters of the system so as to provide the system engineer with information needed to make decisions on future systems. Thus, part of this effort has been an effort to do spectroscopic studies on a small number of LED and laser sources, optical fiber links and WDM devices.

It is important to mention some of the questions that this work did not answer. One fundamental limitation in any WDM system as link lengths are increased should be nonlinear effects in the fiber that would mix the two channels and produce nonlinear crosstalk. [4] In addition, a good statistical sample of spectra of sources, fibers and detectors has not been made. Only items in the EDL were subjected to test. This study has not determined the properties of the overall fiber optic plant with any great statistical certainty.

II. LABORATORY SPECTRAL ANALYSIS SYSTEM

2.1 OPTICAL SPECTRUM ANALYZER

An Anaritsu optical spectrum analyzer was available in the laboratory to be used to perform spectral analysis of coherent and incoherent sources. This piece of test equipment was equipped with an IEEE 488 computer interface which provides for bidirectional computer communication. A portion of the work done under this research effort was to interface the OSA with a Macintosh IIx computer to enable the efficient collection of spectral data in machine readable form. It was envisioned that the operator would manually set up the spectrum analyzer for any given experiment and when a spectrum was collected, activate the computer interface system and acquire a sequential data file containing the maximum wavelength, the minimum wavelength of the scan and 500 data points of optical spectral power density expressed in dBm or milliwatts evenly distributed over the spectral interval.

2.2 THE MACINTOSH IIX COMPUTER

A Macintosh IIx Computer was available for use in data analysis in the laboratory. A IEEE-488 National Instruments interface board was obtained on loan to be used in an attempt to connect the Macintosh with the optical spectrum analyzer. This was accomplished through the use of Hypercard, an object oriented computer language system supplied with all Macintoshes.

The Hypercard stack (program)[5] created to connect the Macintosh with the optical spectrum analyzer is based on three cards or windows. Each has a specific function. The first appears when the stack is activated by double clicking the OSA control icon located on the main directory of the MACFIBER hard disk on the computer. (Note: a backup copy of this program is located on the floppy disk labeled "OSA control".) This first window or card contains the Hypertalk script necessary to link the Macintosh to the optical spectrum analyzer.

A second card shows a display of a subset of the optical spectrum analyzer controls as well as buttons for acquiring a spectrum or transmission data. If the single spectrum button is activated, the program will acquire 500 data points from one of the three data files available from the optical spectrum analyzer. These files will

be saved as "Name".spec in the MACFIBER main directory. Where the "Name" is taken from a text field at the bottom of the card.

If the transmission button is activated, the program will collect two sets of points. One from the reference channel and the other from the sample channel. These files will be saved as "Name".ref and "Name".meas.

The third card in the OSA control stack contains information about using the system.

All spectra obtained during this research effort were taken using this system. Data analysis was accomplished using EXCEL and the results plotted using Cricket Graph.

2.3 DESIGN OF WHITE LIGHT SOURCE FROM AVAILABLE MATERIALS

In order to determine the optical transmission as a function of wavelength of components of a WDM communication system, a source of light was required with energy available over a broad band of wavelengths. Such a source was constructed using a projector lamp, lenses, and a precision translation stage to hold an optical fiber. The optical design is shown in the diagram below.

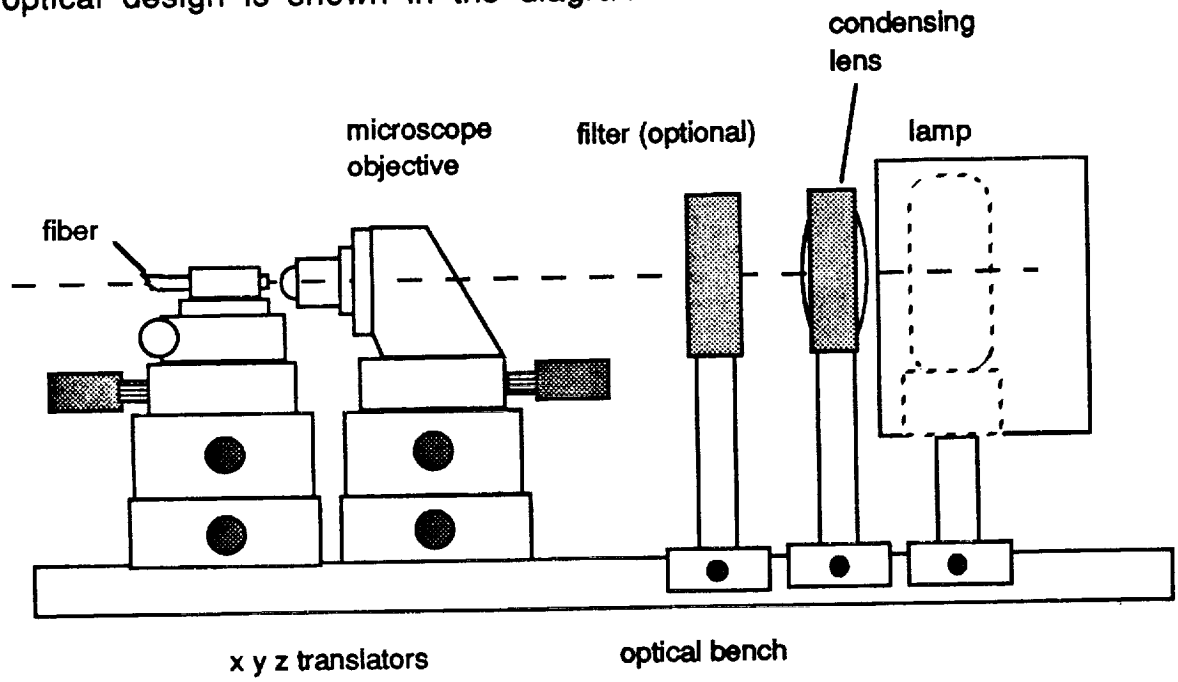

Figure 2-1. Concept Drawing of White Light Source (not to scale)

Experiments were conducted to determine the best microscope objective to use in the system. It was found that a x10 objective having a numerical aperture of 0.25 gave the best results. This closely matches the numerical aperture of the fiber which is 0.20 . The condenser lens was chosen from available stock to have the shortest focal length (2.5 cm) consistent with the physical dimensions of the lamp (GE BXT) and lamp holder. The lamp was rotated to a position so that the filament was oriented about 20 degrees with respect to the optic axis of the bench (looking down at a top view). This gave the most uniform optical field at the microscope objective and maximum power.

The total optical power coupled into the fiber was not only related to the design of the source but was critically related to the alignment of the optics with respect to the fiber. This alignment was accomplished with the x y z translators with the output fiber connected to an optical power meter before each series of tests. The power coupled into a 50 micron-core fiber was measured as a function of lamp power. An optical power of -16 dBm was coupled into the fiber with 10 volts on the lamp and optimum alignment of the system. This proved adequate for all experiments except crosstalk rejection experiments and allowed the lamp to be operated at a reduced voltage for extended life.

2.4 CALIBRATION CHECKS OF THE OPTICAL SPECTRUM ANALYZER

Before conducting spectroscopic experiments on fiber optic communications components, the spectral calibration of the optical spectrum analyzer was cross checked against available filters and a helium neon laser. In addition, saturation and repeatability tests were conducted.

2.4.1 CALIBRATIONS. The HeNe laser was coupled into the optical spectrum analyzer through a multimode fiber using a microscope objective. A high resolution spectrum was collected using the analyzer. This spectrum is shown below.

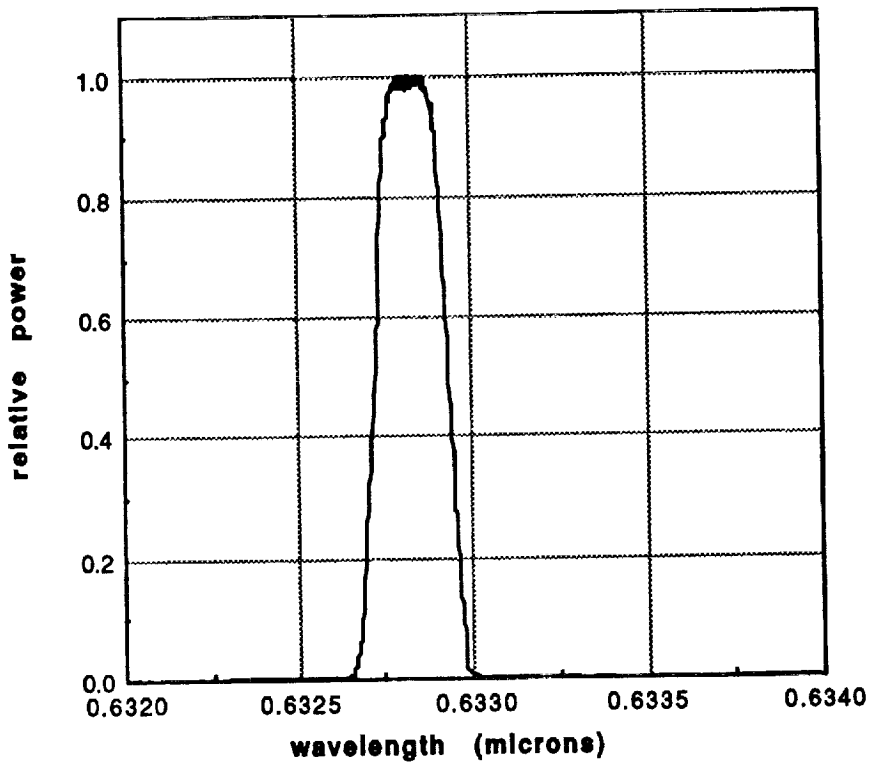

Figure 2-2 Peak Normalized Spectrum of HeNe Laser as Observed With OSA

It should be understood that the HeNe laser spectrum shown in this figure represents the OSA instrument response function and is not an accurate representation of the laser spectrum itself.

A selection of interference filters were inserted into the white light source and the peak of each transmission function measured and compared with the manufacturers values. The filter transmission function data and the HeNe spectral data were summarized and plotted. The graph verifying the spectral calibration of the OSA is shown in Figure 2.-3 below.

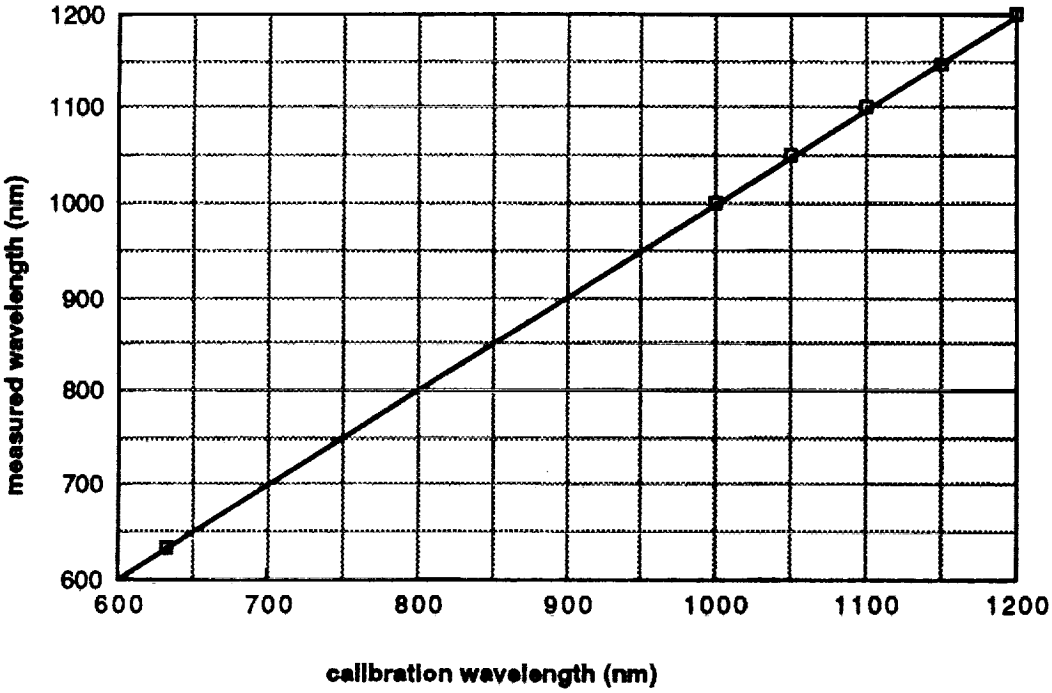

Figure 2-3 OSA Spectral Calibration Summary

2.4.2 OSA DYNAMIC RANGE STUDY. Experiments were conducted to determine the dynamic range of the optical spectrum analyzer operating together with the white light source. A series of spectra were collected each through an optical attenuator which is taken to be the standard. A three dimensional plot of the observed vs actual attenuation values over a range of wavelengths is shown below.

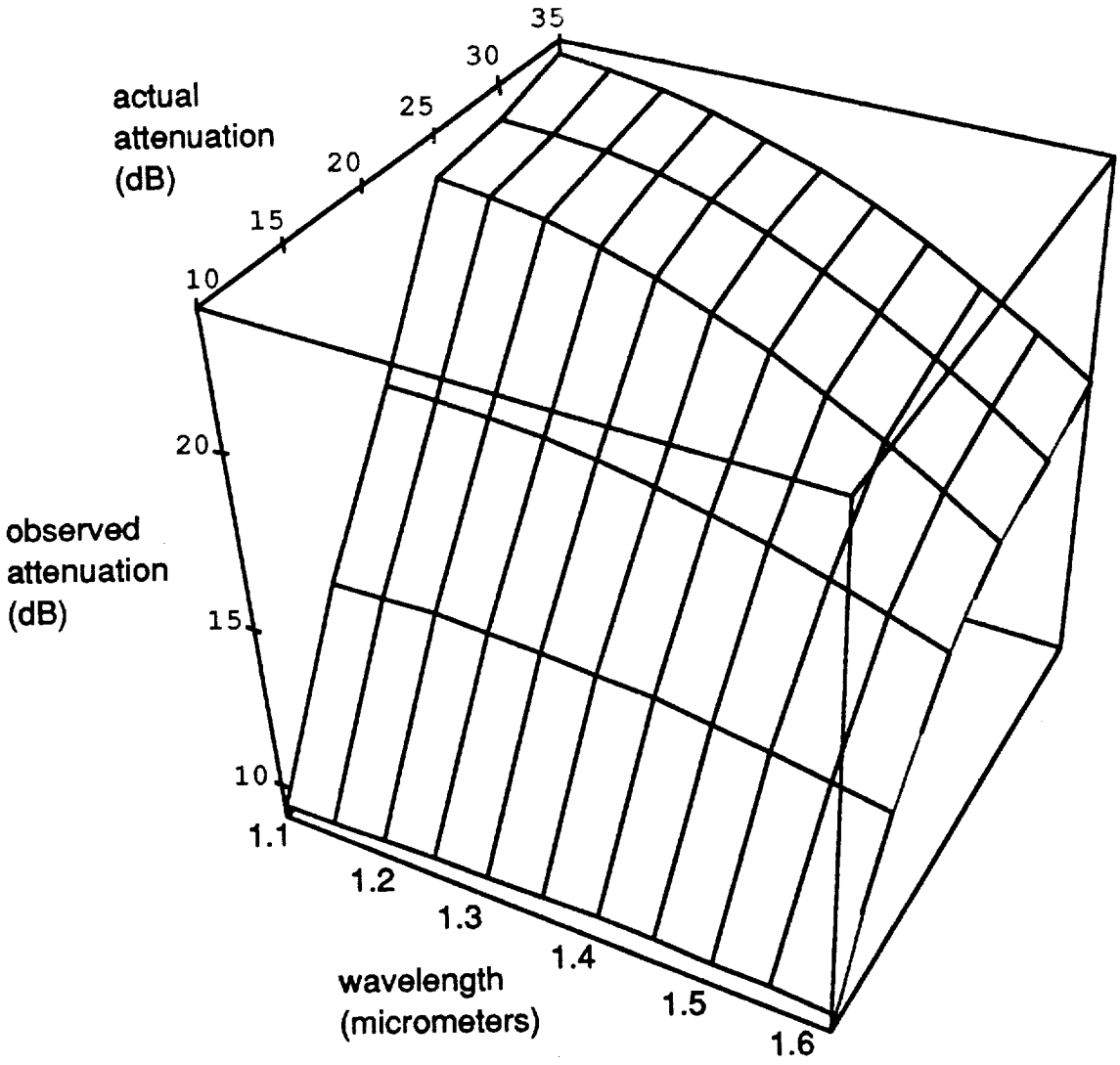

Figure 2-4 Dynamic Range of Optical Spectrum Analyzer White Light Source System

The dynamic range decreases as the system operates at longer wavelengths. Instead of an ideal linear plane, the surface droops as the noise floor is reached at each set of wavelengths plotted. As a result of these observations, no attempt was made to infer the degree of crosstalk in WDM systems using the OSA and white light source. Instead, a single data point was collected using each of the two sources of interest at 1.3 micrometers and 1.55 micrometers respectively.

III. Characterization of KSC Multimode Fiber

3.1 TYPICAL FIBER TEST LINK

The Fiber Optics Laboratory in the EDL building has a series of multimode fiber optic links to the CDSC building. See Figure 6-1 below for a diagram of a typical link. The spectral loss of pairs of these links was measured as a function of wavelength using the white light source and the OSA.

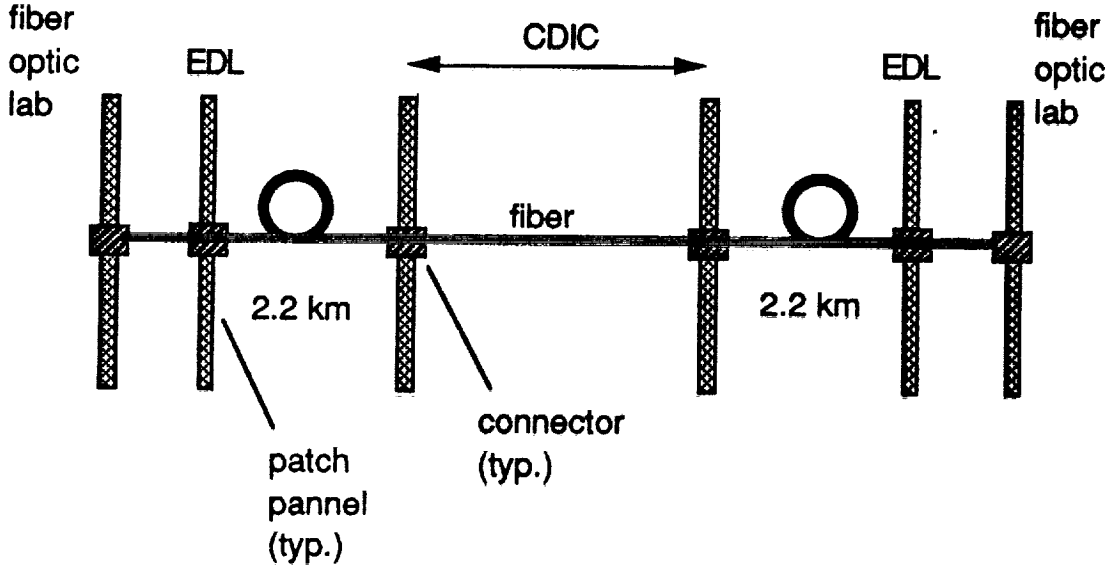

Figure 3-1 Typical Link from Fiber Optic Lab to CDIC and Back

3.2 SPECTROSCOPIC PROPERTIES OF FIBER LINKS IN THE EDL

Measurements were made without using a cladding mode stripper. A cladding mode stripper was constructed and tested. Link 11-12 was remeasured. A linearized loss function due to cladding mode effects was computed and added to the raw data. The resulting loss is plotted as a function of wavelength in a series of graphs that follow (Figures 3-2 through 3-7). The spectra are numbered with the connector numbers located on the patch panel in the Fiber Optic Lab. The average loss of all link pairs was computed and is plotted along with graphs of the average plus and minus one standard deviation in Figure 3-8.

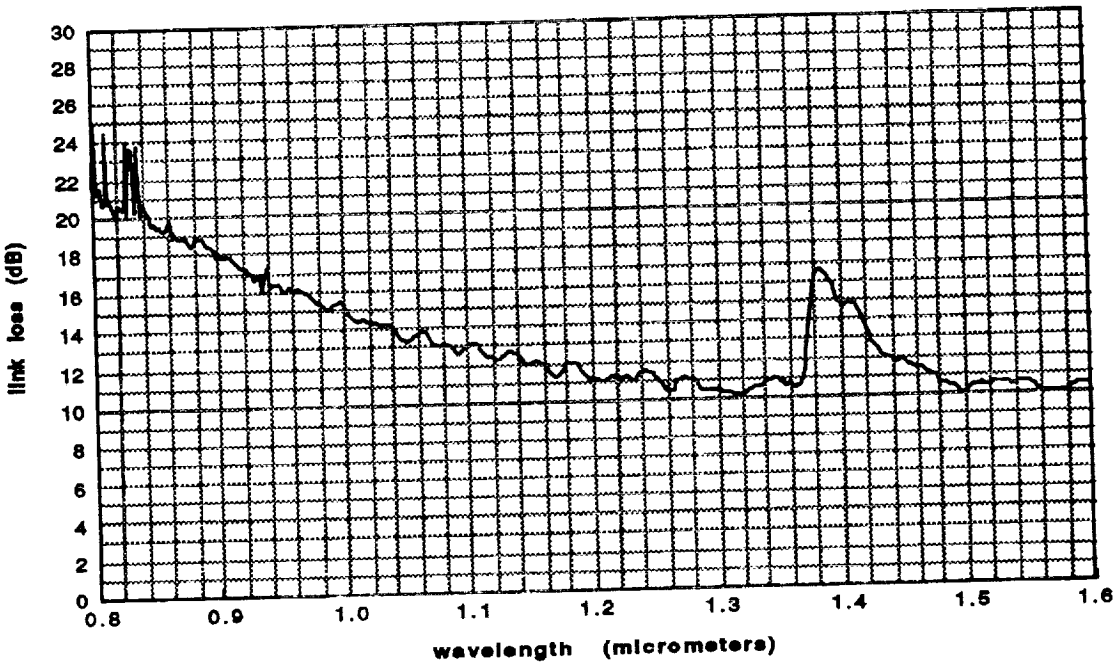

Figure 3-2 Loss in laboratory fiber link 1-2

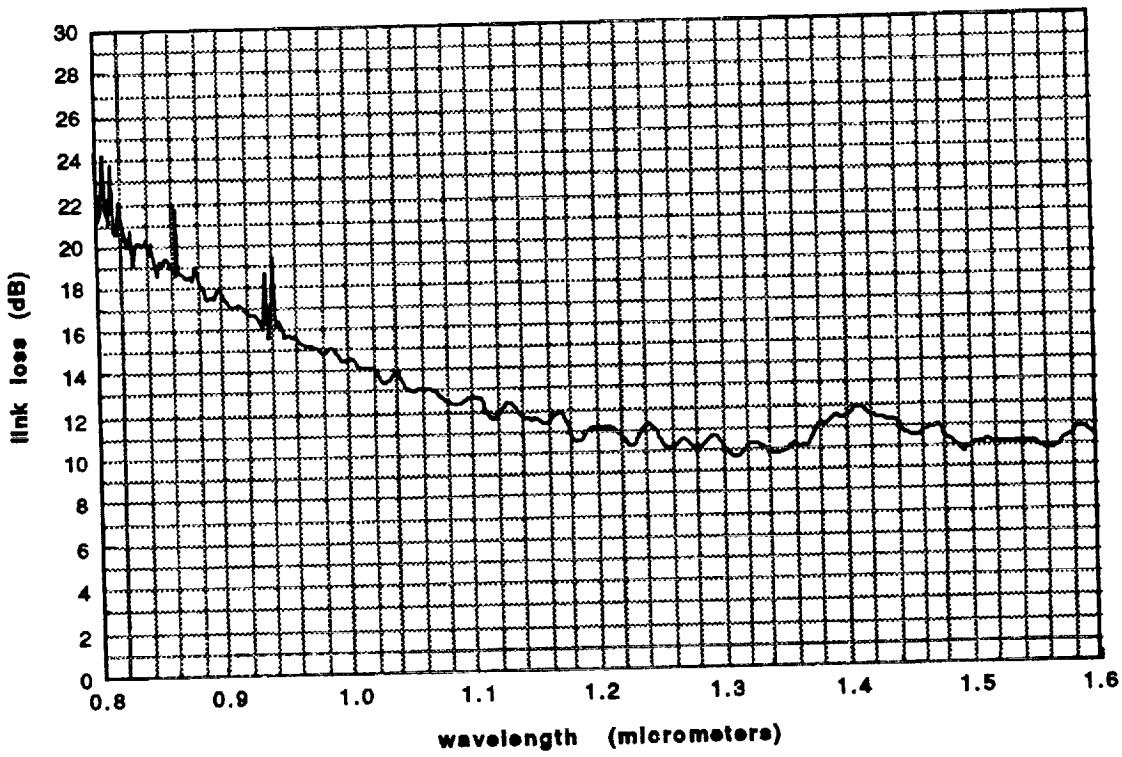

Figure 3-3 Loss in laboratory fiber link 3-4

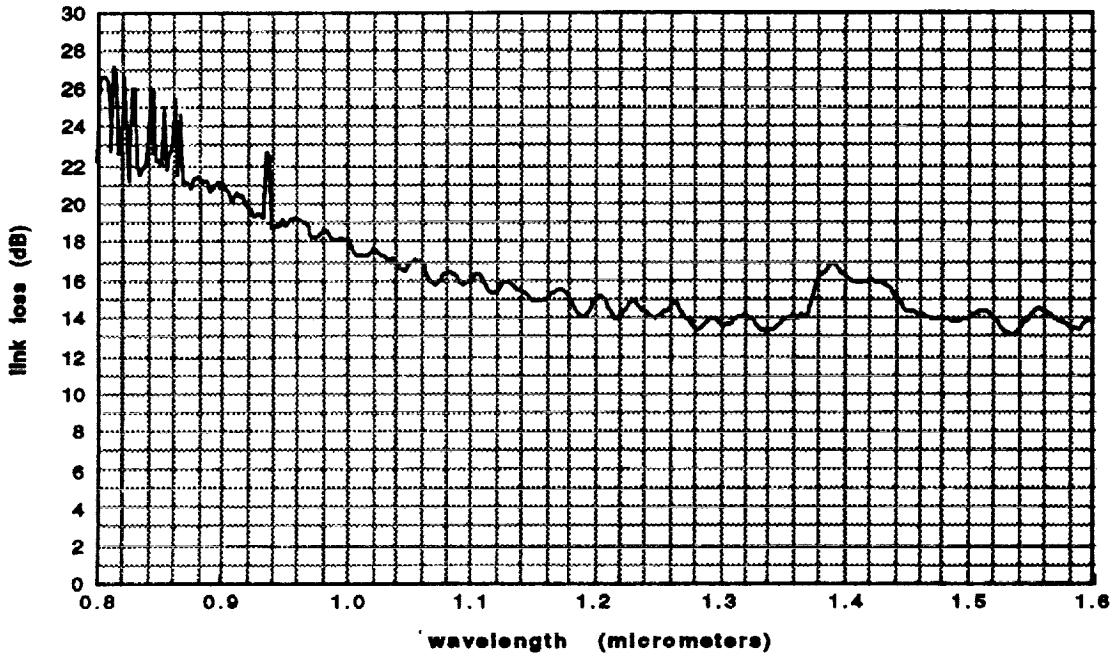

Figure 3-4 Loss in laboratory fiber link 5-6

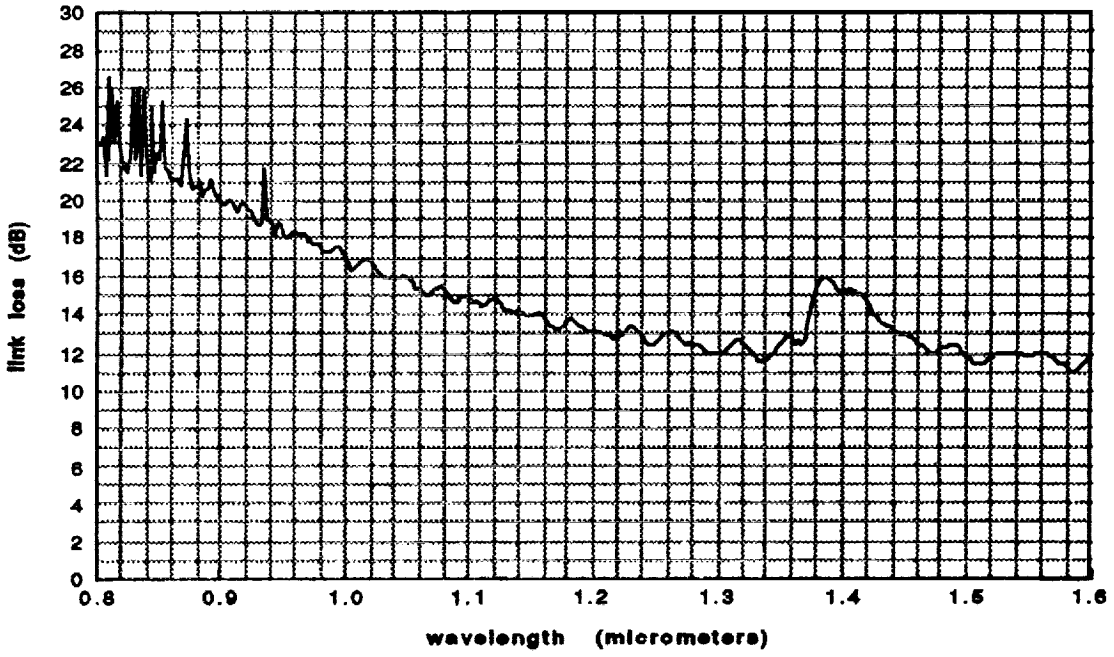

Figure 3-5 Loss in laboratory fiber link 7-8

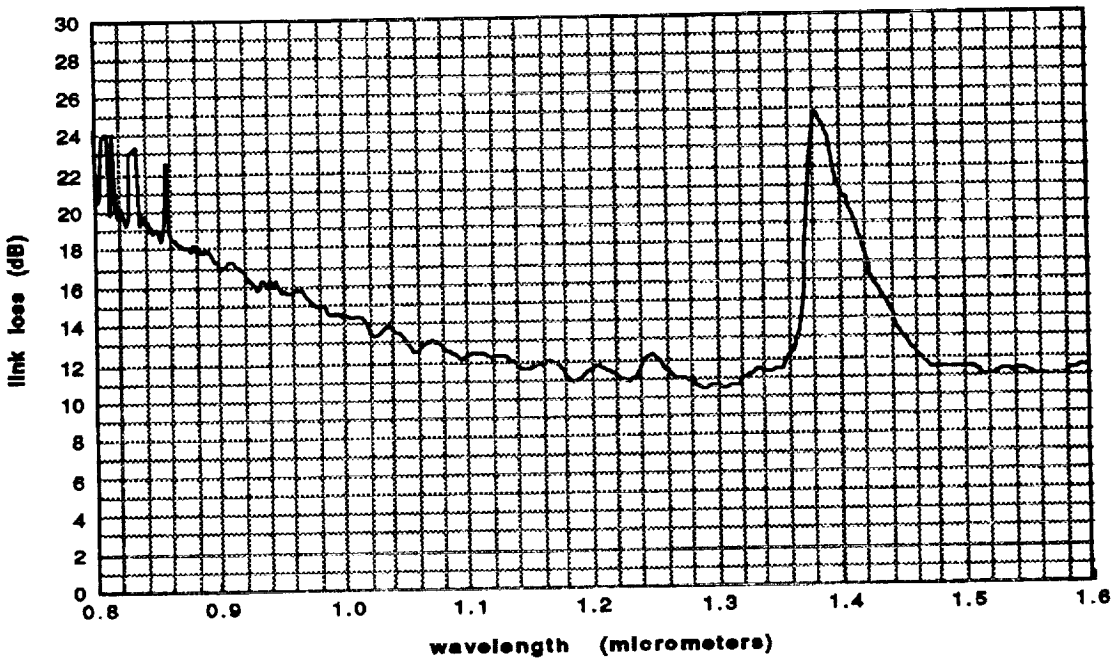

Figure 3-6 Loss in laboratory fiber link 9-10

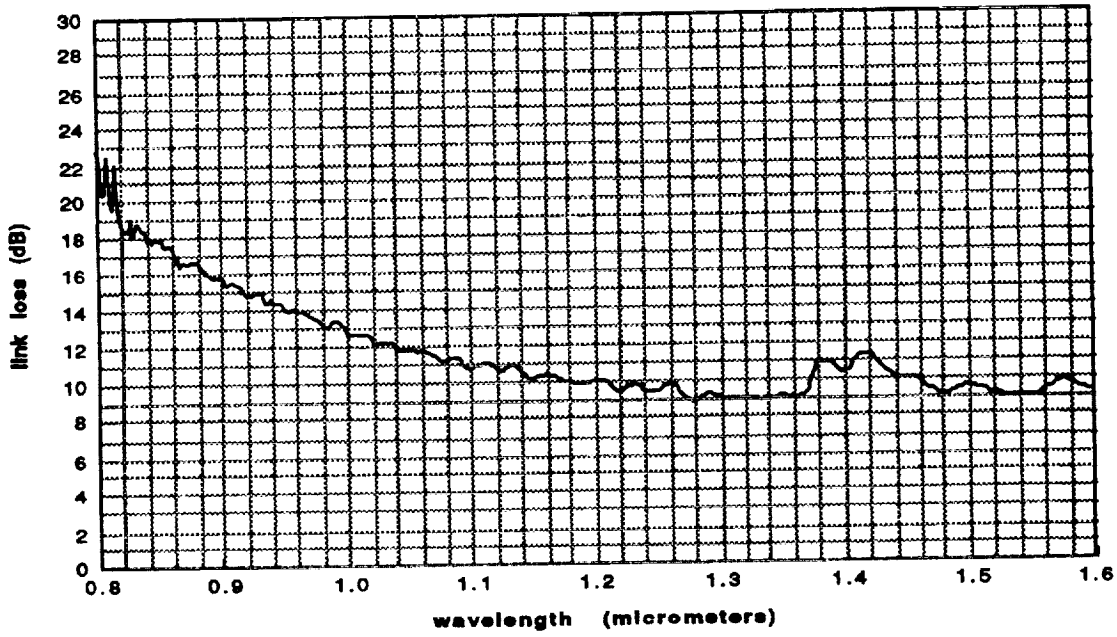

Figure 3-7 Loss in laboratory fiber link 11-12

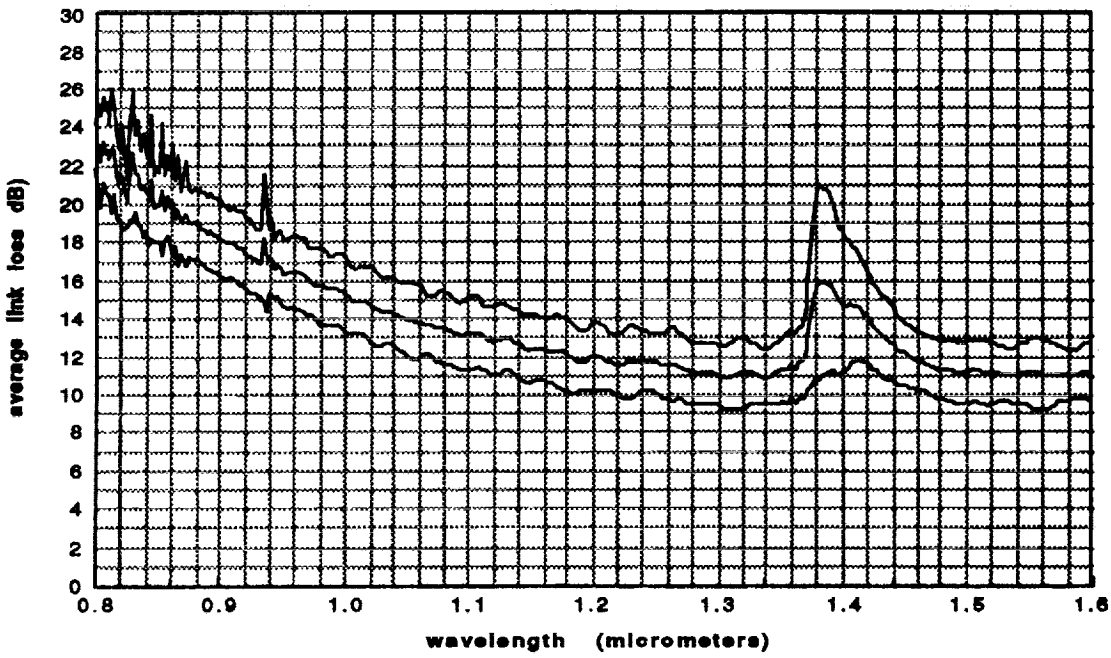

Figure 3-8 Average loss in laboratory fiber links +/- one standard deviation

IV. CHARACTERIZATION OF KSC LEDS AND LASERS

4.1 SPECTROSCOPIC MEASUREMENTS

The OSA was used to collect a selection of spectra of LEDs and laser transmitters. Results of these experimental runs are shown below in Figures 4-1 to 4-3.

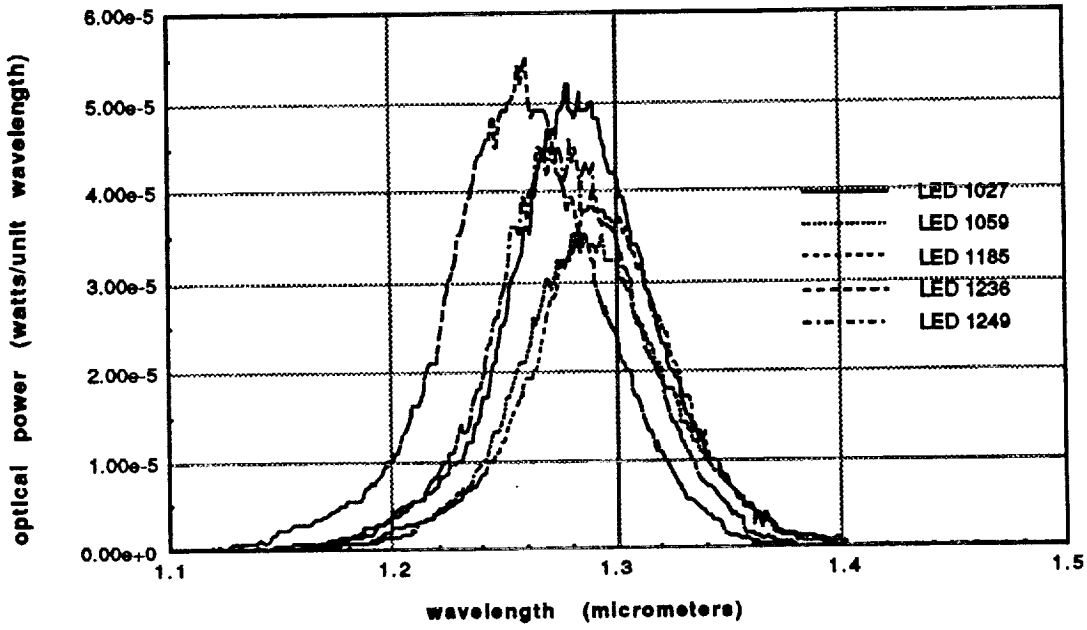

Figure 4-1 Selection of LED Spectra

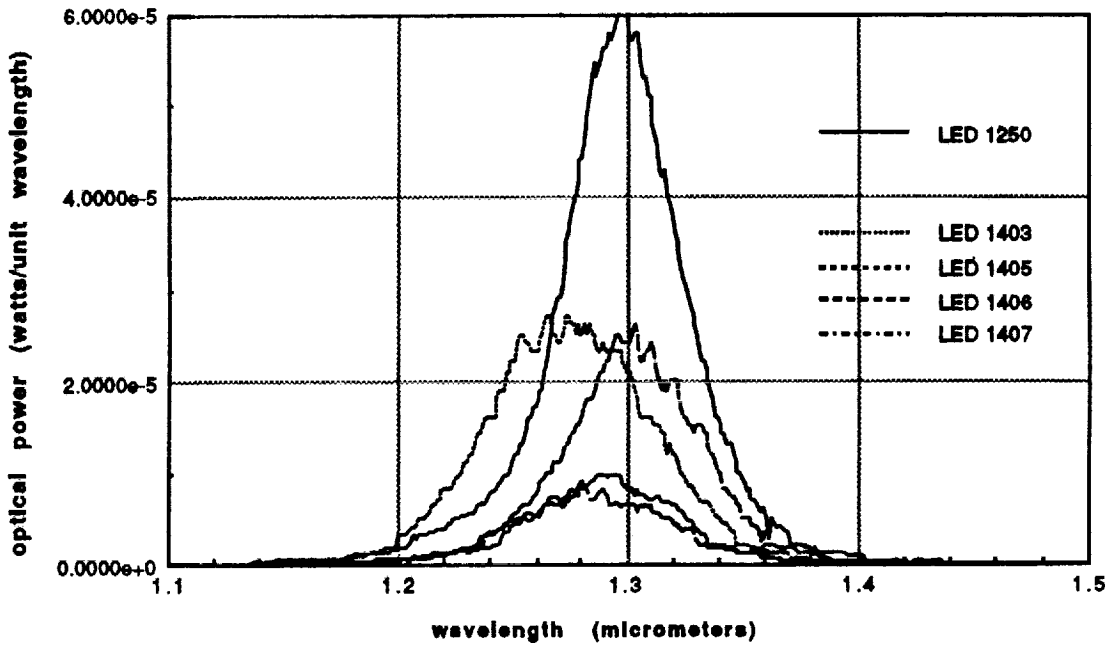

Figure 4-2 Selection of LED Spectra

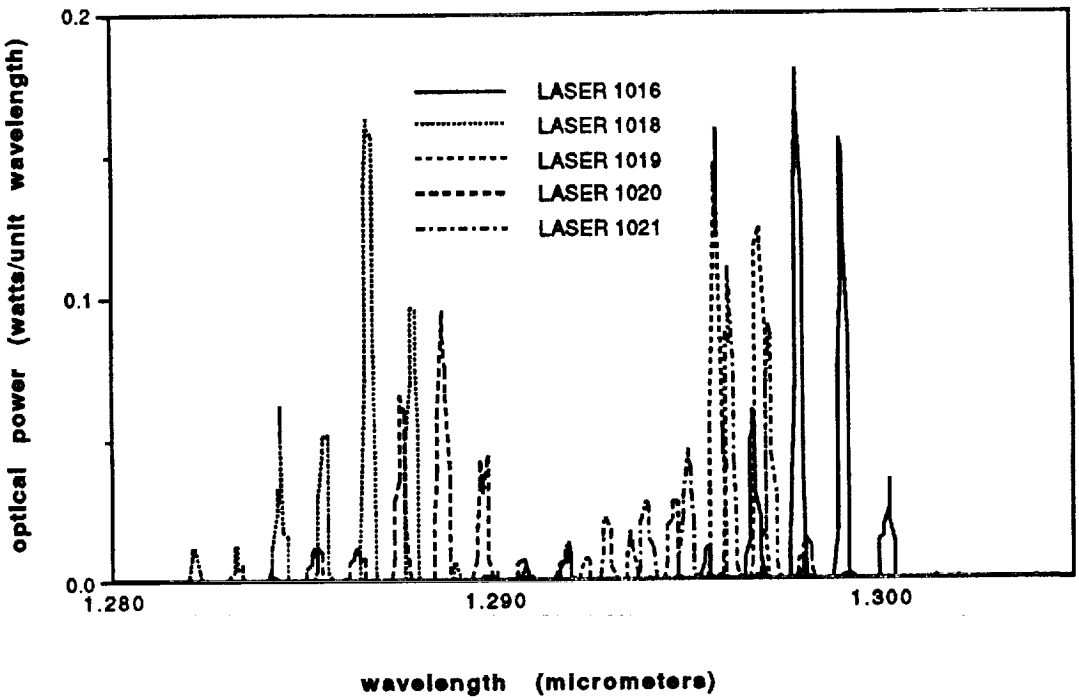

Figure 4-3 Selection of Laser Spectra

It can be seen that each different laser is characterized by a series of simultaneously radiated longitudinal modes. Furthermore, a collection of transmitter modules oscillate at a number of different center wavelengths. This suggests that an experiment to test the ultimate channel density could be performed by carefully selecting pairs of transmitters having specific different wavelength spacings and using these to establish the minimum acceptable channel spacing.

V. CHARACTERIZATION OF A SELECTION OF WDMS

5.1 EXPERIMENTS PERFORMED TO CHARACTERIZE WDMS

Several experiments were performed to characterize the properties of each WDM. The Spectral transmission function of each WDM was measured using the white light source and OSA between each pair of input and output ports. In order to keep the channels consistent between devices, a common numbering system was adopted. Port 1 is designated the common port, port 2 is the 1300 nm input or output port and port 3 is the 1550 nm input or output port. In addition, the insertion loss and crosstalk was measured for each device using a laser source at 1550 nm, a stabilized LED source at 1300 nm and an optical power meter.

5.2 INSERTION LOSS AND CROSSTALK MEASUREMENTS AT SINGLE WAVELENGTHS

These measurements were conducted using a light source, a mode scrambler/cladding mode stripper, the device under study and an optical power meter (Ando AQ 1135E). The input level at the power meter was standardized to 0 dB with the output of the cladding mode stripper directly connected to the meter. The the WDM was inserted in the path and a reading of the loss obtained between the specific pair of ports selected.

Table 5-1 Single Wavelength Insertion Loss and Crosstalk Tests

WDM Tested	Ports (in-out)	1300 nm loss (dB)	1550 nm loss (dB)
Corning M0200061 (1)	1 - 2	4.52	43.4
	1 - 3	33.6	1.48
	2 - 1	4.32	43.5
	3 - 1	34.3	1.87
Corning M0200061 (2)	1 - 2	2.42	43.7
	1 - 3	33.5	4.71
	2 - 1	2.44	40.6
	3 - 1	33.4	4.16
JDS WD13115UC-50 (1)	1 - 2	1.19	43.5
	1 - 3	32.7	0.65
	2 - 1	1.21	43.8
	3 - 1	32.6	0.73
JDS WD13115UC-50 (2)	1 - 2	0.88	43.7
	1 - 3	32.7	0.56
	2 - 1	0.99	43.9
	3 - 1	32.8	0.64
ASTER MWM 12-25-BR (1)	1 - 2	1.90	42.0
	1 - 3	38.2	1.06
	2 - 1	1.68	41.9
	3 - 1	38.1	1.18
ASTER MWM 12-25-BR (2)	1 - 2	2.13	42.2
	1 - 3	38.5	1.39
	2 - 1	2.61	42.4
	3 - 1	39.1	1.59
ALCATEL 7299-C-1 (1)	1 - 2	2.55	42.9
	1 - 3	39.3	1.41
	2 - 1	2.50	42.8
	3 - 1	39.7	1.41
ALCATEL 7299-C-1 (2)	1 - 2	2.23	42.7
	1 - 3	40.0	1.69
	2 - 1	2.06	43.1
	3 - 1	39.1	1.9

In each WDM tested the loss between 2 and 3 and 3 and 2 were measured as well. The result was always greater than 50 dB.

5.2 SPECTRAL TRANSMISSION FUNCTIONS OF WDMS

These measurements were conducted using the white light source, a mode scrambler/cladding mode stripper, the device under study and the OSA. The input level was standardized by collecting a spectrum with the output of the cladding mode stripper directly connected to the OSA. This was stored in memory 1 of the OSA. The the WDM was

inserted in the path and a second spectrum was obtained between the specific pair of ports selected. This was stored in memory 2. The OSA control stack was then activated to collect the spectra in a computer data file. A hard copy was also made from the OSA. The following is two samples of the spectra obtained, one of the best WDM systems studied and one having the least transmission. For lack of space, not every spectrum collected is included in this report.

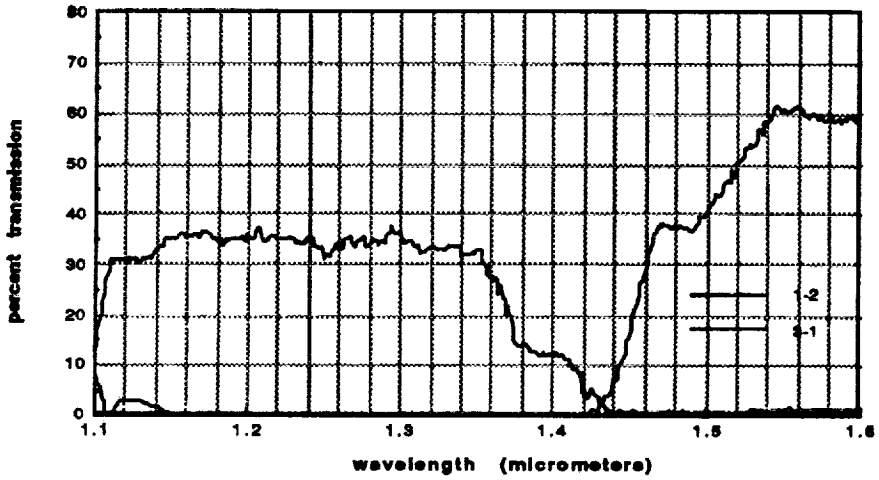

Figure 5-1 Transmission Spectrum of the Corning #1 WDM

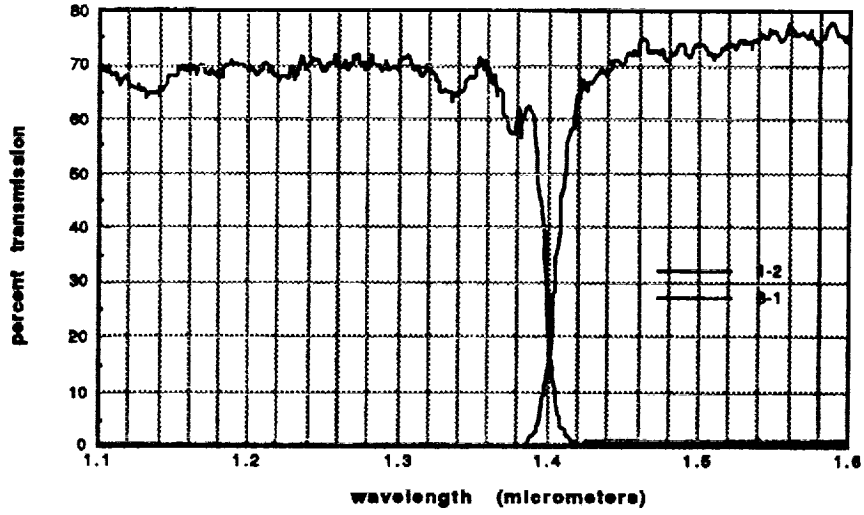

Figure 5-2 Transmission Spectrum of the Aster #1 WDM

VI. THE SIMULTANEOUS TRANSMISSION OF DIGITAL AND VIDEO DATA

6.1 THE SYSTEM TEST

The ultimate test of the two channel WDM concept at KSC was the system test. A complete WDM two channel system was constructed and used to transmit separate signals on a single fiber. The Aster WDM was selected as the best candidate based on tests described in the previous section was used in all of these tests.

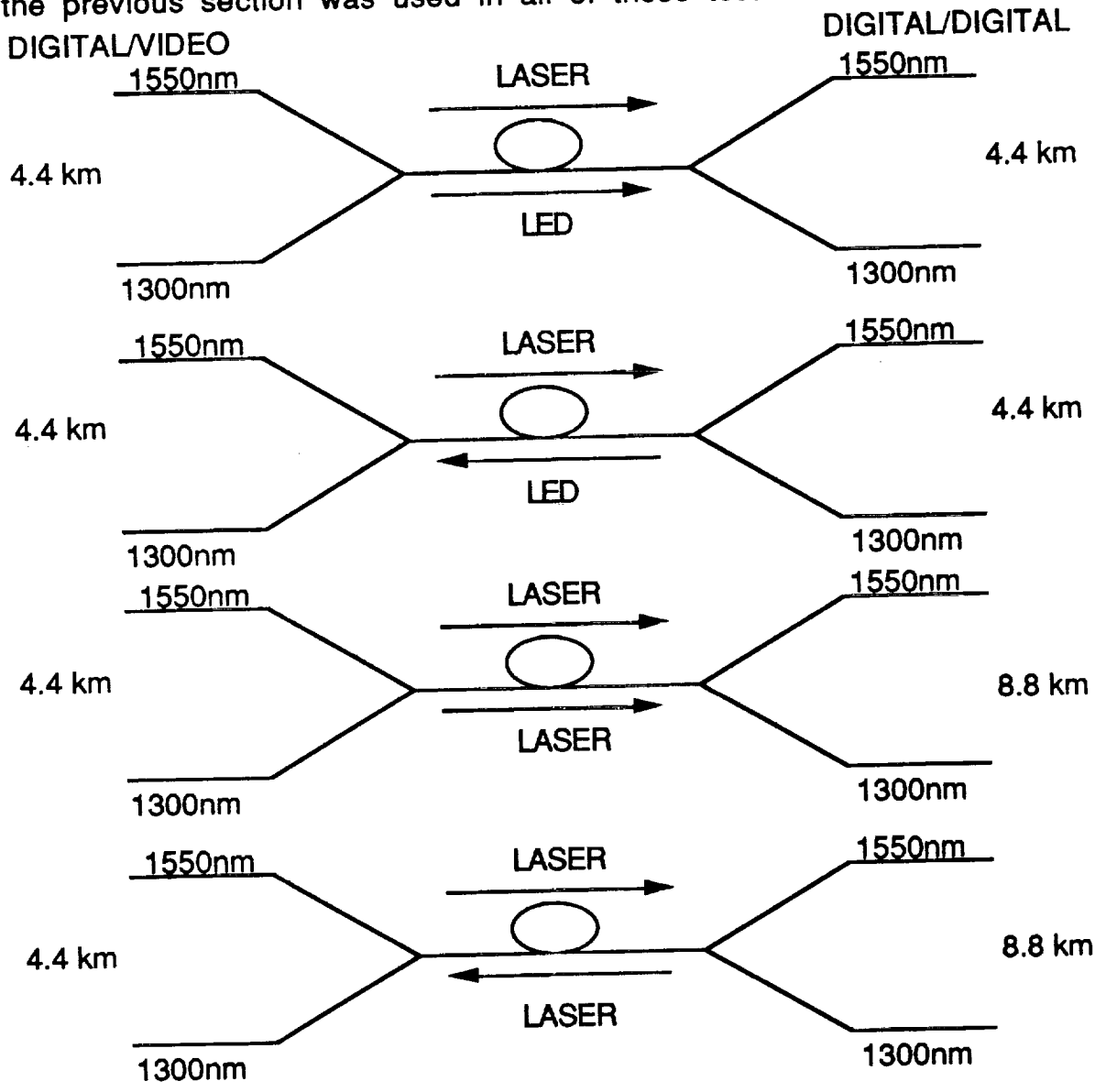

Figure 6-1 WDM System Configurations Tested

A two channel WDM communication system was constructed using these multiplexer/demultiplexer combinations and subjected to rigorous testing in many different configurations. Figure 6-1 shows the different configurations tested. The two vertices in each configuration diagram represent the WDMs. The 4.4 km link is the length of fiber used in a configuration similar to the fiber link described in Figure 3-1 In all cases The 1550 nm source used was a 1550 nm ECL driven laser diode. The 1300 nm channels were lasers or LEDs. neither LEDs nor video signals could be propagated over greater than 4.4 km. Digital signals generated with laser transmitters could be propagated over 8.8 km.

6.2 VIDEO TESTS

Each system configuration was tested with a 1300 nm video signal copropagated with a 1550 nm digital signal. The video signal was checked against the RS 250B short haul standards by transmitting a test pattern using a video generator and analyzing the resulting signal at the receiver end of the link using a Tektronix VM700 test set. The block diagram of a typical test set is shown in Figure 6-2 below.

In all tests, the video channel showed no sensitivity to the presence of the digital data occupying the other wavelength channel. The frequency of the digital data was varied from 1 to 59 MHz. If the video channel could be setup to operate without the 1550 nm channel, It would operate with the potentially interfering signal. Furthermore, the digital data (in the form of a random bit pattern) showed no degradation due to the simultaneous presence of the video signal. Table 6-1 below lists the video parameters checked in these tests.

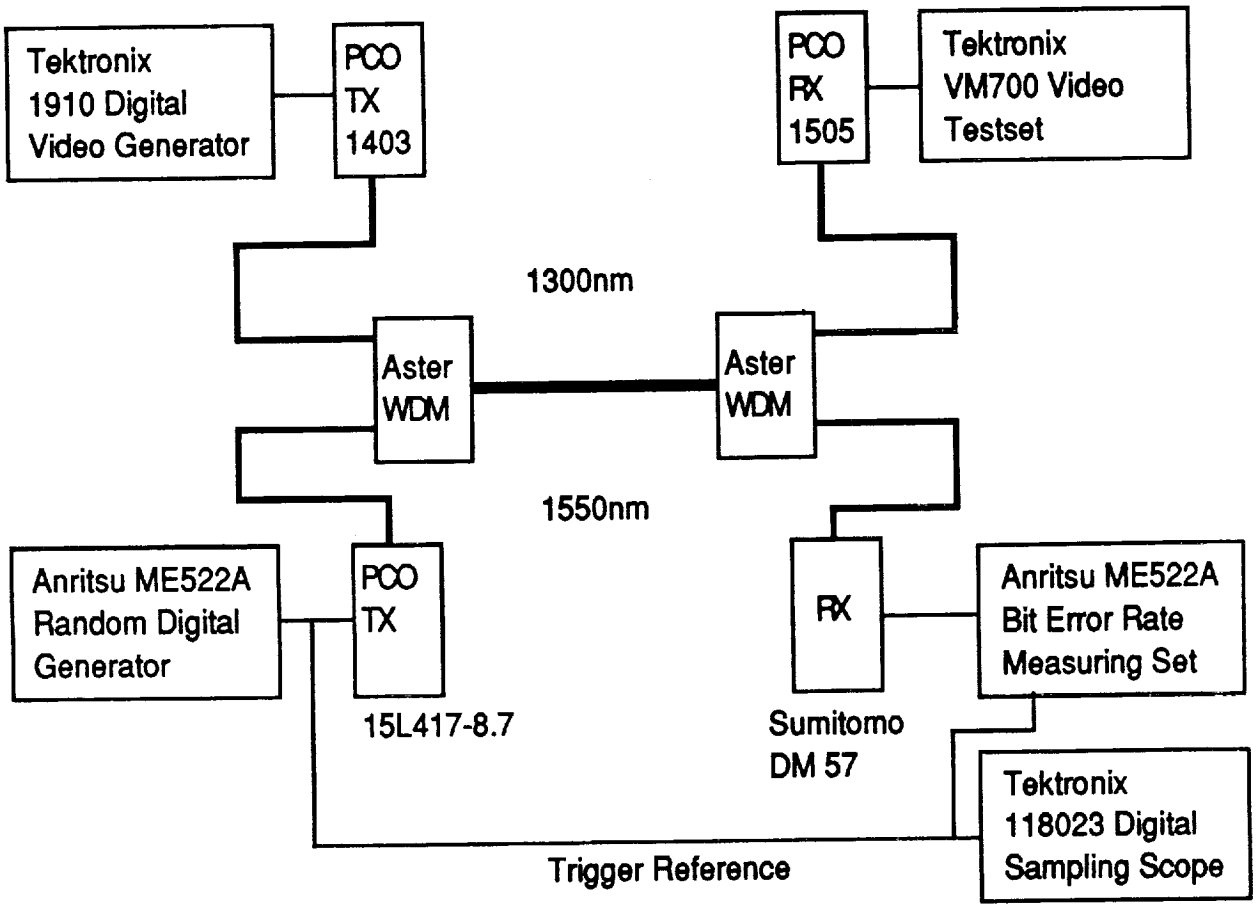

Figure 6-2 Block Diagram of Video/Digital Test Setup

Table 6-1 RS 250B Parameters Checked in System Tests

Avg. Picture Level	51.3 %	S/N Unweighted	58.7 dB
Bar Amplitude	100.6 IRE	S/N Lum-Weighted	68.1 dB
Sync Amplitude (Bar)	40.4 %	S/N Periodic	53.1 dB
Burst Amplitude (Sync)	100.2 %		
		Chroma-Lum Delay	4.1 ns
Sync Risetime	142 ns	Chroma-Lum Gain	100.6 %
Sync Falltime	145 ns		
		Differential Gain	1.98 %
VIRS Chroma Ampl	97.6 %	Differential Phase	0.66 Deg
VIRS Chroma Ampl	39.4 %	Lum Non-Linearity	0.77 %
VIRS Chroma Phase	-0.8 °		
		Relative Burst Gain	-0.06 %
Line Time Distortion	0.4 %	Relative Burst Phase	-0.10 Deg
Pulse/Bar Ratio	97.6 %		
2T Pulse K-Factor	0.3 % Kf		

6.2 DATA/DATA TESTS

Digital data was propagated in all possible combinations along the optical link. One channel would be setup to transmit a random bit pattern and the other would be setup to transmit a clock at the same fundamental frequency. The clock signal along the 1550 nm channel was also be set to the FM signal frequency of the 1300 nm PCO equipment. A bit error rate of better than 1×10^{-9} was maintained over links as long as 8.8 km with no descernible cross-channel interference.

6.3 CROSSTALK SENSITIVITY TESTS

Since no channel failure could be induced in the WDM system tests, it was decided to conduct crosstalk sensitivity tests by feeding both 1300 nm video and 1550 nm interfering light into a PCO receiver. The test setup used is shown below in Figure 6-3.

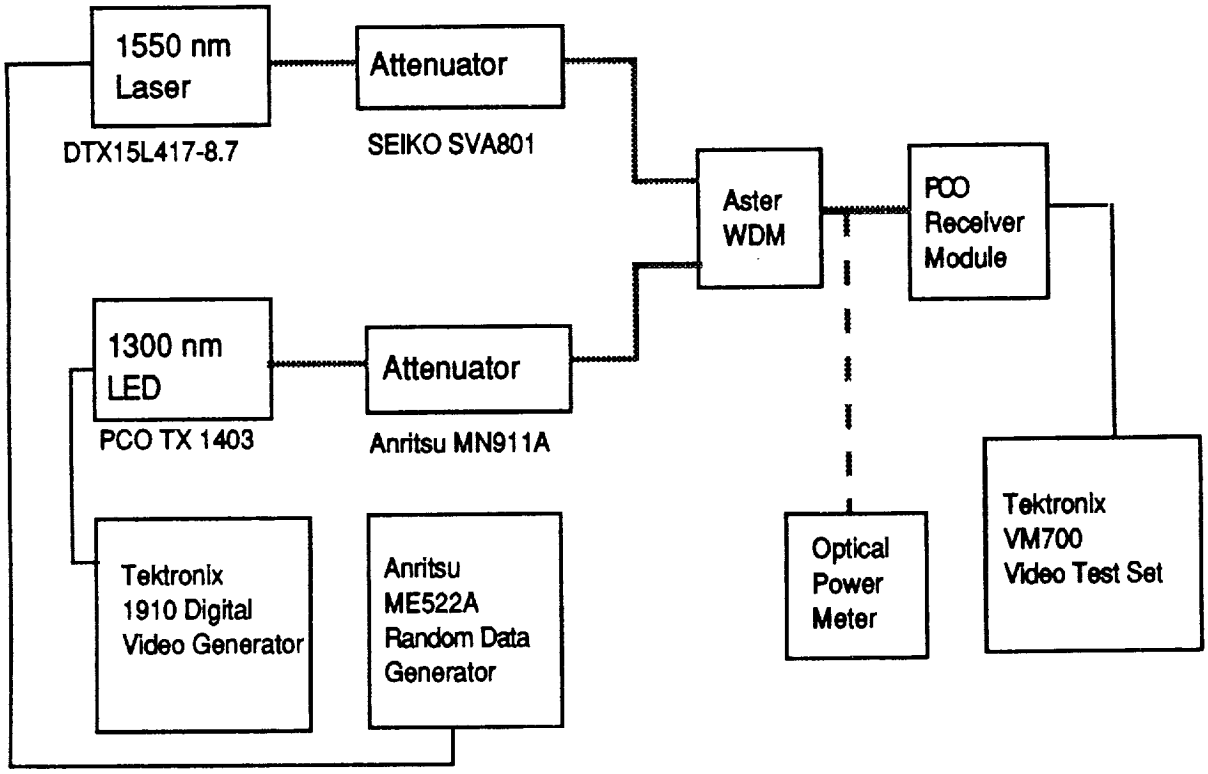

Figure 6-3 Crosstalk Sensitivity Test Setup

The general procedure used in these test was to first calibrate the attenuators. One source at a time was applied to the system. The corresponding attenuator was systematically set to a series of settings and the optical power observed with the power meter. In this way the amount of power at the receiver could be determined by the attenuator setting. Then the interfering source was reduced to negligible level using its attenuator. The video signal was attenuated to the point where it would just meet the RS 250B specifications. The 1550 nm source was then increased in intensity by reducing its attenuator level until the video signal failed the specifications. This combination of attenuator settings was then recorded and the 1300 nm level increased a measured amount until the system passed the test. Again, the interfering light would be increased in intensity until the system failed the attenuator settings would again be recorded...etc. This process was repeated over a wide range of signal levels. The results are shown in the graph below in Figure 6-4. In all cases the observed failure mode was reduction in the periodic signal to noise ratio.

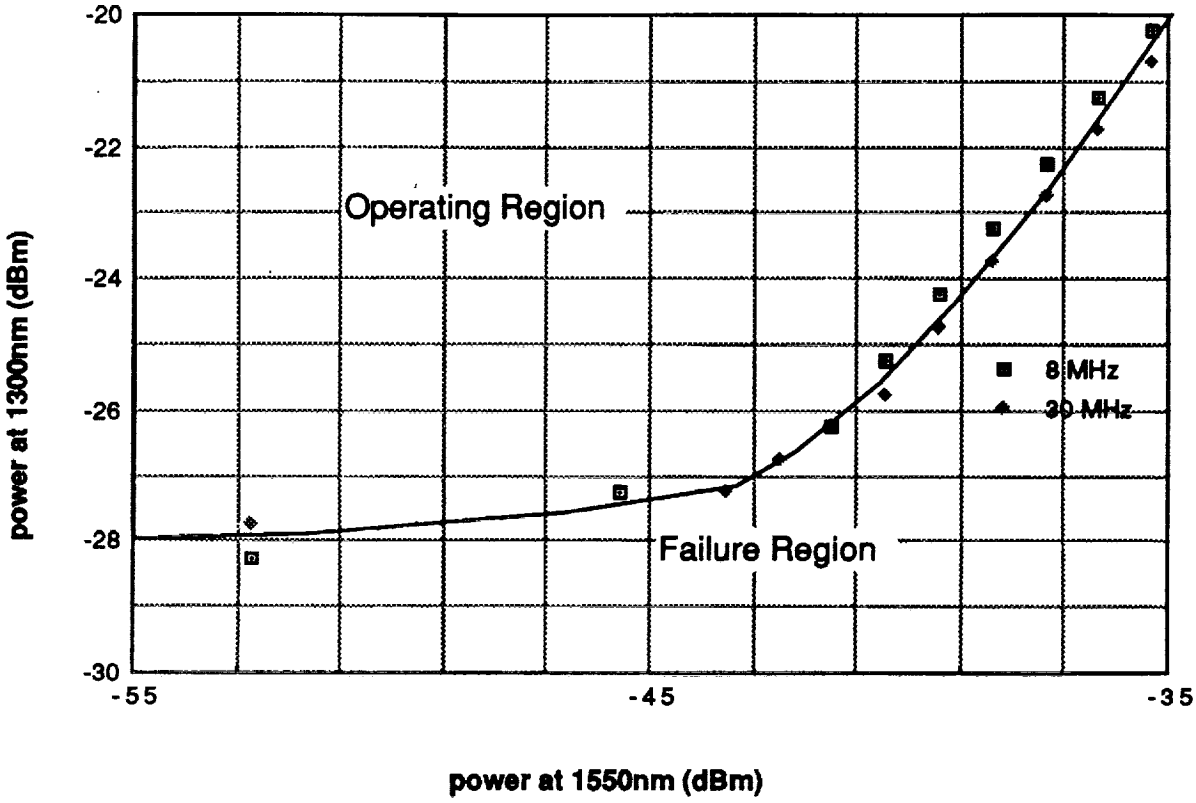

Figure 6-4 WDM Operating Envelope for Video Propagation at 1330 nm

This data will enable the system designer to determine the proper operating parameters or set specifications and safety factors of a 1550 nm/1300 nm WDM system given information about crosstalk, insertion loss, link loss and transmitter spectral power densities.

VII. CONCLUSIONS

The main goals of the research project were met. WDM systems were characterized and a test system constructed using the best WDM devices available to demonstrate the principle. In addition, a considerable amount of data was collected characterizing the spectra of laser and LED transmitter sources, the loss spectra of fiber optic links and crosstalk sensitivity of a typical receiver. This data when taken together can assist the system designer in specifying future systems. By identifying the failure mode for crosstalk in the case of video propagation, this research should also benefit the end user of such systems.

Further work could be done to more completely characterize the nature of the fiber links at KSC and to characterize the transmitters and receivers in the plant. only 10 LED and 10 LID transmitters were measured. In addition the system limits due to fiber nonlinearity could be probed to establish the ultimate transmission distance. The ultimate spectral density of the system using multimode and single mode fiber could be studied as well and a computer system model developed.

REFERENCES

[1]Winzer and Reichelt. "Wavelength Division Multiplex Transmission over Multimode Optical Fibers: Comparison of Multiplexing Principles" Siemens Forsch.vol 9, number 4 (1980)

[2]N. A. Olsen et al., 68.3 km Transmission With 1.37 Tbit Capacity using Wavelength Division Multiplexing of Ten Single Frequency Lasers at 1.5 micrometers", Electronics Letters Vol. 21, Number 3 (January 1985)

[3]J. M. Senior et al. "Devices for wavelength multiplexing and demultiplexing", IEE Proceedings, Vol. 136, No. 3 (June 1989)

[4]A. R. Chraplyvy and P. S. Henry, "Performance Degradation Due to Stimulated Raman Scattering in Wavelength-Division-Multiplexed Optical-Fibre Systems", Electronics Letters, Vol. 19 No. 16 (August 1983)

[5]Danny Goodman, The Complete HyperCard Handbook ,(Bantam Books,New York, 1988)

1990 NASA/ASEE SUMMER FACULTY FELLOWSHIP PROGRAM

P 50

JOHN F. KENNEDY SPACE CENTER
UNIVERSITY OF CENTRAL FLORIDA

ELECTROCHEMICAL IMPEDANCE SPECTROSCOPY OF METAL ALLOYS IN THE SPACE TRANSPORTATION SYSTEM LAUNCH ENVIRONMENT

PREPARED BY: Dr. Luz Calle

ACADEMIC RANK: Associate Professor

UNIVERSITY AND DEPARTMENT: Randolph-Macon Woman's College
Chemistry Department

NASA/KSC

DIVISION: Material Science Laboratory

BRANCH: Materials Testing Branch

NASA COLLEAGUE: Mr. Louis MacDowell

DATE: August 17, 1990

CONTRACT NUMBER: University of Central Florida
NASA-NGT-60002 Supplement: 4

ACKNOWLEDGEMENT

I would like to thank my NASA colleague, Louis G. MacDowell, III, for providing me with the opportunity and orientation to pursue this research. I would also like to thank the people in the Materials Science Laboratory who made me feel welcome at the Kennedy Space Center. Special thanks to Drs. Rupert U. Lee and Cordelia Ontiveros for their friendship and cooperation. I am grateful to NASA/ASEE for my selection as a faculty fellow in the 1989 and 1990 NASA/ASEE program at the Kennedy Space Center. The expertise and kindness of the program director, Dr. Loren A. Anderson is also gladly acknowledged. My gratitude is also extended to Kari L. Baird for her efficient administrative assistance of the program.

ABSTRACT

AC impedance measurements were performed to investigate the corrosion resistance of 18 alloys under conditions similar to the Space Transportation System, STS, launch environment. The alloys were: Zirconium 702, Hastelloy C-22, Inconel 625, Hastelloy C-276, Hastelloy C-4, Inconel 600, 7Mo + N, Ferralium 255, Inco Alloy G-3, 20Cb-3, SS 904L, Inconel 825, 304LN, SS 316L, SS 317L, ES 2205, SS 304L, Hastelloy B-2, and Monel 400. AC impedance data were gathered for each alloy at various immersion times in 3.55% NaCl-0.1N HCl.

Polarization resistance, R_p, values were obtained from the Nyquist plots at each immersion time using the EQUIVALENT CIRCUIT software package available with the 388 Electrochemical Impedance software. Hastelloy C-22 showed the highest overall values for R_p while Monel 400 and Inconel 600 had the lowest overall values. There was a good general correlation between the corrosion performance of the alloys at the beach corrosion testing site and the expected rate of corrosion as predicted based on the R_p values obtained in this investigation. The data indicate that Electrochemical Impedance Spectroscopy can be used to predict the corrosion performance of metal alloys.

SUMMARY

AC impedance techniques were used to study the corrosion of 18 alloys under conditions similar to the Space Transportation System, STS, launch environment which is highly corrosive. The 18 alloys were: Zirconium 702, Hastelloy C-22, Inconel 625, Hastelloy C-276, Hastelloy C-4, Inconel 600, 7Mo + N, Ferralium 255, Inco Alloy G-3, 20Cb-3, SS 904L, Inconel 825, SS 316L, SS 317L, ES 2205, SS 304L, Hastelloy B-2, and Monel 400. AC impedance data were acquired for each of the alloys at various immersion times in 3.55% NaCl-0.1N HCl.

The data were analyzed using the Nyquist plot. R_p values were obtained from the Nyquist plot using the EQUIVALENT CIRCUIT software package available with the 388 Electrochemical Impedance Software.

A comparison of the rates of corrosion expected from the R_p values with the beach corrosion data led to the conclusion that there is, in general, a good correlation between the materials that performed well in both tests as well as between those that performed poorly. However, the ordering of the materials according to their resistance to corrosion cannot be predicted from the values of R_p. It can be concluded that AC impedance techniques can be used to choose what materials should be subjected to long-term corrosion testing.

TABLE OF CONTENTS

LIST OF FIGURES

ELECTROCHEMICAL IMPEDANCE SPECTROSCOPY OF METAL ALLOYS IN THE SPACE TRANSPORTATION SYSTEM LAUNCH ENVIRONMENT

1.0 INTRODUCTION

1.1 Flexible metal hoses are used in various supply lines that service the Orbiter at the launch pad. These convoluted flexible hoses were originally constructed of 304L stainless steel. The severely corrosive environment at the launch site caused pitting corrosion in many of these flex hose lines. In the case of vacuum jacketed cryogenic lines, failure of the flex hose by pitting causes a loss of vacuum and subsequent loss of insulation.

1.2 The environment at the launch site is very corrosive due to the very high chloride content caused by the proximity of the Atlantic Ocean and to the generation of concentrated hydrochloric acid (HCl) as a fuel combustion product of the Solid Rocket Boosters (SRB'S) during a launch. These corrosive conditions cause severe pitting on some of the commonly used stainless steel alloys.

1.3 A previous investigation was undertaken in 1987 to evaluate 19 metal alloys with the purpose of finding a more corrosion resistant replacement material for 304L stainless steel. The tests performed in that investigation were: electrochemical corrosion testing, accelerated corrosion testing in a salt fog chamber, long term exposure at the beach corrosion testing site, and pitting corrosion tests in ferric chloride solution. These tests led to the conclusion that the most corrosion resistant alloys were, in descending order, Hastelloy C-22, Inconel 625, Hastelloy C-276, Hastelloy C-4, and Inco Alloy G-3. Of these top five alloys, the Hastelloy C-22 stood out as being the best of the alloys tested. The details of this investigation are found in report MTB-325-87A (1). Furthermore, on the basis of corrosion resistance combined with weld and mechanical properties, Hastelloy C-22 was determined to be the best material for the construction of flex hoses to be used in fuel lines servicing the Orbiter at the launch site.

1.4 The previous electrochemical corrosion testing was based on the use of DC polarization techniques. In the present investigation, Electrochemical Impedance Spectroscopy (EIS) techniques using AC impedance measurements were utilized in order to study the corrosion of the same 19 alloys tested in

1987. During the first part of the investigation, the 19 alloys were tested after one hour immersion in three different electrolyte conditions: neutral 3.55% NaCl, 3.55% NaCl-0.1N HCl, and 3.55% NaCl-1.0N HCl (2). The second part of the investigation involved the study of 18 of the 19 alloys in 3.55% NaCl-0.1N HCl at different immersion times. The 3.55% NaCl-0.1N HCl electrolyte provides an environment for the corrosion of the alloys similar to the conditions at the launch pad.

2.0 MATERIALS AND EQUIPMENT

2.1 CANDIDATE ALLOYS

The 19 alloys tested and their nominal compositions in weight percent are shown in Table 1. The choice of these alloys for the investigation was based on their reported resistance to corrosion in chloride environments. SS 304LN was excluded from the second part of the investigation due to its similarity to SS 304L and to time limitations.

2.2 AC IMPEDANCE MEASUREMENTS

2.2.1 A Model 378 Electrochemical Impedance system manufactured by EG&G Princeton Applied Research Corporation (PARC) was used for all EIS measurements. The system includes: (1) the Model 273 Computer-Controlled Potentiostat/Galvanostat; (2) the Model 5301A Computer-Controlled Lock-In Amplifier; (3) the IBM XT Microcomputer with peripherals; and (4) the Model 378 Electrochemical Impedance Software. An updated version of the software (PARC version 2.7) including circuit modeling routines was used for the EIS measurements at different immersion times.

2.2.2 Specimens were flat coupons 1.59 cm (5/8") in diameter. The PARC flat specimen holder in the electrochemical cell is designed such that the exposed metal surface area is 1 cm^2.

2.2.3 The electrochemical cell included a saturated calomel reference electrode (SCE), 2 graphite rod counter electrodes, the metal working electrode, and a bubbler/vent tube. Each alloy was studied at different immersion times in aerated 3.55% NaCl-0.1N HCl (similar to the conditions at the launch site). All solutions were prepared using deionized water.

3.0 PROCEDURE FOR AC IMPEDANCE MEASUREMENTS

3.1 The test specimens were polished with 600-grit paper, wiped with methyl-ethyl ketone, ultrasonically degreased for five minutes in a detergent solution, rinsed with deionized water, and dried. Each specimen was observed under the microscope and weighed before and after each experiment to monitor changes caused by corrosion on its appearance and weight. The test samples were immersed in 3.55% NaCl-0.1N HCl. Aeration with dry air was maintained throughout the test.

3.2 The EIS data were acquired at different immersion times starting with one hour (zero hours for 304L and Inconel 625). Data were gathered in the frequency range from 100 kHz to 0.001 Hz using the Auto Execute selection of the EG&G PARC M378 Software System version 2.70. Three experiments were performed covering the following frequency ranges: 100 kHz to 5 Hz, 10-0.1 Hz, and 0.1-0.001 Hz. The data from the three experiments were merged automatically. The AC amplitude was 10 mV.

3.3 The data for each immersion time were plotted in the Nyquist and Bode plot formats.

4.0 TEST RESULTS AND DISCUSSION

4.1 THEORETICAL BACKGROUND

4.1.1 AC impedance techniques offer some distinct advantages over DC techniques (3). First, the small excitation amplitudes that are used, generally in the ranges of 5 to 10 mV peak-to-peak, cause only minimal perturbations of the electrochemical system, thus reducing errors caused by the measuring technique itself. Second, the technique offers valuable information about the mechanisms and kinetics of electrochemical processes such as corrosion. Third, measurements can be made in low conductivity solutions where DC techniques are subject to serious potential-control errors.

4.1.2 Despite the advantages of the EIS techniques mentioned above, their application requires sophisticated methods in order to interpret the data and extract meaningful results. The application of AC impedance measurements to study corrosion has so far resulted in the publication of a large amount of experimental data without much interpretation. The technique is at the present time in a transition from the data collection stage to the data analysis stage (4).

4.1.3 EIS is based on the fact that an electrochemical system, such as those studied in this investigation, can be represented by an equivalent electrical circuit. The equivalent circuit for a simple electrochemical cell is shown in Figure 1 (5). The circuit elements R_s, R_p, and C_{dl} respectively represent the uncompensated resistance (resistance from the reference to the working electrode), the polarization resistance (resistance to electrochemical oxidation), and the capacitance very close to the metal surface (at the double layer). There are several formats that can be used for the graphical representation of the AC impedance data (3,6,7). Each format offers specific advantages for revealing certain characteristics of a given test system. It was determined at the beginning of this research, that the most suitable formats for plotting the AC impedance data were the Nyquist and the Bode plots.

4.1.4 The Nyquist plot is also known as a Cole-Cole plot or a complex impedance plane diagram. Figure 2 (5) shows the Nyquist plot for the equivalent circuit shown in Figure 1. The imaginary component of the impedance (Z") is plotted versus the real component of the impedance (Z') for each excitation frequency. As indicated in Figure 2, this plot can be used to calculate the values of R_Ω, R_p, and C_{dl}.

4.1.5 The Bode plot for the equivalent circuit in Figure 1 is shown in Figure 3 (5). This graphical representation of the AC impedance data involves plotting both the phase angle (θ) and the log of absolute impedance ($\log|Z|$) versus the log of the frequency ($w = 2\pi f$). As indicated on the figure, values for R_Ω, R_p, and C_{dl} can also be obtained from the Bode plot. Of special interest for this research is the determination of the R_p values which can be used to calculate the corrosion rate of an electrode material in a given electrolyte (3,8).

4.2 AC IMPEDANCE MEASUREMENTS AT DIFFERENT IMMERSION TIMES IN 3.55% NACL-0.1N HCL

4.2.1 The data for this part of the investigation were plotted in the Nyquist and Bode plot format. A close examination of both types of plots revealed that the Nyquist plot provided more information for the 18 alloys at each immersion time and are shown in Figures 4-21. The Bode plots were all very similar in shape and are not included in this report for the sake of brevity.

4.2.2 R_p values for the 18 alloys at different immersion times in 3.55% NaCl-0.1N HCl were calculated using the Find Circle option of the Data Cruncher pre-analysis part of the EQUIVALENT CIRCUIT software package available with the Model 388 Electrochemical Impedance Software package. Due to the time limitations imposed on this part of the investigation by the facts that it took 3 hours and ten minutes to collect the data for each immersion time and that the time available to complete the investigation was only ten weeks, a more thorough analysis of the data was not undertaken at this time

using the full capabilities of the software. The R_p values shown on Table 2 are preliminary and it is anticipated that they will be refined within the near future.

4.2.3 Examination of the R_p values at different immersion times for each alloy revealed that R_p changes differently with time for each alloy. This means that the alloys differ significantly in terms of how their rates of corrosion change with immersion time.

4.2.4 Hastelloy C-22 showed the highest overall values of R_p while Monel 400 and Inconel 600 had the lowest overall values. Zirconiumm 702 showed a variation in R_p from 10^5 to 10^1. Data collection for this sample was very difficult because the instrument would stop gathering data when dark spots, indicative of pitting, appeared on the exposed surface of the sample. This is the reason for having used two samples of this material. It should be noted that Zirconium 702 was found to be the most corrosion resistance ally in the one-hour immersion time/different electrolyte investigation. The drastic change in the rate of corrosion for this material at different immersion times points out the importance of performing AC impedance measurements at different immersion times. Other alloys that showed significant changes in the magnitude of R_p with varying immersion times are Ferralium 255 and SS 304L. SS 304L has Rp values indicative of a rate of corrosion that is high at first (low R_p) and then slows down (higher R_p). All the other alloys exhibited R_p values that were on the order of 10^5 to 10^6.

4.3 COMPARISON WITH BEACH CORROSION DATA

4.3.1 A comparison of the R_p values obtained in this part of the investigation with the beach corrosion data for all the alloys given in Figure 9 of reference 2 indicates that AC impedance measurements can discriminate between the best (Hastelloy C-22) and the worst (Monel 400) performing materials at the beach. There is also a good correlation between the best performing materials as a group (those with the highest R_p values) and the poorest performers (those with the lowest R_p values).

4.3.2 There is a discrepancy between the AC impedance results for 20Cb-3 and its performance at the beach corrosion test site. While its R_p values would predict a low rate of corrosion, this material exhibits one of the two highest rates of corrosion at the beach. A possible explanation for this discrepancy can be obtained by examining the one-hour immersion time data in three different electrolytes (Figure 8b in reference 2). The Nyquist plots on this figure clearly show the effect on the R_p value caused by increasing the concentration of HCl. While R_p is high for one hour immersion in neutral 3.55% NaCl and in 3.55% NaCl-0.1N HCl a considerable decrease is observed when the concentration of HCl is increased to 1.0N. It should be noted here that the samples at the beach test site are periodically sprayed with 10% HCl which is a higher concentration than the 0.1N used in this part of the investigation.

5.0 CONCLUSIONS

5.1 AC impedance measurements in 3.55% NaCl-0.1N HCl at different immersion times revealed how the rate of corrosion, as indicated by the R_p values obtained, varies with time for the 18 alloys included in this part of the investigation.

5.2 An examination of the overall R_p values for each alloy over a range of different immersion times allows the prediction of the long-term performance of the alloys under similar conditions.

5.3 AC impedance measurements can be used to rank high performance metal alloys according to their rate of corrosion in order to distinguish between those materials expected to have a low rate of corrosion (high R_p) and those expected to have a high rate of corrosion (low R_p).

5.4 AC impedance measurements, like the ones reported in this investigation, do not provide the information necessary to discriminate among the corrosion rates of the different metal alloys in a way that allows for ordering them exactly according to their rate of corrosion.

5.5 This part of the investigation pointed out the importance or performing AC impedance measurements at different immersion times in order to predict the long-term performance of the metal alloys under similar conditions.

6.0 RECOMMENDATIONS FOR FUTURE WORK

6.1 Further analysis of the data using the full capabilities of the EQUIVALENT CIRCUIT software package.

6.2 Include testing of alloys after exposure to conditions as similar to the STS launch environment as possible.

6.3 Study the effect of protective coatings on the rate of corrosion of the 19 alloys.

6.4 Modify the electrolyte conditions to include other chemicals normally found at the STS launch environment.

6.5 Study the effect that a change in temperature, in a fashion similar to the seasonal changes that occur at the STS launch environment, would have on the rate of corrosion.

REFERENCES

1. MacDowell, L.G. and Ontiveros, C., Evaluation of Candidate Alloys for the Construction of Metal Flex Hoses in the STS Launch Environment, Test Report, Document No. MTB-325-87A, National Aeronautics and Space Administration, Kennedy Space Center, Materials Testing Branch, August 23, 1988.

2. Calle, L.M., Study of Metal Corrosion using AC Impedance Techniques in the STS Launch Environments, 1989 NASA/ASEE Summer Faculty Fellowship Program Research Reports, Kennedy Space Center, 1989.

3. Application Note AC-1, Basics of AC Impedance Measurements, EG&G PARC, Princeton, NJ., 1984.

4. Mansfeld, F., Don't Be Afraid of Electrochemical Techniques -But Use Them with Care!, Corrosion, Vol. 44, pp. 856-868, 1988.

5. Rothstein, M.L., Electrochemical Corrosion Measurements for the Metal Finishing Industry, Application Note Corr-5, EG&G PARC, Princeton, NJ., 1986.

6. Mansfeld, F., Recording and Analysis of AC Impedance Data for Corrosion Studies. I. Background and Methods of Analysis, Corrosion, Vol. 37, pp. 301-307, 1981.

7. Mansfeld, F., Kendig, M.W., and Tsai, S., Recording and Analysis of AC Impedance Data for Corrosion Studies. II. Experimental Approach and Results, Vol. 38, pp. 570-580, 1982.

8. Lorenz, W.J. and Mansfeld, F., Determination of Corrosion Rates by Electrochemical DC and AC Methods, Corrosion Science, Vol. 21, pp. 647-672, 1981.

9. Williams, D.E. and Naish, C.C., An Introduction to the AC Impedance Technique, and its Application to Corrosion Problems, U.K. Atomic Energy Authority, Harwell Report AERE-M3461, pp. 1-10, 1985.

10. Moody, J.R., Quin, X.P., and Strutt, J.E., The Application of a Compurerized impedance Monitoring System to a Study of the Behavior of 347 ss in Nitric Acid, presented at the 166th Meeting of the Electrochemical Society, New Orleans, Louisiana, 1984.

11. Kendig, M.W., Meyer, E.M., Lindberg, G. and Mansfeld, F., A Computer Analysis of Electrochemical Impedance Data, Corrosion Science, Vol. 23, pp. 1007-1015, 1983.

12. Uhlig, H.H., Corrosion and Corrosion Control. An

Introduction to corrosion science and engineering, Second Edition, John Wiley & Sons Inc., p. 368, 1971.

13. Scantlebury, J.D., Ho, K.N. and Eden, D.A., Impedance Measurements on Organic Coatings on Mild Steel in Sodium Chloride Solutions, Electrochemical Corrosion Testing, ASTM STP 727, Mansfeld, F. and Bertocci, U., Eds., American Society for Testing and Materials, pp. 187-197, 1981.

14. Cahan, B.D. and Chien, C., The Nature of the Passive Film of Iron. II. A-C Impedance Studies, J. Electrochem. Soc., Vol. 129, pp. 474-480, 1982.

TABLE 1 CANDIDATE ALLOYS AND THEIR NOMINAL COMPOSITIONS (WT%)

ALLOY	Ni	Fe	Cr	Mo	Mn*	Co*	Cu	C*	Si*	P*	S*	Other
HASTELLOY C-4	Bal.	3.0	18	17	1.0	2.0		0.01	0.08	0.02	0.01	Ti 0.7
HASTELLOY C-22	Bal.	3.0	22	13	0.5	2.5		0.01	0.08	0.02	0.01	V 0.3, W 3
HASTELLOY C-276	Bal.	7.0	17	17	1.0	2.5		0.01	0.08	0.02	0.01	V 0.3, W 4.5
HASTELLOY B-2	Bal.	2.0	1	28	1.0	1.0		0.01	0.1	0.02	0.01	
INCONEL 600	Bal.	8.0	16		1.0		0.5	0.15	0.5		0.01	
INCONEL 625	Bal.	5.0	23	10	0.5	1.0		0.10	0.5	0.01	0.01	Cb 4.1
INCONEL 825	Bal.	22.0	21	3	1.0		2.5	0.05	0.5		0.03	
INCO G-3	Bal.	20.0	22	7	1.0	5.0	2.0	0.02	1.0	0.04	0.03	Cb 0.5, W 1.5
MONEL 400	Bal.	2.5			2.0		31	0.30	0.5		0.02	
ZIRCONIUM 702												Zr 99.2, Hf 4.5
SS 304L	10	Bal.	19		2.0			0.03	1.0			
SS 304LN	10	Bal.	19		2.0			0.03	1.0	0.04	0.03	N 0.13
SS 316L	12	Bal.	17	2.5	2.0			0.03	1.0	0.04	0.03	
SS 317L	13	Bal.	19	3.5	2.0			0.03	1.0			
SS 904L	25	Bal.	21	4.5	2.0		1.5	0.02	1.0	0.04	0.03	
20 Cb-3	35	Bal.	20	2.5	2.0		3.5	0.07	1.0			
7Mo + N	4	Bal.	28	2	2.0			0.03	0.6	0.03	0.01	N 0.25
ES 2205	5	Bal.	22	3	2.0			0.03	1.0	0.03	0.02	N 0.14
FERRALIUM 255	5	Bal.	26	3	1.5		2.0	0.04	1.0	0.04	0.03	N 0.17

* Values are max.

TABLE 2

IMMERSION TIME, POLAR. RESISTANCE (Rp), AND CORR. POTENTIAL (Ecorr)

ALLOY NAME	TIME (hrs)	Rp (ohms)	Ecorr (volts)
HASTELLOY C-4	1	1.9E+05	-0.075
	25	8.2E+05	0.026
	72	1.8E+06	0.073
	168	2.6E+06	0.118
HASTELLOY C-22	1	2.4E+05	-0.037
	4	4.9E+05	-0.005
	28	3.3E+05	0.080
	122	1.4E+06	0.149
	146	4.9E+05	0.272
	170	3.9E+06	0.224
	192	6.3E+06	0.212
	262	3.5E+07	0.177
	286	6.3E+07	0.159
	312	2.0E+07	0.090
	336	1.4E+08	0.138
	360	2.1E+06	0.133
	476	2.1E+06	0.082
	696	8.9E+05	0.116
HASTELLOY C-276	1	2.0E+05	-0.067
	24	8.0E+05	0.023
	144	2.3E+06	0.076
	168	2.3E+06	0.031
HASTELLOY B-2	1	1.7E+03	-0.134
	32	1.8E+03	-0.138
	120	1.6E+03	-0.138
	192	1.6E+03	-0.124
INCONEL 600	1	4.5E+02	-0.223
	28	8.8E+02	-0.238
	72	6.3E+02	-0.221
	224	7.6E+02	-0.232
	268	6.0E+02	-0.209
INCONEL 625	0	1.8E+05	-0.070
	5	5.0E+05	0.138
	31	4.3E+05	0.353
	100	2.5E+05	0.450
	291	1.7E+05	0.451
	396	1.4E+05	0.450

TABLE 2 (cont.)

ALLOY NAME	TIME (hrs)	Rp (ohms)	Ecorr (volts)
INCONEL 825	1	6.2E+05	-0.081
	28	4.9E+05	-0.090
	72	3.2E+06	-0.050
	168	6.5E+05	-0.052
INCO G-3	1	4.5E+05	-0.060
	40	9.4E+05	0.216
	64	1.0E+06	0.242
	88	2.8E+06	0.249
	164	3.3E+06	0.253
	188	3.7E+06	0.254
	337	6.4E+06	0.238
	505	9.6E+06	0.233
MONEL 400	1	9.7E+02	-0.146
	48	6.5E+02	-0.140
	120	5.7E+02	-0.129
	192	6.8E+02	-0.115
ZIRCONIUM 702	1	1.7E+05	-0.089
SAMPLE 1	24	4.3E+02	-0.049
	48	2.0E+03	0.090
	72	1.1E+01	0.157
SAMPLE 2			
	3	5.9E+05	-0.119
	20	7.4E+05	0.136
	43	7.7E+01	0.156
	67	3.3E+02	-0.017
	91	7.6E+01	0.168
	163	3.3E+01	0.152
SS 304L	0	3.8E+02	-0.371
	7	6.5E+02	-0.345
	24	7.8E+02	-0.328
	31	6.2E+02	-0.322
	54	5.0E+05	-0.127
	100	1.3E+05	-0.161
	192	1.4E+05	-0.165
	243	2.3E+05	-0.151

TABLE 2 (cont.)

ALLOY NAME	TIME (hrs)	Rp (ohms)	Ecorr (volts)
SS 316L	1	2.6E+05	-0.117
	48	9.5E+05	-0.077
	120	6.4E+05	-0.140
	192	5.1E+05	-0.120
SS 317L	24	1.4E+06	-0.030
	128	2.1E+06	-0.102
	168	6.5E+06	-0.007
SS 904L	1	6.3E+05	-0.083
	44	4.2E+06	0.032
	120	9.1E+06	0.156
	168	1.6E+06	0.239
20 CB-3	1	3.4E+05	-0.091
	28	2.9E+06	0.066
	96	8.8E+05	-0.020
	168	1.4E+06	0.019
7 MO + N	1	5.3E+05	-0.132
	25	3.1E+06	-0.023
	90	2.3E+06	-0.113
	115	4.6E+05	-0.176
	137	1.5E+06	-0.113
	161	1.5E+06	-0.139
ES-2205	1	3.0E+05	-0.101
	26	2.0E+06	0.018
	73	9.8E+05	-0.097
	166	7.2E+05	-0.126
FERRALIUM 255	1	4.3E+05	-0.115
	24	7.1E+05	-0.068
	48	2.1E+06	0.003
	120	3.0E+05	-0.209
	124	2.9E+05	-0.209
	151	1.1E+07	-0.002
	175	2.3E+07	0.048
	200	3.7E+07	0.067
	223	8.3E+06	0.071
	293	2.0E+06	0.100
	317	7.4E+02	0.117
	343	5.1E+02	0.126
	367	8.6E+05	0.140
	551	1.3E+07	0.249
	654	1.8E+07	0.247

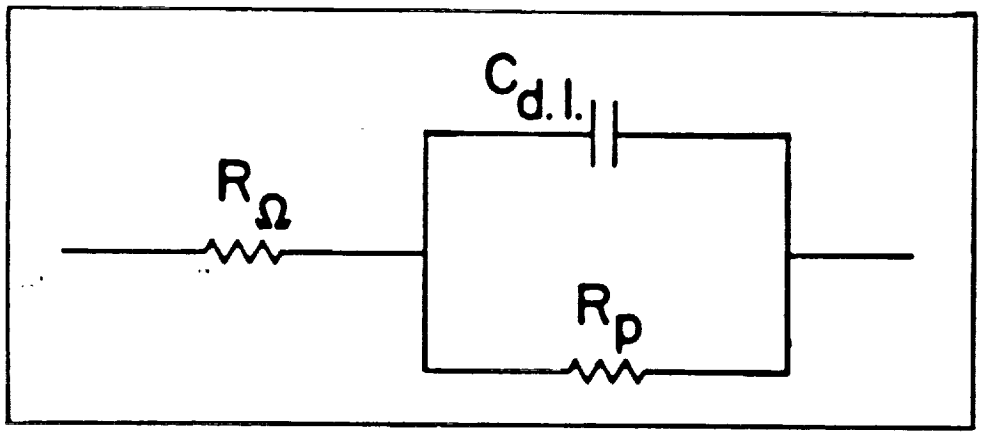

Figure 1. Equivalent circuit for a simple electrochemical cell.

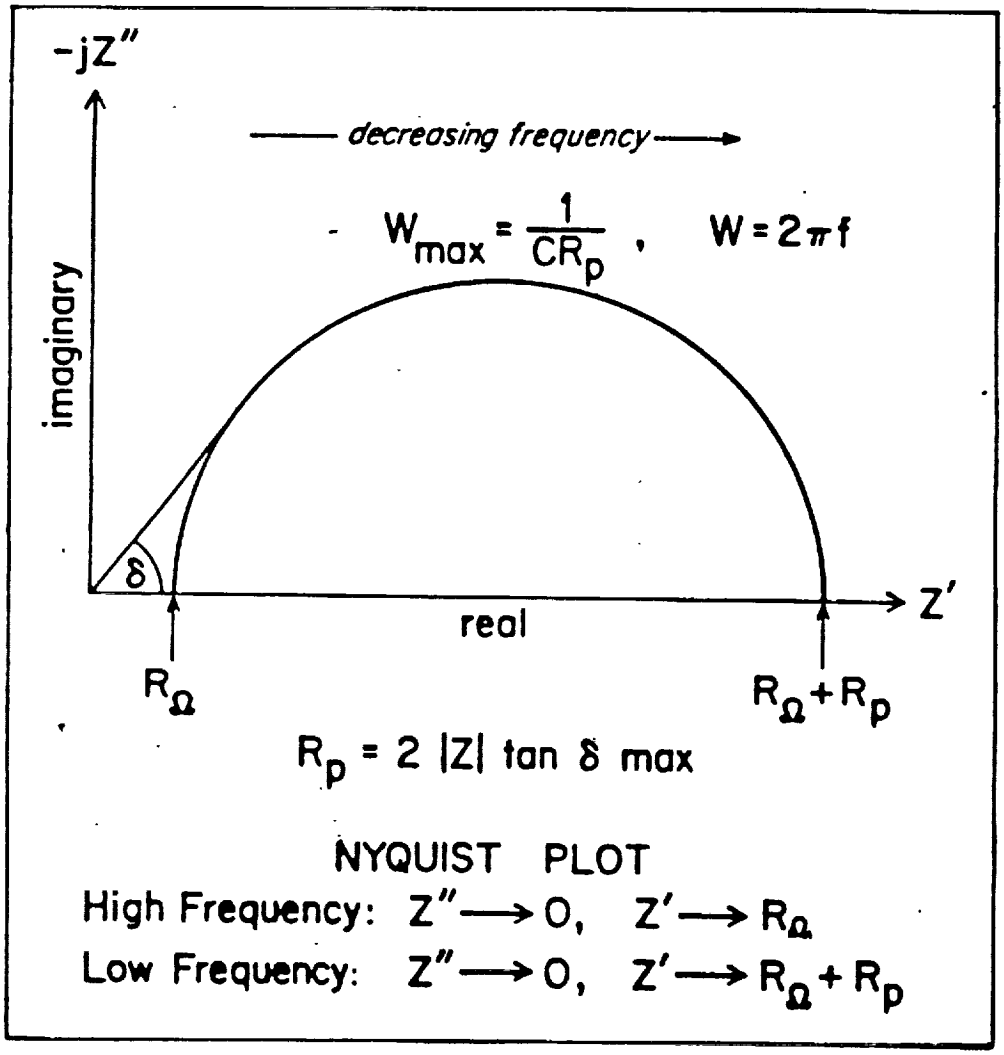

Figure 2. Nyquist plot for equivalent circuit in Figure 1.

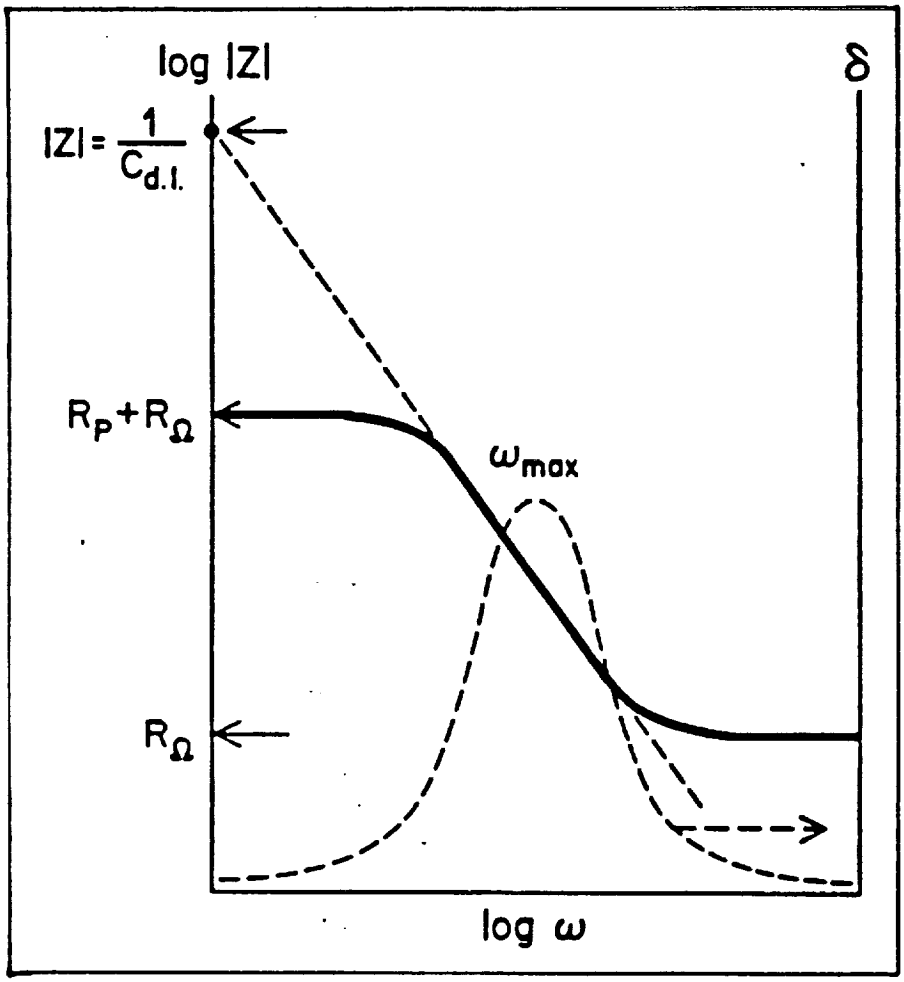

Figure 3. Bode plot for equivalent circuit in Figure 1.

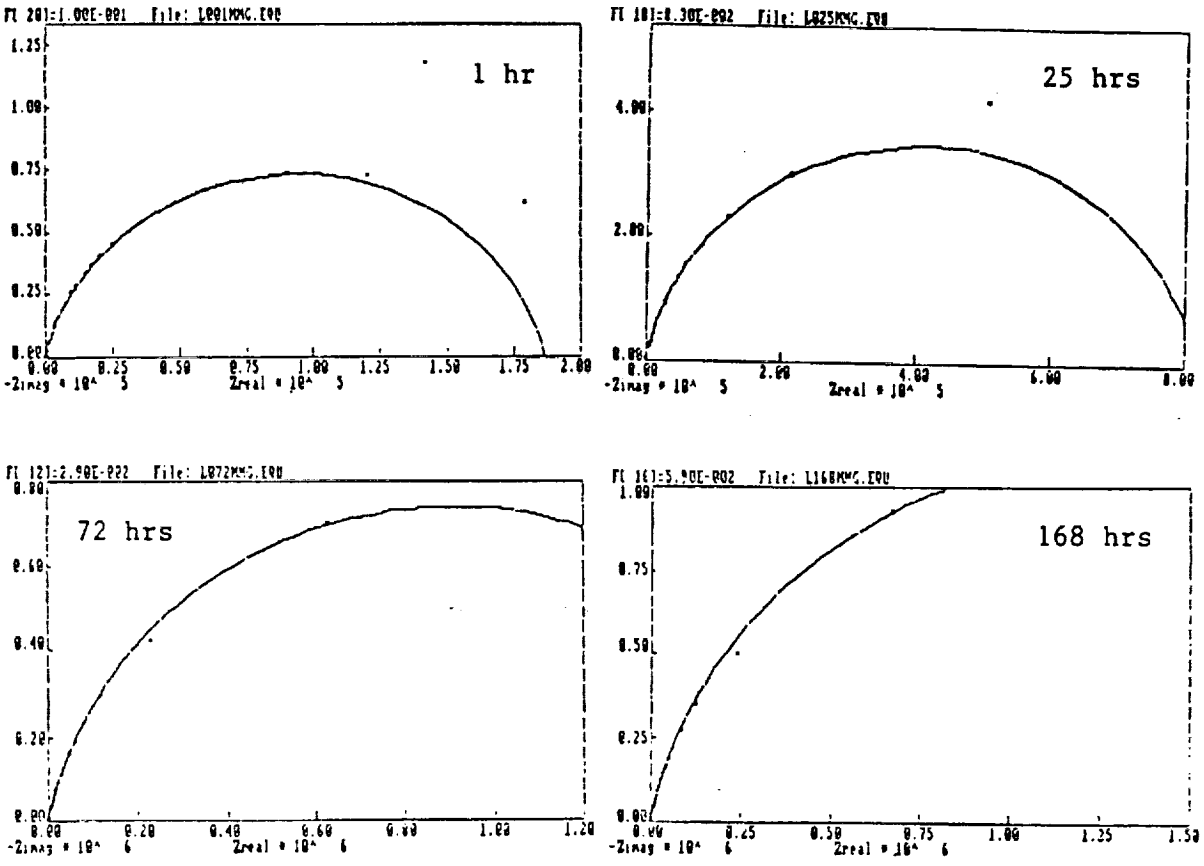

Figure 4 Nyquist Plots for Hastelloy C-4 in 3.55% NaCl-0.1N HCl at Various Immersion Times

C-2

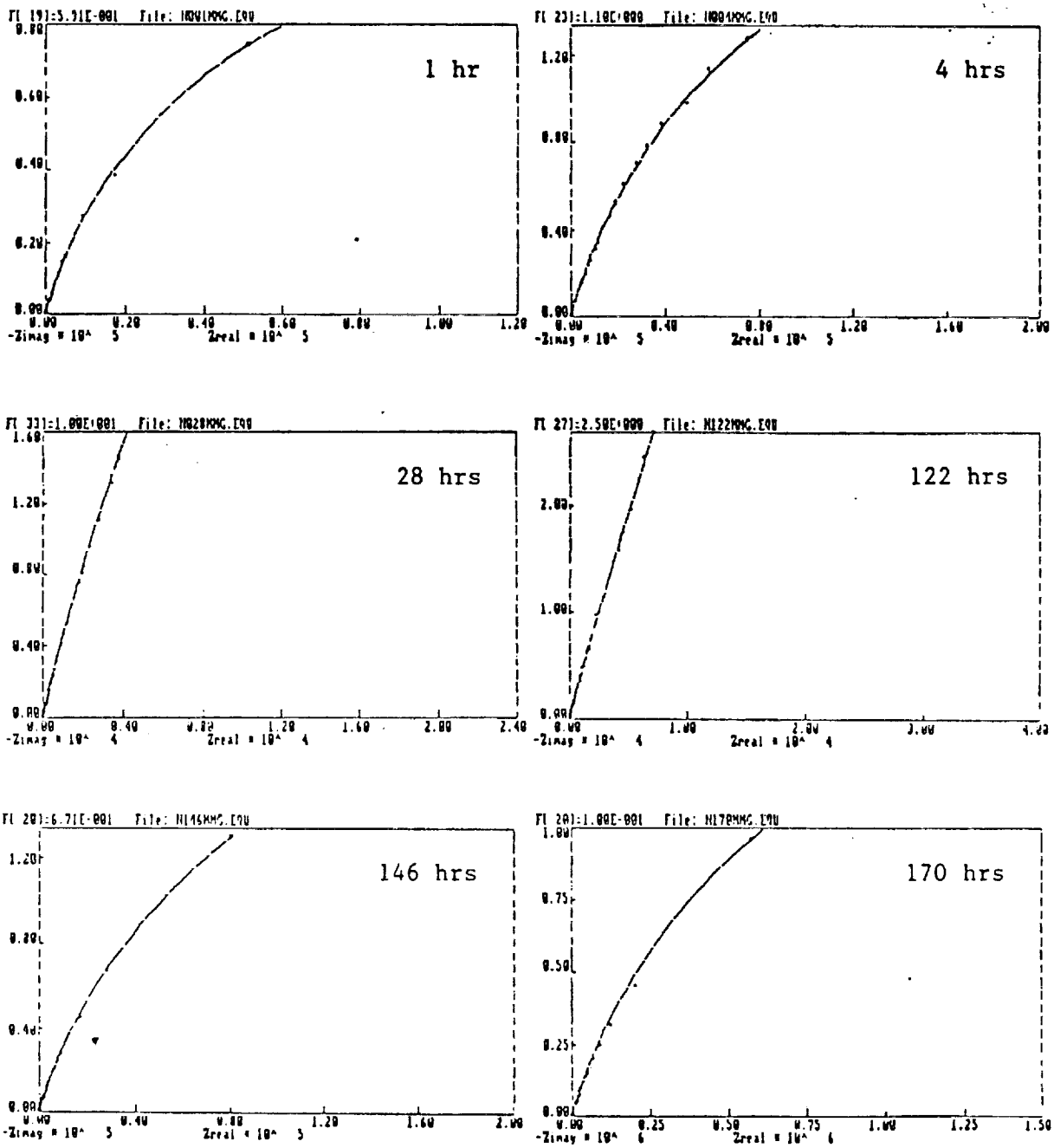

Figure 5 Nyquist Plots for Hastelloy C-22 in 3.55% NaCl-0.1N HCl at Various Immersion Times

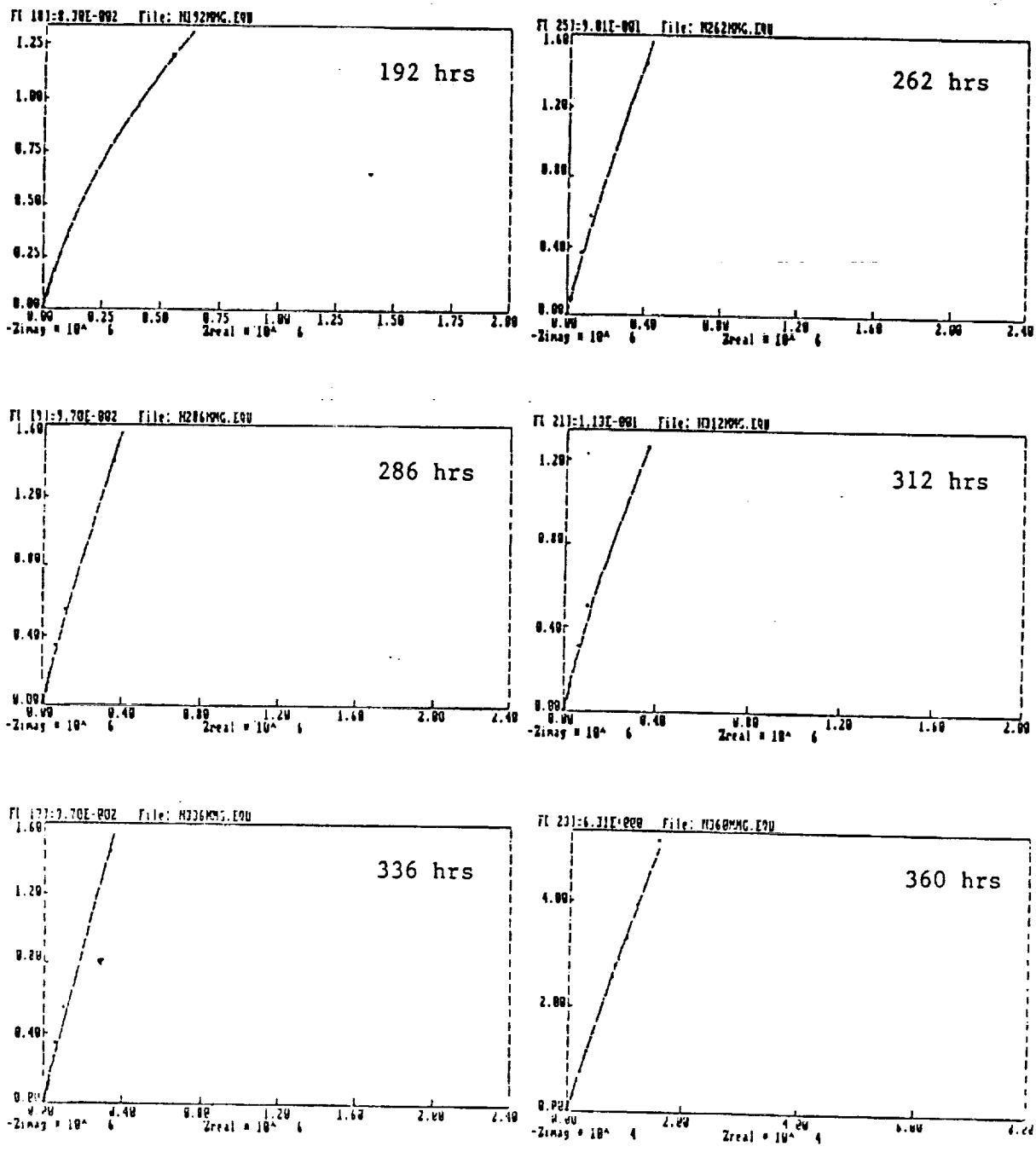

Figure 5 (Cont)

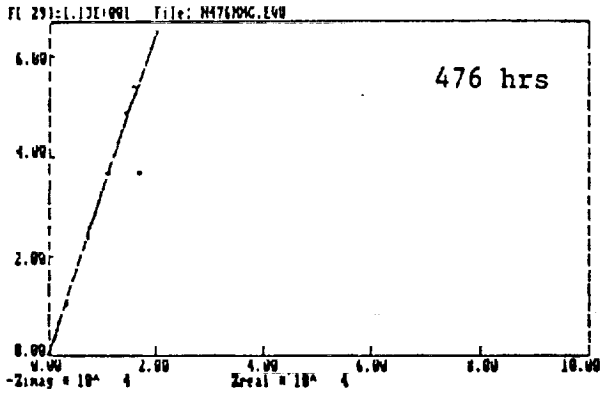

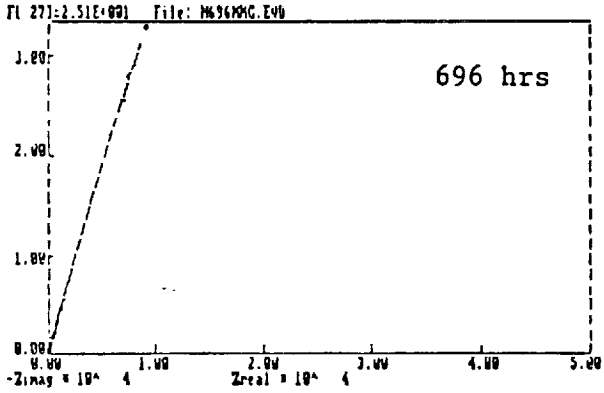

Figure 5 (Cont)

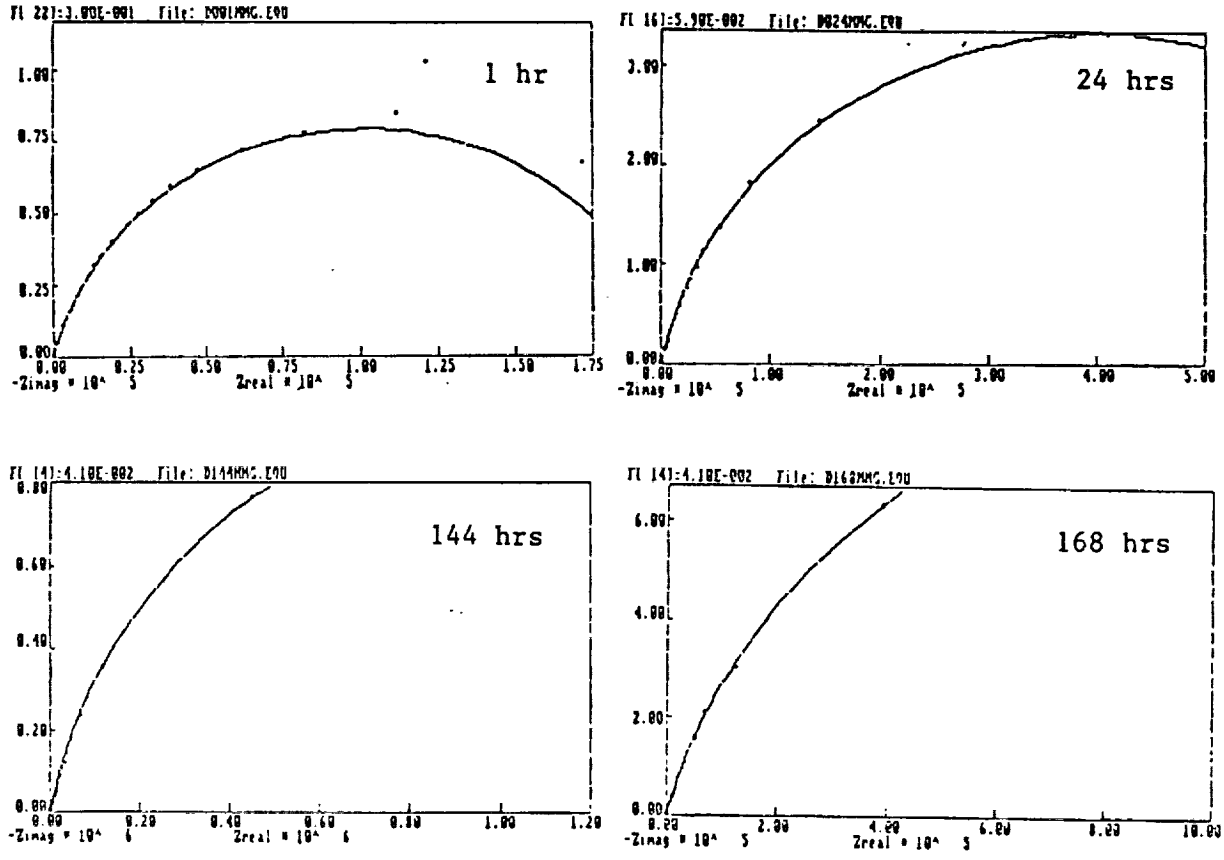

Figure 6 Niquist Plots for Hastelloy C-276 in 3.55% NaCl-0.1N HCl at Various Immersion Times

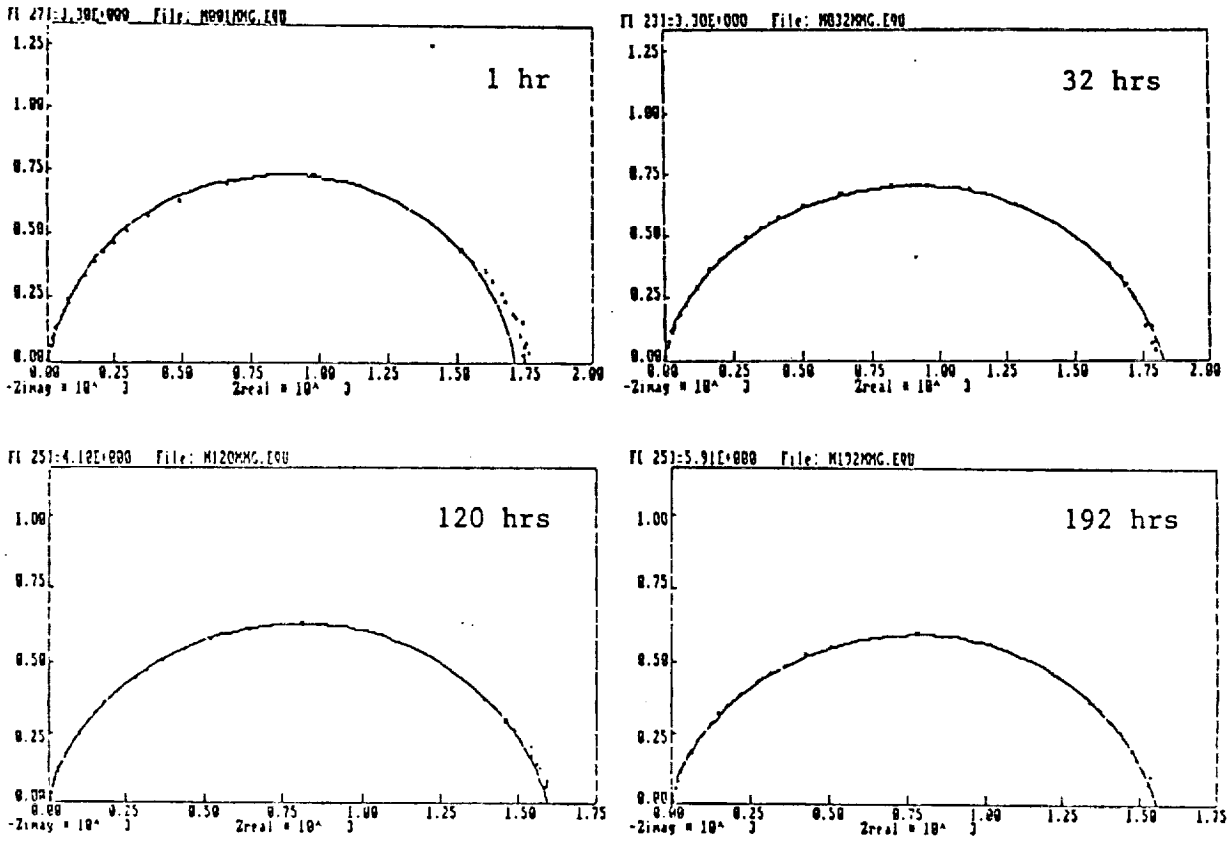

Figure 7 Nyquist Plots for Hastelloy B-2 in 3.55% NaCl-0.1N HCl at Various Immersion Times

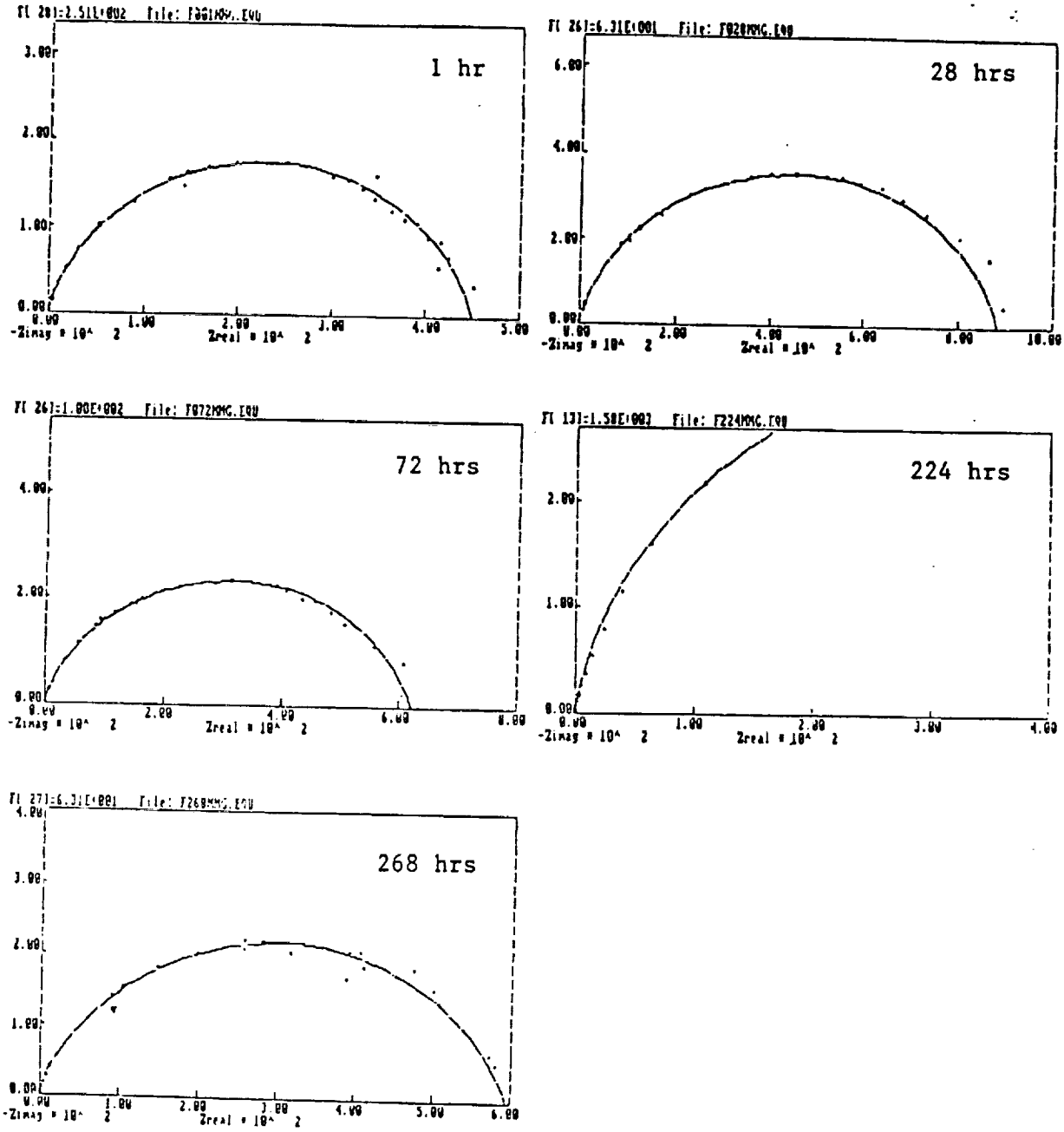

Figure 8 Nyquist Plots for Inconel 600 in 3.55% NaCl-0.1N HCl at Various Immersion Times

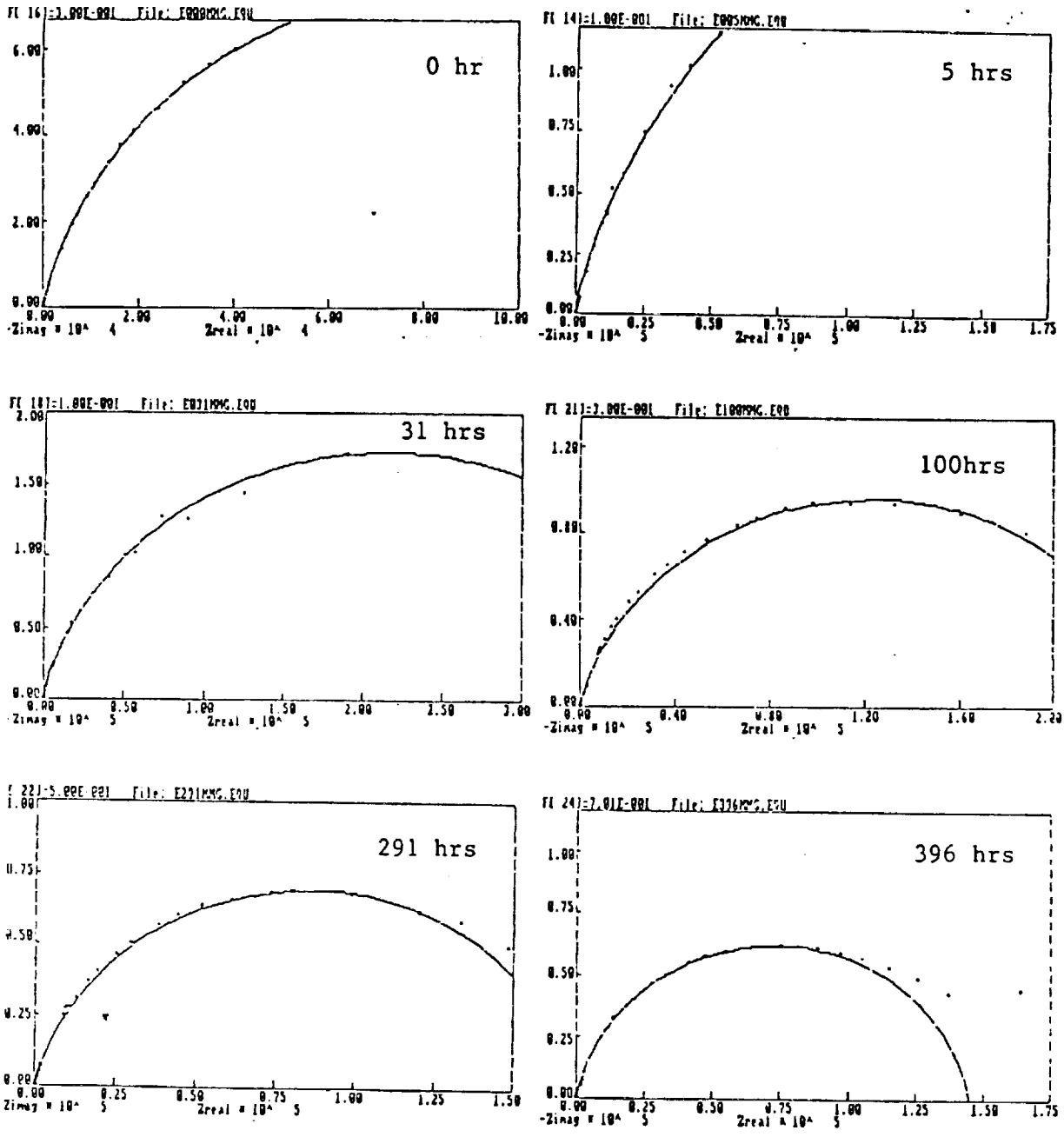

Figure 9 Nyquist Plots for Inconel 625 in 3.55% NaCl-0.1N HCl at Various Immersion Times

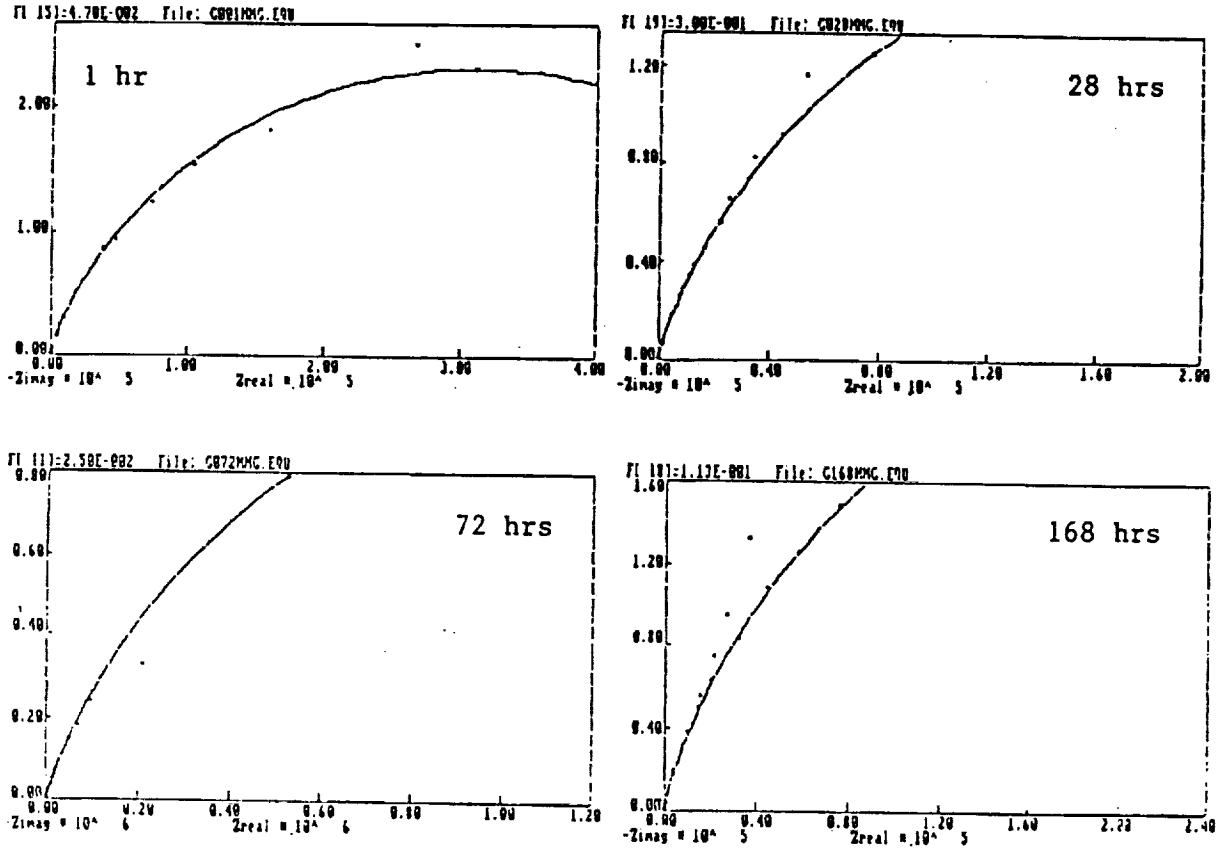

Figure 10 Nyquist Plots for Inconel 825 in 3.55% NaCl-0.1N HCl at Various Immersion Times

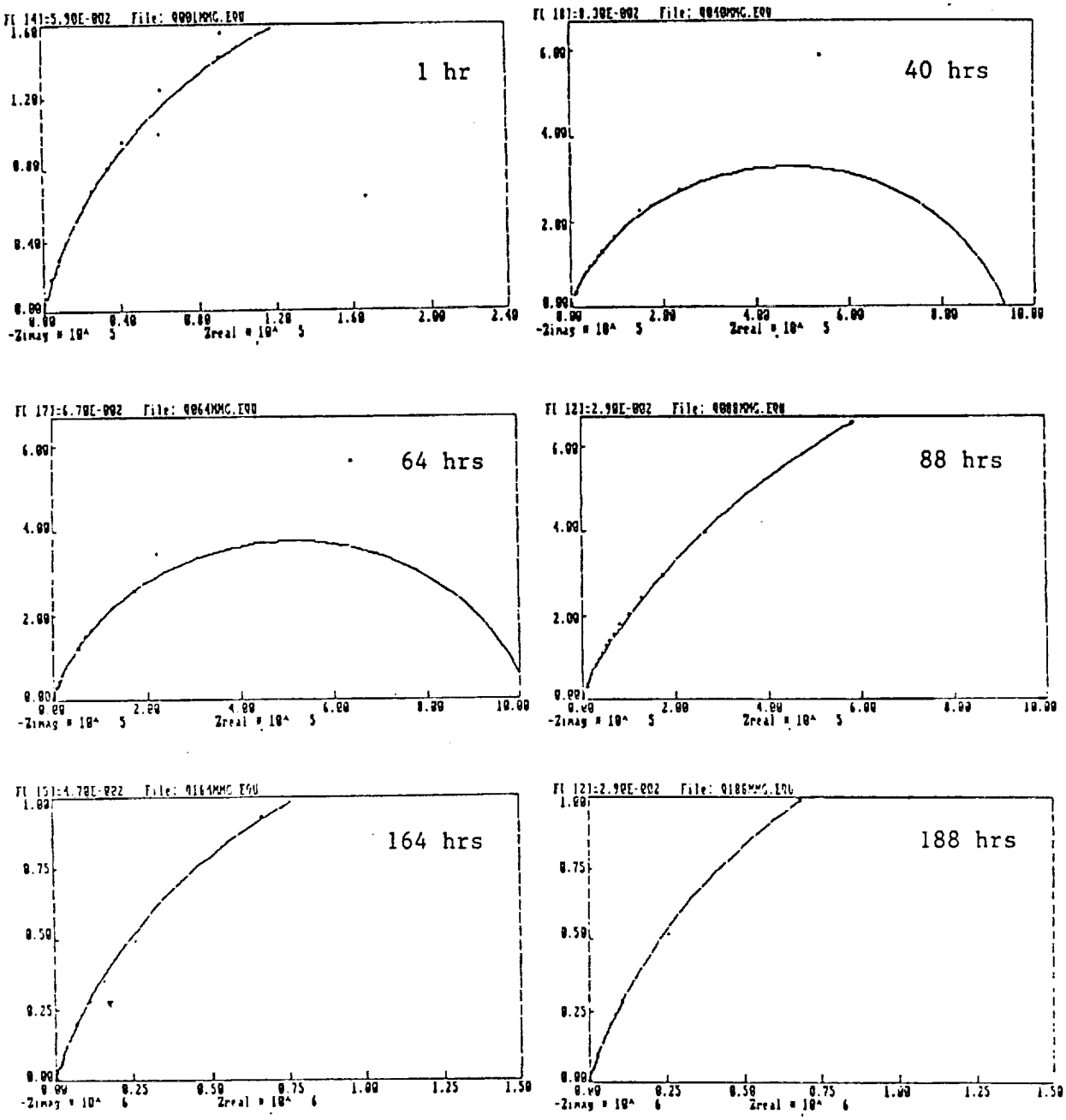

Figure 11 Nyquist Plots for Inco G-3 in 3.55% NaCl-0.1N HCl at Various Immersion Times

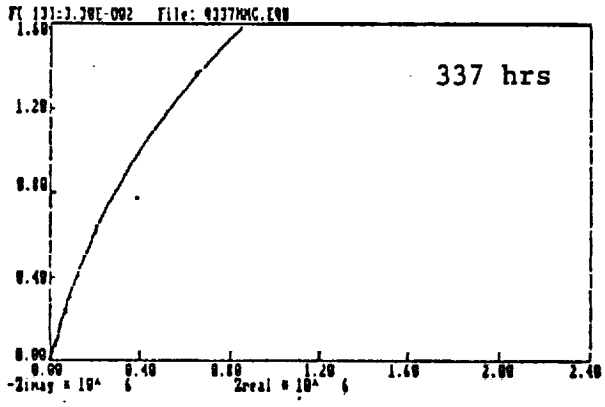

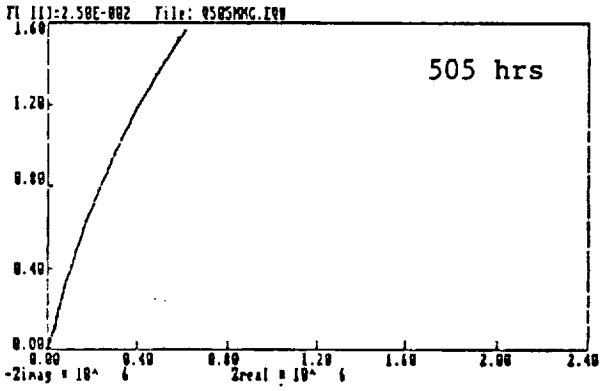

Figure 11 (Cont)

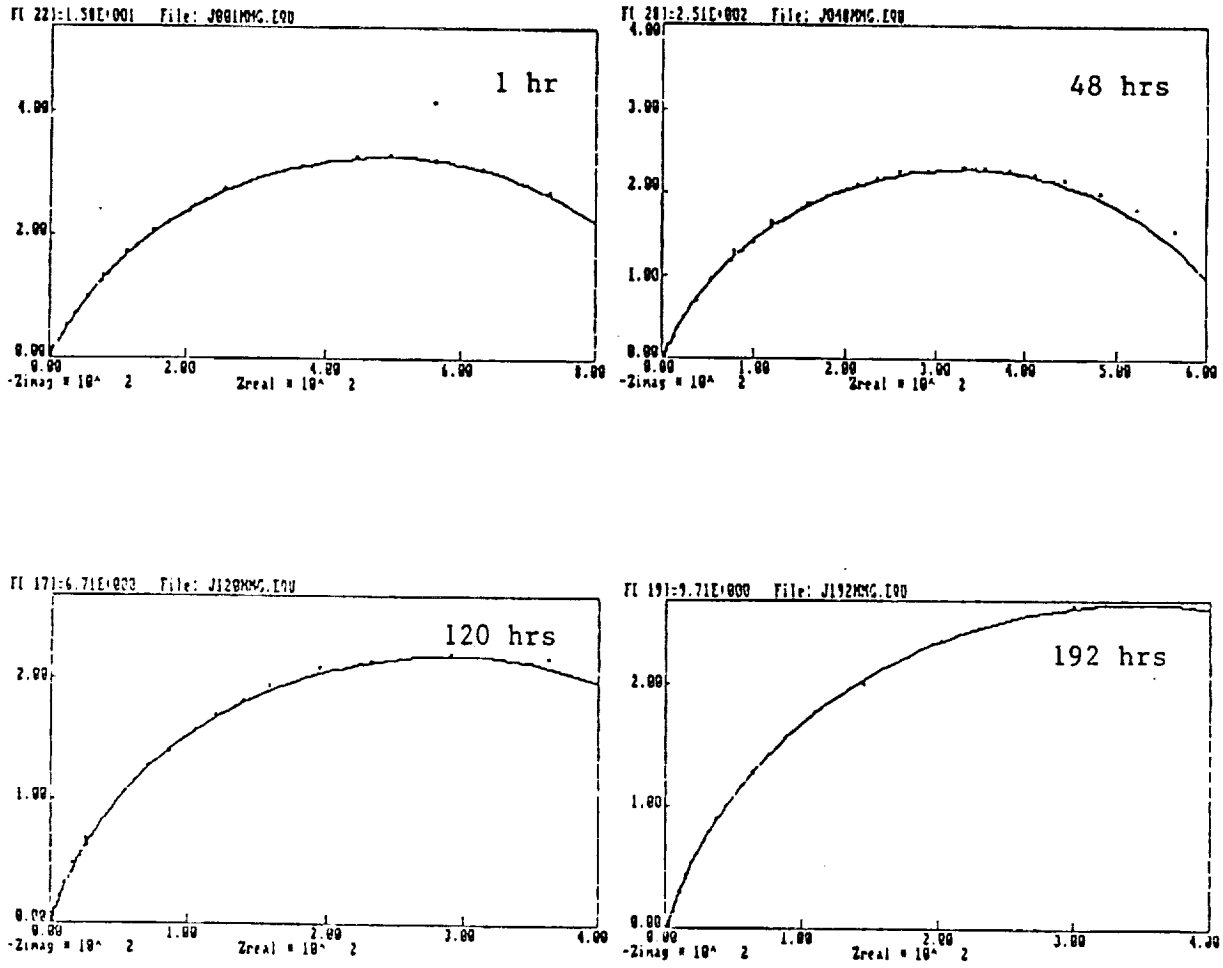

Figure 12 Nyquist Plots for Monel 400 in 3.55% NaCl-0.1N HCl at Various Immersion Times

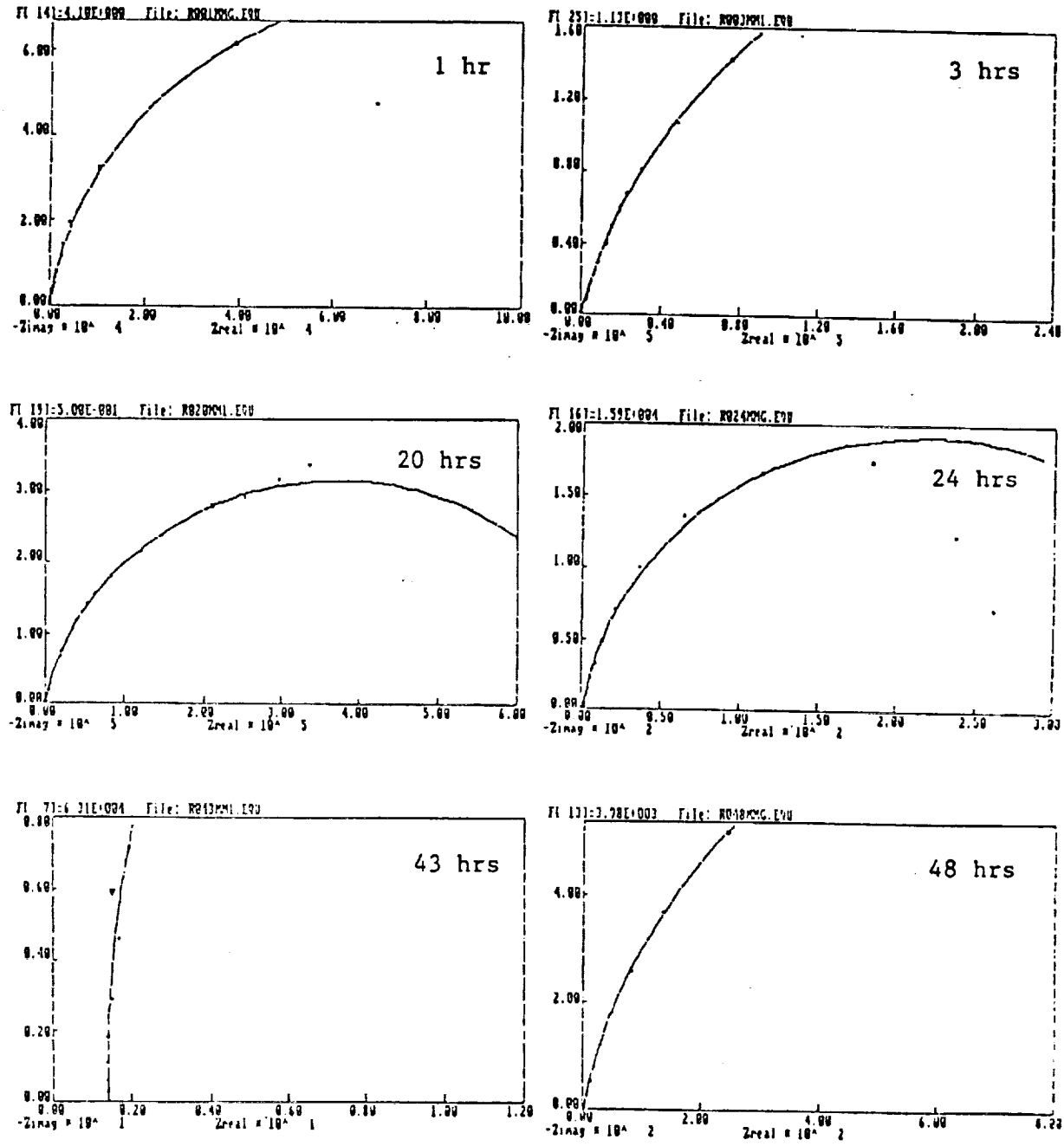

Figure 13 Nyquist Plots for Zirconium 702 in 3.55% NaCl-0.1N HCl in Various Immersion Times

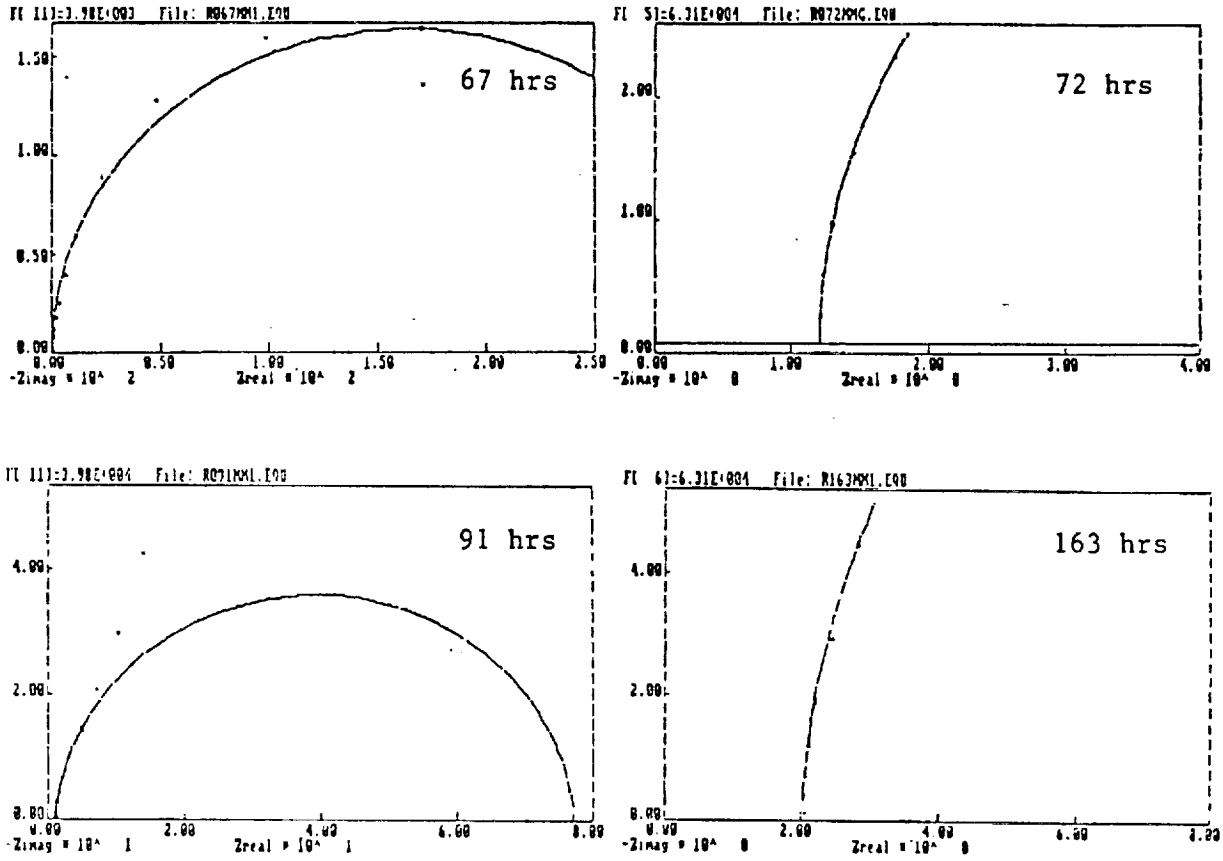

Figure 13 (Cont)

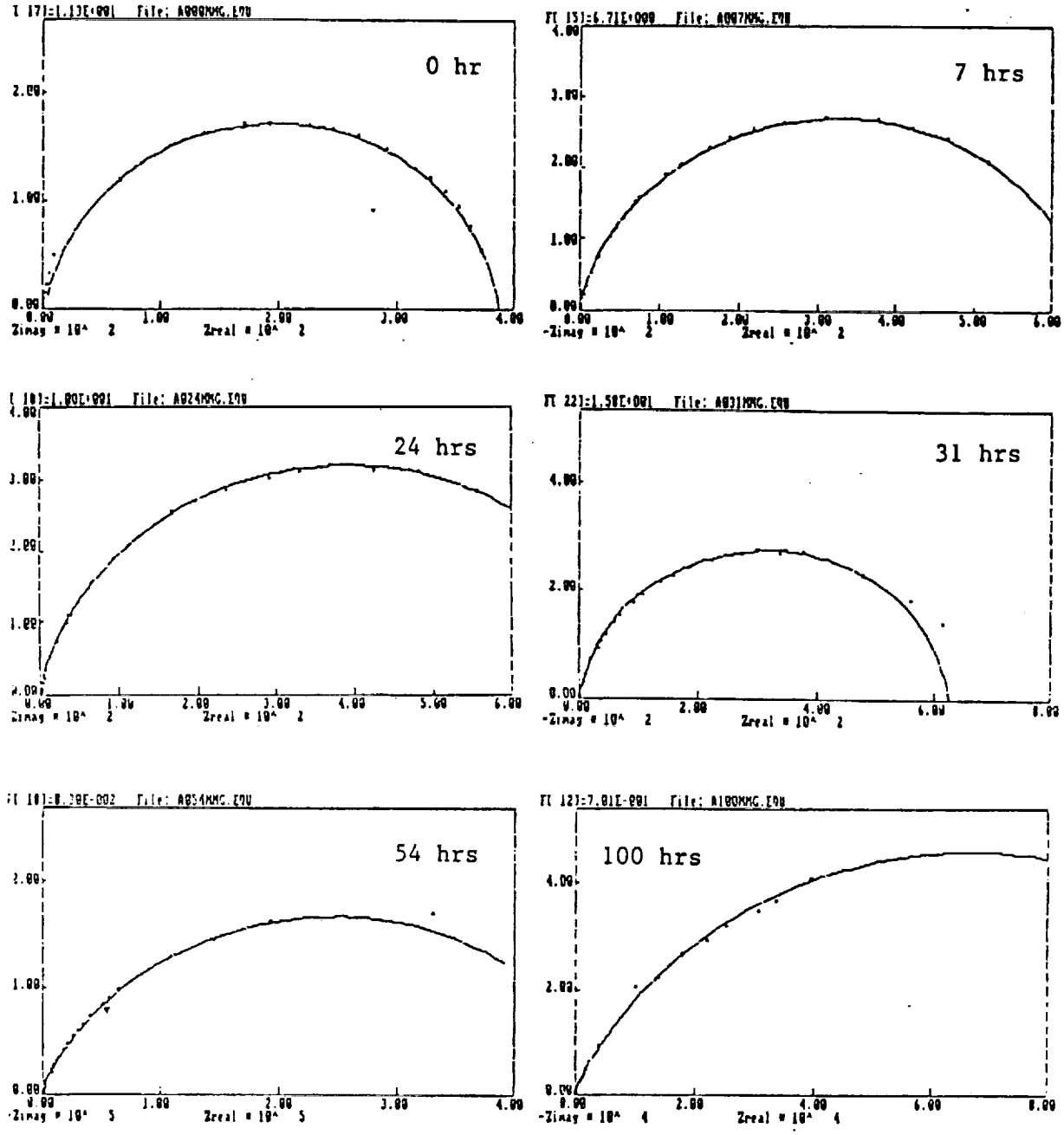

Figure 14 Nyquist Plots for SS 304L in 3.55% NaCl-0.1N HCl at Various Immersion Times

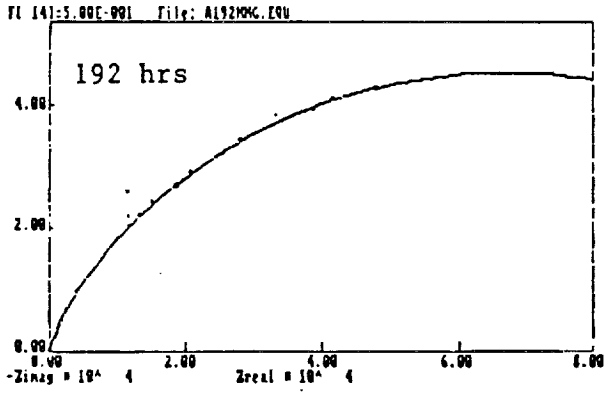

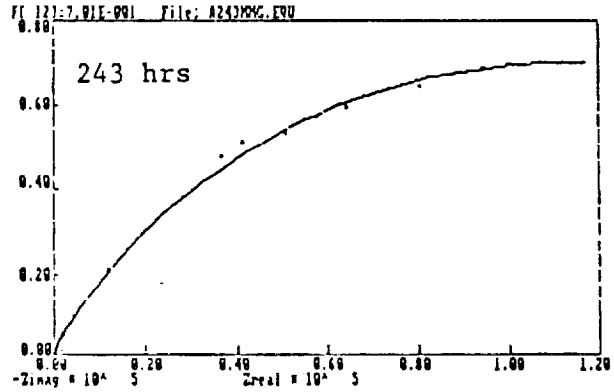

Figure 14 (Cont)

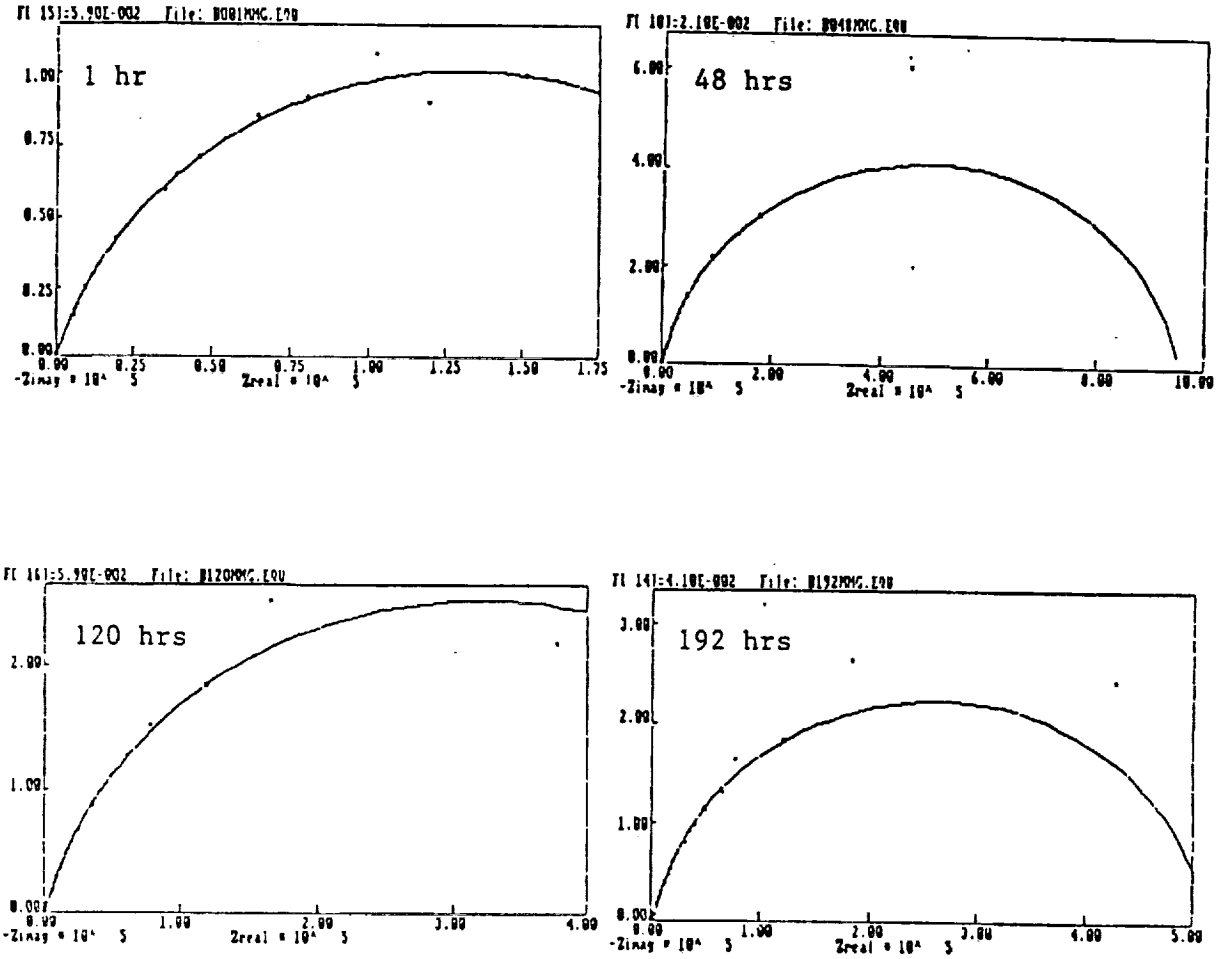

Figure 15 Nyquist Plots for SS 316L in 3.55% NaCl-0.1N HCl at Various Immersion Times

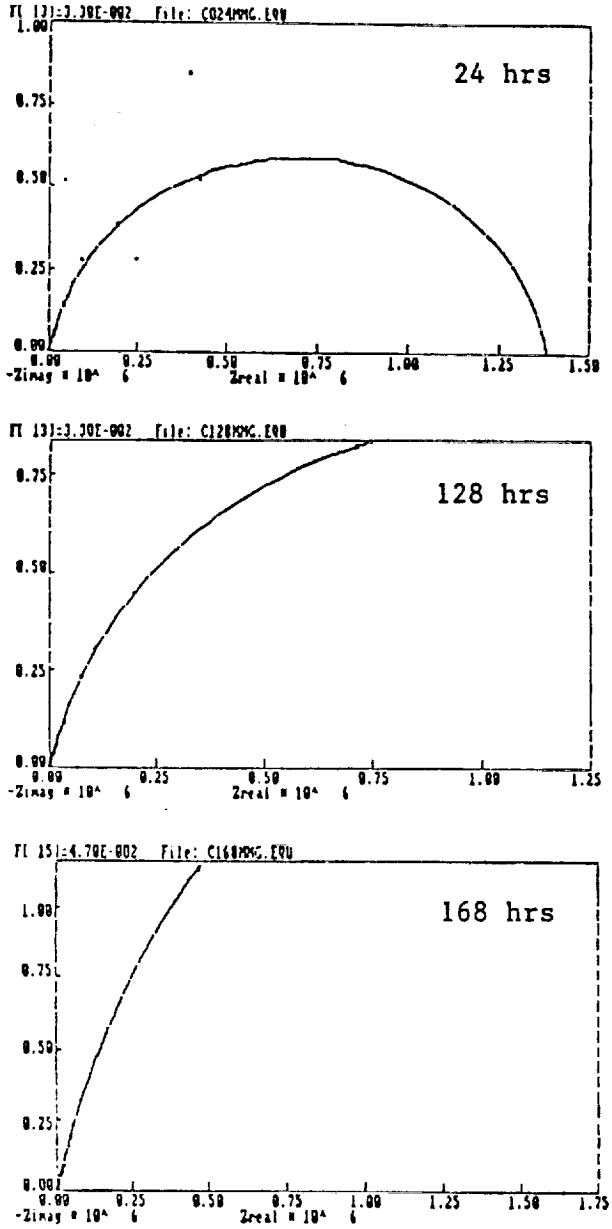

Figure 16 Nyquist Plots for SS 317L in 3.55% NaCl-0.1N HCl at Various Immersion Times

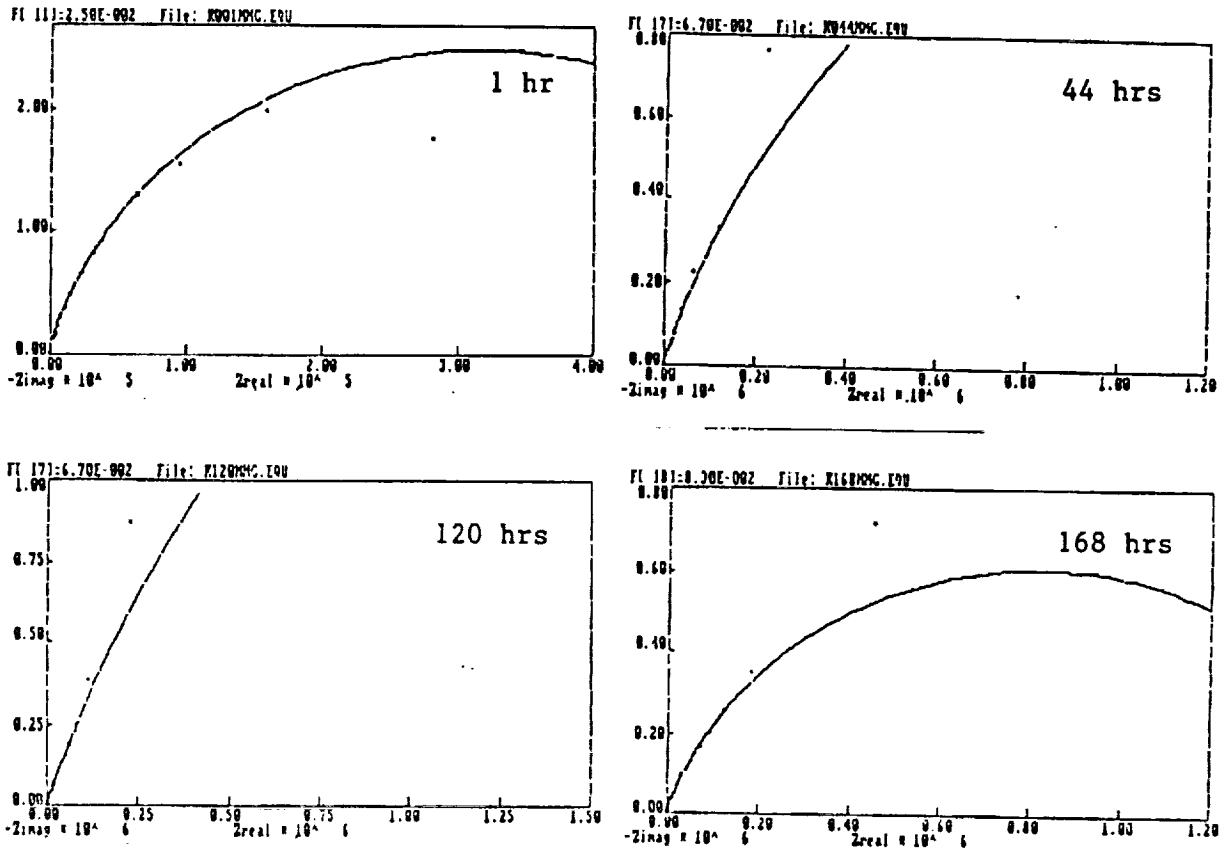

Figure 17 Nyquist Plots for SS 904L in 3.55% NaCl-0.1N HCl at Various Immersion Times

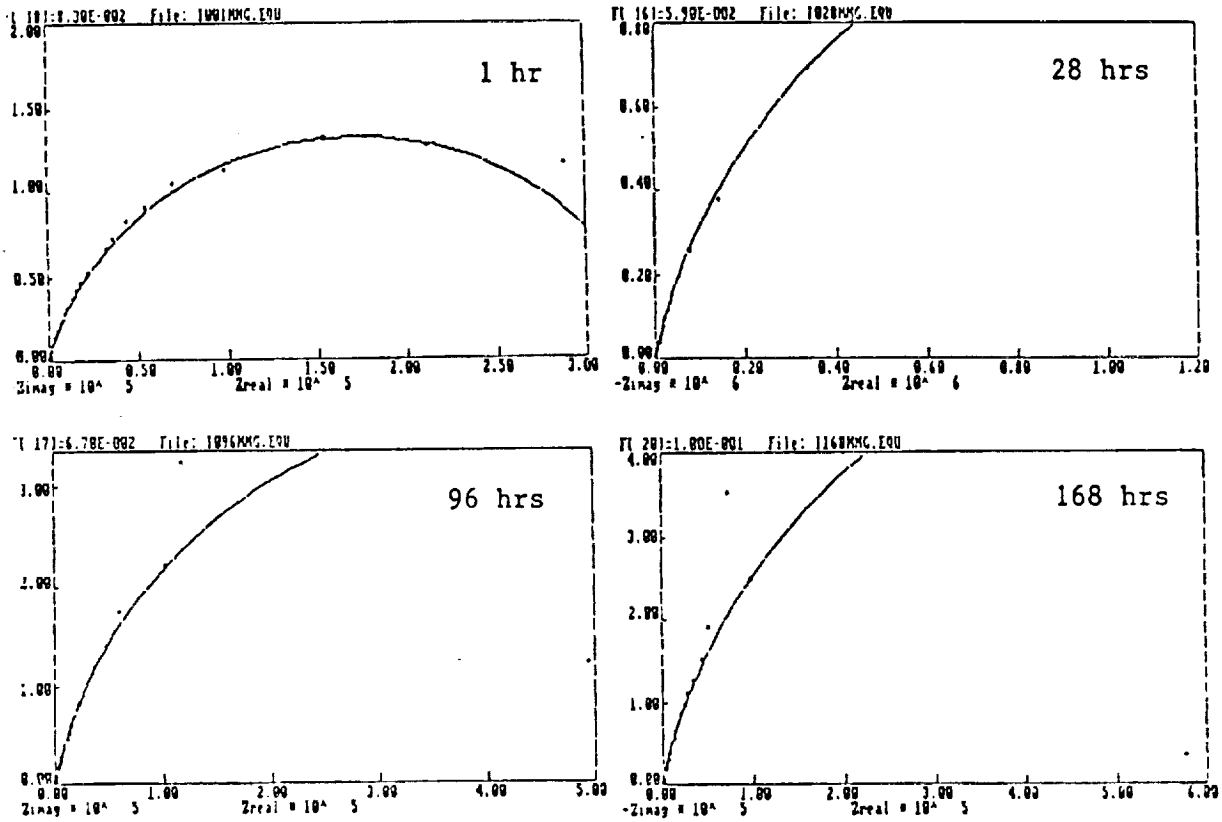

Figure 18 Nyquist Plots for 20 Cb-3 in 3.55% NaCl-0.1N HCl in Various Immersion Times

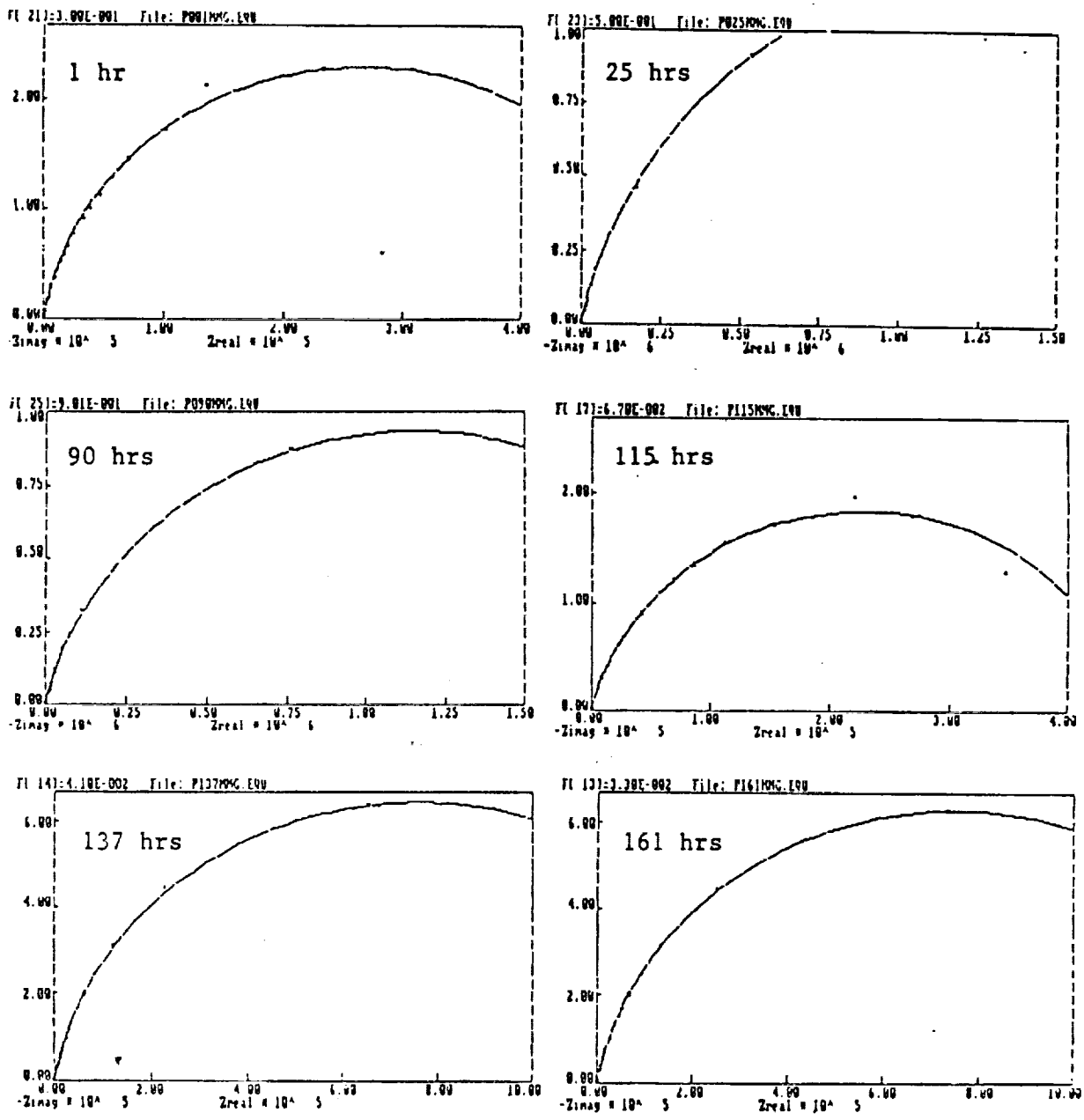

Figure 19 Nyquist Plots for 7 Mo + N in 3.55% NaCl-0.1N HCl at Various Immersion Times

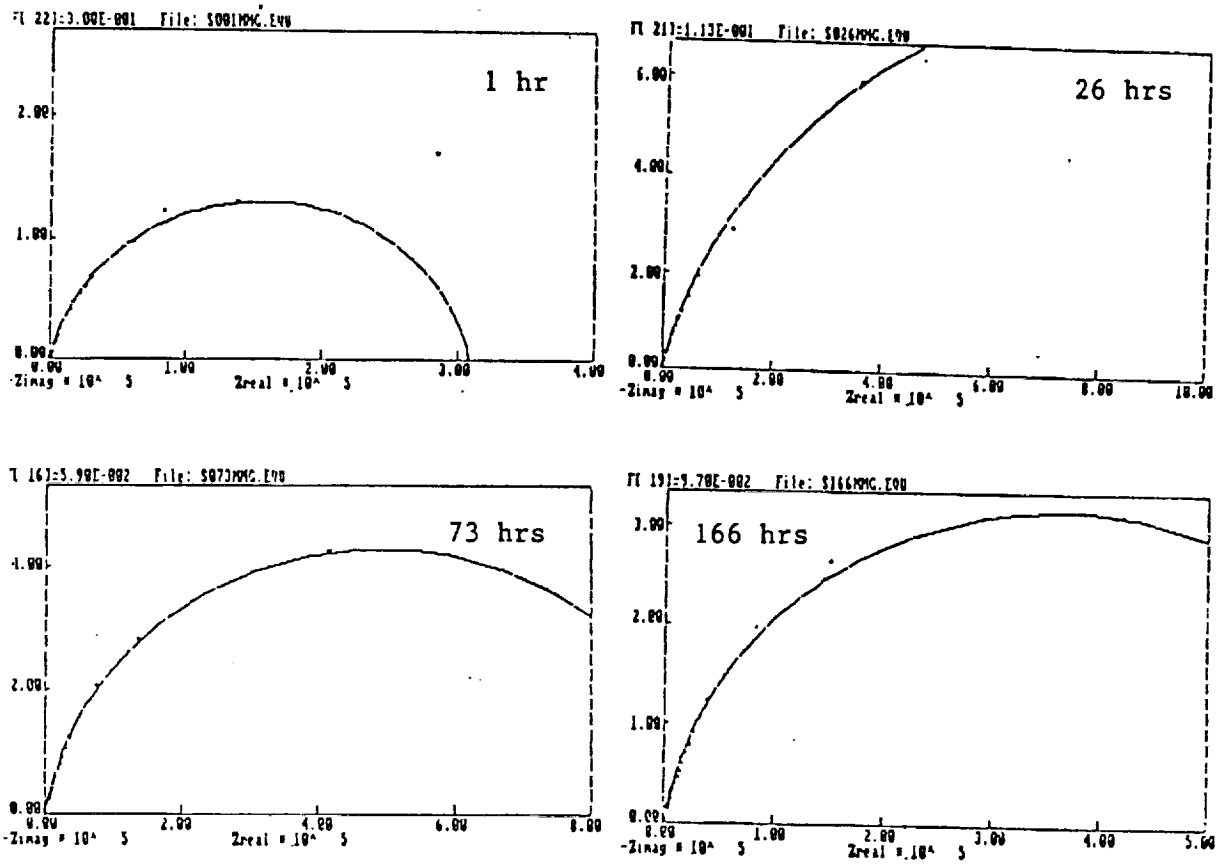

Figure 20 Nyquist Plots for ES-2205 in 3.55% NaCl-0.1N HCl at Various Immersion Times

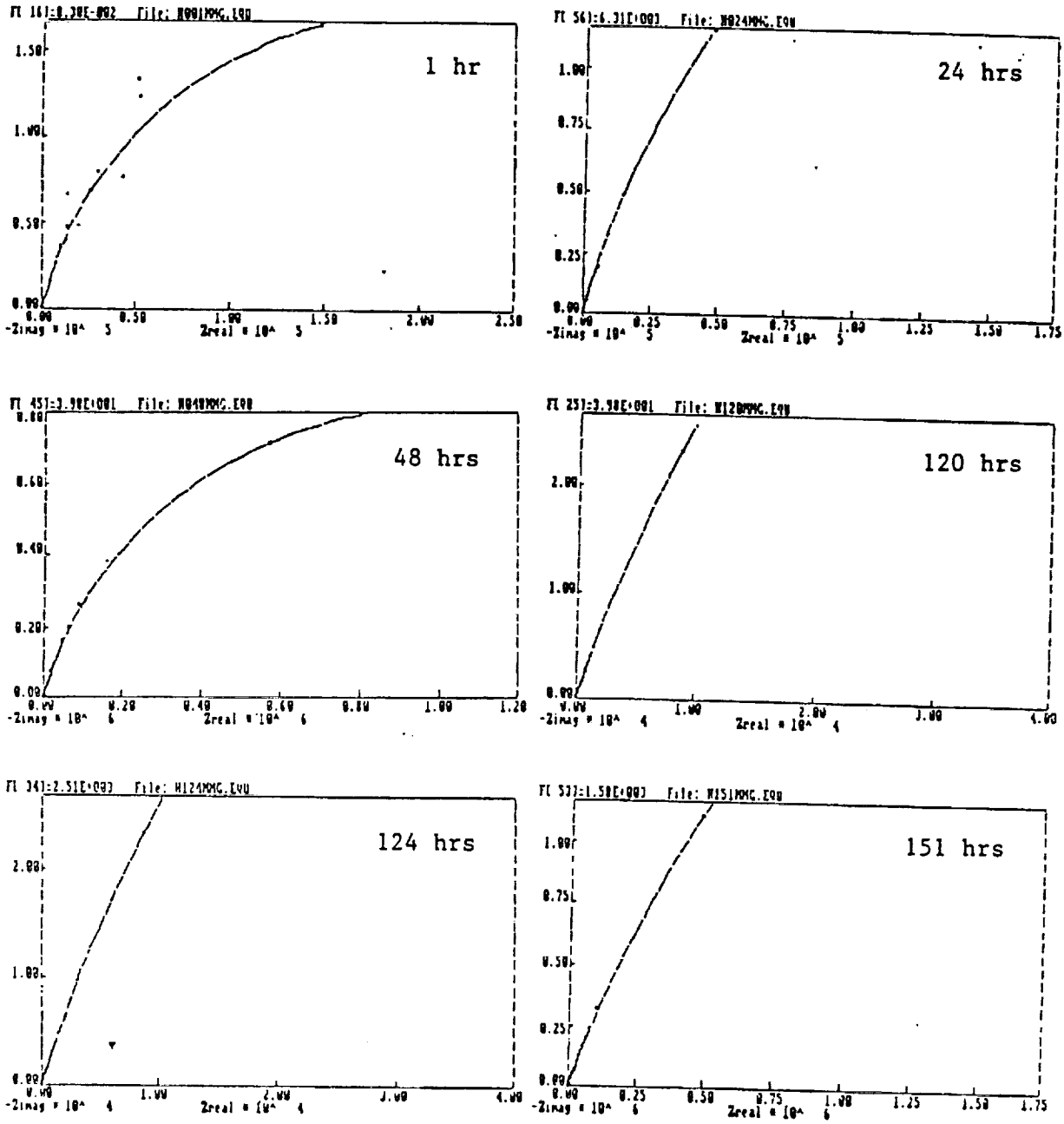

Figure 21 Nyquist Plots for Ferralium 255 in 3.55% NaCl-0.1N HCl in Various Immersion Times

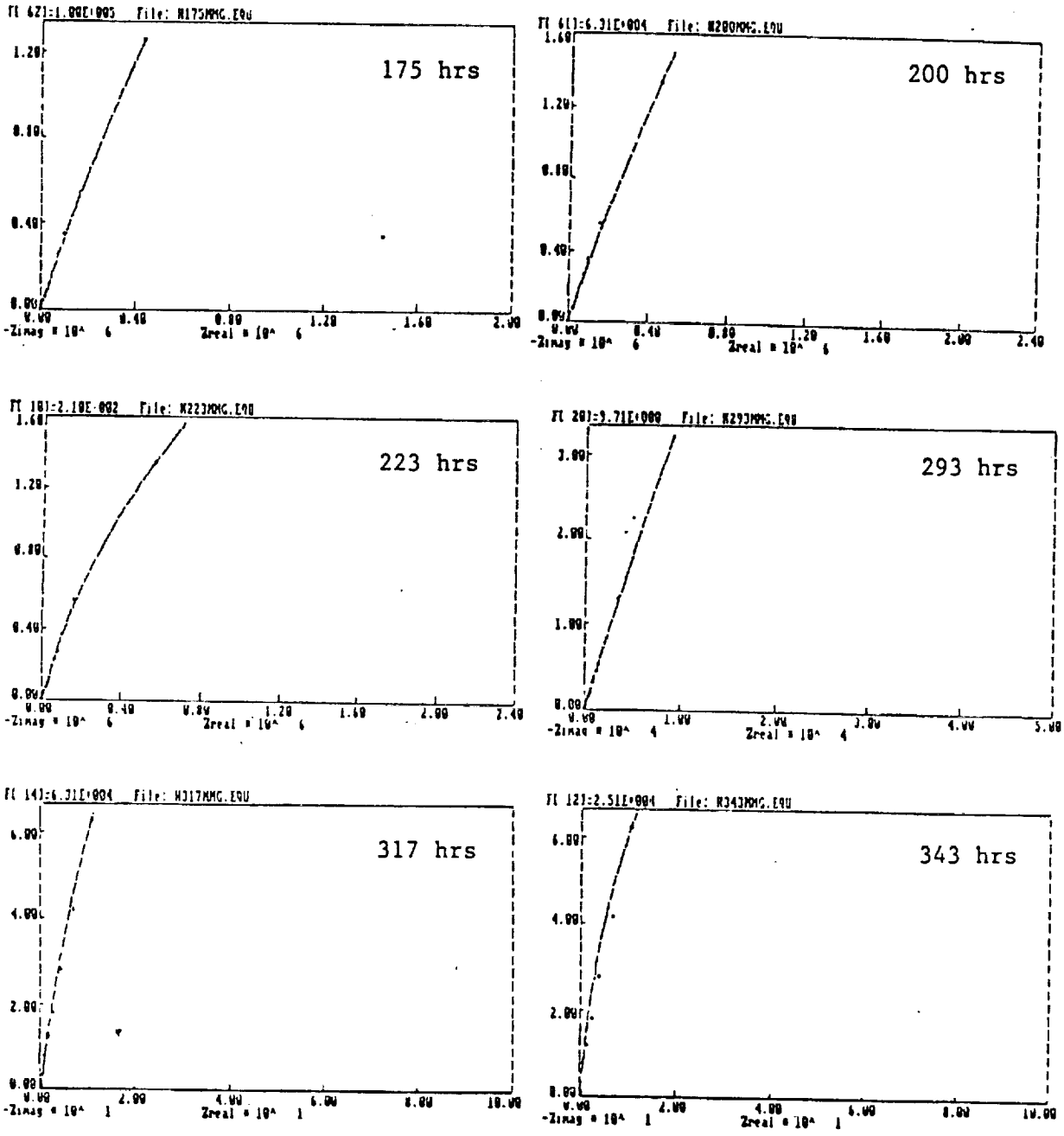

Figure 21 (Cont)

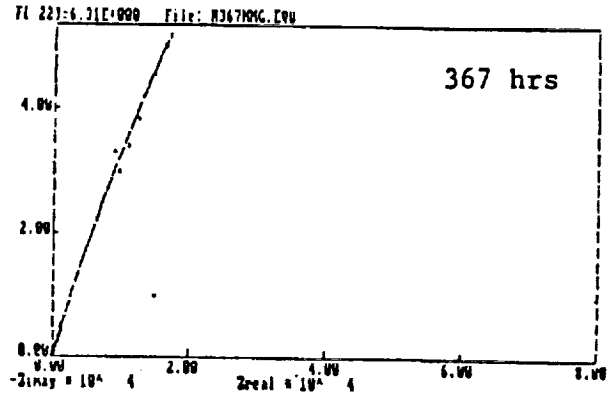

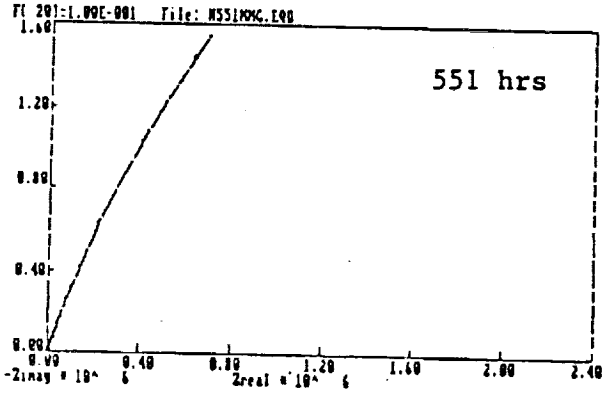

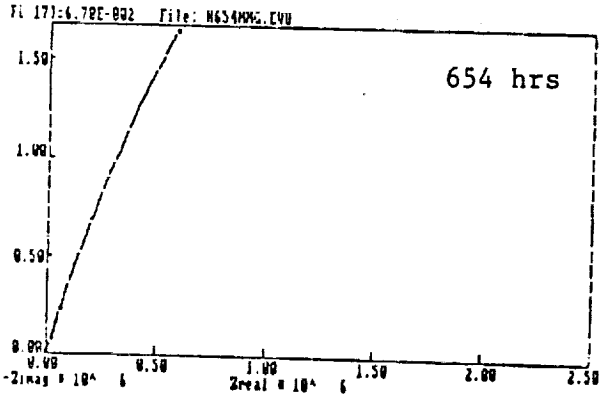

Figure 21 (Cont)

p. 27

1990 NASA/ASEE SUMMER FACULTY FELLOWSHIP PROGRAM

JOHN F. KENNEDY SPACE CENTER
UNIVERSITY OF CENTRAL FLORIDA

CARBON DIOXIDE AND WATER EXCHANGE OF A SOYBEAN STAND GROWN IN THE BIOMASS PRODUCTION CHAMBER

PREPARED BY:	Dr. Kenneth A. Corey
ACADEMIC RANK:	Associate Professor
UNIVERSITY AND DEPARTMENT:	University of Massachusetts Department of Plant & Soil Sciences
NASA/KSC	
DIVISION:	Biomedical Operations and Research
BRANCH:	Life Sciences Research Office
NASA COLLEAGUE:	Mr. John Sager
DATE:	August 3, 1990
CONTRACT NUMBER:	University of Central Florida NASA-NGT-60002 Supplement: 4

ACKNOWLEDGEMENTS

Participation in a second year of the NASA/ASEE Summer Faculty Fellowship Program was a great privilege. It is not possible to identify and thank everyone that contributed to the planning, design, execution, and maintenance of the biomass production chamber which served as the experimental tool over the past 2 summers. To all those individuals who have played a role in work on the BPC I extend thanks. There are several individuals who must be acknowledged for their direct contributions to my project. First, I am most grateful to my working colleague, Dr. Raymond M. Wheeler who established most of the protocol for BPC whole crop physiology experiments. For her careful, rapid, and always cheerful attitude in assisting me with data distillation and other research activities, I thank Ms. Gayle M. Volk, who truly was my personal super number cruncher. To my NASA colleague, Dr. John C. Sager, I extend thanks for the fellowship opportunity and many stimulating "armchair" discussions (i.e. the Sagerian dialectic). Finally, a hearty thanks goes to Dr. Loren A. Anderson, Dr. Mark A. Beymer, and Ms. Kari Baird for their smooth administration of the program.

ABSTRACT

Soybean (Glycine max l. Merr. cv. McCall) plants were grown under metal halide lamps in NASA's Biomass Production Chamber. Experiments were conducted to determine whole stand rates of carbon dioxide exchange and transpiration as influenced by time of day, CO_2 conc, irradiance, and temperature. Plants were grown at a population of 24 plants/m^2, a daily cycle of 12 hour light/12 hour dark, an average temperature regime of 26 C light/20 C dark, and a CO_2 conc enriched and maintained at 1000 ppm during the photoperiod.

A distinct diurnal pattern in the rate of stand transpiration was measured at both ambient and enriched (1000 ppm) conc of CO_2. Transpiration rates declined during the photoperiod, dropped to about 30 % of maximum in the dark, and then increased during the dark period. Water loss increased by a factor of 1.2 when CO_2 was reduced to the ambient level (about 370 ppm). No distinct diurnal rhythm in CER was measured suggesting that rates of NP obtained from early photoperiod drawdowns of CO_2 are representative for characerizing carbon assimilation during growth and development of a soybean stand. Carbon dioxide did not saturate photosynthesis in the range of conc used (up to 1200 ppm). Whole stand CCP values of 66 and 85 ppm were measured at 2 developmental stages.

CER increased linearly with increasing irradiance up to the maximum attainable with the MH lamp source (500 to 550 umol/m^2/s). LCP values for the whole stand were in the range of 76 to 105 umol/m^2/s; an increase occurring with increased stand age presumably attributable to an increased background rate of respiration. Temperature had marked effects on stand CER and transpiration rates. NP increased with temperature from 22 to 26 C but then decreased when the temperature was set at 30 C. DPR increased with increasing temperature. Net carbon assimilation was highest when temperature regimes of 26 C light/18 C dark or 22 C light/22 C dark were used. Water flux increased with increasing VPD, the driving force governed by the saturation vapor pressure of the intercellular leaf spaces.

Data generated in this study represent true whole stand responses to key developmental and environmental variables and will be valuable in database construction for future working CELSS. Crop growth studies in the BPC have been conducted with a high degree of environmental control, gas tightness during growth, and have used large plant stands. These characteristics have placed it in a unique position internationally as a research tool and as a pre-prototype subcomponent to a fully integrated CELSS.

TABLE OF CONTENTS

LIST OF ILLUSTRATIONS

LIST OF ABBREVIATIONS AND ACRONYMS

BPC	Biomass Production Chamber
CER	Carbon dioxide Exchange Rate
CCP	Carbon dioxide Compensation Point
CELSS	Controlled Ecological Life Support System
conc	concentration
DPR	Dark Period Respiration
HPS	High Pressure Sodium
LCP	Light Compensation Point
MH	Metal Halide
NA	Net Assimilation
NP	Net Photosynthesis
PAR	Photosynthetically Active Radiation
PPF	Photosynthetic Photon Flux
ppm	parts per million
RH	Relative Humidity
VPD	Vapor Pressure Deficit

I. INTRODUCTION

The Biomass Production Chamber (BPC) at NASA's Kennedy Space Center is currently a one-of-a-kind plant growth chamber being used as a pre-prototype to a controlled ecological life support system (CELSS). Economically important crop plants are being grown under the semi-closed conditions of the BPC in order to test growth responses to the unique designs and environmental control subsystems developed for the chamber (1,2,3,4). Thus far, complete production grow-outs of wheat (Triticum aestivum), leaf lettuce (Lactuca sativus), and soybean (Glycine max L. Merr.) have been conducted in the BPC.

In comparison to studies in conventional growth chambers, the high degree of environmental control and the large size of the enclosed plant stand combine to provide the BPC with the advantage of a well-integrated sample (5). The BPC has been designed and constructed to be operated as a closed, nearly gas-tight system which enables real time measurements of changes in gas composition throughout growth and development. As a large cuvette, the BPC is extremely "tight"; leak rates in the presence of partial pressure gradients of carbon dioxide have been measured to be in the range of 0.08 to 0.42 % per hour (2; Drese 1989, unpublished data). Such leak rates would have negligible effects on short term determinations of gas exchange rates, particularly those involving the monitoring of changes in atmospheric gas concentrations as influenced by environmental variables.

Rather than relying upon numerous instantaneous measurements of single leaf or single plant measurements to estimate large stand responses, very rapid and reliable rate determinations can be made directly on entire stands. Whole stand measurements avoid the disadvantage of selecting representative sample locations on individual plants for instantaneous rate measurements. The degree of closure of the BPC which has increased for each successive growout conducted is also important for evaluating the performance of crop plants in an environment where trace gas emissions such as ethylene may build up to levels which affect growth and development.

Previous work with wheat (4,5) and soybean (Wheeler, unpublished) has demonstrated that carbon dioxide exchange rates of whole stands are comparable to those obtained from single leaf measurements. With the ratio of plant material to chamber volume and planting configurations used for BPC crop growth experiments, the plant stand responds similarly to single leaves. A notable exception is the light compensation point. Whole stands

typically have light compensation points which are 3 to 5 fold higher than those determined on single leaves (5,6,7).

In this study, a second complete growth and development dataset with soybean as a test crop will be constructed with emphasis on whole stand gas exchange. In the first growout, high pressure sodium lamps were used. The second study will utilize metal halide lamps which provide for lower irradiance but increased spectral emmission in the 400 to 500 nm waveband. The study will thus enable a comparison of growth and yield components under the two light sources.

Specific objectives of this study were to determine the rates of gas exchange (CO_2, O_2, and H_2O) of a soybean stand in response to stage of development, light, CO_2 concentration, and temperature under the semi-closed conditions of the BPC.

II. MATERIALS AND METHODS

2.1 PRODUCTION DETAILS

On May 5, 1990 soybean (cultivar McCall) seed imbibed for 24 hours in a 2.5 mM $Ca(NO_3)_2$ solution were sown in the BPC at the rate of 12 seeds per 0.25 m^2 tray and later thinned to provide a stand of 6 plants/tray or 24 plants/m^2. Environmental conditions in the BPC were as follows: a 12 hour light/12 hour dark daily regime was used, light was provided with metal halide lamps, temperature was set at 26 C for the first 2 days and then a light/dark regime of 26/20 was used after 2 days except when temperature was used as an experimental variable, relative humidity was maintained at 85 % for the first 4 days after planting and then at 65 to 70 % for the remainder of growth, and carbon dioxide concentration was maintained at a setpoint of 1000 ppm during the photoperiod following drawdown to that concentration after the dark respiration period.

As a second growout of soybean in the BPC, most other cultural practices and conditions were the same as the first except that high pressure sodium vapor (HPS) lamps were used in the first. The metal halide (MH) lamps used in this study provided for a lower irradiance at full power (500 to 550 umol/m^2/s after 4 weeks growth) than the HPS lamps. At 100 % power to the lamps the output of the MH lamps in PAR was about 75 % of the HPS lamp output (Wheeler, unpublished data). However, the MH lamps provide considerably greater emissions in the blue waveband (400 to 500 nm) previously shown to reduce internode length and overall stem elongation of soybean (8).

Additional detail on production techniques including the composition of the nutrient solution, system configurations, and manipulations can be found in Wheeler et al. (9).

2.2 GAS EXCHANGE RATE CALCULATIONS

Rates of net photosynthesis (NP) and dark period respiration (DPR) were calculated daily by computing the slopes of the lines fit by linear regression from the changes in CO_2 concentration occurring in the BPC atmosphere following the transitions from lights on and off (Figure 1). Since the dark period respiration led to a CO_2 conc in excess of the 1000 ppm setpoint and no scrubbing device was used, it continued to increase throughout the entire 12 hour dark period. Data points from the first 15 to 30 minutes following a lights on or off transition were not used because there were concomitant changes in temperature which led to changes in the pressure of the BPC atmosphere. These pressure events were transient, but enough to cause mass flow of gases into or out of the BPC depending upon the direction of the total pressure gradient (into the BPC when temperature was decreased). For DPR rates, data from the remainder of the period was used and for NP rates data up to the first injection of CO_2 was used. Calculations were based on a chamber volume of 112,060 liters and a growth area of 20 m^2. Application of the ideal gas law was made to correct the volume for different temperatures used for light and dark periods and for temperature experiments.

Oxygen concentration in the BPC atmosphere was monitored with a S-3A Oxygen Analyzer (Ametek,Thermox Instruments Division, Pittsburgh, PA) which uses a solid oxide (stabilized zirconia) sensor cell. This sensor provides for readings to within +/- 0.02 % O_2. Since very small changes in oxygen were being measured in a large background concentration (i.e. 20.8 %), detection sensitivity was insufficient to be used for reliable short term rate calculations. However, trends were observable and are presented to show a typical diurnal pattern (Figure 1).

Transpiration rates were calculated by measuring the total volume of condensate collected over a given time interval. Rates are expressed in mmol $H_2O/m^2/s$.

2.3 DIURNAL GAS EXCHANGE RATES

Two experiments were conducted to determine if diurnal rhythms in the rates of CO_2 and H_2O exchange exist. For CER, rates from the dark period increase, beginning of photoperiod drawdown, and mass additions over 3-hour time increments were obtained. For transpiration rates, condensate tanks were emptied and the volume

of water measured at 3-hour intervals. The first experiment was conducted 50 days after planting. In the second experiment, the same measurements were made at two CO_2 conc. After the first day at the standard enriched level of 1000 ppm, CO_2 was brought down to the ambient conc (about 370 ppm) 2 hours prior to the dark period. Except for the early photoperiod drawdown following increases due to DPR, CO_2 was maintained at a setpoint of 350 ppm.

2.4 EFFECTS OF ENVIRONMENTAL VARIABLES ON GAS EXCHANGE RATES

2.4.1 EFFECT OF IRRADIANCE

On days 23, 33, and 54 irradiance from the MH lamps was varied to provide 5 levels and a dark treatment. Settings for dimming the light banks were made on the programmable logic controller and adjusted to provide for approximately uniform treatment for the range of irradiances used, since there was considerable variation in the actual output of individual lamps for a given dimming setting. At the start of the experiment, the conc of CO_2 in the BPC was raised to approximately 1600 ppm and each irradiance level maintained for 1-hour segments. Slopes of the changes in CO_2 versus time were obtained from 40-min segments in the middle of each 1-hour treatment. Actual irradiances incident at approximately the top of the canopy for each treatment were measured either immediately following the experiment or the day following the experiment with a sunfleck ceptometer (model SF-40, Decagon Devices Inc., Pullman, WA 99163). Irradiance was measured as a photosynthetic photon flux (PPF), i.e. in the photosynthetically active wavelength region of 400 to 700 nm. Irradiance was measured over each of the 64 growth trays at days 23 and 33. At 54 days, the canopy had developed to the extent that fencing was required for support. Small openings were made in the fencing for tray positions 2, 6, 10, and 14 at each level and incident PPF readings taken at the canopy top over the 4 trays on each level.

2.4.2 EFFECT OF CARBON DIOXIDE CONCENTRATION

On days 24 and 56, the automated control of the 1000 ppm CO_2 setpoint was manually overridden and the CO_2 conc allowed to drawdown to the compensation point. Almost the complete photoperiod was required to achieve this and just prior to the dark period, the CO_2 conc was raised back to the 1000 ppm setpoint. Carbon dioxide exchange rates were determined before, during, and after the drawdowns.

2.4.3 EFFECT OF TEMPERATURE

Temperature setpoints for the light/dark portions of the daily cycle were varied in two separate experiments to provide for 3 different temperatures for each half of the daily cycle. In the first experiment, the light/dark temperature regimes were as follows: 22/18 (day 35), 26/22 (day 36), and 30/26 (day 37). In the second experiment, the order was varied and light/dark regimes were 26/18, 22/22, 26/26, and 30/22 (days 41-44). All temperature and relative humidity readings logged during the different regimes were retrieved and averages across the 4 levels and all times calculated. The actual temperatures and relative humidity values were used to calculate a vapor pressure deficit (VPD) which is the water vapor gradient between the intercellular spaces of the leaf and the BPC atmosphere. The intercellular spaces were assumed to be at saturation. Therefore, the VPD was calculated as the difference between the saturation vapor pressure at a given temperature and the actual vapor pressure (obtained from the product of the relative humidity and the saturation vapor pressure).

III. RESULTS AND DISCUSSION

3.1 DIURNAL GAS EXCHANGE RATES

The CO_2 exchange rate during the photoperiod 50 days after planting was between 25 and 30 umol/m^2/s (Figure 2). The first point was acquired from early photoperiod CO_2 drawdown data while the subsequent 3 points were calculated from mass additions of CO_2. In general, photosynthetic rates calculated from mass additions were 1.12 (standard deviation=0.22; N=47) times higher than those calculated from the drawdowns. It was not determined whether the CER data in Figure 2 is attributable to a distinct diurnal rhythm or if in fact there are inherent differences in the values obtained by the different calculation methods. The mass flow method of calculation should provide a slight overestimate of NP due to the chamber leak rate, but not to the extent of 0.12. Evidence for a diurnal rhythm in stomatal conductance has been obtained (10) and in this experiment there was a distinct decrease in the quantity of condensate collected during the photoperiod, suggesting that stomatal conductance decreases toward the end of the day. However, this daily pattern in stomatal conductance may not affect the CER.

During the dark period, the respiration rate remained relatively constant, but there was a distinct increase in the transpiration rate. Initially, the transpiration rate in the dark was about

one-third of that which occurred at the beginning of the photoperiod. Nevertheless, this represents a substantial rate of water loss during a period when most plants under field conditions have greatly diminished stomatal conductances (7). The data suggest a fairly clear diurnal pattern of transpiration presumably controlled by a rhythm in the degree of stomatal aperture. There does not, however, appear to be as much of an effect of this rhythm on CER, which is in agreement with previous findings in a growth chamber study (10).

Daily measurements of NP and DPR enabled a continuous tracking of gas exchange with growth and development (Figure 3). After 3 weeks from planting the stand was developed sufficiently to observe distinct patterns of CO_2 conc increases and decreases due to DPR and NP, respectively. The rate of NP increased from 15 umol/m^2/s at 3 weeks to about 25 umol/m^2/s after 4 weeks at which time it leveled off. Following pod set and during the early stages of pod fill, the rate of NP declined slowly (after 50 days). The rate of DPR also increased early in development, but not to as great an extent as the rate of NP. Since each portion of the daily cycle was 12 hours in duration, the net assimilation of CO_2 was simply calculated by difference. The lack of smoothness in the data is explained by light, CO_2 drawdown, and temperature experiments conducted at various times throughout development. Following the collection of a complete data set through harvest, the data will be processed to develop a carbon mass budget and to determine if net assimilation can be interpreted and used as a biomass predictor. In general, absolute values for CER determined on whole soybean stands and expressed on a m^2 basis compare within a factor of 1 to 2 of those measured on single leaves and plants (11,12,13).

3.2 IRRADIANCE

Within the range of irradiances tested (0 to 517 umol/m^2/s), CER was related linearly to PPF indicating that light was well below saturation for the stand density and temperatures used (Figure 4). The light compensation points (LCP) as with wheat stands (5) were substantially higher than those measured on single leaves. The LCP values in this study were less than those obtained from the previous growout with HPS lamps. Perhaps there is more efficient utilization of the PAR emitted from the MH lamp source due to differences in both intensity and spectral quality. Some plants have been shown to shift their LCP's in response to decreased irradiance as a part of an 'acclimitization' process (14).

A 36 % increase in the LCP occurred between day 33 and day 54. This may be attributed to a greater background respiration as measured in the dark. While DPR is not the same as respiration occurring in the light, it provides an estimate of the magnitude of CO_2 evolution in the light and does provide an explanation for the increase in LCP with increased stand age (see also Figure 3).

3.3 CARBON DIOXIDE

A total photosynthetic drawdown of CO_2 preceded and followed by DPR increases 24 days after planting is illustrated in Figure 5. Prior to the drawdown, DPR was relatively constant throughout the 12 hours. Following the drawdown DPR was considerably less than that which occurred before the drawdown and a change in slope occurred during the last one-third of the dark period. The rate of DPR before the drawdown was 1.73 times the rate following the drawdown, suggesting that the available pool of carbohydrate was depleted by bringing the CO_2 conc down to near the compensation point (about 66 ppm). The increase in DPR during the latter stages of the dark period was suggestive of a mobilization/metabolism of reserves.

When the same experiment was conducted 56 days after planting the ratio of DPR rates before and after the drawdown was only 1.26. At this stage of development, the absolute DPR rates were 1.5 to 2 times higher than at 24 days. The question is why the stand did not appear to be as carbohydrate depleted by the CO_2 drawdown later in development. Perhaps at this stage of development, the soybean plants are exporting carbohydrate from the leaves to developing pods and converting it into storage compounds (i.e. protein and lipids) at a rapid rate, developing pods contribute more to stand respiration than the leaves, and low free carbohydrate pools affect the rate of pod respiration very little.

Data obtained from the CO_2 drawdowns also enabled the calculation of CER as a function of CO_2 conc. Data at approximately 30 minute intervals were extracted from the entire drawdown data set and slopes calculated between adjacent time points and converted into rates of NP. Data from the day 24 and 56 drawdowns are illustrated in Figure 6. Carbon dioxide compensation points for the 2 drawdowns were about 66 and 85 ppm, respectively. These values are somewhat higher than the CCP measured for wheat (5) and those reported for other C-3 plants (6,7). In the BPC, there is a high rate of air movement (about 4 chamber exchanges/min) and therefore development of boundary layers of gases is probably minimal except deep within a dense canopy. Perhaps the lag in CO_2 diffusion from the root mass resulting from respiratory

activity through the tray covers led to higher CCP values for a whole stand than those measured on leaves or single plants.

In the range of 400 to 500 ppm there was a sharp change in the CER. Over the entire range of CO_2 conc used, NP is apparently not quite saturated as indicated by the slightly positive slope occurring after about 500 ppm. The generation of dose-response relationships such as this for whole crop stands will provide valuable input data for functioning CELSS.

The CER at enriched CO_2 averaged 1.4 times that which occurred at ambient levels (Figure 7). The same general pattern of CO_2 exchange as the previous diurnal experiment (Figure 2) was observed over the 4-day experiment except for the first day at the ambient level. Reduction of CO_2 to ambient conc caused a 1.2 fold increase in the transpiration rate in the light but had no effect on water loss in the dark. This is in agreement with previous findings (15,16) and with the known effect of CO_2 on stomatal conductance (increased CO_2 results in decreased stomatal conductance). As with CER, a diurnal pattern of transpiration similar to that obtained in the 1-day diurnal experiment at the enriched CO_2 was observed.

3.4 TEMPERATURE

In the range of 35 to 37 days after planting the rate of NP was affected little by a temperature increase from 22 to 26 C but decreased by 1.8 umol/m^2/s when increased from 26 to 30 C (Figure 8). Rates of DPR increased progressively with increasing temperature which led to a decrease in the net assimilation of CO_2 with increasing temperatures used for the light/dark periods. A comparison of the 2 common temperatures for NP and DPR (22 and 26 C) shows that there would be no difference in the net assimilation (0.85 mol/m^2/day) in this temperature range. However, this assumes that there is no affect of the order of temperature episodes, which may not hold true.

In a second temperature experiment (42 to 45 days after planting), a comparison of 2 temperature regimes was made with the two common temperatures for NP and DPR used within a 24-hour period. Net assimilation was highest when the 26/18 and 22/22 regimes were used (0.91 and 0.88 mol/m^2/day). In contrast to the first experiment, net assimilation decreased by 0.1 mol/m^2/day when temperature was increased from 22 to 26 C, attributable to both a decline in NP and an increase in DPR. This represents more than a 10 % drop in net carbon fixed. Possible explanations for the disparity in results of CER between the 2 experiments are 1) the later stage of development of the second

experiment was characterized by a larger number of shade senescent leaves which were more sensitive to the increased temperature, and 2) the order in which the temperature epidodes are applied had an affect on the rates.

In a working CELSS, temperature regimes will presumably be used to maximize the rate of net assimilation and therefore the biomass production per unit time. However, at times it may be necessary to manipulate temperature regimes to modulate (slowdown or accelerate) the rates of gas exchange within the system to accomodate mass and energy needs and demands.

The temperature experiments also enabled computation of water fluxes for different water potential gradients (VPD). The VPD varied at different temperatures despite faily rigid control of ambient RH in the BPC because the saturation vapor pressure of water in the intercellular spaces of the plant tissues was assumed to vary. It was assumed that the leaf and other plant tissue temperatures were in equilibrium with the air temperature. Transpiration rate increased linearly with increasing VPD in the light and in the dark (Figure 10). Data points in Figure 10 are from both temperature experiments. This data enables computation of water regeneration capacity under a range of working conditions for a CELSS and as with carbon dioxide exchange may be used to perform manipulations to accomodate or anticipate needs in a CELSS.

IV. CONCLUDING REMARKS

Database construction for crop plants selected for CELSS continued with soybean as a test crop. Whole stand rates of carbon dioxide and water exchange were measured throughout growth and development and as affected by time during a daily cycle, carbon dioxide conc, irradiance, and temperature. As a research cuvette, the BPC is providing whole stand reponses which are currently unrivaled with regard to the degree of environmental control, low gas leakage rate, and large plant sample size. Responses to key environmental variables enable selection of optimum conditions for a CELSS and permit some degree of predictive ability for suboptimum conditions for plants when alterations in growth rates might be dictated by practical considerations such as changing mass and energy availabilities or demands. While many of the responses measured in this study corroborate trends and processes established from classical whole crop physiology studies of the past, the data obtained using the BPC have enabled a higher degree of confidence in the absolute numbers gathered, particularly as they characterize how a large

plant canopy responds. Compared to studies on single leaves and plants, the whole stand gas exchange studies have led to values for carbon dioxide compensation points, light compensation points, and dark transpiration rates generally higher than those reported previously. The gas exchange database gathered using the BPC will also enable mass budget analyses not previously possible with other growth chambers.

V. REFERENCES

1. Prince, R.P., W.M. Knott, J.C. Sager, and S.E. Hilding. 1987. Design and performance of the KSC Biomass Production Chamber. Soc. Auto. Engin. Tech. Paper Ser. No. 871437.

2. Sager, J.C., C.R. Hargrove, R.P. Prince, and W.M. Knott. 1988. CELSS atmospheric control system. Amer. Soc. Agric. Eng. Paper No. 88-4018.

3. Wheeler, R.M., C.L. Mackowiak, T.W. Dreschel, J.C. Sager, R.P. Prince, W.M. Knott, C.R. Hinkle, and R.F. Strayer. 1990. System development and early biological tests in NASA's biomass production chamber. NASA Technical Memorandum 103495.

4. Wheeler, R.M. and J.C. Sager. 1990 Carbon dioxide and water exchange rates by a wheat crop in NASA's biomass production chamber: results from an 86-day study (January to April 1989). NASA Technical Memorandum TM 102788.

5. Corey, Kenneth A. 1989. Dynamics of carbon dioxide exchange of a wheat community grown in a semi-closed environment. NASA/ASEE Summer Faculty Fellowhip Program: 1989 Research Reports. ed. E.R. Hosler and D.W. Armstrong. Contractor Report No. CR-166837, pp 58-84.

6. Larcher, W. 1980. Ch. 3: Carbon utilization and dry matter production. In: Physiological Plant Ecology, 2nd. ed., Springer-Verlag, New York. 303 pages.

7. Salisbury, Frank B. and Cleon W. Ross. 1985. Ch. 11: Photosynthesis: Environmental and Agricultural Aspects. In: Plant Physiology. 3rd ed., Wadsworth, Inc., Belmont, Cal. 540 pages.

8. Wheeler, Raymond M., Cheryl L. Mackowiak, and John C. Sager. 1989. Effect of high pressure sodium (HPS) radiation on stem elongation of soybean. HortScience 24 (Program & Abstracts): 84.

9. Wheeler, R.M., C.L. Mackowiak, and J.C. Sager. 1990. Growth of soybeans in NASA's biomass production chamber using metal halide lighting: a protocol for a biomass (plant) production study. NASA Technical publication BSB901.

10. Wheeler, R.M., C.L. Mackowiak, J.C. Sager and W.M. Knott. 1990 Effects of atmospheric CO_2 on photosynthetic characteristics of soybean leaves. Controlled Ecological Life Support Systems: CELSS '89 Workshop. NASA Technical Memorandum 102277. pp 93-105.

11. Halvelka, U.D., R.C. Ackerson, M.G. Boyle, and V.A. Wittenbach. 1984. Carbon dioxide enrichment effects on soybean physiology. I: Effects of long-term CO_2 exposure. Crop Science 24: 1146-1150.

12. Jones, Pierce, L.H. Allen, Jr., J.W. Jones, K.J. Boote, and W.J. Campbell. 1984. Soybean canopy growth, photosynthesis, and transpiration responses to whole-season carbon dioxide enrichment. Agronomy Journal. 76:633-637.

13. Sionit, N., B.R. Strain, and E.P. Flint. 1987. Interaction of temperature and CO2 enrichment on soybean: photosynthesis and seed yield. Can. J. Plant Sci. 67:629-636.

14. Fonteno, W.C., E.L. McWilliams. 1978. J. Am. Soc. Hort. Sci. 102:52-56.

15. Mackowiak, C.L., R.M. Wheeler, W. Lowery and J.C. Sager. Effects of elevated atmospheric carbon dioxide concentrations on water and acid requirements of soybeans grown in a recirculating hydroponic system. Controlled Ecological Life Support Systems: CELSS '89 Workshop. NASA Technical Memorandum 102277. pp. 107-118.

16. Rogers, H.H., Nasser Sionit, J.D. Cure, J.M. Smith, and G.E. Bingham. 1984. Influence of elevated carbon dioxide on water relations of soybeans. Plant Physiol. 74: 233-238.

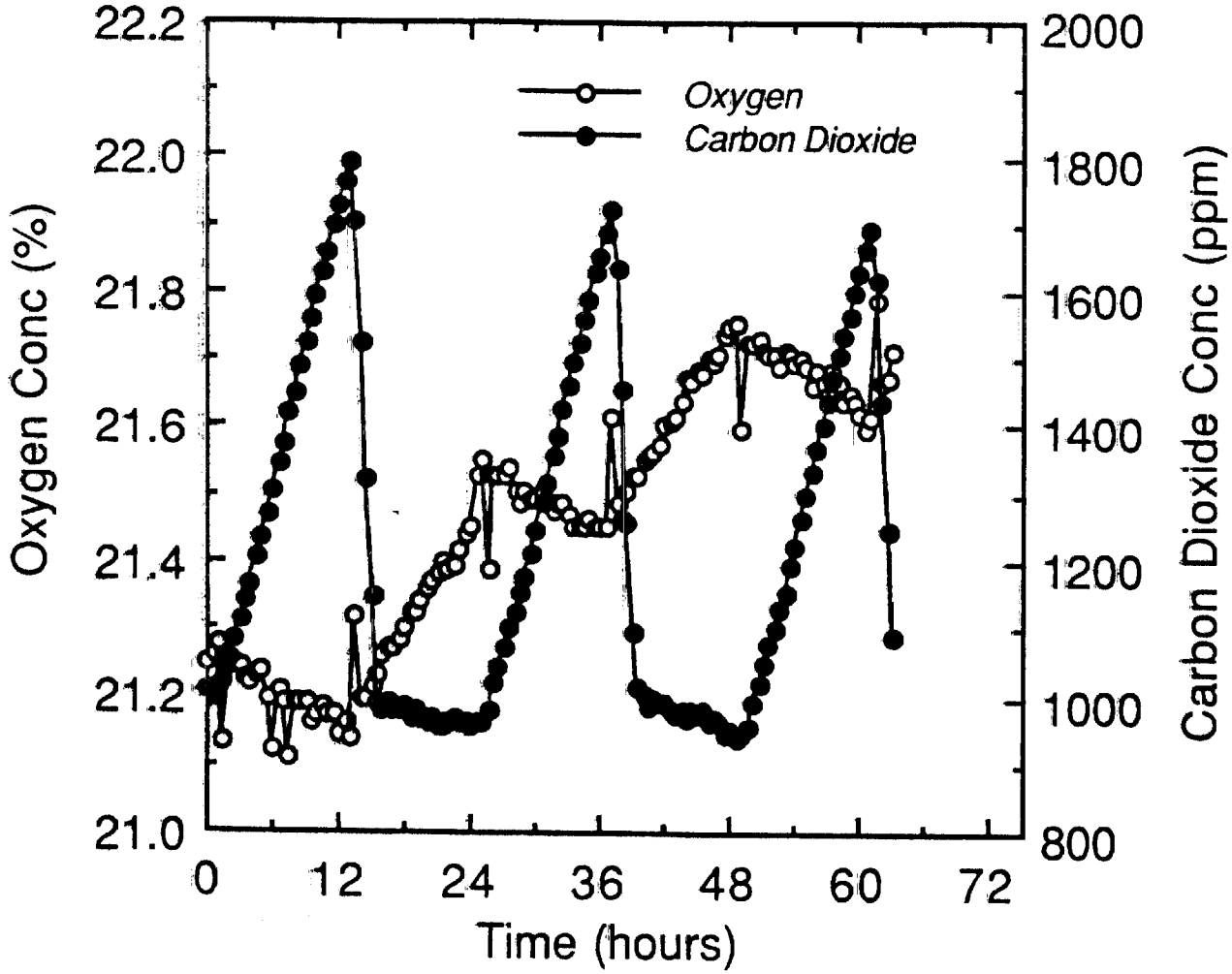
Oxygen
Carbon Dioxide
Oxygen Conc (%)
Carbon Dioxide Conc (ppm)
Time (hours)
22.2
22.0
21.8
21.6
21.4
21.2
21.0
2000
1800
1600
1400
1200
1000
800
0
12
24
36
48
60
72

Figure 1

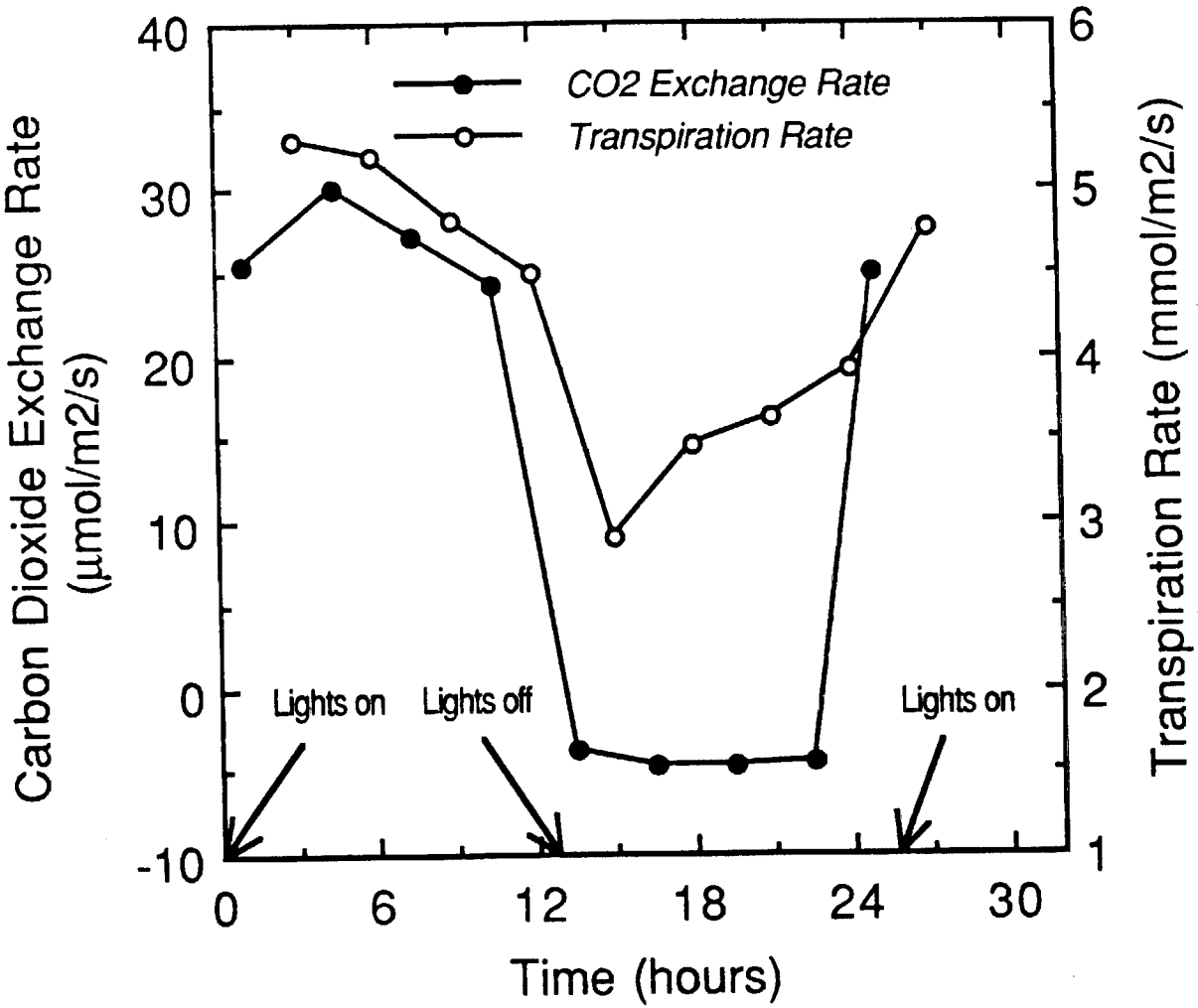
CO2 Exchange Rate
Transpiration Rate
Carbon Dioxide Exchange Rate (µmol/m2/s)
Transpiration Rate (mmol/m2/s)
Time (hours)
Lights on
Lights off
Lights on
40
30
20
10
0
-10
6
5
4
3
2
1
0
6
12
18
24
30

Figure 2

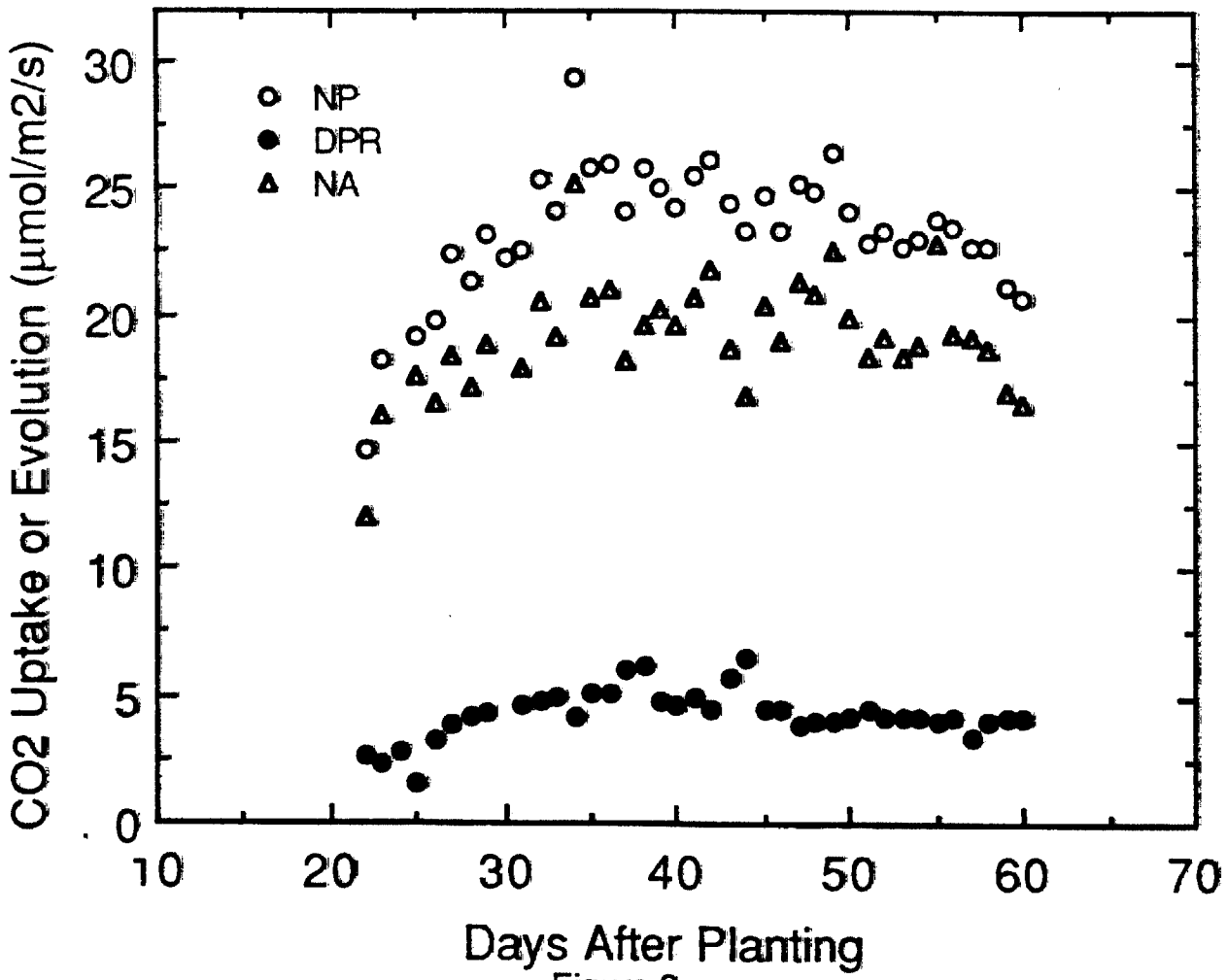
NP
DPR
NA
CO2 Uptake or Evolution (µmol/m2/s)
0
5
10
15
20
25
30
10
20
30
40
50
60
70
Days After Planting

Figure 3

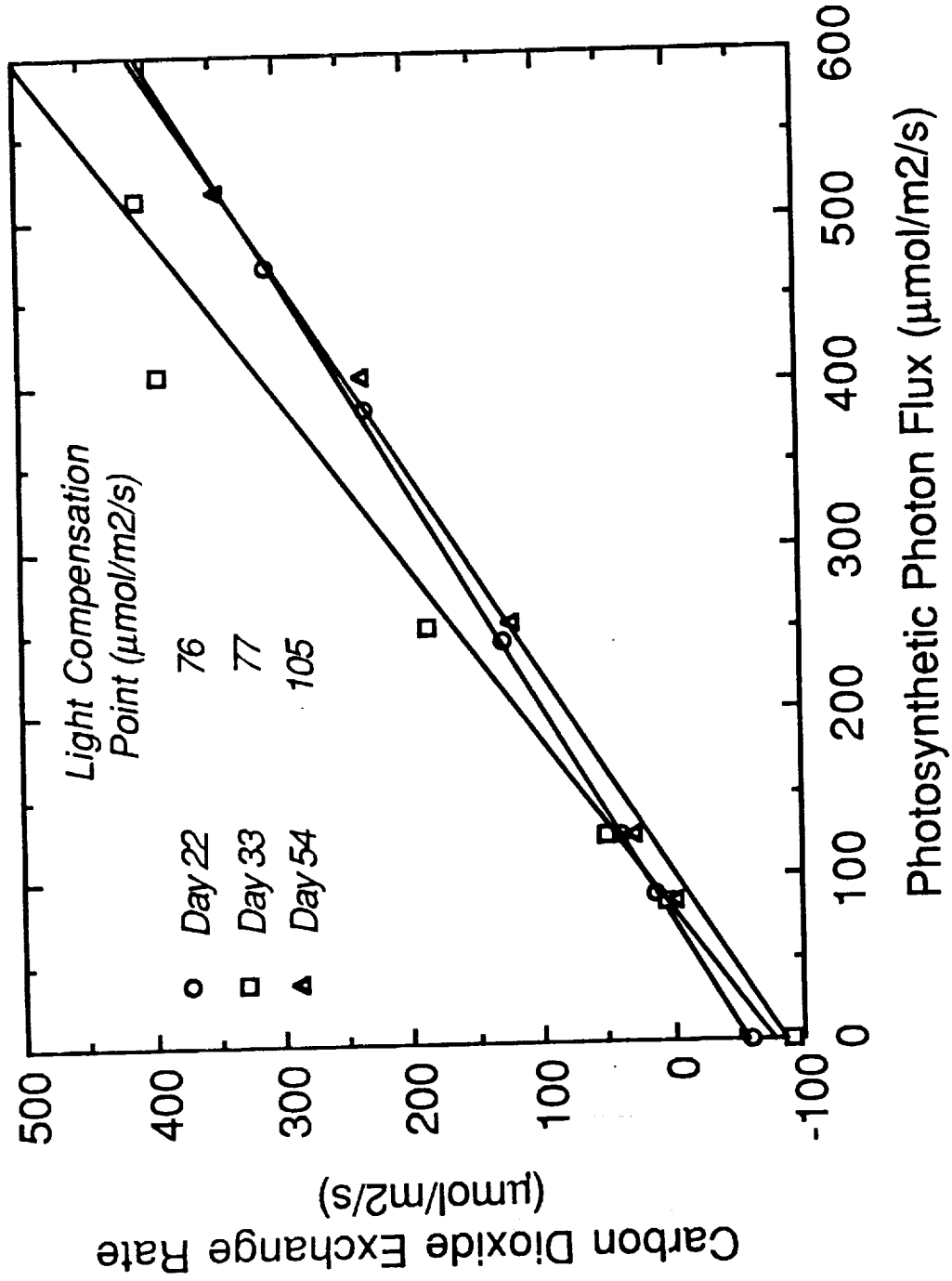
Carbon Dioxide Exchange Rate
(µmol/m2/s)
500
400
300
200
100
0
-100
0
100
200
300
400
500
600
Photosynthetic Photon Flux (µmol/m2/s)
Light Compensation
Point (µmol/m2/s)
Day 22 76
Day 33 77
Day 54 105

Figure 4

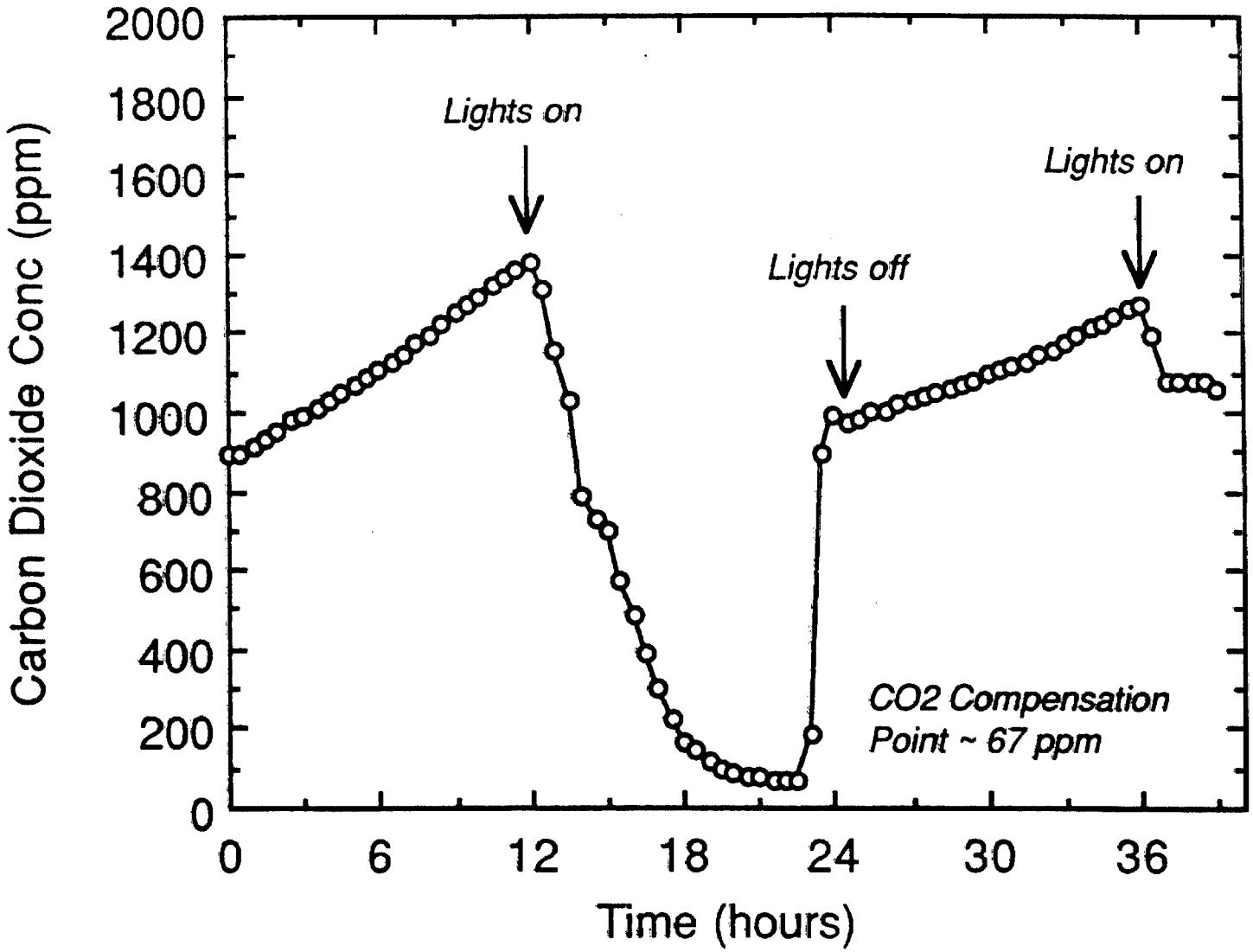
Carbon Dioxide Conc (ppm)
2000
1800
1600
1400
1200
1000
800
600
400
200
0
Lights on
Lights off
Lights on
CO2 Compensation
Point ~ 67 ppm
0
6
12
18
24
30
36
Time (hours)

Figure 5

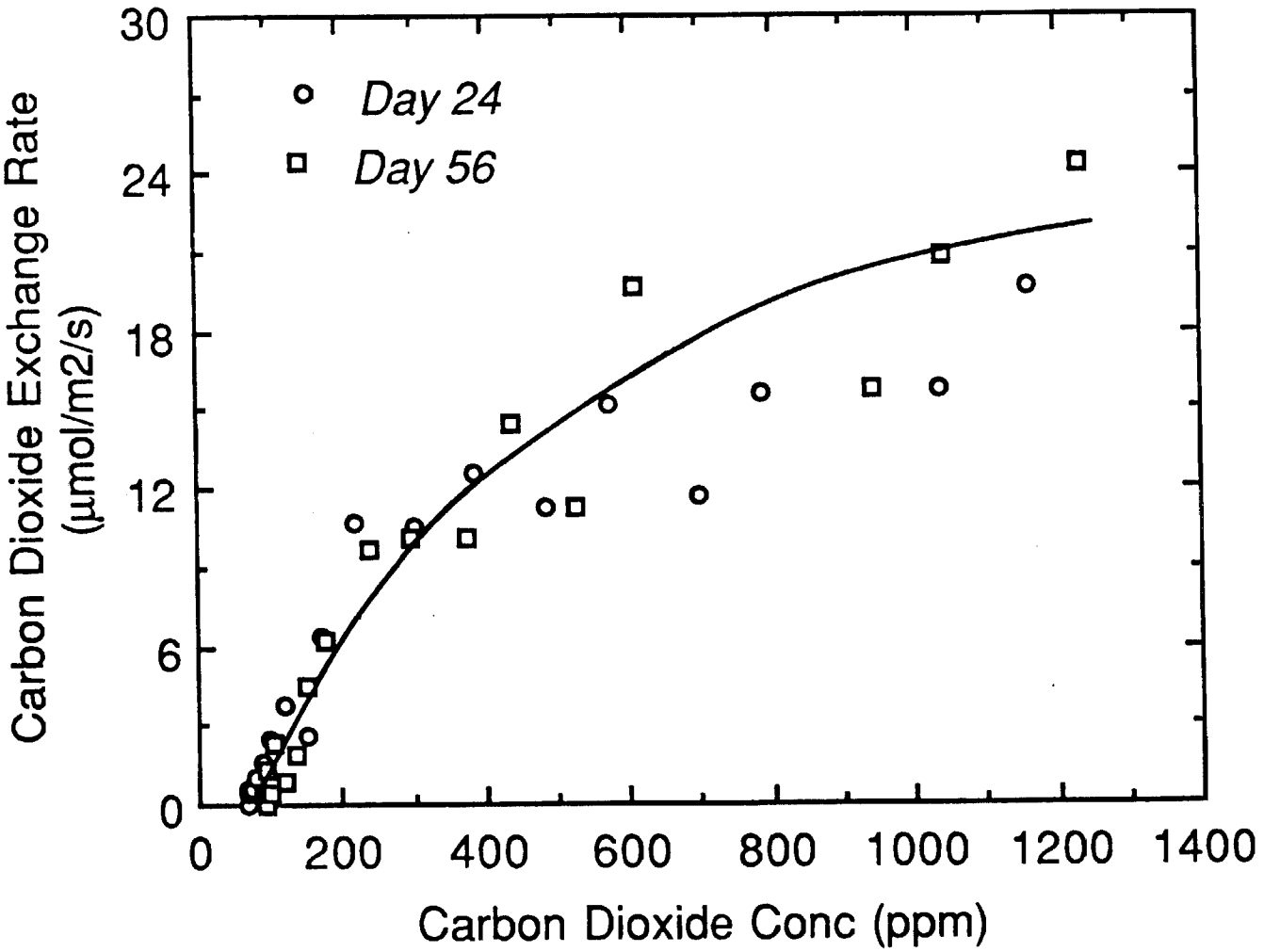
Day 24
Day 56
Carbon Dioxide Exchange Rate (µmol/m2/s)
30
24
18
12
6
0
0
200
400
600
800
1000
1200
1400
Carbon Dioxide Conc (ppm)

Figure 6

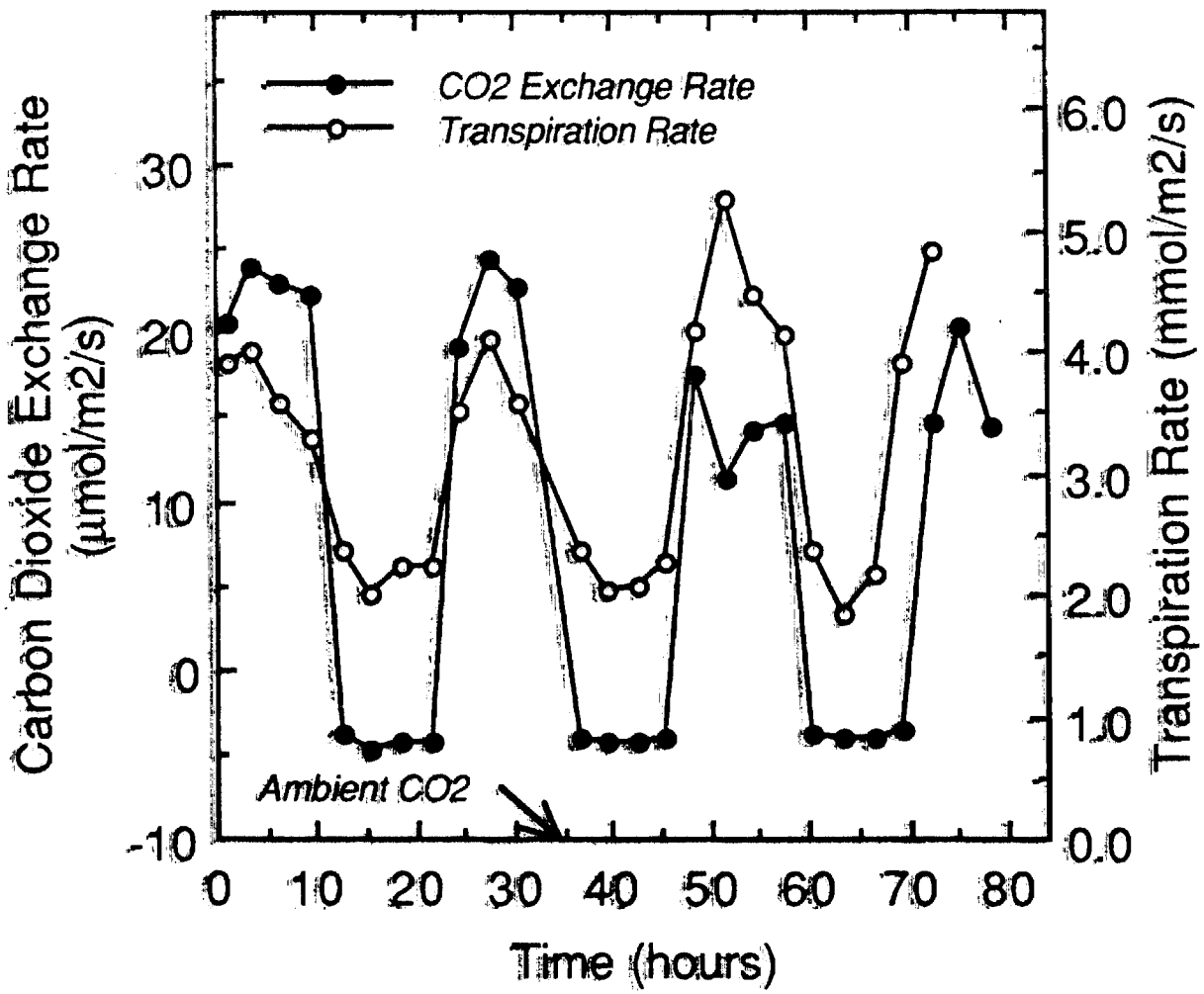
CO2 Exchange Rate
Transpiration Rate
Ambient CO2
Carbon Dioxide Exchange Rate (µmol/m2/s)
Transpiration Rate (mmol/m2/s)
Time (hours)
30
20
10
0
-10
6.0
5.0
4.0
3.0
2.0
1.0
0.0
0
10
20
30
40
50
60
70
80

Figure 7

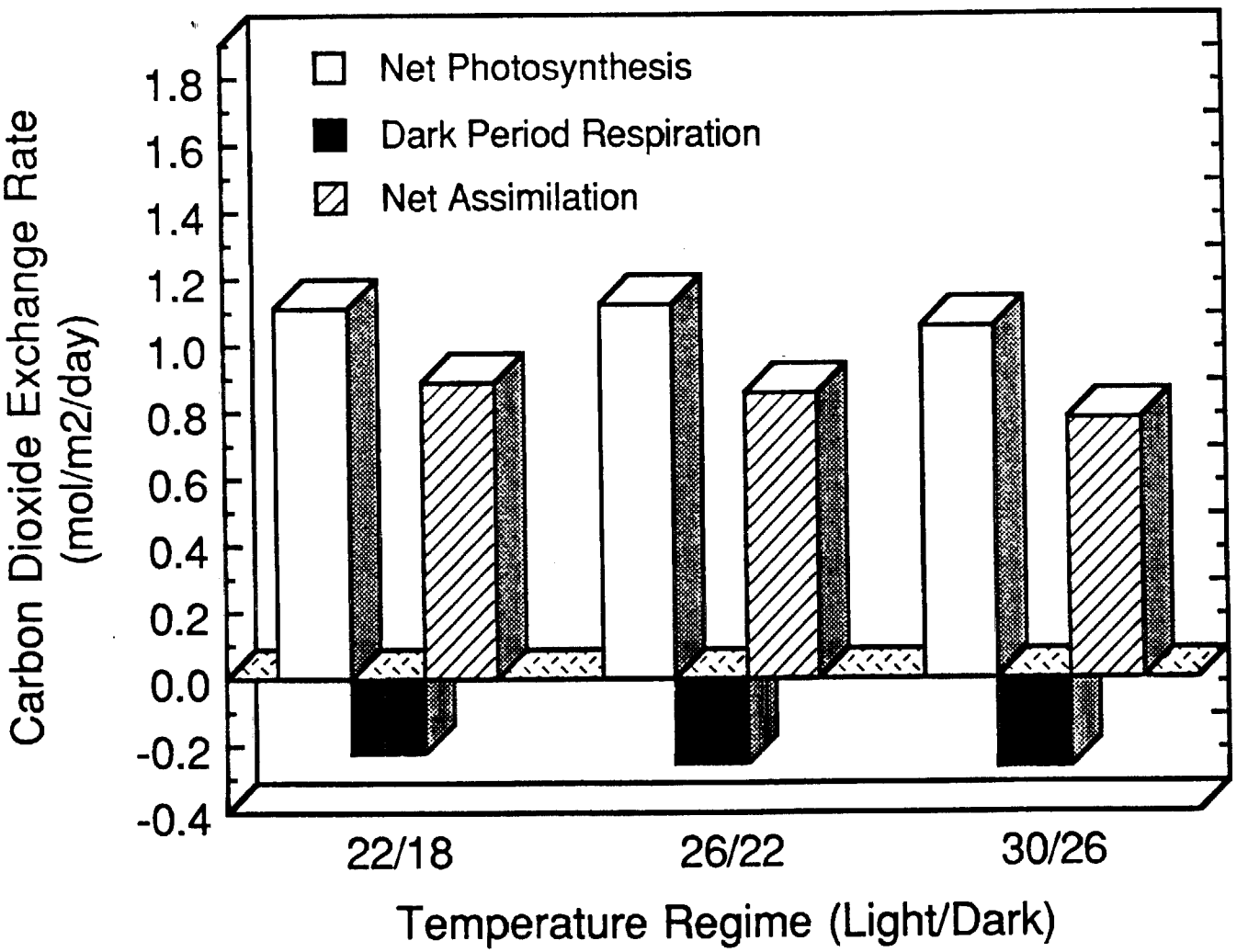
Net Photosynthesis
Dark Period Respiration
Net Assimilation
Carbon Dioxide Exchange Rate
(mol/m2/day)
1.8
1.6
1.4
1.2
1.0
0.8
0.6
0.4
0.2
0.0
-0.2
-0.4
22/18
26/22
30/26
Temperature Regime (Light/Dark)

Figure 8

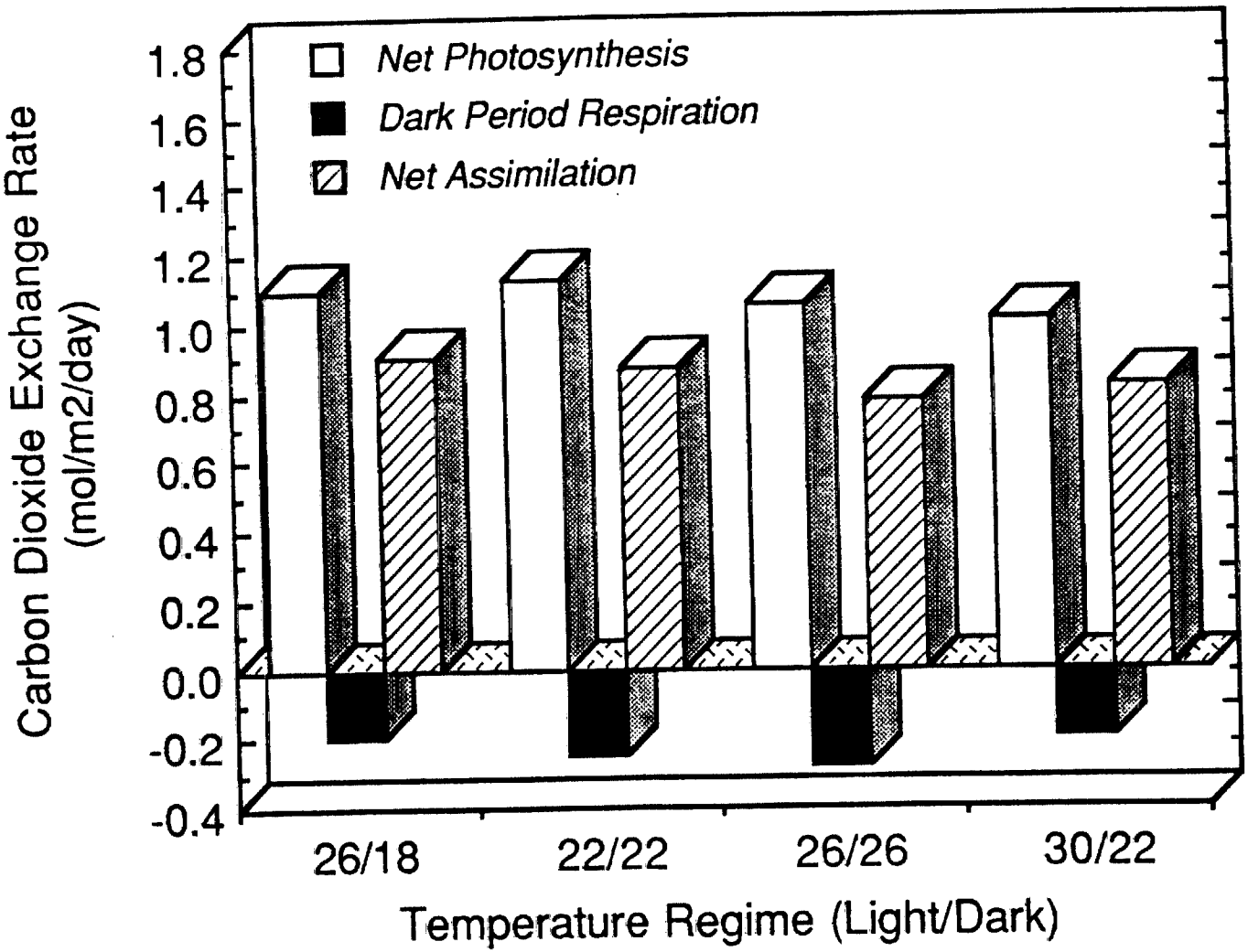
Net Photosynthesis
Dark Period Respiration
Net Assimilation
Carbon Dioxide Exchange Rate
(mol/m2/day)
1.8
1.6
1.4
1.2
1.0
0.8
0.6
0.4
0.2
0.0
-0.2
-0.4
26/18
22/22
26/26
30/22
Temperature Regime (Light/Dark)

Figure 9

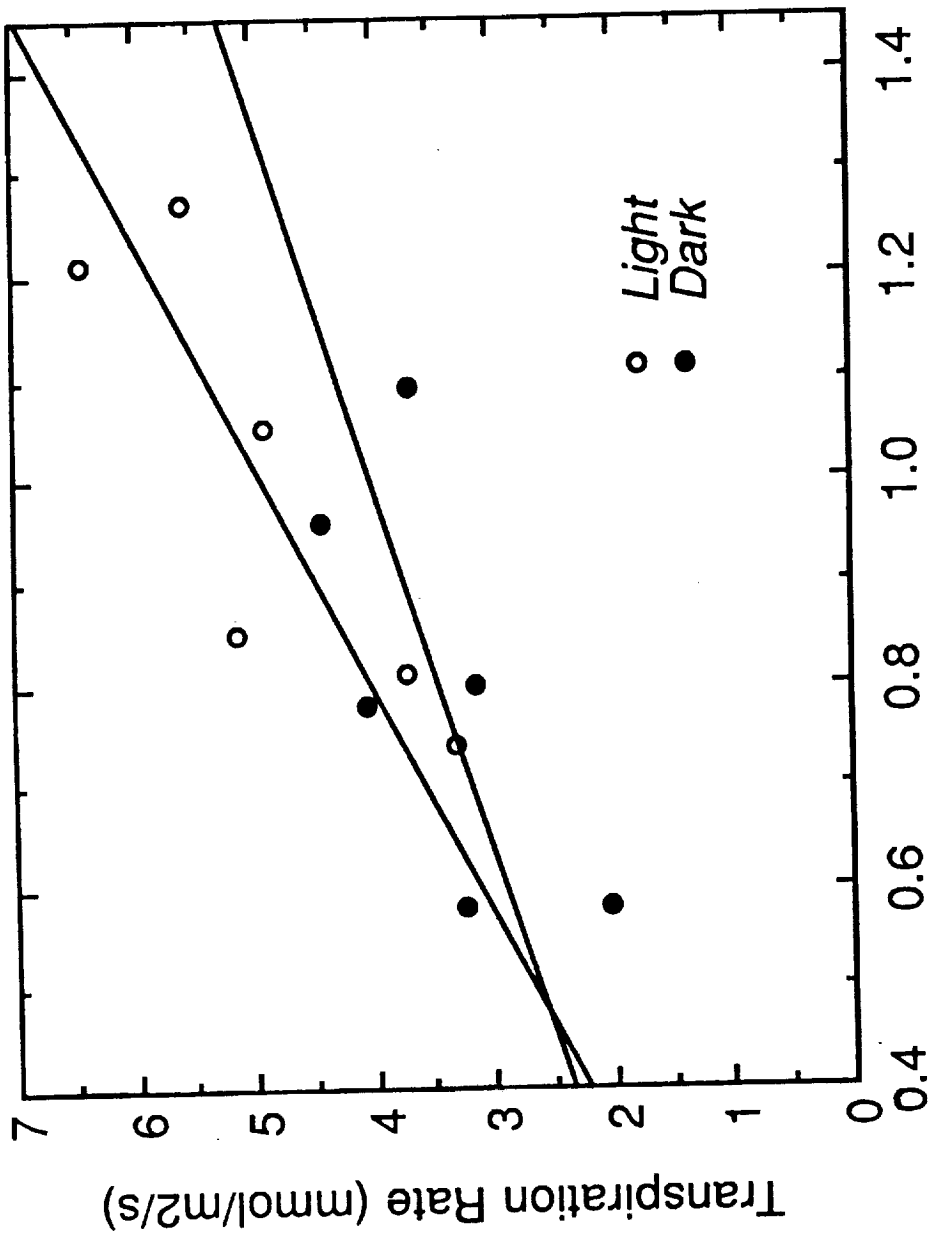
Transpiration Rate (mmol/m2/s)
0
1
2
3
4
5
6
7
0.4
0.6
0.8
1.0
1.2
1.4
Vapor Pressure Deficit (kPa)
Light
Dark

Figure 10

1990 NASA/ASEE SUMMER FACULTY FELLOWSHIP PROGRAM

JOHN F. KENNEDY SPACE CENTER
UNIVERSITY OF CENTRAL FLORIDA

ROCKET-TRIGGERED LIGHTNING STRIKES AND FOREST FIRE IGNITION

PREPARED BY: Dr. James Fenner

ACADEMIC RANK: Assistant Professor

UNIVERSITY AND DEPARTMENT: Auburn University
Aerospace Engineering Department

NASA/KSC

DIVISION: Electronic Systems

BRANCH: Ground Support Equipment

NASA COLLEAGUE: Mr. Bill Jafferis
Mr. Bill McMurran

DATE: August 6, 1990

CONTRACT NUMBER: University of Central Florida
NASA-NGT-60002 Supplement: 4

Abstract

The report presents background information on the rocket-triggered lightning project at Kennedy Space Center (KSC), a summary of the forecasting problem there, the facilities and equipment available for undertaking field experiments at KSC, previous research activity performed, a description of the atmospheric science field laboratory near Mosquito Lagoon on the KSC complex, methods of data acquisition, and present results. New sources of data for the 1990 field experiment include measuring the electric field in the lower few thousand feet of the atmosphere by suspending field measuring devices below a tethered balloon, and measuring the electric field intensity in clouds and in the atmosphere with aircraft. The latter program began in July of 1990. The report also lists future prospects for both triggered lightning and forest fire research at KSC.

Summary

Kennedy Space Center (KSC) is the center for and its operations the focus of the world's most exacting single-point, short-range weather forecasting problems. Thunderstorms, with lightning, hail, strong winds, and possibly tornadoes, represent the greatest hazard at KSC.

The present Atmospheric Science Research Laboratory program at KSC includes ground and airborne electric field measuring instruments (field mills); a ground-based radar; numerical models; rocket triggered lightning experiments; and conventional, fairly dense network of reporting stations and rain gages. When available, KSC will add a high-resolution wind profiler now being developed at Marshall Space Flight Center.

KSC recognizes the critical nature of smaller scale weather phenomenon in the forecasting problem addressed, i.e. short-period, precise, local weather forecasts. No other group has ever attempted to forecast on a routine basis the weather events KSC desires to predict. KSC will first attempt to improve the general understanding of smaller scale weather phenomena. The research project coordinates actions of disparate groups in collecting and analyzing heterogeneous data, and in integrating results into a real-time data display system.

Some significant problem areas: Most of the individual research efforts take place without adequate coordination with either KSC or the other cooperating groups, diluting the effort and rendering it ineffective. KSC must force the research program into a unified effort, demanding top KSC management support, which the program does not now enjoy. Devising a reliable operational forecasting method may take many years and considerable effort from KSC, other government weather-forecasting units, and academia.

Work on lightning-kindled forest fires began at KSC last year, at my initiation, and will continue.

Table of Contents

I

INTRODUCTION

1.1 BACKGROUND INFORMATION

The goal of the rocket-triggered lightning program (RTLP) at Kennedy Space Center (KSC) is to permit more flexibility in the launch criteria, which, as will be mentioned shortly, currently restricts launch operations greatly. Better lightning forecasting would allow more launches without any higher risk to personnel or equipment. However, better forecasts require better knowledge and understanding of the phenomena itself, and that is the object of the rocket-triggered lightning field experiments at KSC.

The lightning program at KSC began in the 1960's, when the National Aeronautics and Space Administration (NASA) began building taller structures on the Center. Lightning strikes to Apollo 12 and, more recently, to an Atlas-Centaur rocket (in 1987), resulting in destruction of both the rocket and its payload, gave rise to added research to understand lightning better. KSC used their own employees, as well as cooperated with academic institutions and private companies in developing its lightning program. The present program includes ground and airborne electric field measuring instruments (field mills), radar, numerical models, rocket triggered lightning experiments, and conventional mesometeorological network of reporting stations and raingages.

The present launch criteria at KSC is very conservative as far as lightning potential is concerned, primarily because of our inadequate knowledge of the following factors: (1) How and under what conditions will aerospace vehicles trigger lighting in electrified clouds; (2) What distance lightning can travel from source to strike object (the aerospace vehicle); and (3) The location and extent of charge sources within clouds for natural and triggered ligthtning. Using lightning simulators and triggering lightning with small sounding rockets can help us determine the vulnerability of facilities and flight vehicles to the effects of direct and indirect lightning strikes.

Most of the individual research efforts by the various participating groups take place without coordination with either KSC or the other cooperating groups. KSC needs to integrate the entire research program into a unified program. Moreover, KSC needs to use the results and techniques developed for its day-to-day operations. Additionally, the limited meteorological expertise at KSC has hampered the research effort, requiring KSC to rely heavily on outside personnel and equipment for this research.

Numerous disparate groups and organizations have some expertise in various aspects of thunderstorm and lightning phenomena. Railroads know about lightning's ability to travel long distances along rail tracks, and to cause damage far from the original strike. Electric power companies also know how lightning travels through its conductors to damage equipment far from the thunderstorm producing the lightning. They also know lightning can couple into lines not originally struck by lightning. Airlines and the military know

lightning strikes aircraft both in the air and on the ground, and that aircraft can trigger lightning flashes even far from a thunderstorm cloud. Radio and television stations, as well as telephone companies know lightning can strike their towers and disrupt their transmissions and communications. It also couples into their equipment. Boaters, anglers, and golfers, among many others, know their recreational equipment (rods, masts, golf clubs) may serve as conductors for lightning strikes--particularly newer graphite materials in rods, masts, and club shafts.

1.2 THE LIGHTNING FORECASTING PROBLEM AT KENNEDY SPACE CENTER

KSC is the center for and its operations the focus of the world's most critical single-point, short-range weather forecasting problems. Many operations at KSC are extremely vulnerable to weather, usually in such novel ways that the forecasting problem has no counterpart in any other realm. The forecaster must develop their own experience at KSC, they cannot rely on any experience gained elsewhere to help them with unique KSC forecasting problems.

The special nature of weather at KSC, as well as extremely high economic and human costs if KSC launches (and therefore missions) fail leads to very precise forecasting criteria with extremely little margin for error. KSC success or failure also impacts directly and significantly on national and international opinion of United States' space effort and expertise. KSC failures draw considerable national and international attention! Thunderstorms, with lightning, hail, strong winds, and possibly tornadoes, represent the greatest hazard at KSC.

In its approach to forecasting extreme weather, KSC recognizes the critical nature of smaller scale weather features and phenomenon (mesoscale components) on the problem addressed: short-period, precise, local weather forecasts. Even the excellent world-wide weather data available through MIDDS cannot by itself make the local weather forecasting problem easier. KSC plans to integrate weather data from satellites, radar, its own local mesonetwork of weather stations, regional weather stations, and data on local lightning strike into the forecasting technique. When available, KSC will add a high-resolution wind profiler (now being developed at NASA Marshall Space Flight Center [MSFC]).

Other data for the weather forecasting scheme envisioned include dual-doppler radar, NEXTRAD at Melbourne, Florida; ground- and airborne electric field measurements from KSC-operated sites; and local lightning-locating data. If at all possible, KSC envisions using its rocket-triggered lightning data into an operational forecasting technique. Since no one, to our knowledge, has ever attempted to forecast on a routine basis the weather events KSC desires to predict, we can only describe the forecasting as experimental. Devising a reliable operational forecasting method may take many years and considerable effort from KSC, other government weather-forecasting units, and academia.

The approach KSC will take will first attempt to improve our understanding of smaller scale (mesoscale) weather phenomena. Only when we obtain an adequate

knowledge of the systems we wish to forecast can we confidently try to predict that phenomenon. This approach requires, however, the close coordination and cooperation of disparate, heterogeneous data, and its integration into a real-time (preferably interactive) data display system. The forecasting problem will also almost require such a technique, because KSC must forecast weather events lasting less than one minute, thus requiring almost instantaneous data collection and display. This requirement may not be unique (airports would also like to have this capability), but the economic and political costs of delays and wrong decisions at KSC are much, much higher than anywhere else.

1.3 RESEARCH PROJECTS AND RESEARCH FACILITIES AND EQUIPMENT

1.3.1 RESEARCH INVESTIGATORS AND THEIR PROJECTS. The rocket-triggered lightning research at KSC involves a number of different research groups from several institutes. They are also working on different, but complimentary, research projects.

The Centre d'Etudes Nucelaires de Grenoble (CENG), from Grenoble, France has two programs at KSC. Their work encompasses launching the rockets to trigger lightning as well as experimental study of the electrostatic fields required for aerospace vehicles to trigger lightning. These two projects will continue at a reduced level during 1990.

The CENG project to launch rockets to trigger lightning also has two parts. The first part is, obviously, to trigger lightning, thus bringing lightning strikes down the conductor trailing behind the rocket to a known location for further study. The second part is to launch instrumented rockets to obtain a fast vertical profile of the electrical fields existing in the atmosphere. The French use two types of rockets, one to reach heights of about 1 kilometer, the other, a Might Mouse rocket, to reach 7 km height. These rocket-derived electric field profiles are then verified by comparison with measurements taken by a series of field mills attached to the tether of an aerostat, as illustrated schematically in **figure 1.1** on the following page. The goal of this second part of this project is to develop a method for taking accurate vertical electric field strength profiles in storm conditions, when the atmospheric electric fields fluctuate rapidly.

The second French project is to study the electrostatic fields that exist at the beginning and ending of electric storms, as the fields oscillate more at those times. The method is to launch a sounding rocket to measure the electric field profile, followed a few seconds later by a rocket designed to trigger a lightning strike. The second rocket trails a copper wire designed to represent the conductive body and charged exhaust gasses of the aerospace vehicle it simulates. The experiements compare theoretical concepts with the results of rocket-borne and ground-based magnetic and electric fields, strike current, and flash luminositiy. The object is to understand and then ultimately to predict the triggered lightning process, which will allow KSC to develop more accurate warning criteria and measuring techniques. A further objective is to measure lightning strike waveforms in order to allow more

accurate simulation of lightning strikes. This will let personnel test the vulnerability of vehicles and associated equipment and facilities prior to their use.

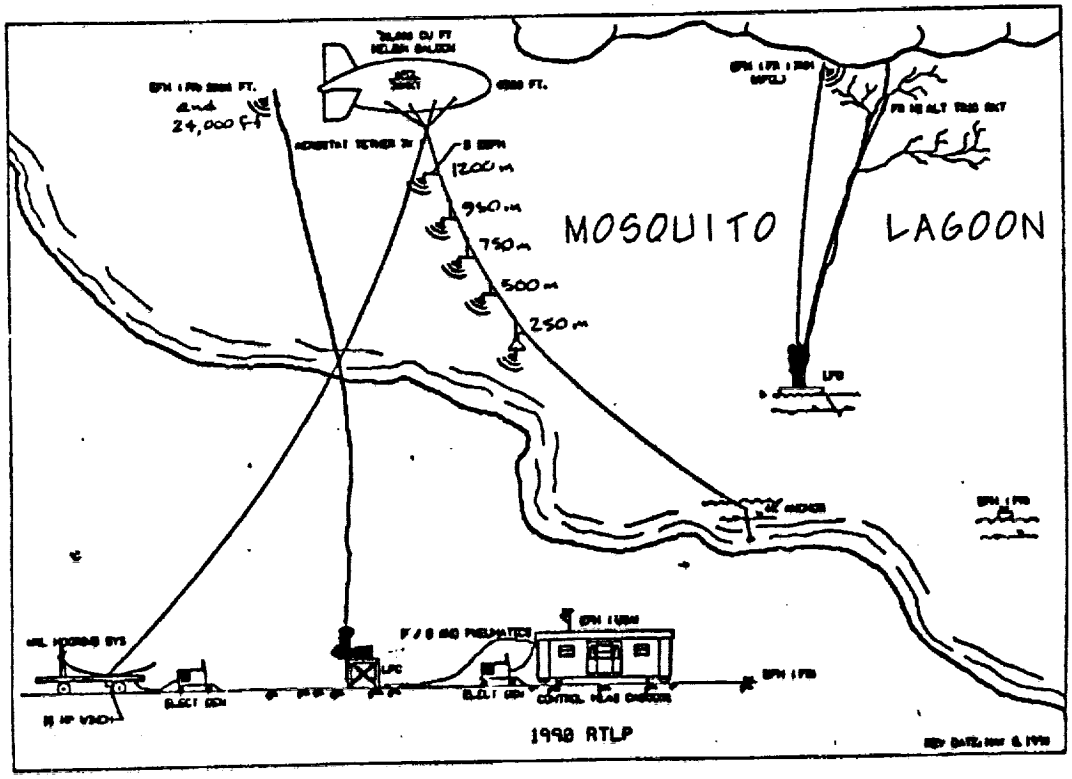

Figure 1-1: The 1990 Rocket Triggered Lightning Project schematic identifying equipment and showing their relative location to each other. (For location of the RTLP, refer to **figure 1-2.**)

Sandia National Laboratories will test the response of aerospace structural materials such as aluminum, titanium, and copper to direct lightning strikes, both natural and triggered. As with part of the French project, the results will also be used to characterize the waveform of lightning strikes for simulations purposes. This project, because it intends to characterize natural as well as triggered lightning, will use a portable launch system for triggered lightning.

Massachusetts Institute of Technology will use microwave radar to measure the plasma temperature of the lightning channel for the triggered lightning strokes. This projects aims at improving our knowledge of the thermodynamics and energetics of lightning discharge.

Embry-Riddle Aeronautical University and the University of Mississippi plan to collaborate on a balloon-tethered field mill experiment above vegetation. This program hopes to understand the shielding effect of low-level space charge produced by corona discharge from the vegetation, which will help interpret ground-based field measurements in relation to fields aloft. This group will compare their measurments with those of the French and the airborne field mill measurements by the Air Force.

Other groups will analyse streak camera images of lightning strikes to help in defining the structure of the strike channel, and measure the ozone and nitrogen produced by the strikes.

1.3.2 THE ATMOSPHERIC SCIENCE FIELD LABORATORY (ASFL) FACILITIES AND EQUIPMENT. Kennedy Space Center (KSC) lies in a region of the United States with one of the highest frequencies of thunderstorms and lightning activity. **Figure 1-2** shows the location of the ASFL and some other sites used for the Rocket-Triggered Lightning Project (RTLP). UCS 10 and UCS 11 refer to the location of unmanned camera sites used to record launches. The headquarters building (HQ Bldg) and launch complex 47 (CX 47) are also shown.

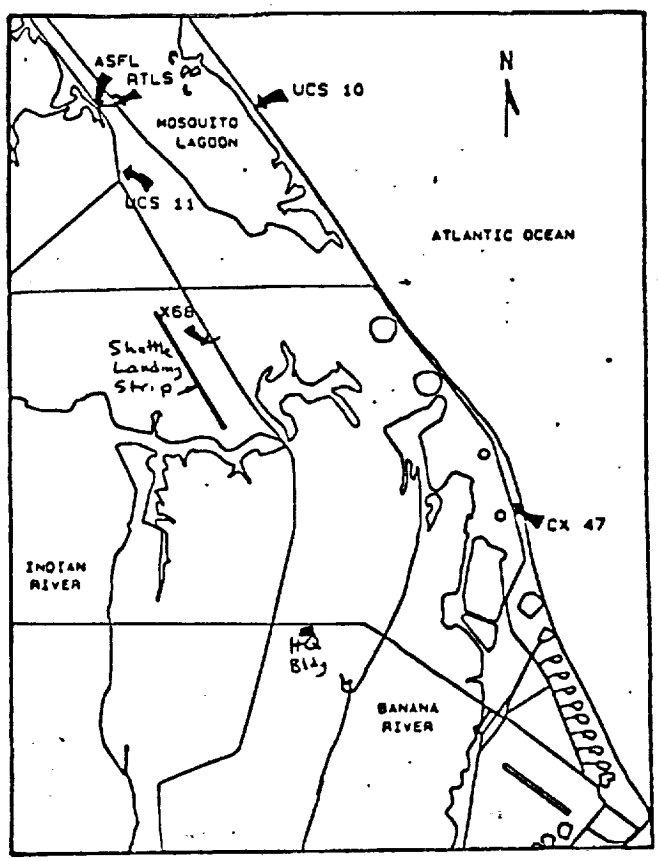

Figure 1-2: Selected site locations used for the 1990 Rocket-Triggerd Lightning Project and their relation to other points on Kennedy Space Center.

KSC operations involve some very expensive equipment (the Shuttle, satellites, and launch vehicles) subject to critical and exacting time schedules. At the same time, launch support equipment such as towers, antennae, above ground and buried cable, are subject to damage or interruption of their function and use from lightning strikes. This combination of conditions make lightning both a hazard to and a significant factor in success or failure of KSC operations. As a result, KSC has been involved in and conducted extensive lightning studies for more than two decades. These studies involved characterizing lightning flashes, devising methods of protecting equipment from lightning strikes, and ways to locate and predict lightning and thunderstorms. Since the early 1980's, KSC, in conjunction with other Government organizations, private companies, and universities, has intensified its studies of thunderstorm and lightning phenomena.

KSC and the Eastern Space Missile Center (ESMC) weather group delve into thunderstorm and lightning forecasting, as well as devising methods of predicting other significant, adverse, or severe weather events (e.g. freezing precipitation, for, icing, or strong or gusty winds). The combination of KSC and ESMC have developed one of the finest facilities for forecasting short-range weather events. The KSC/ESMC facilities include weather satellite and radar data, a mesoscale weather observation network (more than fifty stations), and the Meteorological Interactive Data Display System (MIDDS) which supplies world-wide meteorological data and soundings. The KSC also uses a tethered balloon for research on thunderstorms and lightning, and may be able to include this in future forecasting techniques.

KSC and ESMC wish to create and operate an advanced weather support and forecasting system in order to reduce the weather-related hindrances to KSC operations. The KSC program also plans to transfer to other weather forecasting units (such as the US Air Force or the National Weather Service) the technology and knowledge gained through this research.

The Federal Aviation Administration (FAA), Air Force Wright Aeronautical Laboratories (AFWAL), and the US Naval Research Laboratory (NRL) are among the Government groups interested in lightning studies at KSC. KSC and other groups are interested in (1) characterization of lightning hazards to KSC operations, to communications, to power distribution, and to command and control systems; (2) remote lightning detection; and (3) understanding the "advent and demise" of thunderstorms. In addition, certain groups within the Government are interested in using lightning strikes to simulate the electromagnetic pulse (EMP) nuclear weapon bursts might send out.

After learning more about lighting and its effects on air- and spacecraft, KSC would like to transfer the techniques and knowledge gained from its studies to operational forecasting and to academic institutions training weather forecasters. This should ensure qualified forecasters for future operations.

1.4 DATA ACQUISITION

Items investigated in KSC lightning and thunderstorm studies include static and field charges using electric field measurements in and around KSC; locating and counting lightning discharges (cloud-to-ground strikes, mainly) within 200 miles of KSC; radar data from the KSC region; surface wind data using a mesoscale network of measuring stations within about 50 miles of KSC; electric and magnetic fields and lightning current measurements from the KSC area; and other meteorological data obtained from local, regional, and national sources. These data will, hopefully, be integrated into a forecasting method and applied to improving short-term weather forecasting and verification of numerical weather forecasting, and to evaluating lightning warning procedures.

The Maxwell current and its changes with time may help researchers understand when thunderstorms begin ("turn on") and when they quit ("turn off"). Maxwell current may thus ultimately lead to an approximate threshold for impending lightning strikes. (Lightning and its accompanying thunder define a thunderstorm; without these two phenomena, the event is merely a rain- or hailshower.)

Photo analysis of lightning may be used to quantify several parameters, such as size and shape of strokes. Streak images yield stroke propagation speed. Photography on calibrated film can determine flash luminosity. If luminosity is a function of current, then we can measure lightning current directly. Further, time resolved lightning spectra would then yield electron temperature in the lightning channel. Photographic images can be analyzed by video densitometers, if digitized, or conventional densitometers if not.

The program at KSC is the first program to measure all parameters (electric and magnetic field, current, electron temperature in the lightning plasma, luminosity, spatial orientation, and stroke propagation speed) at the same time, thus allowing case studies to test theoretical and numerical models of lightning behavior.

Kennedy Space Center (KSC) receives wind, temperature, and humidity observations from a network of over 50 instrumented towers covering an area about 53 by 57 km (about 1600 square kilometers) as shown in Watson et al. (1987). Most wind instruments have been mounted on top of standard 54-foot tall telephone poles, and set to record wind data at five-minute intervals. When in use during the RTLP, data from this network is recorded on computer tape and used in mesoanalyses of thunderstorm and lightning case studies.

A network of five direction-finding stations around KSC locate negative lightning flashes (where earth is positive relative to cloud). A paper by Lopez and Holle (1986) describe this lightning direction-finding method.

A United States Air Force WSR-74C radar located at Patrick AFB, approximately 30 km SSE of KSC, supplies data at five-minute intervals. A Weather Bureau radar at Daytona Beach, about 100 km NNW of KSC, also supplies radar imagery at irregular intervals. The Lightning Location and Protection, Inc, (LLP)

Integrated Storm Information System (ISIS), which records negative lightning flash information as well as Daytona Beach radar information, is out of operation for the 1990 RTLP season. When it operates, this ISIS equipment is located at the Range Control building on Cape Canaveral Air Force Station. Until it returns to service, the national lightning location system, operated this year by Sandia National Laboratories, provides similar data.

Lightning triggered when small rockets trailing a conductive wire behind them (rocket-triggered lightning, RTL) are launched near active thunderstorms provide several advantages for scientific study of lightning. First, lightning occurs at a pre-defined place and at a pre-determined time. This allows the researchers to measure parameters seldom--and then only with extreme difficulty--measured in the natural atmosphere. Secondly, it allows a detailed look at the very long "leader" strikes propagating into un-ionized air, close to the conditions prevailing in an unmodified environment. Both of these advantages help researchers understanding lightning leaders, thus understand lightning itself better--and, more importantly, that triggered by aerospace vehicles traversing that region of the atmosphere.

Suspending an isolated metallic object (a cylinder about eight feet long and two feet in diameter) below a tethered balloon as a lightning strike object (LSO) may also simulate an aerospace vehicle-triggered lightning (ATL) object. Lightning flash leaders observed and measured during such strikes will provide data for comparison with prior observations, hopefully to verify or refute the bi-directional ATL model commonly proposed. The series of field mills suspended along the tether cable provides electric field measurements around the LSO. This experimental set-up also allows negative leader current to be measured at the LSO site, possibly permitting return-stroke current measurements at ground and higher levels at the same time. Streak cameras and conventional photography record visual imagery for later quantitative study.

Data taken both over land and over water allows similarities and differences to be observed and measured. Rocket launches over water represent a "purer" electric lightning signature, since there is no distortion of the signal from the ground or support equipment around the launch pad. The 1990 RTLP includes launches from land and water RTLS; my proposal is to launch from each site alternately, or from each at short intervals, i.e. quasi-simultaneously.

Other sensors include microphones to record the sound of thunder, to compliment the photo-recorded lightning flashes; and current sensors in the ground, which are correlated with negative cloud-ground potential.

II

PRESENT RESULTS

2.1 UNIQUE METHODS OF DATA ACQUISITION

The 1990 rocket-triggered lightning strike research season envisions recording positive lightning strike data as well as negative, using a system developed by the State University of New York at Albany (SUNYA). The SUNYA system uses satellite data to provide actual lightning strike location data. Simultaneously, rockets carrying special electric field measuring instruments ("field mills") will be launched to obtain electric field strength data up 7000m altitude.

KSC will also suspend field mills at intervals along a cable attached to a tethered balloon located near the rocket launch site. This will supply a vertical sounding of electric field strength near the triggering site, important data presently missing. From four to six field mills located along the tethering cable will supply field strength at heights up to approximately 1200 m above the ground. This arrangement is shown in **figure 1-1** on a previous page, but repeated here as **figure 2-1** for the reader's convenience.

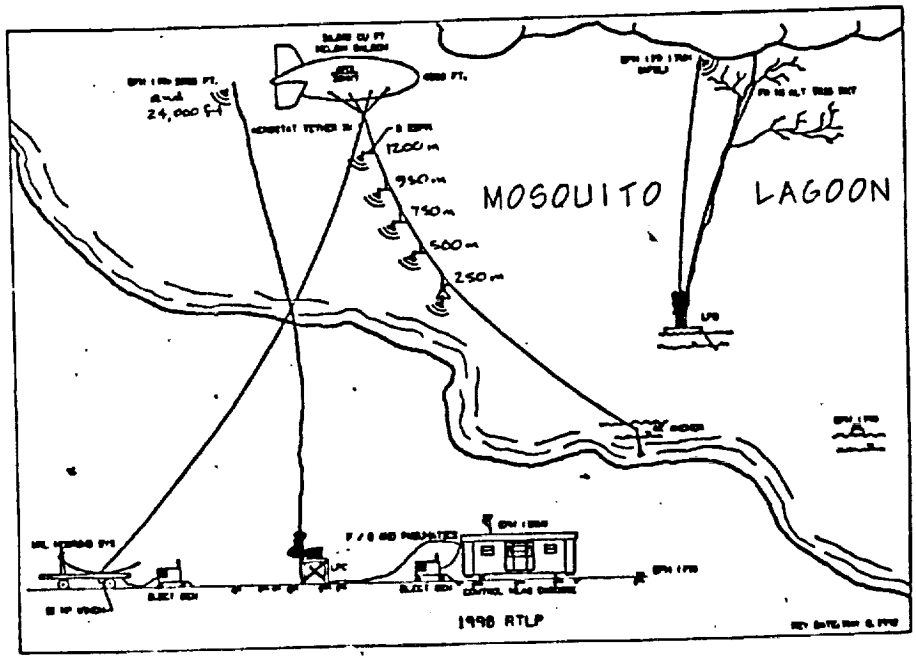

Figure 2-1: The 1990 Rocket Triggered Lightning Site schematic identifying equipment and showing their relative location to each other. (For location of the RTLP, refer back to **figure 1-2**.)

2.2 RESULTS FROM 1990 FIELD EXPERIMENT

2.2.1 PROBLEMS WITH EQUIPMENT. Prior to beginning the 1990 field experiment at the Rocket-Triggered Launch Site (RTLS), KSC had to revise the operating procedures. This delayed the field experiments; consequently, the program had gathered little lightning strike or fire initiation data prior to my departure. This report thus presents results of priliminary case studies for 5 June and 3 July 1990, which I undertook during July.

Another problem, as in 1989, concerned the lightning strike display system, ISIS, which quit functioning entirely in 1990. The ISIS should record both lightning strike location and radar return, and is used both to deduce the physical relationship between the lightning strike and the parent thunderstorm, and to locate sites of fire initiation. Likewise, as in 1989, the French contingent from Grnoble delayed their arrival by about ten days. Since they actually run the RTLS, launch the triggering rockets, and gather data, their delay pushed the start of operational rocket launches back still more.

All RTLP equipment and personnel appeared to be ready for the first rocket launch only on July 31st. Unfortunately, for a number of days thereafter, weather conditions did not produce lightning at the launch site on Mosquito Lagoon.

2.2.2 PROBLEMS WITH COORDINATION AND COOPERATION. With nearly a dozen groups cooperating in the lightning project, occasional lack of coordination seem inevitable. In my view, this need not happen at all. Every group should have been adequately informed of their role in the project and how they were to support every other group. Unfortunately, this certainly did not happen in the case of the Cape Canaveral Air Force Base weather station and its personnel. I called them a number of times between July 6th and July 31st, requesting data for the storm development on the afternoon of July 3rd. To their credit, they sent me data for 12UT July 3rd (figure 2-5), but never for 00UT July 4th, a time closer to actual storm development around 20UT. On each occasion of telephoning the weather station, I seemed to talk to someone new, who did not know anything about my previous requests. The two civilian employees promised to take care of my request (handling such requests apparently is part of their job), but they failed to do so. One apparently became ill, the other apparently merely did not do the job. Finally, after at least a dozen telephone calls, I was informed on August 1st that the weather station only keeps plotted charts and maps for two weeks, and the data for July 4th had been destroyed. As a result, I cannot include this information in this report.

KSC should improve its coordination with support units such as the weather station to improve cooperation in the RTLP.

2.2.3 USING A "STORMSCOPE" TO LOCATE NEW THUNDERSTORM CELL DEVELOPMENT. Bill Jafferis asked me to study the feasibility of using the commercially available Stormscope as an initial indicator of lightning. The idea of using a

Stromscope as a preliminary indicator of thunderstorm activity has merit: Sites without access to the more elaborate lightning detector data or radar could, with help of the Stromscope, get a general indication of lightning activity and direction, even if the Stormscope does not indicate distance to the flash accurately. Further, the Stormscope is relatively inexpensive, has been used in aircraft for many years, and indicates both positively and negatively charged lightning strokes.

As requested, I studied Stormscope displays and compared them with radar returns and the ISIS lightning indicating system. KSC personnel had recorded displays of all instruments and equipment on June 5th, and I looked at all three displays taken from those videotapes. My study confirmed the impression that the Stormscope indicated direction to lightning activity, but the distance was not accurate. As a result, I concluded that a Stromscope located at selected sites would be a good alternative to installing expensive equipment, or running electrical cables to those sites in an effort to remote the data from other locations to these users. Moreover, since Stormscopes display both positive and negative lightning discharges, they can pick up developing and newly developed storms better than the ISIS. This makes the Stormscope a good, reasonably priced, readily available system for use in locating new thunderstorm activity.

2.2.4 SOME PRELIMINARY RESULTS FROM THE 1990 FIELD EXPERIMENT. Due to delays outlined above, coupled with my departure August 7th, this report gives only a few preliminary results from the 1990 field experiment. As noted above, I studied the storm development occurring on 5 June and 3 July 1990, as some interesting new storms developed on those days.

From July 10th through at least August 6th (and possibly continuing for at least another two weeks after my departure), KSC hosted multi-party airborne field mill flights almost daily. During these nearly two dozen flights, Air Force and other parties measured the electric field at various altitudes, both in and out of stratus, cirrus, and cumulus cloud, and correlated them with surface and tethered field mill measurements. The purpose was to be able to extrapolate field mill measurements taken during operational RTLP launches to higher altitudes, i.e. to be able to extend the electric field readings taken from tethered field mills and those measured by small rockets (attaining heights of about 7000m) to the top of the thunderstorm cloud, which often attain altitudes of at least 15,000m. The aircraft measured typically 1kV/m to 2kV/m outside clouds, and also inside stratus or dissipating cumulus clouds. The instruments also recorded up to 60kV/m inside active cumulus and cumulonimbus clouds, and generally noted turbulence, precipitation, and often icing along with higher field strengths. As of August 1st, no operational rocket launches have verified these findings.

Figures 2-2, 2-3, and 2-4 show, respectively, an interesting satellite image, the corresponding radar return, and two soundings for June 5th, 1990. As all the imagery, (satellite, radar, and lightning location) were taken as single frames from videotape of the monitor displays, the reproduction quality is

poor, and I have not included all of the satellite or radar data, nor any of the lightning strike data, in this report. For those who might have an interest, original images are available from Bill Jafferis, DL-ESS-22, HQ Building, Kennedy Space Center, FL 32899.

Figure 2-2 shows GOES 7 satellite imagery from 2031 UT, June 5, 1990. It indicates the arch of clouds (denoted by "A") formed by the downdraft outflow from dissipating thunderstorm "B" forcing moist air to rise. New cell development ("C") on this arch may be the result of interaction between the outflow from "B" and thunderstorm "C," since that thunderstorm cell appeared (from previous imagery not shown here) to be expanding towards the south. New cells "D" and "E" forming upwind of dissipating thunderstorm "F" appear to be developing along a mesoscale boundary between moist and drier low-level air. This apparent boundary is marked by a wedge-shaped region of cumulus clouds extending from the eastern edge of Tampa Bay to cell "F" on the eastern coast of Florida. The overshooting tops on thunderstorm cells "D" and "E," indicating strong updrafts and rapid cloud development, are not apparent in this imagery, but enlargements reveal them. The well developed sea breeze along the eastern coast of Florida shows up as a line of clouds (marked "G") just inland of the coast.

Figure 2-3 shows the radar returns for 2029 universal time (UT), two minutes prior to **figure 2-2**. Thunderstorm cells "D," "E," and "F" can be clearly seen, as well as another storms cell north of "E." This radar echo apparently corresponds to a feature hidden by anvil debris in **figure 2-2**. Other thunderstorm cells visible in satellite imagery are beyond the 60n.mi. radar range selected in this example.

Figure 2-4 shows two soundings (taken at 1015 and 1205 UT) plotted on the same Skew T-Log P diagram the U.S. Air Force normally uses. Lines of equal temperature slope up to the right ("skew-T"), while the logarithm of atmospheric pressure decreases upward ("log-P"). The temperature trace is the solid irregular curve, and the dew point temperature is the dashed irregular curve. Lines of equal moisture, not labeled, appear as dashed straight lines sloping up to the right somewhat more steeply than temperature lines. The solid lines which appear to converge as they slope up to the left denote the change in temperature with pressure dry air ascending adiabatically in the atmosphere would experience, while the four dashed lines curving up to the left denote the temperature change with pressure that rising saturated air would experience. Together with the temperature and dew point traces, these sets of lines can be used to evaluate static stability of the atmosphere, potential for thunderstorm formation, and estimated thunderstorm cell height. The final items depicted are short barbs indicating wind direction and speed, plotted along the right margin. The length of the line segment indicates relative wind speed (the actual value is given to its right, in knots), and the orientation of the line indicates compass direction clockwise from true north. Most wind directions lie between southwest and northwest in this case.

Figures 2-5 and 2-6 show weather facsimile products for July 3rd, 1990. Due to the poor quality of other images available, and lack of data for other times, I have not included any in this report.

Figure 2.5 shows the weather analyses for the 200 (A), 500 (B), 700 (C), and 850mbar (D) levels for 12:00 UT, July 3, 1990. Light lines in each map denote height contours on the pressure surface, which correspond to lines of constant pressure (isobars) on a surface analysis. Centers of high height contours are marked "H," those of lower contours "L." The heavy curves emanating out from low centers depict troughs, while heavy wavy lines from highs denote ridges. Isotherms are dashed. The jet stream is shaded on the 200mbar map.

Figure 2-6 shows a locally produced surface weather map for 12:00 UT, July 3, 1990. A low pressure center lies along the eastern Florida coast, midway between Miami and KSC at this time. The troughs (marked "Trof") radiating outward from this low pressure center induced convergence, which, when combined with the sea-breeze convergence later in the day, gave rise to thunderstorm development. The outflow from one of these storms forced new storm cell development ahead of the original storm. This new thunderstorm passed over Titusville, producing considerable lightning and rain. (The data, charts, and maps for this case cannot be shown or included in this report, because the original data was not recorded, and the maps were destroyed, as noted previously. However, I noted the development with my own eyes, as I was physically present in the Technology Transfer Unit (TTU) on that afternoon and watched this storm develop on radar and through satellite imagery and the convergence indicated by the mesoscale wind network around KSC.)

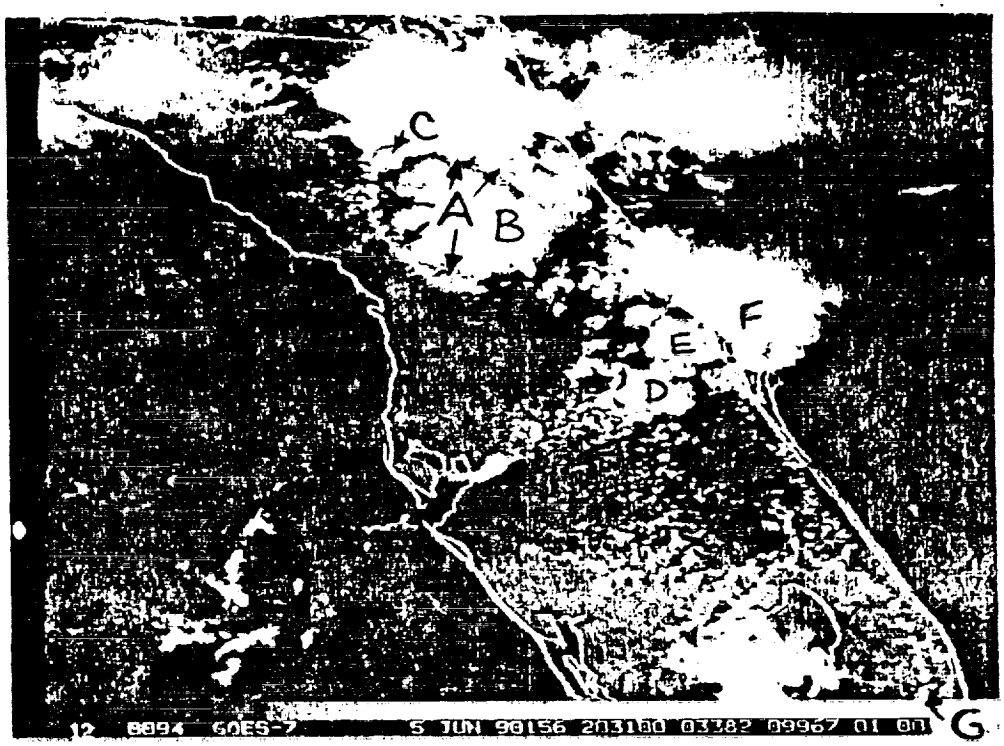

Figure 2-2: GOES 7 satellite imagery from 2031 UT, June 5, 1990, showing the outflow arch (**A**) from a dissipating thunderstorm (**B**), new cell development (**C**) on this arch, and new cells (**D**) and (**E**) forming on the upwind side of storm (**F**), along a mesoscale boundary between moist and drier low-level air.

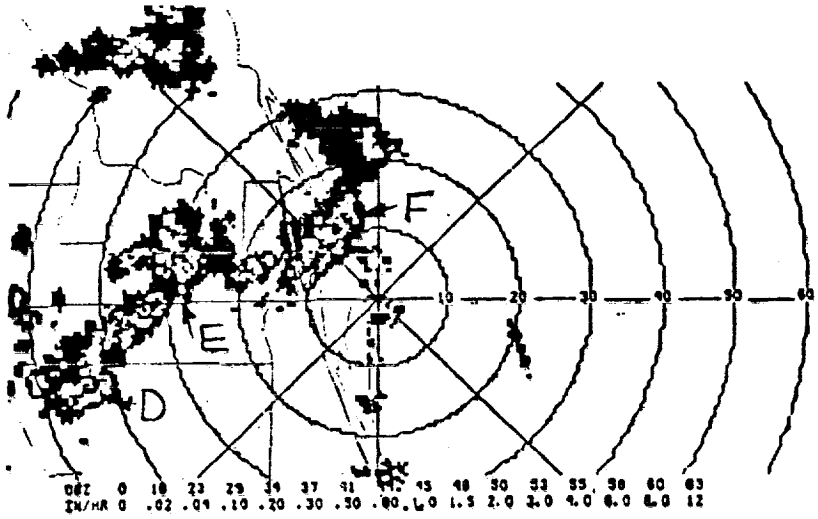

Figure 2-3: Radar return for 2029 UT, June 5, 1990, for the Kenned Space Center. Range is in nautical miles. Lighter areas within darker radar echos indicate higher radar reflectivity.

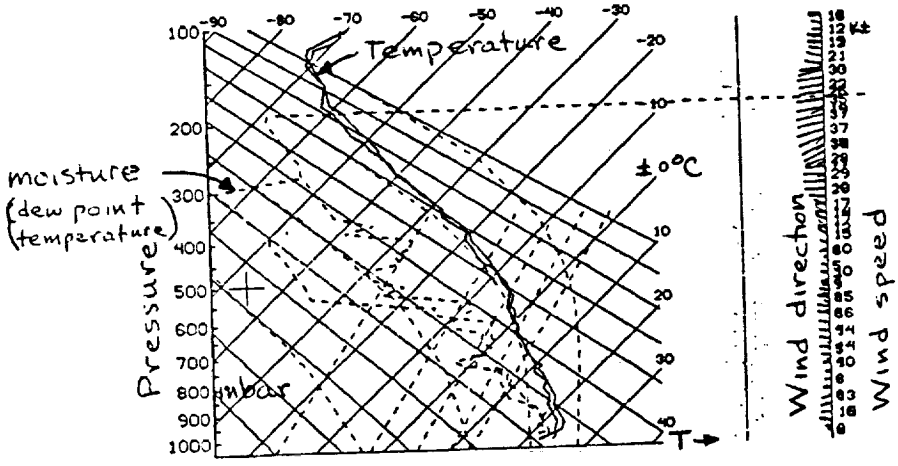

Figure 2-4: Temperature, moisture, and wind soundings for Kennedy Space Center for 1015 and 1205 UT, June 5, 1990. The two soundings have been inadvertently plotted on top of each other.

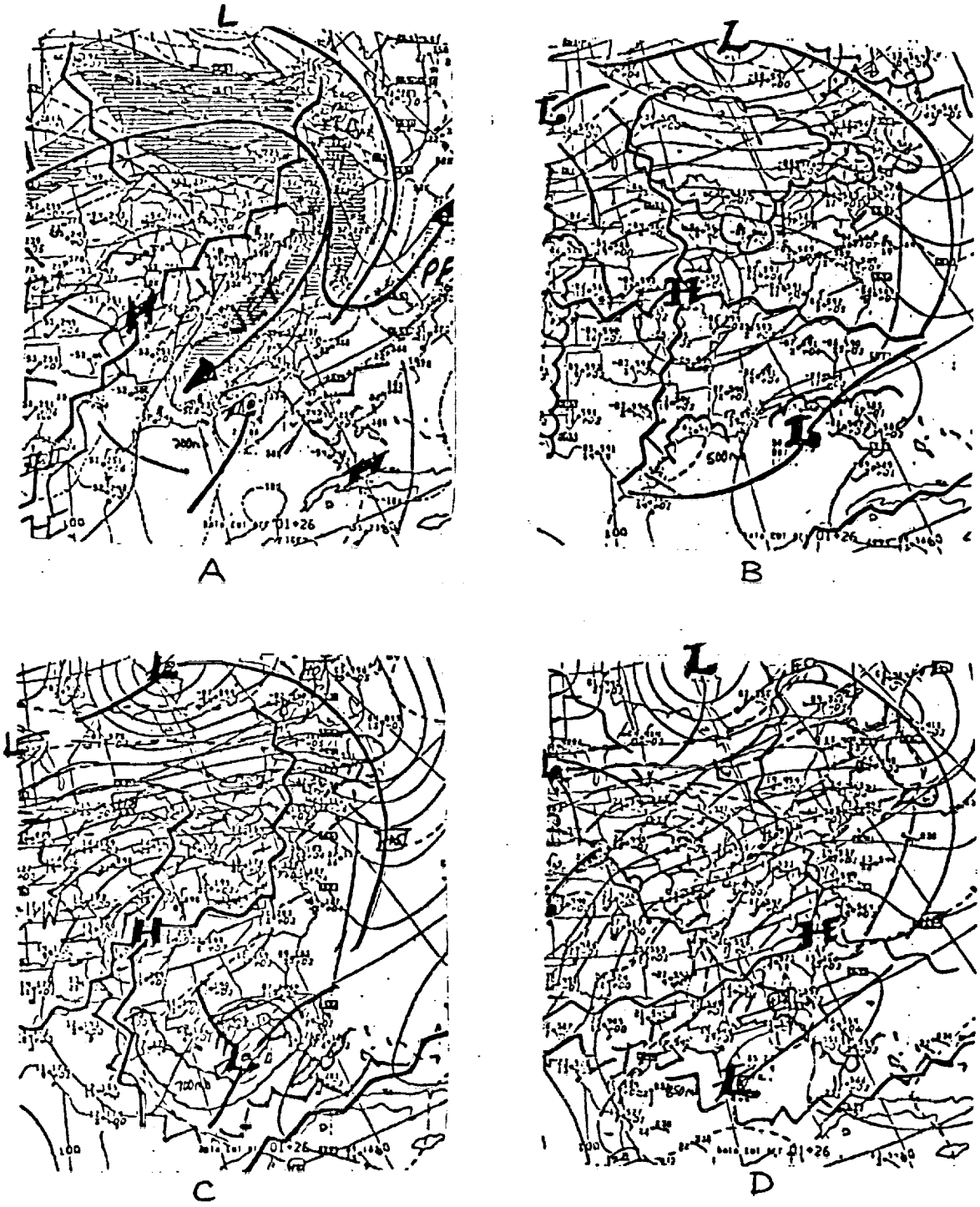

Figure 2.5: Analyses of 200 (A), 500 (B), 700 (C), and 850mbar (D) levels for 12:00 UT, July 3, 1990. Light lines denote contours of height of the pressure surface; heavy curves depict trought, while heavy wavy lines denote ridges. Centers of high height contours are marked "H," those of lower contours "L." Isotherms are dashed. The jet stream is shaded on the 200mbar map.

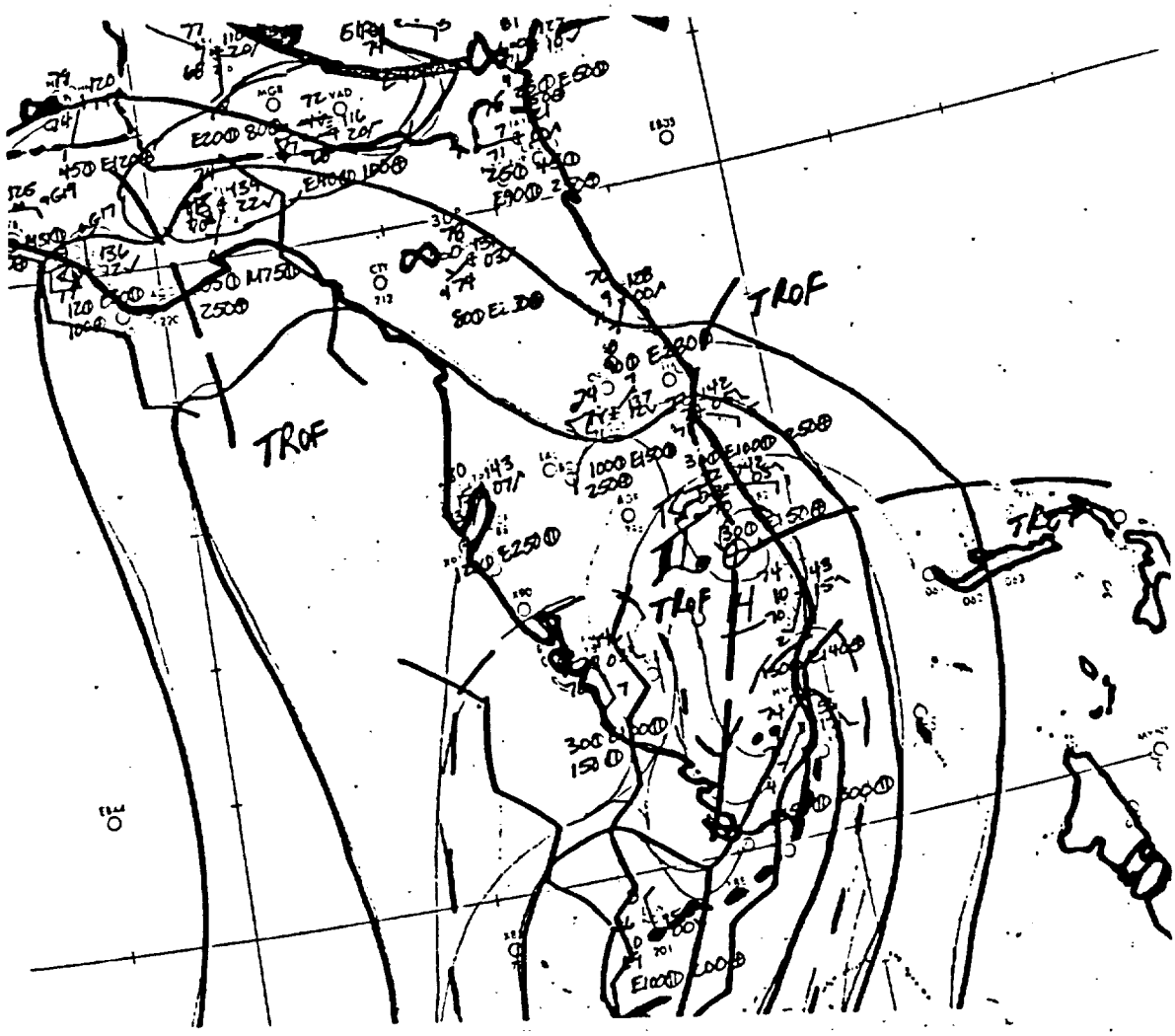

Figure 2-6: Locally produced surface weather map for 12:00 UT, July 3, 1990. A low pressure center lies along the eastern Florida coast, midway between Miami and KSC at this time. The troughs ("Trof") radiating outward from this low pressure center induced convergence, which, when combined with the sea-breeze convergence later in the day, gave rise to thunderstorm development near Titusville about 19:00 UT.

2.3 LIGHTNING-KINDLED FIRES IN FOREST PRODUCTS

The plan was to place piles of toothpicks, 1/4-inch, 1/2-inch, and 1-inch wood dowels; kindling sawn from 1/4-inch plywood, 1-by-1's, and 2-by-2's; and ultimately actual examples of local plants collected with the help and permission of the FIsh and Wildlife Service at the launch site to see which ones ignite. KSC also intends to measure the current in each strike. The idea of using well defined sizes of wood is to achieve reproducible results. Again, no results have been obtained due to paucity of triggered lightning.

Kennedy Space Center personnel involved in the lightning project are to lay this kindling near the launch site and record the results. They are to forward the data to me for my analysis and interpretation.

III

CONCLUDING REMARKS

3.1 NEW DEVELOPMENTS AND PROPOSED METHODS FOR FORECASTING LIGHTNING

The current system for forecasting thunderstorm location and lightning strike location uses a composite technique including maximum radar reflectivity of thunderstorm cells; rate of change in radar reflectivity; gradient of radar reflectivity; location, number, and frequency of negative lightning strikes; surface wind convergence; and surface wind pattern. (Surface wind pattern typically varies with stage of thunderstorm development. See Byers and Braham [1949] or Watson et al. [1989])

As Shuttle and other launches become scheduled more frequently, KSC operations become less tolerant of delays. Thus, KSC forecasters need to identify more low-risk launch window, requiring improved forecasting of weather events such as triggered lightning, wind shear, and turbulence with accuracy and timeliness unique to space programs. Measurements of electric fields, for example, have not yet been included in the forecasting process for triggered lightning. Moreover, many critical weather factors cannot even be measured directly; the forecasters infer their value from their relationship to other parameters they can measure.

Launch safety needs both accurate current weather data and forecasts for two hours or less. Observations limit the accuracy and quality of forecasts, particularly on this short-term forecasting, or nowcasting, time scale. KSC must improve its observations, including new instrumentation and measuring systems, to improve operational forecasts.

New instrumentation is no panacea, however. New instruments improve detection, not necessarily forecasting. Forecasting methods use the data available when those methods were developed. KSC needs to modify forecasting methods and techniques to include new data sources. Displays for lightning detection networks and new instruments to detect in-cloud and cloud-to-cloud lightning, for example, should be incorporated into KSC weather forecasting. Likewise, local weather analysis and forecasting techniques specific to KSC need to be developed. KSC should also develop an interactive, computer-aided weather decision-making system, and possibly numerical weather prediction models specific to KSC operations.

Local convergence of surface winds still induce thunderstorm formation at KSC. Byers and Rodebush (1948) and Byers and Braham (1949) suggested this cause, and many later experiments and studies supported them. The comparatively dense network of surface wind measurements at KSC allow use of local convergence for short-period forecasting. In particular, the forecaster must locate and follow the movements of the sea breeze, as it dominates all other convergence forces in and around KSC. A proposed, new prediction method (not yet completed) is to write computer programs to calculate and plot convergence over several sub-areas within the KSC research area (fig. 1-2), and to

locate lines and regions of convergence within the same area. Breaking the KSC research area down into four or nine smaller regions, or sub-areas, should be adequate. Watson and Blanchard (1984) noted that smaller areas provide reasonably good predictions of thunderstorm development using average convergence data, but Watson et al. (1989) noted that larger ones do not, since the averaging process dilutes the convergence (large on a small scale) when averaged over an area as large as the KSC research area. My proposal to break the KSC area down into smaller units for automatic convergence computation would solve the apparent dilution problem.

Surface convergence does not, of course, take into account any dynamic processes occurring higher in the atmosphere. The MIDDS provides upper-level information. By writing programs to analyze and plot various combinations of data (the best combinations have yet to be determined), the forecaster should be able to predict at least the potential for triggered lightning. One thing the previous research at KSC has shown: Lightning appears to begin just after maximum convergence (averaged over a fairly small area), to peak before average divergence over the same area reaches a maximum, and to decrease as divergence decreases.

3.2 FUTURE PROSPECTS AND RECOMMENDATIONS

From its start seven years ago on the shores of Merritt Island's Mosquito Lagoon, about eight miles north of KSC's Vehicle Assembly Building, NASA's Rocket-Triggered Lightning Program (RTLP) has developed progressively into a formidable research effort. NASA's desire to improve KSC lightning protection and lightning forecasting gave the RTLP emphasis. Each year adds new features to improve scientific knowledge. The RTLP added a tethered balloon in 1988. In 1990, the French will be using two different rockets to measure electric fields up to about 7000m above the ground.

Other new elements added in 1990 included raising the height of the tethered balloon to about 1500m in order to measure the electric fields to greater height with the field mills suspended below the tethered balloon; aircraft flying into clouds at various altitudes to measure the electric fields inside and outside these clouds (the airborne field mill experiment); and attempts at quantifying lightning-initiated kindling of forest materials. Placing field mills at intervals between the ground and the height of the balloon provides data on change of atmospheric electric field strength with altitude, the better to help characterize the lightning strike potential over land and water. Field mills detect and help locate the lightning, as well as allow study of the electric field environment prior to lightning strikes. The series of field mills suspended below the tethered balloon provide a more complete view of weather conditions conducive to rocket- or aircraft-triggered lightning.

The future thrust should be in combining and assimilating the many diverse data sources into an integrated short-term predictive technique. One main thrust should lie in setting up an expert system or knowledge bank, a

"forecaster's helper" along the lines of the artificial-intelligence based "doctor's associate" used by some physicians and in some hospitals. A second main effort, writing programs to analyze the myriad data sources (KSC local wind fields, electric fields, radar, and other data from the Meteorological Interactive Data Display System [MIDDS] and the Digital Weather Image Processing System [D-WIPS]) automatically, should support development of an expert system. KSC apparently recognizes the fact that too little work has been done in integrating the excellent data sources available, because they are looking for help in this vital area. I plan to continue helping KSC in these areas.

Eventual civilian "spin-off" applications of RTLP results include aircraft lightning avoidance, and lightning protection systems to thwart electrical power and/or telecommunication outages.

To undertake the Rocket Triggered Lightning Program at Kennedy Space Center gives it some unique advantages due to KSC facilities and location. The program also offers very positive potential benefits. However, to achieve the goal of the program--to improve the accuracy of lightning forecasting, thus increasing the launch window--the RTLP needs to overcome some very significant problems and shortcomings:

1. Lack of a coherent goal and the specific objectives leading there. Although I perceive the main goal of the RTLP as more flexibility in the launch criteria, with all subordinated projects leading to that goal, I have not been able to ascertain that upper KSC management has a specific goal in mind. It seems that objectives supporting the ultimate goal--things such as understanding the phenomena or developing a forecasting technique to improve thunderstorm and lightning forecasting--may be, and often have been, confused with the goal itself. Without a defined goal and a plan to achieve that goal, KSC will be doomed to flounder about, not knowing where it's going or how to get there.

2. Lack of top management support. As I perceive the situation, top KSC management does not really support the RTLP. Without that support and commitment, the program is doomed. Again, a program coordinator higher in the bureaucracy, reporting directly to top management, would enhance the RTLP.

3. Lack of adequate coordination among the diverse groups undertaking research essentially independently of each other. Each research group seems to place its own project above the total program. An example this year was the Airborne Field Mill Experiment (AFME), obviously supporting the RTLP. However, the AFME apparently enjoyed upper KSC management support and took precedence over the RTLP in allocation of resources, equipment, and personnel. To improve the RTLP, top KSC management must make a commitment to support the project. Further, program coordination should rest at a much higher level. The current coordinator is lower in rank than some of the supposedly subordinate research project leaders. Moreover, some project leaders of lower rank appear to have more influence on the RTLP than the coordinator does. There also appears to be some personal animosities.

4. Lack of cooperation. Along with coordination, cooperation among the groups does not exist, at least not as it should. Each group appears to hord its data as if it were proprietary information, which it should not be. The individual research projects within the RTLP to not share data effectively, limiting the integration of diverse data sources into a unified forecasting method which should be the strength of the program at KSC. The potential benefit of having the RTLP at KSC is its unique data sources; lack of cooperation robs the program of its main virtue. Reorganizing program structure to place every individual research project under the RTLP, even when performed by an outside group, and demanding that every group share its results with all other groups, would improve cooperation. Last year, not one of the research groups involved in the RTLP sent me the data I requested; this year has thus far been no better.

Again let me stress that Kennedy Space Center not only offers the best location and climate for thunderstorm and lightning studies, it also offers unique and extremely valuable resources, capabilities, and expertise for conducting and managing such a research effort. Unfortunately, those assets have not yet been channeled into the cohesive, fully functioning program it could and should be. With a bit more management guidance and support, a firm goal and plan for achieving that goal, plus the required top management support, KSC could have a potent and dynamic rocket triggered lightning program. Any number of groups and individuals (including me) would be eager to contribute to the success of such a well designed and planned research effort.

IV

LITERATURE AND BIBLIOGRAPHY

Byers, H.R. and R.R. Braham, 1949: The Thunderstorm. U.S. Government Printing Office, Washington, D.C. 287pp.

Byers, H.R. and H.R. Rodebush, 1948: "Causes of thunderstorms of the Florida peninsula" J Meteor., Vol.5, pp.275-280.

Krider, E.P., R.C. Noggle, and M.A. Uman, 1976: "A gated, wideband magnetic direction finder for lightning return strokes" J. Appl. Meteor., Vol.15, pp.301-306.

Lopez, R.E. and R.L. Holle, 1986: "Diurnal and spatial variability of lightning in northeastern Colorado and central Florida during summer" Mon. Wea. Rev., Vol.114, pp.1288-1312.

Maier, M.W. and W. Jafferis, 1985: "Locating rocket-triggered lightning using the LLP lightning locating system at the NASA Kennedy Space Center" Paper presented at the 10th International Conference on Lightning and Static Electricity, Paris, France.

Pielka, R.A., 1974: "A three-dimensional numerical model of the sea breeze over south Florida" Mon. Wea. Rev., Vol.102, pp.115-139.

Watson, A.I. and D.O. Blanchard, 1984: "The relationship between total area divergence and convective precipitation in south Florida" Mon. Wea. Rev., Vol.112, pp.673-685.

Watson, A.I., R.L. Holle, R.E. Lopez, R. Ortiz, and J.R. Daugherty, 1989: "Use of the surface wind field as a predictor of thunderstorms and cloud-to-ground lightning at Kennedy Space Center" Paper to be presented at the 1989 International Conference on Lightning and Static Electricity, 26-28 Sep, Bath, England. 7pp.

Watson, A.I., R.E. Lopez, R.L. Holle, and J.R. Daugherty, 1987: "The relationship of lightning to surface convergence at Kennedy Space Center: A preliminary study" Wea. Forecasting, Vol.2, pp.140-157.

Watson, A.I., R.E. Lopez, J.R. Daugherty, R. Ortiz, and R.L. Holle, 1989: "A composite study of Florida thunderstorms using radar, cloud-to-ground lightning, and surface winds" Paper presented at the 24th Conference on Radar Meteorology, Talahassee, FL, 27-31 Mar 1989. 4pp.

Williams, E.R., 1985: "Large-scale charge separation in thunderclouds" J. Geophys. Res., Vol.90, pp.6013-6025.

Ulanski, S.L. and M. Garstang, 1978: "The role of surface convergence and vorticity in the life cycle of convective rainfall. Part I: Observation and analysis" J. Atmos. Sci., Vol.35, pp.1047-1062.

V

ACRONYMS AND ABBREVIATIONS

AFWAL - Air Force Wright Aeronautical Laboratories

ASFL - Atmospheric Science Field Laboratory
Building near Mosquito Lagoon, about 15 miles north of the main KSC building complex, housing equipment, research space, and offices for conducting field experiments in lightning and other aspects of atmospheric science.

D-WIPS - Digital Weather Image Processing System
A suite of electronics, computer, and four video monitors for acquiering and displaying radar, satellite, and conventional weather data in real time and as loops.

EMP - Electromagnetic Pulse
Pulse of electromagnetic radiation emitted by nuclear explosions.

ESMC - Eastern Space Missile Center

FAA - Federal Aviation Administration

ISIS - Integrated Storm Information System
System for storage and display of digital radar data and/or cloud-to-ground lightning strike location. Displays either radar or lightning data separately on the video terminal, or both together.

KSC - Kennedy Space Center

LLP - Lightning Location and Protection, Inc
Manufactures of ISIS.

MSFC - Marshall Space Flight Center

MIDDS - Meteorological Interactive Data Display System
World-wide weather data dissemination and display system capable of displaying radar, satellite, and conventional weather data in a variety of modes and combinations, including overlaying.

NASA - National Aeronautics and Space Administration

NRL - Naval Research Laboratories

RTLP - Rocket Triggered Lightning Program
Program at KSC to launch small rockets into thunderstorm clouds, triggering lightning at the launch site.

RTLS - Rocket Triggered Launch Site
Site on Mosquito Lagoon, near the ASFL, where RTLP personnel launch small rockets into active thunderstorm clouds. Contains launch sites over land and water.

SUNYA - State University of New York at Albany

1990 NASA/ASEE SUMMER FACULTY FELLOWSHIP PROGRAM

p 28

JOHN F. KENNEDY SPACE CENTER
UNIVERSITY OF CENTRAL FLORIDA

AN EXPANSION PLAN FOR THE 60 HZ POWER DISTRIBUTION SYSTEM AT KSC: LC-39 SUBSTATIONS LOAD ALLOCATION PLAN

PREPARED BY:	Dr. Alex Kalu
ACADEMIC RANK:	Assistant Professor
UNIVERSITY AND DEPARTMENT:	Savannah State College Department of Engineering Technology
NASA/KSC	
DIVISION:	Facilities Engineering
BRANCH:	Electrical
NASA COLLEAGUE:	Mr. Julian King
DATE:	August 7, 1990
CONTRACT NUMBER:	University of Central Florida NASA-NGT-60002 Supplement: 4

ACKNOLWEDGEMENT

The author expresses his indebtedness to Mr. Julian King for his resourcefulness and assistance during this study. Many thanks are also due to Mr. Patrick Hanan, a Florida Atlantic University student, for reproducing the diagrams, and to Mrs. Imogene Smith for typing the script.

The author is above all grateful to NASA, Kennedy Space Center, authorities and the ASEE program coordinators at the University of Central Florida for the opportunity.

ABSTRACT

The increasing load density in the LC-39 area of Kennedy Space Center (KSC) can be met by either modifying the existing substation and increasing its capacity or by planning an additional new substation. This report provides evidence that the later approach is more economic, enhances the system reliability and would produce more satisfactory performance indices.

The proposed substation is optimally located based on network theory. A load reallocation plan which minimizes investment cost and power losses and meets other desirable system features is drafted. The report should be useful to the system designer and can be a useful guideline to future facility planners.

SUMMARY

This report compares the relative investment costs of expanding the C-5 substation or building a new substation to meet the power need due to increasing load density in the LC-39 area of Kennedy Space Center. In addition to more intensive labor demand, the distribution cost was determined to be higher for the C-5 expansion alternative. Similarly, this alternative suffers more power losses than the new substation approach. For these reasons and for other heuristic reasons the report recommends the building of an additional substation to meet the electric power need and projected need at LC-39 area distribution system.

Using minimum path algorithm the report suggests an optimal location for the proposed substation. A load allocation plan based on simple network theory is then used to reallocate some of the loads to the new substation. The plan suggested in this report would result in minimum investment cost and minimum system losses. Most importantly, the plan will enhance system reliability and meet desirable system performance characteristics.

The thrust of this research is to determine an optimal location for a proposed substation and based on this to evaluate the two alternative means of meeting the increasing load density. The process is based on data which contain uncertainties and thus results should be seen as a guide not a design of the system. The location of the proposed substation is determined by classical methods with environmental and social constraints taken into consideration. Also considered is an economic availability of power to future facilities.

TABLE OF CONTENTS

LIST OF FIGURES

II. INTRODUCTION

2.1 Statement of Problem

The load demand in the Kennedy Space Center (KSC) power system has been increasing continuously since its inception twenty-five years ago. This increase has become more rapid in recent years due to increased frequency of vehicle launches and associated activities. A rather misleading average shows a predicted load growth of about 1.5 MVA per year. To keep up with this ever-increasing load density, effective expansion plans for the distribution systems are essential. Two alternative means to ensure no loss of load due to low installed capacity are: (a) to expand (increase) the capacity of the existing substations or, (b) to build new substations.

An essential part of the expansion planning is to determine which of the two alternatives should be implemented. This decision should be based on sound principles rather than be made arbitrarily. The criteria for determining which alternative should be adopted are investment and construction cost, power loss, reliability, and system performance indices, such as voltage regulation, etc. In addition to the above quantifiable measures, one also needs to look at other matters which are not easily quantifiable, such as long term economic and technical considerations, expected area of future (long term) expansion, and environmental and social constraints.

The system under study is the LC-39 area distribution system. Presently, it is supplied from a 45 MVA substation consisting of four 10 MVA main transformers and two 2.5 MVA transformers. Though the demand is fast approaching the capacity, several new facilities have been planned for the area in the next few years, thus creating a need for capacity expansion. The proposed facilities are mostly concentrated in the area between the VAB and Swartz Road and bounded by Contractors Road to the west. This study is based on the proposed load and the capacity-demand conditions of the feeders which presently supply electric power to the sub-area. The study shows that the winning alternative is building of a new substation which should be located in the area with high density of projected load growth. Based on this decision, a load reallocation plan between C-5 substation and the proposed substation is suggested.

2.2 Description of the Study System

Only a subsection of the LC-39 area of Kennedy Space Center is affected by the load allocation scheme. This area is bounded to the west by Contractors Road and lies between VAB and Swartz Road. The real estate in this area suffers considerable discontinuities due to patches of wetland. Several facilities have been planned for the area in the next few years and are sited at buildable columns of the real estate. None-the-less, there is still ample room for growth in the southeast portion of this sub-area. To the south of Swartz Road, adjoining the industrial area, lies substantial real estate for possible future expansion. This area, however, has high percentage of wetland. A diagram of the area affected by our study showing the facilities, the proposed facilities, the wetland patches and other geographic conditions is shown in Figure 1.

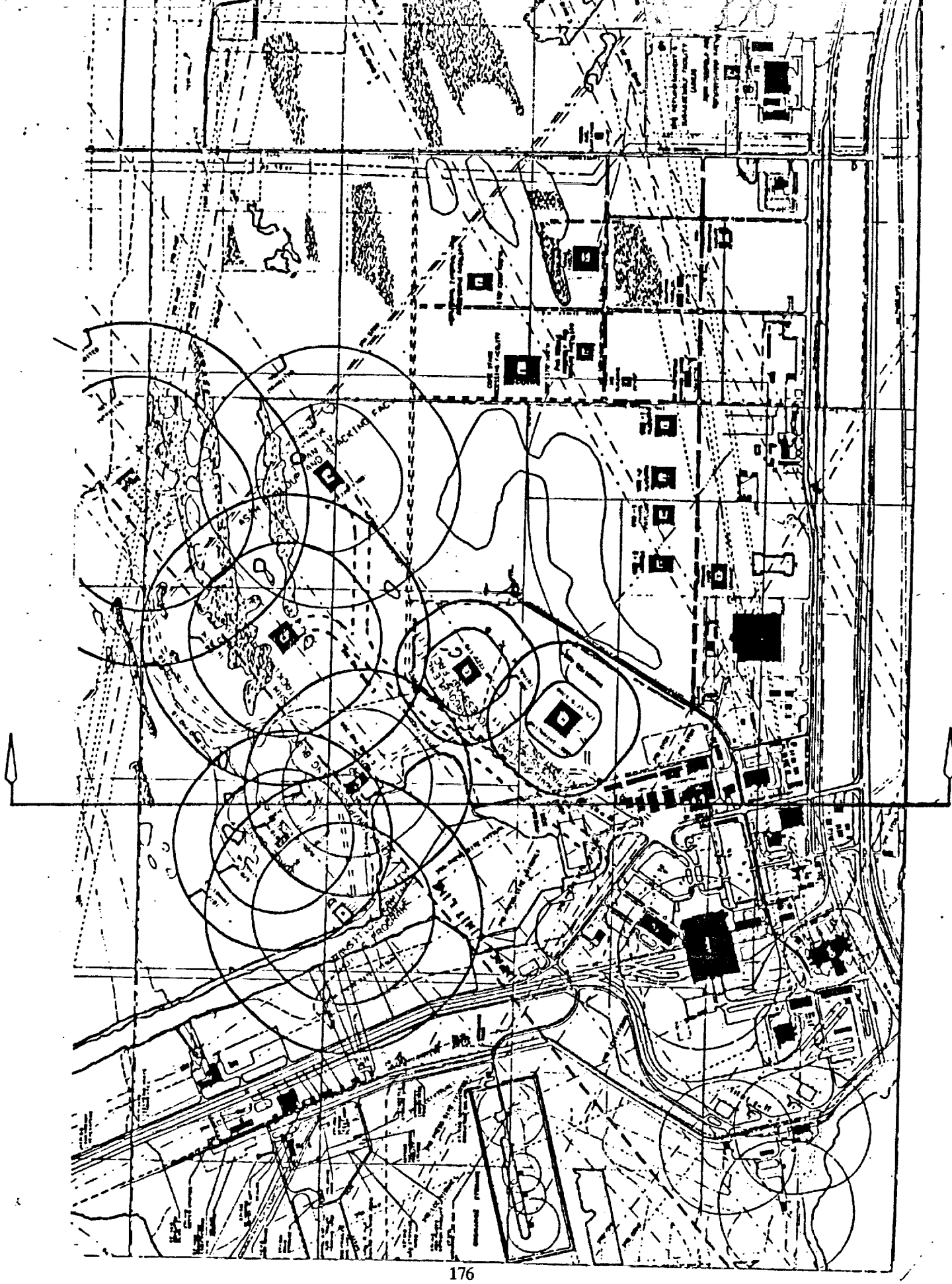

FIGURE 1. SUB-AREA OF 39 DISTRIBUTION SYSTEM UNDER STUDY

One of the four main transformers at C-5 substation is reserve. This leaves normal operating capacity of 30 MVA in the distribution system. The demand is approximately 98 percent of the rated normal operation capacity at the present but substantially below the maximum capacity.

Two feeders (FDR 605 and FDR 616) out of this substation supply electric power to the sub-area of interest. FDR 605 supplies power to the facilities in the sub-area under discussion through load break switches LBS 731, LBS 732, LBS 710, and LBS 709. Utilization facilities in the sub-area which draw power from FDR 616 are connected to one of the following load break switches - LBS 717, LBS 716, LBS 715, LBS 714, LBS 713, LBS 712, LBS 711, LBS 708, and LBS 50. See Figure 2 for the single line diagram showing the distribution network in sub-area affected by the load reallocation plan. This area was carved out for the study to cover most of the proposed utilization facilities. It is also the sub-area of the LC-39 distribution zone that has room for future facilities siting. Figure 3 is a diagram of the sub-area showing present distribution system and the proposed facilities.

2.3 Capacity-Demand Status of Substation and Feeders Under Load Reallocation Plan

To estimate the loss of load probability (LOLP) it is necessary to determine the capacity-demand margin. In the case of the substation, judgement can be based on one of several margins depending on the required level of reliability. The margins range from normal operation rated capacity-demand margin to maximum available capacity-demand margin. For the feeders the margins of interest are the differences between rated ampacities and the maximum demand current. Tables 1 and 2 show the present capacity-demand conditions relevant to the study.

III. LOCATING THE NEW SUBSTATION AND THE LOAD REALLOCATION PLAN

3.1 Optimal Location for the New Substation

The primary assumption for choosing a location for the new substation is that much of what necessitates the building of the substation are proposed facilities and anticipated growth. This is based on the reasoning that since the present capacity-demand margins (based on the normal operation rated capacity of C-5 substation) is virtually zero, it will be prudent to consider a new substation to support the proposed loads. By the same token, since there is no loss of load in the system at present, none of the present load needs to be transferred to another substation unless the transfer enhances system reliability while reducing cost and system losses. The basic variables for computing the location of the new substation are thus the distribution of the proposed utilization facilities and the area of greatest likelihood for future growth.

The underlining-philosphy is to determine a location for the proposed substation P-LC-39 that will result in minimum investment cost and system losses. If we assume that the construction and equipment costs are fixed (not dependent on location) then investment cost becomes a function of cable length L. Thus the problem of minimizing investment cost reduces to minimizing feeder length. A simple minimal path algorithm is suitable for this purpose, [1]. This is shown in paragraph 3.1.1

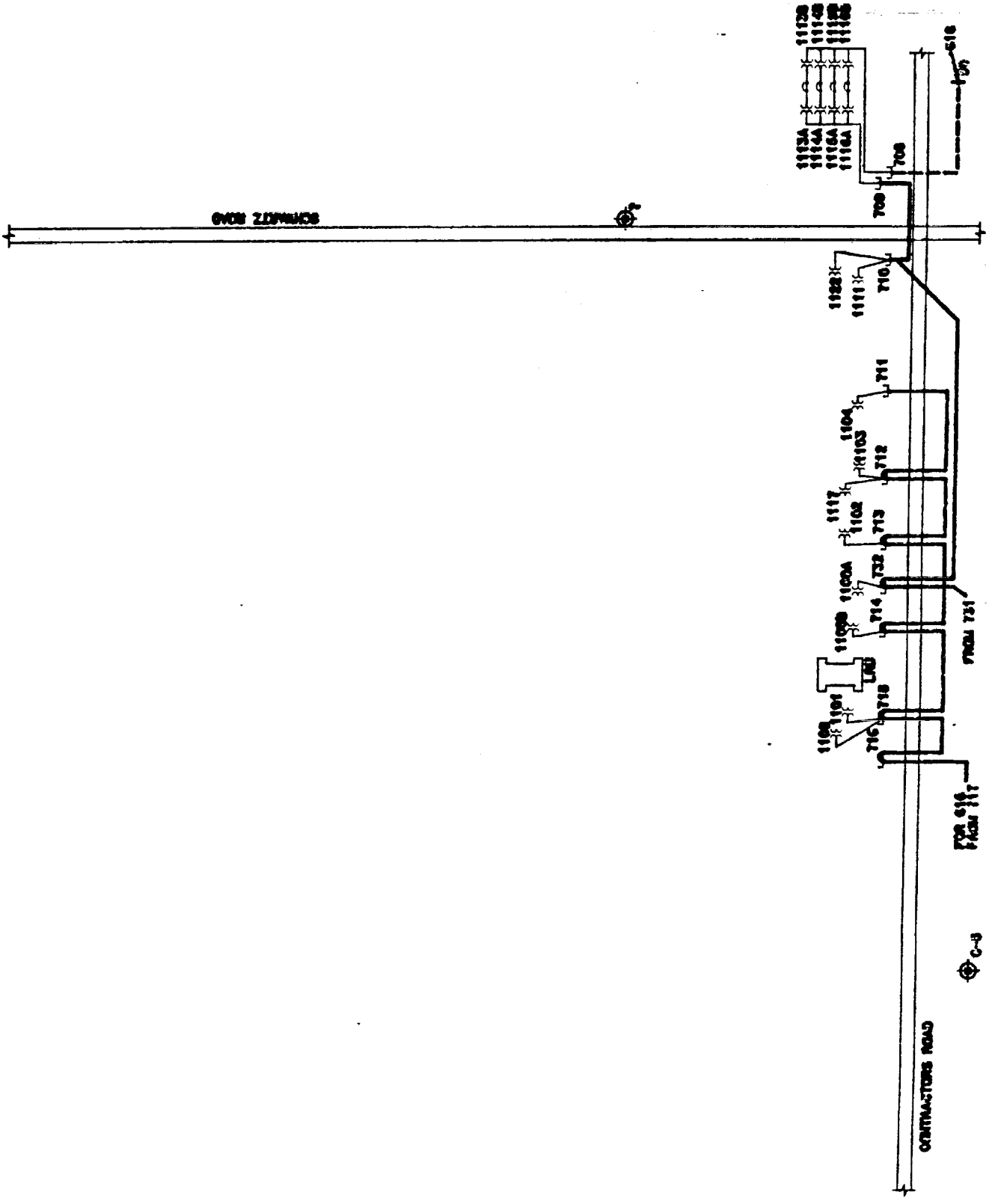

FIGURE 2. THE ELECTRIC POWER DISTRIBUTION NETWORK IN AREA UNDER STUDY

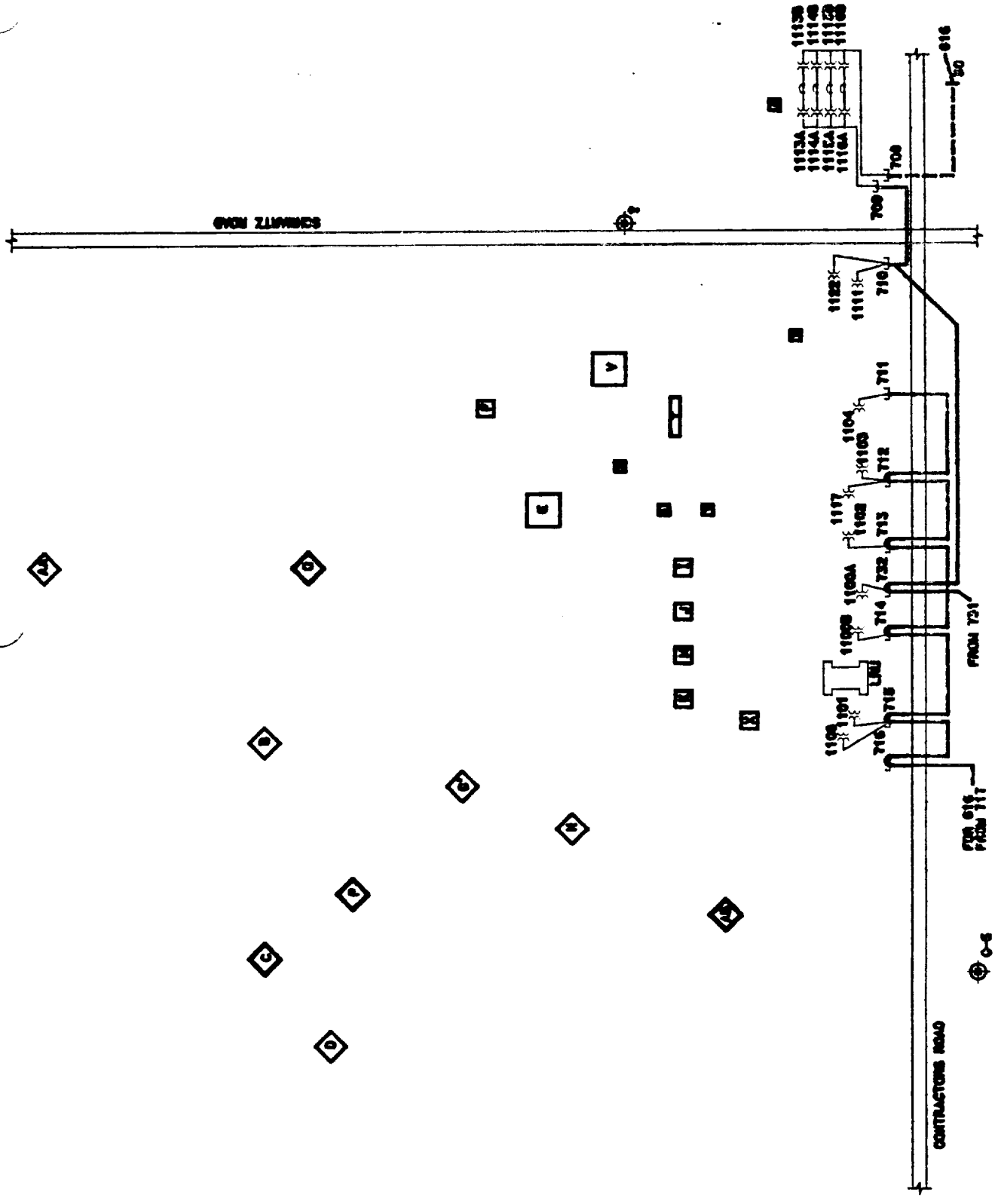

FIGURE 3. SHORT TERM PROPOSED FACILITIES AND PRESENT ELECTRIC SUPPLY NETWORK IN SUB-AREA

TABLE 1

C-5 SUBSTATION CAPACITY-LOAD MARGIN INFORMATION 1990

	CAPACITY (MVA)	LOAD (MVA)		MARGIN		
		CONNECTED	DEMAND	CAPACITY-CONNECTED (MVA)	CAPACITY-DEMAND MVA	%
55^{o} C, NO FAN	30.0	189.168	29.4	-159.168	0.6	2.0
65^{o} C, NO FAN	33.6	189.168	29.4	-155.568	3.6	10.7
55^{o} C, FAN COOLING	37.5	189.168	29.4	-151.668	8.1	21.6
65^{o} C, FAN COOLING	42.0	189.168	29.4	-147.168	12.6	3.0

The ratio of peak load to connected load is 15.54 percent which indicates that the capacity-connected load margin is not a good measure of system reliability. An overwhelming percentage of the connected load does not draw power simultaneously.

TABLE 2

AMPACITY-DEMAND MARGINS FOR FEEDERS UNDER LOAD REALLOCATION

FDR #	CONDUCTOR AMPACITY (AMPS)	DEMAND* (AMPS)	MARGIN AMPS	MARGIN %
605	307	120	187	60.9
616	280	180	100	35.7

*These are the maximum demand (peak values) for the year 1990. (Available data at time of study, July 1990.)

If optimal conditions are attained by all the new loads being connected to P-LC-39 and the integrity of the present system preserved, then the minimum investment cost scheme will also produce a minimum system loss. However, if the location of P-LC-39 as obtained by the minimum cost algorithm (based on the proposed loads) results in a possible load reallocation, then the minimum power loss algorithm must be introduced. Indeed this may result in a shift in the position of P-LC-39, i.e., the minimum cost algorithm is used again to determine the final and optimal location of P-LC-39 based on the reallocation plan and the minimum power loss scheme. The minimum power loss algorithm is discussed in paragraph 3.1.2

3.1.1 The Minimum Cost Algorithm

With reference to figure 4. which shows the distribution of the proposed loads, define two sets:

S = {Connected Nodes}

$\overline{S}$ = {Unconnected Nodes} = {A, B, C, V, W, T, N, F, E, C', I, J, M, K, X, H, AA, D, U, Y, AB, P, LRU, O}

The problem is to determine the branches that will join all the nodes (load points) in $\overline{S}$ to form a network S, such that the sum of the lengths of the chosen branches is minimized. The process is a sequence of transitions of the elements (nodes) in $\overline{S}$ to S such that the distance i between elements i + 1 and any element in S is a minimum for i = 1, 2, 3, ...N, where N is the number of proposed load points in $\overline{S}$. The starting point is arbitrary. Let D be the starting node. The sets S and $\overline{S}$ now become:

S = { D }

$\overline{S}$ = {A, B, C, V, W, T, N, F, E, C', I, J, K, X, H, AA, U, Y, AB, P, LRU, O}.

Now compare the distances between D and the nodes in $\overline{S}$. The shortest distance is between D and C. Thus the sets S and $\overline{S}$ now become S = {D, C},$\overline{S}$ = {A, B, V, W, T, N, F, E, C', I, J, K, X, H, AA, U, Y, AB, P, LRU, O}. Now connect D to C and compare the distances from all the nodes in $\overline{S}$ to all the nodes in S. We select a node in $\overline{S}$ closest to a node in S. This node is P. Consequently, S = {D, C, P,}, $\overline{S}$ = {A , B, V, W, T, N, F, E, C', I, J, K, X, H, AA, U, AB, LRU, O}. P is connected to C (shortest link).

This procedure is continued until all load points are connected, i.e.:

S = {A, B, C, V, W, T, N, F, E, C', I, J, K, M, X, H, AA, D, U, Y, AB, P, LRU, O}.

$\overline{S} = \phi$

The number of iterations is N-1 where N is the number of proposed load points. The minimum spanning tree is shown in figure 5. If the proposed substation P-LC-39 is located on any of the branches it will result in minimum feeder cost. It should be noted that unlike in traditional application of minimum path algorithm, here a loop is allowable, but only if there

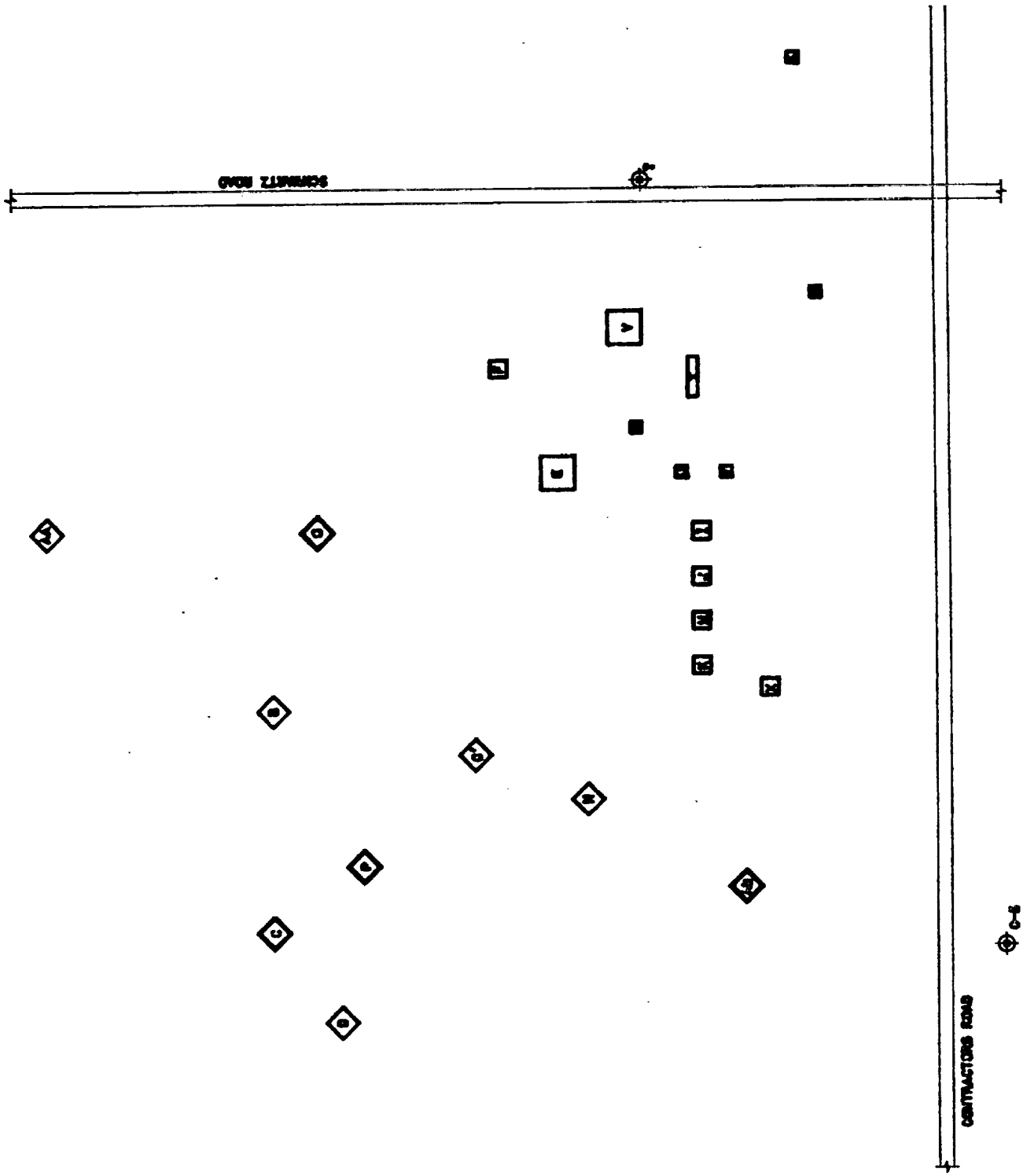

FIGURE 4(a). THE DISTRIBUTION OF PROPOSED UTILIZATION FACILITIES

FIGURE 4(b). THE DISTRIBUTION OF PROPOSED FACILITIES AND PRESENT ELECTRIC LOAD PO[illegible]S

C-3

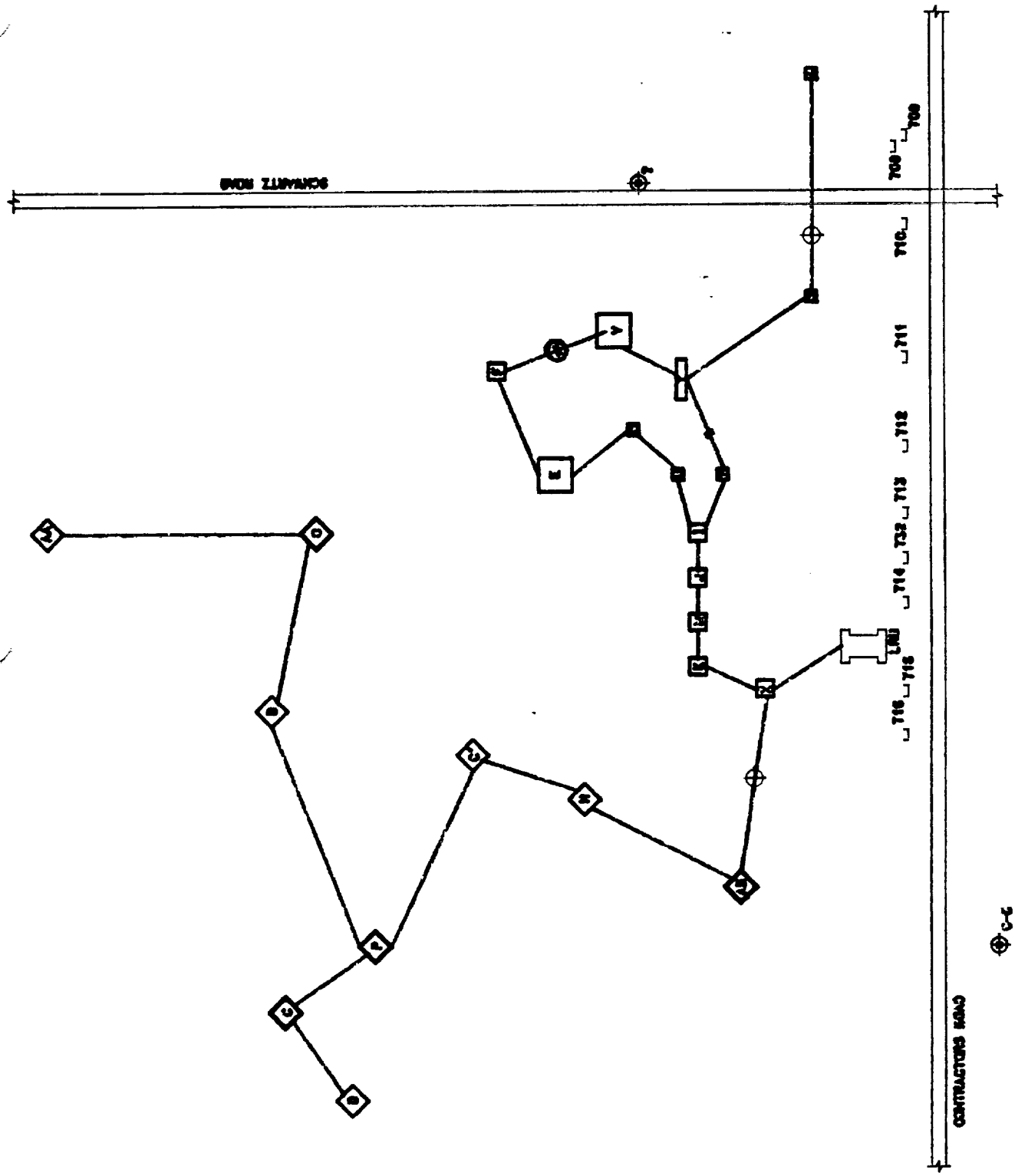

FIGURE 5. MINIMUM LENGTH NETWORK FOR CONNECTING ALL PROPOSED LOADS

is a tie. If this happens the equal links should be marked. Usually one of them will be eliminated or used to tie two feeders for switching purposes.

3.1.2 Load Reallocation and the Minimum Loss Algorithm

The power loss of a feeder is given by:

$$\text{Loss} = I^2R \qquad (1)$$

Where

I = the demand in amps

R = the resistance.

Since I, the current drawn by the loads is fixed for a given set of loads, loss can only be reduced by a reduction in R. But:

$$R = \frac{\rho L}{A} \qquad (2)$$

Where A, the cross sectional area and ρ the resistivity of the conductor are constant for a given feeder. Hence a reduction in R and consequently a reduction in feeder loss can be achieved by a reduction in the feeder length L. This means that to achieve minimum system loss, system feeder lengths must be minimum or the load reallocation plan must insist that loads be connected to sources closest to them. Thus the minimum loss algorithm is essentially the load allocation algorithm.

Having determined a location for the new substation, P-LC-39, the load reallocation algorithm is as follows:

With center P-LC-39 describe a circle radius r_1 in the load field. With center C-5, describe a circle of same radius r_1 in the load field. With these two centers, describe circles of equal radii r_2, r_3, r_4.--. The number of pairs of circles depends on engineering judgement based on the load distribution. Similarly, spacing of the circles $r = r_{i+1} - r_i$ is arbitrarily chosen due to the load distribution. Label the circles, see figure 6. Circles with center P-LC-39 are labeled P_1, P_2, P_3... in order of increasing radius. Circles with center C-5 are labeled C_1, C_2, C_3.-- in order of increasing radii. Compare the load points with respect to the circles and the load allocation rule is:

Assign Load Point X to P-LC-39

if $X \in P_i$ and $X \notin C_i$, $i = 1, 2, 3$---

Assign Load Point X to C-5

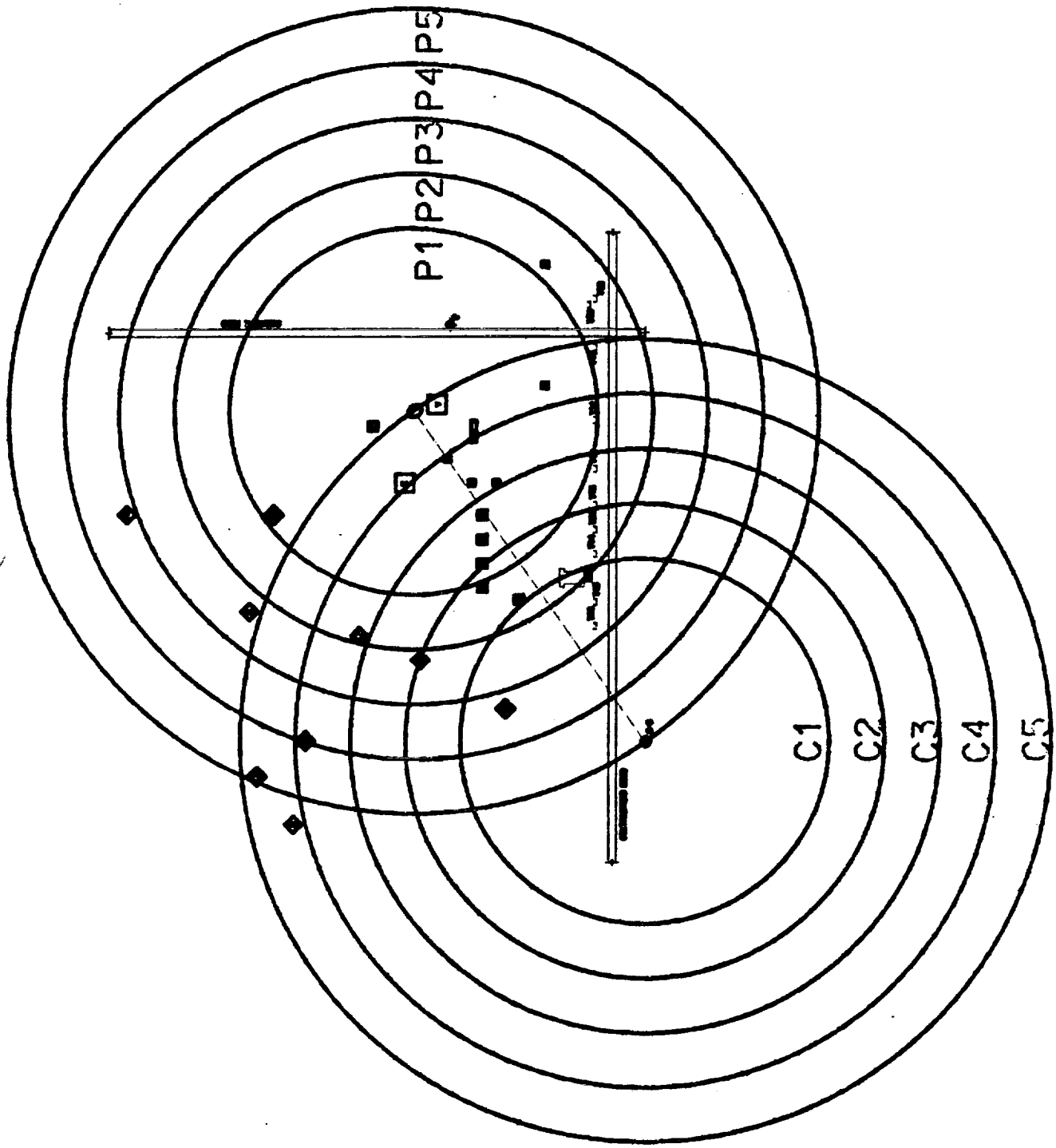

FIGURE 6. LOAD ALLOCATION CHART

if $X \in C_i$ and $X \notin P_i$.

It must be noted that the application of this rule is subject to some heuristic rules set by the system management. Examples of such rules are given in section 3.2. Also, if $X \in \{C_i \cap P_i\}$ assignment is arbitrary subject to some heuristic rules.

Using this load allocation plan feeders FDR 616 and FDR 605 are relieved of 5.175 MVA and 5.925 MVA, respectively, from the existing load while substation C-5 picks up 10.7 MVA of the proposed load. (See Table 3.) It can be observed that the effectiveness of this plan has resulted in a relief on the two feeders in C-5 which at the present suffer the highest demand/ampacity ratios (highest load factors).

3.1.3 The Optimal System

The algorithm just described produces a minimum power loss load allocation. To further optimize the system each substation distribution network must be connected subject to some rules.

3.1.3a The Proposed Substation P-LC-39 Distribution Network

Now that loads have been assigned to the proposed substation, the algorithm of Section 3.1.1 is used to determine the final set of points (links) on which P-LC-39 can be located. This time the initial set $\overline{S}$ (iteration 0) shall consist of all the loads (present and proposed) that were allocated to P-LC-39 by the algorithm of section 3.1.2. This recursive relationship between the two algorithms guarantees a simultaneous minimization of investment cost and system losses in the load allocation scheme. The minimum spanning tree for the final selection of P-LC-39 location is shown in Figure 7. It may be noted that this tree coincides with that of Figure 5, thus, the recursive process terminates.

After the load reallocation and the final selection of P-LC-39 location, the minimum power loss algorithm proceeds thus for P-LC-39:

STEP 1: Connect the load points in P_1 to P-LC-39 forming new feeders for P-LC-39. These feeders should not violate the constraints set by management. Otherwise, another location must be chosen for P-LC-39 and this step repeated.

STEP 2: Connect each load point in P_2, but not in C_2 to any one of the load points in P_1.

STEP 3: Repeat step 2 for i = 3, 4, ..., connecting load points in P_i to any load point in P_{i-1}, provided other constraints are not violated.

3.1.3b. Connection of Load Reallocated to C-5

A rule that must be followed for reaching a minimum power loss and investment cost load allocation plan for C-5 is:

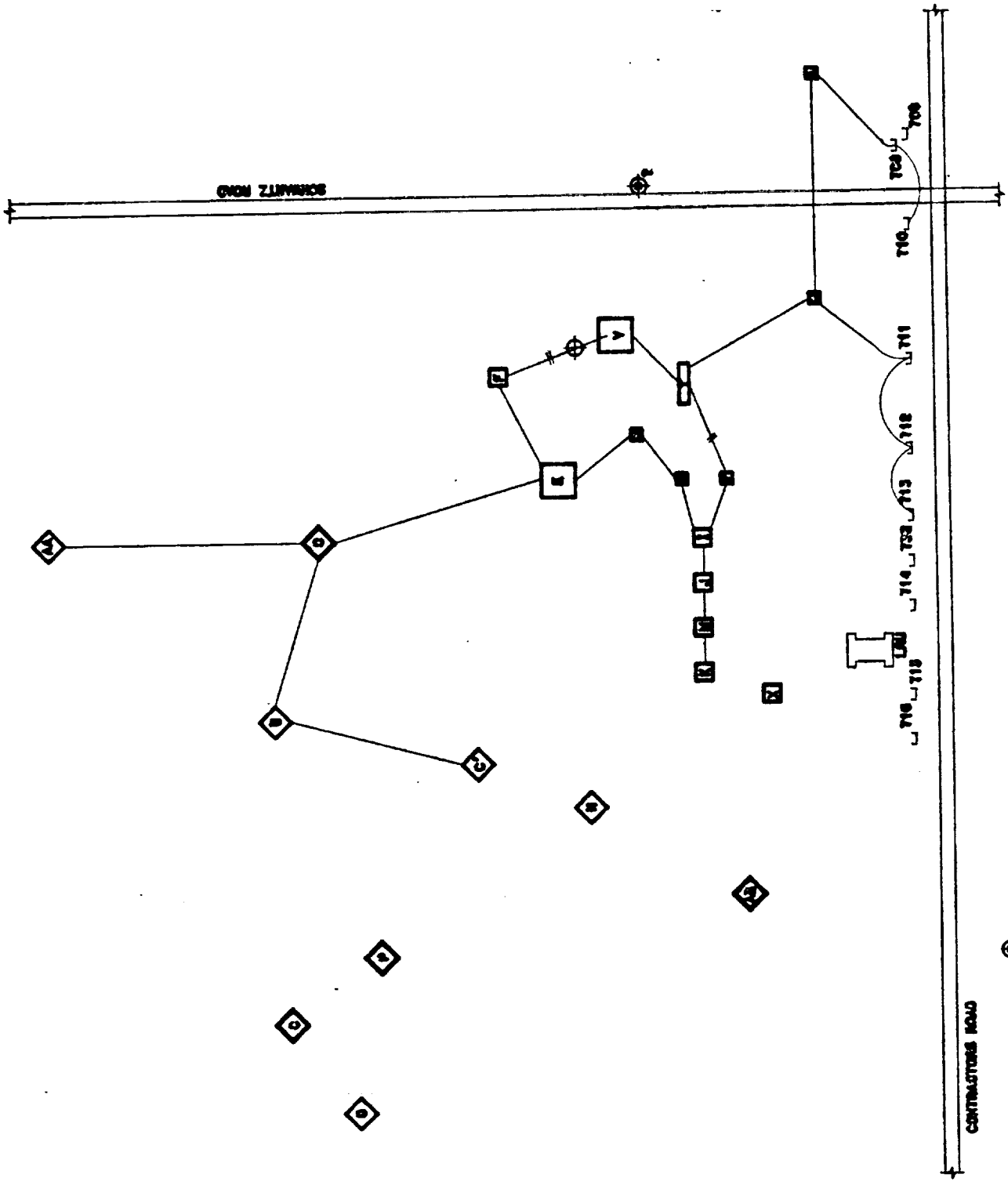

FIGURE 7. THE OPTIMAL LOCATION SET FOR P-LC-39

TABLE 3

LOAD POINTS AFFECTED BY LOAD RELOCATION

A. TRANSFER FROM C-5 TO P-LC-39

FDR#	LBS #	USS #	SIZE (KVA)
605	709	1113A'	2000
		1114A	750
		1115A	1000
		1116A	300
	710	1111	150
		1122	225
	732	1100A	1500
616	708	1113B	2000
		1114B	750
		1115B	1000
		1116B	300
	711	1104	75
	712	1103	750
		1117	225
	713	1102	75

Total transfer from C-5 = 11.1 MVA.

B. CONNECT TO C-5 FEEDERS

PROPOSED LOAD ID	ESTIMATED SIZE (KVA)
P	2000
C	300
D	200
H	3000
LRU	1000
X	200
AB	4000

Total new load to be connected to C-5 = 10.7 MVA, estimated value.

The load points which are connected to an existing feeder and fall within the same circle C_i must be connected in the load allocation plan. In addition to this rule, connection of load points in C_i to load points in C_{i-1} should also be followed subject to capacity constraints.

3.2 Heuristic Rules for Load Reallocation

The mathematical procedures outlined in section 3.1 result in an optimum system in an ideal world. The application of those rules, however, must be subject to some constraints which are determined by engineers based on their experience, environment, and required level of reliability. The following are examples of such constraints:

1. Constraints on Substations

   (a) The location of the new substation P-LC-39 is subject to (i) Environmental Constraints: These are the existence of wetland in the area and danger to wild life. From discussions with the environmental staff, it is noted that these constraints are relaxed for LC-39 area. (ii) Social constraints: The substations must be built not to interfere with planned streets and roads, or with probable area of facility location. There are indications from the real estate managers that this constraint is very soft particularly relative to the branches of the minimum spanning tree of figure 7.

   (b) It is the place of the system planners to determine the capacity of the new substation based on their need. It is also the system planners engineering judgement that sets the allowable demand/capacity ratio according as the level of reliability required. A typical rule is [2]: If the load of a substation is greater than 70% of its installed capacity, another substation is needed.

   (c) If the substation design does not tie the main transformers in parallel (connected to one bus) then the planners must set the allowable connected load/capacity ratio for a transformer. Under the same situation, the allowable number of feeders to a transformer should also be specified.

2. Constraints on Feeders

   (a) The load factor should not exceed a set value.

   (b) The maximum load (MVA) to be supported by a feeder should be specified.

   (c) The maximum number of load break switches to be connected to a load break switch should be specified.

   (d) An acceptable voltage regulation for each load break switch (or load point) must be specified.

The actual implementation of the load allocation feeder design, substation design, and load connections should take these rules into consideration while conforming with the guidelines of the algorithms of section 3.1

IV. RESULTS AND RECOMMENDATIONS

The main goals of this study are (a) to determine whether to build a new substation or expand the capacity of C-5; (b) to determine the best possible location(s) of the new substation if one should be built.

(a) The study concludes that a new substation should be built based on the following:

(1) There will be a reduction in system losses if this option is adopted and the load allocation scheme implemented.

Suppose all the proposed loads are to be connected to an expanded C-5 substation. Then in comparison to connecting them or some of them to a new P-LC-39 substation which is optimally located, the distance between C-5 and the furthest load AA is greater than the distance between P-LC-39 and any of the proposed loads. This implies that the minimum power loss chart for C-5 will consist of more zones (circles) than that of P-LC-39 to cover all the loads. From the discussions of section 3.1.3, it is obvious that power loss is proportional to the number of zones (concentric circles). Measurements show that the ratio of power losses for the two alternatives is 3.5:8.0 in favor of the new substation alternative. (See Figure 8.)

(2) The new substation option will result in savings in investment cost.

Suppose it is proposed to expand C-5 to accommodate all the new loads. Then new feeders must be added to connect those loads. A minimum length network for this purpose is shown in Figure 9. In comparison to Figure 7, this scheme uses (302-206) 96 more unit lengths of feeder. This alternative would thus cost more.

(3) In addition to the above deterministic criteria, other reasons for choosing the new substation alternative which are not readily quantifiable include:

a) Avoiding the mixture of new main transformers with twenty-six year old transformers. If new transformers with possibly different specifications are connected in parallel to the existing old transformers in C-5 it may create impedance mismatch problems, stability problems, and increase uncertainty in system reliability. The mixture will also create maintenance scheduling problems.

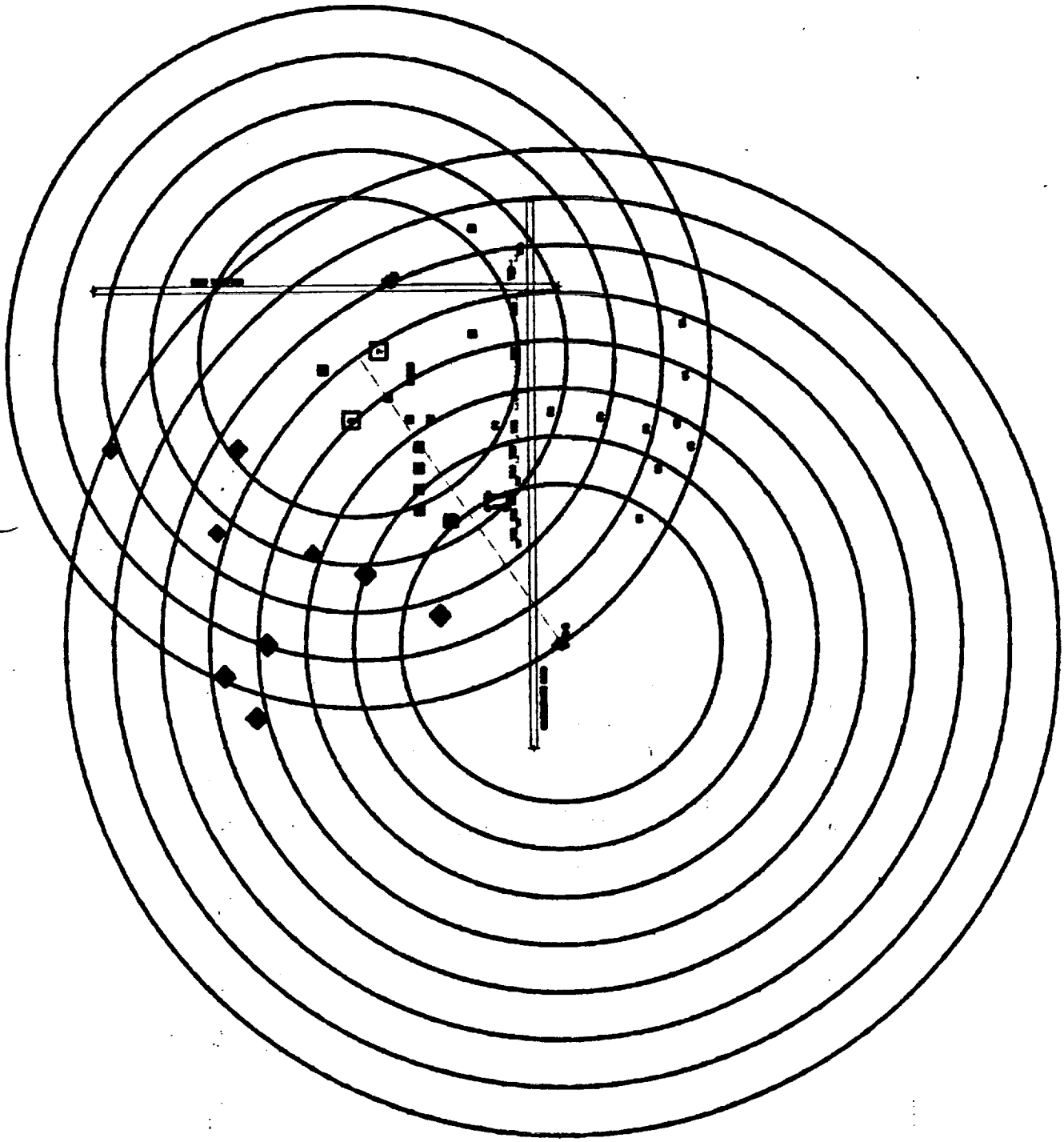

FIGURE 8. A COMPARISON OF THE MINIMUM-LOSS CHARTS FOR THE COMPETING ALTERNATIVES

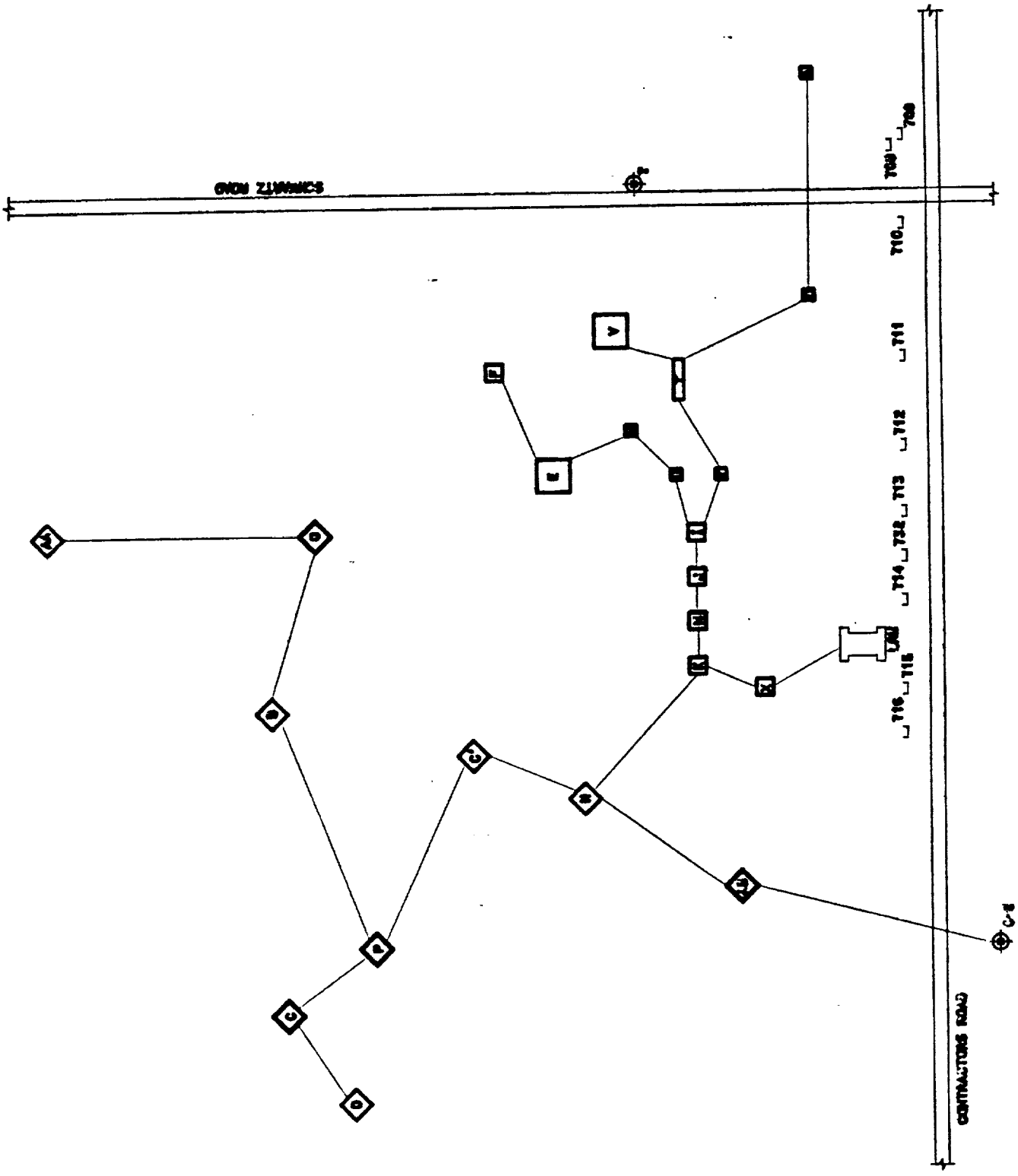

FIGURE 9. MINIMUM LENGTH NETWORK FOR CONNECTING ALL NEW LOADS TO C-5

b) Considering the area of greatest likelihood of growth, the new substation will result in greater long term savings.

c) System reliability will be enhanced by the construction of a new substation which can have an emergency assistance tie with the existing substation.

d) System studies will be much easier if the loads are divided into two substations.

V. CONCLUDING REMARKS

This study concludes that a new substation should be built to support the proposed loads and any future growth. The load reallocation of table 3 is based on the authors choice of the location of the new substation. (See Figure 7.) This choice is based on the fact that future growths are most likely to occur in the southeast portion of the area. Figures 5 and 7 show a set of points where the substation can be located. Any point on the links on the tree of Figure 7 will yield the same result. The case of locating the substation close to the transmission line should be irrelevant if the primary concern is to save cost to NASA-KSC. Transmission line is a delivery mechanism whereby the power supplier (FP&L) delivers power to its customers. One would then expect the cost of transmission to be borne by FP&L. More importantly, KSC power consumption is metered at its substations. This excludes the power losses in the transmission line. It is therefore more important to optimize P-LC-39 location with respect to distribution feeder lengths and losses in the feeders than with respect to its proximity to the transmission line. The actual size and location of the substation will depend on the system planners and designers. This note is intended to be a guide, if followed will result in a reliable system with desirable performance indices, and reduce cost.

REFERENCES

[1] Chan, J., and Y. Hsu; "An Expert System for Load Allocation in Distribution Expansion Planning," IEEE Trans Power Delivery, Vol. H, No 3., July 1989.

[2] Akoi, K., et al; "Normal State Optimal Load Allocation in Distribution Systems," IEEE Trans Power Delivery, Vol. 2, No. 1, 1987.

1990 NASA/ASEE SUMMER FACULTY FELLOWSHIP PROGRAM

JOHN F. KENNEDY SPACE CENTER
UNIVERSITY OF CENTRAL FLORIDA

STUDY OF THE AVAILABLE FINITE ELEMENT SOFTWARE PACKAGES AT KSC

PREPARED BY:	Dr. Chu-Ho Lu
ACADEMIC RANK:	Assistant Professor
UNIVERSITY AND DEPARTMENT:	Memphis State University Department of Mechanical Engineering
NASA/KSC	
DIVISION:	Data Systems
BRANCH:	CAD/CAE
NASA COLLEAGUE:	Mr. Hank Perkins Mr. Ed Bertot
DATE:	August 10, 1990
CONTRACT NUMBER:	University of Central Florida NASA-NGT-60002 Supplement: 4

ACKNOWLEDGMENTS

I would like to thank my NASA colleagues, Mr. Eddie Bertot and Mr. Hank Perkins of DL-DSD-22 for their support In obtaining the necessary resources to do this research. The technical support from Mr. Drew Hope of EG&G in using I/FEM, and Mr. Rudy Werlink and Mr. Raoul Caimi of NASA DM-MED-11 of and Mr. Richard Hall and Mr. Lloyd Albright of EG&G in using SDRC/I-DEAS and MSC/NASTRAN was also deeply appreciated.

Additionally, I would like to thank the administrative support of Dr. Loren A. Anderson and Ms. Kari Baird, University of Central Florida, and Dr. Mark Beymer, the director of the summer faculty fellowship program at NASA/KSC.

ABSTRACT

This research report concerns the interaction among the three finite element software packages - SDRC/I-DEAS, MSC/NASTRAN and I/FEM, used at NASA, John F. Kennedy Space Center. The procedures of using more than one of these application software packages to model and analysis a structure design are discussed. Design and stress analysis of a solid rocket booster fixture is illustrated by using four different combinations of the three software packages. Their results are compared and show small yet acceptable differences.

SUMMARY

In this research report the use of the three finite element software packages, SDRC/I-DEAS, MSC/NASTRAN and I/FEM, in model construction and statics analysis is studied. The procedures in using highly interactive and graphics software such as SDRC/I-DEAS and I/FEM to construct a working model are briefly summarized in Section II and illustrated in Figures 1, 2 and 3.

Due to the very general capabilities of structural analysis contained within MSC/NASTRAN, the applicability of using SDRC/I-DEAS (or I/FEM) in preprocessing and postprocessing and MSC/NASTRAN in analysis are discussed in Sections III and IV. Although transferring files between SDRC/I-DEAS and I/FEM is not supported by either software, it is found that it can be done with the aid of MSC/NASTRAN.

The design and statics analysis of a solid rocket booster fixture was studied in Section V. The purpose of studying this problem is twofold: the strength of the fixture so that it won't fail in use can be assured through stress analysis, and the interfacing of more than one software packages can be tested via four different combinations as shown in Table 1. As expected, the different combinations of the three finite element software packages yielded similar results. The effective use of these software packages and the strengths and weaknesses of each software package are discussed in the conclusions.

TABLE OF CONTENTS

LIST OF ILLUSTRATIONS

LIST OF TABLES

I. INTRODUCTION

The finite element method has been established as a powerful and popular numerical procedure for solving many different problems of continua governed by differential equations. The method, in general, can be considered a definite set of seven basic steps: Discretization, Interpolation, Elemental Formulation, Assembly, Constraints, Solution and Computation of derived variables. As a result of the first three steps, a continuous model with infinite degreeS of freedom is converted into a discrete model having finite degree of freedom, and a mathematical model including differential equations is generally converted into a mathematical model involving algebraic equations. After these algebraic equations are assembled and the constraints are introduced, the solution and the derived variables can be obtained with the aid of computers.

It is possible to write computer code which will create and analyze a finite element model just described. In fact, hundreds of commercial finite element programs are available, from small to large. The most well known large general-purpose analysis software packages are NASTRAN, ANSYS and ABAQUS. They provide many different element types, so that almost any conceivable structure, loads and boundary conditions can be treated. Linear problems of statics and dynamics are certainly included. Several nonlinear capabilities are also provided.

Using the commercially available finite element programs to solve problems, one does not begin with differential equations. Instead, there are three basic phases which can be identified (i.e., preprocessing, analysis modeling and solution, and postprocessing). In the preprocessing phase, a continuous media is discretized, element types are selected, loads and constraints are provided, and material and physical properties of the problem are specified. Then the problem is solved in the analysis phase. The derived variables are also computed. The results are finally analyzed and managed in the form of reports or plots in the postprocessing phase. The process is repeated if mesh refinement is necessary.

Although the large general-purpose finite element software packages offer an extremely versatile capability, engineers typically consume more than 65% of their time in the model analysis process. It is clear that the effort in this process can be reduced if a third-party analysis package, with powerful pre- and post-processing capabilities can be used. The purpose of this project is therefore devoted to studying the performance of the interaction among the available finite element software packages at NASA, John F. Kennedy Space Center. In the following sections the procedures combining the powerful pre- and post-processing capabilities of SDRC/I-DEAS and I/FEM with MSC/NASTRAN's analysis capabilities will be summarized and the design of a solid rocket booster fixture will be examined. The last section contains discussions and conclusions.

II. FINITE ELEMENT MODEL DEVELOPMENT

The procedures to creating a finite element model can be very different depending on which application software package is used. However the basic concepts may be the same. The procedures in the model construction process for the available finite element software packages at NASA-KSC: SDRC/I-DEAS (version 4.1), MSC/NASTRAN (version 65) and I/FEM (version 1.3), will be briefly summarized in this section. It will be clear that the I-DEAS and I/FEM software packages are easier to use and save time when compared to NASTRAN.

2.1 SDRC/I-DEAS

I-DEAS (Integrated Design Engineering Analysis Software) developed by Structural Dynamics Research Corporation provides a comprehensive package for mechanical design engineers. Its capabilities are packaged as a set of software modules in which the I-DEAS Supertab modules offer finite element applications. The software provides highly interactive, graphic-oriented and menu-driven modules. Figures 1 and 2 show I-DEAS Supertab modules and Pre/Post processing module [1], respectively.

The geometry and elements of a finite element model can be constructed in the Model Preparation module for simple structures (e.g. truss). This module offers creation, generation, and manipulation of nodes, elements, coordinate systems, physical tables and material tables. For more complicated structures one can first use the Free Mesh Geometry module or the Geometry Definition module to prepare and manipulate the geometry. The element mesh can then be generated automatically by using Free Mesh Generation module or generated semi-automatically by using the Mapped Mesh Generation module. The mesh just created may have different sizes so that high mesh density can be developed in critical regions. The validity of the model is verified in the Model Checking module. The preprocessing phase is finally done by specifying the boundary conditions and loads of the model in the Analysis Cases module.

2.2 MSC/NASTRAN

The software package NASTRAN (NASA Structural Analysis) which was developed by NASA has been expanded to be a large-scale general purpose structural analysis package and is marketed by The MacNeal-Schwendler Corporation since 1972. MSC/NASTRAN is designed to operate in the batch mode. As such, a job submitted resembles a card deck stacked in the following order: NASTRAN Card, Executive Control Deck, Case Control Deck and Bulk Data Deck.

Similar to the preprocessing phase in I-DEAS, the Bulk Data Deck deals with structural modeling. The deck contains all the data necessary to define the geometry, and the constraints and loading conditions. It is the major portion of the input data for MSC/NASTRAN. For a large problem the Bulk Data Deck may consist of several thousand cards [2].

In preparing the Bulk Data Deck engineers usually record the data from the model's sketch. Without any typing mistakes, the time spent in this preparation is approximately twice as long as one would spend by using I-DEAS.

2.3 I/FEM

The Intergraph Finite Element Modeling System (I/FEM) is a computer-aided engineering software package for finite element analysis. The software operates with highly interactive graphics on Intergraph's workstation. The analyst creates the model by first selecting commands from icon-based graphic menus and then by drawing the geometry on the screen in one of the four windows which provides the top view, front view, right view and isometric view (Figure 3).

Like I-DEAS, two methods of building a finite element mesh are available in I/FEM. In using automatic meshing the analyst is restricted to 3-node or 6-node triangles for plane elements or 4-node tetrahedrons for solid elements. With semiautomatic mapped meshing any type of finite element can be used. However the mapped meshing requires more user interactions and therefore is more time consuming than automatic meshing.

One additional attractive feature in I/FEM is the geometry-based modeling [3] which enables users to define boundary conditions (constraints, loads, temperatures, etc.,) on the design geometry so that users do not need to modify the automatically generated mesh to assure accurate placement of the boundary conditions.

III. ANALYSIS AND USING THE INTERFACE

After the completion of the model construction process in I-DEAS or I/FEM, the analyst can do the analysis on third-party software packages or use their own analysis capabilities which are relatively small when compared to NASTRAN's capabilities. In this section the interface among I-DEAS, NASTRAN and I/FEM will be discussed.

3.1 The Interface Between SDRC/I-DEAS and MSC/NASTRAN

To create an analysis input file for MSC/NASTRAN in I-DEAS, we use the following command sequence which is available in any task: MAnage_fe_model, Write, Nastran_(msc). A file containing the Case Control Deck and the Bulk Data Deck is then generated. With the addition of an Executive Control Deck, which requests a specific solver, and an OUTPUT2 file storing all the data blocks generated via the Case Control Deck, the job can be submitted in NASTRAN. If the data block is not requested via Case Control, the OUTPUT2 functional module will ignore it. As an example, the Executive Control Deck for statics analysis [1] is shown below:

```
$   THE FOLLOWING DATA BLOCKS ARE RECOVERED:
$
$         CSTM      - COORIDNATE SYSTEM TRANSFORMATION MATRICES
$         GPL       - GRID POINT LIST
$         GPDT      - GRID POINT DEFINITION TABLE
$         EPT       - PHYSICAL PROPERTY DEFINITIONS
$         MPT       - MATERIAL PROPERTY DEFINITIONS
$         GEOM2     - ELEMENT DEFINITIONS
$         GEOM3     - LOAD DEFINITIONS
$         GEOM4     - RESTRAINT DEFINITIONS
$         OUGV1     - GRID POINT DISPLACEMENTS
$         OSTR1     - ELEMENTAL STRAIN
$         OES1      - ELEMENTAL STRESS
$         OEF1      - ELEMENT FORCES (STRESS RESULTANTS)
$         ONRGY1    - ELEMENTAL STRAIN ENERGY
$
ID STATICS, EXAMPLE
TIME 10
SOL 24
READ 9
ALTER     210 $
OUTPUT2   CSTM,GPL,GPDT,EPT,MPT//0/11 $
OUTPUT2   GEOM2,GEOM3,GEOM4,,//0/11 $
OUTPUT2   OUGV1,OSTR1,OES1,OEF1,ONRGY1//0/11 $
OUTPUT2   ,,,,//-9/11 $
CEND
```

In the above example the OUTPUT2 file is written to FORTRAN unit 11. Usually a .com file which contains a .dat file assigned to FORTRAN unit 11 (e.g. $ASSIGN OUTPUT.DAT FOR011) must be submitted along with the NASTRAN job so that the OUTPUT2 file can be automatically placed in the .dat file.

Using the I-DEAS Supertab Data Loader module the analyst can recover the analysis results in the NASTRAN OUTPUT2 binary file and create a universal file which in turn be read by the pre/post processing module into a model file. Once a model file has

analysis result data in it, the postprocessing phase is ready to be studied.

3.2 The Interface Between I/FEM and MSC/NASTRAN

Translation of an I/FEM design model to an MSC/NASTRAN bulk data deck is done in two steps: first by translating the model to a neutral file (an ASCII file) and then by running the following translator:

```
/usr/ip32/msc/bin/ifmsc  [-l] [-s] <i_fn> <o_fn>
```

where -l and -s stand for the long format and the short format for the bulk data deck,respectively. The <i_fn> is the name of the neutral file and <o_fn> is the name of the resultant bulk data deck.

To run the job the analyst must add the MSC/NASTRAN executive control deck and case control deck. The request of an MSC punched output file is necessary so that the results can be transferred back to I/FEM. For running a statics problem, the executive control deck and case control deck may have the following form:

```
ID STATICS, EXAMPLE
TIME 10
SOL 24
CEND
DISPLACEMENT (PUNCH) = ALL
STRESS (PUNCH) = ALL
```

Because the punched files are written to FORTRAN unit 7, the NASTRAN job should be submitted along with a .com file which assigns a .pch file to FORTRAN unit 7 (e.g. $ASSIGN OUTPUT.PCH FOR007) so that all the output data is stored in the .pch file.

To load the MSC .pch file into I/FEM model, first run the following loader:

```
/usr/ip32/msc/bin/ilmsc  <i_fn>  <o_fn>
```

where <i_fn> is the name of the MSC punch file and <o_fn> is the name of the generic file which can then be loaded from the I/FEM environment.

3.3 The Interface Between SDRC/I-DEAS and I/FEM

Direct interaction between SDRC/I-DEAS and I/FEM is not supported by either software package. However, it can be accomplished with the aid of NASTRAN. For a model designed in I-DEAS the corresponding MSC bulk data deck can be obtained as described in Section 3.1. If the analysis is going to be done in I/FEM, one first brings the bulk data file to the workstation and then runs the following translator to create a neutral file:

```
/usr/ip32/msc/bin/ibmsc  <i_fn> <o_fn>
```

where <i_fn> is the name of the MSC file and <o_fn> is the name of the neutral file. Then, the design model can be recovered in I/FEM by translating the neutral file from

the I/FEM environment .

For a model designed in I/FEM which is going to be analyzed in I-DEAS, the following procedure applies:

(1) Create an MSC bulk data file from I/FEM as stated in Section 3.2.
(2) Add MSC executive control deck as described in Section 3.1 omitting the following card (which corresponds to the output data, such as displacements, strain, stress, etc):

```
OUTPUT2 OUGV1,OSTR1,OES1,OEF1,ONRGY1//0/11 $
```

(3) Run the job with an alter card RF24D32 (used to read the design model without running analysis) and with a .com file storing the OUTPUT2 files.
(4) Retrieve the model in I-DEAS as described in Section 3.1.

The interfacing procedures discussed so far could also support other two combinations among the three software packages: design model in I-DEAS (I/FEM), analysis in NASTRAN, postprocessing in I/FEM (I-DEAS).

IV. THE POSTPROCESSING PHASE IN FINITE ELEMENT ANALYSIS

Highly interactive graphics capabilities in I-DEAS and I/FEM provide advantages in postprocessing. The analyst can display, manipulate and manage analysis results from the graphics environment. The results are then stored in the working design file. Some of the features of the two software packages are listed below:

1) Plot of deformed shape based on loading conditions.
2) Line contours of stress, displacement, strain and moment, which are all based on the results on grid points.
3) Criterion display (used in I-DEAS) or color-coded elements (used in I/FEM) for stress, strain and moment, which are all based on elements.

One may check the plots of stress (or strain) to determine whether the element mesh of the design model should be refined. Refining mesh may be necessary if the contour lines are not smooth enough.

V. AN EXAMPLE OF APPLICATION - DESIGN OF SOLID ROCKET BOOSTER FIXTURE

The purpose of studying this problem is twofold. We want to assure the fixture has enough strength so that it will not fail when used, and we want to verify the procedures described in the previous sections. The results based on using different combinations of the three software packages will be compared.

The fixture is made of aluminum alloy. The components of the fixture consist of a circular plate of 0.379 inches thick and 155 inches in diameter, a cylindrical plate of the same thickness welded under the circular plate, and three lifters which are welded on the outside surface of the cylindrical plate and located 120 degrees apart. To connect the fixture with a solid rocket booster by means of bolts, four sets of small holes are drilled in a circle of 148 inches diameter on the circular plate. Each set are located 90 degree apart and contains eight holes. A crane can then apply load through the three lifters to move the 1200 pound solid rocket booster.

In studying the response of the fixture in statics analysis the boundary conditions are considered to be fixed on the locations where the solid rocket booster is connected. The loads are modeled to be concentrated, upward and equally applied to each lifter. In other words, each lifter carries 400 lbs. To illustrate the procedures stated in Sections II and III, one can analyze the problem just described by means of four different combinations of the three software packages as listed in the following table:

Table 1 - Different Combinations of The Three Software Packages

	Preprocessing	Analysis	Postprocessing
(i)	I/FEM	I/FEM	I/FEM
(ii)	I/FEM	MSC/NASTRAN	I/FEM
(iii)	SDRC/I-DEAS	SDRC/I-DEAS	SDRC/I-DEAS
(iv)	SDRC/I-DEAS	MSC/NASTRAN	SDRC/I-DEAS

The geometry and element mesh of the fixture developed in I/FEM is shown in Figure 4. It contains 640 nodes and 723 elements of linear triangles and quadrilaterals. The element mesh is designed so that the areas near the constraints and loads have higher mesh density. In order to obtain a meaningful comparison of the results by using different software combinations, the working model created in the preprocessing phase should be the same. Instead of developing of the same element mesh in I-DEAS, analysts can obtain the same working model created in I/FEM by following the procedures stated in Section 3.3. Using combination (iii) from Table 1 above, the result of deformation is shown in Figure 5 (the dash lines represent the undeformed shape). The deformation was scaled by 100 so that the difference between the two shapes can be shown. The CPU times spent doing the analysis phase were 56 minutes in I/FEM, 6 hours 39 minutes in MSC/NASTRAN and 1 hour 36 minutes in SDRC/I-DEAS (the latter two software packages run on the VAX 11/780).

The results based on combination (iv) are shown in Figures 6 and 7. Figure 6 depicts the contours for the displacement field. The maximum displacement is shown to occur at the

lifters. The contouring plot of the principle stress field is shown in Figure 7. Both figures show symmetric distribution of the variables about one plane (yz-plane). This should be the case because the geometry, boundary conditions, loads, material and physical properties are all symmetric with respect to this plane. As a matter of fact, the same results can be obtained by studying half of the fixture together with an appropriate boundary condition along the x axis.

The contouring plots of the results based on the other analysis combinations show similar curves for displacement fields but somewhat different curves for principle stress fields. For example, the results based on the combination (iii) are shown in Figures 8 and 9. The following table shows the critical values for the whole structure based on the different solver combinations.

Table 2 - Comparison for The Max. Displacement and Nodal Principle Stress

Analysis Combination	Maximum Displacement	Maximum Principle Stress
(i)	0.157"	5717 psi
(ii)	0.166"	6094 psi
(iii)	0.156"	5891 psi
(iv)	0.166"	2307 psi

It is seen that combination (iv) yields much different maximum principle stress results. The discrepancy may be explained as follows. The output of stresses in MSC/NASTRAN are the stresses related to Gauss points which are the centroid of the elements if linear elements are used. On the other hand, the output of the stresses when using I-DEAS or I/FEM are the stresses computed at each node, which can then be used in contouring plots. Although the grid point stresses in NASTRAN can be assigned to write to a punch file and then be brought to I/FEM, the translation of grid point stress from NASTRAN to I-DEAS is not supported by I-DEAS. However, when the analysis results of MSC/NASTRAN are translated back to I-DEAS for postprocessing, the stresses at each node are accessible. Obviously, the interpolation and extrapolation, from the stresses at the centroids of the elements to the nodal stresses, has been executed. The stresses are therefore different from the one obtained by the actual calculation of the stresses at the nodes. In fact, the stresses related to elements rather than nodes can be obtained by the "criterion" command in I-DEAS and by selecting the "color-coded element" icon in I/FEM. The elemental stresses obtained from MSC/NASTRAN can be retrieved by using these commands. Therefore it may be more reliable to compare the principle stresses at the centroids of elements, as shown in the following table:

Table 3 - Comparison for The Max. Elemental Principle Stress

Analysis Combination	Maximum Principle Stress
(i)	3203 psi
(ii)	3414 psi
(iii)	3225 psi
(iv)	3414 psi

The table shows that the accuracy of the maximum displacement can be obtained for the maximum principle stress if they are based on the centroids of elements. Indeed stresses usually give the most accurate values on the Gauss points [4]. To overlook the stresses at the nodes may be misleading when arriving at conclusions.

All the stresses shown on table 3 are one order lower than the yield stress of the aluminum alloy. Hence the fixture should have enough strength for lifting the solid rocket booster.

VI. CONCLUSIONS

Investigations of model design and statics analysis on three finite element software packages - SDRC/I-DEAS, MSC/NASTRAN and I/FEM were performed. The interfaces between these software packages were tested via the design and analysis of a solid rocket booster fixture. It was found that with the aid of MSC/NASTRAN a model can be developed in I/FEM and translated into SDRC/I-DEAS and vice versa.

Although MSC/NASTRAN provides a very broad range of capabilities in structural analysis, this study shows that for the analysis of the SRB fixture model MSC/NASTRAN consumed large CPU time. Analysts should consider using SDRC/I-DEAS or I/FEM in the analysis as long as it can solve the problem at hand.

Disagreement on nodal stress contours was found between the results from SDRC/I-DEAS and from MSC/NASTRAN. The discrepancy may be due to different computation schemes. However, it is known that the stresses give the most accuracy on the Gauss points. The comparison of these critical elemental stresses does give differences, yet they are within an a

Based on the currently released versions of the software packages, SDRC/I-DEAS has a wider range than I/FEM as to the types of problem it can solve. Also, when compared to I/FEM, SDRC/I-DEAS can create MSC/NASTRAN files for a wider array of problems. For example, a problem like laminated analysis of fiber-oriented composite structure can be solved in SDRC/I-DEAS but I/FEM lacks the capability to solve a problem of this type. However, I/FEM provides a "geometry-based finite element modeling" feature which is not provided in SDRC/I-DEAS. Even in the next version of SDRC/I-DEAS (version 5), only loads (or generalized forces) can be applied on geometry before the element mesh is crated.

REFERENCES

1. Supertab Pre- and Post- Processing Engineering Analysis User's Guide, I-DEAS Level 4, SDRC, 1988

2. MSC/NASTRAN Handbook for Linear Analysis, MSC/NASTRAN Version 64, The MacNeal-Schwendler Corporation, August, 1985.

3. Intergraph/Finite Element Modeling (I/FEM) Operation Training Guide, Intergraph, December, 1988.

4. Cook, R.D., Malkus, D.S. and Plesha, M.E., Concepts and Applications of Finite Element Analysis, 3rd Edition, John Wiley & Sons, 1989.

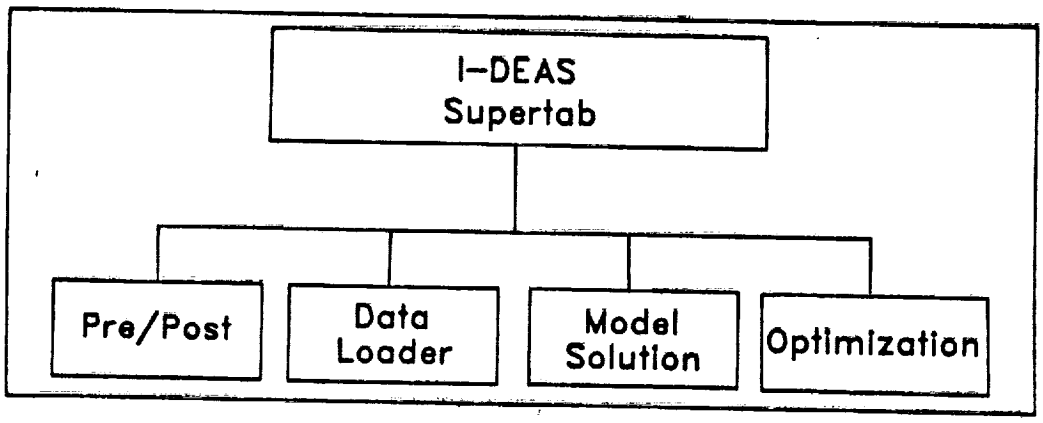

Figure 1. I-DEAS Supertab Modules

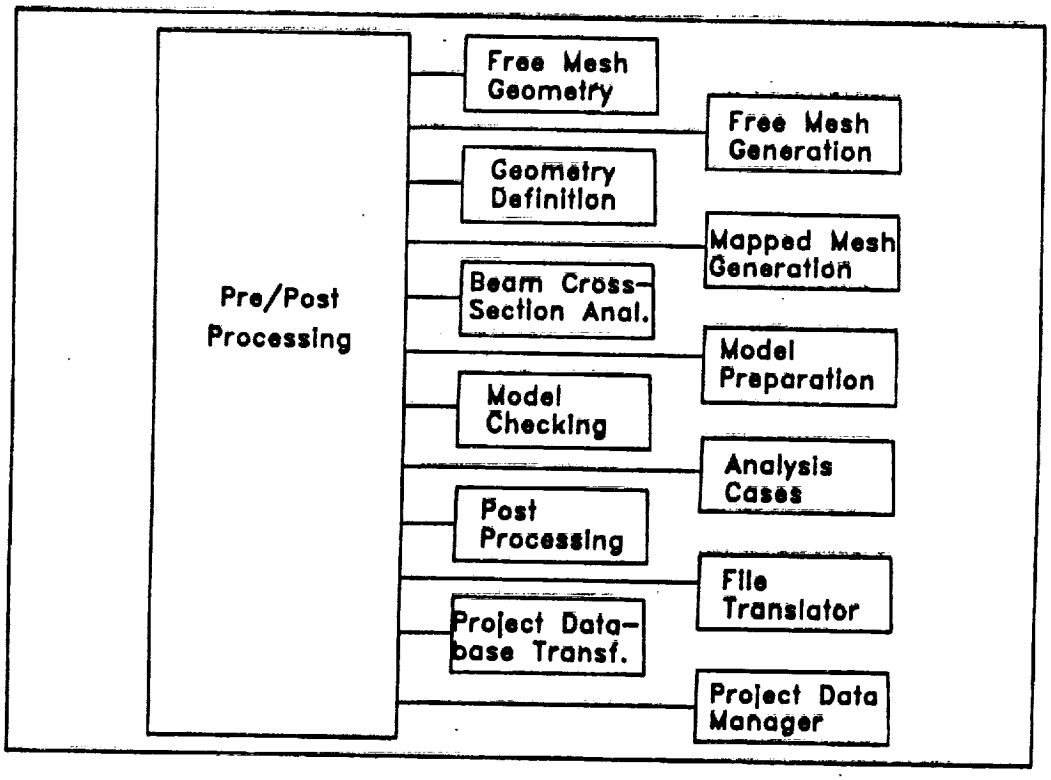

Figure 2. I-DEAS Pre/Post Processing Module

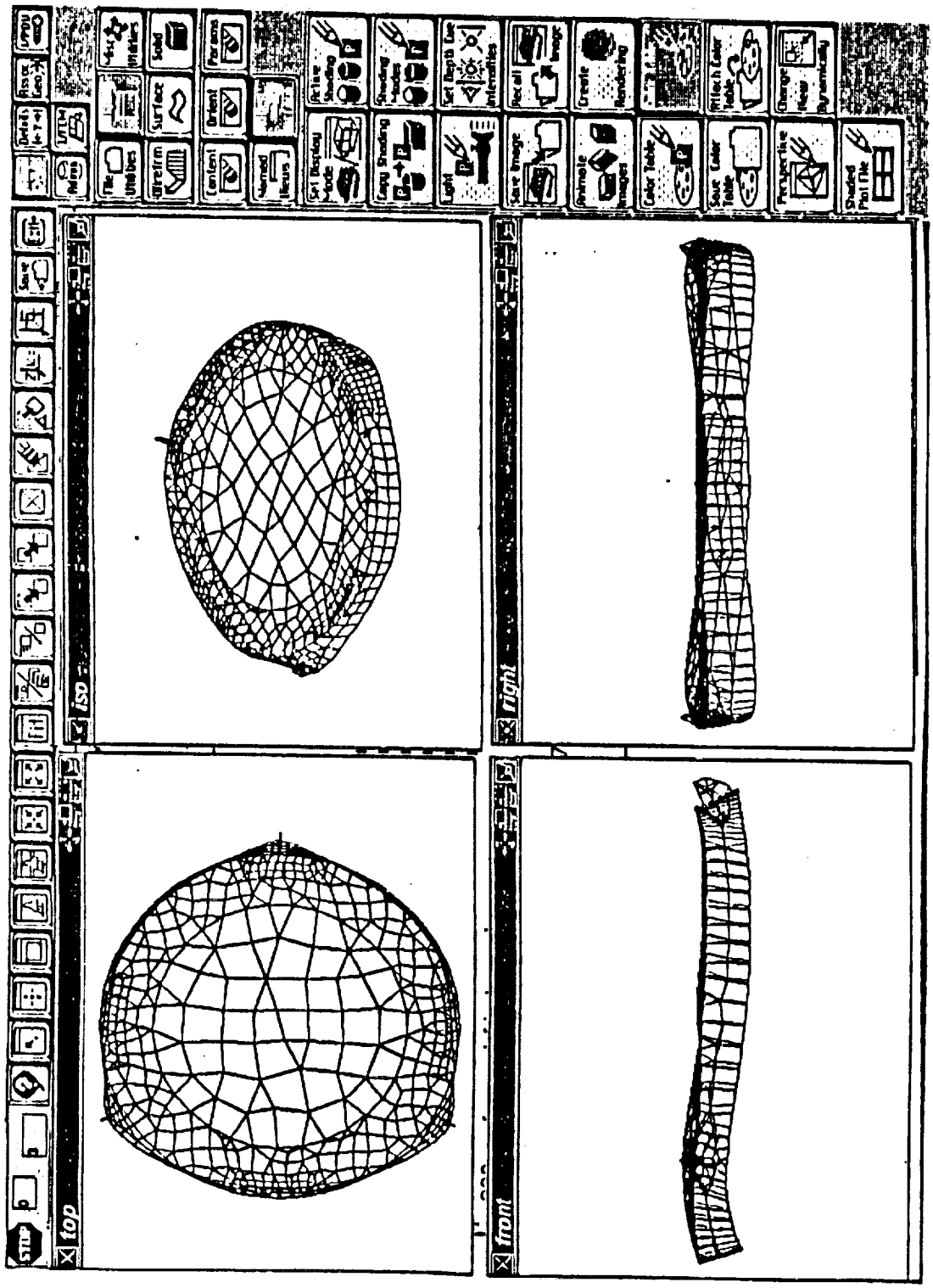

Figure 3. Graphics Menu and Working Windows of I/FEM

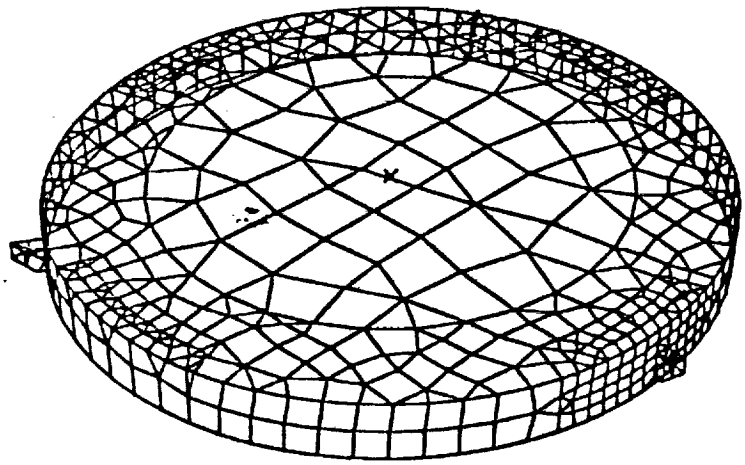

Figure 4. Design of Solid Rocket Booster Fixture in I/FEM

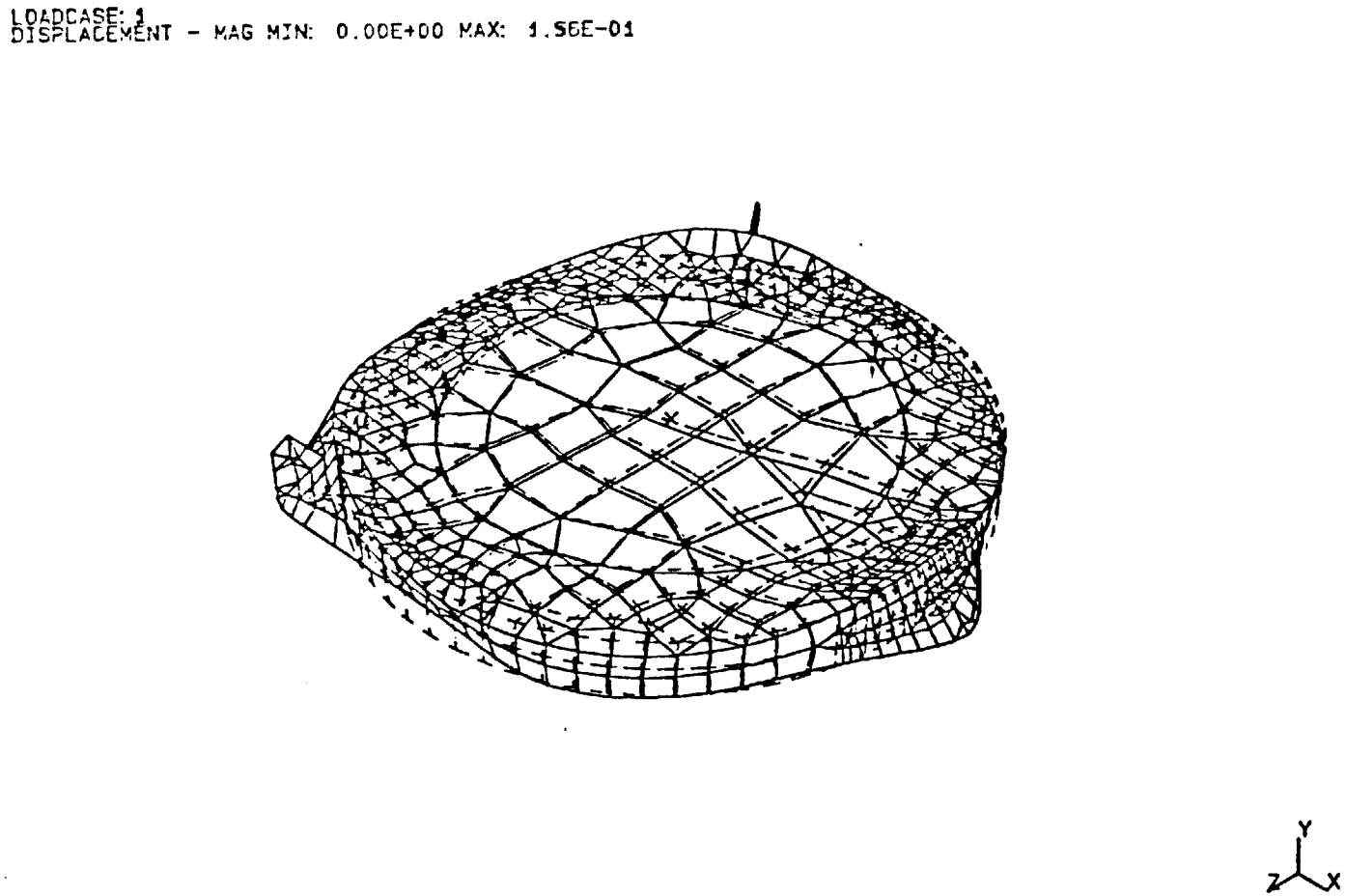

Figure 5. Deformed and Undeformed Geometries of SRB Fixture - Based on the Analysis in I-DEAS

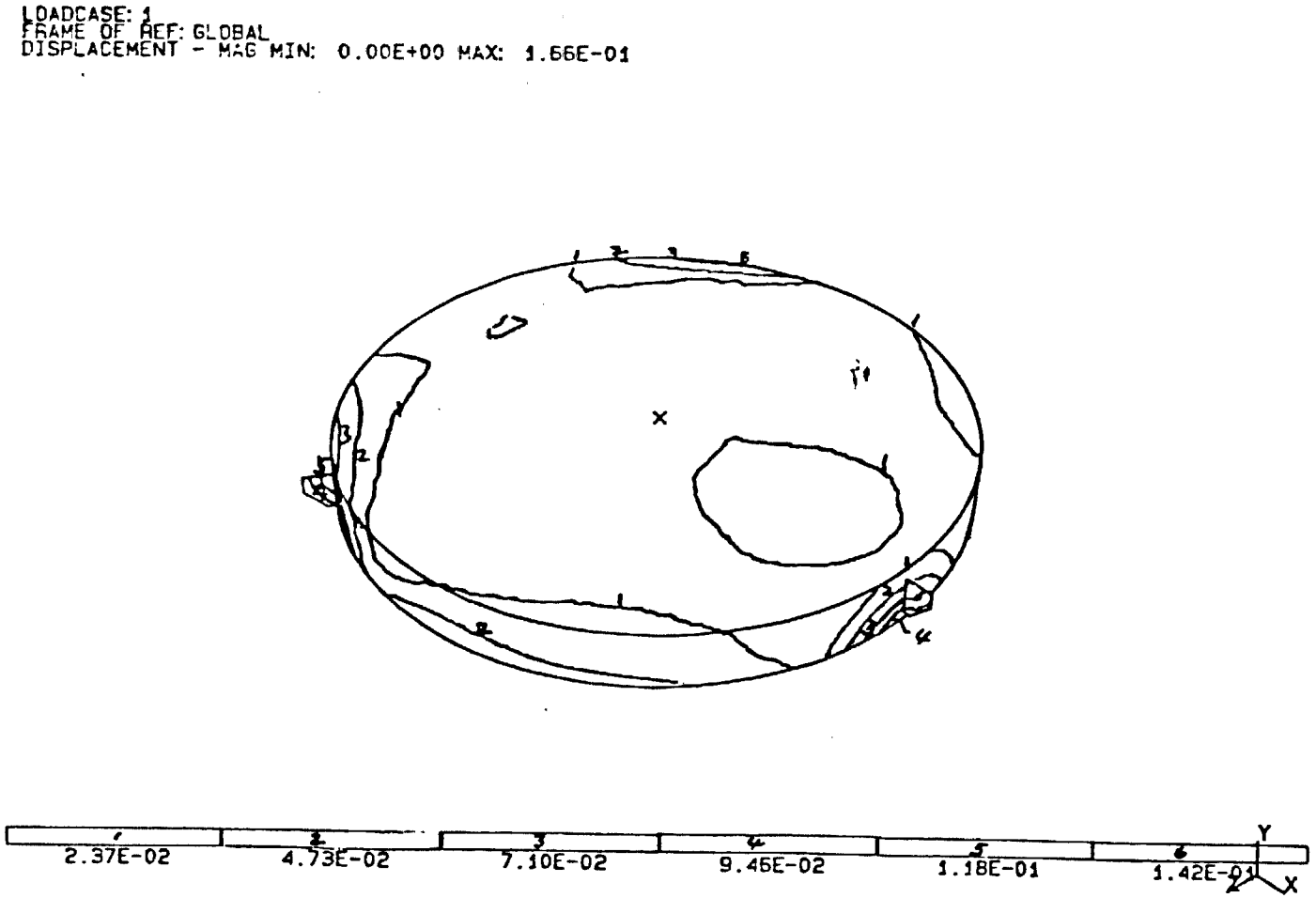

Figure 6. Nodal Displacement Contour - Based on the Analysis in NASTRAN

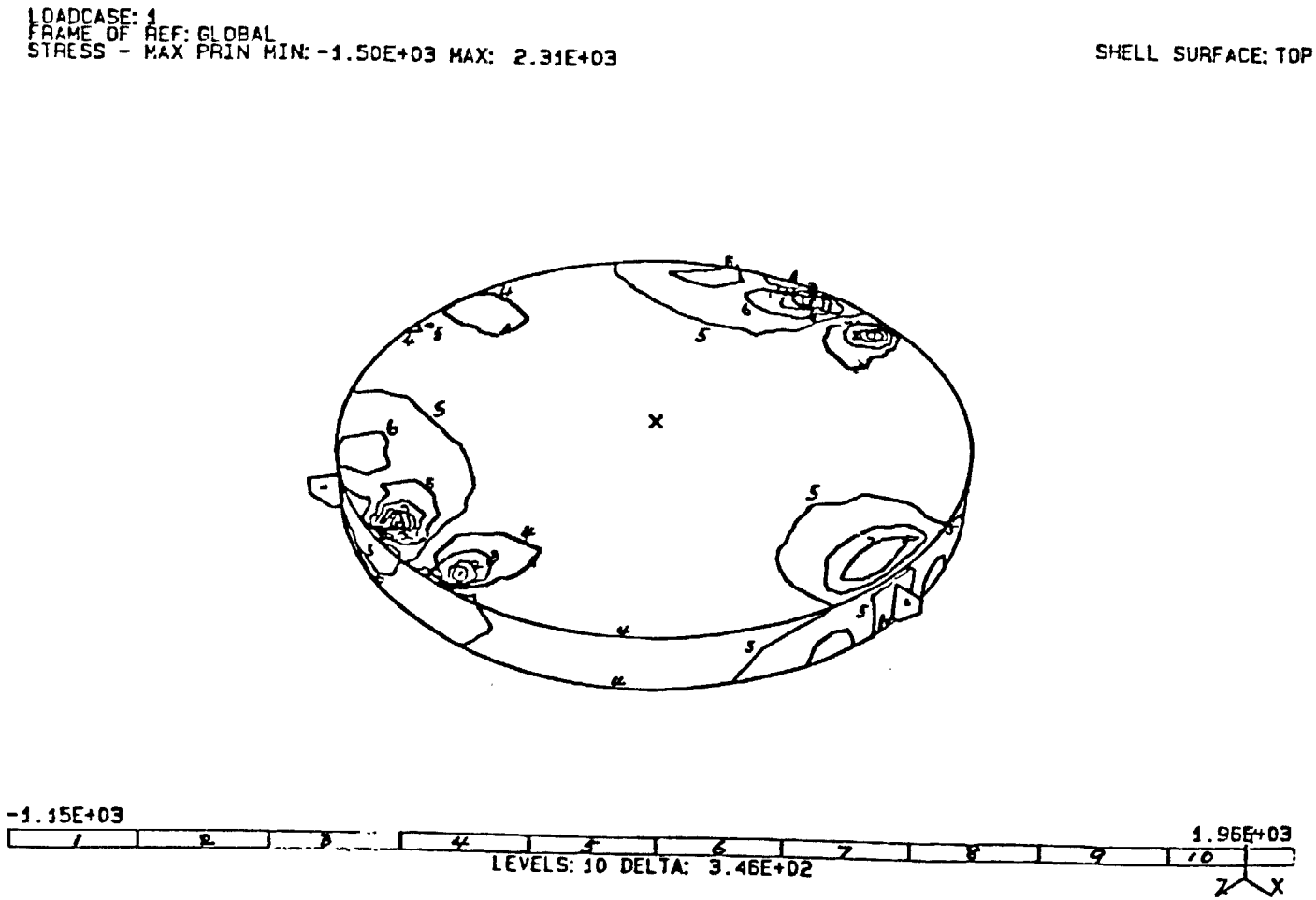

Figure 7. Nodal Stress Contour - Based on the Analysis in NASTRAN

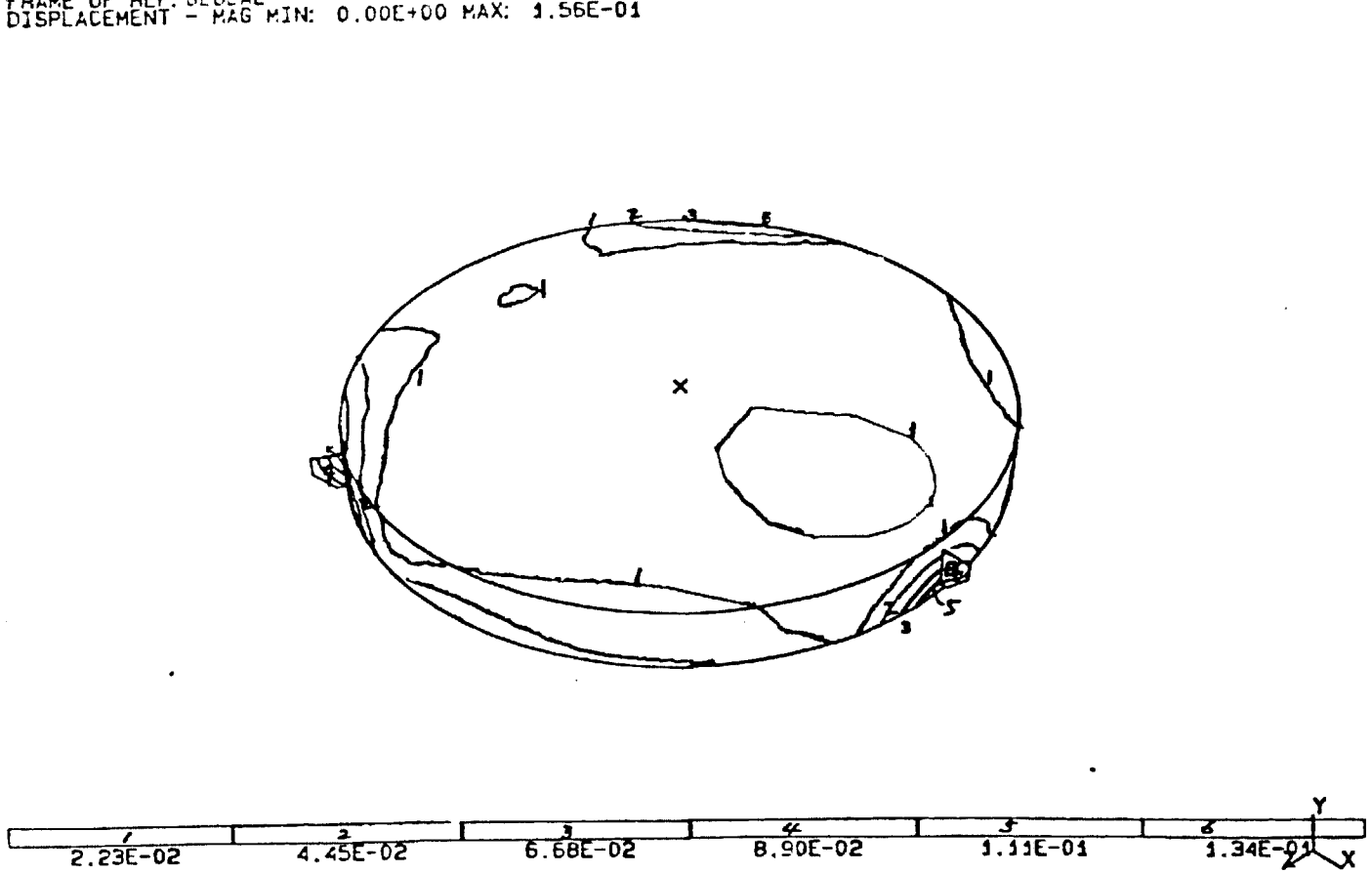

Figure 8. Nodal Displacement Contour - Based on the Analysis in I-DEAS

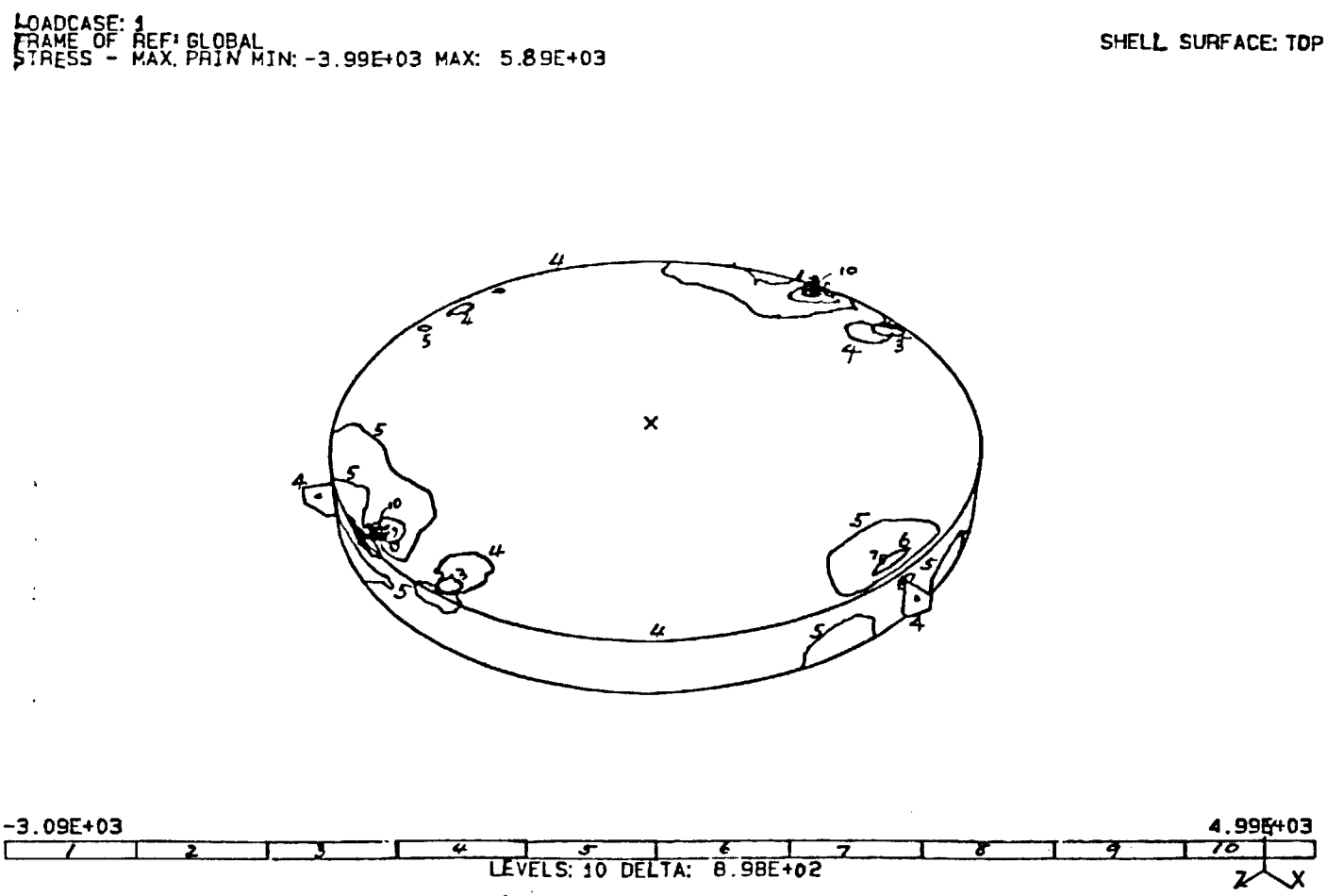

Figure 9. Nodal Stress Contour - Based on the Analysis in I-DEAS

N91-20030

1990 NASA/ASEE SUMMER FACULTY FELLOWSHIP PROGRAM

p 22

JOHN F. KENNEDY SPACE CENTER
UNIVERSITY OF CENTRAL FLORIDA

CAROTID-CARDIAC BAROREFLEX INFLUENCE ON FOREARM VASCULAR RESISTANCE DURING LOW LEVEL LBNP

PREPARED BY:	Dr. David Ludwig
ACADEMIC RANK:	Associate Professor
UNIVERSITY AND DEPARTMENT:	University of North Carolina - Greensboro Department of Mathematics and Statistics
NASA/KSC	
DIVISION:	Biomedical Operations and Research Office
BRANCH:	Life Sciences Research Office
NASA COLLEAGUE:	Dr. Victor Convertino
DATE:	July 24, 1990
CONTRACT NUMBER:	University of Central Florida NASA-NGT-60002 Supplement: 4

I

ABSTRACT

Twelve healthy males were tested at low levels of lower body negative pressure (LBNP) with and without artificial stimulation of the carotid-cardiac baroreceptors. The carotid-cardiac baroreceptors were stimulated by applying a pressure of +10 mmHg to the carotid artery via a pressurized neck chamber. During the procedure, forearm blood flow (FBF) and forearm vascular resistance (FVR) were measured using a Whitney mercury silastic strain gauge technique. FBF decreased while FVR increased with increased intensity of LBNP. Both FBF and FVR were unaffected by carotid-cardiac baroreceptor stimulation.

II

SUMMARY

Lower body negative pressure (LBNP) at low levels is an accepted method for inducing forearm vasoconstriction (elevated peripheral vascular resistance) which in turn is used as a measure of cardiopulmonary baroreflex responsiveness. It is assumed that arterial baroreflexes are not stimulated and do not influence the cardiopulmonary baroreflex test results. As with any intact living organism, complete isolation of a physiological system is a tenuous assumption. If carotid baroreceptor unloading does exist during low levels of LBNP (-20 mmHg or less), does it alter the results in any significant way to deem the measure of cardiopulmonary baroreflex responses invalid? To address this question, 12 subjects underwent low levels of LBNP exposures (-15 and -20 mmHg) with and without additional artificial (+10 mmHg neck pressure) unloading of the carotid baroreceptors. The results indicated no measurable influence of carotid unloading on forearm vascular resistance. Forearm vascular resistance measured during cardiopulmonary baroreceptor unloading is unaffected by carotid baroreceptor unloading within the magnitude encountered during low levels of LBNP.

TABLE OF CONTENTS

IV

TEXT

4.1 INTRODUCTION

Lower body negative pressure (LBNP) has been extensively used as a tool to create intravascular fluid shifts from the upper body into the lower extremities in order to examine cardiovascular reflex adjustments. Several investigators have suggested [9,20] that low levels of LBNP (maximum of -20 mmHg) induce reflex adjustments of vascular resistance primarily resulting from the unloading of the cardiopulmonary baroreceptors. This conclusion was based on the observations that LBNP levels down to -20 mmHg cause reductions in central venous pressure which induce forearm vasoconstriction. These alterations occur without measurable changes in determinants of arterial baroreceptor activity such as arterial blood pressure, aortic pulse pressure, arterial dp/dt (rate of change of pulse pressure), and heart rate [9,17,20]. Consequently, low levels of LBNP have been used to examine the stimulus-response characteristics of the cardiopulmonary baroreflex [6,8,10,16,18].

In recent experiments [6,16], we have observed small (two to four beats), but consistent increases in heart rate across increasing LBNP stages down to -20 mmHg, suggesting the unloading of arterial as well as cardiopulmonary baroreceptors. Data from

other investigations have confirmed these observations [12,17,18].

Unloading of carotid baroreceptor activity during low levels of LBNP may influence the response of the cardiopulmonary baroreflex. Some experiments have provided evidence that the carotid-cardiac baroreflex acts to maintain blood pressure by increasing forearm vascular resistance as well as heart rate [1,2,3,18]. If low levels of LBNP unload carotid baroreceptors and increase forearm vascular resistance, the interpretation of the cardiopulmonary baroreflex response measured by this procedure could be compromised. The purpose of our study was to determine if additional unloading of the carotid baroreceptors influences changes in forearm vascular resistance observed during low levels of LBNP.

4.2 METHODS

4.2.1 SUBJECTS. Twelve healthy, nonsmoking, normotensive men, with a mean (±SE) age of 36 ± 2 years (range 28-51), a height of 178 ± 1 cm (range 169 - 180), and a weight of 81.2 ± 2 kg (range 68 - 93), gave written informed consent to participate in this study. Selection of subjects was based on normal clinical results of a screening evaluation comprised of a detailed medical history, physical examination, complete blood count, a

panel of blood chemistry analyses, urinalysis, resting and treadmill elecrtrocardiograms, and pulmonary function tests.

4.2.2 PROTOCOL. During a preliminary visit to the laboratory, subjects were made familiar with the protocol and testing procedures. All subjects were instructed to abstain from exercise and caffeine for 12 hours prior to the testing period.

Subject instrumentation for the test procedures occurred simultaneously with a supine stabilization period which lasted approximately 30 minutes. Subjects were positioned in the LBNP device with both the right and left arms extended outward at heart level. The right arm was used for measurement of forearm blood flow and the left was used for beat-to-beat finger blood pressure measurements.

The experimental protocol consisted of six different combinations of LBNP and neck chamber pressure administered to each subject in a random order. LBNP was either off (0mmHg), decompressed to -15 mmHg, or decompressed to -20 mmHg. The neck chamber device [15] was either off (0 mmHg) or on at a pressure of +10 mmHg, i.e., baroreceptor unloading. Each treatment was applied over a 2-min period with a 5-min rest interval separating each of the six treatments. Lower body negative pressure was used to unload cardiopulmonary baroreceptors whereas the neck chamber was used to provide additional unloading of carotid baroreceptors. A neck cuff pressure of +10 mmHg was chosen since

this pressure has previously been shown to be within the responsive range of the baroreflex to cause a shortening of the R-R interval in most normotensive subjects [6,15,16]. A between treatment interval of five minutes was chosen to ensure that heart rate and blood pressure returned to pre-LBNP baseline values. Electrocardiograph measurements, using standard leads I, II, III, and beat-to-beat blood pressures, measured with the Finapress finger blood pressure technique [4] were recorded continuously throughout the protocol on a strip chart. Mean arterial pressure was calculated by dividing the sum of systolic blood pressure and twice diastolic pressure by three. At alternate 10-sec intervals during the 2-min test periods, forearm blood flow was measured by venous occlusion plethysmography, using a Whitney mercury-in-silastic strain gauge placed around the left forearm with circulation to the hand occluded [10,16,19]. An index of forearm vascular resistance was calculated by dividing mean arterial pressure by forearm blood flow and expressed in peripheral resistance units (PRU). Although data were collected continuously throughout the two minutes of testing, only measurements made in the last minute of testing were retained for statistical analysis. This was done to allow subjects to stabilized once the treatment was applied.

4.2.3 STATISTICAL METHODS. Data analysis was based on a 2 (barocuff status) x 3 (LBNP stage) factorial analysis of variance run in 12 randomized blocks (subjects). This was in keeping with

the experimental design in which each of the 12 subjects received each of the six treatment combinations in random order. When appropriate, orthogonal polynomials were fit and tested across LBNP stage to further describe observed treatment differences. Barocuff by LBNP pressure stage means are graphically presented since the interactive effects of these two treatments were of primary interest. Measures of variability are presented graphically as standard errors both adjusted and unadjusted for subject variation. Probabilities associated with tests of statistical inference reflect the chances of falsely concluding that the observed differences were attributable to the experimental manipulation and not random variability associated with the experimental methods or selection of the subjects for the given sample size of this experiment.

4.3 RESULTS

Figure 1 graghically presents the barocuff by LBNP stage interaction means for heart rate. Heart rate tended to increase with increasing levels of negative lower body pressure when the barocuff was at ambient pressure. Conversely, heart rate was elevated and tended to remain unchanged across LBNP stage when the barocuff was pressurized. However, the large TYPE I error rate generated from the analysis of variance for the barocuff by LBNP stage interaction indicated that this observed difference could be accounted for by random variation ($F(2,55) = 1.06$, $p = 0.3535$).

The results of a polynomial (linear) trend analysis across LBNP stages when the cuff was at ambient pressure indicated that the observed heart rate change of 3 beats from ambient LBNP to -20 mmHg was large enough to be detected within a TYPE I error rate of 10 percent ($F(1,55) = 2.81$, $p = 0.0994$). A comparison of heart rate between the pressurized and unpressurized barocuff at ambient lower body pressure yielded a moderately high TYPE I error rate ($F(1,55) = 2.27$, $p = 0.1379$). Overall, the results tend to indicate small differences in heart rate (one to three beats) as a result of the two types of stress with little or no interaction existing between the two procedures. Since the overall statistical model explained 89 percent of the total variation in heart rate, the results indicate that the observed differences were probably real but difficult to detect due to the small effect size.

Figure 2, Panel A presents the interaction means for forearm blood flow. The graph indicates a strong linear main effect of LBNP stage with a slight interaction with barocuff status. The low TYPE I error rate for the overall LBNP linear component ($F(1,55) = 23.64$, $p = 0.0001$) and the moderately high Type I error rate for the barocuff by LBNP linear interaction ($F(1,55) = 1.75$, $p = 0.1914$) support the idea that forearm blood flow decreases with increasing LBNP and that this decrease was unaffected to any significant extent by barocuff pressurization, i.e., carotid baroreceptor unloading, at +10 mmHg. The overall

statistical model explained 78 percent of the total variation in forearm blood flow.

Figure 2, Panel B presents the interaction means for forearm vascular resistance. Except for a change in direction, the results are similar to those for forearm blood flow. The strong overall linear component across LBNP stage ($F(1,55) = 15.84$, $p = 0.0002$) does not seem to interact (change) with barocuff pressurization ($F(1,55) = 0.07$, $p = 0.7923$). The overall statistical model explained 68 percent of the total variation in forearm vascular resistance. This lower percentage of explained variation as compared to forearm blood flow probably reflects the fact that true forearm vascular resistance is not actually measured but calculated from mean arterial pressure.

4.4 DISCUSSION

Although it is generally accepted that low levels of LBNP (20 mmHg or less) exclusively unload the cardiopulmonary baroreceptors [8,9,10,12,20], our data from the present study suggest that carotid baroreceptors may also be unloaded since small but consistent linear increases in heart rate were observed during LBNP levels of -15 and -20 mmHg, and that unloading of carotid baroreceptors at rest produced similar elevation in heart rate as that observed during LBNP. These findings are supported by the data of other investigators [12,17,18] and are consistent with unpublished observations from our previous investigations in

which mean (±SE) heart rate increased from 62 ± 3 to 67 ± 3 bpm ($F(1,23) = 17.23$, $P = 0.0004$) in 24 subjects [6] and from 58 ± 4 to 62 ± 4 bpm ($F(1,7) = 12.75$, $P = 0.0091$) in 8 subjects [16] when exposed from zero to -20 mmHg LBNP, respectively. The consistent observation that heart rate is elevated during low levels of LBNP suggests the possibility of carotid baroreceptor unloading and refutes the assumption that this technique isolates the cardiopulmonary baroreflex [8,10]. These data raise the concern that carotid baroreceptor unloading may accentuate the reduction in forearm vascular resistance during LBNP levels of 20 mmHg or less [5,7] and thus influence the measured response of the cardiopulmonary baroreflex.

There is some discrepancy in the literature as to the contribution of the carotid baroreceptors in controlling forearm vascular resistance responses. Loading of the carotid baroreceptors by neck suction or manual compression of the carotid arteries has been shown in some investigations to have negligible effects on vasomotor tone [1,11,13,14]. In contrast, Epstein et al. [7] found a 16 percent reduction in forearm vascular resistance when directly stimulating the carotid nerves of patients undergoing implantation of carotid sinus nerve stimulators. This finding supported the work of Carlsten et al. [5] who also demonstrated a reduction in vascular resistance with direct stimulation to the carotid sinus nerve. Significant alterations in vasomotor tone have also been observed by several

investigators during baroreceptor loading induced by neck suction [2,3] and unloading induced by neck pressure [18]. In our study, carotid baroreceptor unloading with +10 mmHg neck cuff pressure caused increases in heart rate compared to control values indicating that we successfully induced a reflex response. We observed no effect of carotid unloading on forearm vascular resistance. Our results suggest that a carotid baroreceptor stimulus equivalent to slight hypotension (-10 mmHg) does not influence forearm vascular resistance either directly or through an interaction with cardiopulmonary baroreceptor responses.

Victor and Mark [18] performed an experiment very similar to ours using neck cuff pressures of +20 mmHg and +30mmHg during -10 mmHg LBNP. Neck cuff pressure at +20 mmHg caused no alteration in forearm vascular resistance while +30 mmHg neck pressure resulted in increases in FVR with and without LBNP. The forearm vascular resistance response to +30 mmHg neck pressure during LBNP was greater than the sum of the separate responses to LBNP and neck pressure alone. These investigators concluded that not only do the carotid baroreceptors have a direct effect on forearm vascular resistance, but they also have a potentiating effect on the cardiopulmonary baroreceptor FVR responses to LBNP.

Although our data and those of others [1,11,13,14] may appear contradictory to the findings of several investigations [2,3,5,7], the magnitude of stimulation may provide an

explanation for all findings. Taken together, the results of our experiment and those of Victor and Mark [18] suggest that a hypotensive stimulus of 20 to 30 mmHg may be required to elicit a threshold response for initiating a vasoconstriction from carotid baroreceptor unloading. The degree to which we unloaded the carotids was greater than that expected by the small blood pressure reductions of 2 to 4 mmHg reported during 20 mmHg of LBNP [10,17,20]. Further, concommitant application of LBNP and neck cuff pressure in our experiment assured greater unloading of the carotid baroreceptors than that experienced by LBNP alone. Therefore, it is unlikely that the small degree of carotid baroreceptor unloading that occurs in most human subjects during LBNP of 20 mmHg or less influences forearm vascular resistance. Consequently, protocols of low levels of LBNP (-20 mmHg or less) can be employed to measure the stimulus-response relationship of the cardiopulmonary baroreflex with the confidence that carotid baroreceptor unloading is not affecting the response.

V

CONCLUSIONS

Artificial stimulation of the carotid-cardiac baroreceptors (to approximate a +10 mmHg drop in pressure) does not effect the measurement of FBF or FVR during exposure to low levels of LBNP. Limited levels of stimulation and undescribed mechanisms of heart rate alterations suggest areas for future research.

VI

REFERENCES

1. Abboud, F. M., D.L. Eckberg, U.J. Johannsen, and A.L. Mark. Carotid and cardiopulmonary baroreceptor control of splanchnic and forearm vascular resistance during venous pooling in man. J. Physiol. 286:163-184, 1979.

2. Beiser, G. D., R. Zelis, S.E. Epstein, D.T. Mason and E. Braunwald. The role of skin and muscle resistance vessels in reflexes mediated by the baroreceptor system. J. Clin. Invest. 49:225-231, 1970.

3. Bevegard, B.S. and J. T. Shepherd. Circulatory effects of stimulating the carotid arterial stretch receptors in man at rest and during exercise. J. Clin. Invest. 45: 132-142, 1966.

4. Boehmer, R.D. Continuous real-time noninvasive monitor of blood pressure: Penaz methodology applied to the finger. J. Clin. Monit. 3:282-287, 1987.

5. Carlsten A., B. Folkow, G. Grimby, C. Hamberger, and O. Thulesius. Cardiovascular effects of direct stimulation of the carotid sinus nerve in man. Acta Physiol. Scand. 44:138-145, 1958.

6. Convertino, V.A., C.A. Thompson, D.L. Eckberg, J.M. Fritsch, G.W. Mack, and E.R. Nadel. Baroreflex responses and LBNP

tolerance following exercise training. Physiologist 33:S40-S41, 1990.

7. Epstein,S.E., G.D. Beiser, R.E. Goldstein, M. Stampfer, A.S. Wechsler, G. Glick, and E. Braunwald. Circulatory effects of electrical stimulation of the carotid sinus nerves in man. Circulation 40:269-276, 1969.

8. Gauer, O.H.., and H.O. Sieker. The continuous recording of central venous presure changes from an arm vein. Circ. Res. 4:74-78, 1956.

9. Johnson, J.M., L.B. Rowell, M. Niederberger, and M.M. Eisman. Human splanchnic and forearm vasoconstrictor responses to reductions of right atrial and aortic pressures. Circ. Res. 24:515-524, 1974.

10. Mack, G.W., X. Shi, H. Nose, A. Tripathi, and E.R. Nadel. Diminished baroreflex control of forearm vascular resistance in physically fit humans. J. Appl. Physiol. 63:105-110, 1987.

11. Mark, A.L., D.L. Eckberg, F.M. Abboud, and U.J. Johannsen. Relative contribution of low and high pressure baroreceptors in circulatory adjustments to venous pooling in man. J. Clin. Invest. 53:50A-51A, 1974.

12. Pawelczyk, J.A., and P. B. Raven. Reductions in central venous pressure improve carotid baroreflex responses in conscious men. Am. J. Physiol. 257:H1389-H1395, 1989.

13. Roddie, I. C., and J. T. Shepherd. Receptors in the high-pressure and low-pressure vascular systems: their role in the reflex control of the human circulation. Lancet 1:493-496, 1958.

14. Roddie, I. C., and J. T. Shepherd. The effects of carotid artery compression in man with special reference to changes in vascular resistance in the limbs. J. Physol. 139:377-384, 1957.

15. Sprenkle, J.M., D. L. Eckberg, R.L. Goble, J.J. Schelhorn and H.C. Halliday. Device for rapid quantification of human carotid baroreceptor-cardiac reflex responses. J. Appl. Physiol. 60:727-732, 1986.

16. Thompson, C.A., D.L. Tatro, D.A. Ludwig, and V.A. Convertino. Baroreflex responses to acute changes in blood volume in man. Am. J. Physiol. (Regulatory, Integrative Comp. Physiol.) 1990 (in press).

17. Tripathi, A., G. Mack, E.R. Nadel. Peripheral vascular reflexes elicited during lower body negative pressure. Aviat. Space Environ. Med. 60:1187-1193, 1989.

18. Victor, R.G., and A.L. Mark. Interaction of cardiopulmonary and carotid baroreflex control of vascular resistance in humans. J. Clin. Invest. 76:1592-1598, 1985.

19. Whitney, R. J. The measurement of volume changes in human limbs. J. Physiol. Lond. 121:1-27, 1953.

20. Zoller, R.P., A.L. Mark, F.M. Abboud, P.G. Schmid, and D.D. Heistad. The role of low pressure baroreceptors in reflex vasoconstrictor responses in man. J. Clin. Invest. 51:2967-2972, 1972.

VII

FIGURES AND LEGENDS

Figure 1. Mean (±SE) heart rates by barocuff status (neck pressure) and LBNP stage. The pooled SE is calculated from the analysis of variance and is adjusted for between subject variation.

Figure 2. Mean (±SE) forearm blood flows (Panel A) and forearm vascular resistance (Panel B) by barocuff status and LBNP stage. The pooled SE is calculated from the analysis of variance and is adjusted for between subject variation.

FIGURE 1

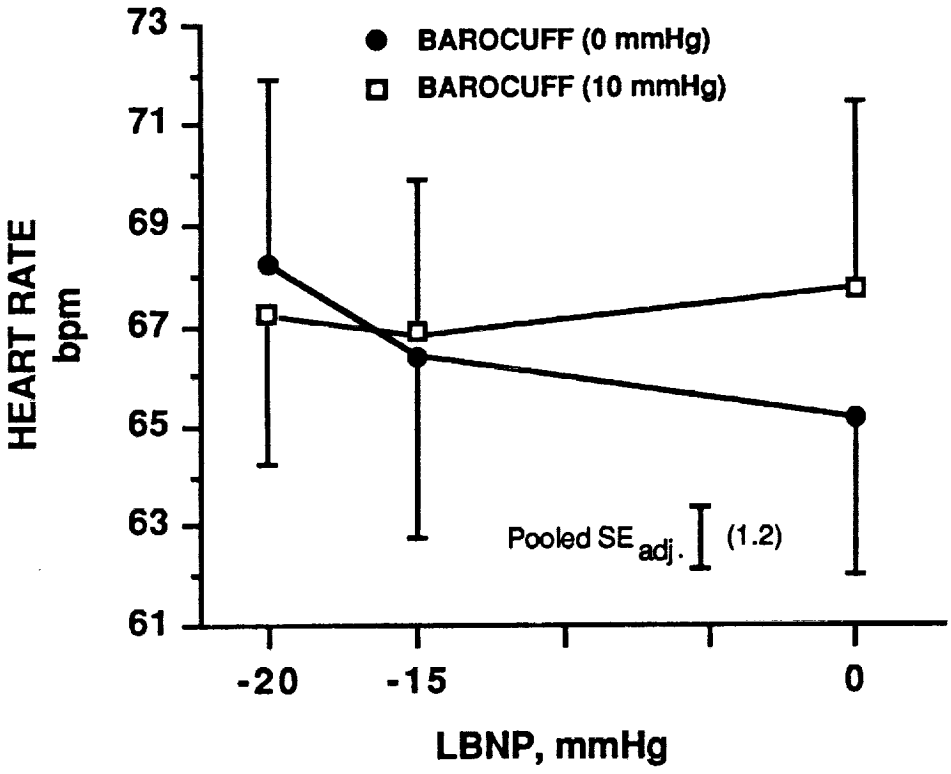
73
71
69
67
65
63
61
HEART RATE
bpm
BAROCUFF (0 mmHg)
BAROCUFF (10 mmHg)
Pooled SE adj.
(1.2)
-20
-15
0
LBNP, mmHg

FIGURE 2

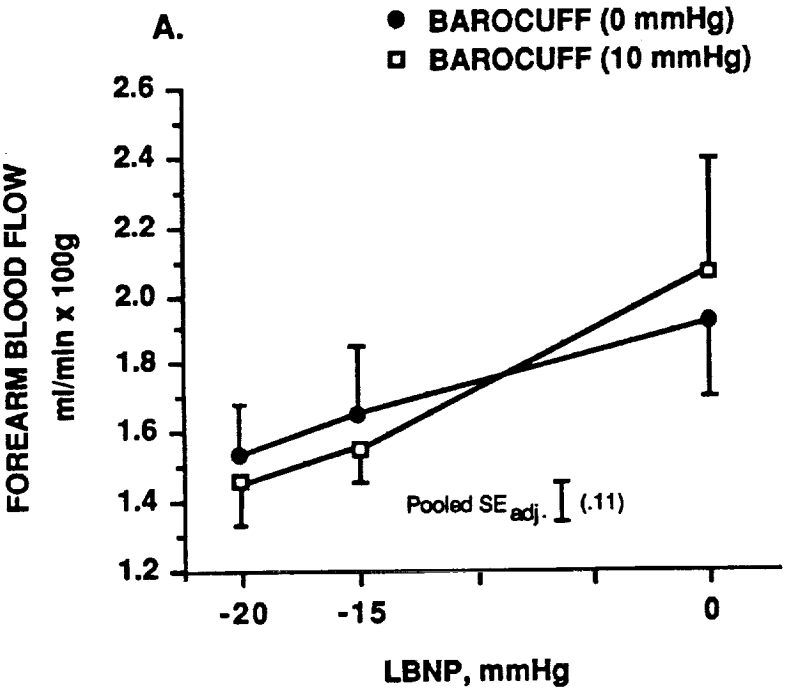
A.
BAROCUFF (0 mmHg)
BAROCUFF (10 mmHg)
FOREARM BLOOD FLOW
ml/min x 100g
2.6
2.4
2.2
2.0
1.8
1.6
1.4
1.2
Pooled SE adj. (.11)
-20
-15
0
LBNP, mmHg

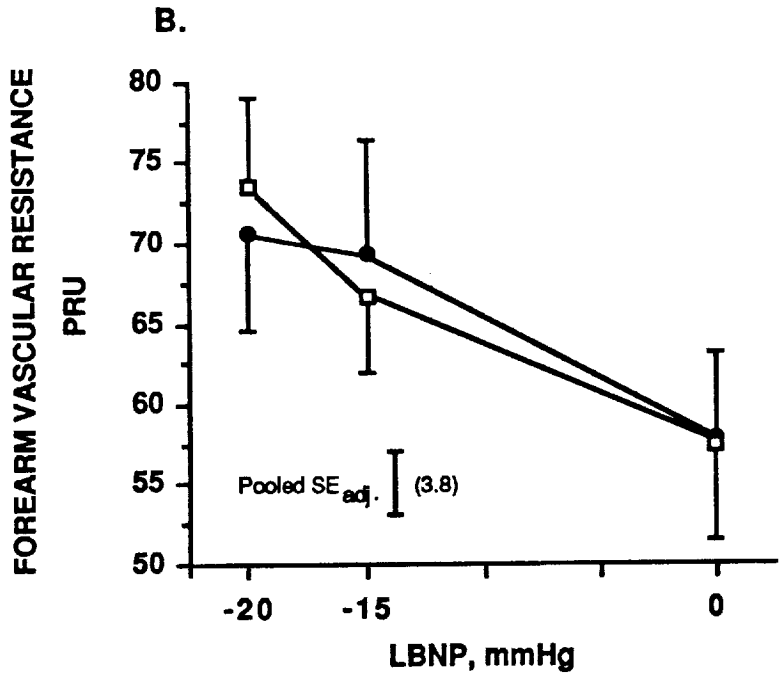
B.
FOREARM VASCULAR RESISTANCE
PRU
80
75
70
65
60
55
50
Pooled SE adj. (3.8)
-20
-15
0
LBNP, mmHg

1990 NASA/ASEE SUMMER FACULTY FELLOWSHIP PROGRAM

JOHN F. KENNEDY SPACE CENTER
UNIVERSITY OF CENTRAL FLORIDA

ROCKET NOISE FILTERING SYSTEM USING DIGITAL FILTERS

PREPARED BY:	Dr. David Mauritzen
ACADEMIC RANK:	Assistant Professor
UNIVERSITY AND DEPARTMENT:	Indiana - Purdue University - Fort Wayne Department of Engineering
NASA/KSC	
DIVISION:	Mechanical Engineering
BRANCH:	Special Projects
NASA COLLEAGUE:	Dr. Gary Lin
DATE:	August 10, 1990
CONTRACT NUMBER:	University of Central Florida NASA-NGT-60002 Supplement: 4

ACKNOWLEDGMENTS

I would like to thank my NASA colleague, Dr. Gary Lin, and his supervisor, Mr. Willis Crumpler for the opportunity to work on this interesting project and for the very professional atmosphere they have provided. I also would like to express my gratitude to Mr. Nick Schultz and Mr. Rudy Werlink who provided information on the current system and sample data with which to work. The American Society of Engineering Educators (ASEE) is to be commended for this outstanding program which provides such opportunities for professors. The program has been smoothly administered by Professor Loren Anderson of the University of Central Florida, and Ms. Kari Baird who has provided cordial assistance. I also appreciate the support of my home institution, Indiana - Purdue University at Fort Wayne, the Chairman of the Department of Engineering, Professor Muhammad Rashid, and the various members of the administration who are helping us build our program through support of faculty participation in programs such as this.

ABSTRACT

A set of digital filters is designed to filter rocket noise to various bandwidths. The filters are designed to have constant group delay and are implemented in software on a general purpose computer. The Parks-McClellan algorithm is used. Preliminary tests are performed to verify the design and implementation. An analog filter which was previously employed is also simulated.

SUMMARY

Acoustic data is collected by a field of sensors during launch. Although data is collected which contains valid data up to about 2 kHz, not all users require full bandwidth data. Filtering the data to remove spectral components which are not of interest results in savings in storage volume and processing time. For some applications it is important to maintain constant group delay. A set of digital filters has been designed and implemented which provide constant delay, very sharp roll off, and large stop band attenuation. Complete processing time for a typical field of sensors is less than 30 hours and could readily be reduced to less than 8 hours. A program was written to simulate a single analog filter which had previously been used for this application was written but not tested because of time limitations. The digital design eliminates data manipulation which is time consuming and potentially error prone while providing performance which is much superior to analog filtering.

TABLE OF CONTENTS

LIST OF ILLUSTRATIONS

LIST OF TABLES

SECTION I

INTRODUCTION

1.1 THE CURRENT ROCKET NOISE DATA PROCESSING SYSTEM

The input to the current rocket noise filtering system is an analog signal proportional to absolute pressure. The present system utilizes a 5th order analog Butterworth filter having a 3 dB bandwidth of 2 kHz for its anti-aliasing filter. The data is then sampled at a rate of 9091 samples per second (sps) and converted to digital form by employing a 10 bit analog to digital (A/D) converter. This resolution is equivalent to 1024 cells and corresponds to a dynamic range of about 60 dB. The data is then stored in digital form on magnetic tapes with four decimal place precision. Four decimal place precision provides about 80 dB of dynamic range.

When it is necessary to reduce the bandwidth of the signal for some applications and generate samples at a lower sampling rate (down sampling), the digital data is played back and fed to a digital to analog (D/A) converter. The converter output is then filtered by an appropriate low pass filter and re-sampled at the lower rate. If the data is then to be processed digitally, it is re-digitized and stored.

One typical down sampling operation employs a 5th order analog Butterworth filter which has a bandwidth of 1 kHz. The 9091 sps digital data is pulled from tape, converted to analog form and filtered. It is then sampled at one-half of the original sampling rate, 4545.5 sps.

1.2 DISADVANTAGES OF CURRENT SYSTEM.

The data playback, reconstruction, and resampling process exhibits several shortcomings.

1. The process is time consuming since the original data tapes must be obtained and remounted. The process is repeated for each data pull.

2. The analog filter must be redesigned and rebuilt or, at a minimum, reconfigured whenever a new bandwidth is desired.

3. The Butterworth filter is not very selective so that either more aliasing noise must be accepted or higher sampling rates must be used for a given bandwidth.

4. The Butterworth filters intrinsically generate time delay distortion.

5. There are many opportunities for error in the procedure. Since the tape playback is repeated for each data pull, there is opportunity for the introduction of extraneous noise each time. The tape heads may be dirty or misaligned. The hardware may be incorrect. The wrong analog filter or the wrong sampling rate may be employed.

6. Errors may be insidious. Since they tend to add noise to the noise already present, they may be very difficult to detect. (Interestingly, there was noise in the first set of processed

data that was provided as test data. Figure 1-1a depicts histograms of the filtered and unfiltered data for sensor #1. The cell width for the histograms is 0.2 pounds per square inch (psi). Comparison of the original 9 ksps data with the down sampled data reveals that the mean of the filtered data differs from that of the unfiltered data. This indicates an error since the mean value should propagate through the filter without change. Histograms for sensor #2, shown in figure 1-1b, do not exhibit this anomaly.)

It is not necessary that the signal be reconstructed in analog form, refiltered, and re-sampled. Once the data has been acquired in digital form all processing can be done digitally. Once operational, digital processing will be reliable and repeatable and overcome the disadvantages cited above.

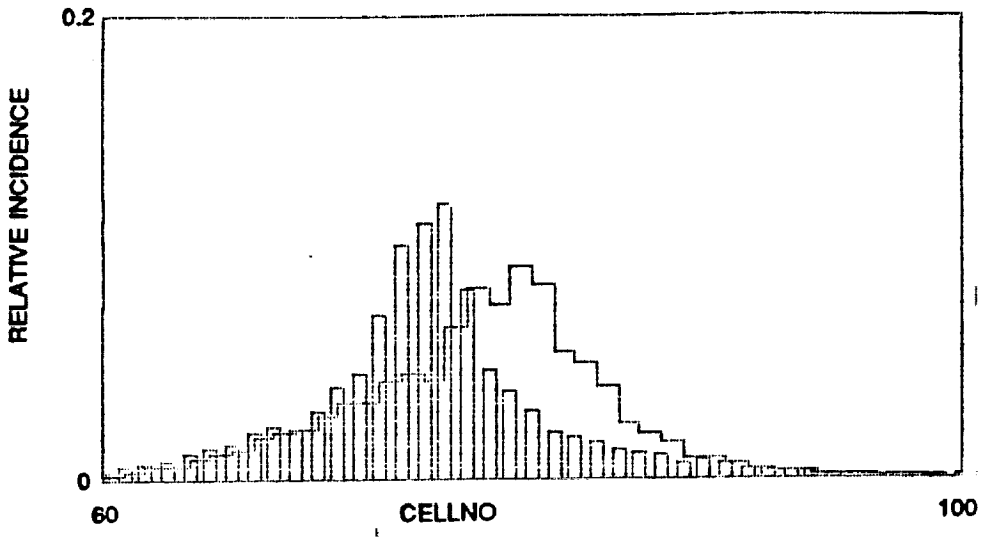

Figure 1-1a. Histogram of Filtered and Unfiltered Data for Sensor #1
Unfiltered Data drawn with vertical bars.
Cell width = 0.2 psi

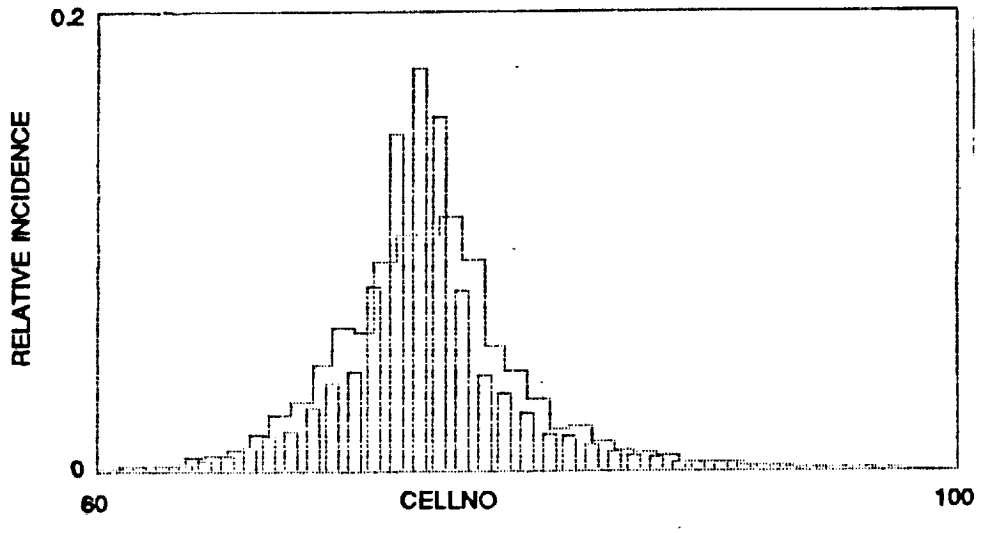

Figure 1-1b. Histogram of Filtered and Unfiltered Data for Sensor #2
Unfiltered data drawn with vertical bars.
Cell width = 0.2 psi

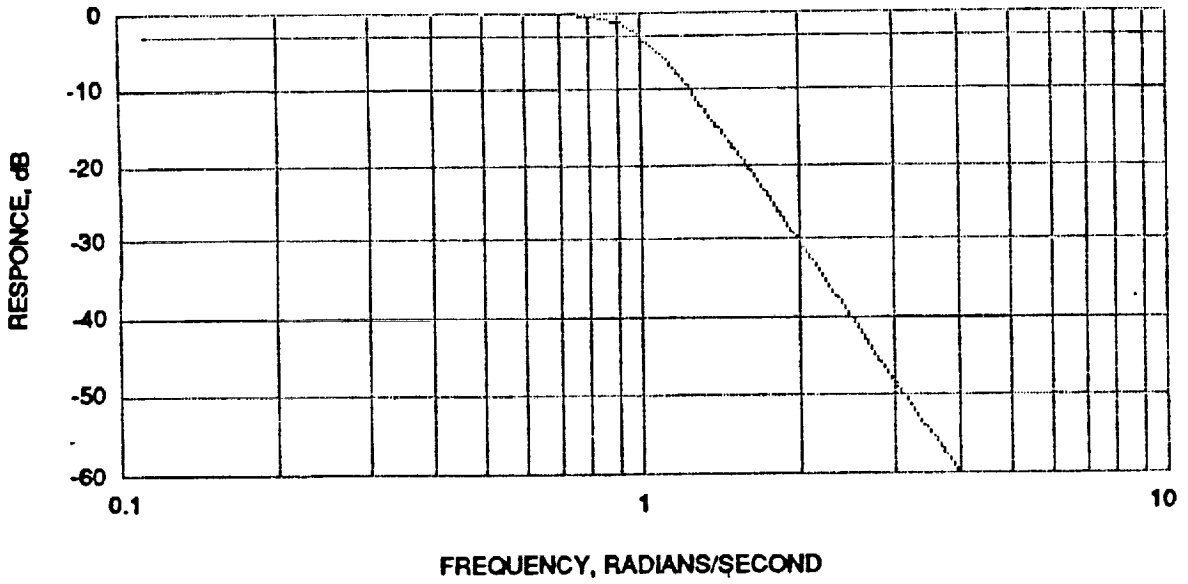

Figure 2-1. Bode Plot Response of 5th Order Butterworth Analog Filter
Normalized to a corner frequency of 1.
horizontal line is -3 dB.

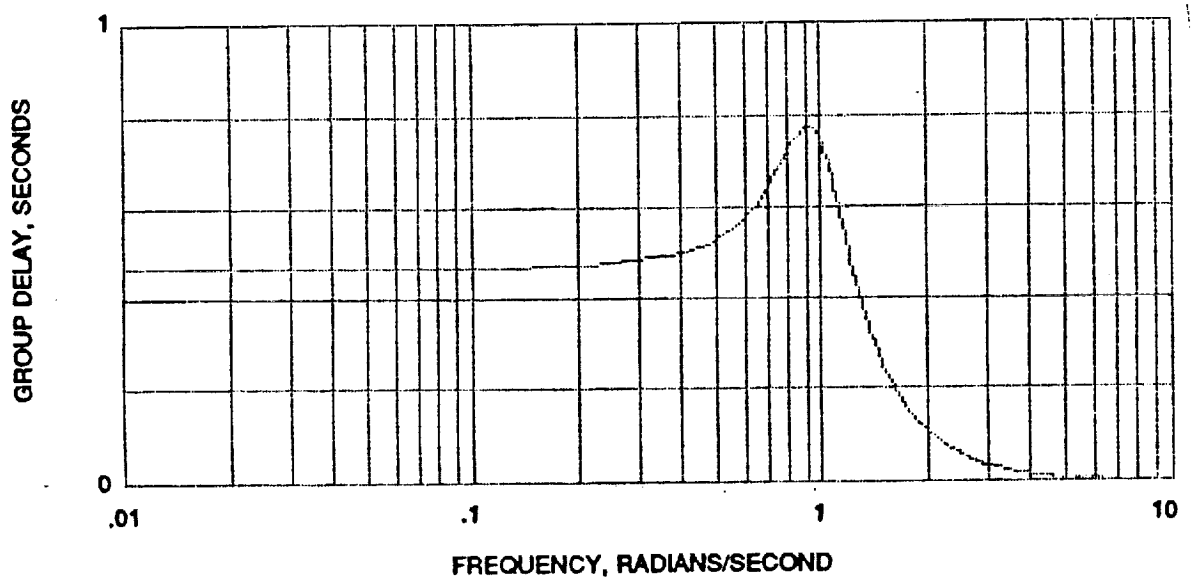

Figure 2-2. Group Delay of 5th Order Butterworth Filter
(for a 1 radian/second bandwidth filter)

SECTION II

ANALOG AND DIGITAL FILTERS

2.1 SIMULATION OF THE CURRENT ANALOG FILTER

It was decided to simulate the operation of the analog filter and the half rate down sampler which is often used. This would provide continuity with previous operations, and affords the opportunity to cross check results and detect errors. It was anticipated that this work could be done along with the digital filter development effort within the allotted ten week interval.

The analog filter used in the 2:1 down sampling operation has a 5th order Butterworth response, and a corner frequency of 1000 Hz. The poles of this filter lie on a circle of radius 2000*pi radians/second in the complex plane, with one pole on the negative real axis and angular spacings between successive poles of 36 degrees. The poles are therefore at -2000*pi, -1618*pi +/- j*1176*pi, and -618*pi +/- j*1902*pi. Figure 2-1 is a Bode plot of the 5th order Butterworth response, normalized to a cut off frequency of 1 radian/second. The group delay of this filter is shown in figure 2-2. The time delay is approximately constant for low frequencies (far below the cut off frequency) but rises rapidly to a maximum in the vicinity of the cut off frequency.

2.1.1 The Impulse Response of the 5th Order Butterworth Filter

The impulse response, h(t), for the filter will be used in the simulation of the analog filter, and may be determined by taking the inverse Laplace transform of the transfer function of the filter, which can be written in the form

$$B5(s) = \frac{Ao * B1 * B2}{(s + Ao) * (s^2 + A1 * s + B1) * (s^2 + A2 * s + B2)} \qquad (1)$$

where the name B5 was used to indicate that this is the transfer function of a 5th order Butterworth filter. A partial fraction expansion of this transfer function may be made in the form

$$B5(s) = \frac{Co}{(s+Ao)} + \frac{C1 * s + D1}{(s^2 + A1 * s + B1)} + \frac{C2 * s + D2}{(s^2 + A2 * s + B2)} \qquad (2)$$

The constants Co, C1, C2, D1, and D2 of this expansion may be determined by expressing the partial fraction expansion expression as a single term, over a common denominator and equating the coefficients of the powers of s. The resulting equations may be written in matrix form as

$$[C] * [U] = [K] \tag{4}$$

where the coefficient matrix [C] is

$$[C] = \begin{bmatrix} 1 & 1 & 1 & 0 & 0 \\ (A1+A2) & (A0+A2) & (A0+A1) & 1 & 1 \\ (B1+B2+A1A2) & (B2+A0A2) & (B1+A0A1) & (A0+A2) & (A0+A1) \\ (A1B2+A2B1) & A0B2 & A0B1 & (B2+A0A2) & (B1+A0A1) \\ B1B2 & 0 & 0 & A0B2 & A0B1 \end{bmatrix} \tag{5}$$

and the unknown matrix [U] and constant matrix [K] are

$$[U] = \begin{bmatrix} C0 \\ C1 \\ C2 \\ D1 \\ D2 \end{bmatrix} \qquad [K] = \begin{bmatrix} 0 \\ 0 \\ 0 \\ 0 \\ A0B1B2 \end{bmatrix} \tag{6}$$

The unknowns are therefore

$$[U] = [C]^{-1} * [K] \tag{7}$$

Equation (2) may be inverted on a term by term basis. The inverse transform of the first term of (2), defined as h1(t), is

$$h1(t) = C0 * \exp\{-A0*t\} \tag{8}$$

The second term of (2) is

$$\frac{C1 * s + D1}{(s^2 + A1 * s + B1)} \tag{9}$$

which may be inverted to yield h2(t)

$$h2(t) = \exp\{-A1*t/2\} * [C1 * \cos(wd1*t) + CF1 * \sin(wd1*t)] \quad (10)$$

where

$$wd1 = (B1 - A1\text{^}2/4)\text{^}.5$$

and

$$CF1 = (D1 - A1*C1/2)/wd1$$

Since the form of the third term of (2) is the same as that of the second term, its inverse transform, h3(t) has the same form as h2(t) except that 2 replaces 1 in the definition of the constants C1, D1, A1, B1, wd1, and CF1. The total impulse response is the sum of y1(t), y2(t) and y3(t).

The calculations to generate the constants and evaluate and graph h(t) have been performed in program B5HOFT.MCD. This program stores sample values of h(t) in a disk file. A related program is GB5CONST.MCD, which evaluates the constants A0, A1, A2, B1, B2, C0, C1, C2, D1, and D2 and defines the maximum significant duration time of h(t), MAXTH and stores this data in file B5H1K.CON for convenient use in the filtering program.

2.1.2 The Analog Filter Simulation Program

The analog filter simulation program B5A1K19.BAS simulates the 5th order Butterworth analog filter with a 1 kHz cut off frequency that is used as an anti-aliasing filter for the 2:1 down sampling system currently in use. This program may be used either to cross check the data produced by the traditional down sampling process or in lieu of it if so desired.

The program reads the constants which define the impulse response of the filter from file B5H1K.CON and defines the function H(T). It then loads the data from file ZMIPH1_9.DAT which contains zero mean pressure data which has been scaled by a factor of 100 and stored in zero mean integer form. This data originated from sensor #1 and was acquired at 9091 sps. (It was more efficient to work with scaled integer values of the pressure data.) The data is read into arrays which are stored in ephemeral memory (RAM) in arrays IDH19A and IDH19B. Two arrays were necessary because of array size limitations in Quick Basic 4.5. The filter output is estimated by forming a numerical approximation for the convolution of the input data with the impulse response for every multiple of the read out time interval, i.e. the reciprocal of the output sampling rate. There were 42,976 samples in the input file. The first 32,000 points are from array IDH19A, the rest from IDH19B. The progress of the program is reported to the console by printing the output point number and the time for points 1, 40, 50, 1000, and 2000. This information may then used to estimate the time to completion. The progress information may be omitted if so desired, but the savings in execution time will not be great. The filter output is then stored in file YF1910KA.DAT. This file is nominally half as large as the input file because of the 2:1 down sampling.

2.2 THE DIGITAL FILTER

Digital filters have the potential to outperform their analog counterparts in many respects. Since they may be implemented as computer programs they can be of relatively high order with essentially no increase in complexity, thus leading to steep selectivity skirts. Since no hardware is involved, they may be readily and quickly changed. They can be designed to have phase characteristics which are exactly linear. The group delay will then be constant for all frequencies. They are completely stable with respect to environmental factors such as temperature and humidity. Component aging is not a factor. Once operational, they are reliable. Should a system fail, it will typically fail completely so that there is no uncertainty with respect to the occurrence.

2.2.1 Selection of the Digital Filter Type

Digital filters may be classified as having either infinite impulse response (IIR) or finite impulse response (FIR). The output of an IIR filter may extend to infinity because samples of the output are fed back through the system. The impulse response of FIR filters must be zero after the last non-zero input has propagated through the system. The choice of the filter type depends upon the nature of the application and circumstance.

Although IIR filters may be unstable, FIR filters are always absolutely stable; with no feedback there is no possibility of unbounded oscillation. Closed form design equations for IIR filters exist for many filters, whereas there is no analogous set of design equations for FIR filters. For similar levels of performance, a FIR filter tends to be of higher order than an IIR filter. This leads to reduced hardware requirements and faster execution times for IIR implementations. A FIR filter may be designed to have exactly linear phase so that the time delay of the filter can be constant for all frequencies. A more extensive comparison of the relative differences between FIR and IIR filters is contained in reference 1.

Execution time is not of great consequence for our application since filtering need not be done on a real time basis. Also, since the filter will be implemented on a general purpose computer, hardware complexity is not a factor. The advantage of constant time delay afforded by FIR filters is highly desirable for our application; therefore our choice is to use a FIR filter.

2.2.2 Linear Phase FIR Filters

It can be shown that a sufficient condition for linear phase response is that the unit sample response of the system, h(n), be even symmetric about its midpoint. See, for example, reference 2.

2.2.3 Design Algorithms

Although no general closed form design algorithm exists for FIR filters, there are known design procedures. Impulse invariance techniques are the simple, easy to employ and allow translation of analog filter designs to digital designs, but exhibit aliasing problems and are not usually optimum. Modifications may include the use of weighting functions (windowing) to yield improved response. Bilinear transformation can also afford a means by which analog filters may be translated to digital filters. These eliminate the aliasing problem associated with

the previous technique, but the mapping involved distorts the frequency scale. (Pre-warping can be employed to produce acceptable results in the case of filters having piecewise constant transfer functions.) The design techniques cited are derivatives of analog filter designs. As such, they lose much of the potential advantage of digital filters.

Techniques analogous to impulse invariance exist in the frequency domain. The unit sample response of a digital filter may be obtained by taking the inverse discrete transform of samples of the desired response in the frequency domain.

Direct approaches which do not rely on prior analog filter designs have also been developed. Consider the design of a low pass filter having equal ripple in the pass band and in the stop band. The parameters of interest are the order of the filter, the frequency of the upper edge of the pass band, the frequency of the lower edge of the stop band, the ripple in the pass band and the ripple in the stop band. These parameters are interrelated; they can not be chosen independently. Although the problem has been formulated with many choices for the independent variables, Parks and McClellan have developed the mathematical conditions and a computer program which employs iterative techniques to design linear phase filters when the order of the filter, the edge of the pass band and the edge of the stop band are given. Please refer to references 3 and 4. The program minimizes the maximum error. The resulting filters show nearly equal ripple throughout the band. Even high order filters may be designed relatively quickly, although it may be desirable to repeat the design process to minimize the width of the transition band.

2.2.4 Digital Filter Design

The performance of digital filters of various orders was explored empirically using the Parks and McClellan design algorithm. Filters of order 128 were selected and used exclusively because of their performance. Although such high order filters increase computation time, this was considered to be a relatively insignificant for this application; the rapid transition from pass band to stop band and large attenuation in the stop band were considered to be more desirable than reduced computation time.

Figure 2-3 indicates the topology for the filter, while figure 2-4 shows the performance of a filter designed to have a cut off frequency of 1 kHz, the same as the fifth order analog Butterworth filter used in the current down sampling process. At the corner frequency the analog filter is down by 3 dB, as for any order Butterworth filter. The digital filter output is down only a fraction of a dB at the corner frequency. The original analog filter response is down about 30 dB one octave above the cut off frequency; the digital filter is down about 92 dB for any frequency above 1.12 kHz.

2.2.5 Filter Bank Definition

It was decided that a set of filters be designed and implemented on a general purpose computer. Each filter output would produce a separate file. The set of bandwidths chosen for the filters was 2.0 kHz, 1.5 kHz, 1.0 kHz, 800 Hz, 600 Hz, 400 Hz, 300 Hz, 200 Hz, 150 Hz, 100 Hz, 60 Hz, 40 Hz, 30 Hz, 20 Hz, 15 Hz, and 10 Hz. The ratio of successive filter bandwidths was chosen to be no less than 0.6. The set of filter bandwidths selected is felt to be reasonably complete, although filters having different bandwidths may be designed.

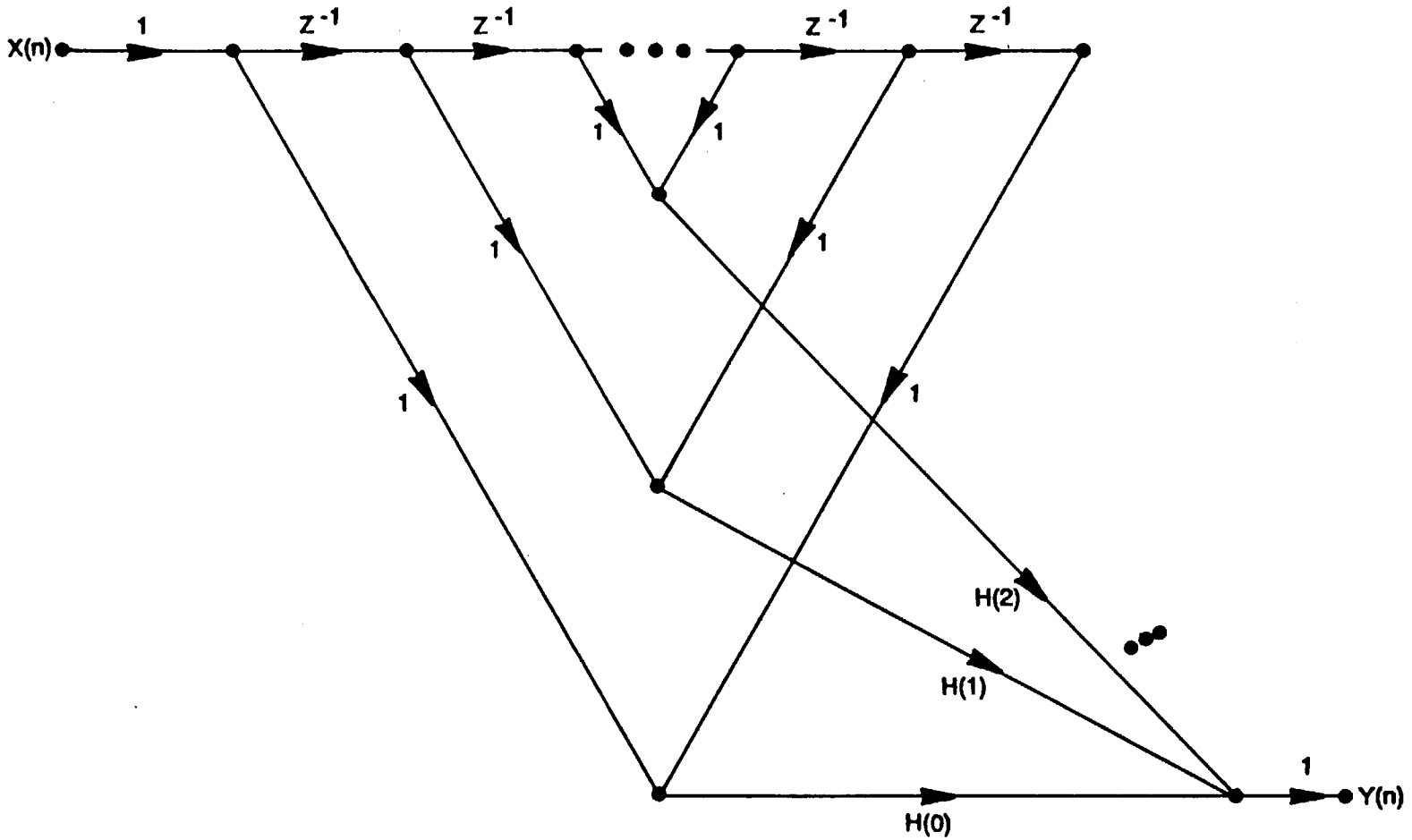

Figure 2-3. Topology of Digital Filter.

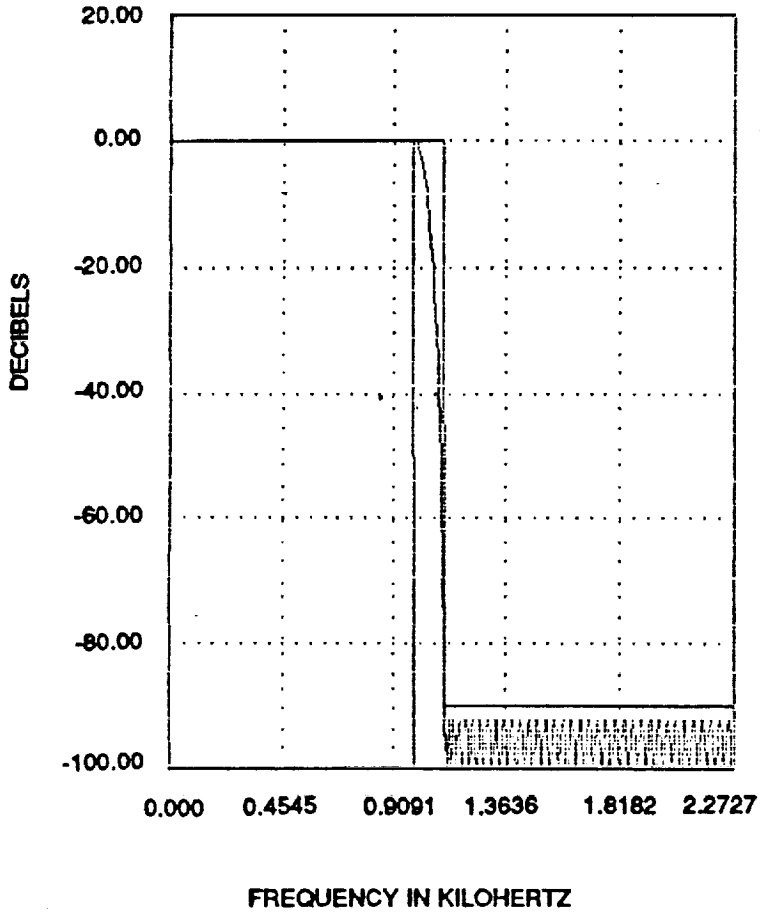

Figure 2-4. Performance of a 1 kHz Digital Filter.

Not all filters have been designed with the same sampling rate. As the spectral width of the data is reduced by filtering to less than one-fourth the input data sampling rate, it is possible to reduce the sampling rate by a factor of two and still meet the Nyquist sampling rate criterion. This is done whenever possible to reduce the volume of stored data. This also enables us to maintain the sharp selectivity skirt of the ensuing filter. Finally, the computation time is correspondingly reduced with no loss of information.

2.2.6 Block Diagram of Filter Bank and Designations

A block diagram of the filter bank which has been implemented is shown in figure 2-5. Low pass filters are designated by a lead L followed by a number indicating their bandwidth. Output files are designated by a lead Y followed by a number indicating the data bandwidth and a letter specifying their input sampling rate. The convention used to define the sampling rate is as follows:

N - 9.091 ksps	W - 1.136 ksps	E - .142 ksps
F - 4.546 ksps	H - .568 ksps	S - .071 ksps
T - 2.273 ksps	Q - .284 ksps	D - .036 ksps

The logic behind these designators is that the rates are nominally Nine, Four, Two, Won, Half, Quarter, one Eighth, one Sixteenth, and one thirty seconD ksps. The use of "Won" allows us to avoid the use of O which might be confusing. The author apologizes for the misuse of won, but the reduced probability of error warrants the potentail wrath of grammarians. The other rather odd usage is the D for one thirty second, but occurs because T had already been used to designate two ksps.

The input data from file ZMIPH1_9.DAT came from sensor #1 at a 9091 sps rate. (This has been rounded to 9 ksps in the figure.) It contains data which is the integer part of 100 times the original pressure data minus the mean value. No information has been lost by this process. The data is filtered by the 2 kHz wide low pass filter, and data is stored in output file Y2_0N. The same input data is also filtered by the 1.5 kHz wide low pass filter, but since this is less than one fourth the sample frequency, it is only necessary to store alternate samples. The two to one down sampling operation is indicated in the diagram by a circle with an arrow pointing downward. Similar logic was used to define the rest of the filters and files.

2.2.7 Digital Filter Definition

The sixteen filters cited in the previous section may be defined by citing their unit sample responses. The array defining the unit sample responses of the filters is in disk file available upon request.

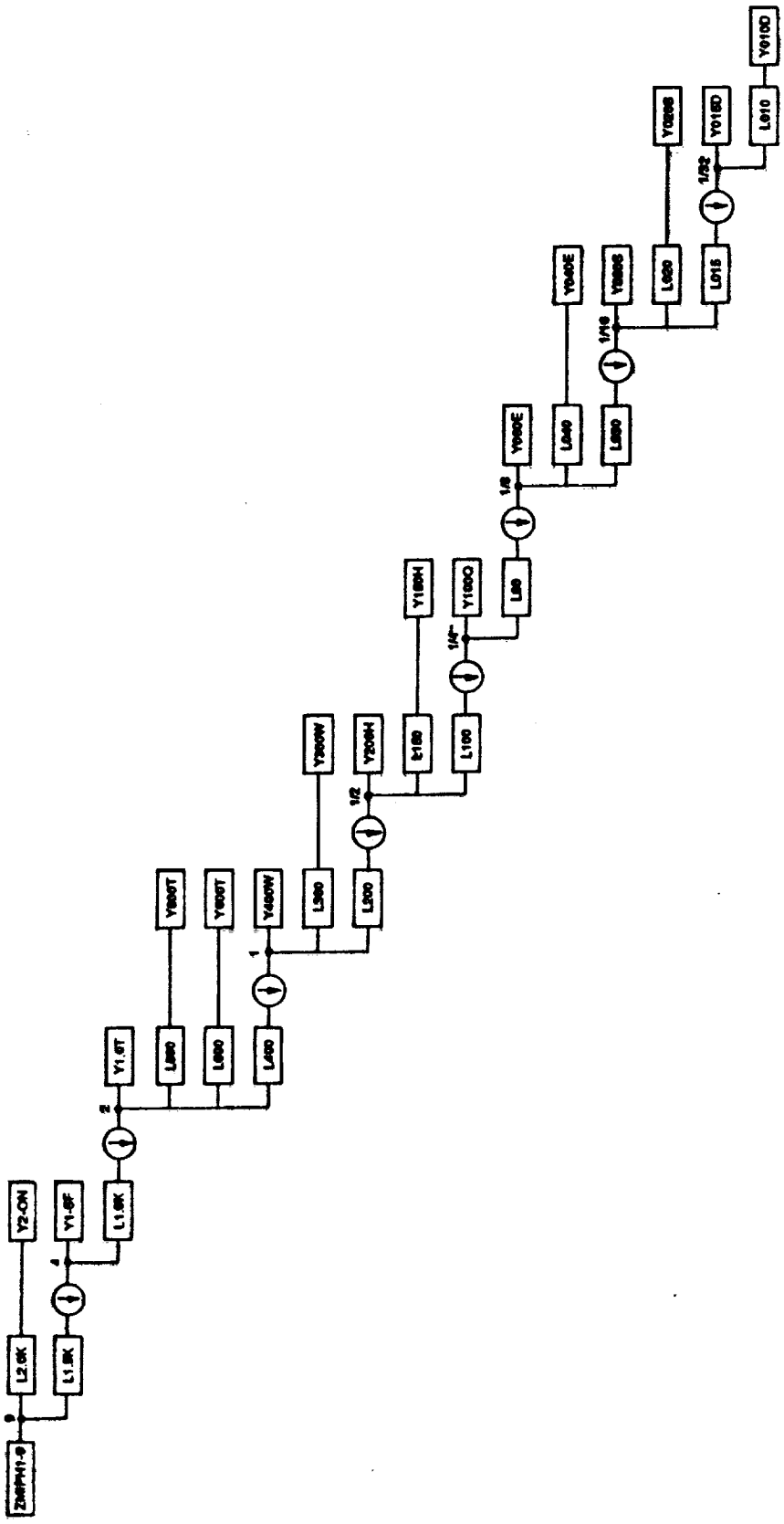

Figure 2-5. Block Diagram of Digital Filter Bank.

SECTION III

RESULTS AND DISCUSSION

3.1 PERFORMANCE OF FILTERS

The performance of each of the sixteen filters is similar to that of the 1 kHz digital filter which was cited previously, so Bode plots for each individual filter have not been included. Table 3-1, below, summarizes the performance of each filter more compactly. The column labeled Bandwidth is the width of the passband of the filter. The Stopband is the frequency of the lower edge of the stopband. The % BW is the width of the transition band measured as a percentage of the pass band width. Fsample is the sampling rate of the input data. Ripple is the peak value occurring within the passband. Attenuation is the minimum value of loss occurring within the stop band.

Bandwidth (Hz)	Stopband (Hz)	% BW	Fsample (Hz)	Ripple (dB)	Atten. (dB)
2000	2400	20	9091	0.005	> 100
1500	1800	20	9091	0.05	> 100
1000	1120	12	4546	0.15	92
800	860	8	2273	0.14	92
600	660	10	2273	0.15	92
400	460	15	2273	0.15	92
300	330	10	1136	0.15	92
200	230	15	1136	0.15	92
150	165	10	568	0.15	92
100	115	15	568	0.15	92
60	68	13	284	0.15	92
40	47	19	284	0.15	91
30	34	12	142	0.19	90
20	22	9	71	0.18	90
15	17	12	71	0.19	90
10	11	9	36	0.18	90

Table 3-1. Summary of Filter Performance

3.2 DIGITAL FILTER BANK IMPLEMENTATION

The digital filter band program is named DFILTER. The program was written in BASIC because this language is familiar and ubiquitous. Current versions of the language have extensive capability and very convenient debug and test features. A brief discussion of the operation of the program is included in this section of the report.

3.2.1 The Digital Filtering Program

DFILTER first reads the constants which define the unit sample response of each of the sixteen digital filters into a two dimensional array, H(K,FILTNO). The source data is contained in file HKFILTNO.FDT which was produced by a utility program which was written to extract the values of H(K) from the design program DFDP. (DFDP, Digital Filter Design Program, is part of a digital filter design program which is commercially available.)

After initializing the output point number (OUTPTNO&), and defining the length of the filter (FLTLEN, which is 128 for all the filters at present), the filter length plus 1 (FLPLUS1), the filter length divided by 2 (FLDIVBY2), and the number of filters (NOOFFILT), the input array (X) is dimensioned to the length of the filter and the output array (Y) is dimensioned to the number of filters. The constants FLPLUS1 and FLDIVBY2 are evaluated outside the ensuing loops to eliminate unnecessary repetitive calculation.

The file to be processed is then opened for input. In the listing, the file ' being processed, ZMIPH1_9.DAT, is from sensor #1. File ZMIPH2_9.DAT or any other data file sampled at 9091 sps could be processed. The filters having cut off frequencies of 2.0 kHz and 1.5 kHz are designed to operate at this sampling rate. The files for the output (Y2_0N.DAT and Y1_5F.DAT) are then opened.

Next the input array (X) is loaded with the first 128 samples of the input file. Pairs of input values which share the same unit sample weighting are summed, multiplied by the appropriate value of H(K) and accumulated for the 2.0 kHz cut off frequency filter which is defined to be filter #1. Since the 1.5 kHz filter, #2, also operates on input data having the same sample rate, similar processing is done for this filter. However, the spectral content of its output is low enough that it may be down sampled; this is done by calculating its output for only odd numbered output points. This also reduces computation time. Having completed calculations for the filter outputs, the input array is shifted by one sample and a new input sample is read into the first cell of the input array. This process is repeated until the input data array is exhausted. The filtering process is then repeated for the remaining filters with the source file updated to provide data at the correct sampling rate.

The last portion of the program evaluates the mean squared value of the data in the output arrays. This is the AC power of the input array since the mean value has already been subtracted. The value is scaled by 10,000 because of the conversion to integer format, which included multiplication by a factor of 100.

At present, any input file will produce the output files cited. It is suggested that the output files be renamed so that they are not inadvertently overwritten. The primary names of the output files are only 5 places long, so there are 3 additional places which could be used to designate the sensor number and launch.

3.2.2 Initial Filter Program Tests

Preliminary tests have been run on the digital filter bank program to verify its operation. Tests included sinusoidal and noise excitation.

3.2.2.1 Sinusoidal Excitation Test

Sums of unit sine waves at various frequencies were sampled at 9091 sps and 100,000 data points were stored. The frequencies were chosen so that one additional sine wave would be included in each successively wider filter. A few sine waves were then added near the corner frequency of the widest (2.0 kHz) filter and above its cut off frequency. The power calculations should then show a decrease of 1/2 for each successively narrower band, except that the widest filter (2 kHz) would partially respond to the additional sine waves around its cut off frequency. Specifically, the unit sine waves were at frequencies of 5, 12, 18, 28, 38, 58, 90, 140, 190, 290, 390, 590, 790, 990, 1490, 1990, 2100, 2200, 2500, and 3000 Hz. Table 3-2 contains data for theoretical and calculated filter output power when the filter bank is excited by the sum of these sine waves. The ripple in the pass band has been ignored.

File Source	Theoretical Power	Calculated Power	Percent Error
Input File	10.00	9.99941	-0.006
2.0 kHz	8.35	8.33643	-0.163
1.5 kHz	7.50	7.50658	0.088
1.0 kHz	7.00	7.02102	0.300
800 Hz	6.50	6.52702	0.416
600 Hz	6.00	6.02446	0.408
400 Hz	5.50	5.55879	1.069
300 Hz	5.00	5.04134	0.827
200 Hz	4.50	4.50858	0.191
150 Hz	4.00	4.07841	1.960
100 Hz	3.50	3.49527	-0.135
60 Hz	3.00	2.93645	-2.118
40 Hz	2.50	2.47886	-0.846
30 Hz	2.00	1.99582	-0.209
20 Hz	1.50	1.49261	-0.493
15 Hz	1.00	1.01627	1.627
10 Hz	0.50	0.99467	98.934

Table 3-2. Comparison of Theoretical and Calculated Power Outputs

The theoretical power calculation includes observable effects of the components at 2.1 and 2.2 kHz in the output of the 2.0 kHz wide filter. Despite ignoring the ripple in the pass band, the error build up from a large number of calculations and variations due to sampling, the maximum error is only 2.118% and the mean absolute error is about .68 % excluding the results from the 10 Hz filter. It is felt that there is an error in this filter. The origin of this error was not pursued since this is the least important filter and because of time limitations.

3.2.2 White Noise Excitation Test

An alternate test was also performed to increase confidence in the digital filtering program. The pseudo-random number generator available in the BASIC language was used to provide samples which were interpreted as originating from bandlimited white noise. The bandwidth of the source was assumed to be 4545.5 Hz and the sample rate was defined to be 9091 in order to be compatible with the filter sample rate requirement. The amplitude of the samples was

scaled to provide a noise power spectral density of 1 volt squared per Hz, and 100,000 samples were generated and stored in a file.

The file of noise samples was then fed to the filter bank program as input data. The power of the data in the input file and in the data of each output file were estimated. The power in the output files should be proportional to the equivalent noise bandwidth. Since the spectral density was scaled to unity, we expect the output power to be numerically equal to the equivalent noise bandwidth of the filter in a statistical sense. The equivalent noise bandwidth of the filters was not calculated, but may reasonably expected to be limited to a value greater than the pass band width but less than the edge of the stop band. These limits are only valid in a statistical sense, and only one random noise sample file was run. The number of samples in outputs of the wider filters is quite large, and the variability of the power should be relatively small. Table 3-3 is a tabulation of the power in the input file, the power in each of filter outputs, and the limits cited.

File Name	Power Estimated	Power Limits Lower	Upper
INPUT	4553.666	4546	4546
Y2_0NWN	2126.869	2000	2400
Y1_5FWN	1583.643	1500	1800
Y1_0TWN	1032.652	1000	1120
Y800TWN	820.728	800	860
Y600TWN	623.858	600	660
Y400WWN	420.640	400	460
Y300WWN	316.196	300	330
Y200HWN	214.496	200	230
Y150HWN	156.262	150	165
Y100QWN	106.328	100	115
Y060EWN	61.536	60	68
Y040EWN	40.286	40	47
Y030SWN	31.766	30	34
Y020SWN	19.942	20	22
Y015DWN	14.566	15	17
Y010DWN	13.660	10	11

Table 3-3. Power in Volts squared for the input and output files.

Agreement is excellent for nearly all the files, although the power in the filters having bandwidths of 20 Hz and 15 Hz is very slightly low, this may be a consequence of statistical variation and the relatively small sample size available at these low frequencies. The only questionable result is once again that from the 10 Hz filter. Its output appears to be unduly high. This result again makes this filter implementation suspect.

3.3 EXECUTION TIME AND DATA VOLUME

A complete run, including filter output power calculations in BASIC, for the white noise test sample, which consisted of 100,000 points of data, took less than three hours to complete

on a computer having a 80386 CPU and a 80387 co-processor chip running at a speed of 16 MHz. This volume of data is equivalent to the output of one sensor for 11 seconds, so the execution time is about .27 hours/sensor-second. A set of 10 sensors collecting data for 11 seconds each would lead to a total processing time of about 30 hours under the conditions cited. Since this is a non-recurrent operation for a given launch, the current execution time may be acceptable.

3.3.1 Reduction of Execution Time

Run time could be reduced by using a faster machine, say a 33 MHz system, thus speeding execution by a factor of 2. It would be possible to use one of the new 80486 systems, which are reputed to be 2 to 4 times faster than the 80386 machines. The program could also be run on a mini, mainframe, or other faster machines. A compiled language program would also execute more rapidly. Additionally, the program could be modified to reduce computation time. For example, the shift register operation, which mimics a hardware implemented shift register could be replaced by a functionally equivalent system in which the data is loaded into an array in RAM and accessed by pointers. This implementation would most likely be quicker. It is also possible that transform techniques may be faster.

3.3.2 Data Volume

The data volume may be reduced with no loss of information by storing only the sampling interval and a sequential set of pressure samples. The pressure samples may be stored in integer format rather than floating point. Data compression techniques, which are currently in use, should be continued for archival purposes.

SECTION 4

CONCLUSIONS

A filter bank of 15 digital filters has been designed and implemented in software for this project and appears to be functioning correctly, although additional verification work would further increase confidence.

The all-digital filtering program is far more versatile than the previous system. It is much more extensive.

Should different applications require different bandwidths, a new set of digital filters could be quickly, easily, and inexpensively designed and implemented.

The performance attained by the digital filters far exceeds that of their analog predecessor both in roll off rate and attenuation. Aliasing errors are correspondingly reduced, assuming the adequacy of the analog anti-aliasing filter.

The time delay for the digital filters is constant for all frequencies, so there is no distortion caused by relative time shifts between the spectral components of a signal.

The time to process 11 seconds of data from 10 sensors may be filtered and the power in the filter outputs calculated in less than 30 hours. The processing time could be easily reduced to less than 8 hours.

Once operational, the digital filtering system is reliable and error free. No analog signal reconstruction, filtering and resampling operations are necessary, thus eliminating many opportunities for error.

The volume of data could be further reduced and subsequent processing time decreased if the sampling rate were made close to the Nyquist rate for each filter bandwidth. This would require non-integer changes in the sampling frequency. It is possible, through a process of upsampling and down sampling, to produce sampling rates which related by any rational number.

The analog filter simulation was written but not verified due to time limitations. It was a secondary goal, intended to provide cross comparison and verification of the current processing system. It was therefore given lower priority than the digital effort.

References

1. L. R. Rabiner, J. F. Kaiser, O. Herrmann, and M. T. Dolan, "Some Comparisons between FIR and IIR Digital Filters," Bell System Technical Journal, Volume 53, Number 2, February, 1974, pages 305 - 331.

2. Alan V. Oppenheim and Ronald W. Schafer, "Digital Signal Processing," Prentice-Hall, 1975.

3. T. W. Parks and J. H. McClellan, "Chebyshev Approximation for Non-recursive Digital Filters with Linear Phase," IEEE Transactions Circuit Theory, Volume CT-19, March, 1972, pages 189 - 194.

4. T. W. Parks and J. H. McClellan, "A Program for the Design of Linear Phase Finite Impulse Response Filters," IEEE Transactions Audio Electroacoustics, Volume AU-20, Number 3, August, 1972, pages 195 - 199.

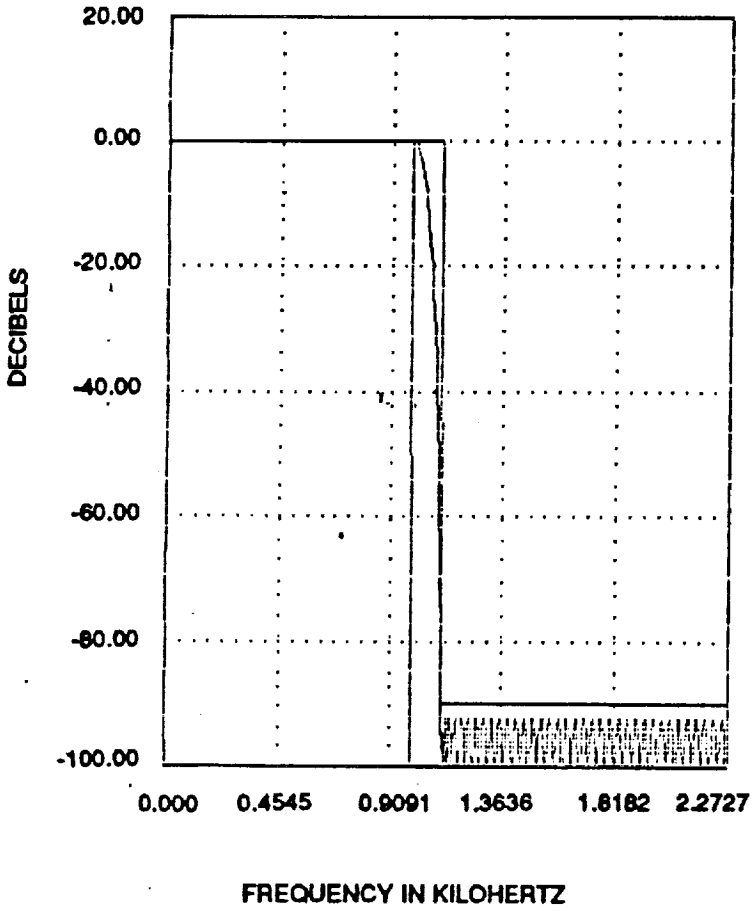

Log Magnitude Response

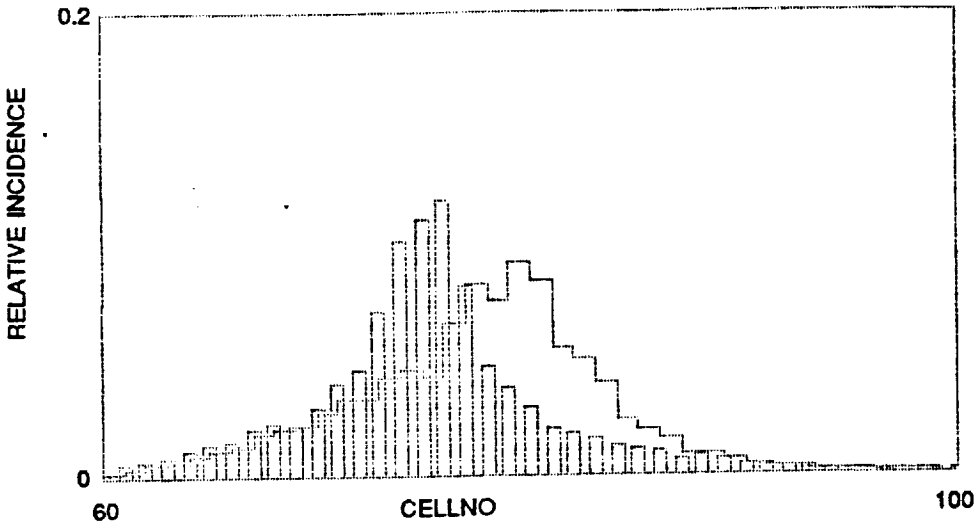

Figure 1-1a. Histogram of Filtered and Unfiltered Data for Sensor #1
Unfiltered Data drawn with vertical bars.
Cell width = 0.2 psi

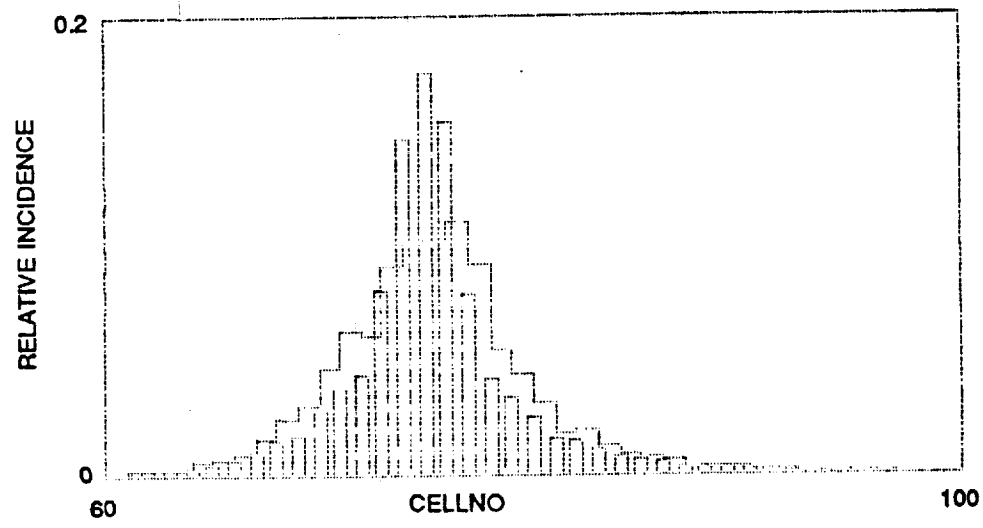

Figure 1-1b. Histogram of Filtered and Unfiltered Data for Sensor #2
Unfiltered data drawn with vertical bars.
Cell width = 0.2 psi

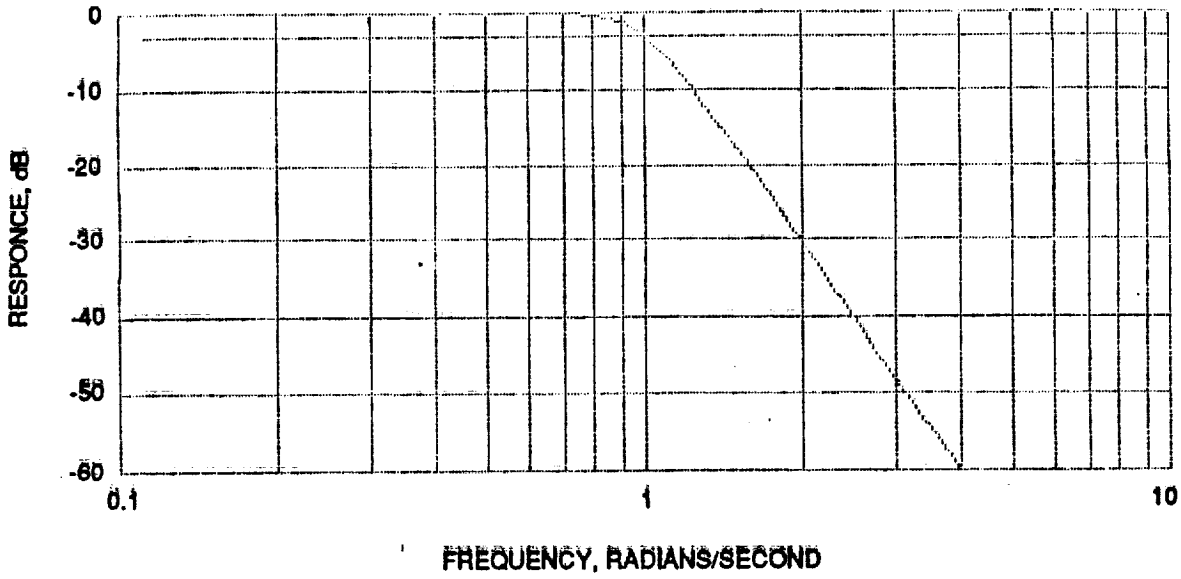

Figure 2-1. Bode Plot Response of 5th Order Butterworth Analog Filter
Normalized to a corner frequency of 1.
horizontal line is -3 dB.

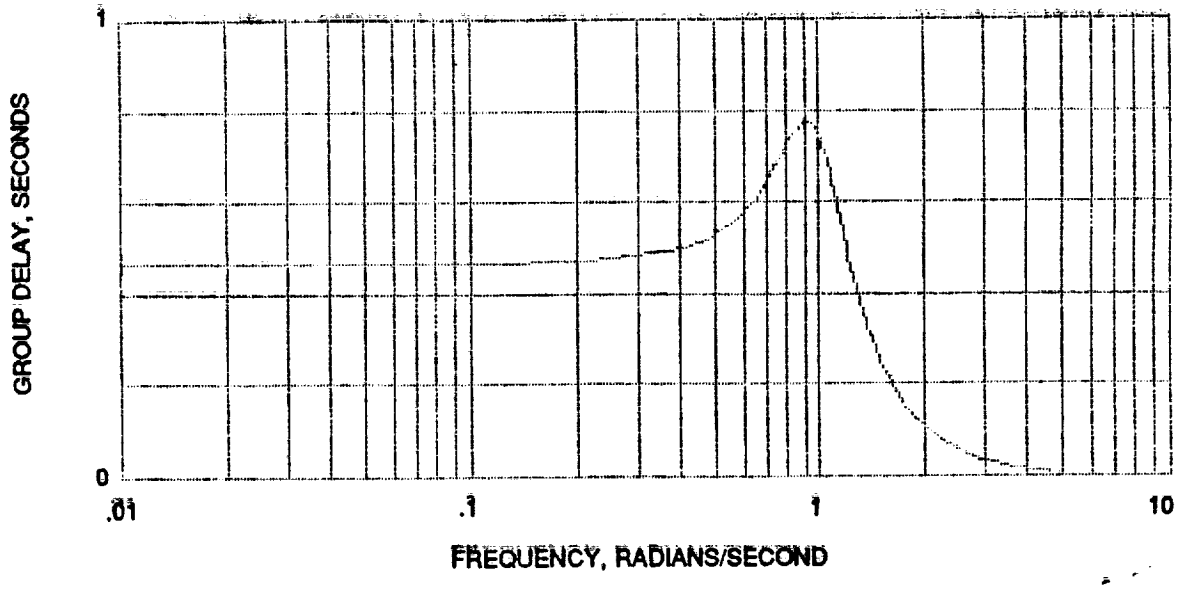

Figure 2-2. Group Delay of 5th Order Butterworth Filter
(for a 1 radian/second bandwidth filter)

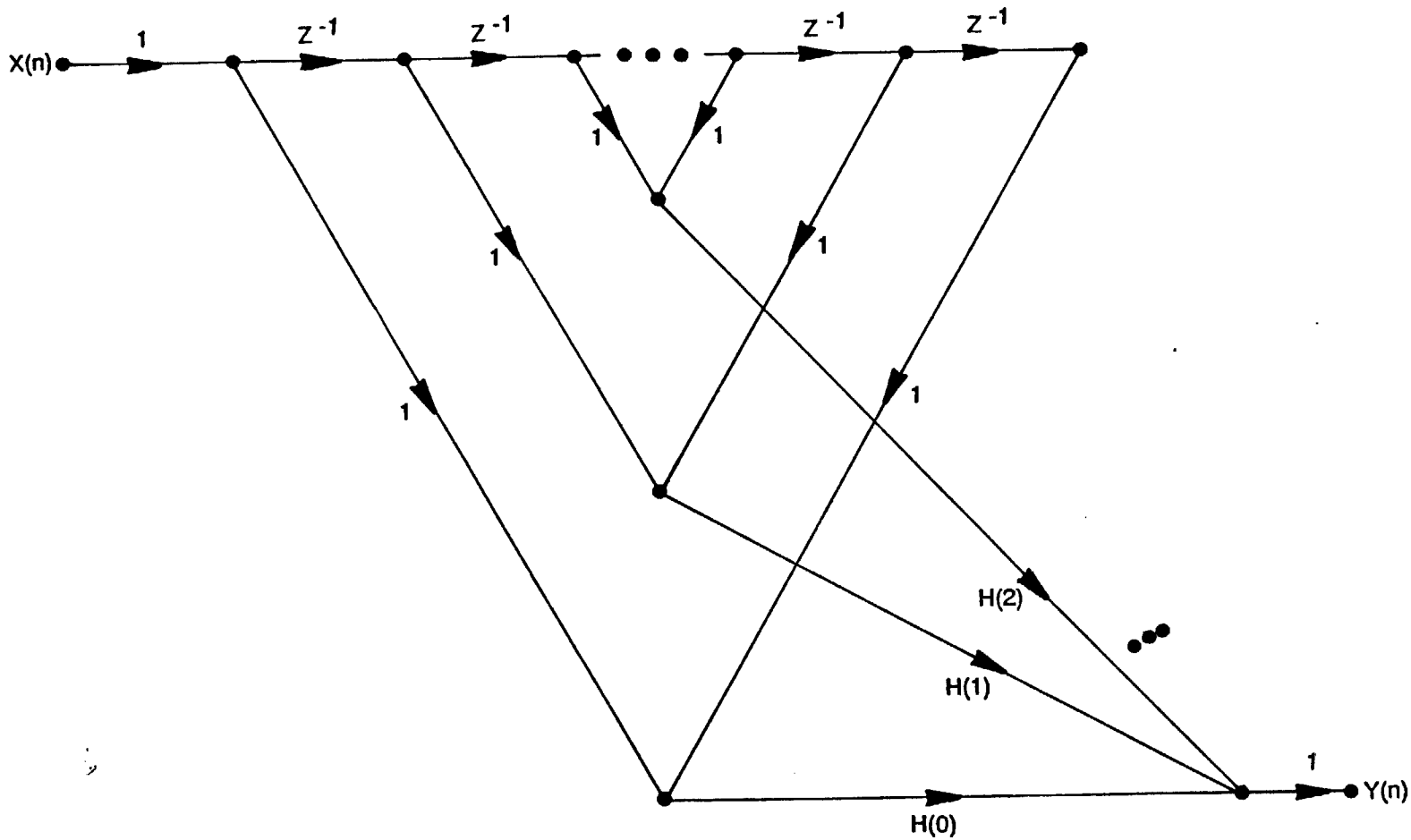

Figure 2-3. Topology of Digital Filter.

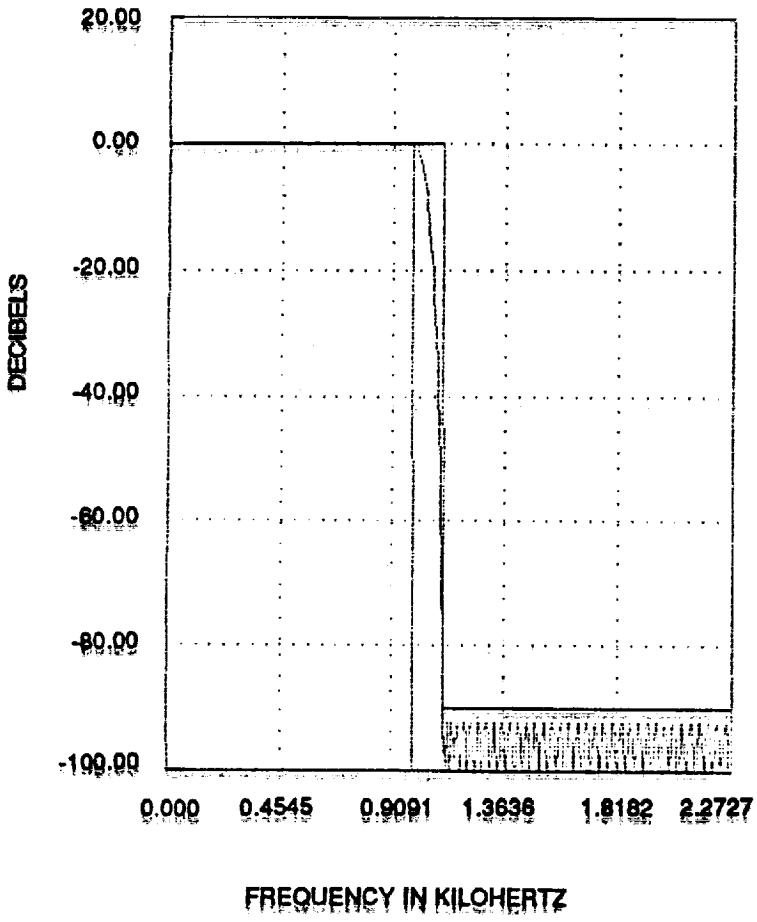

Figure 2-4. Performance of a 1 kHz Digital Filter.

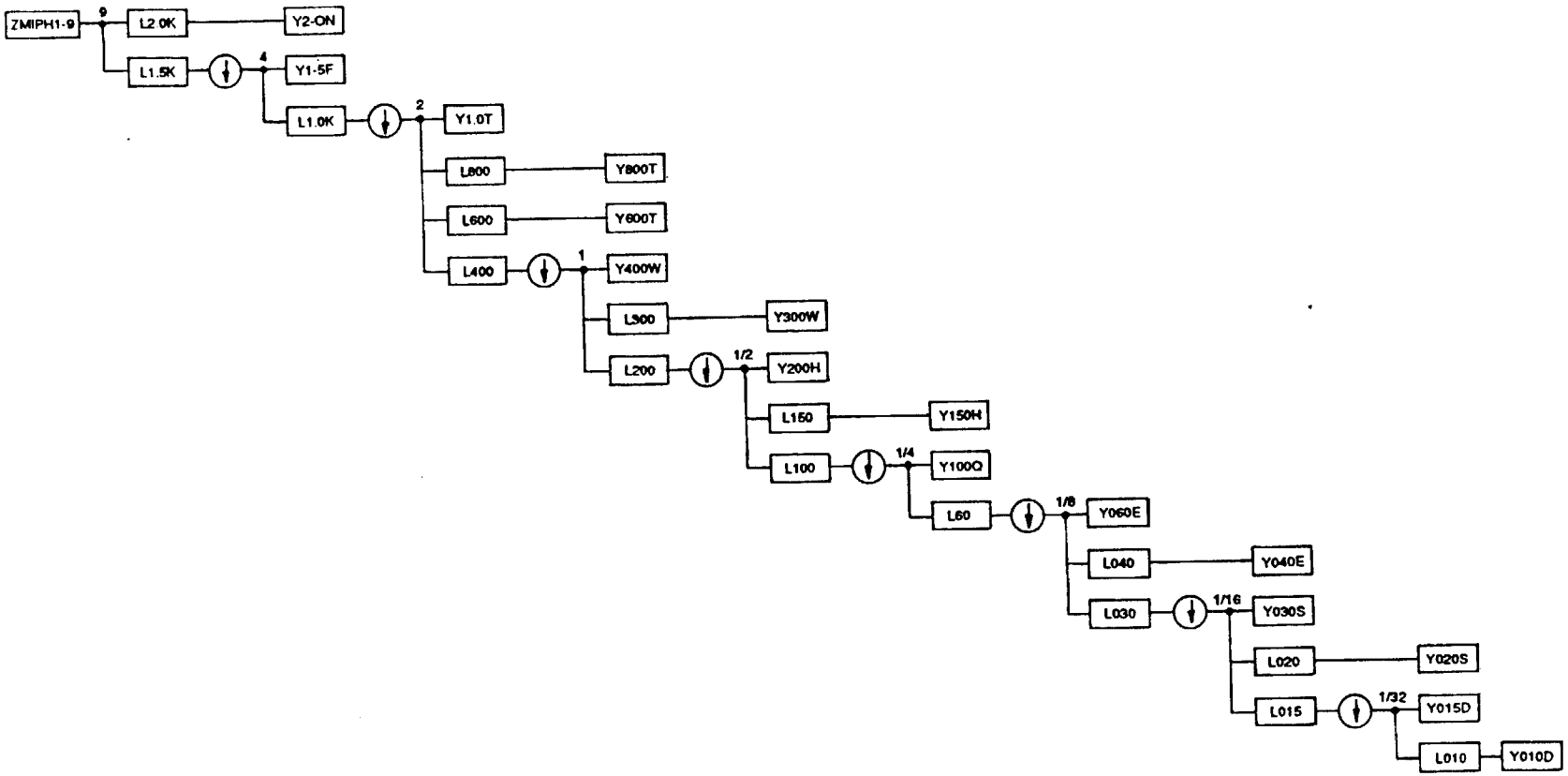

Figure 2-5. Block Diagram of Digital Filter Bank.

1990 NASA/ASEE SUMMER FACULTY FELLOWSHIP PROGRAM p. 32

JOHN F. KENNEDY SPACE CENTER
UNIVERSITY OF CENTRAL FLORIDA

LOW LEVEL VAPOR VERIFICATION OF MONOMETHYL HYDRAZINE

PREPARED BY:	Dr. Narinder Mehta
ACADEMIC RANK:	Investigator
UNIVERSITY AND DEPARTMENT:	University of Puerto Rico - Mayaguez Research Center, College of Engineering
NASA/KSC	
DIVISION:	Engineering Development
BRANCH:	Instrumentation
NASA COLLEAGUE:	Ms. Rebecca Young
DATE:	August 2, 1990
CONTRACT NUMBER:	University of Central Florida NASA-NGT-60002 Supplement: 4

ACKNOWLEDGEMENT

I would like to thank NASA / ASEE Summer Faculty Fellowship Program, to Dr. Loren Anderson of the University of Central Florida, to Mr. William (Bill) Helms and Dr. Mark Beymer of the Kennedy Space Center (KSC) for providing me with the opportunity to work at KSC for a second summer. Many thanks to Ms. Kari Baird for her willingness to help in all administrative matters.

Special thanks are extended to Mrs. Rebecca Young, KSC project coordinator for suggesting the project, and for her guidance and encouragement in all phases of this project. Grateful acknowledgment is due to Mr. Dave Collins, Mr. Josh Travis and Mr. Paul Mogan for their assistance and support during my stay at KSC.

Special appreciation is due to professionals working in the TVD laboratory who made me feel welcome, and for the pleasant interactions we all had while working in the laboratory.

The support of Dr. Rafael Munoz Candelario of my home institute, the University of Puerto Rico is gratefully acknowledged.

ABSTRACT

The purpose of this summer project was to evaluate the vapor scrubbing system and the coulometric test procedure for the low level vapor verification of monomethyl hydrazine (MMH). Experimental data on precision, efficiency of the scrubbing liquid, instrument response, detection and reliable quantitation limits, stability of the vapor scrubbed solution and interference were obtained to assess the applicability of the method for the low ppb level detection of the analyte vapor in air. The results indicated that the analyte vapor scrubbing system and the coulometric test procedure can be utilized for the quantitative detection of low ppb level vapor of MMH in air.

SUMMARY

American Conference of Governamental Industrial Hygienists on toxic vapors has recently proposed to reduce the Threshold Limit Value (TLV) of hydrazines to 10 ppb level in air. NASA's Toxic Vapor Detection (TVD) group at the Kennedy Space Center (KSC) is working on to develop sensors for meeting this requirement. For the testing of the potential sensors, test vapor of the analyte must be verified at the low ppb level of concentration. TVD group has opted to use the coulometric titration method for the vapor verification of hydrazines since it is a routine TVD lab's procedure for the detection of hydrazines at the ppm levels. In this project, experimental data is obtained to assess the applicability of the coulometric test procedure at low ppb level after scrubbing the monomethyl hydrazine (MMH) vapor in acidic absorbing solution.

0.1 M H_2SO_4 is found to be an effective scrubbing medium for absorbing MMH vapors without any carry-over loss of the analyte. Coulometric response to MMH is found to be linear and consistent in the low ppb concentration range. The acidic solution containing scrubbed MMH vapors is stable up to a period of 3-day and a slight loss of the analyte is detected after seven days. Ammonia gas is found to be a potential negative interferent at twice its TLV value and higher. Experimental data obtained demonstrate that the vapor scrubbing system and the coulometric titration test procedure can be utilized for the low ppb level verification of MMH vapor in air.

TABLE OF CONTENTS

LIST OF ILLUSTRATIONS

LIST OF TABLES

LOW LEVEL VAPOR VERIFICATION OF MONOMETHYL HYDRAZINE

I - INTRODUCTION

Hydrazines are used as hypergolic propellants for the in-flight shuttle maneuvering systems. Their vapors are highly toxic at low parts per million (ppm) levels and form hazardous explosive air mixtures at higher concentrations. These fuels affect the performance capabilities of humans and have been shown to cause tetragenic and mutagenic activity.

The American Conference of Governmental Industrial Hygienists (ACGIH) has proposed to reduce in 1991 the Threshold Limit Value (TLV) of hydrazine (N_2H_4) and monomethyl hydrazine (MMH) to 10 parts per billion (ppb) level from their respective 100 and 200 ppb levels. NASA's Toxic Vapor Detection (TVD) Group of the Instrumentation Branch at the Kennedy Space Center (KSC) has been working to develop sensors to meet this new requirement.

Prior to the testing of the potential sensors, test vapors must be accurately analyzed for hydrazines. A coulometric titration procedure has been in use at KSC for many years for the detection of ppm concentration level of hydrazines. Due to its simplicity and accuracy, the TVD group has opted to use this method; however, use of this test procedure requires experimental data on precision, accuracy, efficiency, etc., to assess the applicability of the method for the ppb level detection of hydrazines. This project focussed on the evaluation of the vapor scrubbing system and the coulometric titration test procedure for the ppb level vapor verification of MMH in air.

II - MATERIALS AND METHODS

2.1 MMH Vapor Generator System:

Kin-Tek's Span Pac 361 Precision Standard Vapor Generator is used in conjuction with Miller-Nelson HCS-301 flow-humidity-temperature control system for the generation of the MMH vapors.

Span-Pac consists of three permeation devices housed in three temperature-controlled ovens. Each permeation device is a stainless steel dewar containing a coil of polymeric capillary tube submerged in MMH. Nitrogen flows through the polymeric tubes at all times. Standard vapor of the analyte at various levels of relative humidities may be generated by diluting the analyte-nitrogen mixture with varying conditioned air from Miller-Nelson unit. Activating the SPAN or ZERO mode in conjuction with activating a combination of channel switches of the permeation devices on the Kin-Tek vapor generator, zero air and various concentration levels of the analyte in vapor phase may be generated at various levels of percent relative humidity.

2.1.1 MMH Vapor Standards

Using the standard laboratory set-up, the system generated MMH vapors in the concentration range of 3-149 ppb in air at approximately 80% relative humidity, a requirement for meeting the OSHA's protocol for the development of a new methodology[1,2].

2.1.2 MMH Scrub Solutions for Spiking

0.1 M H_2SO_4 scrubbing solutions containing MMH were prepared using a 10% solution of high purity MMH supplied by Wiltech Corporation in KSC. 25 ml of these solutions were spiked with various MMH standard vapors for recovery, detection and reliable quantitation limits. Actual concentration of MMH present in these scrubbing solutions was determined by coulometric titration[3] method using the following formula:

$$\text{ppb (in liquid)} = \frac{10^{-4}\ \text{amp} \times (\text{distance in cm} \times 60\ \text{sec} / 2\ \text{cm}) \times (46 \times 10^{6}\ \text{ug / mole of MMH})}{(9.6484 \times 10^{4}\ \text{amp-seconds / mole e}^{-}) \times 4\ \text{mole e}^{-}\ \text{/ mole MMH} \times \text{sample volume, Lit's.}}$$

2.1.3 Interference Study

Interference by ammonia gas present in the sample stream on the detection of MMH vapor in the scrubbed liquid was determined. K-bottle containing known concentration of ammonia in nitrogen was connected into the air inlet of the MMH vapor generating system. Outlet flow of the K-bottle was controlled so that the standard MMH vapor produced by the system contained approximately 50 ppm (2xTLV) and higher concentration of ammonia gas.

2.2 Vapor Collection System:

Cole-Palmer masterflex peristallic type air sampling pump with variable control speed was used for scrubbing the standard MMH vapors for having the experimental data to assess the applicability of the coulometric method for the ppb level detection of MMH. MMH vapors were scrubbed through a glass straight tube impingers having 25 ml of 0.1 M H2SO4 as the scrubbing solution at a rate of about 0.8-1 liter per minute. At all times, the volume of the MMH vapor passing through the impingers was calculated from the wet test meter readings. 15 liters of the MMH vapors were scrubbed for all the standards except for the low level concentration standards (< 10 ppb) where 30 liters of the vapors were also scrubbed to have a readable titration time (net chart distance) in the coulometric analysis over blank (bkg) reading.

Most of the scrubbing was done using single impingers; however, two impingers were also used in series to determine the absorbing efficiency of the scrubbing solution for the MMH vapors. The standard laboratory sampling setup is presented in Figure 2-1.

2.3 Coulometric Titration System

The circuits of a typical standard coulometric titration system[4] is shown in Figure 2-2. The oxidant generator circuit consists of a platinum anode (+), an auxiliary platinum cathode (-) and a constant-current power supply. The potential monitoring circuit contains a platinum indicator electrode, a reference electrode and a strip chart recorder. The schematics and the list of the components of a NRL coulometer used for this study are presented in the Appendix A.

2.3.1 Coulometric Titration Method:

Following vapor absorption, MMH concentration was determined by constant-current coulometric titration method.

> Hydrazines are titrated in acidic solution with electrically-generated bromine. Coulometric method analyzes hydrazines collectively. Quantification of hydrazines are obtained by counting the electrons produced by the oxidation of the analyte since each mole of hydrazines produces four moles of electrons. The electrons produced during the titration enter an electric circuit and are counted by integrating the electric current as a function of time since time and current are related to the number of electrons by Faradays constant (96484.56 amp-sec per mole). In other words, time or net recorder chart distance required for the titration is directly related to the analyte concentration in the scrubbed solution.

Basically, NASA's TVD lab's analysis procedure TVD-00003-GP was followed for the titration of the MMH vapor in the scrubbed solutions and is presented in Appendix B. A small amount of potassium bromide (KBr) crystals were dissolved in the vapor-absorbed scrubbing solution. A direct electric current passing through the solution electrolyzed KBr at the anode (+) to produce bromine (Br_2) which immediately oxidized MMH present in the scrubbing solution. The length of the titration (Figure 2-3) reflected the amount of MMH present in the solution. Soltec 1241 recorder having a chart speed of 2 cm / min at a recorder sensitivity of 100mv was used for all the coulometric titration runs. Proper coulometric operation was checked by titrating standard solutions of MMH and hydrazine prepared in the laboratory.

Analyte vapor concentration was calculated using the following simple formula:

$$\text{ppb (in air)} = \frac{\text{Net titration length in cm} \times 0.38 \times 10^3}{\text{Chart speed (cm / min)} \times \text{Liters of vapor scrubbed}}$$

$$\text{where } 0.38 = \frac{(10^{-4}\ \text{amp}) \times (60\ \text{sec / min}) \times (24.5\ \text{Lit / mole}) \times (10^6\ \text{ul / Lit})}{(9.65 \times 10^4\ \text{amp-sec / mole e}^-) \times (4\ \text{mole e}^- / \text{mole MMH})}$$

No volume correction was applied since all the MMH vapor scrubbing was done at 23-25 ^{0}C and at one atmospheric pressure. However, the following formula may be used for obtaining the correct sample volume if significant variation in temperature and pressure exists.

$$\text{Volume, Liters} = \frac{\text{Volume scrubbed , Liters} \times (273 + {}^0\text{C}) \times 760\ \text{mm of Hg}}{\text{Pressure in mm of Hg} \times 298}$$

2.3.2 Chemical Reaction in Coulometric Titration

N_2H_4 and its alkylated derivative (MMH) do not go oxidation at anode (+) spontaneously given by the equations

$$N_2H_4 \not\rightarrow N_2 + 4H^+ + 4e^-$$

$$CH_3HN_2H_2 + H_2O \not\rightarrow CH_3OH + N_2 + 4H^+ + 4e^-$$

They are forced to do so by applying potential across the solution between two

oppositely-charged electrodes. As the scrubbing solution is acidic, H^+ are reduced to H_2 at cathode (-).

$$4H^+ + 4e^- \longrightarrow 2\,H_2$$

Hydrazines are protonated in acidic scrubbing solution as follows

$$N_2H_4 + H^+ \longrightarrow N_2H_5^+$$

$$CH_3HN_2H_2 + H^+ \longrightarrow CH_3HN_2H_3^+$$

Protonated hydrazines are not oxidized directly on an anode (+). An intermediate electrolyte is used which oxidizes easily at the anode (+) and then oxidizes hydrazines. KBr is used for this purpose.

$$4KBr \longrightarrow 2Br_2 + 4e^- + 4K^+$$

Liberated oxidant, Br_2, immediately oxidizes hydrazines

$$N_2H_5^+ + 2Br_2 \longrightarrow N_2 + 5H^+ + 4Br^-$$

$$CH_3HN_2H_3^+ + 2Br_2 + H_2O \longrightarrow CH_3OH + N_2 + 5H^+ + 4Br^-$$

Each mole of hydrazine or MMH produces four moles of electrons. Hydrazines are titrated with electrons which act as a universal standard. There is no need of an external standard. Moreover, there are no reference standards available from National Institute of Standards and Technology (NIST).

III - RESULTS AND DISCUSSIONS

3.1 Efficiency of the Vapor Scrubbing Solution

The results obtained for the scrubbing of the various MMH vapor standards into the 25 ml of the 0.1 M H_2SO_4 absorbing solutions under the standard laboratory setup are presented in Table 3-1. Scrubbing of 15 liters over 10 ppb level and 30 liters under 10 ppb level MMH standard vapors did not show any carryover of the analyte vapor into the second impinger except for the 149 ppb level MMH standard where a slight carryover of MMH vapors was observed into the second impinger. Higher scrubbing volume (overnight run) resulted in the carryover of the MMH vapor into the second impinger for the standards having 42 ppb MMH and above. The data indicate that 15 liters over 10 ppb level and 30 liters under 10 ppb level are the optimum scrubbing volumes and that 0.1 M H_2SO_4 is an efficient scrubbing medium for absorbing the MMH vapors at low ppb levels without any carryover losses.

3.2 Precision of the Analytical Procedure

The precision of the analytical procedure for the MMH vapor verification study includes the sample collection system as well as the coulometric titration analysis. Data obtained for a series of MMH vapor standards scrubbed and analyzed by the coulometric method are presented in Table 3-2. The variation in the results of the MMH concentration found in the scrubbed solutions for most of the vapor standards was found to be approximately 10%. The scattering in the data obtained for the 15 liter vapor scrubbing done for std-20 on June 11 was found to be higher; however, another run of July 3 of the same standard for the same scrubbing volume was found to be less than 10%. The variation of approximately 30% on June 11 may be attributed to the air inlet pressure fluctuations in the standard vapor generation system observed during the early part of this investigation. Scattering in the data is also observed for the higher MMH vapor standards but the variation is less compared to std-20.

The calculated percent coefficient of variation for all the standards was found to be 10% or less except for std-20 scrubbed on June 11. Using 30 liters

scrubbed volume for std-7.5 and std-20, and 15 liters scrubbed volume for all other standards, the calculated pooled percent coefficient of variation was found to be 6.7% which is better than 8% required by OSHA for the development of a new methodology .

3.3 Instrument Response to MMH

The linear curve obtained for the net chart distance obtained in cm at a chart speed of 2 cm / min in the coulometric analysis versus the average MMH vapor concentration determined experimentally by scrubbing is presented in Figure 3-1. The curve demonstrates the consistency in the coulometric response in determining MMH in the absorbing solution after scrubbing. It also demonstrates a linear response of the analytical method to the concentration range (3-149 ppb) of the analyte vapor scrubbed and analyzed under the prescribed conditions of the test procedure.

3.4 Spiking of the Scrubbing Solution Containing MMH

Spiking of the various MMH vapor standards was done into 0.1 H_2SO_4 scrubbing solutions containing 72 and 7.9 ppb average concentration levels of MMH. The purpose was to evaluate if we could recover the amount of MMH vapors spiked into a scrubbing solution containing MMH. Data obtained for this spiking are presented in Tables 3-3 and 3-4. The results reflect that the average %recovery for all of the standard MMH vapors spiked into the scrubbing solution containing a known amount of the analyte was in the range of 81-113% for 15 or 30 liters of sample volume scrubbed except for the std-20 where average %recovery was found to be 71% for 15 liter scrubbing volume. No explanation can be given for this low recovery except to attribute this to the air pressure fluctuations in the vapor generation system; however, 30 liter scrubbing volume of std-20 gave 105 and 103 average percent recovery for scrubbing solutions containing 72 and 7.9 ppb average concentration of the analyte respectively.

3.5 Detection Limits

3.5.1 Detection Limit of the Analytical Procedure

Detection limit of an analytical procedure is normally a factor of the base-line noise in any analytical instrumentation. In coulometric analysis, the type of base-line (bkg) information obtained is a line trace. It was decided to use the detection limit equal to the blank line trace obtained by running the scrubbing solution through the coulometric titration procedure. 0.1 M H_2SO_4 scrubbing solutions gave an average chart distance of approximately 0.4 cm at a chart speed of 2 cm / min which when calculated using the standard formula gave an equivalent value of approximately 5 ppb. Hence 5 ppb was selected as a detection limit of the analytical procedure.

3.5.2 Detection Limit of the Overall Procedure

The detection limit of the overall procedure is the amount of the analyte spiked which allows recovery equivalent to the detection limit of the analytical procedure. Figure 3-2 is a recovery curve of the MMH vapor concentration recovered versus average MMH vapor concentration of various spiked standards. Data used for the preparation of this recovery curve is the spiking data presented in Table 3-4. The detection limit of the overall procedure was found to be 5 ppb. It was decided to evaluate if we can go below 5 ppb as the detection limit of the overall procedure. A set of six absorbing solutions having 2.1 ppb average MMH concentration were spiked with a 2.7 ppb average MMH vapor concentration standard using 30 liters of the scrubbing volume. MMH concentrations recovered in this test are also plotted on to Figure 3-2 and are presented in Table 3-5. It demonstrates that we can detect less than 5 ppb level of MMH vapor absorbed in 0.1 H_2SO_4. So we may conclude that the detection limit of the overall procedure is less than 5 ppb.

3.6 Reliable MMH Quantitation Limit

The reliable quantitation limit is the smallest amount of the analyte which can be quantitated with at least 75% recovery and a precision ($\mp$ 1.96 Std Dev) of $\mp$ 25% or better. The data obtained (Table 3-5) for spiking 30 liters of MMH vapor std-20 into six of 0.1 M H_2SO_4 absorbing solutions containing 7.9 ppb concentration level of MMH were used to calculate the reliable quantitation limit. The average percent recovery of six runs was found to be 103% and a precision of $\mp$ 12%. As the precision obtained was better than required for OSHA methodology, it was decided to use the scrubbing data of 30 liters of the MMH vapor standard having 2.7 ppb average MMH vapor concentration spiked

individually into six absorbing solutions having 2.1 ppb average MMH concentration (Table 3-5). The average percent recovery was found to be 87% with a precision of +20%. Hence it is appropriate to consider 3 ppb as the reliable quantitation limit of the analytical method.

3.7 Stability of the MMH Vapor Scrubbed Solutions

30 liters of std-20 was spiked into each of the six absorbing solutions and the MMH concentration was determined at an interval of three and seven days. The scrubbed solutions were stored at the room temperature and analyzed at the required time interval. No variation in the average MMH concentration in the three scrubbed solutions was found after three days; however, an average decrease of approximately 15% was observed in the other three solutions after a period of 7-day; average concentration of 6.1 ppb (6.3 ppb, 5.7 ppb and 6.3 ppb) MMH versus 7.2 ppb MMH.

3.8 Determination of MMH vapor in the presence of ammonia as interferent

The study indicates that ammonia is a negative interferent. The higher the concentration of ammonia in the stream of the MMH vapor for scrubbing, the lower is the MMH concentration detected in the scrubbed solution. 50 ppm of ammonia gas present in the MMH vapor std-20 stream resulted in a 25% average detection loss of MMH in the scrubbed solution while for 588 ppm ammonia, the loss was found to be 58% of the original concentration. The results obtained are as follows:

NH_3, ppm	Std-20 MMH, ppb	MMH, ppb detected	Av MMH detected	% MMH loss
50	7.2	5.4 5.4	5.4	25%
588	7.2	2.9 3.2 2.9	3.0	58%

IV - CONCLUSIONS

1. 0.1 M $H2SO_4$ is an effective scrubbing solution for absorbing MMH vapors at low ppb levels. 15-30 liters scrubbing of the vapor sample at approximately 0.8-1 liter / min is optimum without any carry-over loss of the analyte.

2. The pooled percent coefficient of variation of the method (sample collection system and the coulometric analysis) is found to be 6.7.

3. Coulometric response to MMH in the absorbing solution is found to be linear and consistent in the concentration range of 3-149 ppb under the prescribed conditions of the test procedure.

4. The average percent recovery of the spiked MMH vapor standards into the scrubbing solutions having various levels of MMH is found to be in the range of 71-113%.

5. The detection limit of the overall procedure and the reliable quantitation limit are found to be less than 5 ppb and 3 ppb respectively.

6. No variation in the average concentration of MMH vapor in the scrubbed liquids is found for std-20 after three days; however, a slight reduction in the detection of the analyte is observed after a period of 7-day.

7. Ammonia is found to be a potential negative interferent. The higher the ammonia in the sample stream, the lower is the amount of the analyte detected in the scrubbed solutions i.e. 25% and 58% average detection loss at 50 ppm and 588 ppm levels of ammonia respectively.

8. The present study demonstrates that the analyte vapor scrubbing system and the coulometric titration test procedure can be utilized for the quantitative analytical low ppb level detection of MMH vapor in air.

V - RECOMMENDATIONS

1. For the testing of any potential sensor at low ppb level detection of MMH vapor using the Span-Pac MMH vapor generator system, the following is recommended

   - The vapor generator system should be optimized with a constant air flow and a standard laboratory setup procedure.

   - There should not be any interference with the test setup during the course of the investigation for having a constant and reliable analyte vapor concentration.

2. Interference study using H_2S, alcohols and other interferents should be carried out to have information about the impact of the interferents on the detection of MMH in the scrubbed solution.

3. Since hydrazine behaves like MMH in acidic solution for the coulometric titration analysis, the data obtained in this study may also be utilized for the vapor verification of hydrazine at low ppb level. However, it is worth to generate independent experimental data in the laboratory for the detection of hydrazine at low ppb level.

REFERENCES

1. Schultz, G., et. al., "An outline for the Evaluation of Organic Sampling and Analytical Methods," Organic Methods Evaluation Branch, OSHA Analytical Laboratory, November 1987.

2. Hull, R. D., "Development and Evaluation of Methods," NIOSH / DPSE.

3. Johnson, R. P. and Miller, E. L., "Quantitation of Hydrazines and Hydrazones," Lockheed E & M Service Company, NASA / Johnson Space Center, Los Cruces, New Mexico.

4. Willard et. al., Instrumental Methods of Analysis, 5th ed. New York: D. Van Nostrand Co., 1974.

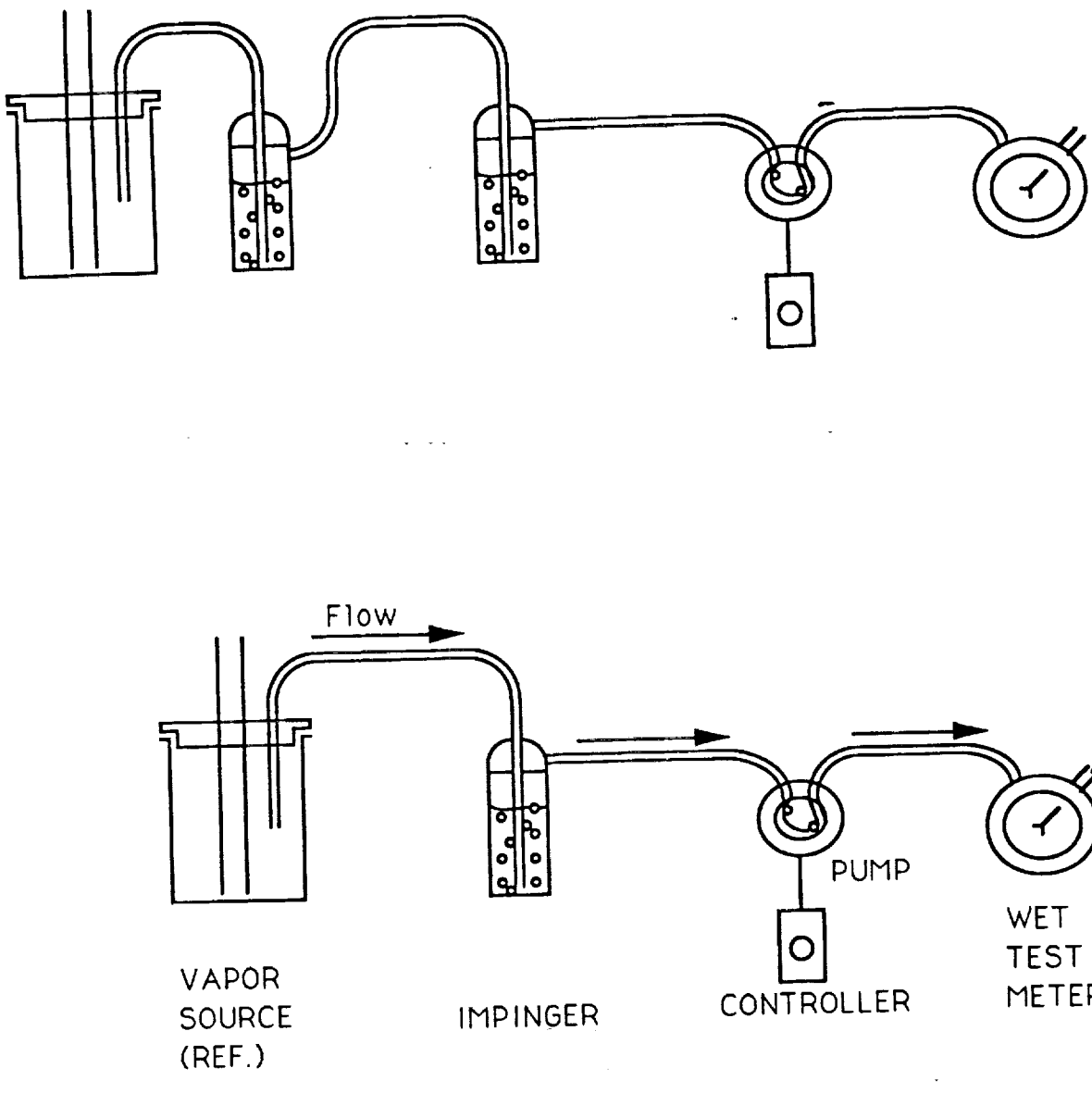

Figure 2-1 Vapor Collection System Setup

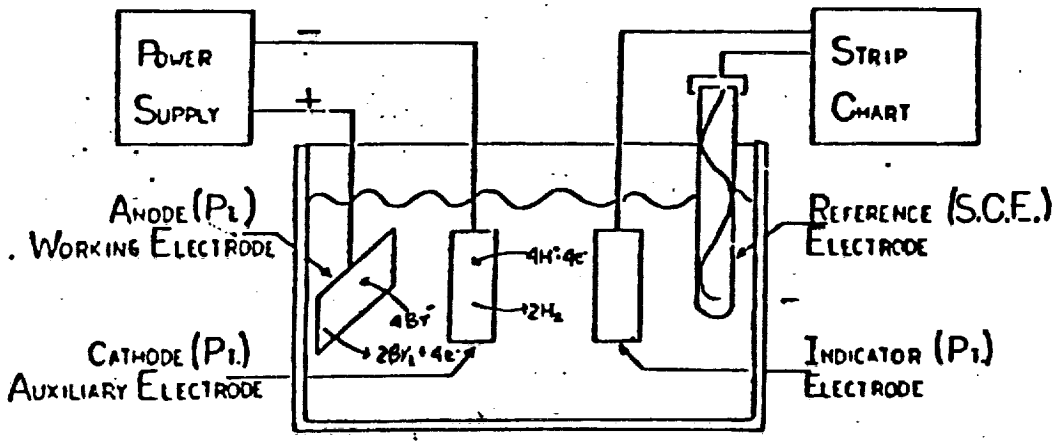

Figure 2-2 Typical Standard Coulometric Titration System

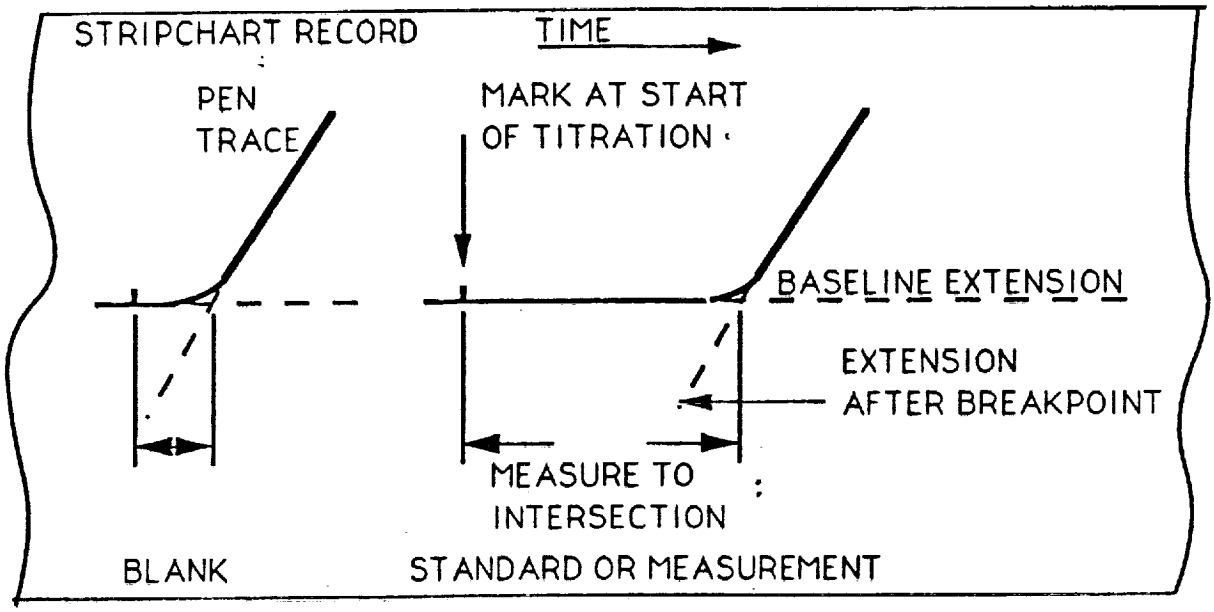

Figure 2-3 Measurement of Coulometric Titration Length

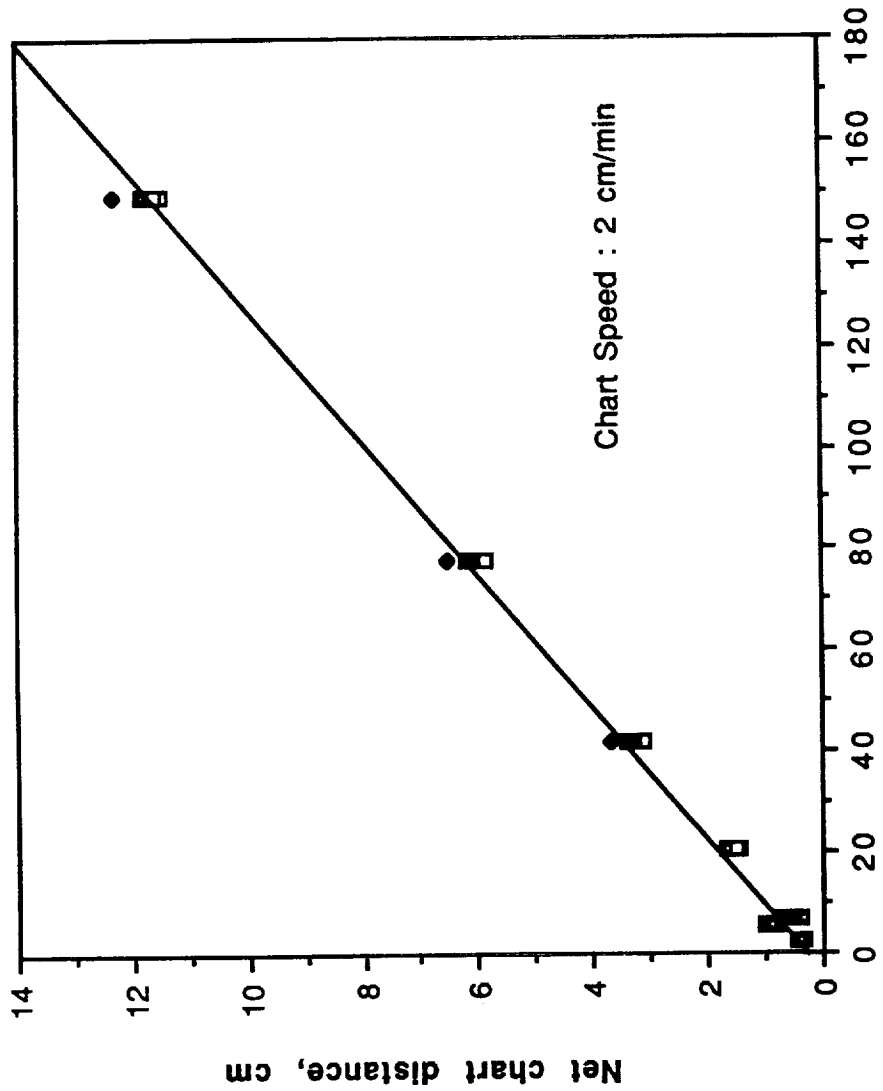

Figure 3-1. Instrument (Coulometer) Response to MMH

Detection limit of the analytical procedure
= Blank (coulometric) line trace
≅ 0.4 cm at a chart speed of 2cm / min
which is equivalent to 5 ppb

In exp work, scrubbing solution having 7.9 ppb MMH was spiked with various MMH vapor standards

AND

Scrubbing solution having 2.1 ppb MMH was also spiked with a 2.7 ppb MMH vapor std to see how low we can detect MMH.

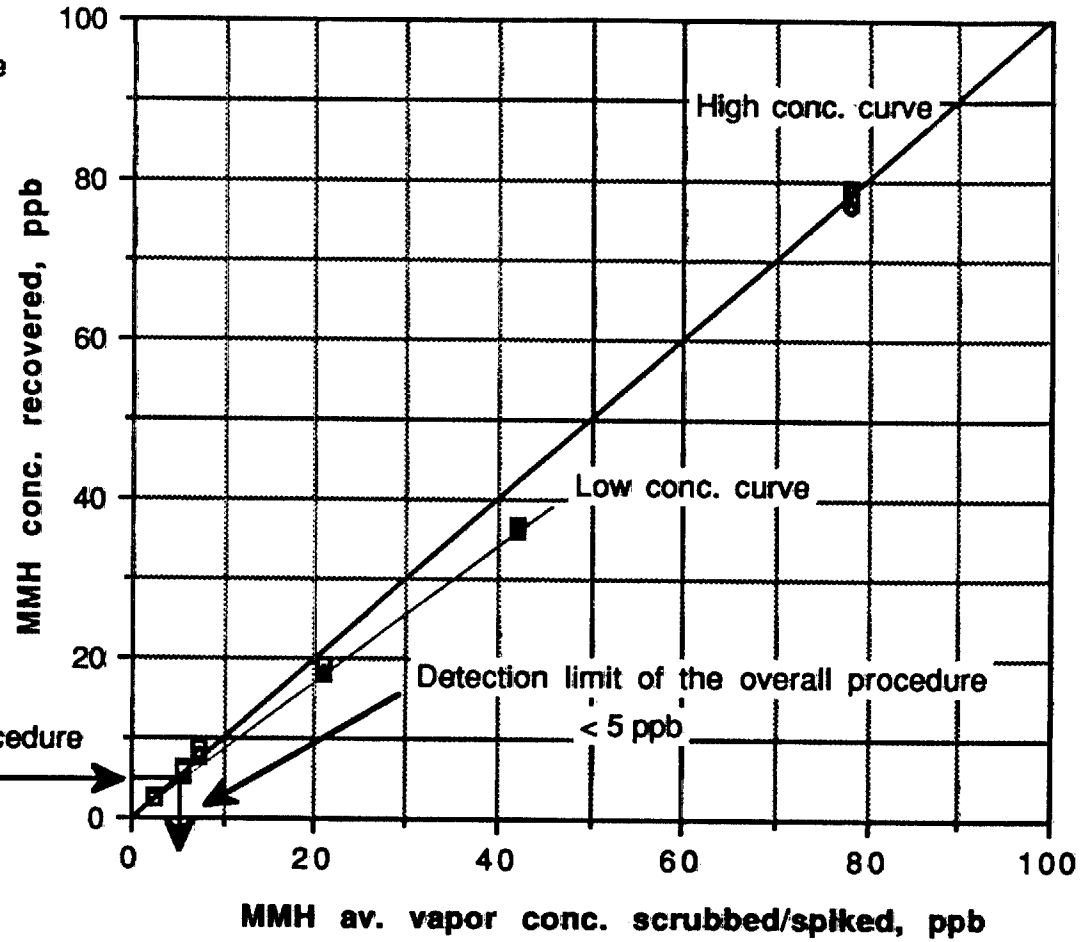

Figure 3-2. Detection Limit of the Overall Procedure for MMH

TABLE 3-1

MMH Vapor Generated By Span-Pak Under Standard Lab Procedure

Temp : 23-25 C and % R. H. : 80-81
Scrubber (0.1 M H_2SO_4) Volume : 25 ml
Scrub rate : 0.8-1 liter / min

MMH vapor standard	Liters of vapor scrubbed	Airflow	Av MMH found in Ist impinger ppb	MMH found in 2nd impinger ppb
Std-7.5	30 (July 2)	4+1	2.7	
Std-20	15 (June 11)	4+1	7.2	
	15 (July 3)	4+1	8	
	30 (June 18)	4+1	5.7	
Std-79	15 (June 8)	39+1	21	0
Std-158	15 (June 5)	19+1	42	0
	831 (overnight)		38	<1
Std-316	15 (June 7)	9+1	78	0
	836 (overnight)		84	2
Std-632	15 (June 8)	4+1	149	2

TABLE 3-2

PRECISION OF THE ANALYTICAL PROCEDURE FOR MMH VAPOR VARIFICATION STUDY

(Sample collection and Coulometric Titration Analysis)

Recorder Chart Speed and Sensitivity : 2 cm/min and 100mv
Scrubbing Solution Volume : 25 ml of 0.1 M H_2SO_4

Vap scrub vol	Std-7.5 30 Lit	Std-20 15 Lit 11-Jun	Std-20 15 Lit 3-Jul	Std-20 30 Lit 18-Jun	Std-79 15 Lit	Std-158 15 Lit	Std-316 15 Lit	Std-632 15 Lit
Run 1	2.2 ppb	7 ppb	7.6 ppb	6 ppb	22 ppb	42 ppb	79 ppb	146 ppb
2	2.5	7.6	8.2	5.4	22	47	82	156
3	2.5	7	7.6	6.3	20	43	75	150
4	2.9	5.1	8.2	5.7	22	41	79	147
5	2.5	7	8.2	6	19	41	77	147
6	2.9	8.8	8.2	5.1	19	39	74	147
7	2.9	10		5.4		42		
8	2.9	5.1		5.9		44		
Average, ppb	2.7	7.2	8	5.7	21	42	78	149
ppb Variation	2.7+0.2 -0.2	7.2+2.8 -2.1	8+0.2 -0.4	5.7+0.6 -0.6	21+1 -2	42+5 -3	78+4 -4	149+7 -3
% Variation	7%	29-39%	3-5%	11%	5-10%	7-12%	5%	2-5%
Std Deviation	0.27	1.67	0.31	0.4	1.51	2.39	2.94	3.76
% Co Variation	* 10	23.2	3.9	* 7	* 7.2	* 5.7	* 3.8	* 2.5

* Pooled % Coefficient of Variation : 6.7

* Using15 Lit vap scrub vol data for all std's except 30 Lit vap scrub vol data for Std-20 and Std-7.5

Table 3-3

STUDY OF MMH VAPOR SPIKING-1

Av conc of MMH in the scrubbing solution (by coulometric method) : 72 ppb.
Scrubbing solution volume : 25 ml of 0.1 M H_2SO_4

Lit's of vapor scrubbed	MMH vapor standard	MMH av conc in scrubbed vapor, ppb	MMH found in solution after scrub, ppb	% Recovery	Average % Recovery
15	Zero gas	0	72+1 72+0 72+1		
15	Std-20	7.2	72+5.1 72+5.1 72+5.1	71 71 71	71
30	Std-20	5.7	72+5.7 72+6.3	100 111	105
15	Std-79	21	72+17 72+15 72+20 72+16	81 71 95 76	81
15	Std-158	42	72+39 72+38 72+33	93 91 79	88

Table 3-4

STUDY OF MMH VAPOR SPIKING-2

Av conc of MMH in the scrubbing solution (by coulometric method) : 7.9 ppb
Scrubbing solution volume : 25 ml of 0.1 M H_2SO_4

Lit's of vapor scrubbed	MMH vapor standard	MMH av conc in scrubbed vapor, ppb	MMH found in solution after scrub, ppb	% Recovery	Average % Recovery
15	Zero gas	0	7.9+0		
			7.9+0		
			7.9+0		
15	Std-20	7.2	7.9+8.9	124	113
			7.9+7.6	106	
			7.9+7.6	106	
			7.9+8.2	114	
30	Std-20	5.7	7.9+6.3	111	103
			7.9+6.0	105	
			7.9+5.3	93	
			7.9+5.7	100	
			7.9+6.0	105	
			7.9+6.0	105	
15	Std-79	21	7.9+19	91	87
			7.9+18	86	
			7.9+18	86	
			7.9+18	86	
15	Std-158	42	7.9+36	86	87
			7.9+36	86	
			7.9+37	88	
			7.9+36	86	
15	Std-316	78	7.9+78	100	100
			7.9+77	99	
			7.9+79	101	
			7.9+77	99	

Table 3-5

RELIABLE QUANTITATION LIMIT FOR MMH

Av conc of MMH in the 0.1 M H2SO4 scrubbing solution : 7.9 ppb
MMH standard vapor scrubbed volume : 30 Liters

MMH conc in scrubbed vap ppb	# Run	MMH found in solution after scrub, ppb	% Recovered after scrub
5.7	1	6.3	111
18-Jun	2	6	105
	3	5.3	93
	4	5.7	100
	5	6	105
	6	6	105
	Average	5.9	103
	Std Deviation		6.1

Precision = ∓ 1.96 Std Deviation = ∓ 12 %

Av conc of MMH in the 0.1 M H2SO4 scrubbing solution : 2.1 ppb
MMH standard vapor scrubbed volume : 30 liters

MMH conc in scrubbed vap ppb	# Run	MMH found in solution after scrub, ppb	% Recovered after scrub
2.7	1	2.9	107
2-Jul	2	2.5	93
	3	2.2	81
	4	2.2	81
	5	2.2	81
	6	2.2	81
	Average		87
	Std Deviation		10

Precision = ∓ 1.96 Std Deviation = ∓ 20 %

PARTS LIST NRL COULOMETER

PART NO.	AMT REQ'D	COMPONENT	MFR	MFR'S NO.	or equiv.	Net ea $	Cost $	Bd'd.
A1	4	REG. DUAL POWER SUPPLY,						
		±15VDC, 0.150A	ACO	D15-15A		79.—	316.—	
A2	4	SOCKET (FOR A1)	"	EL-1		5.—	20.—	
A3	4	ISOLATED DC-DC CONVERTER	"	15E15D25		105.—	420.—	
A4	4	SOCKET (FOR A3)	"	ES-1		5.—	20.—	
A5	12	ULTRA LOW OFFSET VOLTAGE						
		OP AMP	AD	ADOP-07-DH		3.—	36.—	
A6	6	PRECISION LOW POWER FET INPUT		—				
		ELECTROMETER OP AMP	AD	AD515-JH		28.50	171.—	
A7	6	HIGH PRECISION 10V IC REFERENCE	AD	AD581-JH		6.90	41.40	
A8	1pk	RESISTOR, 100K, 1/4W, 5%, (100/pk)	ALL	823-1717		5.04	5.04	
A9	1pk	" , 1K, " , " , "	ALL	823-1356		5.04	5.04	
A10	1pk	" , 11K, " , 1%, "	"	832-6528		4.94	~~5.04~~	4.94
A11	1pk	" , 10K, " , " , "	"	832-6522		4.94	4.94	
A12	1pk	" , 1M, " , 5%, "	"	823-1877		5.04	5.04	
A13	1pk	" , 15K, " , " , "	"	823-1550		5.04	5.04	
A14	12	500Ω, TRIMMER POT, PC MOUNT	"	753-4720		1.68	20.16	
A15	12	0.22μF CAPACITOR	"					
A16	12	SWITCH, MINIATURE, DPDT	"					
A17	12	INSULATED TIP JACK - RED	"	920-0181		.81	9.72	
A18	12	" " " - BLACK	"	920-0182		.81	9.72	
A19	12	" " " - YELLOW	"	920-0208		.81	9.72	
A20	12	" " " - GREEN	"	920-0206		.81	9.72	
A21	12	" " PLUG - RED	"	920-0578		.76	9.12	
A22	12	" " " - BLACK	"	920-0577		.76	9.12	
A23	12	" " " - YELLOW	"	920-0590		.76	9.12	
A24	12	" " " - GREEN	"	920-0580		.76	9.12	
A25	4	BNC CONNECTOR, PANEL MT.	"	885-4160		2.95	11.80	
A26	4	CABINET, 2½ x 15 x 7, STEEL	"	736-3613		16.20	64.80	
A27	4	EDGE CONNECTOR, 44 CONTACT	"	780-1039		17.55	70.20	
A28	4pr	HANDLES, CHROME, 1 5/16" CTRS	"	736-4366		7.05	28.20	
A29	1pk	RECESSED BUMPERS, 100/pk	"	859-2439		20.40	20.40	
A30	2pk	INSULATED BANANA JACK, RED, 5/pk	"	920-1485		1.75	3.50	
A31	2pk	" " " BLACK, "	"	920-1519		1.75	3.50	
A32	2pk	" " " YELLOW, "	"	920-1526		1.75	3.50	
A33	2pk	" " " GREEN, "	"	920-1527		1.75	3.50	
A34	2pk	" " PLUG, RED, "	"	920-0185		3.85	7.70	
A35	2pk	" " " BLACK "	"	920-0186		3.85	7.70	
A36	2pk	" " " YELLOW "	"	920-0237		3.85	7.70	
A37	2pk	" " " GREEN "	"	920-0233		3.85	7.70	

7-69

(BROMINE GENERATOR)

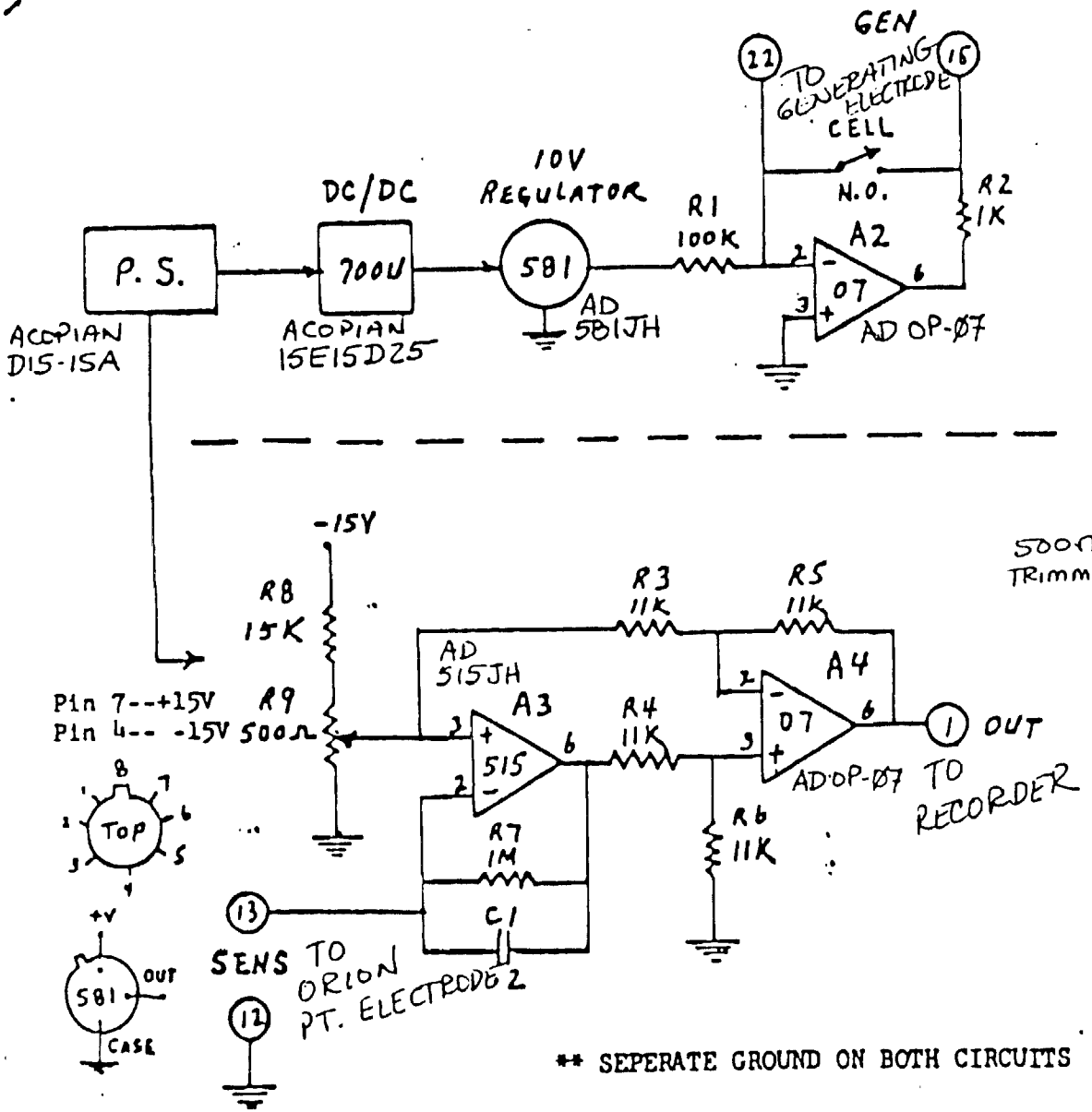

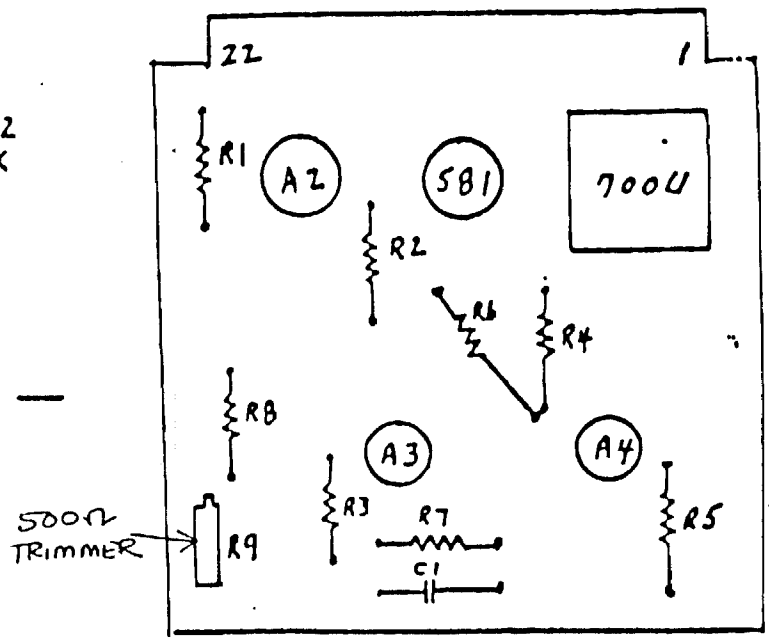

PC CONNECTOR

1--OUT
5--+15V
10--GRD
12--GRD
13--SENS
15--BR GEN
17-- +15V
20-- -15V
22--BR GEN

** SEPERATE GROUND ON BOTH CIRCUITS

Appendix B

2. DETERMINATION OF N2H4 OR MMH VAPOR CONCENTRATION IN NITROGEN OR AIR - COULOMETRIC TITRATION METHOD

2.1 Apparatus

2.1.1 Coulometer, 0.1 ma, 30 mv, with platinum wire electrodes.

2.1.2 Reaction vessel, 100 ml beaker.

2.1.3 Stirring bar and magnetic stirrer.

2.1.4 Recorder, Soltec Model 1241 or equal, calibrated for chart speed.

2.1.5 Pipets, 25 ml volumetric, 10 ml measuring.

2.1.6 Volumetric flasks, 1000 ml, 100 ml.

2.1.7 Wet test meter, Singer AL-17-1 or equal, calibrated.

2.1.8 Air sampling pump, Cole Parmer, masterflex, peristaltic type with variable speed control or equal.

2.1.9 Glass midget impingers, 25 ml, straight tubing.

2.1.10 Autopipet: Eppendorf or equal, 10 ul to 1000 ul adjustable.

2.1.11 Flowmeter, Sensidyne, EZ cal/Digital flowmeter or equal, calibrated.

2.1.12 Scoop, two scoops yield approximately 0.4 g KBr.

2.1.13 Tubings, Bev-A-Line, Tygon, assorted sizes and lengths.

2.1.14 Beaker, 100 ml, containing D.I. water.

2.2 Chemicals

2.2.1 Potassium Bromide (KBr), reagent grade.

2.2.2 Sulfuric acid (H2SO4), concentrated, reagent grade.

2.2.3 D.I. water.

2.2.4 Hydrazine (N2H4), reagent grade.

2.3 Safety

General - Refer to TVD-00004-SP, Toxic Vapor Detection Laboratory Hazards and Safety Manual for safety requirements and specific hazards, precautions, and emergency procedures concerning fire

(paragraph 4.4.1), hypergols (paragraph 4.4.4), acid and base (paragraph 4.4.5) and toxic vapors and solvents (paragraph 4.4.3).

2.3.2 Safety Equipment (Personal)

2.3.2.1 Face shield or safety glasses

2.3.2.2 Laboratory coat or rubber apron.

2.3.2.3 Gloves, chemical resistant.

WARNING

Monomethyl hydrazine and hydrazine are suspected carcinogenic chemicals. The current OSHA maximum allowable concentrations in air ceiling exposure are 0.2 ppm and 0.1 ppm, respectively.

WARNING

Concentrated sulfuric acid is very corrosive. Wear gloves while handling this chemical.

2.3.3 Safety Equipment (Laboratory)

2.3.3.1 Fume hood.

2.3.3.2 Safety shower and eyewash fountain.

2.3.3.3 MMH and N2H4 vapor concentration monitoring devices.

2.3.3.4 Fire extinguisher.

WARNING

Handle MMH and N2H4 in a fume hood. Avoid all oxidizing agents. Wear personal safety equipment. Note location of the closest fire extinguisher, safety shower, and eyewash fountain. Ensure test area conforms to good housekeeping standards. Monitor working area MMH and N2H4 concentrations with a calibrated monitoring device.

2.4 Preparation of Reagents

2.4.1 Sulfuric acid 0.1M - Pipet 5.6 ml of H2SO4 conc. into a 1000 ml volumetric flask containing approximately 700 ml of D.I. water. Add D.I. water to the mark. Mix well.

2.4.2 Hydrazine Stock Solution 100 ppm - Fill a 100 ml volumetric flask to the mark with 0.1 M H_2SO_4 solution. Add, below the surface, 10 ul of N_2H_4 into the solution. Mix well. Solution is stable for one month.

2.5 Sampling of N_2H_4 or MMH Vapor.

2.5.1 Set up the sampling apparatus as in Figure 1.

2.5.2 Pipet 25 ml of 0.1 M H_2SO_4 into the impinger. Stopper the impinger and water seal.

2.5.3 Turn on the air pump and adjust the flow control valve for 0.5 liter per minute flow. The flowrate shall be verified by calibrated EZ cal digital flowmeter.

2.5.4 Attach the inlet of impinger to vapor source using Bev-A-Line tubing.

2.5.5 As a guide, sample 6 liters for less than 0.5 ppm concentration of vapor, sample 3 liters for more 1.0 ppm concentration.

2.6 Analysis of Sample

2.6.1 Set recorder parameters as follows:

Range - 500 mV
Speed - 60 cm per hour

2.6.2 Turn coulometer power on.

2.6.3 Fill the reaction vessel containing a stirring bar to 40 ml mark with 0.1M H_2SO_4.

2.6.4 Place the raction vessel on the magnetic stirrer. Stir at medium speed.

2.6.5 Add 0.5 scoops of KBr to the solution. Stir until KBr is dissolved.

2.6.6 Place the electrodes in the solution. Ensure the electrolyte (0.1M H_2SO_4) in the Bromine generating electrode is approximately 1 inch above the solution in the vessel.

2.6.7 Turn on the recorder and lower the pen to start recording. When the line on the chart paper is level, simultaneously activate the coulometer CELL switch and the recorder marker.

2.6.8 When the recording line deflects upward approximately 1-1/2 inches (see figure 2), deactivate the cell switch, lift up the recorder pen, and promptly place the electrode in clean D.I. water.

2.6.9 Discard the solution in the vessel; rinse the vessel with D.I. water, then with 0.1M H_2SO_4.

2.6.10 Measure the reaction time in terms of distance in cm as in figure 2.

2.6.11 Repeat paragraphs 2.6.3 through 2.6.10 until three consecutive runs indicate the same distance. This is the blank value.

2.6.12 To ensure that the instrument is functioning properly, repeat pararaphs 2.6.3 to 2.6.10 with 30 ul of N_2H_4 stock solution added to 0.1 M H_2SO_4 in the vessel. The measured distance should be 6.0 cm $\pm$0.1 cm. If this distance cannot be achieved, notify supervisor.

2.6.13 Quantitatively transfer (or take an aliquot of) the sample in the impingers to the glass vessel. Add 0.1M H_2SO_4 to 40 ml mark of the vessel. Repeat paragraphs 2.6.4 to 2.6.10.

2.7 Calculation

ppm MMH or N_2H_4 in air (or nitrogen) =

$$\frac{[\text{Sample (cm)} - \text{blank (cm)}] \times 0.38 \times \text{aliquot factor}}{\text{volume sampled (l)}}$$

1990 NASA/ASEE SUMMER FACULTY FELLOWSHIP PROGRAM

p 31

JOHN F. KENNEDY SPACE CENTER
UNIVERSITY OF CENTRAL FLORIDA

CORRELATION OF LEAK RATES OF VARIOUS FLUIDS WITH THE LEAK RATE OF AN INERT GAS IN THE SAME CONFIGURATION

PREPARED BY: Mr. Howard Schleier

ACADEMIC RANK: Associate Professor

UNIVERSITY AND DEPARTMENT: Norwalk State Technical College
Department of Mathematics/Science

NASA/KSC

DIVISION: Mechanical Engineering

BRANCH: Propellants & Gases

NASA COLLEAGUE: Mr. William I. Moore, Jr.

DATE: August 23, 1990

CONTRACT NUMBER: University of Central Florida
NASA-NGT-60002 Supplement: 4

I

ACKNOWLEDGMENTS

THIS WORK WOULD NOT HAVE POSSIBLE WITHOUT THE HELP THAT I RECEIVED FROM THE STAFFS AT KSC AND UCF. I ESPECIALLY WANT TO MENTION DR. LOREN ANDERSEN, KARI BAIRD, JEAN EPPINGER, KIM BALLARD, JAMES FESMIRE AND, OF COURSE, MY NASA COLLEAGUE IRBY MOORE.

I ALSO WANT TO GIVE SPECIAL MENTION TO ANDY RODRIGUEZ, RON FOX, AND ELAINE WHITE WHO PERFORMED THE LABORATORY OPERATIONS NECESSARY TO SUPPORT THIS EFFORT.

MANY THANKS ARE AFFORDED TO ROBERT NEELY OF EG&G FOR AIDING ME IN THE USE OF THE PLOTTING SOFTWARE AT KSC.

II. ABSTRACT

NASA IS INTERESTED IN FIELD TESTING FOR POSSIBLE LEAKAGE IN THEIR FUELING SYSTEMS. HOWEVER, MANY FUELS ARE HAZARDOUS TO THE EXTENT THAT PERSONNEL CANNOT BE ON HAND WHEN THE SYSTEM IS BEING MONITORED. IT IS PROPOSED THAT AN INERT MATERIAL SUCH AS HELIUM BE USED ON THE FIELD TEST, AND THAT THOSE RESULTS BE CALIBRATED TO SIMULATE THE ACTUAL PROCESS. A TECHNIQUE SUCH AS THIS WOULD ALLOW PERSONNEL TO BE ON SITE DURING THE TESTING, AND USE TECHNIQUES TO DETERMINE THE BEHAVIOR OF THE SYSTEM THAT COULD NOT BE USED OTHERWISE. THIS ENDEAVOR ATTEMPTS TO DEVELOP SUCH A CORRELATION. THE RESULTS SHOW PROMISE, BUT MORE REFINEMENT AND MORE DATA ARE NEEDED.

III. SUMMARY

IT WAS DESIRED TO PREDICT THE LEAKAGE OF VARIOUS FLUIDS WITH THE KNOWN LEAKAGE OF A KNOWN GAS FOR A FIXED CONFIGURATION. A SIMPLE MODEL WAS CONTRIVED, SOFTWARE WAS DEVELOPED, AND AN EXPERIMENT WAS RUN TO TEST THE MODEL.

CORRELATION WAS SIGNIFICANT AT THE 99% LEVEL FOR SEVENTEEN RUNS ON THREE DIFFERENT GASES. HOWEVER A LEAST SQUARES REGRESSION ON THE DATA, PRODUCED A DESIRABLE SLOPE BUT A QUESTIONABLE INTERCEPT. AT WORST, THIS WOULD INDICATE THAT THE RANGEABILITY OF THE PREDICTOR IS GOOD ONLY AT HIGHER LEAKAGE RATES, BUT THE AUTHOR BELIEVES THAT THE DISCREPANCIES THAT OCCUR AT LOWER FLOWS ARE PROBABLY DUE TO ERRORS IN FLOWMETER CALIBRATION.

IT WAS RECOMMENDED THAT A LARGER NUMBER OF TESTS OVER A WIDER VARIETY OF CONDITIONS BE RUN, AND THAT SOME SLIGHT MODIFICATIONS IN THE TESTING PROCEDURE BE MADE. THE AUTHOR BELIEVES THAT THE MODEL OR SOME MINOR VARIATION THEREOF WOULD BE AN ADEQUATE PREDICTOR FOR LEAK DETECTION.

TABLE OF CONTENTS

V

NOMENCLATURE

SYMBOL	DEFINITION	UNITS
A	ACOUSTIC VELOCITY	M/S
C	SPECIFIC HEAT	J/KG/K
CD	DISCHARGE COEFFICIENT	LESS
F	SCALING FACTOR	LESS
G	MASS VELOCITY	KG/M**2/S
H	SPECIFIC ENTHALPY	J/KG
K	SPECIFIC HEAT RATIO	LESS
M	MOLECULAR MASS	AMU
MDOT	MOLAR FLOW	MOL/S
P	ABSOLUTE PRESSURE	N/M**2
R	GAS CONSTANT	J/MOL/K
RHO	DENSITY	KG/M**3
S	CROSS-SECTIONAL AREA	M**2
T	ABSOLUTE TEMPERATURE	K
V	VELOCITY	M/S

SUBSCRIPT	EXPLANATION
a	UPSTREAM CONDITION
b	DOWNSTREAM CONDITION
c	CRITICAL FLOW CONDITION
gas	GAS
liq	LIQUID
o	STAGNATION CONDITION
p	CONSTANT PRESSURE CONDITION
pro	PROCESS CONDITION
ref	REFERENCE CONDITION
s	ISENTROPIC CONDITION
v	CONSTANT VOLUME CONDITION

6.1 INTRODUCTION

THE LEAKING CONFIGURATION WAS ASSUMED TO BE THAT OF A SHARP EDGED ORIFICE. THE CASES OF: 1) THE SINGLE PHASE GAS, 2) TWO-PHASE FLOW, AND 3) THE SINGLE PHASE LIQUID WERE CONSIDERED. FURTHER INVESTIGATION SHOWED THAT ONLY THE CASES OF THE IDEAL GAS UNDER A CRITICAL PRESSURE DROP, AND THE INCOMPRESSIBLE LIQUID WOULD BE CONSIDERED FOR THIS INVESTIGATION. HELIUM OR ANY OTHER GAS IS USED AS THE TEST (OR REFERENCE) GAS AND ANY SINGLE PHASE FLUID (LIQUID OR GAS) MAY BE CONSIDERED AS THE PROCESS FLUID. THE ORIFICE EQUATION FOR A SHARP EDGED ORIFICE HAVING A SMALL BETA IS APPLIED IN BOTH SITUATIONS AND THE MOLAR FLOW OF THE REFERENCE FLUID IS DYNAMICALLY SCALED TO PREDICT THE MOLAR FLOW OF THE PROCESS FLUID.

UNDER EACH CONDITION ONE HOPES THAT THE DISCHARGE COEFFICIENTS ARE THE SAME. IN REALITY THESE COEFFICIENTS HAVE A MAXIMUM RANGE OF ROUGHLY 0.61 TO 1.0. THE LOWER EXTREME IS FAVORED FOR SHARP EDGED ORIFICES AT HIGH REYNOLDS NUMBER INCOMPRESSIBLE FLOW. THE UPPER FOR CAREFULLY MACHINED VENTURI TUBES. INDUSTRIAL PRACTICE ROUTINELY ASSUMES A CONSTANT DISCHARGE COEFFICIENT IN THE SIZING OF CONTROL VALVES, SAFETY VALVES, AND RUPTURE DISCS (1).

6.2 MAIN TEXT

6.2.1 DESCRIPTIVE INFORMATION

A LABORATORY TEST WAS DESIGNED TO TEST FOR THE LEAKAGE OF VARIOUS GASES UNDER DIFFERENT CONDITIONS. THE GASES WERE FED THROUGH A PRESSURE REGULATOR TO A BALLAST TANK. ATTACHED TO THE BALLAST TANK WAS A SMALL BAR STOCK GATE VALVE THAT WAS SLIGHTLY CRACKED. A SMALL ROTAMETER WAS THEN ATTACHED TO THE OTHER END OF THAT VALVE. THE RUNS CONSISTED OF VARYING THE UPSTREAM PRESSURE, FOR THE VARIOUS GASES AND RECORDING THE PRESSURE, TEMPERATURE, AND FLOW READINGS FOR EACH INDIVIDUAL RUN. SEVENTEEN DIFFERENT CONDITIONS WERE RECORDED. THREE DIFFERENT GASES WERE USED, NAMELY HELIUM, NITROGEN, AND ARGON.

6.2.2 MATHEMATICAL PRESENTATION

CONSIDER A CAREFULLY MACHINED CONVERGING-DIVERGING NOZZLE IN A HORIZONTAL PLANE WITH AN IDEAL GAS FLOWING ISENTROPICALLY IN STEADY STATE IN ONE DIMENSION WITH A FLAT VELOCITY PROFILE, AND STAGNATION UPSTREAM.

THEN: $dH + V*dV = 0,$ (1)

$P/RHO = 1000*R*T/M,$ (2)

$dH = Cp*dT,$ (3)

$Cp = Cv + 1000 * R/M$ (4)

$K = Cp/Cv,$ (5)

& $A**2 = [(\text{partial of } P)/(\text{partial of } RHO)]s$ (6)

COMBINING THE ABOVE WE GET:

$P/RHO**K = Po/RHOo**K,$ (FOR ISENTROPIC STAGNATION) (7)

& $T/P**((K-1)/K) = To/Po**((K-1)/K)$ (8)

SINCE $G = RHO*V,$ & $Gc = RHO*A$ (9)

AND $A**2 = 1000*K*R*T/M$ (10)

$Gc = RHO*sqrt(1000*K*R*T/M)$ (11)

OR $Gc = M*P/1000/R/T*sqrt(1000*K*R*T/M)$ (12)

$Gc = P*sqrt(K*M/1000/R/T)$ (13)

ADJUSTING FOR STAGNATION

$Gc = Po*sqrt(K*(2/(K+1))**((K+1)/(K-1))*M/1000/R/To)$ (14)

IF THE PROCESS IS NOT ISENTROPIC

$Gc = CD*Po*sqrt(K*(2/(K+1))**((K+1)/(K-1))*M/1000/R/To)$ (15)

WHERE CD IS THE DISCHARGE COEFFICIENT.

ACCORDING TO SHAPIRO (2)(CH.4,FIG.4.17)THE RANGE FOR CD IN CRITICAL FLOW VARIES BETWEEN 0.74 AND 0.85, AND DEPENDS ONLY ON THE RATIO OF DOWN-STREAM TO UPSTREAM PRESSURES.

NOW LET US CONSIDER THE ALTERNATIVE CONDITION OF AN INCOMPRESSIBLE LIQUID UNDERGOING ISOTHERMAL FLOW IN A PERFECT CONVERGING-DIVERGING NOZZLE. THE FLOW IS AGAIN ISENTROPIC WITH STAGNATION UPSTREAM. THEN THE BERNOULLI EQUATION STATES:

$(Pb-Pa)/RHO + (Vb**2-Va**2)/2 = 0$ (16)

FOR Va = 0, LET Vb = V AND WE GET

$(Pb-Pa)/RHO + V**2/2 = 0$ (17)

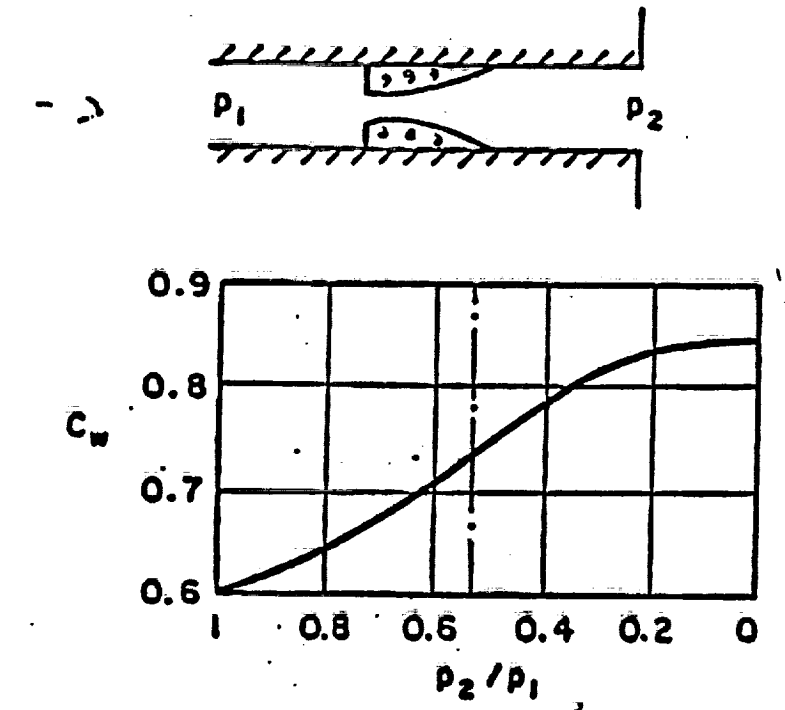

FIG. 4.17. Discharge coefficient of sharp-edged orifice meters with zero velocity of approach (after J. A. Perry).

SINCE $Gliq = RHO*V$ (18)

$(Pb-Pa)/RHO + (Gliq/RHO)**2/2 = 0$ (19)

OR $Gliq = sqrt(2*(Pa-Pb)*RHO)$ (20)

SIMILARLY FOR NON-ISENTROPIC FLOW

$Gliq = CD*sqrt(2*(Pa-Pb)*RHO)$ (21)

WHERE CD IS THE DISCHARGE COEFFICIENT.

DISCHARGE COEFFICIENTS FOR LIQUIDS FOR ORIFICES WITH SMALL BETAS RUN ABOUT 0.61 (3)(P.5-15).THERE IS NO RECOVERY OF THE LOSS (3)(P.5-17).

THE THIRD POSSIBILITY WE WERE GOING TO CONSIDER WAS THE CASE OF TWO-PHASE CRITICAL FLOW. THE LITERATURE PROVIDES A LARGE AMOUNT OF INTER-ESTING APPROACHES TO THE PROBLEM, AND THE MODELING IS NOT THE OBVIOUS (4), (5), (6), (7), (8), (9). HOWEVER, THERE ARE INDICATIONS (4) THAT FOR SHARP EDGED ORIFICES WITH SATURATED LIQUID OR SATURATED VAPOR UPSTREAM THAT ONLY THE 100% LIQUID OR THE 100% VAPOR CASE NEED TO BE CONSIDERED. THEREFORE, FOR THE PURPOSES OF THIS REPORT ONLY SINGLE PHASE FLOW WAS INVESTIGATED.

THEN FOR A GAS LEAK CONSIDER

$$Gc = CD*Po*sqrt(K*(2/(K+1))**((K+1)/(K-1))*M/1000/R/To) \quad (15)$$

OR

$$\frac{[Gc]pro}{[Gc]ref} = \frac{[CD]pro*[Po*sqrt(K*(2/(K+1))**((K+1)/(K-1))*M/To)]pro}{[CD]ref*[Po*sqrt(K*(2/(K+1))**((K+1)/(K-1))*M/To)]ref} \quad (22)$$

OR

$$\frac{[Gc]pro}{[Gc]ref} = \frac{[CD]pro}{[CD]ref} * Fgas \quad (23)$$

WHERE

$$Fgas = \frac{[Po*sqrt(K*(2/(K+1))**((K+1)/(K-1))*M/To)]pro}{[Po*sqrt(K*(2/(K+1))**((K+1)/(K-1))*M/To)]ref} \quad (24)$$

NOTING THAT Fgas IS A DIMENSIONLESS FACTOR DEPENDING ONLY ON THE UPSTREAM PRESSURES, TEMPERATURES, AND IDENTITIES OF THE PROCESS AND REFERENCE GASES, OUR FOCUS SHIFTS TO THE RATIO OF THE DISCHARGE COEFFICIENTS - [CD]pro/[CD]ref. RE SHAPIRO (2) THE EXTREMES OF CD IN THE CRITICAL PRESSURE RATIO RANGE ARE FROM 0.74 T0 0.85 IMPLYING A MAXIMUM DIFFERENCE OF ABOUT 15% BETWEEN REFERENCE AND PROCESS CONDITIONS. HOWEVER IT IS EXPECTED THAT THE PRESSURE RATIOS WOULD BE SUFFICIENTLY

SIMILAR OVER BOTH TEST AND REFERENCE CONDITIONS SO THAT THE RATIO [CD]pro/[CD] ref COULD BE TAKEN AT UNITY, AND

$$[Gc]pro = [Gc]ref * Fgas \quad (25)$$

SIMILARLY FOR THE CASE OF THE PROCESS FLUID BEING A LIQUID WE GET:

$$Gliq = CD*sqrt(2*(Pa-Pa)*RHO) \quad (26)$$

$$\frac{[Gc]pro}{[Gc]ref} = \frac{[CD]pro}{[CD]ref} * Fliq \quad (27)$$

WHERE

$$Fliq = \frac{[sqrt(2*(Pa-Pb)*RHO)]pro}{[Po*sqrt(K*(2/(K+1))**((K+1)/(K-1))*M/1000/R/To)]ref} \quad (28)$$

IT IS NOTED THAT Fliq IS A DIMENSIONLESS FACTOR BASED ON THE DENSITY AND PRESSURE DROP OF THE PROCESS LIQUID, AND ON THE IDENTITY AND UPSTREAM CONDITIONS OF THE REFERENCE GAS. SHARP EDGED ORIFICES WITH HIGH VELOCITY LIQUID FLOWS HAVE BEEN SHOWN TO DEMONSTRATE A CD OF 0.61 QUITE RELIABLY (3)(CH.5, FIG.5-20).

HOWEVER, OTHER CONFIGURATIONS DEMONSTRATE CD'S BETWEEN 0.61 AND 1.0. CONSIDERING THE PREVIOUSLY MENTIONED GAS CD'S RANGING FROM 0.74 TO 0.85 WE MAY ESTIMATE A RATE NO MORE THAN 20% LOWER THAN AN ESTIMATE BASED ON Fliq ALONE. NEVERTHELESS THIS IS AN EXTREME CONDITION, CONFIGURATIONS OTHER THAN SHARP EDGED ORIFICES TEND TO HAVE CD'S GREATER THAN 0.61, AND UNTIL EXPERIMENTAL DATA SHOWS OTHERWISE, ESTIMATES WILL BASED ON Fliq ONLY. THAT IS, THE [CD]pro/[CD]ref RATIO WILL BE TAKEN AT UNITY.

THEREFORE FOR GASES

$$[Gc]pro = [Gc]ref * Fgas \quad (29)$$

AND FOR LIQUIDS

$$[Gliq]pro = [Gc]ref * Fliq \quad (30)$$

SINCE $$MDOT = G*S/M \quad (31)$$

WE GET $$[MDOT]pro = [MDOT]ref /([Mref]/[Mpro]) * Fgas \quad (32)$$

OR $$[MDOT]pro = [MDOT]ref /([Mref]/[Mpro]) * Fliq \quad (33)$$

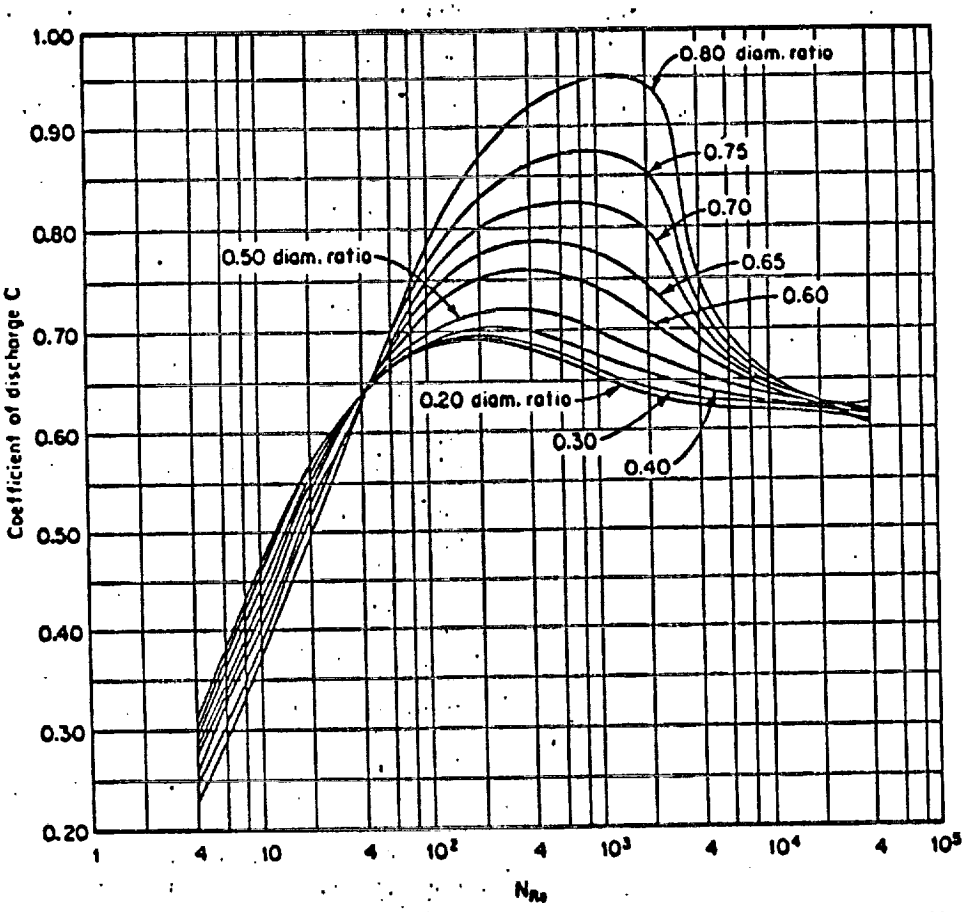

FIG. 5-20 Coefficient of discharge for square-edged circular orifices with corner taps. [*Tuve and Sprenkle, Instruments, 6, 201 (1933).*]

6.2.3 RESULTS AND DISCUSSION

THE ROTAMETER DETERMINED FLOW RATES WERE CORRECTED FROM HELIUM TO THE PROCESS GAS INVOLVED (10)(FIG 8-27). THE DATA WERE THEN EVALUATED PER PROGRAM LEAX () DEVELOPED BY THE AUTHOR FOR THIS PROJECT. PICTORIAL REPRESENTATION OF THE RESULTS WERE THEN OBTAINED VIA AN ADAPTATION OF THE IN HOUSE REGIS SOFTWARE. A LINEAR REGRESSION WAS APPLIED TO THE DATA AND A LEAST SQUARES FIT INDICATED A SLOPE OF ABOUT 0.9 AND AN INTERCEPT OF ABOUT 15 SCCM WITH SIGNIFICANCE AT THE 99% LEVEL. IDEALLY ONE WOULD EXPECT A SLOPE OF 1.0 AND AN INTERCEPT OF ZERO. THE AUTHOR REGARDED THE SLOPE AS INDICATIVE OF THE RATIO OF THE CD'S WHICH WAS TAKEN AT UNITY. THOUGH THE 0.9 SLOPE IS QUITE SATISFACTORY, THE INTERCEPT OF 15 SCCM WAS CONSIDERED TO BE HIGH AT LOW LEAK RATES. IN ORDER TO DEMONSTRATE THAT THE EFFECT OF THE NONE ZERO INTERCEPT WAS NOT DUE TO THE EFFECTS OF THE CD ASSUMPTIONS THE DATA WERE AGAIN EXAMINED WITH LEAX2 WHICH CORRECTED FOR THIS DISCREPANCY AND VERY SIMILAR RESULTS WERE OBTAINED. (TABLE 1, FIGURE 1, TABLE 2, FIGURE 2)

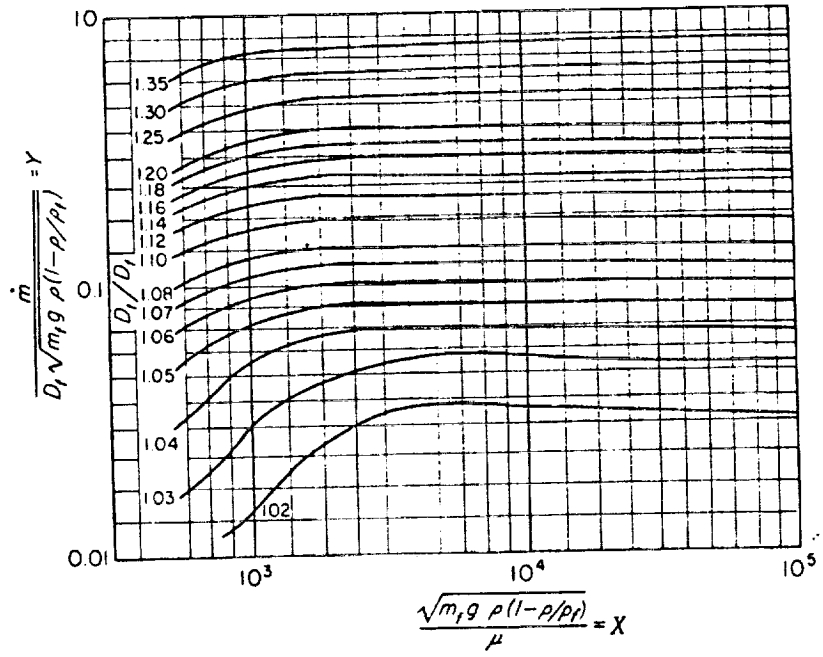

Figure 8-27 *Rotameter calibration curves.*

TABLE 1

FILE NAME = TESTRUN
TITLE = UG. 1,1990
STATUS = NEW
DEVICE = 22

RUN	GAMMAREF	MWREF AMU	PREF PSIG	TREF DEGF	MFREF SCCM	GAMMAPRO	MWPRO AMU	PPRO PSIG	TPRO DEGF	MFPRO SCCM	MFOBS SCCM
1	0.167E+01	0.400E+01	0.677E+02	0.797E+02	0.105E+03	0.167E+01	0.400E+01	0.151E+02	0.797E+02	0.380E+02	0.120E+02
2	0.167E+01	0.400E+01	0.677E+02	0.797E+02	0.105E+03	0.167E+01	0.400E+01	0.299E+02	0.797E+02	0.568E+02	0.390E+02
3	0.167E+01	0.400E+01	0.677E+02	0.797E+02	0.105E+03	0.167E+01	0.400E+01	0.448E+02	0.797E+02	0.758E+02	0.600E+02
4	0.167E+01	0.400E+01	0.677E+02	0.797E+02	0.105E+03	0.167E+01	0.400E+01	0.601E+02	0.797E+02	0.953E+02	0.925E+02
5	0.167E+01	0.400E+01	0.677E+02	0.797E+02	0.105E+03	0.167E+01	0.400E+01	0.677E+02	0.797E+02	0.105E+03	0.105E+03
6	0.167E+01	0.400E+01	0.677E+02	0.797E+02	0.105E+03	0.140E+01	0.280E+02	0.150E+02	0.757E+02	0.135E+02	0.472E+01
7	0.167E+01	0.400E+01	0.677E+02	0.797E+02	0.105E+03	0.140E+01	0.280E+02	0.300E+02	0.789E+02	0.203E+02	0.104E+02
8	0.167E+01	0.400E+01	0.677E+02	0.797E+02	0.105E+03	0.140E+01	0.280E+02	0.451E+02	0.797E+02	0.271E+02	0.159E+02
9	0.167E+01	0.400E+01	0.677E+02	0.797E+02	0.105E+03	0.140E+01	0.280E+02	0.600E+02	0.805E+02	0.339E+02	0.181E+02
10	0.167E+01	0.400E+01	0.677E+02	0.797E+02	0.105E+03	0.140E+01	0.280E+02	0.752E+02	0.813E+02	0.407E+02	0.234E+02
11	0.167E+01	0.400E+01	0.677E+02	0.797E+02	0.105E+03	0.140E+01	0.280E+02	0.900E+02	0.813E+02	0.474E+02	0.291E+02
12	0.167E+01	0.400E+01	0.677E+02	0.797E+02	0.105E+03	0.167E+01	0.399E+02	0.149E+02	0.773E+02	0.120E+02	0.475E+01
13	0.167E+01	0.400E+01	0.677E+02	0.797E+02	0.105E+03	0.167E+01	0.399E+02	0.300E+02	0.797E+02	0.180E+02	0.101E+02
14	0.167E+01	0.400E+01	0.677E+02	0.797E+02	0.105E+03	0.167E+01	0.399E+02	0.450E+02	0.797E+02	0.241E+02	0.139E+02
15	0.167E+01	0.400E+01	0.677E+02	0.797E+02	0.105E+03	0.167E+01	0.399E+02	0.601E+02	0.797E+02	0.302E+02	0.171E+02
16	0.167E+01	0.400E+01	0.677E+02	0.797E+02	0.105E+03	0.167E+01	0.399E+02	0.753E+02	0.797E+02	0.363E+02	0.221E+02
17	0.167E+01	0.400E+01	0.677E+02	0.797E+02	0.105E+03	0.167E+01	0.399E+02	0.904E+02	0.797E+02	0.424E+02	0.266E+02

F(CALCULATED) = 0.336E+03 F.95 = 0.454E+01 F.99 = 0.868E+01
Y(PREDICTED) = 0.153E+02 + (0.904E+00)*X(OBSERVED)
CORRELATION IS SIGNIFICANT AT THE 95% LEVEL
CORRELATION IS SIGNIFICANT AT THE 99% LEVEL

FIGURE 1

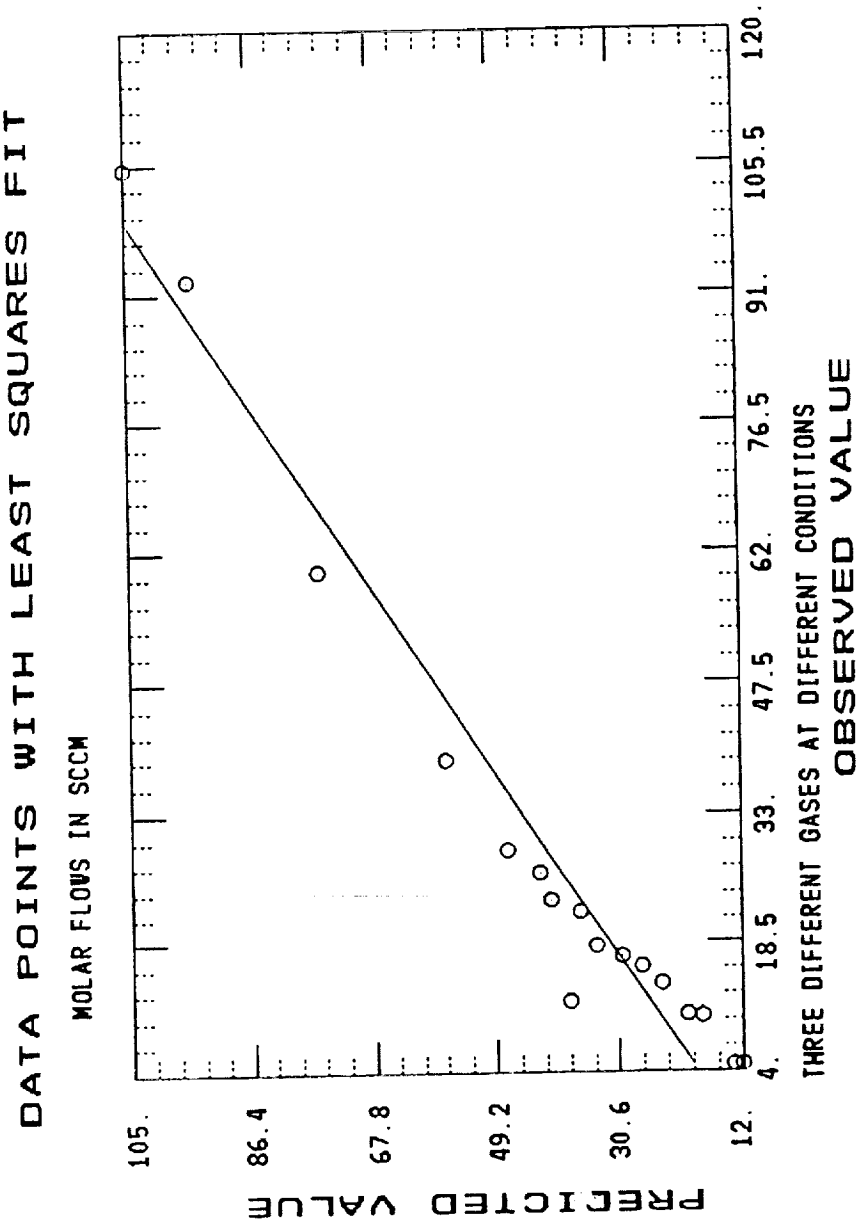
DATA POINTS WITH LEAST SQUARES FIT
MOLAR FLOWS IN SCCM
PREDICTED VALUE
105.
86.4
67.8
49.2
30.6
12.
4.
18.5
33.
47.5
62.
76.5
91.
105.5
120.
THREE DIFFERENT GASES AT DIFFERENT CONDITIONS
OBSERVED VALUE

TABLE 2

FILE NAME = TEST2
TITLE = AGAIN AUG 6,1990
STATUS = NEW
DEVICE = 22

RUN	GAMMAREF	MUREF AMU	PREF PSIG	TREF DEGF	MFREF SCCM	GAMMAPRO	MUPRO AMU	PPRO PSIG	TPRO DEGF	MFPRO SCCM	MFOBS SCCM
1	0.167E+01	0.400E+01	0.677E+02	0.797E+02	0.105E+03	0.167E+01	0.400E+01	0.151E+02	0.797E+02	0.345E+02	0.120E+02
2	0.167E+01	0.400E+01	0.677E+02	0.797E+02	0.105E+03	0.167E+01	0.400E+01	0.299E+02	0.797E+02	0.549E+02	0.390E+02
3	0.167E+01	0.400E+01	0.677E+02	0.797E+02	0.105E+03	0.167E+01	0.400E+01	0.448E+02	0.797E+02	0.749E+02	0.600E+02
4	0.167E+01	0.400E+01	0.677E+02	0.797E+02	0.105E+03	0.167E+01	0.400E+01	0.601E+02	0.797E+02	0.950E+02	0.925E+02
5	0.167E+01	0.400E+01	0.677E+02	0.797E+02	0.105E+03	0.167E+01	0.400E+01	0.677E+02	0.797E+02	0.105E+03	0.105E+03
6	0.167E+01	0.400E+01	0.677E+02	0.797E+02	0.105E+03	0.140E+01	0.280E+02	0.150E+02	0.757E+02	0.123E+02	0.472E+01
7	0.167E+01	0.400E+01	0.677E+02	0.797E+02	0.105E+03	0.140E+01	0.280E+02	0.300E+02	0.789E+02	0.196E+02	0.104E+02
8	0.167E+01	0.400E+01	0.677E+02	0.797E+02	0.105E+03	0.167E+01	0.280E+02	0.451E+02	0.797E+02	0.284E+02	0.159E+02
9	0.167E+01	0.400E+01	0.677E+02	0.797E+02	0.105E+03	0.140E+01	0.280E+02	0.600E+02	0.805E+02	0.338E+02	0.181E+02
10	0.167E+01	0.400E+01	0.677E+02	0.797E+02	0.105E+03	0.140E+01	0.280E+02	0.752E+02	0.813E+02	0.409E+02	0.234E+02
11	0.167E+01	0.400E+01	0.677E+02	0.797E+02	0.105E+03	0.140E+01	0.280E+02	0.900E+02	0.813E+02	0.477E+02	0.291E+02
12	0.167E+01	0.400E+01	0.677E+02	0.797E+02	0.105E+03	0.167E+01	0.399E+02	0.149E+02	0.773E+02	0.108E+02	0.475E+01
13	0.167E+01	0.400E+01	0.677E+02	0.797E+02	0.105E+03	0.167E+01	0.399E+02	0.300E+02	0.797E+02	0.174E+02	0.101E+02
14	0.167E+01	0.400E+01	0.677E+02	0.797E+02	0.105E+03	0.167E+01	0.399E+02	0.450E+02	0.797E+02	0.238E+02	0.139E+02
15	0.167E+01	0.400E+01	0.677E+02	0.797E+02	0.105E+03	0.167E+01	0.399E+02	0.601E+02	0.797E+02	0.301E+02	0.171E+02
16	0.167E+01	0.400E+01	0.677E+02	0.797E+02	0.105E+03	0.167E+01	0.399E+02	0.753E+02	0.797E+02	0.364E+02	0.221E+02
17	0.167E+01	0.400E+01	0.677E+02	0.797E+02	0.105E+03	0.167E+01	0.399E+02	0.904E+02	0.797E+02	0.426E+02	0.266E+02

F(CALCULATED) = 0.379E+03 F.95 = 0.454E+01 F.99 = 0.868E+01
X(PREDICTED) = 0.147E+02 + (0.989E+00)*X(OBSERVED)
CORRELATION IS SIGNIFICANT AT THE 95% LEVEL
CORRELATION IS SIGNIFICANT AT THE 99% LEVEL

FIGURE 2

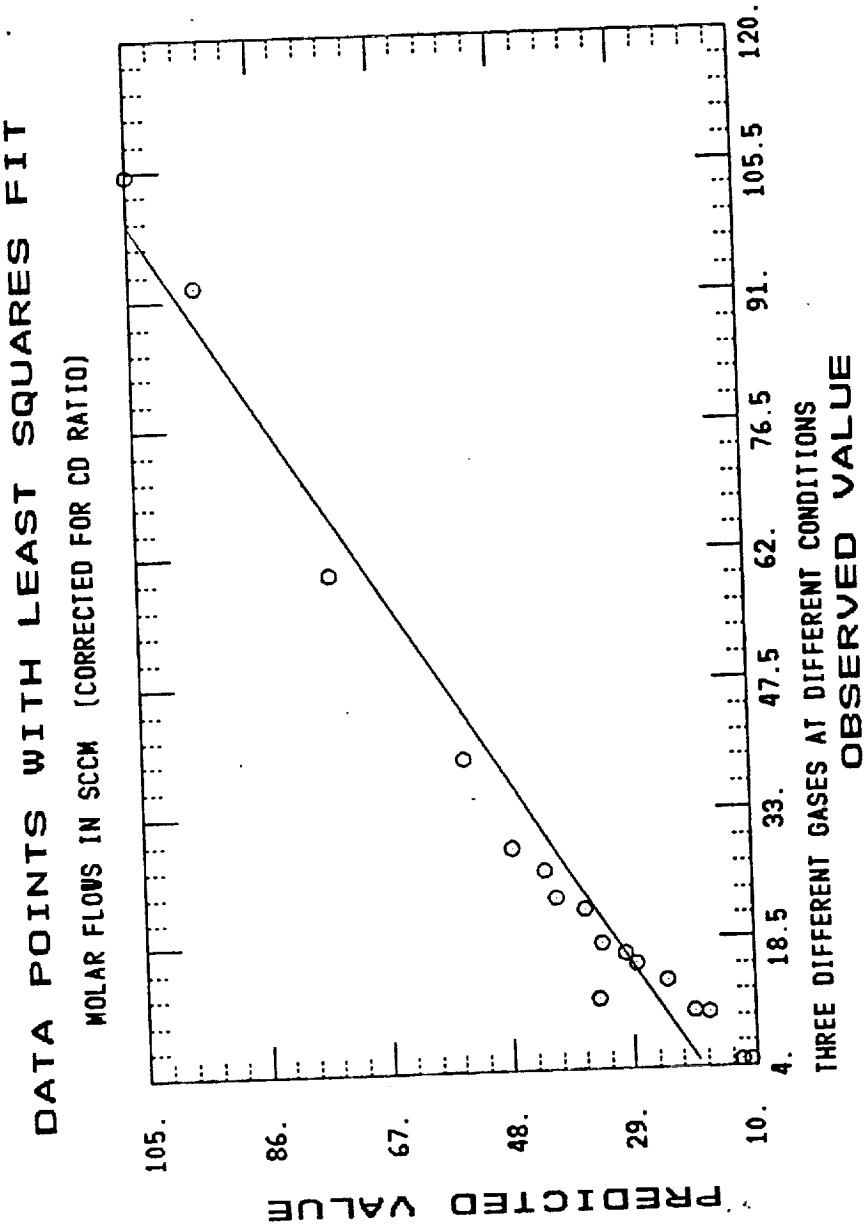
DATA POINTS WITH LEAST SQUARES FIT
MOLAR FLOWS IN SCCM (CORRECTED FOR CO RATIO)
THREE DIFFERENT GASES AT DIFFERENT CONDITIONS
PREDICTED VALUE
OBSERVED VALUE
105.
86.
67.
48.
29.
10.
4.
18.5
33.
47.5
62.
76.5
91.
105.5
120.

VII CONCLUDING SECTION

7.1 CONCLUDING REMARKS

X (PREDICTED) = 0.9 * X (OBSERVED) + B WAS SIGNIFICANT AT A LEVEL OF 99%, X REFERRING TO THE MOLAR FLOW RATE. OF COURSE ONE WOULD IDEALLY EXPECT THAT X (PREDICTED) = X (OBSERVED). HOWEVER DUE TO THE ROUGH NATURE OF THE PREDICTOR 0.9 SEEMS TO BE ACCEPTABLE AS THE SLOPE AND IS INDICATIVE OF THE ASSUMPTION THAT THE RATIO OF THE DISCHARGE COEFFICIENTS BE UNITY. THE INTERCEPT B WOULD EXERT LITTLE INFLUENCE AT THE HIGHER FLOWS BUT WOULD BE SIGNIFICANT AT LOWER FLOW RATES.

THE DATA WERE AGAIN PROCESSED USING AN ALGORITHM THAT ACCOUNTED FOR THE RATIO OF THE DISCHARGE COEFFICIENTS. VERY SIMILAR RESULTS WERE ACHIEVED, INDICATING THAT THE RESIDUAL INTERCEPT MAY HAVE ARISEN FROM FLOWMETER CALIBRATION. IT IS RECOMMENDED, THAT THE DATA BE RETAKEN ON A "TIME-WEIGH" BASIS TO DETERMINE WHETHER OR NOT THE FLOW MEASUREMENT GAVE RISE TO THE SOMETIMES UNDESIRABLE INTERCEPT.

VIII APPENDIX

LABORATORY DOCUMENTATION

COMMENTS TO ELAINE WHITE REPORT

Add Title to report. "SPECIAL LEAK RATES TEST".

ABBREVIATIONS/ACRONYMS

PSIG	Pounds Per Square Inches
OF	Degrees Farenheit
SCCM	Standard Cubic Centimer
KC	Kennedy Space Center fittings
GN2	Gaseous Nitrogen
GHe	Gaseous Helium
Ar	Gaseous Argon

George
4526

INTRODUCTION

A need to know small leak rates for different gases at ambient temperatures was the test objective. The Prototype Lab (DM-MED-2) was used to contruct the test tool to perform (See fig. AA). The tool made of 6061 Aluminum pipe measuring 12 inch by 8 inch had both end capped with an 6061 Aluminum plate. Ports were drilled and tapped at one end for installing the pressure, temperature and flowrate instrumentation.

PRELIMINARY MEETING

A preliminary meeting was held on July 26, 1990 to discuss the test project requirements. Personnel attending the meeting were: John Puppert, Ernie Walters, and Ron Fox with DM-MED-2, and Andy Rodriguez, Elaine White with DM-MED-4.

DISCUSSION

Figure AA shows a pictorial of the test setup. The instrumentation used is also shown on this figure. The test result is shown on Table A. Flow rates were measured at each pressure increment of 15 PSIG.

CONCLUSION

There were no anomalies during the fabrication/test phase and all the test objectives were accomplished.

INTRODUCTION

ON 26 JULY 1990 @ 0930 HRS., JOHN POPPERT, ERNIE WALTERS, RON FOX (DM-MED-2), ANDY RODRIGUEZ, AND ELAINE WHITE (DM-MED-4) MET IN THE PROTOTYPE SHOP BUILDING TO DISCUSS FABRICATION OF A TEST SET-UP TO RECORD LEAK RATES OF VARIOUS GASEOUS MEDIUMS IN A VESSEL WITH A KNOWN AMBIENT TEMPERATURE AND PRESSURE. WITH A CONTROLLED LEAK, THE FLOWRATE WOULD BE MEASURED AND CONVERTED TO SCCM.

AFTER CONSTRUCTION OF THE VESSEL ON 27 JULY 1990, IT WAS CHECKED FOR LEAKS BY A DU PONT INSTRUMENTS 120 SSA LEAK DETECTOR. THE TESTS WERE CONDUCTED ON 01 AUG 1990 AFTER A TWO DAY DELAY BECAUSE OF OTHER HIGHER PRIORITY PROJECTS AT THE PROTOTYPE LAB. THE TEST CONDUCTOR WAS ELAINE WHITE (DM-MED-4) AND THE TECHNICIAN WAS RON FOX (DM-MED-2).

TEST SET-UP

A HEISE DIGITAL PRESS. INDICATOR
RANGE 0-100 PSI, ACCURACY 0.1 %
CALIBRATION CAL/CERT # M06071
DATE 11 JAN 90

B FLOWMETER
MATHESON # 610A RANGE 0-100
MAX PRESS. 250 PSI
KC-116 FITTING WITH TEFLON TAPE
CALIBRATION CAL/CERT # M05881
DATE 05 DEC 89

C [SEE NEXT SHEET]

D ASTRO-MED, INC. STRIP CHART
MT-9500
PRESSURE READING 0-100 PSI
TEMPERATURE READING 0-100 % ≅ 23° - 104° F

[C] VESSEL

PIPING AND PLATES
BOTH ALUMINUM

TOP VIEW

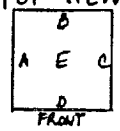

A SHUTOFF VALVE
TESCOM CORP.
KEL-F-81 SEATS
6000 PSI MAX
SERIAL # L46004

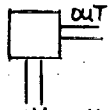

KC112-C4
KC171-C4
(3) PACKINGS
(1) SEAL RING KC103-4

B PRESSURE TRANSDUCER
TELEDYNE TABER
MODEL # 2403
RANGE 0-100 PSI, ACCURACY 1% FULL SCALE
SERIAL # 848388
SPEC # 79K 0034-38-S3N1Z REV G
CALIBRATION CAL/CERT Z80276
DATE 29 NOV 89

C METERING VALVE
PARKER HANNIFIN CORP.
CPV-84-1-11
(2) KC116-C4-2
(1) KC103-4

D TANK BLEED VALVE
TESCOM CORP.
KEL-F-81 SEATS
6000 PSI MAX
SERIAL # L46023

E TEMPERATURE TRANSDUCER
SCIENTIFIC INSTR. INC.
MODEL # 49WT-02-13
RANGE -5C to +40° C, ACCURACY ± 1%
SPEC # 79K03499-02-13S
CALIBRATION CAL/CERT Z06160
DATE 1 APR 90

TEST RUN DATA - TEST DATE 01 AUG 1990

	PRESS (PSI)	LEAKRATE (SCCM)	TEMP (°F)
NITROGEN	15.0	12.5	75.7°
	30.0	27.5	78.9°
	45.1	42	79.7°
	60.0	48	80.5°
	75.2	62	81.3°
	90.0	77	81.3°
HELIUM	15.1	12	79.7°
	29.9	39	79.7°
	44.8	60	79.7°
	60.1	92.5	79.7°
	67.7	105	79.7°
ARGON	14.9	15	77.3°
	30.0	32	79.7°
	45.0	44	79.7°
	60.1	54	79.7°
	75.3	70	79.7°
	90.4	84	79.7°

8/1/90

Test setup stripchart →

1

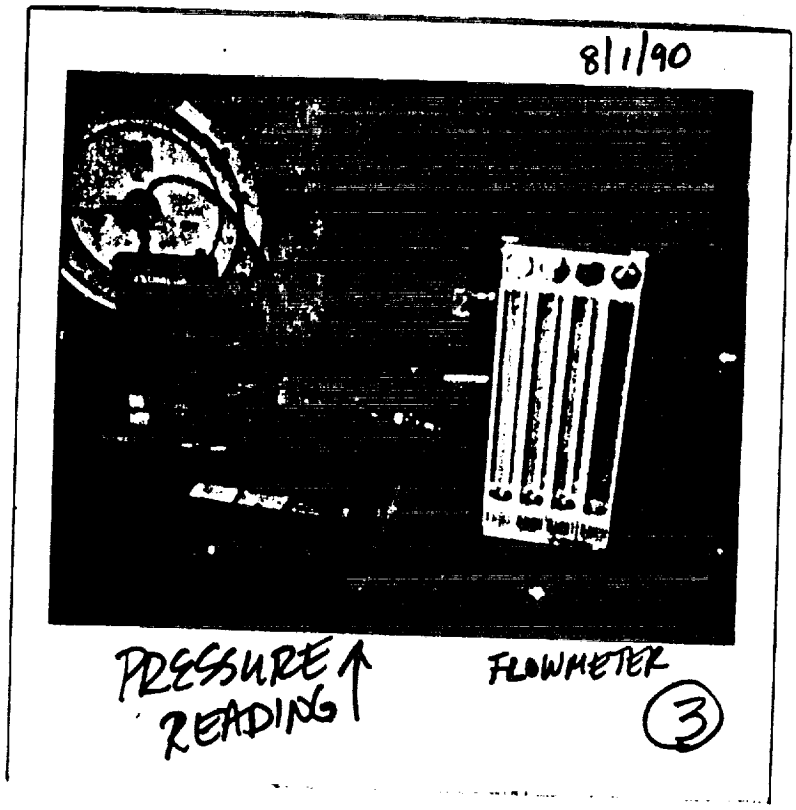

ORIGINAL PAGE IS
OF POOR QUALITY

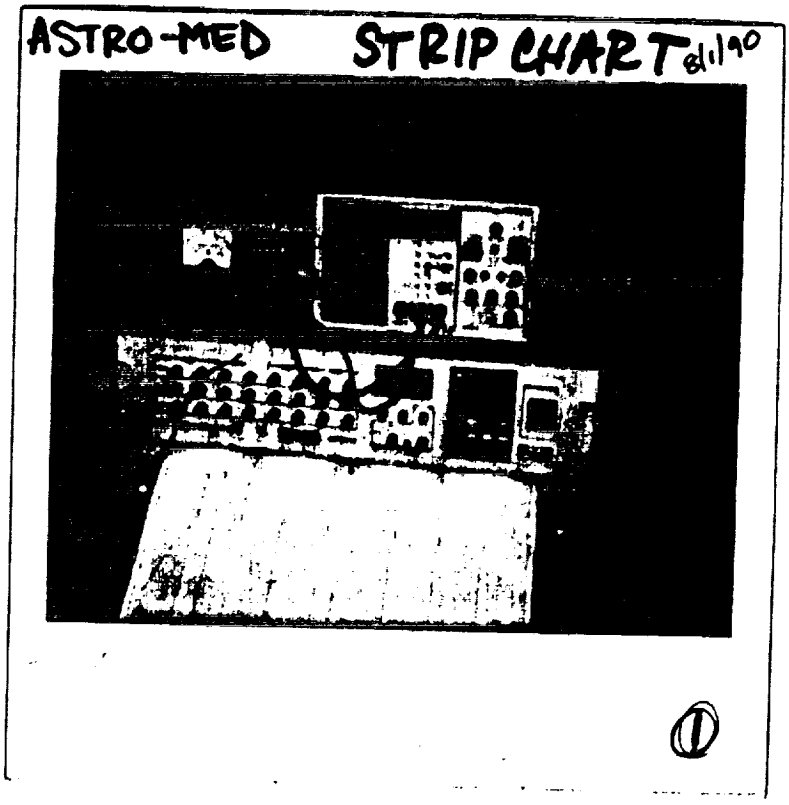

8/1/90

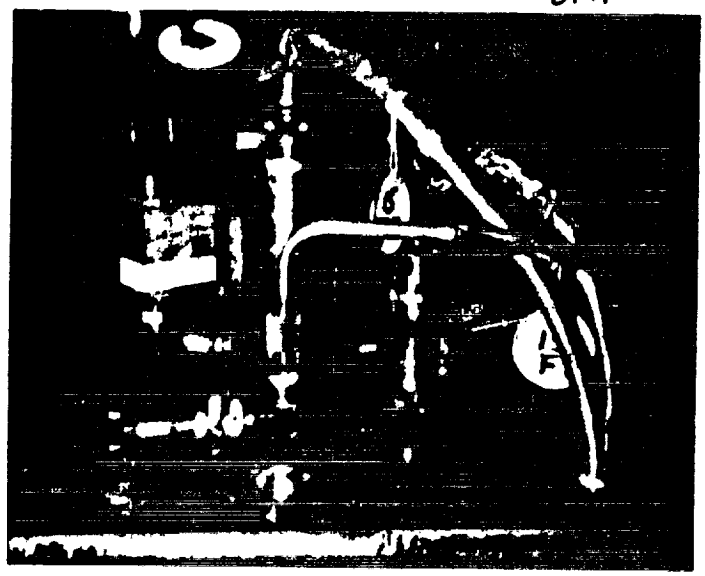

MTR VLV SIDE (5)

IX REFERENCES

1. LONERGAN VALVE DIVISION, 'TECHNICAL MANUAL', LONERGAN 1989

2. SHAPIRO, A. H., 'THE DYNAMICS AND THERMODYNAMICS OF COMPRESSIBLE FLOW', RONALD PRESS, NEW YORK (1953)

3. PERRY, R. H., 'PERRY'S CHEMICAL ENGINEERS' HANDBOOK', SIXTH EDITION', McGRAW-HILL, NEW YORK (1984)

4. BENJAMIN ,M. W., 'THE FLOW OF WATER THROUGH THROTTLING ORIFICES', TRANS. ASME, VOL.71, NO.5, JULY 1941,PP 419-429

5. CRUVER, J. E., 'CRITICAL FLOW OF LIQUID-VAPOR MIXTURES', JOURN. AIChE, VOL.13, NO.1, JANUARY 1967, PP 52-60

6. HESSON, J. C., 'FLOW OF TWO-PHASE CARBON DIOXIDE THROUGH ORIFICES', JOURN. AIChE, VOL.4, NO.2, JUNE 1958, PP 207-210

7. SMITH, R. V., 'CRITICAL TWO-PHASE FLOW OF HELIUM', CRYOGENICS, OCTOBER 1973, PP 616-619

8. HENRY, R. E., 'THE TWO-PHASE CRITICAL FLOW OF ONE-COMPONENT MIXTURES IN NOZZLES, ORIFICES, AND SHORT TUBES', J. HEAT TRANSFER, MAY 1971, PP 179-187

9. LEVY, S. 'PREDICTION OF TWO-PHASE CRITICAL FLOW RATE, J. HEAT TRANSFER, FEBRUARY 1965, PP 53-58

10. MCCABE, W. R. 'UNIT OPERATIONS OF CHEMICAL ENGINEERING' MCGRAW-HILL, NEW YORK (1962)

1990 NASA/ASEE SUMMER FACULTY FELLOWSHIP PROGRAM

JOHN F. KENNEDY SPACE CENTER
UNIVERSITY OF CENTRAL FLORIDA

A FLAMMABILITY STUDY OF THIN PLASTIC FILM MATERIALS

PREPARED BY:	Dr. S. Ballou Skinner
ACADEMIC RANK:	Professor
UNIVERSITY AND DEPARTMENT:	The University of South Carolina Coastal Carolina College Department of Physics
NASA/KSC	
DIVISION:	Materials Science Laboratory
BRANCH:	Materials Testing Branch
NASA COLLEAGUE:	Mr. Charles Hoppesch
DATE:	August 17, 1990
CONTRACT NUMBER:	University of Central Florida NASA-NGT-60002 Supplement: 4

ACKNOWLEDGMENT

I am grateful to the NASA/ASEE Summer Faculty Fellowship Program and to Mr. Charles W. Hoppesch, Chief of the Materials Science Laboratory of the Engineering Development Directorate at the Kennedy Space Center (KSC), for the opportunity of spending an enjoyable, productive and rewarding summer conducting a flammability study of thin plastic film materials. I greatly value the helpfulness and assistance of Mr. Ed Dumas for the preparation of videos, graphs and figures. Also, I am thankful to Mr. Billy Dearing for his assistance in the temperature profile study and in the heat sink effect study.

I further acknowledge the generous assistance provided by Mr. Carlos Springfield, Chief of the Materials Testing Branch, Mr. Coleman Bryan, a summer faculty mentor in the program, Messrs. Jon A. Bayliss and Robert J. Frankfort.

Also, appreciation goes to Mr. Paul Zombo of EG&G, NDE, for his assistance in the infrared imaging; the Microchemical Analysis Branch for determining melting temperatures; Miss Marsha Maxwell for determining fire points; Mr. Terry Boodhoo for his help in sample preparation; and, Ms. Gayle Krisingha for typing this paper.

The expertise and kindness of the program director, Dr. Loren A. Anderson, is also gladly acknowledged.

ABSTRACT

The Materials Science Laboratory at the Kennedy Space Center presently conducts flammability tests on thin plastic film materials by using a small needle rake method. In this study, flammability data from twenty-two thin plastic film materials were obtained and cross-checked by using three different testing methods: (a) the presently used small needle rake, (b) the newly developed large needle rake, and (c) the previously used frame.

In order to better discern the melting-burning phenomenon of thin plastic film materials, five additional specific experiments were performed. These experiments determined (1) the heat sink effect of each testing method, (2) the effect of the burn angle on the burn length or melting/shrinkage length, (3) the temperature profile above the ignition source, (4) the melting point and the fire point of each material, and (5) the melting/burning profile of each material via infrared (IR) imaging.

The experimentations gave the following results: Comparison of the three flammability test methods revealed inconsistent pass/fail results in four of the twenty-two samples. The heat sink effect experimentation depicts that the frame method acted like a large heat sink. Increasing the burn angles affected both the burn length and the melting/shrinkage length. The temperature profile above the ignition source revealed that convection currents affect the air temperature gradient. Melting point data, fire point data and infrared imaging discerned whether the material was burning or shrinking (i.e., melting).

TABLE OF CONTENTS

List of Illustrations

List of Tables

I. Introduction

1.1 Background Information

A fire near the Orbiters, payloads, ordnance materials, hypergols or practically any place at KSC could potentially cause catastrophic results. Fires have the capability to destroy millions of dollars worth of equipment and endanger hundreds of lives. Therefore, careful flammability testing must be performed to eliminate fire hazardous materials.

Thin plastic film materials are used widely at KSC for an extensive variety of needs. Some of these needs are (1) the packaging of small items such as transistors, (2) the crating of large items such as satellites, (3) the draping of items up to the size of a spacecraft, and (4) the shielding of workers and equipment from debris.

Thin plastic film materials used at KSC must pass flammability tests conducted in the Materials Science Laboratory. The flammability tests measure and describe the properties of materials in response to heat and flame under ambient conditions. The results from these tests are used to classify materials proposed for use in spacecraft and associated equipment as Group I and Group II. Group I materials can be used without restrictions. Group II materials do not pass Group I criteria and must be subjected to additional flammability testing. Group II materials are restricted from use in spacecraft and associated equipment.

1.2 NASA's Upward Propagation Test (NHB 8060.1B Test 1)

Specifications for NASA's upward propagation test can be found in the NASA publication NHB 8060.1B Test 1, "Flammability, Odor, and Offgassing Requirements and Test Procedures for Materials and Environments that Support Combustion" (reprint May 1988). The publication requires that thin plastic film samples be cut into 2.5 by 12 inch rectangles and placed on a framed or needle rake sample holder. The sample's bottom edge must be located at least three inches from the base of a hood. Ignition of the sample is accomplished by employing a regulated energy source. The ignition source consists of a length of No. 20 gauge bare nickle-chromium wire sufficient to wind a minimum of three turns around a standard clean weld "B" igniter (hexamethylenetetramine based). See Figure 1. The nominal

diameter of this igniter is 0.125" with a length of one inch. The flame temperature is 2000°F ± 200°F and burns for a duration of 25 ± 5 seconds. The upper edge of the igniter surface is placed 0.25 inches from the bottom edge of the sample. See Figure 2 for a picture of a burning sample.

The acceptance criteria states that the material shall be considered noncombustible, or self-extinguishing, if less than six inches of the sample is consumed and the time of burning does not exceed 10 minutes. There must be no sparking, sputtering or dripping of flaming particles from the test sample. A minimum of three samples must be tested. A failure of any one of the three samples constitutes failure of the material.

The thin plastic film materials are burned in a non-oxygen enriched atmosphere, i.e., air (79% N_2 and 21% O_2) at 14.7 psia in a hood.

In regard to sample preparation, samples are cut from the same batches of materials for all tests in order to reduce variability.

II. Procedures

2.1 Test Materials

Twenty-two thin plastic film materials were tested. Table 1 lists each thin plastic film material with the following information: generic type, thickness, type of sample holder, burn length, burn time, propagation rate, dripping of flaming particles, self-extinguishing, and pass or fail.

2.2 Description of Sample Holders

Frame Sample Holder: This sample holder consists of a vertically mounted steel clamped frame that overlaps 1/4 inch on each side of a sample along the full 12 inch minimum length of the sample, leaving a 2 inch wide by 12 inch long exposed center section (see Figure 3).

Small Needle Rake Sample Holder: This sample holder is made of steel with needles spaced 3 inches apart lengthwise. A 2 1/2 by 12 inch sample is impaled onto the needle rake. It is also mounted vertically (see Figure 4).

Large Needle Rake Holder: This sample holder is identical to the small needle rake holder except it is larger. It impales a 12 by 12 inch sample onto its needle rake (see Figure 5).

Specifications for NASA's upward propagation test (NHB 8060.1B Test 1) allows one to use either the frame or small needle rake in testing thin plastic film materials. The large needle rake was devised by the author of this paper and is not yet approved by NASA.

2.3 Tests Performed

The Materials Science Laboratory at KSC presently conducts flammability tests on thin plastic film materials by using a small needle rate method. In this study, data from twenty-two thin plastic film materials was obtained and cross-checked by using three different methods: (1) the presently used small needle rake, (2) the newly developed large needle rake, and (3) the previously used frame. Documentation of data from these three tests was recorded on video tapes.

In order to better discern the melting-burning phenomenon of thin plastic film materials, five additional tests were performed. These experiments (1) determined the heat sink effect of each method, (2) determined the effect of the burn angle on the burn length or the shrinkage length, (3) determined the temperature profile above the ignition source, (4) determined the melting point and the fire point for each thin plastic film material, and (5) employed infrared imaging to determine the melting/burning profile of the thin plastic film materials in question.

III. Results

3.1 Comparison of The Three Different Flammability Methods

Table 2 gives a comparison of the three different flammability test methods (frame, small needle rake, and large needle rake) for twenty-two thin plastic film materials. Eleven of the twenty-two materials were consistent in passing all three test methods while seven were consistent in failing all three test methods. There were inconsistencies in pass/fail results among three test methods for four of the materials (FRAS Sheet MG-3 mils, Staticure FR, RCAS 2400 and 3M 2100). All four of these materials passed the frame test but failed the small needle rake test. Only 3M 2100 failed the large needle rake test method.

3.2 Heat Sink Effect

In order to investigate the heat sink effect of the frame, the small needle rake, and the large needle rake, thermocouples were placed in the air 1/16 inch from the bottom inside corner of the frame and 1/16 inch above the bottom needle of the small and the large needle rakes. Thermocouples were also placed on all three sample holders at three inches and six inches above the base. Figures 6, 7 and 8 reveal the placement of the thermocouples.

Fixture comparisons at the base (Figure 9), three inches above the base (Figure 10), and six inches above the base (Figure 11) depict that the temperatures are much lower in air near the frame holder than for the small needle rake. Since the frame and the needle rake holders are the same size, this means that the frame is absorbing much more heat than the small needle rake, i.e., the frame is a much better heat sink. Temperatures are low near the large needle rake holder because of the distance from the flame.

3.3 Burn Length or Shrinkage Length as a Function of Burn Angle

Four materials (An 120, Halar, Herculite 80 and Polyethylene) were burned at various angles (0, 5, 10, 15, 20, 25, 30 degrees. See Figure 12 for the burn angle orientation). For materials like polyethylene that burned 12 inches, i.e., entirely consumed, the burn angle had no effect upon burn length (Figure 13). For materials like AN 120 and Halar, the consumed length was due to burn and

shrinkage. Figures 14 and 15 reveal that angles of 20 degrees or larger eliminates the shrinkage. For materials that consistently burn a definite length without any shrinkage, like Herculite 80, Figure 16 depicts that the burn length is almost inversely proportioned to burn angle.

3.4 Temperature Profile Above the Ignition Source

Figure 17 shows the small needle rake holder with thermocouples placed at the base and at one inch intervals up to seven inches. Figure 18, The Vertical Flame Temperature Profile, reveals the peak temperatures from the base of the frame to seven inches above the frame at one inch intervals. The peak temperatures from four to seven inches above the base ranges from 250° to 500°F, a temperature exceeding the melting point for each thin plastic film material tested. It is understandable that a seven inch consumed length for a material like AN 120 is due to melt and/or shrinkage rather than burn since AN 120 has a melting point of 374°F.

3.5 Melting Point and Fire Points

The melting point is the temperature at which the material disappears as if it were dissolving. Shrinkage is the contraction or curling up of the material. The fire point is the lowest temperature at which the mixture of vapors from the surface of the material and the test atmosphere continue to burn after ignition. In most thin plastic film materials, shrinkage will occur before melting and melting will occur before burning.

The Microchemical Analysis Branch of the Materials Science Laboratory determined the melting points (peak apex), onsets and joules per gram for the thin plastic film materials (Table 3). The Materials Testing Branch provided auto-ignition testing graphs via the interactive DSC V3.0 program. See Figures 19 and 20 for auto-ignition graphs of polyethylene and FRAS sheet MG, respectively.

3.6 Infrared Imaging

Figures 21 and 22 show the progression of a melting front of FRAS sheet MG via photos of infrared imaging. Analysis of the IR spectrum reveals that the temperature of

the melting front is a blue color, which on the scale at the bottom of the photo equals 225°F (107°C), the melting point of FRAS sheet MG. This example is one of many IR examples depicting thin plastic film materials melting instead of burning. IR documentation for all twenty-two thin plastic film materials was recorded on video tape.

IV. Conclusions and Recommendations

Section 3.1 shows that inconsistent results can be obtained using the three different methods of testing. Four out of twenty-two materials exhibited inconsistencies among the three methods. This research project attempts to discover the reasons for these discrepancies.

Section 3.2 reveals that the frame holder serves as a large heat sink, absorbing and dissipating heat required for material combustion. Materials that burn completely, such as polyethylene, are often extinguished when the flame comes near the edge of the frame holder. The small needle rake method, although an insignificant heat source, also has a flaw in that melted material often accumulates on the tips of the needle rakes, bursts into flame and sometimes drip as flaming particles from the tips. Many thin plastic film materials will not burn at their manufactured thickness but will burn when increased to a thicker dimension. The large needle rake holder is also an insignificant heat source. It eliminates the accumulation of melted material around the tips because the horizontal burn is not wide enough to reach the tips.

I recommend that consideration be given to using a needle rake holder larger than the one that is presently being used at KSC. A needle rake that holds a 6 inch by 12 inch sample will be a good compromise between the small needle rake holder and the large needle rake holder used in these experiments.

The experimentations described in Section 3.3 makes it clear that the burn angle should be zero degrees. These experiments show that varying the burn angle is successful in eliminating the melt length on some of the materials. This is good because it is advantageous to eliminate the shrinkage length. But, varying the burn angle also affects the burn length (which we do not desire to eliminate or interfere with). Materials that ignite and burn completely are not affected by the burn angle. I recommend a zero degree burn angle as presently deployed.

Section 3.4, The Temperature Profile Above the Ignition Source, reveals that the air temperature seven inches above the bottom of the sample is sufficient to melt some of the materials. After examining the melting point temperatures for the twenty-two materials in Section 3.5, it is

understandable why the melt lengths of materials like AN 110, AN 120 and FRAS sheet MG exceed six inches. Infrared imaging of the burning thin plastic film materials, as described in Section 3.6, answers a very important question: "Is the material burning or melting?" Infrared imaging of materials such as AN 110, AN 120, FRAS sheet MG, Proguard, Llumaloy and Staticure reveal that all have melt lengths exceeding six inches in at least one of the three test methods. The tester should not fail these materials because consumption exceeded six inches. If there is a question of whether a six inch or greater consumed length is due to burn or melt, I recommend using infrared imaging analysis.

Flammability investigations have revealed that most thin plastic film materials are either clear-cut failures or clear-cut passes no matter which of the three test methods are used. However, there are a few marginal materials which are not clear-cut pass or fail. These marginal materials require a closer examination and I recommend for these materials a minimum of six (preferably ten) samples be tested. Testing three samples, as specified in NASA publication NHB 8060.1B Test 1, may not be sufficient in marginal materials.

It is important and essential that the flammability test method eliminates subjectivity and ambiguity on the part of the test operator. The test operator must place special scrutiny on marginal materials.

A more realistic and practical flammability classification for thin plastic film materials in regard to burn/melt (shrinkage) length is suggested by the following criteria:

CLASS	CRITERIA OF ACCEPTABILITY	WHERE IT CAN BE USED
A	No damage to the sample exceeding 6 inches (burning, melting, or shrinkage), burn time may not exceed 10 minutes and no sparking, sputtering or dripping of flaming particles.	Anywhere in a spacecraft or in ground support equipment (GSE) areas.

CLASS	CRITERIA OF ACCEPTABILITY	WHERE IT CAN BE USED
B	No damage to the sample exceeding 9 inches (burning, melting, shrinkage), burn time may not exceed 10 minutes and no sparking, sputtering or dripping of flaming particles.	Anywhere outside of a 5 foot perimeter around the spacecraft.
C	Any materials not meeting the criteria of acceptability defined in Class A and B.	Nowhere.

V. References

1. Comparison of Results of the European Space Agency Oxygen Index Test and The NASA Upward Propagation Test, Document No. TR-581-001, NASA, Johnson Space Center, White Sands Test Facility, 1989.

2. Flammability, Odor and Offgassing for Materials in Environments that Support Combustion, Document No. NHB 8060.1B, Office of Space Transportation Systems, 1988.

3. Physical and Chemical Test Results of Plastic Films, Document No. MTB-402-85, NASA, Kennedy Space Center, Materials Testing Branch, 1986.

4. Physical and Chemical Test Results of Plastic Films (addition of materials #60 through #96), Document No. MTB-402-85, Addendum 1-88, NASA, Kennedy Space Center, Materials Testing Branch, 1988.

5. Unpublished Paper, Recommendations for Test 1 (Upward Flame Propagation).

TABLE 1 - FLAMMABILITY RESULTS FOR THIN PLASTIC FILM MATERIALS

MATERIAL NAME	GENERIC NAME	THICKNESS (MILS)	METHOD	BURN LENGTH (INCHES)	BURN TIME (SEC)	PROPAGATION RATE (IN/S)	DRIPPING FLAMING PARTICLES	SELF EXTINGUISH.	PASS OR FAIL
ACLAR 33 C	PCTFE	3	FRAME	3.0	10	18.0	NO	YES	PASS
			SM. NEEDLE	2.6	4	39.0	NO	YES	PASS
			LG. NEEDLE	4.0	8	30.0	NO	YES	PASS
WRIGHTLON 7400	NYLON	2	FRAME	4.8	8	36.0	NO	YES	PASS
			SM. NEEDLE	2.8	3	56.0	NO	YES	PASS
			LG. NEEDLE	3.1	6	31.0	NO	YES	PASS
HERCULITE 80	PVC/DACRON	19	FRAME	5.7	17	10.6	NO	YES	PASS
			SM. NEEDLE	3.0	20	6.3	NO	YES	PASS
			LG. NEEDLE	3.5	22	9.5	NO	YES	PASS
HALAR	ECTFE	2	FRAME	4.7	12	21.7	NO	YES	PASS
			SM. NEEDLE	5.0	10	25.0	NO	YES	PASS
			LG. NEEDLE	4.5	16	27.0	NO	YES	PASS
PROGUARD	ANTISTATIC NYLON	2	FRAME	3.7	7	31.7	NO	YES	PASS
			SM. NEEDLE	4.0	14	17.1	NO	YES	PASS
			LG. NEEDLE	6.0	16	22.5	NO	YES	PASS
AN-35	METALIZED PVF	13	FRAME	4.2	15	16.8	NO	YES	PASS
			SM. NEEDLE	4.3	14	18.4	NO	YES	PASS
			LG. NEEDLE	4.7	16	17.6	NO	YES	PASS
AN-110	PVF/POLYESTER	3	FRAME	8.0*	16	30.0	NO	YES	PASS
			SM. NEEDLE	6.0*	7	51.4	NO	YES	PASS
			LG. NEEDLE	6.5*	11	35.5	NO	YES	PASS
AN-120	PVF/POLYESTER	6	FRAME	6.1*	17	21.5	NO	YES	PASS
			SM. NEEDLE	6.3*	9	42.0	NO	YES	PASS
			LG. NEEDLE	6.3*	14	27.0	NO	YES	PASS

TABLE 1 (CONTINUED)

MATERIAL NAME	GENERIC NAME	THICKNESS (MILS)	METHOD	BURN LENGTH (INCHES)	BURN TIME (SEC)	PROPAGATION RATE (IN/S)	DRIPPING FLAMING PARTICLES	SELF EXTINGUISH.	PASS OR FAIL
LLUMALOY (35%)	METALIZED POLYESTER	1	FRAME	7.0*	4	105.0	NO	YES	PASS
			SM. NEEDLE	4.2	4	63.0	NO	YES	PASS
			LG. NEEDLE	5.3	6	53.0	NO	YES	PASS
LLUMALOY (50%)	METALIZED POLYESTER	1	FRAME	6.8*	4	102.0	NO	YES	PASS
			SM. NEEDLE	5.3	7	45.4	NO	YES	PASS
			LG. NEEDLE	5.0	6	50.0	NO	YES	PASS
FRAS sheet MG (2 mils)	POLYETHYLENE	2	FRAME	4.0	14	17.1	NO	YES	PASS
			SM. NEEDLE	7.5*	13	34.7	NO	YES	PASS
			LG. NEEDLE	6.3*	12	31.5	NO	YES	PASS
FRAS sheet MG (3 mils)	POLYETHYLENE	3	FRAME	6.1*	12	30.5	NO	YES	PASS
			SM. NEEDLE	5.4	11	29.4	YES	YES	FAIL
			LG. NEEDLE	6.0*	13	27.7	NO	YES	PASS
STATICURE FR	NYLON/STATICURE COATING	2	FRAME	6.3*	10	37.8	NO	YES	PASS
			SM. NEEDLE	4.2	8	31.5	YES	YES	FAIL
			LG. NEEDLE	4.5	14	19.3	NO	YES	PASS
RCAS 2400	POLYAMIDE NYLON	2	FRAME	4.5	12	22.5	NO	YES	PASS
			SM. NEEDLE	3.8	10	22.8	YES	YES	FAIL
			LG. NEEDLE	3.2	7	27.4	NO	YES	PASS
3M-2100	POLYESTER/NICKEL	3	FRAME	5.3	14	22.7	NO	YES	PASS
			SM. NEEDLE	6.2	40	9.3	YES	YES	FAIL
			LG. NEEDLE	12.0	153	4.7	YES	YES	FAIL
AS-6000	NYLON	2	FRAME	7.3	16	27.4	YES	YES	FAIL
			SM. NEEDLE	6.0	17	21.2	YES	YES	FAIL
			LG. NEEDLE	7.0	36	11.7	YES	YES	FAIL

TABLE 1 (CONTINUED)

MATERIAL NAME	GENERIC NAME	THICKNESS (MILS)	METHOD	BURN LENGTH (INCHES)	BURN TIME (SEC)	PROPAGATION RATE (IN/S)	DRIPPING FLAMING PARTICLES	SELF EXTINGUISH.	PASS OR FAIL
BAYSTAT (antistatic grid	NYLON/POLYETHYLENE/ CARBON	3	FRAME	6.3	20	18.9	YES	YES	FAIL
			SM. NEEDLE	12.0	30	24.0	YES	YES	FAIL
			LG. NEEDLE	5.0	20	15.0	YES	YES	FAIL
RCAS 1200	POLYETHYLENE	6	FRAME	7.0	15	28.0	YES	YES	FAIL
			SM. NEEDLE	12.0	47	15.3	YES	NO	FAIL
			LG. NEEDLE	12.0	98	7.3	YES	NO	FAIL
PVC	POLYVINYL CHLORIDE	4	FRAME	10.0	15	40.0	YES	YES	FAIL
			SM. NEEDLE	12.0	21	34.2	YES	NO	FAIL
			LG. NEEDLE	12.0	15	48.0	YES	YES	FAIL
POLYETHYLENE	POLYETHYLENE	4	FRAME	5.8	13	26.8	YES	YES	FAIL
			SM. NEEDLE	12.0	42	17.1	YES	NO	FAIL
			LG. NEEDLE	12.0	92	7.8	YES	NO	FAIL
ST-600	PE/PVA/CARBON	4	FRAME	12	25	28.8	YES	NO	FAIL
			SM. NEEDLE	12	22	32.7	YES	NO	FAIL
			LG. NEEDLE	12	27	26.7	YES	NO	FAIL
VELOSTAT	POLYOLEFIN (BLACK)	9	FRAME	12.0	60	12.0	YES	NO	FAIL
			SM. NEEDLE	12.0	45	16.0	YES	NO	FAIL
			LG. NEEDLE	12.0	112	6.4	YES	NO	FAIL

* Material passed because a portion of the length is attributable to shrinkage

TABLE 2

COMPARISON OF THE THREE FLAMMABILITY TEST METHODS

MATERIAL NAME	GENERIC TYPE	METHOD		
		FRAME	SMALL NEEDLE RAKE	LARGE NEEDLE RAKE
ACLAR 33 C	PCTFE	PASS	PASS	PASS
WRIGHTLON 7400	NYLON	PASS	PASS	PASS
HERCULITE 80	PVC/DACRON	PASS	PASS	PASS
HALAR	ECTFE	PASS	PASS	PASS
PROGUARD	ANTISTATIC NYLON	PASS	PASS	PASS*
AN-35	METALIZED PVF	PASS	PASS	PASS
AN-110	PVF/POLYESTER	PASS*	PASS*	PASS*
AN-120	PVF/POLYESTER	PASS*	PASS*	PASS*
LLUMALOY (35%)	METALIZED POLYESTER	PASS*	PASS	PASS
LLUMALOY (50%)	METALIZED POLYESTER	PASS*	PASS	PASS
FRAS sheet MG (2 mils)	POLYETHYLENE	PASS	PASS*	PASS*
FRAS sheet MB (3 mils)	POLYETHYLENE	PASS*	FAIL (4 OF 10)	PASS*
STATICURE FR	NYLON/STATICURE COATING	PASS*	FAIL (2 OF 10)	PASS*
RCAS 2400	POLYAMIDE NYLON	PASS	FAIL (3 OF 10)	PASS
3M-2100	POLYESTER/NICKEL	PASS	FAIL	FAIL
AS-6000	NYLON	FAIL	FAIL	FAIL
BAYSTAT (antistatic grid)	NYLON/POLYETHYLENE/CARBON	FAIL	FAIL	FAIL
RCAS 1200	POLYETHYLENE	FAIL	FAIL	FAIL
PVC	POLYVINYL CHLORIDE	FAIL	FAIL	FAIL
POLYETHYLENE	POLYETHYLENE	FAIL	FAIL	FAIL
ST-600	PE/PVA/CARBON	FAIL	FAIL	FAIL
VELOSTAT	POLYOLEFIN (BLACK)	FAIL	FAIL	FAIL

* Passed the test even though the shrinkage carried the consumed length beyond six inches.

TABLE 3

MELTING POINTS AND FIRE POINTS
FOR THIN PLASTIC FILM MATERIALS

	Melting Points			Fire Point
Sample	Peak Apex (C)	Onset (C)	Joules/gram	(C)
3M2100	106.9	95.7	52.0	Above 600
PVC	Decomposes w/o melting			
RCAS 1200	108.8	95.7	79.7	Above 600
Velostat	96.4	77.6	36.2	Above 600
Baystat	106.8	93.5	53.9	Above 600
AN 120	190.5	167.3	26.6	Above 600
Polyethylene	108.0	96.6	77.9	300
AN 110	191.1	177.9	6.3	Above 600
RCAS 2400	214.0	200.9	49.7	Above 600
FRAS Sheet MG	107.1	97.1	71.8	Above 600
Staticure	214.5	204.7	60.0	Above 600
AN 35	251.7	247.1	18.9	Above 600
Aclar 33C	202.0	194.6	12.6	Above 600
Wrightlon 7400	210.9	198.3	29.5	Above 600
Llumaloy (35%)	247.7	238.3	37.2	Above 600
Llumaloy (50%)	247.3	240.2	37.4	Above 600
Herculate 80	244.2	231.1	8.2	Above 600
AS 6000	214.6	206.2	46.6	Above 600
Proguard	212.7	196.5	37.9	Above 600

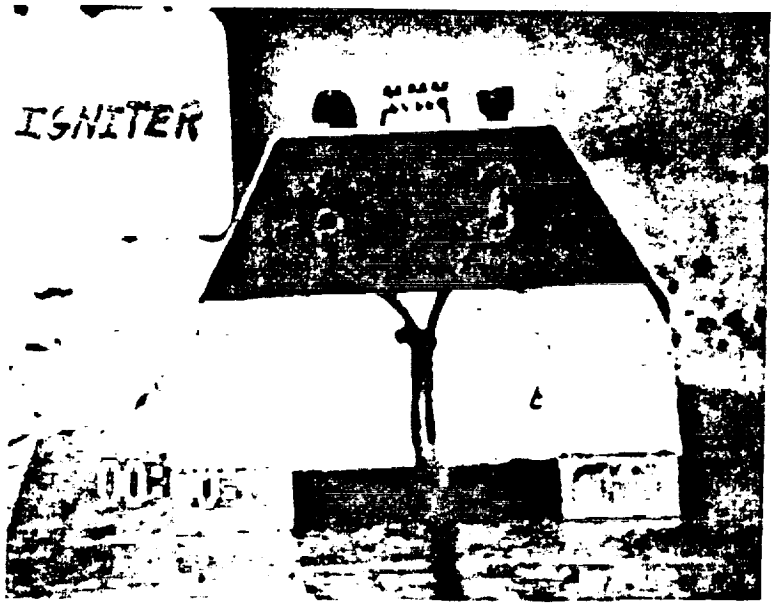

FIGURE 1. IGNITER SOURCE

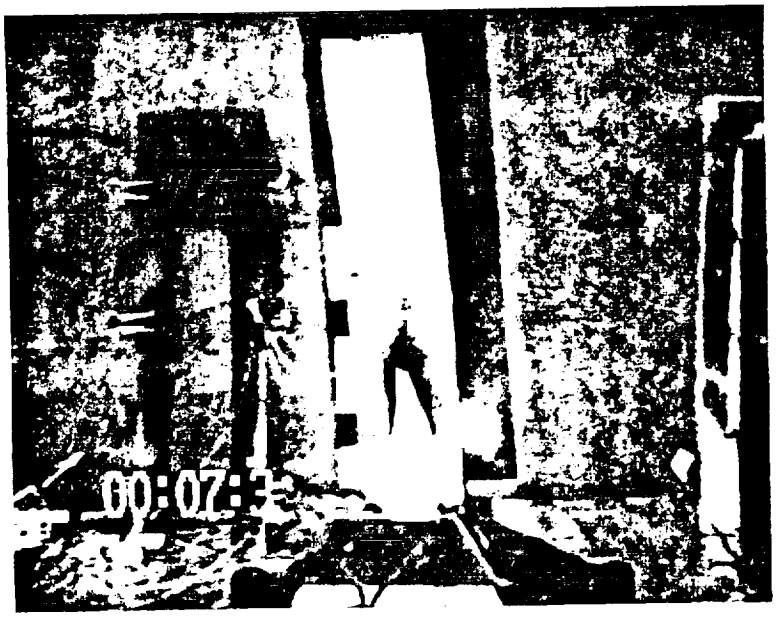

FIGURE 2. BURNING SAMPLE

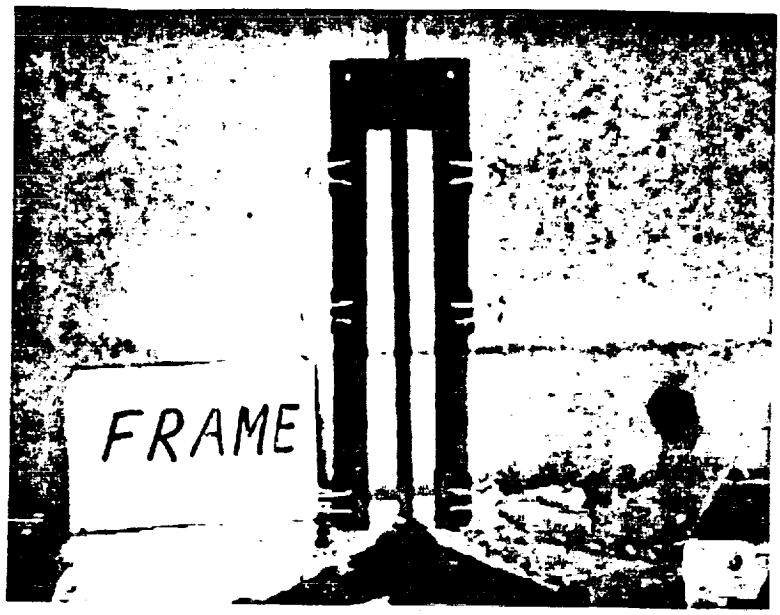

FIGURE 3. FRAME SAMPLE HOLDER

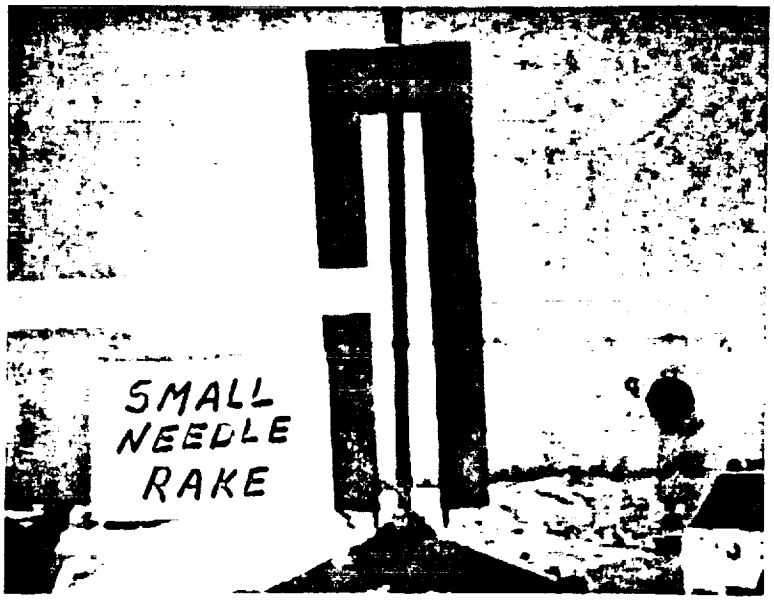

FIGURE 4. SMALL NEEDLE RAKE SAMPLE HOLDER

FIGURE 5. LARGE NEEDLE RAKE SAMPLE HOLDER

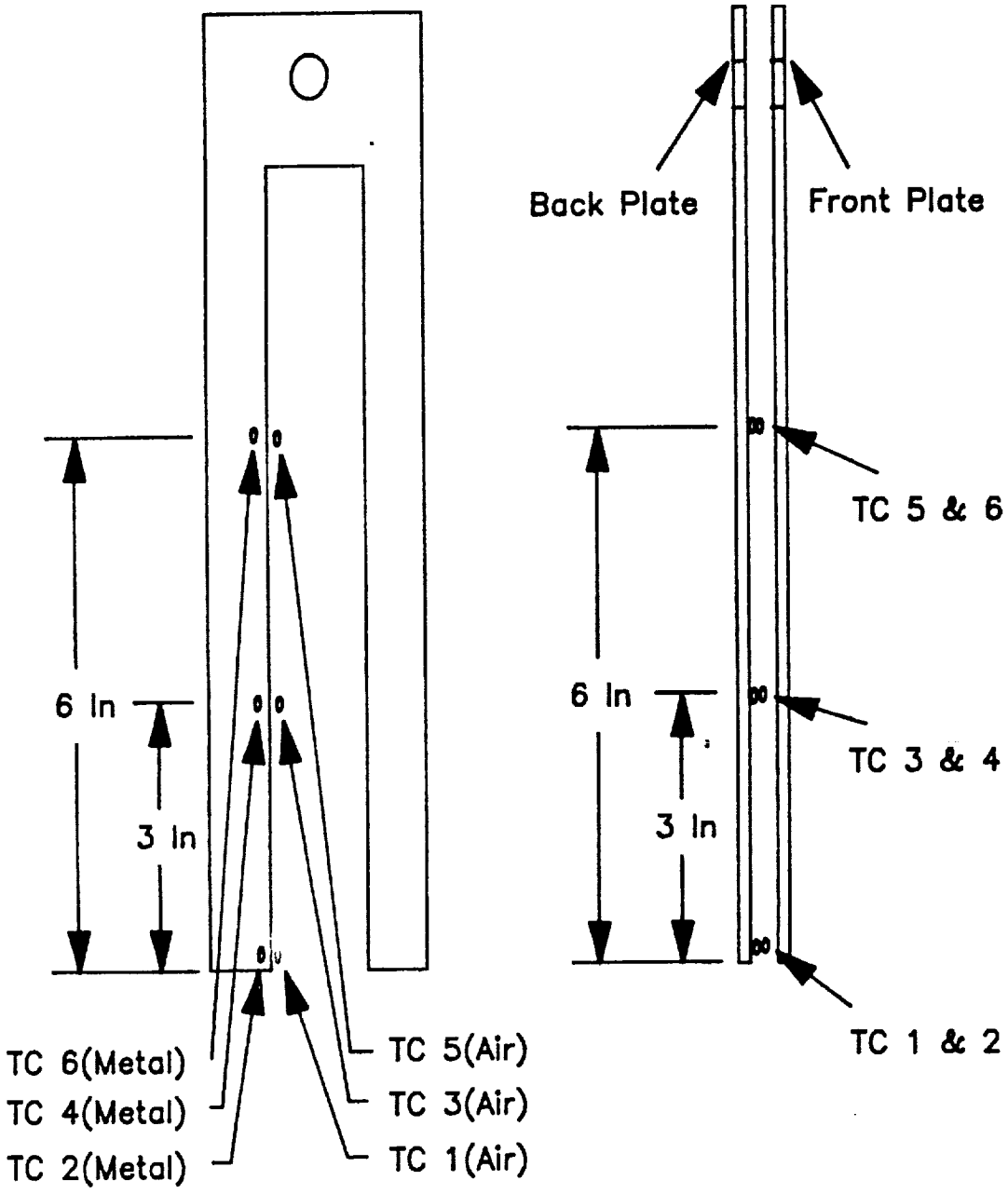

Figure 6. Frame Thermocouple Locations

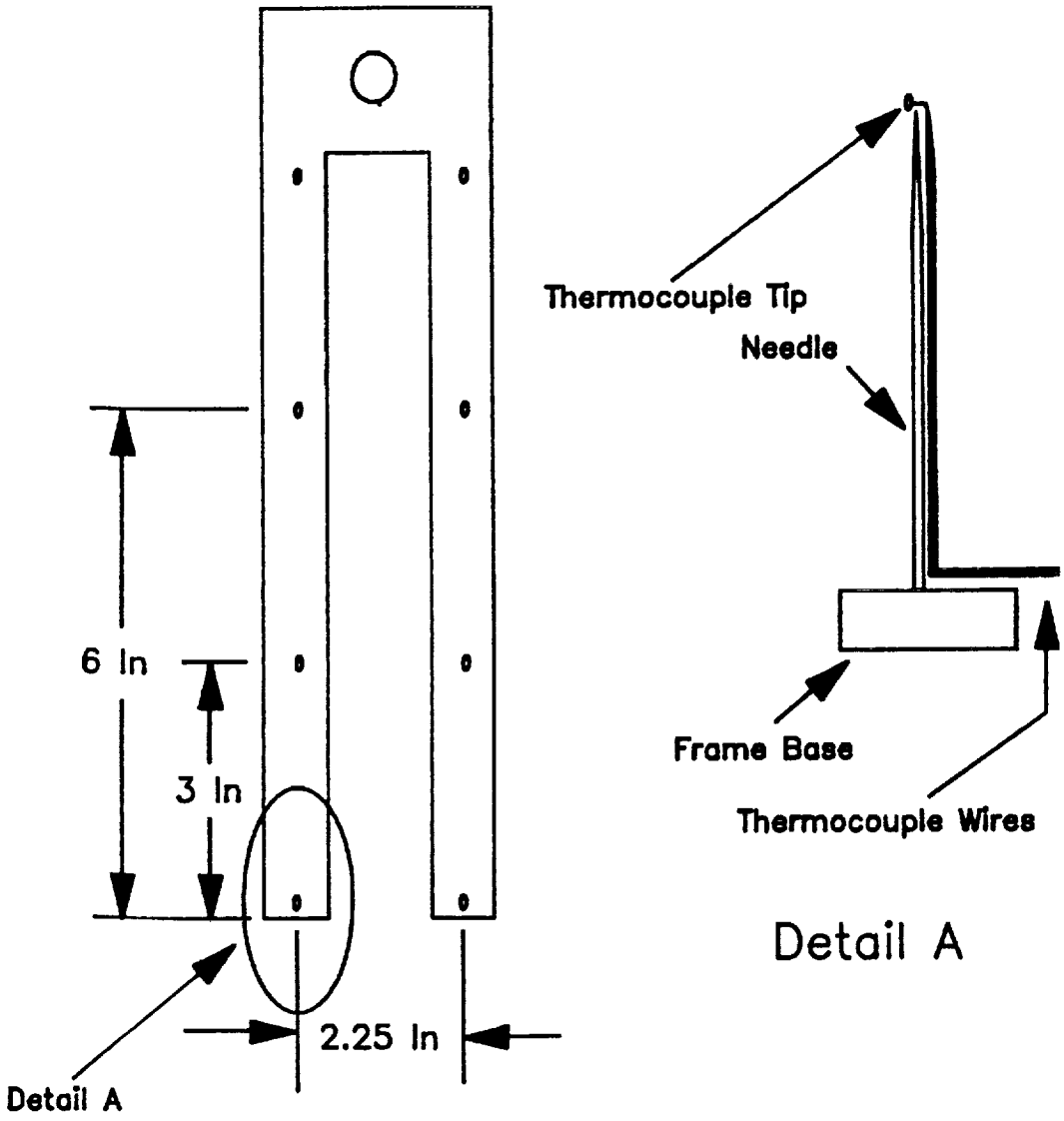

Figure 7. Small Needle Rake Thermocouple Locations

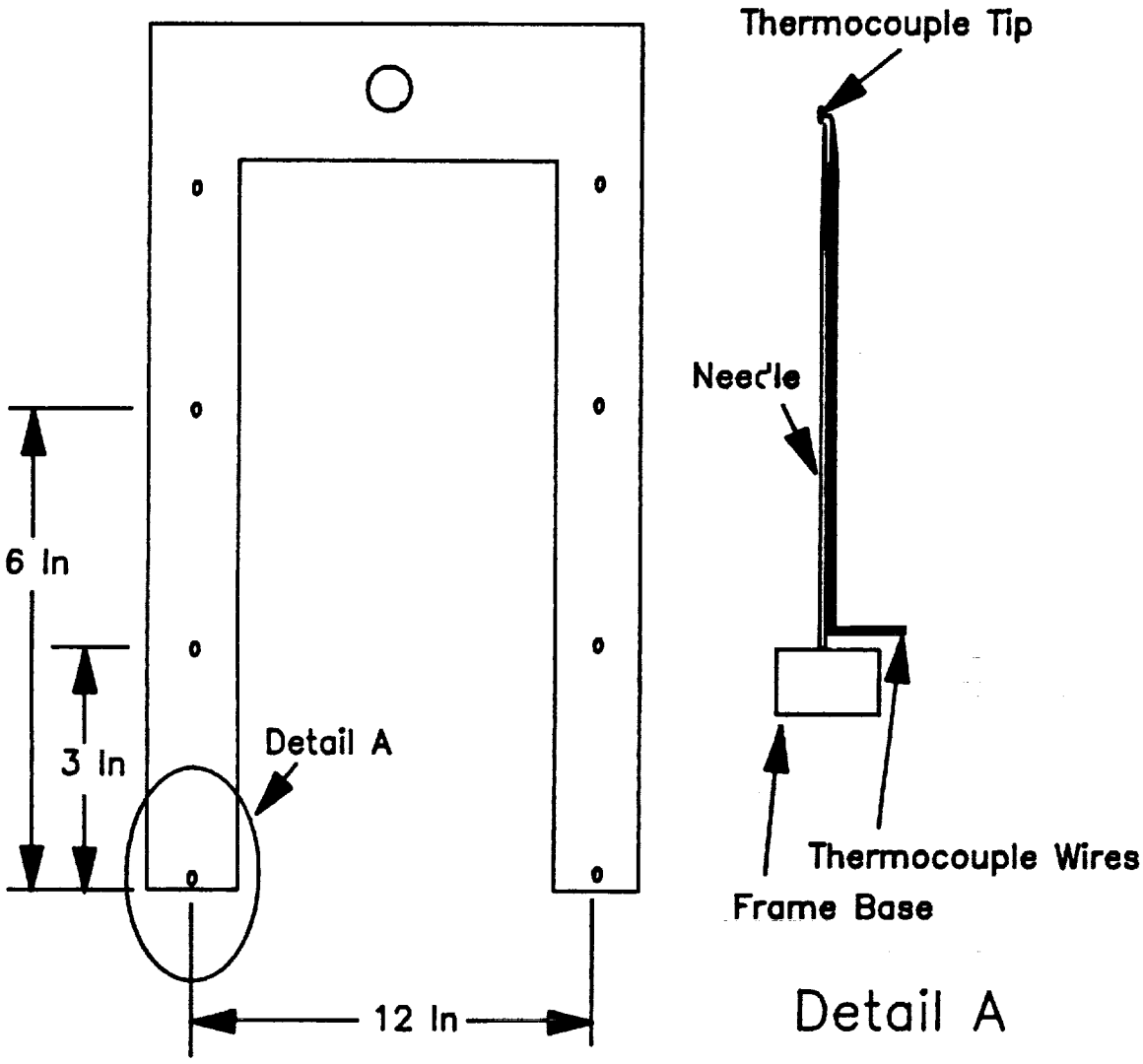

Figure 8. Large Needle Rake Thermocouple Locations

Figure 9
Fixture Comparison At Flame Base
No Sample Present In Fixture

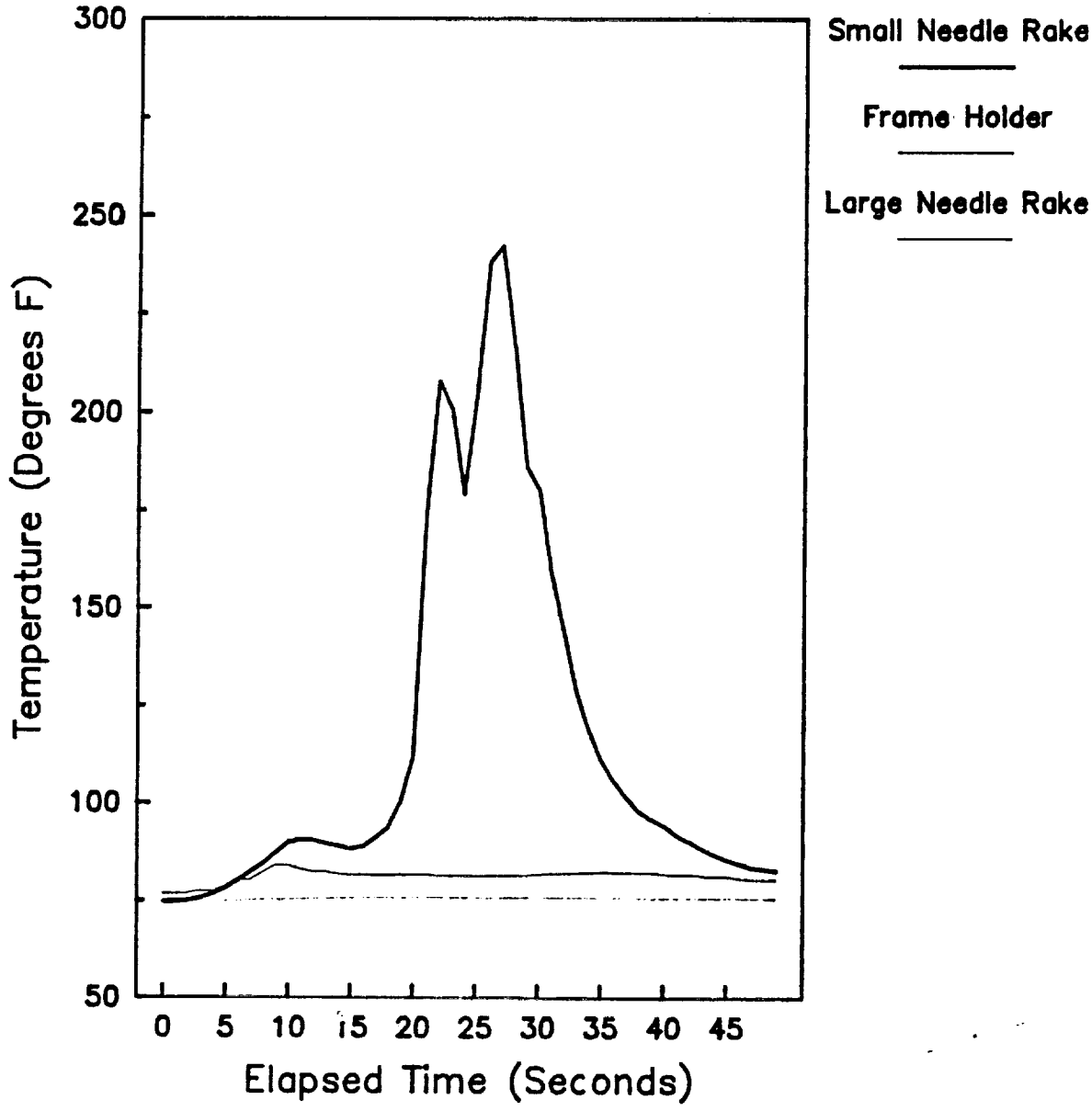

Figure 10

Fixture Comparison At 3" From Flame Base
No Sample Present In Fixture

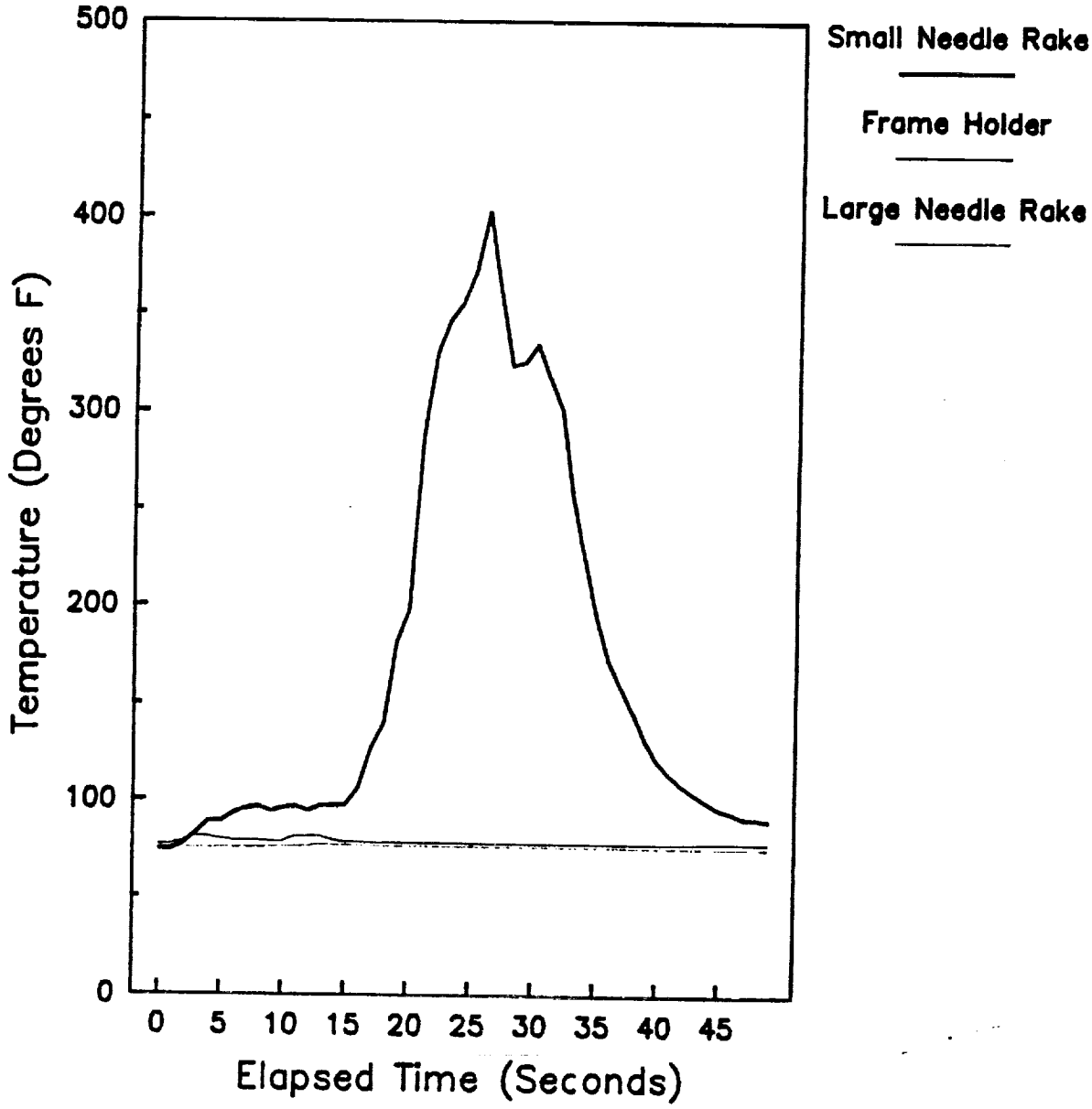

Figure 11

Fixture Comparison At 6" From Flame Base
No Sample Present In Fixture

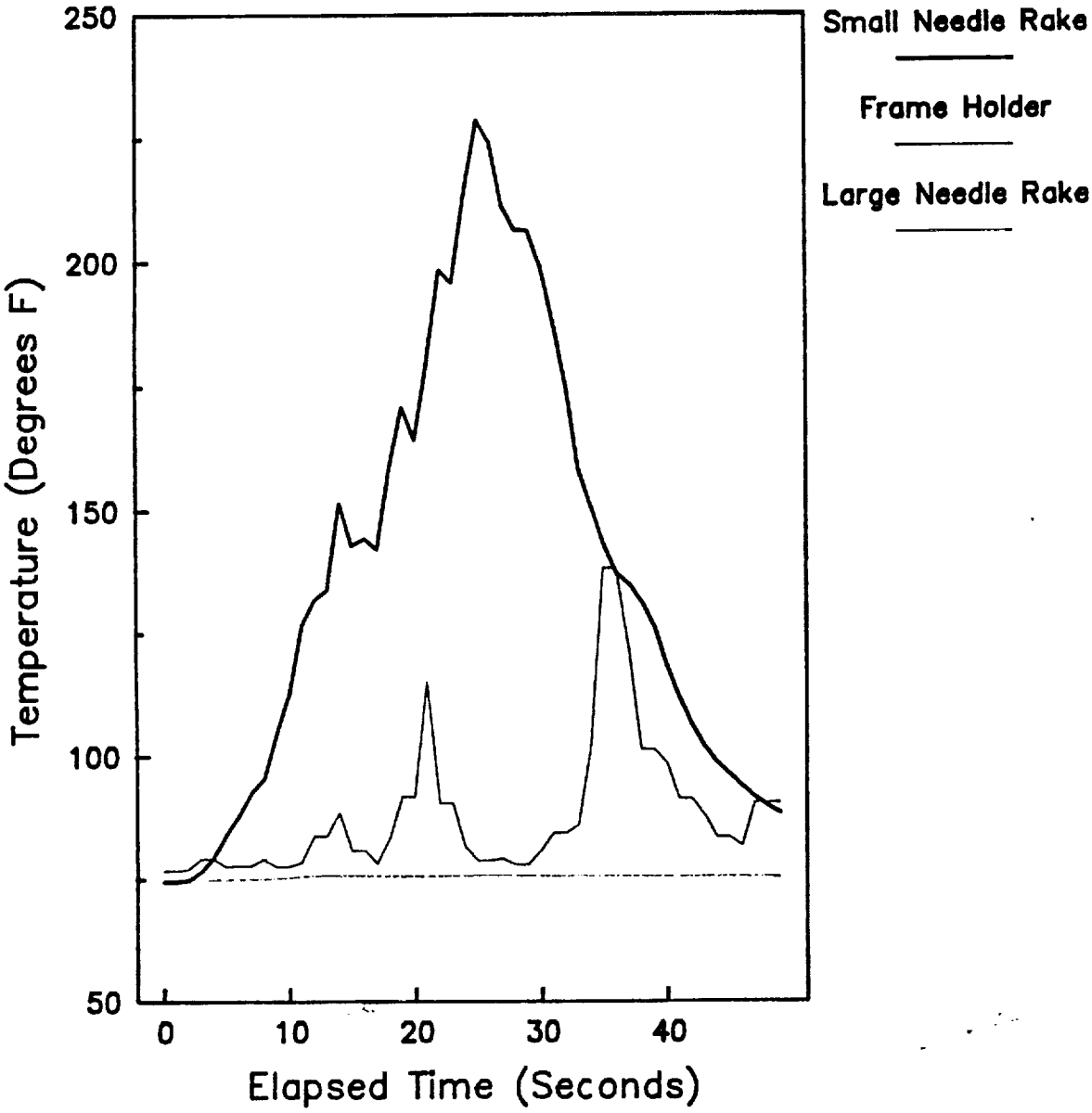

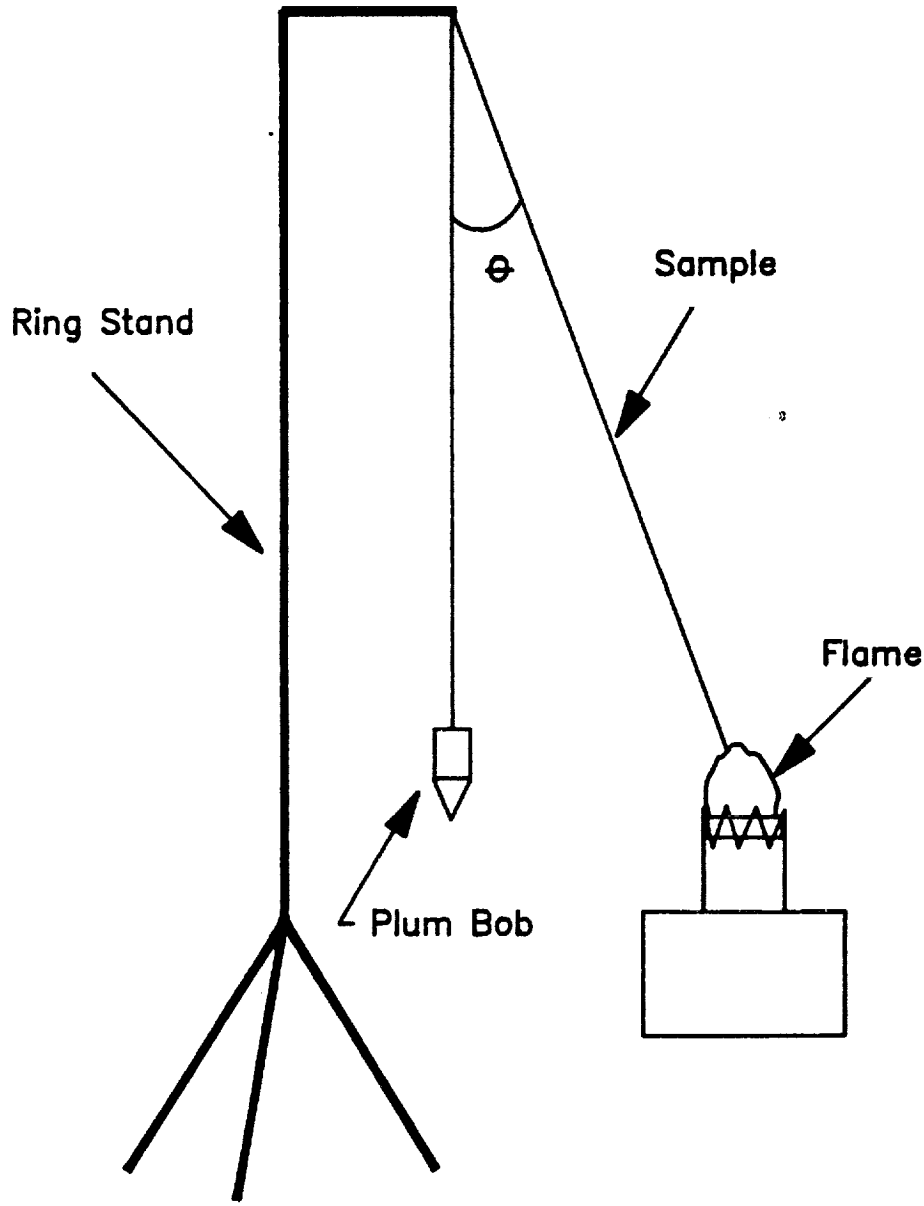

Figure 12. Burn Angle Orientation

θ = Burn Angle

Figure 13
Burn Length Of Polyethylene As A Function Of Angle

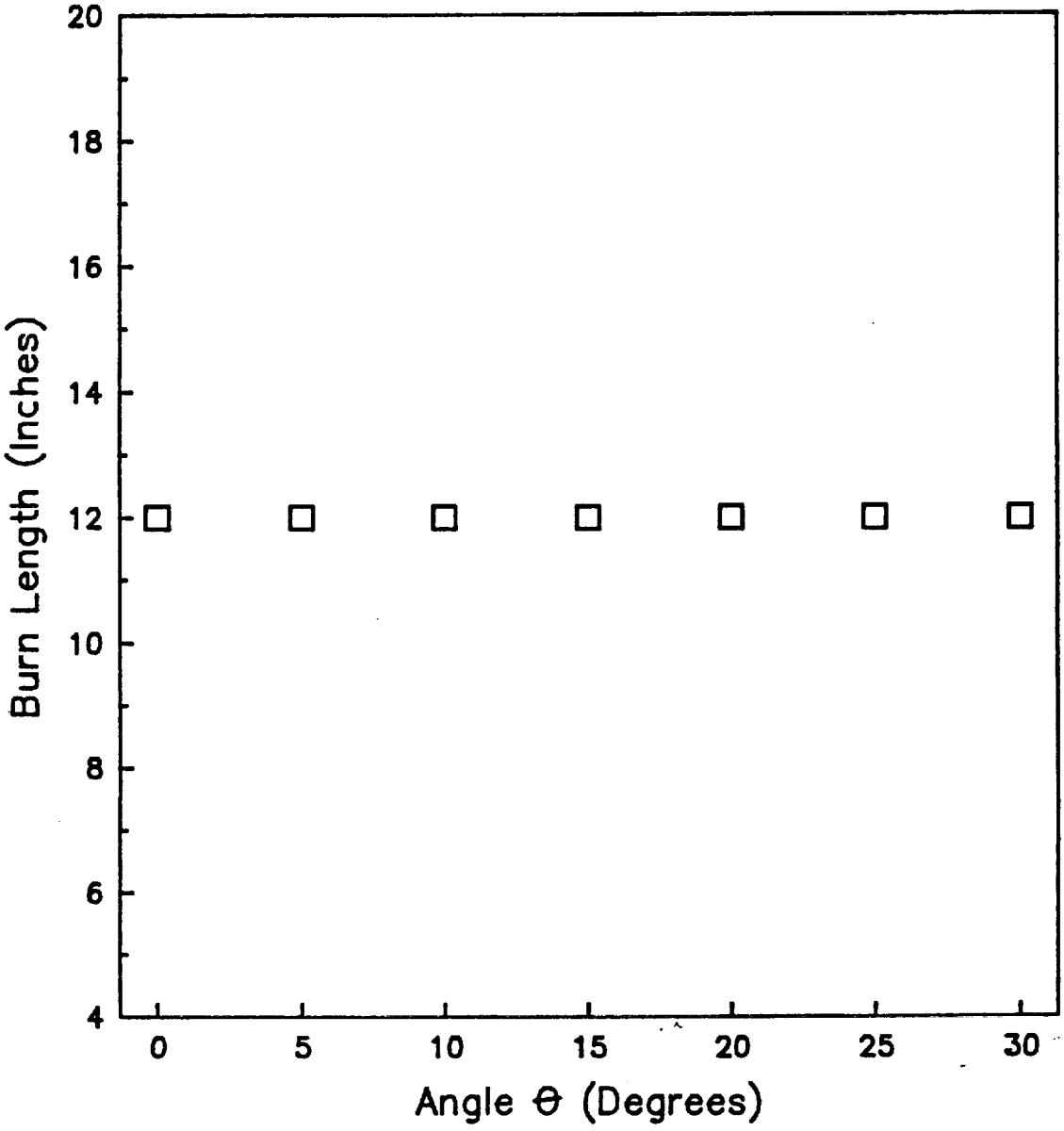

Figure 14
Shrinkage Of AN 120
As A Function Of Angle

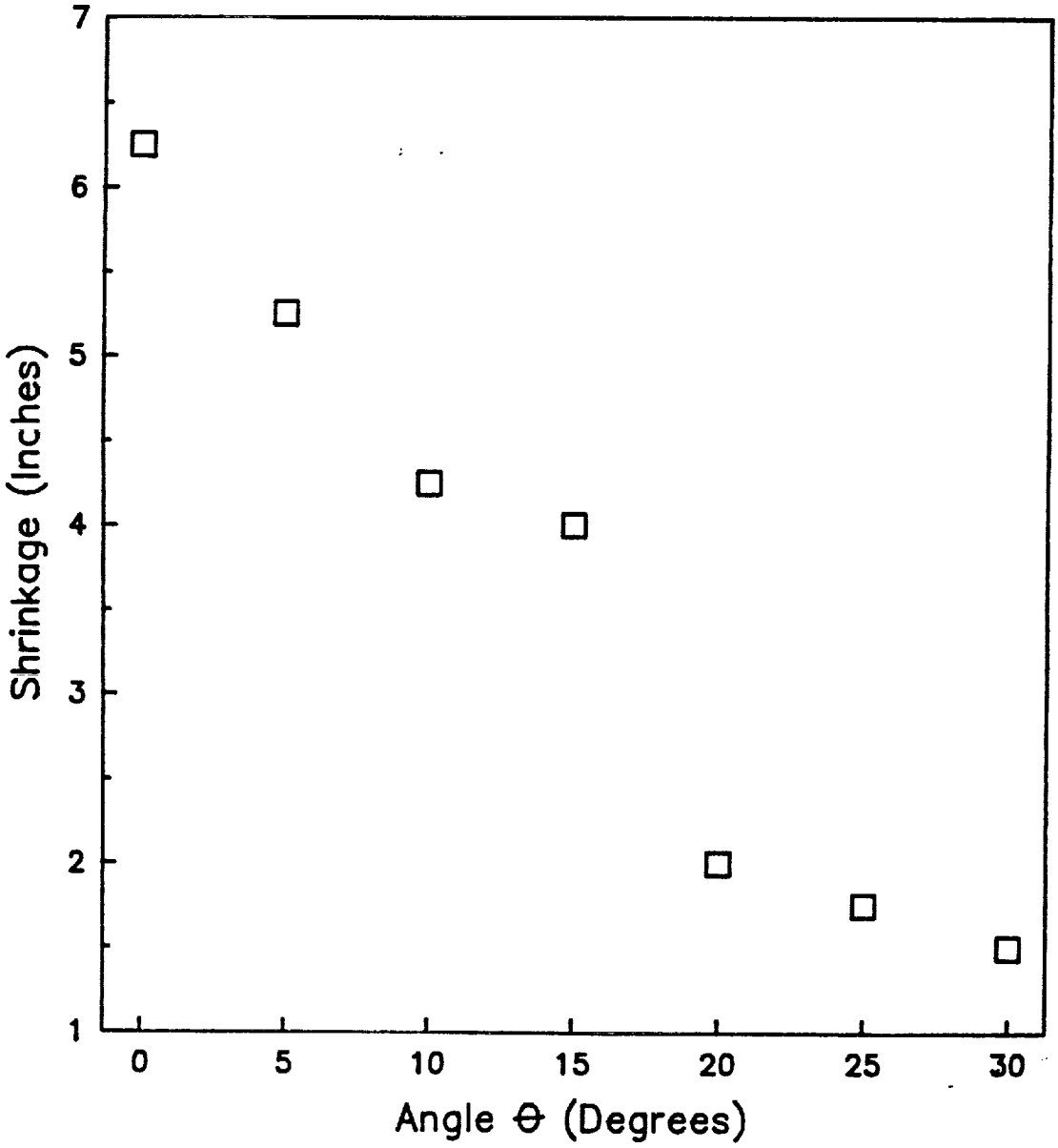

C-5

Figure 15
Shrinkage Of Halar
As A Function Of Angle

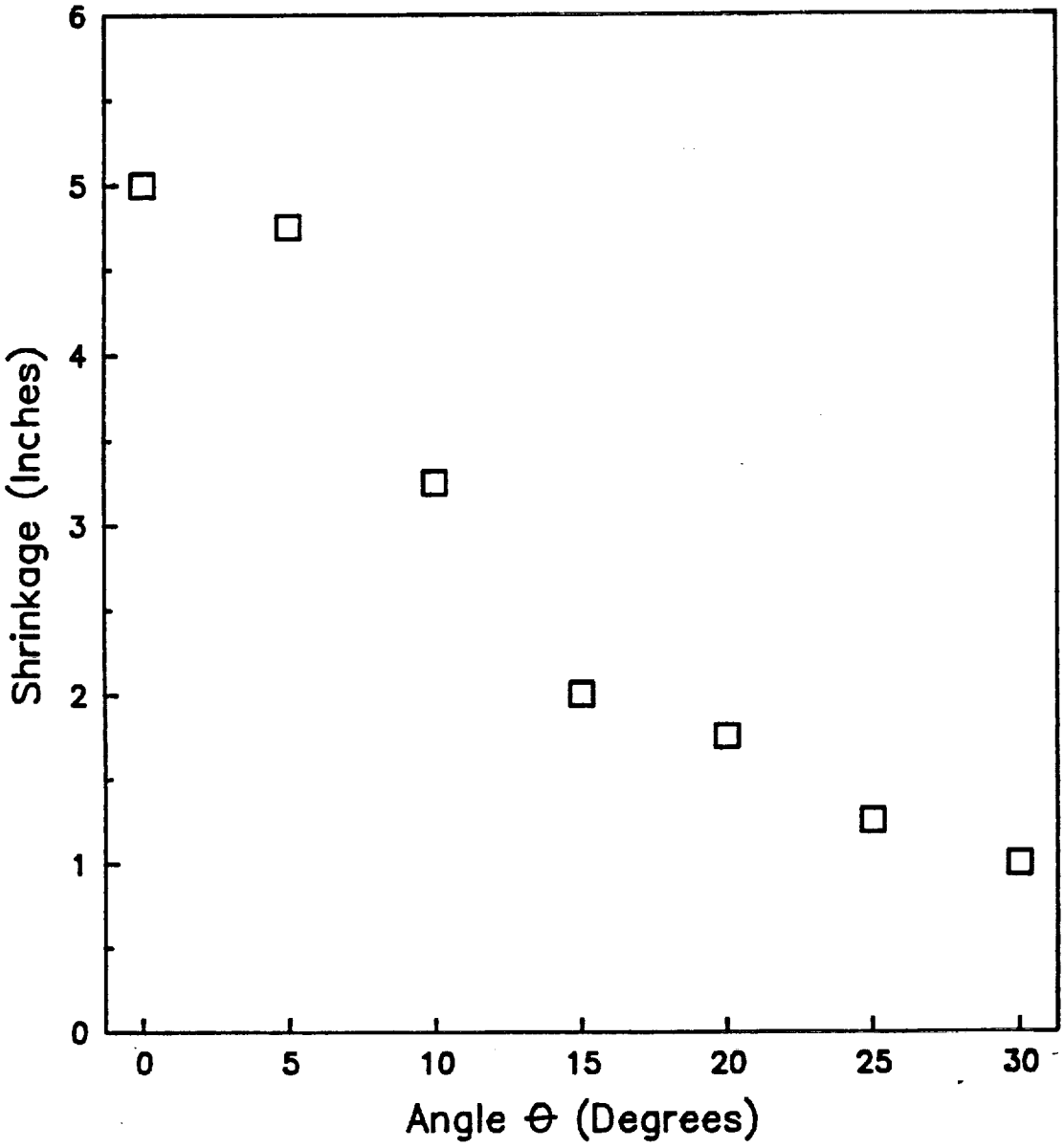

Figure 16
Burn Length Of Herculite 80 As A Function Of Angle

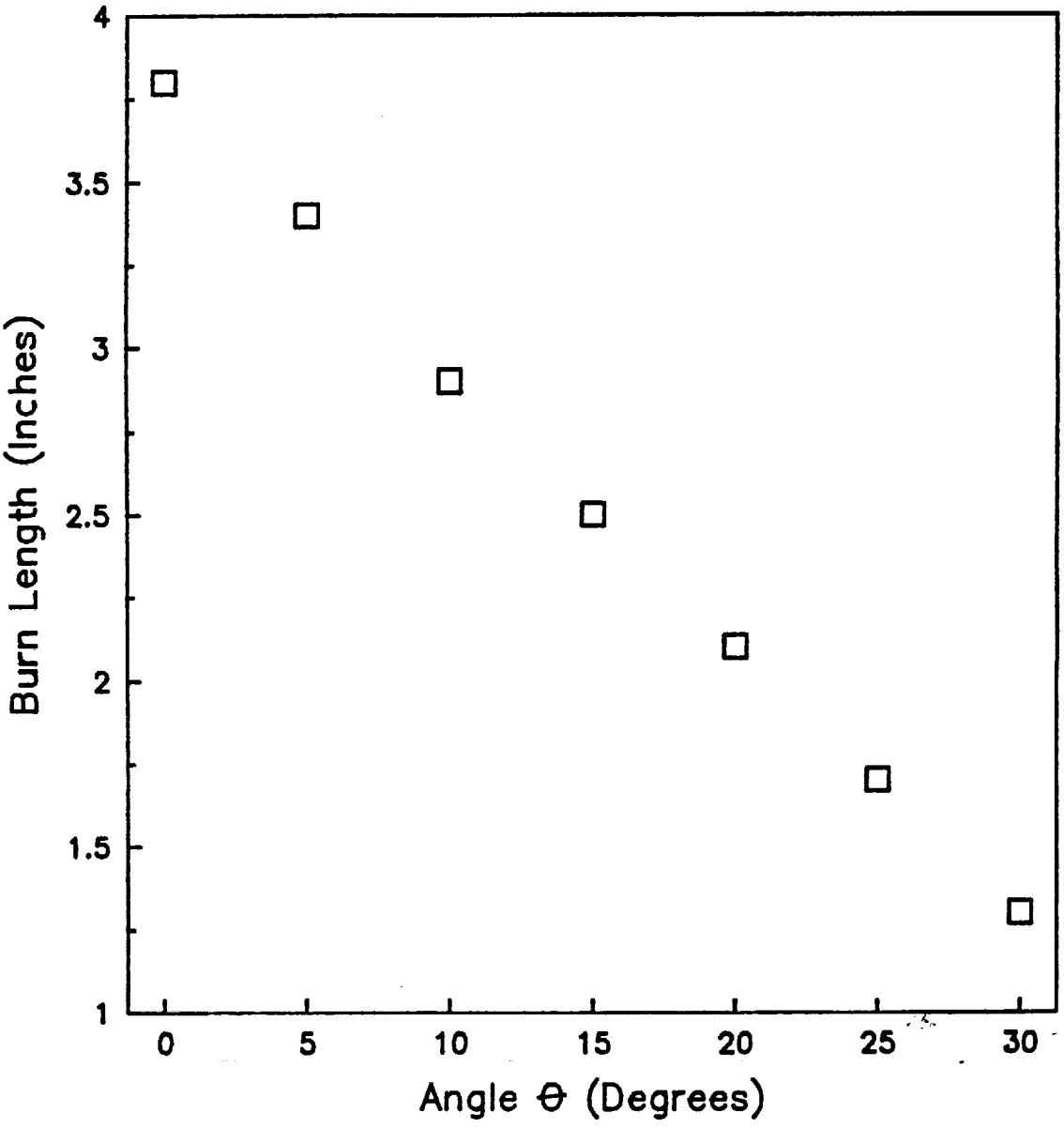

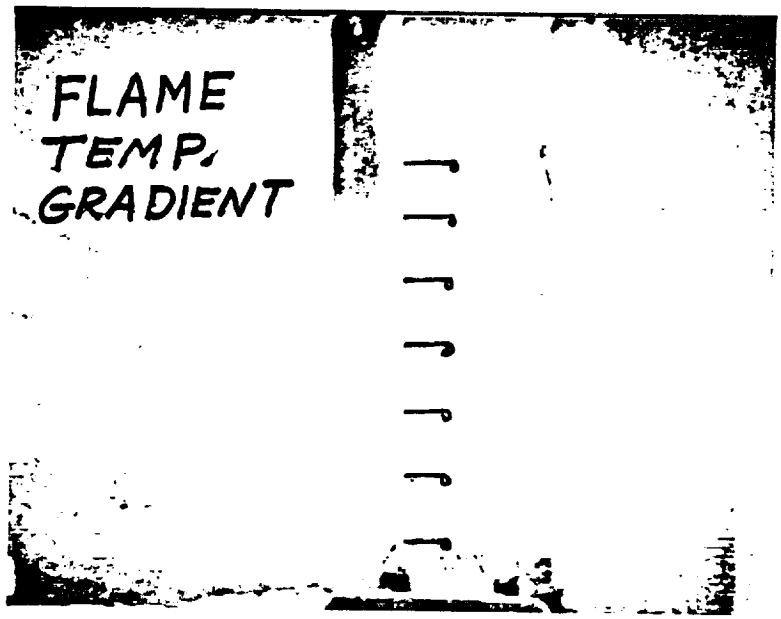

FIGURE 17. THERMOCOUPLE PLACEMENT FOR TEMPERATURE PROFILE ABOVE IGNITION SOURCE

Figure 18
Vertical Flame Temperature Profile

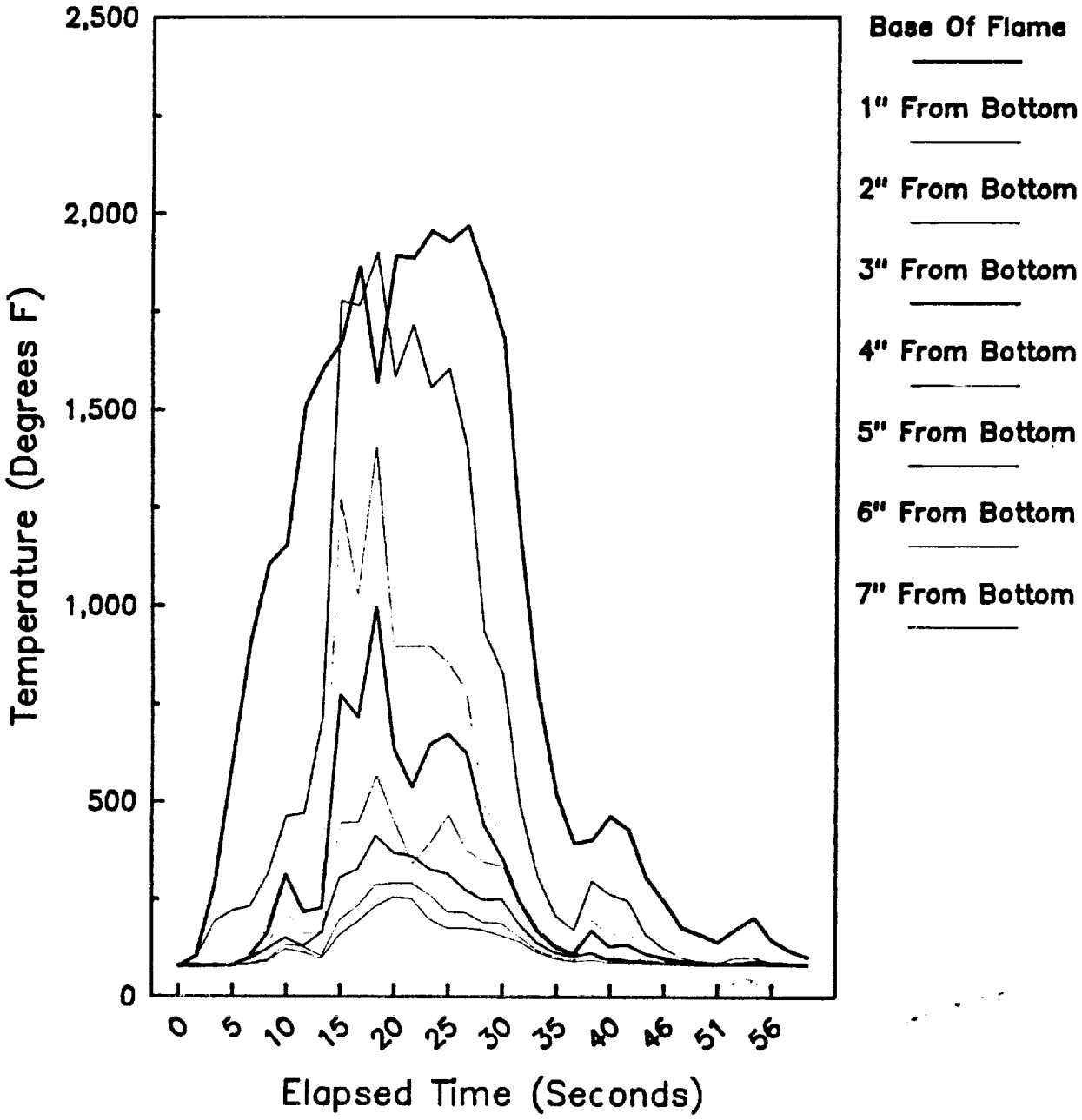

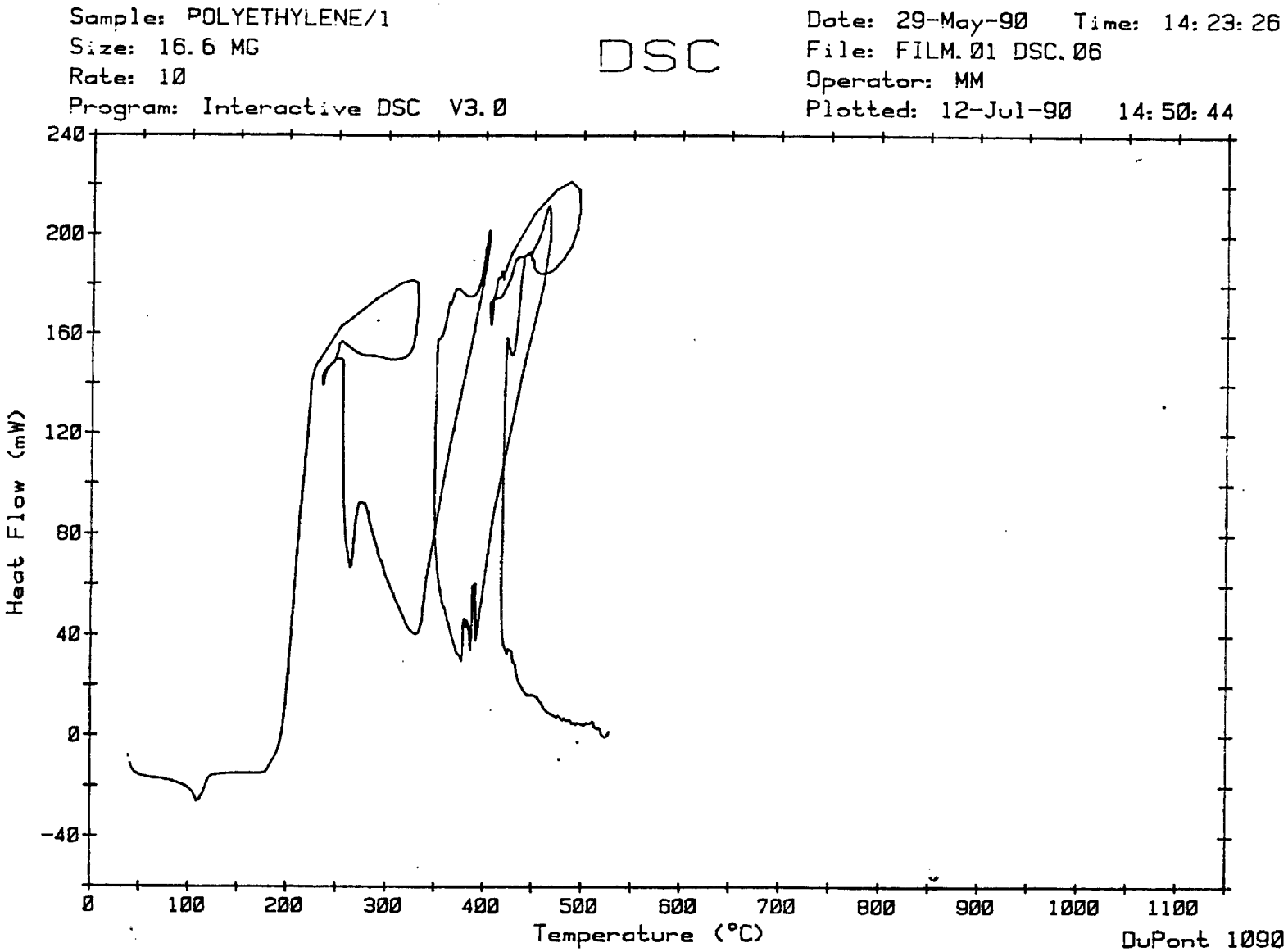

FIGURE 19. AUTO-IGNITION GRAPH FOR POLYETHYLENE

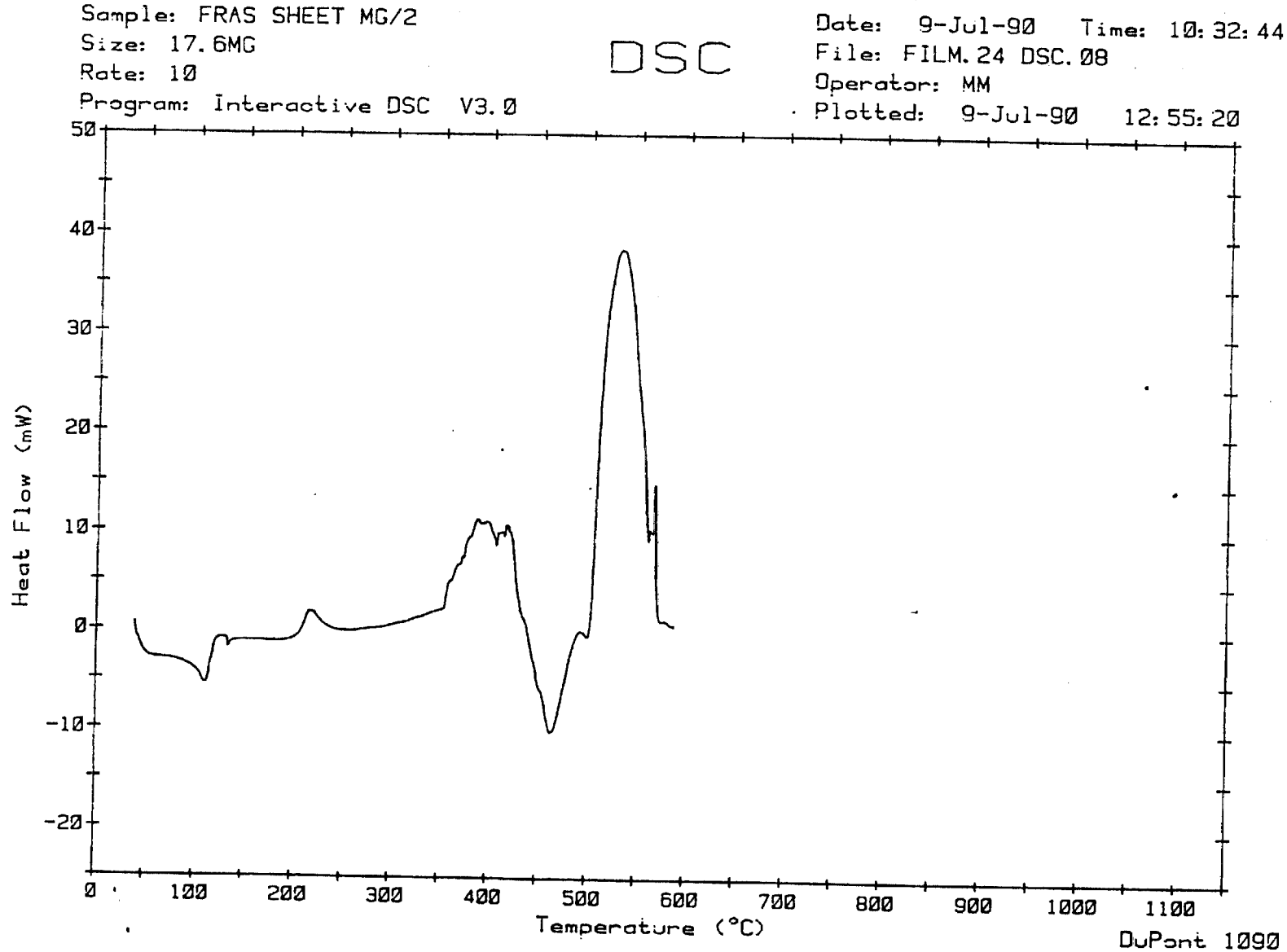

FIGURE 20. AUTO-IGNITION GRAPH FOR FRAS SHEET MG

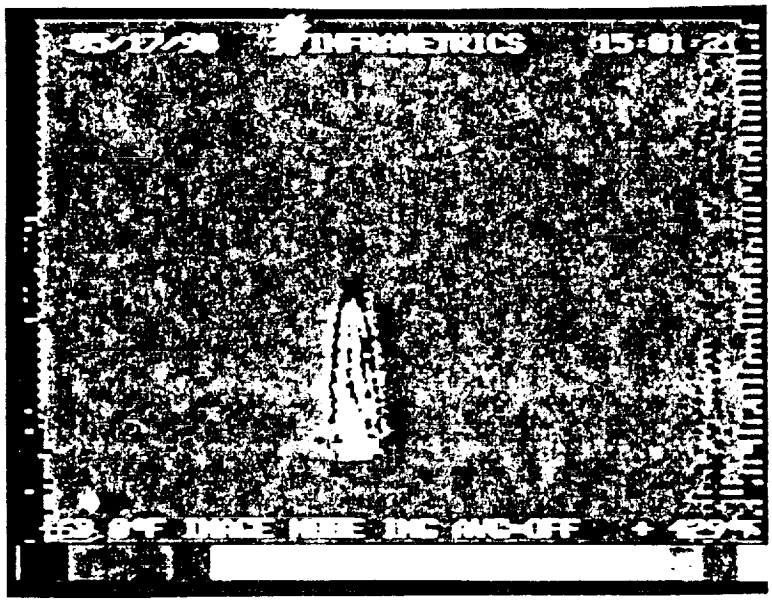

FIGURE 21. INFRARED IMAGING AT TIME X

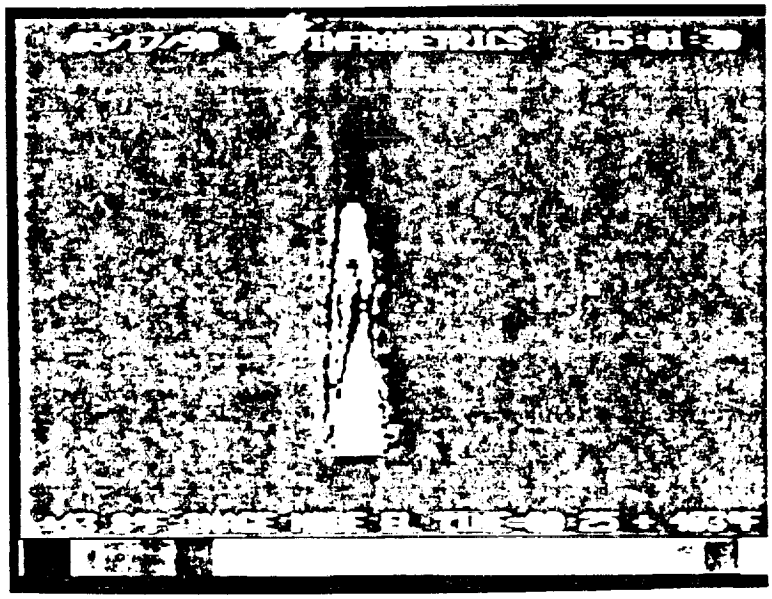

FIGURE 22. INFRARED IMAGING AT TIME X + 2 SECONDS

1990 NASA/ASEE SUMMER FACULTY FELLOWSHIP PROGRAM

JOHN F. KENNEDY SPACE CENTER
UNIVERSITY OF CENTRAL FLORIDA

SOME ASPECTS OF ROBOTICS CALIBRATION, DESIGN AND CONTROL

PREPARED BY:	Dr. Hazem Tawfik
ACADEMIC RANK:	Associate Professor
UNIVERSITY AND DEPARTMENT:	State University of New York - Farmingdale Mechanical Engineering Technology
NASA/KSC	
DIVISION:	Mechanical Engineering
BRANCH:	Special Projects (RADL)
NASA COLLEAGUE:	Mr. V. Leon Davis
DATE:	August 8, 1990
CONTRACT NUMBER:	University of Central Florida NASA-NGT-60002 Supplement: 4

ACKNOWLEDGEMENTS

I would like to thank my KSC colleague Mr. Leon Davis for giving me such a wonderful opportunity to participate in the interesting activities taking place in his robotics section at KSC. Also, thanks should be extended to the whole robotics engineering team for their cooperation; especially the coop student Mr. Tom Woods.

I am also grateful to the UCF program director Dr. Loren Anderson for making the summer program as much fun as it was a challenge. Ms. Kari Baird's enthusiasm and helpfulness was very much appreciated.

Many thanks to the NASA/KSC summer program director Dr. Mark Beymer for his friendliness.

ABSTRACT

The main objective of this project was to introduce the reader to techniques in the areas of testing and calibration, design, and control of robotics systems. A statistical technique was described to analyze a robot's performance and provide quantitative three dimensional evaluation of its repeatability, accuracy, and linearity. Based on this analysis; a corrective action should be taken to compensate for any existing error(s) and enhance the robot's overall accuracy and performance.

A comparison between robotics simulation software packages that were commercially available (SILMA, IGRIP) and that of KSC (ROBSIM) was also included in this report. These computer codes simulated the kinematics and dynamics patterns of various robotics arms geometry to help the design engineer in sizing and building the robot manipulator and its control system.

Finally, this report provided a brief discussion on an adaptive control algorithm.

SUMMARY

Robots are becoming increasingly viable in various applications within NASA/KSC. Most of these applications require more precision and sensory sophistication such as remote umbilical, radiator, tile, payload inspection etc. The mechanical structure of a robot manipulator usually consists of a number of interacting links and joints with separate drive and control systems. Therefore, the various sources of error that each joint could experience will result in a cumulative error and inaccuracy in the positioning of the end effector's tool center point.

Accordingly, a simple and straight forward technique to calibrate a robot and analyze its performance was deemed necessary.

The present report gives a detailed description of both the hardware and software that are used in the development of a statistical technique that provides a three dimensional evaluation of the robot's overall repeatability, accuracy, and linearity. Based on the obtained results and analysis, corrective measures could be taken such that the robot's inverse and forward kinematic software and/or control system would account for the errors to enhance accuracy and performance. In addition, for trouble shooting an operational problem, this technique could also be conducted to examine the accuracy of every individual joint that will help trace and rectify the problem.

The second part of this project provides a comparison between two commercially available computer codes (SILMA and IGRIP) and NASA's (ROBSIM) program. This comparison will help NASA/KSC make a decision regarding the selection of a computer simulation package for the robotics kinematics, dynamics, and control system. Such a package is very useful for an engineer during the design stage to size the various components of a robotics system. The SILMA package was found to be the easiest to use and equipped with the best graphical display that could be integrated with various work stations.

The third part of the report gives a brief discussion on the adaptive control algorithm for the radiator inspection robot. Because of the variation in the manipulator's inertia through the robot trajectory, the torque requirement at the joints will also change with the robot's position. Accordingly, the PID loop optimum gains will also change. The proposed algorithm is based on a closed form polynomial of the 8th order or more to yield the optimum gain values for the PID loop that corresponds with robot location.

TABLE OF CONTENTS

LIST OF ABBREVIATIONS AND ACRONYMS

IGRIP	-	Interactive Graphics Robot Instruction Program
KSC	-	Kennedy Space Center
LaRC	-	Langley Research Center
RADL	-	Robotics Applications Development Laboratory
ROBSIM	-	ROBotics SIMulation program
TCP	-	Tool Center Point

LIST OF ILLUSTRATIONS

I INTRODUCTION

1.1 ROBOTICS IN INDUSTRY

The economical value of the use of robots in industry has been proven because robots increase productivity, enhance quality, and reduce the price per units. Most of the industrial applications require high precision and sensory sophistication such as assembly, deburring etc. However, due to operational, environmental, and manufacturing factors the robot's accuracy deteriorates. Accordingly, initial and periodical testing and calibration of robots is a very important task. Since the beginning of the use of robots in industry back in the 70's until the present time there is no satisfactory calibration and testing scheme to examine the robot's performance and accuracy. The present report provides a detailed description of a precise, simple, and straight forward technique that evaluates the repeatability, relative accuracy, and linearity.

1.2 ROBOTICS At NASA/KSC

As soon as the shuttle returns back from a space mission and rolls into the Orbit Processing Facility it goes through rigorous inspection, service and maintenance routines. Some of these inspection routines lend themselves well as a robotics application such as the radiator, tiles, etc. Also, in the shuttle program at KSC there are other robotics applications that are still in the research and development stage such as remote umbilical connection, payload inspection, etc. In addition, robots are currently used in other processes at KSC such as the coat removing process of the booster rockets using water jets after having been picked up from the ocean.

All these robots previously indicated require routine calibration and testing every four to six months depending on the accuracy requirement of the task to be accomplished. The technique described in this report will not only calibrate the robot but also will help the trouble shooting process by testing each individual joint separately.

1.3 WHEN TO CALIBRATE AND TEST A ROBOT?

Any robot should be tested as indicated in the following:

- After Initial Instalation
- Periodically During Operation
- Trouble Shooting A Problem

II ROBOTICS CALIBRATION AND TESTING

2.1 SOURCES OF ERRORS

The robot manipulator is simply described as an open chain that consists of a number of links and joints to provide the arm with a certain degree of freedom (DOF). The manipulator is fitted to a firm base at one end and an end effector is mounted to the other end of the arm. The arm is designed to provide accurate positioning of the end effector's tool center point (TCP) in the space to conduct certain tasks such as material handling, welding, visual inspection etc.

However, the cumulative errors in all links and joints combined with the possible inaccuracy of the robot's control system will result in an overall error in the location of the TCP. These sources of error could be summarized in the following:

- Servo positioning error (Due to linearization)
- Variations in the links dimensions due to manufacturing tolerances.
- Backlash and wear in the joints due to operation
- Arm deflection due to its flexibility and variation in the environment temperature.
- The zero of the encoder does not coincide with the zero of the joint.
- Forward and inverse kinematics error due to linearization around a nominal operating point.

Accordingly, a simple and straight forward technique was found necessary to evaluate the overall error in the X,Y, and Z directions experienced by the end effector in the positioning of the TCP. The few robotics calibration techniques that are recently available in the literature can be described as rather complicated; and some of them do not reach an acceptable level of accuracy.

2.2 PARAMETERS OF TESTING AND CALIBRATION

The present robotics calibration techniques enjoy both precision and simplicity in the evaluation of the following calibration parameters:

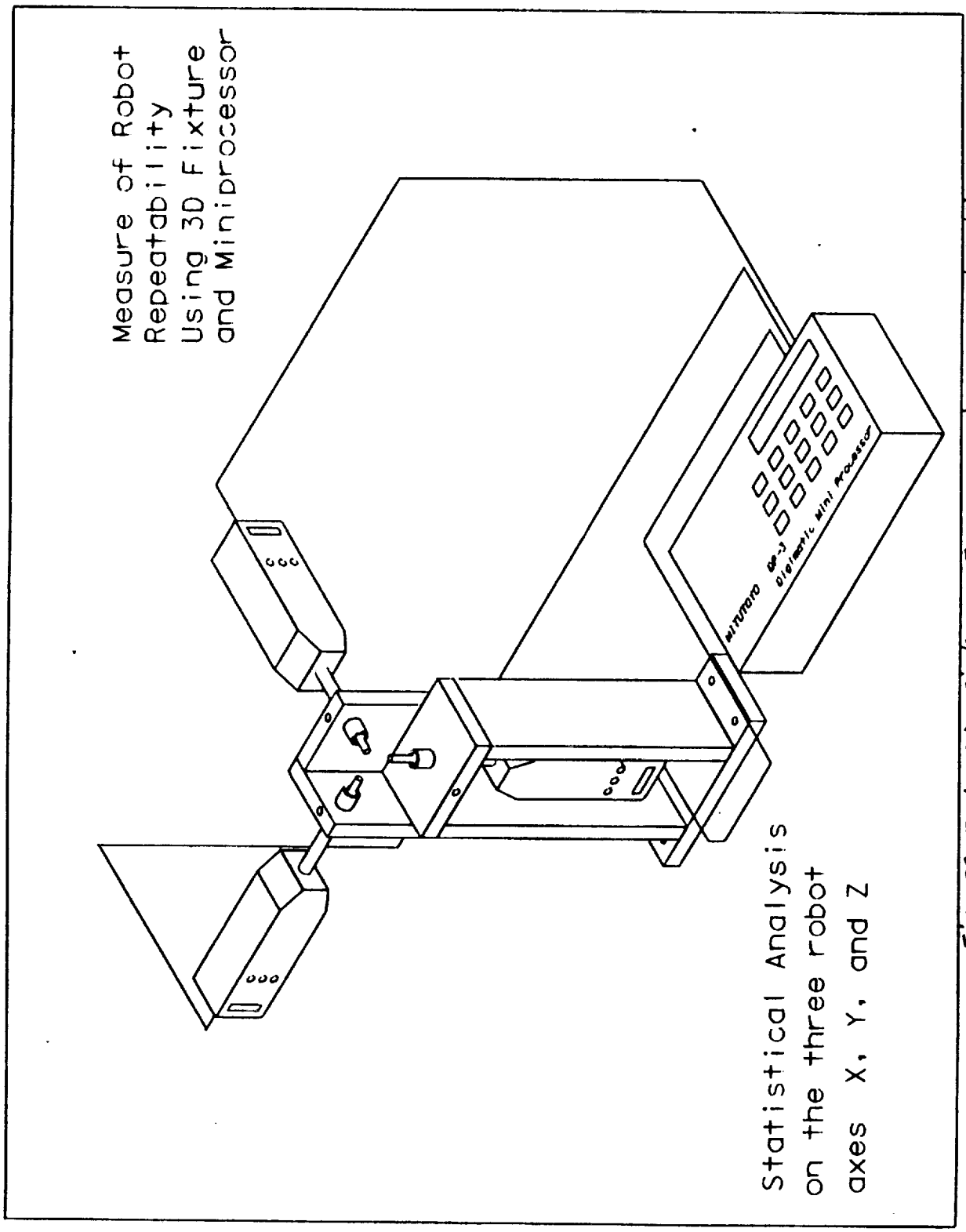

Figure 2-1 3D Fixture For measuring repeatability

E:\DUN\TAWFIK2.MLN JUL. 31, 1990 14:44:58

- Repeatability
- Accuracy
- Linearity

This report provides a detailed description of such a technique supported with illustrative figures and diagrams of both hardware and software that are used in the study, analysis, and evaluation of the previously mentioned parameters. This analysis will help the corrective action decision so the robot forward and inverse kinematic software as well as the control system will account for the calculated errors and improve the overall accuracy of the robot manipulator.

2.3 EVALUATION OF THE ROBOT'S REPEATABILITY IN THREE DIMENSIONAL X,Y,AND Z AXES

The repeatability of a robot is defined as how close the robot will locate the TCP to a previously taught position. A taught position means that the robot should be physically at this point and all the encoder or resolver readings are recorded. This means that the goal points are never specified in cartesian coordinates and the inverse kinematic computation never arises. Simply, repeatability is a teach and playback process. Therefore, the first step in the robot's calibration procedure is the examination of its repeatability. The measurement of the repeatability could be conducted using the calibration fixture with three dial or digimatic indicators as shown in Figure 2-1.

2.4 HARDWARE DESCRIPTION

The hardware consists of the following:

- 3D Calibration Fixture
- Cube With Blunt Front Corner
- Digimatic Mini Processor
- Digimatic Data Logger
- Digimatic Data Transmitter
- Digimatic Dial Indicator
- PC Computer With Math Co-processor and 640K memory
- Communication Cables

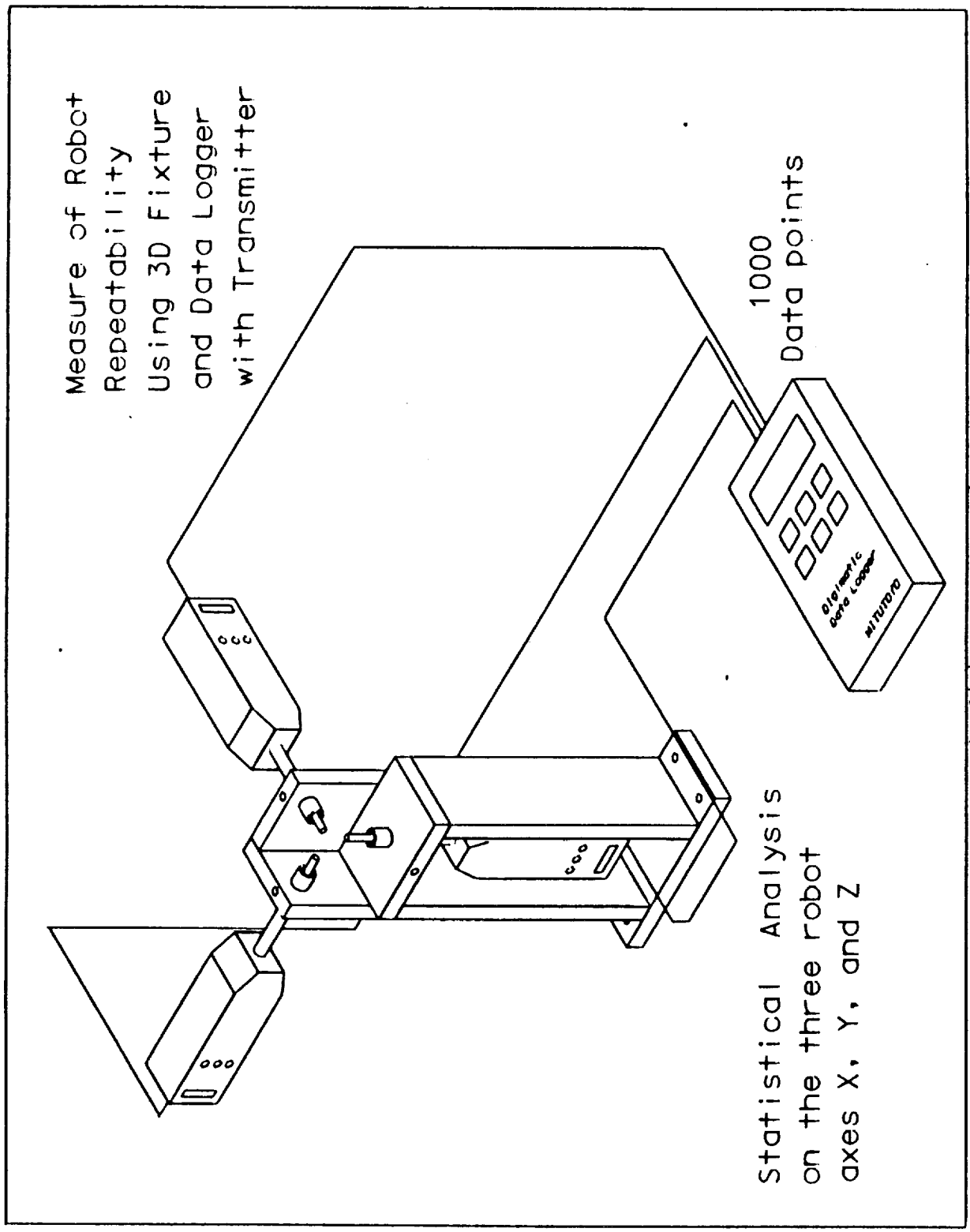

Figure 2-2 3D Fixture connected to Data Logger

E:\DGN\TAWFIK2.HLN Aug 01, 1990 11:02:28

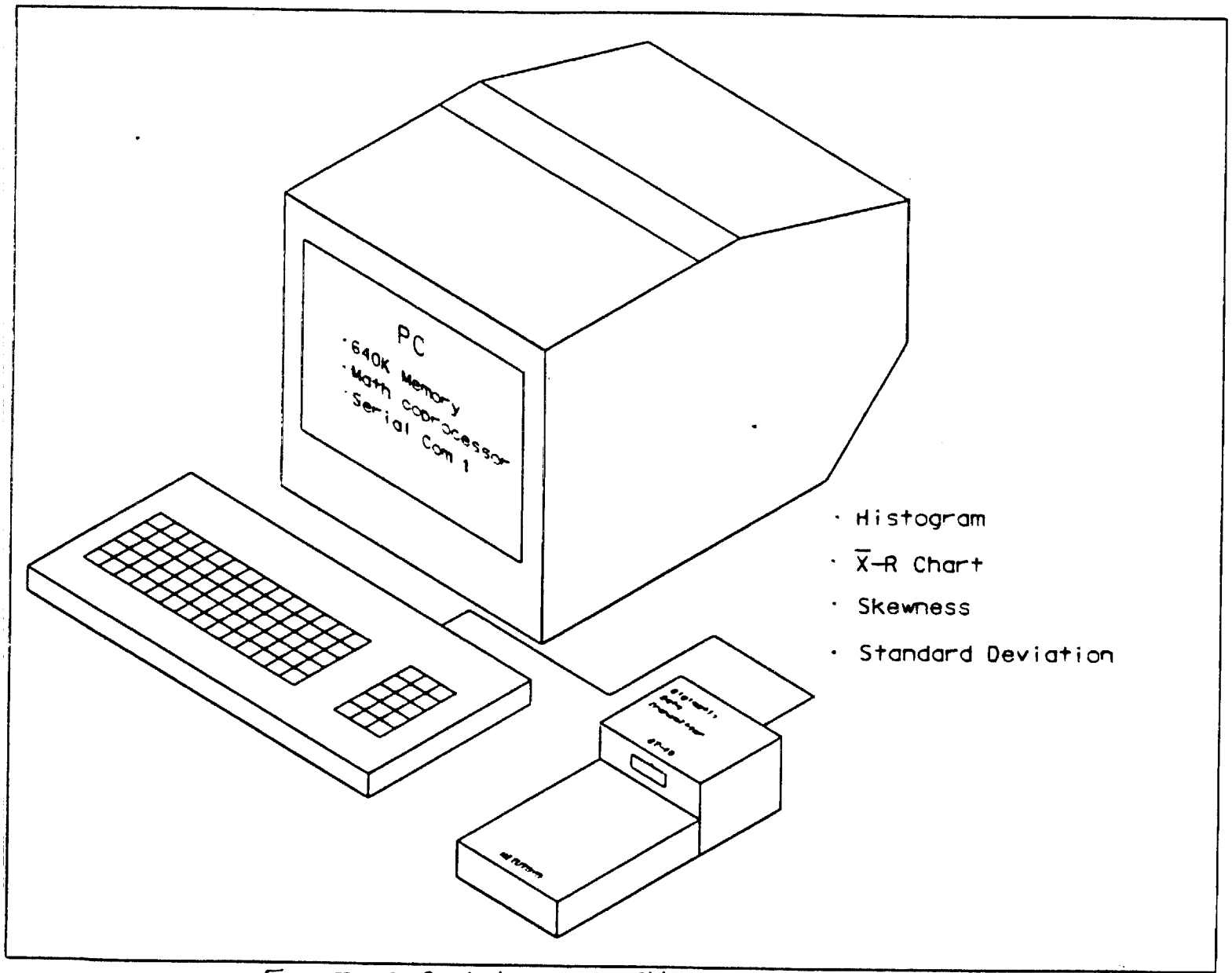

Figure 2-3 Data transmitted to Computer

2.5 DESCRIPTION OF THE SOFTWARE

Two software packages are used to perform the required analyzes and evaluate the following statistical parameters:

- Average or Mean
- Mode
- Standard Deviation
- Skewness
- Range

Also, these packages provide plots of the Histogram, and the Xbar-R charts.

2.6 EXPERIMENTAL PROCEDURE

The experimental procedure consists of the following steps:

- Bolt or clamp the 3D fixture to a surface plate within the work envelope of the robot.
- Install the digimatic dial indicators and lock them to the X,Y, and Z axes as shown in Figure 2-1.
- Mount a cube with a blunt front corner on the end effector of the robot under examination.
- Move the robot such that the cube will fit between the three indicators and cause approximately a 3/8 inch deflection in each indicator.
- Teach that position (A) to the robot controller
- Move the robot about one inch away from the fixture and teach that position (B) to the robot controller.
- Move the robot to any arbitrary position within the work envelope and return back to position (A) via position (B).
- Record or Dump the three indicators readings to the Data Logger device Figure 2-2 and then to the PC computer through the Data Transmitter device and RS232 communication board Figure 2-3.
- Repeat this process 25 to 30 times.

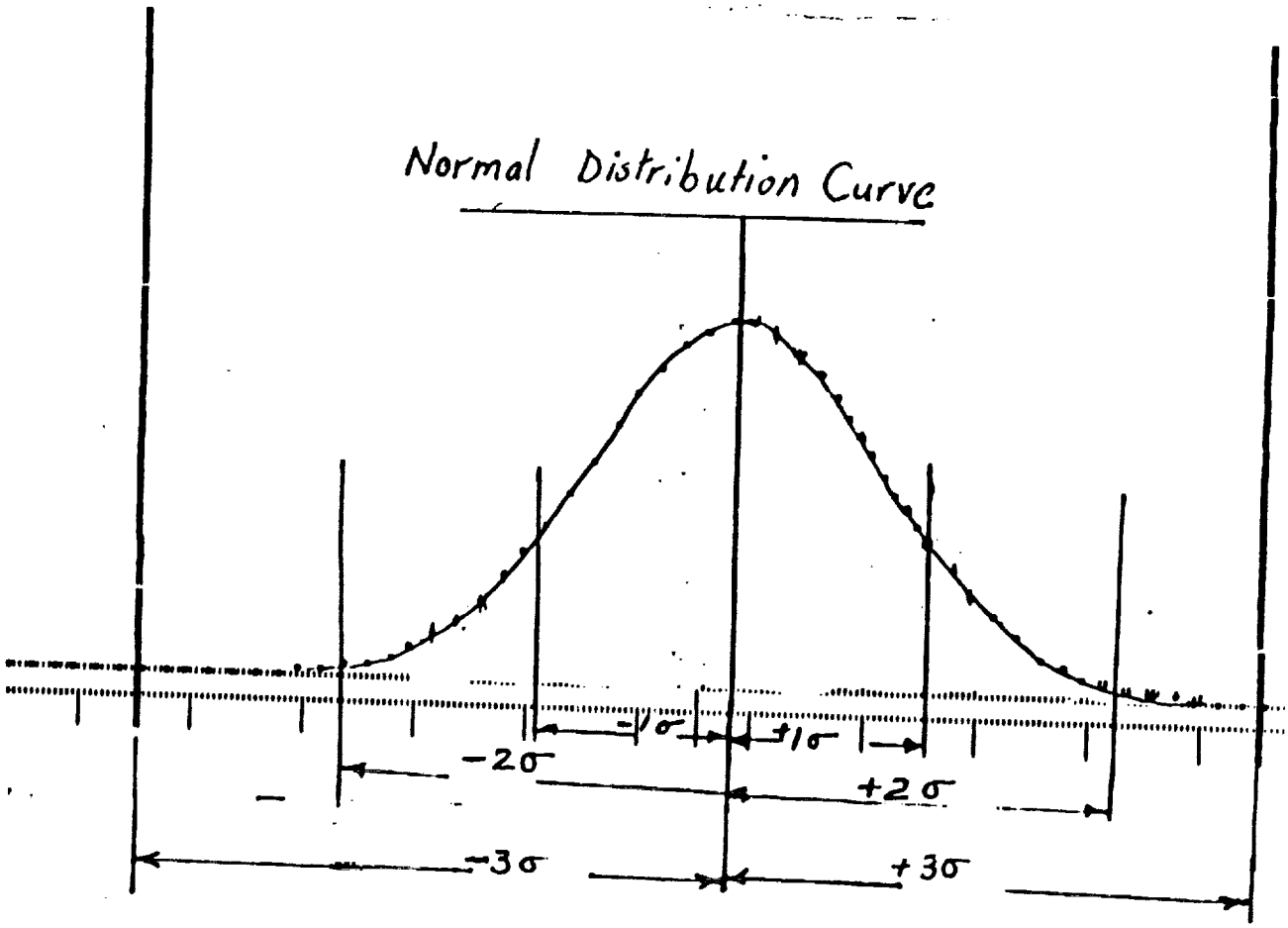

Between ±1σ 68% of the Data

±2σ 95% of the Data

±3σ 99% of the Data

Figure 2-4 Normal Distribution Curve

2.7 DATA ANALYSIS

The data analysis is mainly performed by the two previously mentioned software packages. Also, a numerical example is given later on in this report to support and clarify the procedure.

2.7.1 Visual Observation of the Histogram

The first step of the analysis is the visual observation of the histogram to determine the existence of any skewness. The value of the skewness parameter a_3 given by the software provides an estimate for the degree of skewness in the histogram as shown in the following:

a_3	=	0	Symmetrical Histogram (Figure 2-4)
a_3	>	0	Skewed to the right
a_3	<	0	Skewed to the left

If a_3 is close to the value of + 1 or higher this is an indication that the histogram is highly skewed to the right or to the left; this skewness is usually attributed to an instability in the robot's control system. A corrective action should be taken.

2.7.2 The Location of the Average Line (X bar)

If the average value does not coincide with the nominal value, this amount of error could be attributed to the linearization of the inverse kinematics software and/or the effect of the ambient temperature.

2.7.3 The Robotics Capability Index

When evaluating the robotics system to determine if it is capable of meeting the specification requirements of a certain task, three parameters have to be evaluated as defined by the following three equations, also see Figure 2-4:

$$C_p = \frac{USL - LSL}{6 * \sigma}$$

$$C_{pk1} = \frac{USL - \bar{X}}{3 * \sigma}$$

$$C_{pk2} = \frac{\bar{X} - LSL}{3 * \sigma}$$

as

C_p = Robotics Capability Index (RCI)- The robot will be classified as capable of meeting the task's accuracy requirements if the value of this parameter equals unity or more. If the value of the RCI is less than unity the robot is classified as incapable of performing the task.

C_{pk1} = This parameter will indicate if the robotics system is experiencing any shift off the nominal value. Accordingly, the value of this parameter should exceed unity.

C_{pk2} = Similar to the previous parameter

USL = Upper specification Limit

LSL = Lower Specification Limit

Sigma = Standard Deviation

2.7.4 Xbar-R Chart

The Xbar-R Chart should be examined for out of control signs and/or patterns. Some of these patterns could be summarized in the following:

- One point above the UCL or below the LCL

  UCL = X bar + 3 sigma

  LCL = X bar - 3 sigma

- Seven points in the row going up or down
- Fifteen points in the row going up and down
- Two points out of three are in zone "C"

2.7.5 Numerical Example

Consider a robot that is used in the assembly of mechanical parts, the nature of the task requires robot's repeatability as 0.001 in.

The following table 2-1 shows 30 arbitrary data points chosen to numerically present the procedure and analyses for only one axis the X axis say. Also, a Histogram was drawn for this set of data as shown in Figure 2-5.

In this example the average (X-bar) = 0.00008 inch which also indicates the repeatability in the X direction.

Accordingly, Total Repeatability = SQR((X-barx)^2 + (X-bary)^2 + (X-barz)^2)

Skewness (a_3) = - 0.356

This value of the skewness parameter indicates that the robot's control system could be experiencing a certain degree of bias. However, if the value of a_3 exceeded unity a corrective action should be considered.

Robot Capability Index C_p = (USL LSL)/(6 * sigma)

USL = + 0.001 inch

LSL = - 0.001 inch

The Standard Deviation (sigma) = 0.00026

C_p = 1.28 (Robot is Capable)

C_{pu} = (USL - X bar)/ (3*sigma)

= (.001 - .0008) / (3 * 0.00026) = 0.256

C_{pl} = (X bar - LSL) / (3 * sigma)

= (.0008 - (- 0.001)) / (3 * 0.00026) = 2.3

Both C_{pu} and C_{pl} should be larger than unity for no corrective action

The current numerical example indicates that the robot needs adjustment.

X bar - R Charts

The data shown in table 2-1 are plotted in an X bar - R chart as depicted in Figure (2-6). The study of this X bar - R chart shows no patterns or signs of out of control as previously explained.

DATE PRINTED 08-02-1990

PAGE

BASIC STATISTICS COMPREHENSIVE REPORT ON hht1

PART DESCRIPTION: calib

LOT DESCRIPTION: calib

SUBGROUP NUMBER: 1 SUBGROUP CODE: 1 08-02-1990 19:14

FEATURE: A NO. SUBGROUPS: 1 NO. PIECES/SUBGROUP: 30

MAXIMUM: +0.00070 AVERAGE: +0.00008 MINIMUM: -0.0005(

UPPER SPEC: +0.00100 NOMINAL: +0.00000 LOWER SPEC: -0.0010(

TOTAL NUMBER OF PIECES: 30 SIGMA: +0.00026 RANGE: 0.0012(

PIECES ABOVE UPPER SPEC: 0 PERCENT ABOVE UPPER SPEC: 0.00

PIECES BELOW LOWER SPEC: 0 PERCENT BELOW LOWER SPEC: 0.00

PIECE	MEASUREMENT	PIECE	MEASUREMENT	PIECE	MEASUREMEN
1	+0.00020	11	+0.00030	21	+0.00040
2	+0.00010	12	-0.00020	22	-0.00020
3	-0.00010	13	+0.00010	23	+0.00000
4	-0.00040	14	+0.00020	24	+0.00000
5	+0.00040	15	+0.00070	25	+0.00020
6	+0.00030	16	+0.00010	26	-0.00010
7	+0.00010	17	+0.00020	27	+0.00020
8	-0.00050	18	-0.00050	28	+0.00010
9	+0.00020	19	+0.00030	29	+0.00020
10	+0.00010	20	-0.00010	30	+0.00000

Table 2-1 Data Points Collected from One Axis of the 3D Fixture

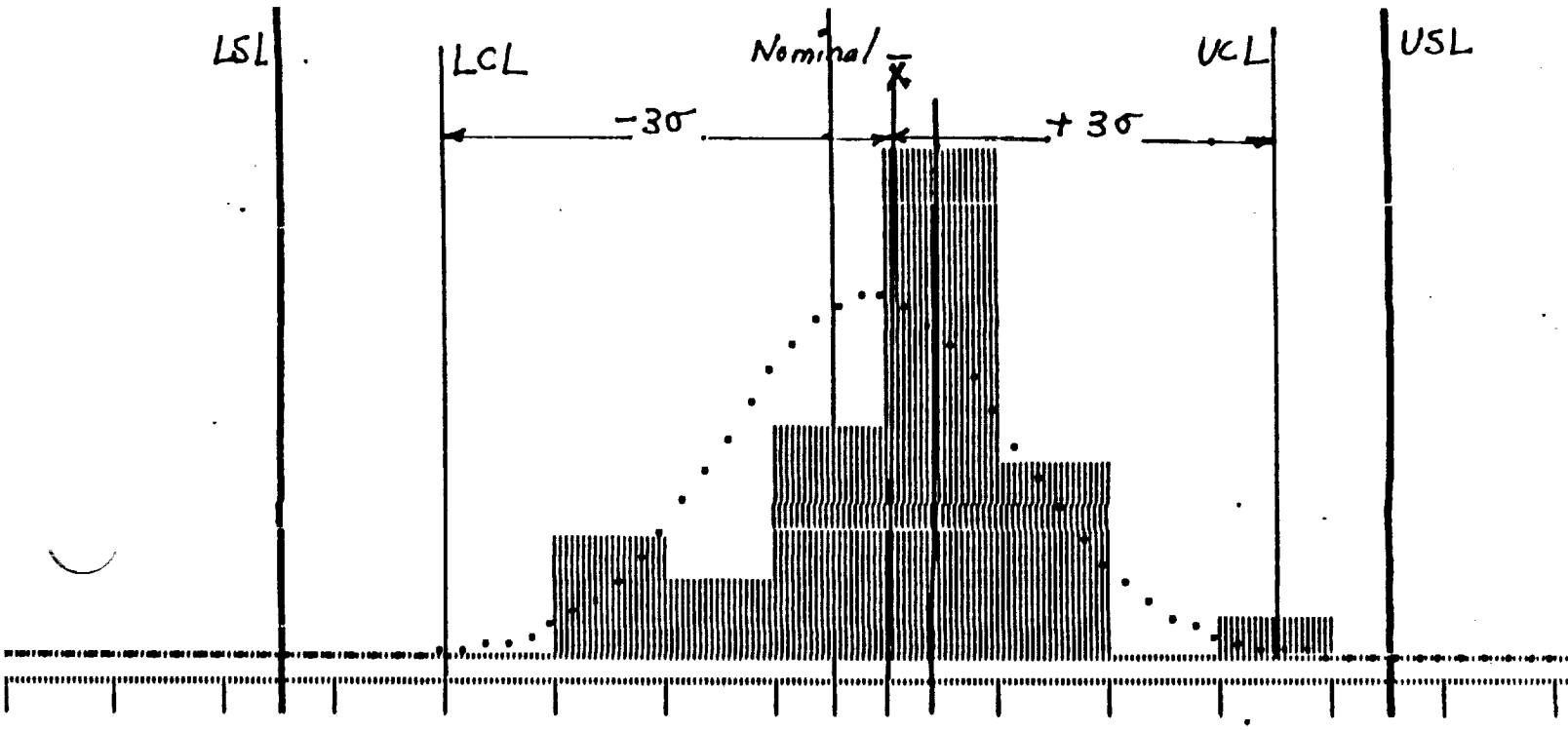

MAX:	+0.00070	USL:	+0.00
⟨BAR:	+0.00008	NOM:	+0.00
MIN:	−0.00050	LSL:	−0.00
SIG:	+0.00026	RNG:	0.00
MODE:	+0.00020	INTERVAL:	+0.00

Figure 2-5 Histogram

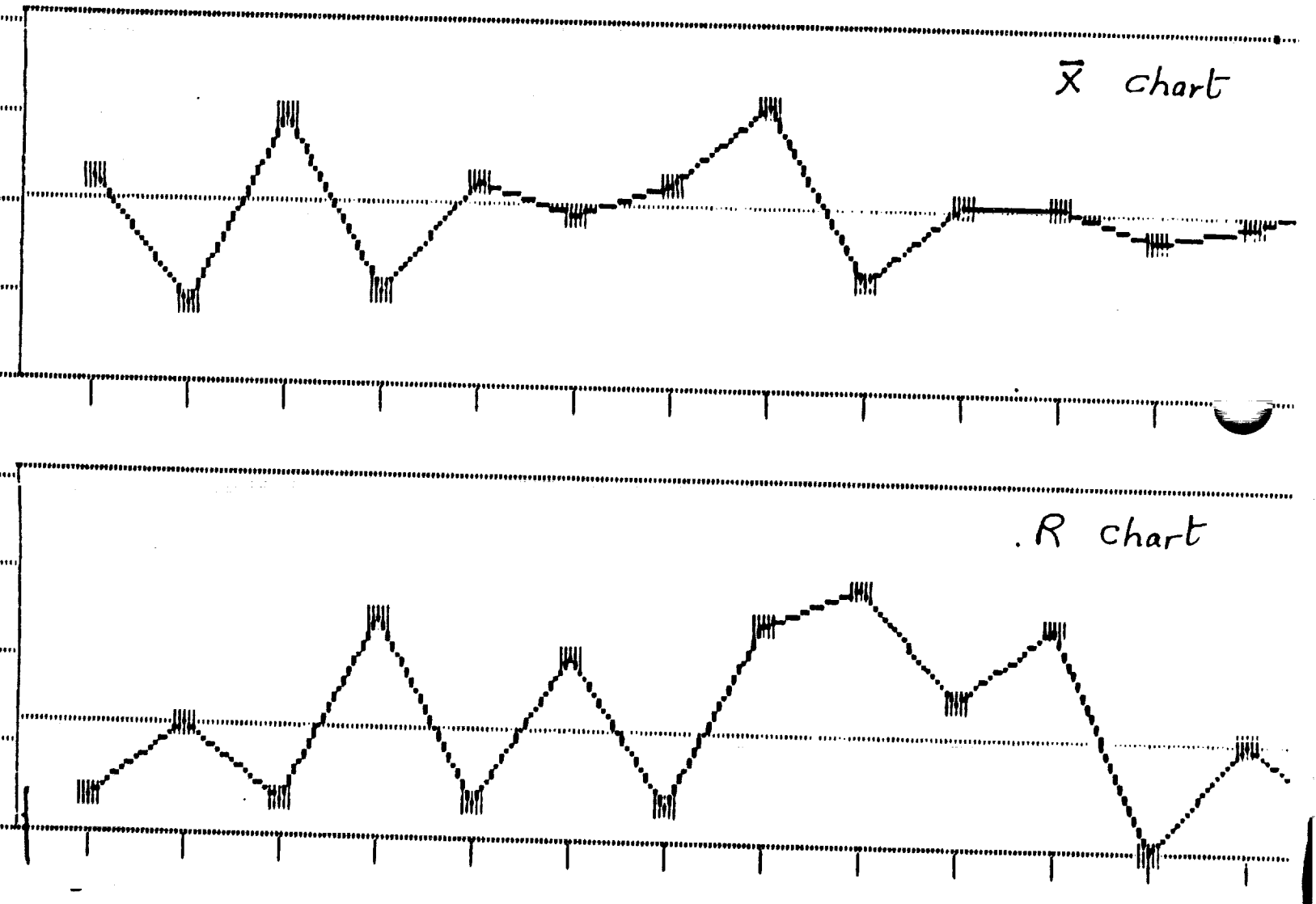

Figure 2-6 $\bar{X}$-R charts

2.8 TESTING ROBOT'S ACCURACY IN THE THREE X,Y, and Z AXES

If the robot's repeatability is proven to be acceptable this will lead to the second step which is the checking of its accuracy. Accuracy, however, is defined as the precision with which a goal position, specified in cartesian terms, is attained. Accordingly, the inverse kinematics must be computed to find the required joint angle that yield the precise positioning of the TCP at the specified point. This will represent an additional source of error that will only influence the robot's accuracy but not its repeatability. Due to the linearization and approximation of most robotics inverse kinematic models associated with the possibility of more than one solution, robots in general are more repeatable than accurate.

Therefore, a good analytical technique, precise measurements and efficient data acquisition scheme are deemed necessary for detailed examination of any robot performance. Such a technique could also be used to trouble shoot an operational problem by monitoring the individual performance of the manipulator's joints.

According to the previous definition of accuracy the following two types should be considered they are as follows:

- Absolute Accuracy
  Measured with respect to the world coordinate system of the robot

- Relative Accuracy
  Measured in reference to any other coordinate system such as TCP, Encoders, etc.

The knowledge of the relative accuracy of a robot is much more important than the absolute in most applications. Therefore, this report is only concerned with the evaluation of the robot 's relative accuracy with respect to its encoder's reference points.

2.8.1 Experimental Set Up

The experimental set up is clearly exhibited in Figure (2-7) it consists of two 3D fixtures similar to that used in the repeatability measurement.

2.8.2 Experimental Procedure

The experimental procedure could be simply described in the following:

- Place the two fixtures as far apart as possible and still be within the work envelope of the robot.

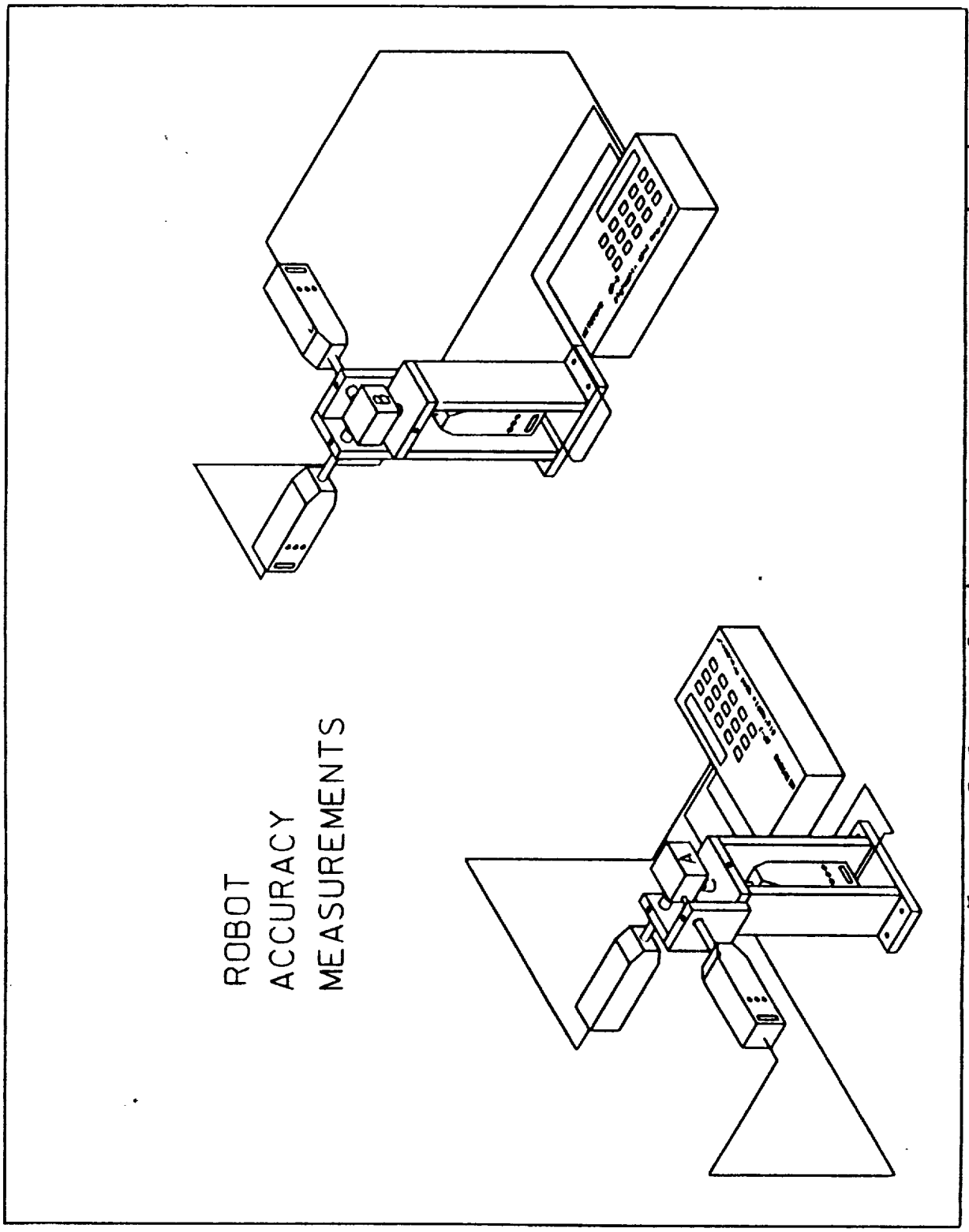

Figure 2-7 3D Robot Accuracy measurement set up

E. \DGN\TAWFIK2.HLN Jul. 31, 1990 13.19.33

- Place the blunt nose cube that is fitted to the end effector of the robot between the indicators of the first fixture to cause an approximate deflection of .5 inch in each indicator.
- Zero off the indicators and set this position as home for the robot arm i.e. all robot's encoders will read zero at this point.
- Move the arm to the second fixture and place the cube between the indicators tips to depress them for about .5 inch each.
- Read and record the teach pendent display of the X,Y, and Z coordinates of this second point.
- Zero off all indicators once more as well as set this position to home.
- Command the robot to go back to the first fixture through an inverse sign of the previously recorded point.
- Record or transmit the readings of the X,Y, and Z indicators to the computer for analysis and evaluation of the mean relative accuracy in each axis.
- Change the positions of these fixtures and repeat the procedure a few times to cover most of the work envelope.
- Evaluate the overall average accuracy in the direction of each axis.

2.8.3 Data Analysis

The analysis of the accuracy evaluation is similar to the previously described analysis for the evaluation of repeatability.

However, if the overall accuracy of each axis is within an acceptable range and the robot has not been classified as out of control, the error could be accounted for either in the control system gains or the inverse kinematic model of the robot. This will result in better accuracy and general improvement in the robot performance.

2.9 Testing of Robot's Linearity

The testing of the robot's linearity means examining its ability to move in straight line trajectories. To evaluate such ability an experimental set up is shown in Figure (2-8).

2.9.1 Equipment Requirement

The Equipment needed to evaluate the linearity of a robot consists of the following:

- Right angle holder for fitting two perpendicular indicators
- Parallel bar with parallelism and perpendicularity up to + 0.0001
- Linear scale with resolution of 0.0001 inch

2.9.2 Experimental Set Up

The experimental set up is summarized in the following:

- Mount the indicators on the holder such that they will be perpendicular to each other to few seconds
- Fit the combination of the holder and indicators to the end effector of the robot.
- Screw the linear scale to the side of the parallel bar
- Prepare a rigid connection between the linear scale and the indicator holder so the position of the TCP along the bar could be monitored.

2.9.3 Experimental procedure

The experimental procedure is as follows:

- Move the end effector until the indicators touch the horizontal and vertical surfaces of the parallel bar near one of its ends.
- Move further in till both indicators are depressed against the bar surfaces approximately .5 inch each.
- Connect the linear scale to the indicators holder
- Zero off the indicators as well as the linear scale and teach the robot this position (A)

Figure 2-8 Experimental set up for linearity measurements

E:\DGN\TAMFIK2.HLN Aug. 01, 1990 13:06:53

- Move the end effector with the holder near the other end of the bar in a straight line motion to the best of the robots ability.
- Teach the robot this point (B)
- Zero off the indicators and the linear scale once more
- Command the robot to shuttle between (A) and (B) for 25 to 30 times
- Collect data through each stroke and perform analysis similar to that previously described to evaluate the robot's linearity.

III EVALUATION OF "ROBSIM" AND ITS USEABILITY AT NASA/KSC

3.1 Introduction

Due to the continuous expansion in the Robotics Application Development Laboratory (RADL) at KSC a good computer software package is needed to help the engineers design and size Robotics components. Currently, there are few packages that are commercially available as well as ROBSIM that is developed by NASA contractors.

Naturally, the ROBSIM package is available for any of NASA's Centers free of charge. However, the package that was given to KSC in 1989 or earlier, was found to be an incomplete according to Langley Research Center (LaRC) personnel. This was the reason that Dr. Gregory L. Tonkay could not use ROBSIM and give a fair evaluation of the package during his NASA/ASEE Summer Faculty Fellowship program in 1989. One of Dr. Tonkay concluding remarks was that " ROBSIM is awkward to learn, and use".

3.2 Package evaluation

Although the package has been completed, according to KSC personnel, I still concur with Gregory's findings with regard to ROBSIM's poor interaction with the user and it is not user friendly.

Also, it has limited graphics capability using Evans & Shutherland as well as poor collision avoidance model.

On the other hand, one should not ignore ROBSIM's good points such as:

- It provides a wide range of robotics design and analysis capabilities
- It models the kinematics and dynamics patterns of a robot manipulator
- It simulates linear control system with a PID loop
- It provides adaptive control algorithm

A comparison between ROBSIM package and other packages that are commercially available is given in table (3-1) next page.

Table 3-1 Comparison Of Robotics Simulation Software

Feature	ROMSIM	IGRIP	SILMA
Ease of Use	Cumbersome, Difficult, May not be Free of Errors	Easy, Mouse-driven Menus	Easy, Mouse-driven Menus
Control System Simulation	Adaptive Control System Algorithm	Linear Control	Linear Control with PID Loop
Kinematic Solution	Internal Solution	Provide Multiple Arm Configuration And Allows Adding More Through C-Program	Provide efficient Closed Form Solutions for Inverse Kinematics of Multiple Configuration and Allows To Add New Robots Config. To The Cimstation Library
Dynamics	Requires Too Much Detailed Information To Generate Interactive Forces and Torques At The Joints.	The Robot Controller Could Be Connected to the Work Station and Directly Drive the Robot Model on the screen.	Simulate general Dynamics Of Manipulator, Compute Forces and Torques At Joints
Collision	Poor Model For Collision Avoidance	Collision Detection, Exact Intersection of Surfaces	Collision Detection, Min. Distance Analysis
Graphics	Poor Wireframe	Wireframe, Shaded Surfaces	Wireframe, Shaded Surfaces
Graphics Hardware	Evans & Shutherland For Full Graphics, VT 240 For Limited Graphics	Intergraph Workstation	Intergraph Workstation or Similar

Table 3-/ Comparison of Robotics Simulation Software (Cont.)

Feature	ROBSIM	IGRIP	SILMA
Workcell Integration	Not Available	Not Available	Generate Simulation Programes for actual Workcell Devices
Animation	Not Available	Not Available	Graphical Representation Of Workcell Simulation
Cost	No Cost	$ 70,000 - 100,000	$ 70,000 - 100,000
Systems	VMS operating System		UNIX Environment

3.3 Results and Discussion

In view of the current study and the comparison table (3-1) one could come to the following recommendations:

- In case of budget availability IGRIP or SILMA package is recommended
- In case of budget unavailability a good manual should be prepared for ROBSIM so its inverse kinematic, Dynamics, and Control models could be easily used for calculating the torque requirements at the joints, arm configuration, control system specifications, etc.

IV ADAPTIVE ALGORITHM FOR THE CONTROL SYSTEM OF THE RADIATOR INSPECTION ROBOT

4.1 Introduction

The motors of the control system of the radiator inspection robot are currently being selected. The sizing of these motors are based on the maximum torque requirement calculations given be Todd Graham's planer model that is based on Kane's equations. Also, this model provides the interaction forces and moments at the joints that have been incorporated in the design and configuration of the control system.

4.2 The Servo Control System

The control system for the three joints of the robot arm are outlined in Figure 4-1. It could be noted that each joint is controlled with a similar system. However, the transfer function of the linearized inertia terms of each link and the interactive torques on each joint are different and varying with position and time. Therefore, the optimum PID loop gains that provide the most smooth and accurate operation with each joint control system will also vary with time and location.

However, for a repeatable task like that performed by the radiator inspection robot the optimum gains could be only related to the robot's positions.

4.3 Adaptive Algorithm

The proposed adaptive control algorithm is to overcome the effects of the position-varying manipulator dynamics on system performance by providing updated values of the control system gains. This could be achieved by finding the optimum gains at few positions through the robot's path that include both the beginning and end points Figure 4-2. MATRIXX7.1 could be used to find these gains. A least square or equivalent curve fitting technique will provide a polynomial that yields each gain as a function of joint location (q). For example:

$$K = a_0 + a_1 q + a_2 q^2 + a_3 q^3 + \ldots\ldots\ldots\ldots\ldots + a_n q^n$$

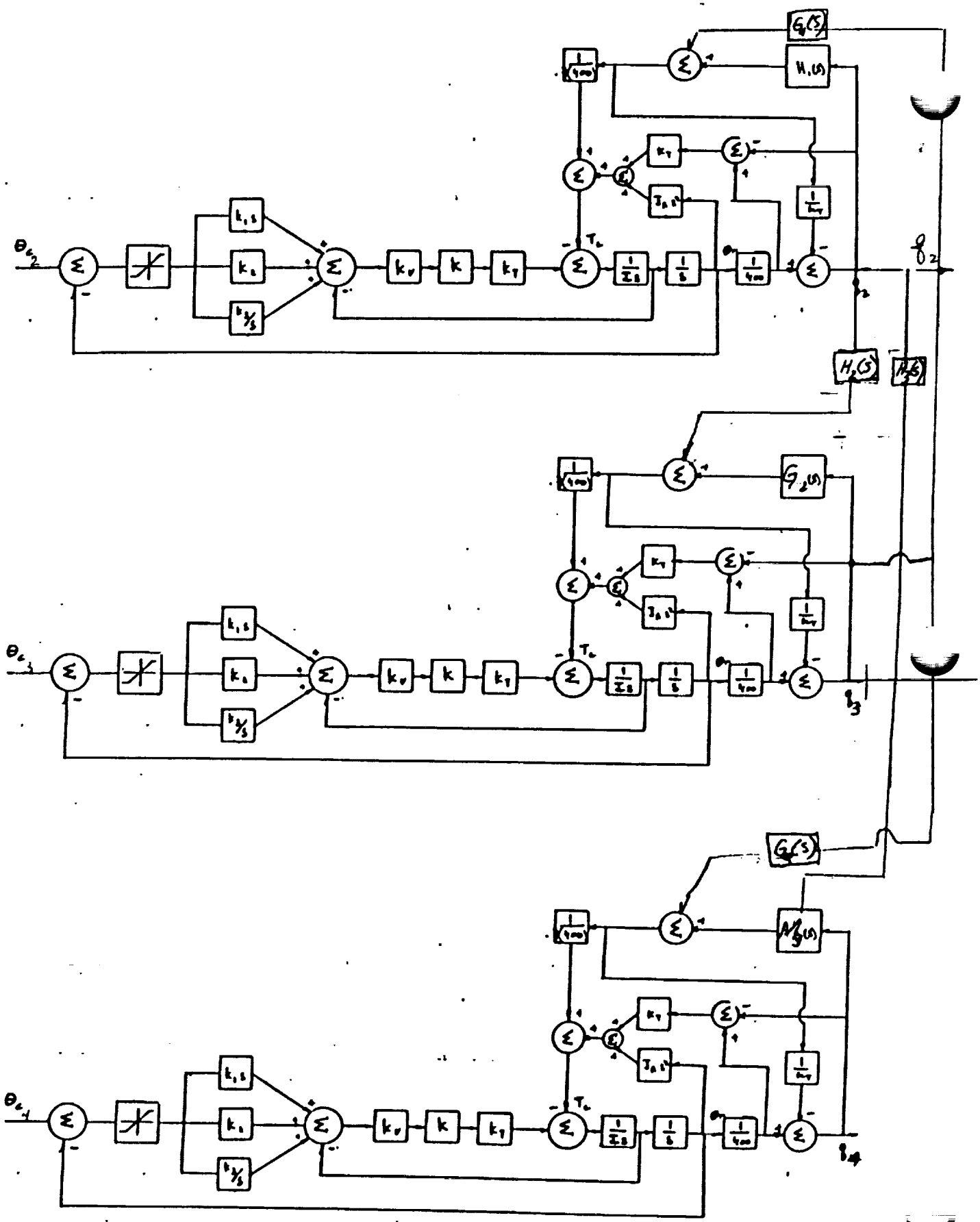

Figure 4-1 servo control system for Radiator Inspection Robot

ORBITER RADIATOR INSPECTION

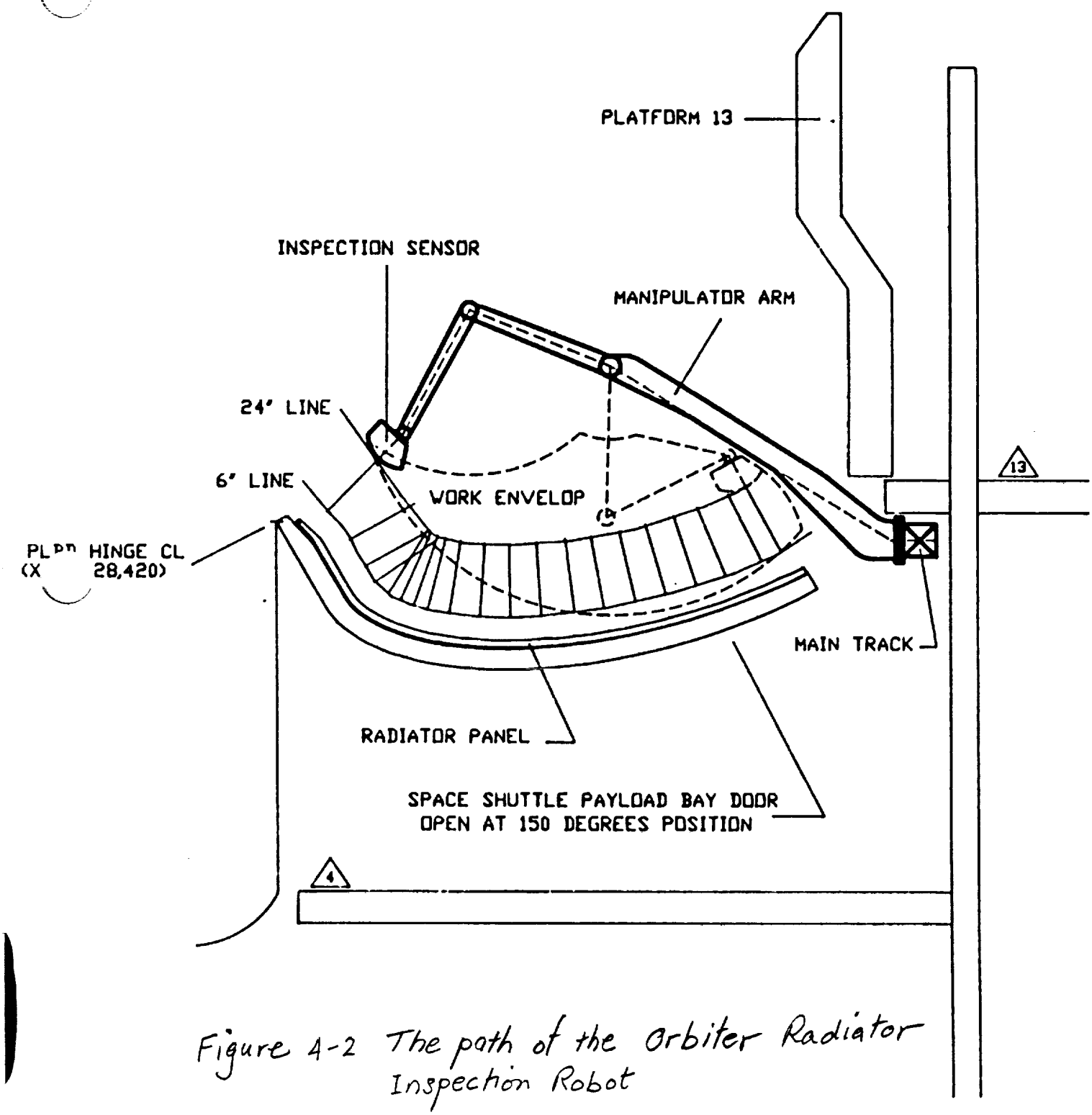

Figure 4-2 The path of the Orbiter Radiator Inspection Robot

V CONCLUSIONS

(1) A statistical technique could be used to calibrate, test, and trouble shoot a robot.

(2) The present technique provides a straight forward method to evaluate the robotics accuracy, repeatability, and linearity.

(3) In case of budget availability it would be advisable to obtain either SILMA or IGRIP as robotics design packages at RADL.

(4) In case of budget unavailability, a good manual should be developed for ROBSIM so its kinematics, dynamics, and control system packages could be used at RADL.

(5) An adaptive algorithm should be used with the radiator inspection robot's control system to minimize the servo system errors due to the variation of the inertia matrix with time and location.

REFERENCES

[1] Davis, Virgil Leon, " Systems Integration for the Kennedy Space Center Robotics Applications Development Laboratory" MS 87-482 SME Technical Report, 1987.

[2] Evaluation of Automated Decisionmaking Methodologies and Development of an Integrated Robotic System Simulation: Appendix A - Robsim User's Guide, NASA Contractor Report - 178051, March 1986

[3] Craig, John, " Introduction to Robotics Mechanics and Control", 1989 Addison-Wesley Publishing Company, Inc.

[4] Tawfik, Hazem "Computer Integrated Manufacturing Work Cell Process Capability", ASME Manufacturing International '90, Atlanta, Gorgia, March 1990.

[5] Kuo, Benjamin " Automatic Control Systems", Prentice-Hall, Inc., Englewood Cliffs, New Jersey, 1987.

[6] Nof, Shimon, " Handbook of Industrial Robotics", John Wiley & sons Inc.,1985.

1990 NASA/ASEE SUMMER FACULTY FELLOWSHIP PROGRAM

JOHN F. KENNEDY SPACE CENTER
UNIVERSITY OF CENTRAL FLORIDA

EVALUATION OF THE EFFECT OF LOW STRAIN RATE OVER TIME ON TITANIUM HOSE CLAMPS USED IN THE ORBITER

PREPARED BY:	Mr. Delbert Taylor
ACADEMIC RANK:	Instructor
UNIVERSITY AND DEPARTMENT:	Murray State College Engineering Technology
NASA/KSC	
DIVISION:	Materials Science Laboratory
BRANCH:	Malfunction Analysis Branch
NASA COLLEAGUE:	Mr. Charles Denaburg Mr. Scott Murray
DATE:	August 10, 1990
CONTRACT NUMBER:	University of Central Florida NASA-NGT-60002 Supplement: 4

ACKNOWLEDGEMENTS

I am extremely grateful for the opportunity to have participated in the 1989 and 1990 NASA/ASEE Summer Faculty Fellowship Programs. The experiences of the past two summers have been most enjoyable and rewarding.

First of all, I would like to thank the people at NASA/KSC and at the University of Central Florida for their hospitality and enthusiastic helpfulness. Special recognition for the overall planning and implementation of the program is given to Dr. Loren A. Anderson and Dr. E. Ramon Hosler, University of Central Florida Program Directors and their administrative assistant, Ms. Kari L. Baird; Kennedy Space Center Program Directors, Mr. Dennis W. Armstrong and Dr. Mark A. Beymer.

A special thanks to Bob Denaburg, Scott Murray, Gino Gaudino and Peter Marciniak for making room for me in their laboratory, and for providing their expertise, guidance and assistance throughout the project. The stimulating discussions about metallurgy and laboratory techniques have been inspirational.

Thanks to Mr. Charles W. Hoppesch, Chief of the Materials Science Laboratory, for making all the areas and equipment available for my use.

I would like to acknowledge the support of colleagues from my home institution, Murray State College, particularly, Dr. Clyde Kindell, President, Mr. Dennis Toews, Mr. Joe Reid and Mr. Bill Malone.

My acknowledgements would not be complete, however, without special mention of my wife, Vern. She continues to furnish help and support as always.

ABSTRACT

Titanium is available in both commercially pure and alloy grades. These grades can be grouped into three basic categories according to the predominant phase or phases in their microstructure. The titanium hose clamps are manufactured from single phase titanium, classified as being in the alpha category and designated as an unalloyed grade called commercially pure titanium. This commercially pure grade is characterized by a hexagonal, close-packed crystalline grain structure, is not heat treatable, is easily welded and is stable from room temperature up to 1625 degrees F. Commercially pure titanium is commonly used in applications where optimum corrosion resistance is desired and where high strength is not a factor. The failure of several commercially pure titanium hose clamps used in the orbiter is believed to be the result of strain over an extended period of time. This study will focus on the long time duration of low strain rate and evaluation of the results.

SUMMARY

Hose clamps manufactured out of commercially pure titanium reportedly failed in use aboard the orbiter. Subsequent tests indicate this failure may be due to sustained load cracking. The samples were analyzed by inductively coupled argon plasma emission spectrometric methods. The samples met the compositional requirements for commercially pure titanium. The samples contained hydrogen in the amount of approximately 30 ppm both in the strap and in the holder area. Scanning electron microscope fracture analysis depicts features characteristic of a brittle failure mode. The failure fracture appeared to initiate in the center of a spot weld and terminated with a fracture at the interface of the fusion zone and the heat affected zone. Additional tests were conducted to further investigate the slow strain embrittlement with emphasis on the detection of hydride precipitation in the leading edge of the crack. Test results indicate a loss of ductility and the embrittlement of the sample.

TABLE OF CONTENTS

LIST OF FIGURES

LIST OF ABBREVIATIONS AND ACRONYMS

FUZ	Fusion Zone
HAZ	Heat Affected Zone
HRB	Rockwell Hardness Number
ICAP	Inductively Coupled Argon Plasma
PPM	Parts per million
SEM	Scanning Electron Microscope
SLC	Sustained Load Cracking

I. INTRODUCTION

1.1 BACKGROUND

Titanium is commercially available in several different compositions and grades. Selection of the grade that is precisely correct for a specific application usually makes the difference between the safe profitable use of titanium in a high performance structure and a marginal application.

Titanium base alloys are similar to many other engineering metals. Pure titanium is soft, weak and very ductile. When alloyed with other elements, the titanium metal base is converted to a material with characteristics of high strength, stiffness, useable ductility, corrosion resistance and a lower density than other engineering materials. The most predominant of these characteristics in any given composition is a function of the alloying element selected (1).

Titanium has a hexagonal close-packed crystal grain structure called alpha, which transforms to a body centered cubic structure, called beta at 1625 degrees F. Alloying elements favor one or the other of the two structures. Aluminum, for example, stabilizes the alpha structure raising the transformation temperature from alpha to beta. Chrominum, iron, molybdenum, manganese and vanadium lower the transformation temperature making the beta phase stable at lower temperatures. Tin is considered neutral.

Titanium grades fall into three major classes depending on the phase or phases present in their microstructures. The three classes are alpha, beta, and the combination of phases referred to as alpha-beta. The alpha-beta class includes most of the titanium as used today.

Alpha alloys, the hexagonal structured compositions, possess the highest strength and oxidation resistance at elevated temperatures and the best weldability of the titanium grades. Room temperature strength levels, however, are the lowest. These compositions do not respond to heat treatment (2).

Within the alpha alloy classification are grades with high aluminum content, grades with such lean beta present to be almost pure alphas, and the commercially pure or unalloyed grades.

Commercially pure titanium was the first titanium melted and currently is produced in five different strength levels determined by the interstitials present, primarily oxygen.

Titanium alloys also have a great affinity to the beta stabilizing interstitial, hydrogen. There are basically two types of hydrogen embrittlement exhibited. These have been designated as impact embrittlement and low strain rate embrittlement. Sensitivity of titanium alloys to low strain rate embrittlement appears to increase with increasing strength, notch severity, alpha grain size, continuity of the beta phase and the hydrogen content (3).

In commercially pure titanium, as in all other metals, as the strength increases, toughness, ductility and formability decrease.

1.2 HOSE CLAMP FAILURES

Broken titanium hose clamps were found lying on the deck in the crew compartment of the orbiter. These clamps of various sizes are used to hold low pressure ducting in place. It was reported that the failures occurred during the installation tightening process. However, discussions with the system engineers and technicians indicated that some were found broken. Others had failed on reinstallation, having been stressed in use over a long period of time. It was reported that the failure occurred to a few being reinstalled, not representing a failure of all the reused clamps. The subject clamps, P?N ME277-0015, were manufactured by Aeroquip Manufacturing Company (4).

1.3 PRIOR INVESTIGATIVE RESULTS

An investigation of the failures was conducted by NASA/KSC Failure Analysis Lab (4). The investigation procedures included visual, metallography, scanning electron microscope (SEM) and analytical tests.

1.4 PRIOR CONCLUSIONS

The initial investigation concluded that the failure was due to sustained load cracking (SLC). Normally this type of fracture would be caused by an excess of one of the interstitial elements, primarily hydrogen and the precipitation of hydrides. The subject hose clamps were manufactured from commercially pure titanium (4).

1.5 OBJECTIVES

The overall objective of this investigation was to establish a similar type low strain rate under controlled conditions using the same type titanium hose clamps to establish the brittleness, hydrogen content and the changes in the microstructure.

II. TEST PROCEDURES

2.1 TESTS

The tests were conducted using the small hose clamps shown in Figures 2-1 and 2-2. Previous metallic samples selected from the clamps were dissolved in concentrated HCL and analyzed by inductively coupled plasma (ICAP) spectrometric methods. The subject material met the composition requirements for unalloyed titanium, essentially 100% Ti. This is the same criteria for the alpha class commonly called commercially pure titanium. Fracture surface samples were also analyzed using a scanning electron microscope for fractgraphic studies. The sample hose clamps were stressed by installing them around a piece of pipe. An Instron tensile testing machine was used to subject the clamps to a low strain rate of .002 inches per minute until the fracture point was reached.

2.2 TEST RESULTS

The failures of the hose clamps were primarily in the area where spot welding was performed between the strap and bolt-holding bracket. The fracture appeared to originate from the edge of a spot weld. The grains of the microstructure near the edge of a weld appeared to be distorted. Linear marks that can be attributed to the welding machine also were seen. The fracture surface showed dimples arranged in areas that appear to be separated by crack arrest lines. Many of the dimpled lines were elongated indicating that the origin of the fracture was at the center of the spot weld. This failure is in the area of the fusion zone (FUZ) and the heat affected zone (HAZ) interface (HAZ/FUZ) as shown in Figure 2-3. SEM photomicrographs of the fracture are shown in Figures 2-4 through 2-7. Most of the fracture surfaces had a sharp, faceted appearance which is indicative of brittle fracture. There was also a slight indication of fatigue in the area.

Metallographic samples were made of the HAZ and FUZ weld areas. These were compared with a sample from an unstressed clamp. There was no indication of any microstructure change which could contribute to the premature failure. The metallographic samples were primarily etched with Kroll's etchant for grain examination. Some were etched with an Hf-Hcl etchant to investigate for the presence of hydrides.

Hardness tests were conducted using a Universal Microhardness Tester. All values were converted to a Rockwell Hardness Number (HRN). All hardness readings fell within a range of HRB 92 to HRB 100. There was no noticeable hardness difference between the stressed and the unstressed samples.

Hydrogen analysis conducted by the Lewis Research Center of similar clamps, both stressed and unstressed, determined that the hydrogen level of the samples was approximately 30 ppm. The composition of the samples met the requirements for commercially pure titanium (99.2+%).

III. CONCLUSION

When subjected to a low strain rate over a period of time, commercially pure titanium hose clamps are subject to failure due to sustained load cracking (SLC). Although slow strain rate is most often observed in the alpha/beta class titanium, it has also been observed in the alpha and the beta class metals. The loss of ductility was pronounced at near room temperature. The embrittlement of the low strain rate can be attributed to the hydride precipitate that formed during the strain. This formation of the hydride took place in the area of the slip planes. The large volume of the hydride stressed the slip plan causing a crack. Beginning at the leading edge of the crack, this process is again repeated until complete failure occurs. Additional testing would be required to determine whether the hydride nucleation is initiated by the attainment of a critical stress or by the mount of strain developed in the metal.

REFERENCES

1. Donachie, M.J. Introduction to Titanium and Titanium Alloys. Source Book, ASM, 1982.

2. "A General Summary of the Physical Metallurgy of Titanium Alloys." TML Report No. 19, 1955.

3. Groeneveld, T.P., Fletcher, E.E., Elsea, A.R. A Study of Hydrogen Embrittlement of Various Alloys. Battelle Annual Report, 1966.

4. Metals Handbook, 9th Edition. Metallography and Microstructures. ASM, Vol. 9, 1985.

5. Metals Handbook, 9th Edition. Mechanical Testing. ASM, Vol. 8, 1985.

6. "Hydrogen Embrittlement Testing." ASM-STP543, 1974.

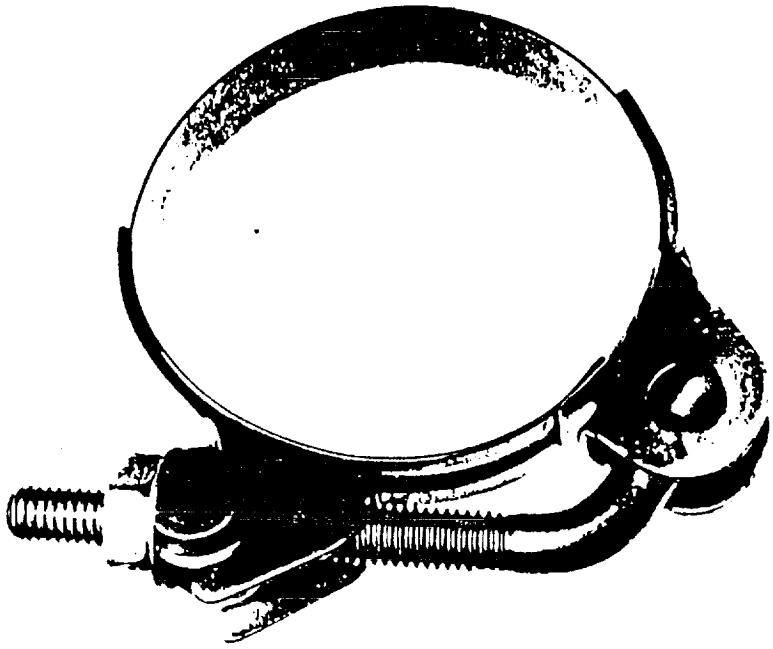

Figure 2-1. Titanium Hose Clamp

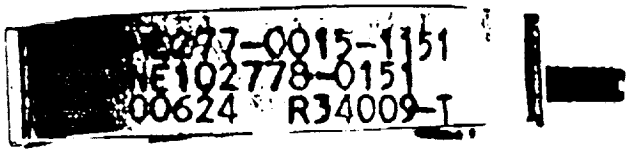

Figure 2-2. Titanium Hose Clamp Identification

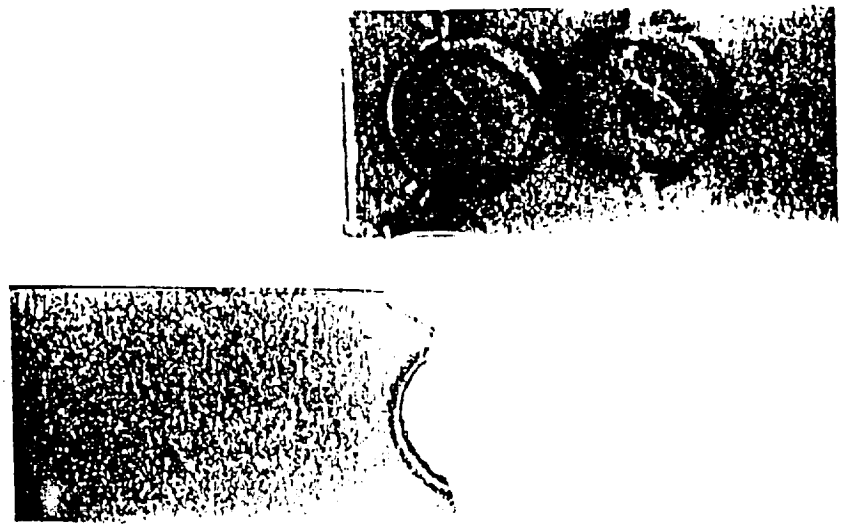

Figure 2-3. Weld Fracture

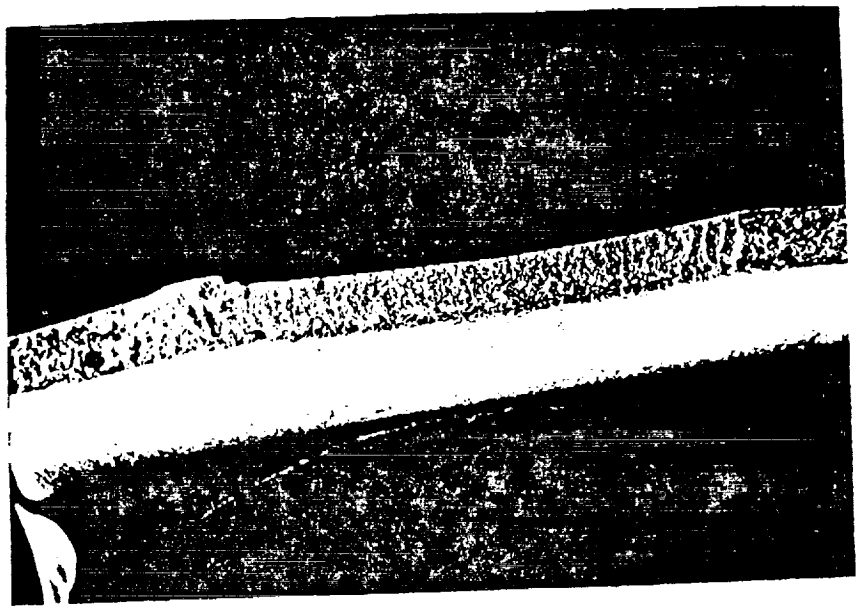

Figure 2-4. SEM Micrograph of Fracture, 17X

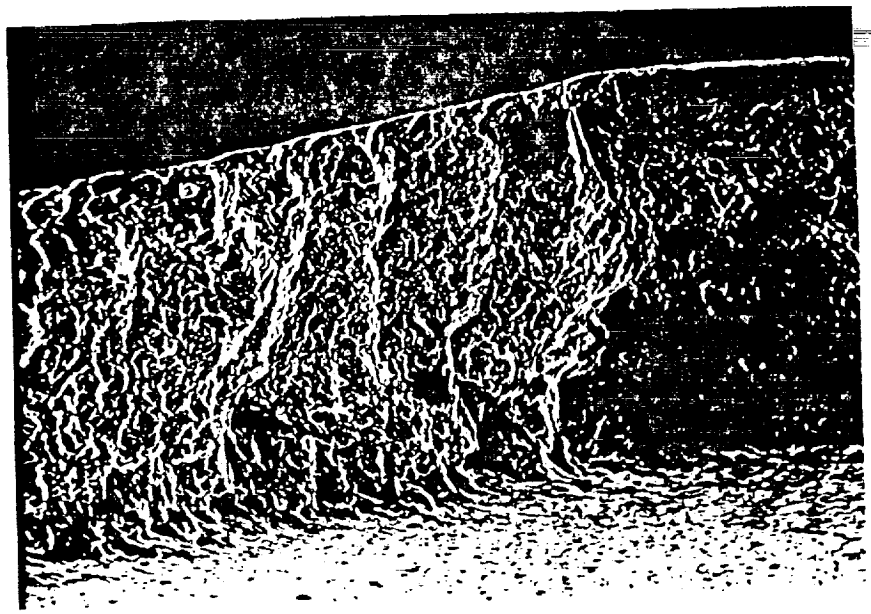

Figure 2-5. SEM Micrograph of Fracture, 107X

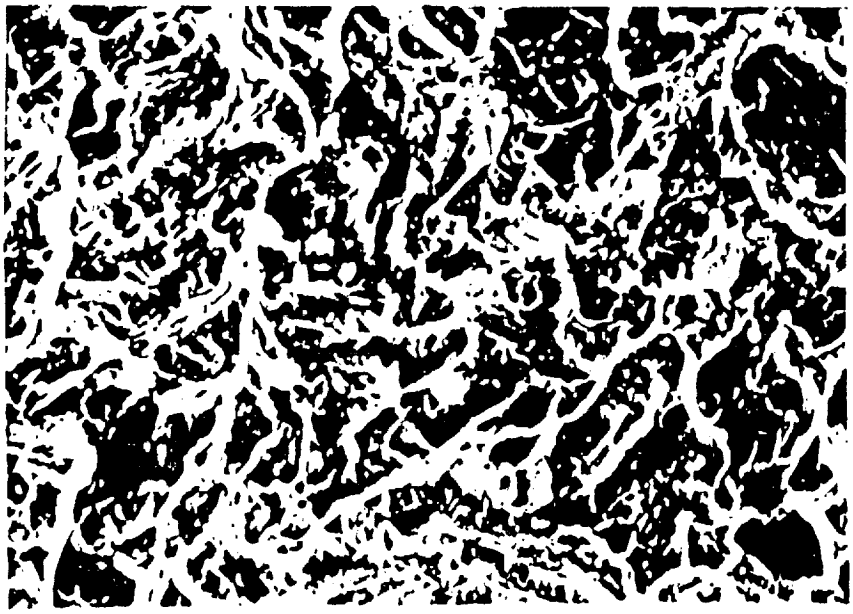

Figure 2-6. SEM Micrograph of Fracture, 1230X

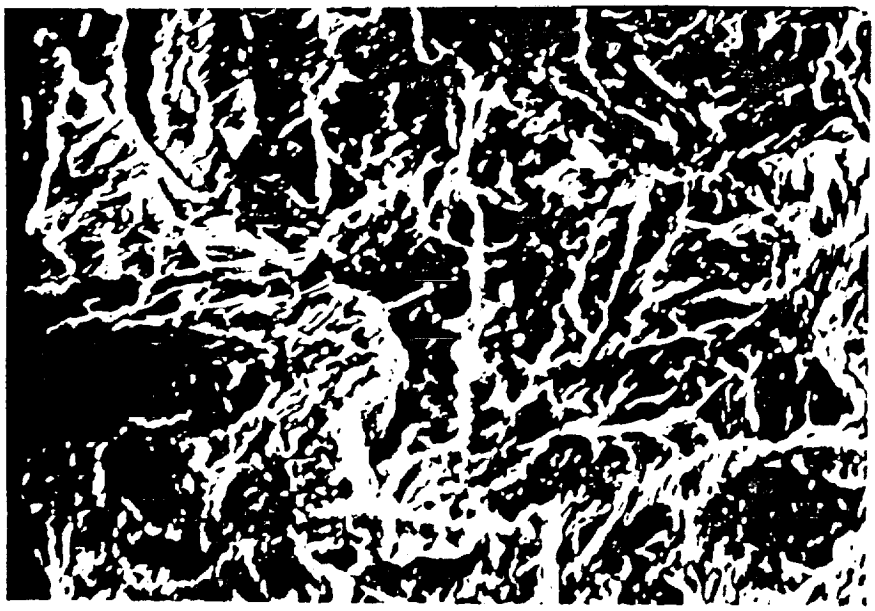

Figure 2-7. SEM Micrograph of Fracture, 1210X

1990 NASA/ASEE SUMMER FACULTY FELLOWSHIP PROGRAM

p. 30

JOHN F. KENNEDY SPACE CENTER
UNIVERSITY OF CENTRAL FLORIDA

LOW FLOW VORTEX SHEDDING FLOWMETER FOR HYPERGOLICS/ALL MEDIA

PREPARED BY:	Dr. Ngo Thinh
ACADEMIC RANK:	Professor
UNIVERSITY AND DEPARTMENT:	California State University - Sacramento Mechanical Engineering Department
NASA/KSC	
DIVISION:	Electronic Systems Support
BRANCH:	Instrumentation - Transducers Section
NASA COLLEAGUE:	Mr. Robert Howard
DATE:	August 10, 1990
CONTRACT NUMBER:	University of Central Florida NASA-NGT-60002 Supplement: 4

SUMMARY

Current turbine type flowmeters have been used to measure the loading of hypergolics into the Space Shuttle Orbiter. Because of the problems associated with the refurbishment of these meters after each launch, NASA has considered the development of a vortex shedding flowmeter without internal moving parts. The objective of the current project was to test an existing vortex shedding prototype for 1/2" outside diameter pipe and to develop a family of vortex shedding flowmeters for larger line sizes and flow ranges.

In order to test the meter for the flow of Freon 113, which is similar to hypergols, a flow test loop was designed and built. A series of tests were performed on the existing vortex shedding flowmeter to evaluate its output characteristics. Results of the tests indicated a linear relationship between vortex shedding frequencies and flow rates.

A family of vortex shedding flowmeters for larger sizes of 3/4", 1", 1 1/2" and 2" with three different geometries for the shedder bar, were designed and submitted to the prototype shop for fabrication. Test runs on this family of vortex shedding flowmeters are scheduled for next summer.

ACKNOWLEDGEMENTS

I would like to thank all members of the Transducer Section for their help during my tenure of this summer project. I am grateful to **Bob Howard** for his encouraging words which brought me to the Kennedy Space Center and his strong support toward my research endeavour. I also would like to thank **Dr. Loren A. Anderson** and **Dr. Mark A. Beymer** , Directors of the NASA/ASEE Summer Faculty Fellowship Program, for their assistance and hospitality which make my days at KSC very educational and enjoyable.

ABSTRACT

The purpose of this summer project was to further develop a family of vortex shedding flowmeters for flow measurement of hypergols that requires a long term operation without removal from system lines. A family of vortex shedding flowmeters without moving parts have been designed. The test loop to evaluate the meters for the Freon flow which simulates the hypergolic fluids, has been modified and reconstructed. Preliminary results were obtained on the output frequency characteristics of an 1/2" flowmeter as a function of the flow rate.

TABLE OF CONTENTS

LIST OF ILLUSTRATIONS

LIST OF TABLES

1.1 STATEMENT OF PROJECT NEEDS.

During the loading of hypergolic fuels and oxidizers, flow meters are used to measure the amount of fluid. The current method of metering these fluids involves turbine type meters and shuttle-ball type vortex shedding meters. One of the problems that occurs with these meters is that after each launch the meters have to be taken apart and refurbished then recalibrated. The reason for this process is that there are moving parts of the meters in contact with the flowing fluid. Figure 1.1 shows a typical turbine flowmeter. The bushings and bearings of these meters are susceptible to wear, especially during the purge phase of fuel loading process when severe over speeds of the rotor occur due to gas flow through the lines. The process of refurbishment of the meters is costly due to the techniques required to handle the very toxic hypergols. It is estimated that a saving of about $1000 per flowmeter per launch can be made if the meters do not require this maintenance. There are about 6000 flowmeters of all sorts on the Space Shuttle.

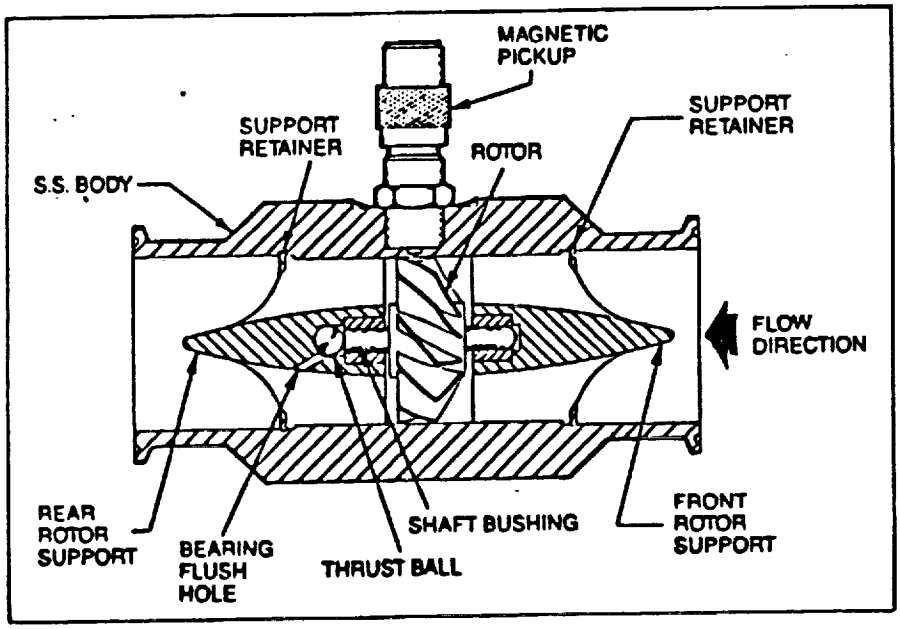

Figure 1.1 EXAMPLE OF A TURBINE FLOWMETER

1.2 OBJECTIVE OF THE PROJECT.

The objective of this project is to develop a family of vortex shedding flowmeters for applications that require long term operation without removal from system lines. This family of vortex shedding flowmeters would have no moving parts. The linearlarity between the frequency and the flow rate would be as close as that of the turbine type. The flowmeters could be installed permanently after the initial calibration and only the signal conditioner would be removed for calibration. This procedure would not affect the totalcalibration accuracy of the meter.

II. VORTEX SHEDDING FLOWMETERS

2.1 BACKGROUND OF VORTEX SHEDDING PHENOMENA.

The phenomenon of vortices being shed from a surface in a flowing fluid is not new, and the application of the vortex shedding to the measurement of flowrate is well established.

For an uniform flow past a circular cylinder, vortices are formed at the two separation points and shed off regularly in an alternating fashion, as shown in figure 2.1. These vortices move downstream in a regular pattern. Von Karman did the initial analysis of the stability of vortex trail behind a cylinder. According to his analysis, a stable vortex pattern must have a geometry such that

$$h/l = 0.281 \qquad (1)$$

where h and l are the linear dimensions.

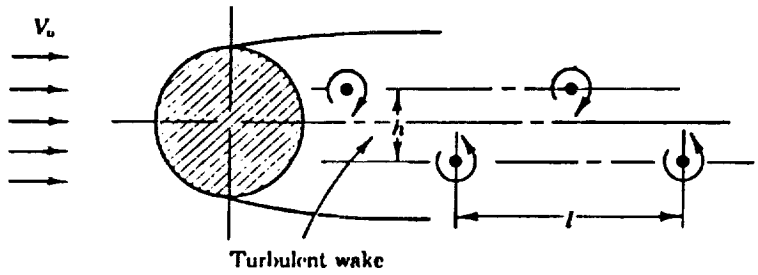

Fig. 2.1. VON KARMAN VORTEX TRAIL

The vortices move downstream with a velocity u which is less than the mainstream velocity U. Von Karman derived the following formula for calculating the drag force per unit length of the cylinder:

$$F = Rho*U**2*h*(2.83*(u/U)**2-1.12*(u/U)**2) \qquad (2)$$

where U is the velocity of the freestream, h and u are determined from experimental measurements, Rho is the density of the fluid.

The alternating shedding of vortices from the separation points on the surface of a circular cylinder produces transverse forces on the cylinder and causes the cylinder to oscillate. Such effects were first studied in the laboratory about 1878 by Strouhal, who showed that the vibrations would cause the sound to transverse to the fluid. He also showed that the frequency f of the vibration was related to the

air speed U and the cylinder diameter d by the approximate equation:

$$f = U/6d \qquad (3)$$

Vortex shedding flowmeters work on the principle that the frequency of the vortex shedding behind a bluff body is proportional to the fluid velocity past that body as shown in Figure 2.2.

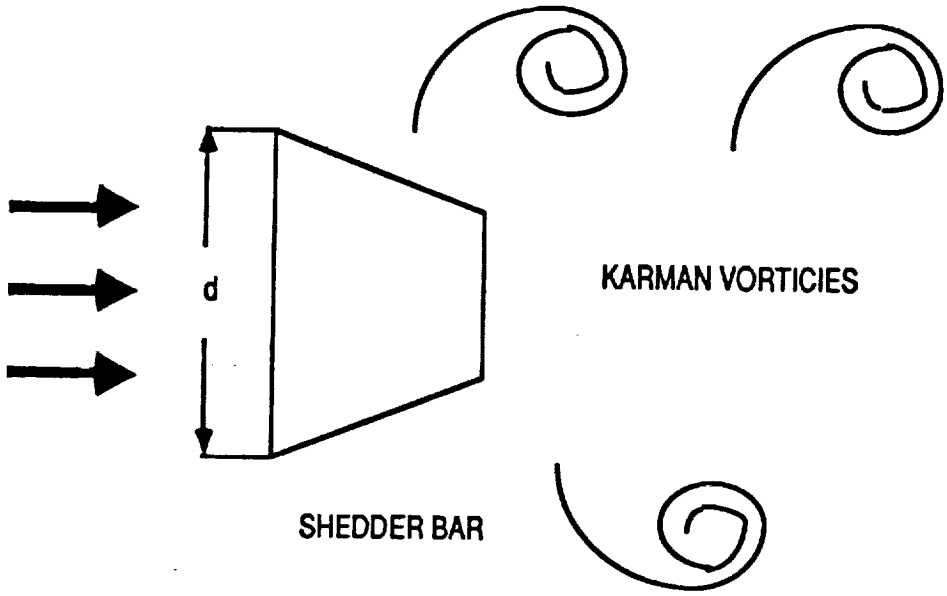

Figure 2.2 VORTEX SHEDDING PHENOMENON

The proportionality constant or the relationship between the vortex shedding frequency and velocity of the uniform flow is called the Strouhal number which is related to the vortex shedding frequency in the following equation:

$$f = St*U/d*(1-20/Re) \qquad (4)$$

where:

- f Vortex shedding frequency, Hz
- St Strouhal number
- U Fluid flow velocity, ft/sec
- d Characteristic dimension of bluff body, ft
- Re Reynolds number of pipe flow

Equation (4) can be simplified if the ratio 20/Re is assumed negligible:

$$f = St*U/d \qquad (5)$$

or

$$St = f*d/U \qquad (6)$$

2.2 DESIGN OF THE PROTOTYPES.

Figure 2.3 shows the design for an one-inch vortex shedding flowmeter with a rectangular shedder bar. The meter was scaled down to 1/2", 3/4" and up to 1 1/2" and 2" models. The prototypes were designed to use the same pressure transducer type to simplify the testing procedures. With 3 different types of shedder bar which will be mentioned in the next section, there will be 15 different flowmeter models to study experimentally.

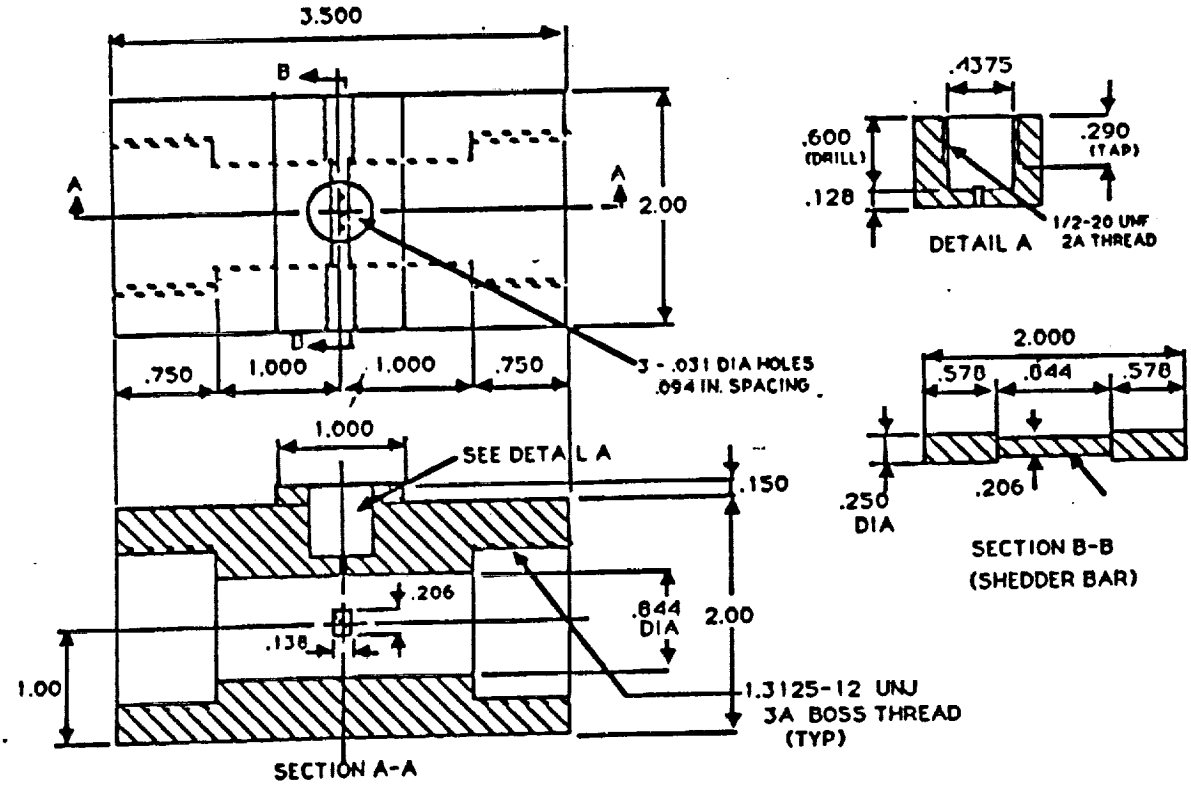

Figure 2.3 ONE-INCH VORTEX SHEDDING FLOWMETER

The geometry of the shedder bar determines the characteristic of the frequency of vortices. Three shapes for the shedder bar were selected for this study. They are circle, rectangular, and reversed wedge as shown in following figure 2.4.

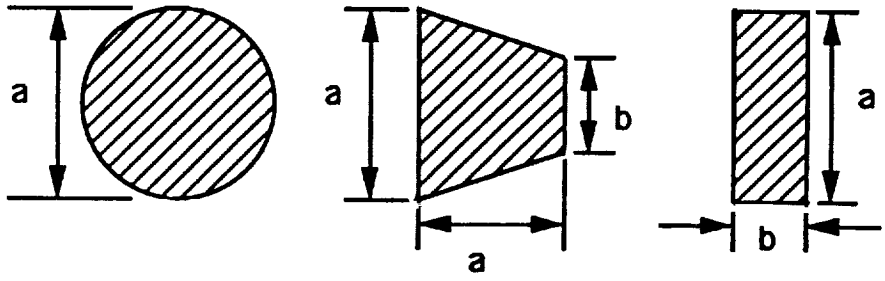

Figure 2.4 SHEDDER BAR GEOMETRY

Table 2.1 shows the geometrical dimensions of the flow meter components related to the flow field as well as the shedder bar dimensions.

TABLE 2.1

SHEDDER BAR DIMENSIONS

FLOWMETER (O.D)	1/2"	3/4"	1"	1 1/2"	2"
I.D (in.)	.410	.609	.844	1.312	1.781
a (in.)	.110	.170	.235	.367	.500
b (in.)	.075	.115	.155	.245	.335

III. EXPERIMENTAL STUDY

3.1 INTRODUCTION

The basic goal of the project were to design and construct a flow bench to test a family of vortex shedding flowmeters. The prototype flowmeters have been designed and the development stage will follow. The test considered in this section is on an existing KSC modified prototype for 1/2" O.D. pipe. Freon 113 (Trichlorotrifluoroethane) is the working fluid. Freon was chosen because it has similar properties to the hypergolic fluids which will be metered by the flowmeter considered in this project.

3.2 FLOW BENCH DESIGN

The flow bench to test the family of vortex shedding flowmeters has been designed using the existing set up to measure the 1/2" KSC prototype flowmeter.

The existing flow loop is shown schematically in figure 3.1. The test section in which the flowmeters are located have been modified to accommodate all the pipe sizes of the flowmeters. Two 50-gallon dewars were used as containers for the freon fluid. Dewar #1 was located inside the laboratory and was placed on a load platform used to measure the mass flow rate of Freon 113. Dewar #2 was located outside of the laboratory window and was connected to the flow loop through the window. By proper adjustment of the valve system Freon 113 could flow through the loop from either dewar. High pressurized nitrogen gas was used to vent Freon from one dewar through the test section into another dewar. The quantities measured in the loop include the output signals from the turbine flowmeter used as a reference, from the vortex shedding flowmeter under test, from the pressure transducers at various locations in the test loop, and from the load cell transducers installed under Dewar #1. The vortex flowmeter output signals were detected by a Kistler transducer (model 206). The Kistler transducer was a piezoelectric type of device and came with a Kistler signal coupler (model 5116) which could produce an AC coupled

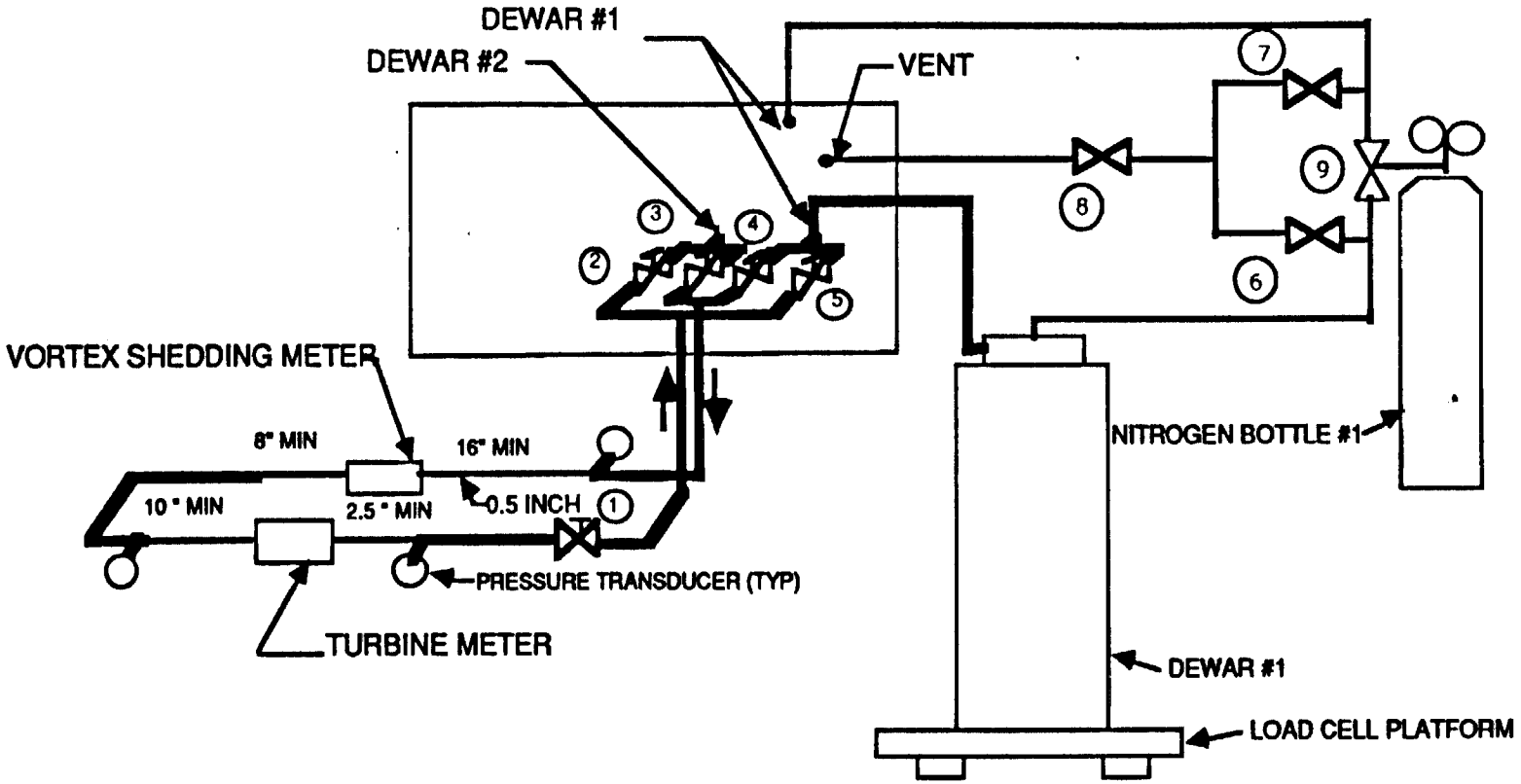

Figure 3.1 FLOW TEST SCHEMATIC

millivolt output proportional to pressure fluctuations. A Philips oscilloscope PM3320A was used to analyze the pressure fluctuations. The frequency of the vortex shedding was then obtained.

3.3 1/2" FLOWMETER TEST

One of the goals for this summer project was to study experimentally the existing 1/2" vortex shedding flowmeter to obtain some characteristic data using the turbine meter as a reference. To vary the flow rate, more or less pressure was applied to the Freon dewar using the three-way valve connected to Nitrogen Bottle #1. Steady flow was indicated by a steady output reading from the calibrated turbine meter in series with the vortex meter. The turbine meter output consists of a voltage from the signal conditioner which is linearly proportional to the flow rate. The calibration curve relating gallons per minute (GPM) and frequency in Hz to output voltage are shown in Figure 3.2, 3.3 and Appendix A.

The output from the vortex shedding flowmeter was analyzed using the Philips oscilloscope PM33204. The output signal from the Kistler pressure transducer was clearly picked up on the oscilloscope and the frequency results were easily obtained. The oscilloscope used had a storage capability which permitted a freeze on the trace for easy pulse counting and frequency determination.

The measurement of pressures and temperatures at various locations in the flow loop were also needed. However, only one pressure reading at the inlet of the flowmeter was obtained at this time. A thermocouple will be used to determine the temperature Freon in the flowmeter.

Mass flow rate measurements were also taken for three conditions. The output data was read from three Dynasco pressure transducers which were connected to three Lebow load cells. The Freon dewar #1 was placed on a load platform which in turn was placed on the three Lebow load cells. Results of the mass flow rate measurement were tabulated and shown in Appendix B.

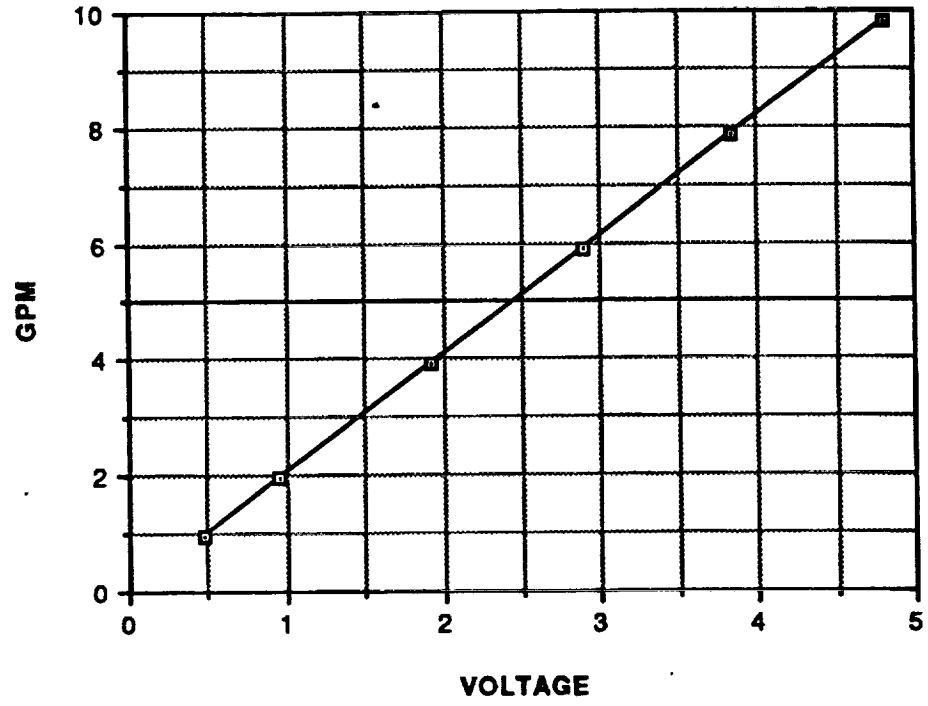

Figure 3.2 TURBINE FLOWMETER CALIBRATION, V vs Q

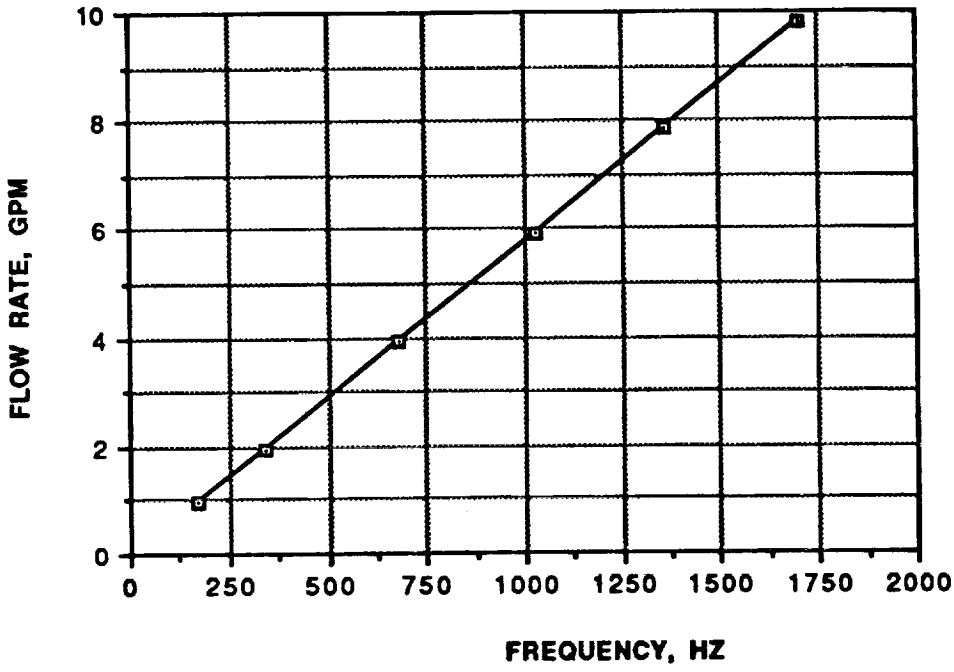

Figure 3.3 TURBINE FLOWMETER CALIBRATION, Q vs FREQ.

3.4 RESULTS AND DISCUSSION

The experimental results consist of a determination of the vortex shedding frequency versus flow rate which was interpreted from the calibration curve of the turbine flow meter. Test results for the 1/2" KSC flowmeter are shown in Appendix C. As can be seen from Figure 3.4, the relationship between vortex frequency and flow rate is linear. The Kistler pressure transducer and the Philips oscilloscope produced excellent output signals which help make the analysis simple. Appendix D shows the pressure pulses recorded on the oscilloscope screen and plotted with an HP ThinkJet printer. The frequency of the vortex shedding was analyzed and appeared on the output screen.

Table 3.1 shows the average frequency from 2 test cases and the corresponding mass flow rate interpolated from the turbine flowmeter calibration. The Reynolds number and the Strouhal numbers as well as the velocity of the Freon flow were also calculated.

The calculated mass flow rate of Freon 113 compared well with measured results (Appendix C) within a 5% discrepancy. This discrepancy would be less if one Dynasco transducer was connected to read the total mass from the three separate readings.

TABLE 3.1

TEST CASE RESULTS

Freq. (Hz)	Q (gpm)	Q (ft3/s)	m (lbm/s)	u (ft/s)	St	Re	Turb/Ref Voltage
164	2.032	.004526	.440	4.941	.277	360	1.0
241	3.058	.006811	.663	7.436	.270	540	1.5
332	4.083	.009094	.885	9.928	.279	725	2.0
387	5.104	.011367	1.106	12.409	.260	900	2.5
440	6.125	.013641	1.327	14.892	.246	1085	3.0
509	7.146	.015915	1.549	17.374	.244	1265	3.5

Density = 97.31 Lbm/ft3, Viscosity = .00142 Lbf-sec/ft2

Results shown on Figure 3.5 and 3.5 also indicate a linear relationship between the vortex shedding frequency and the Reynolds & Strouhal numbers.

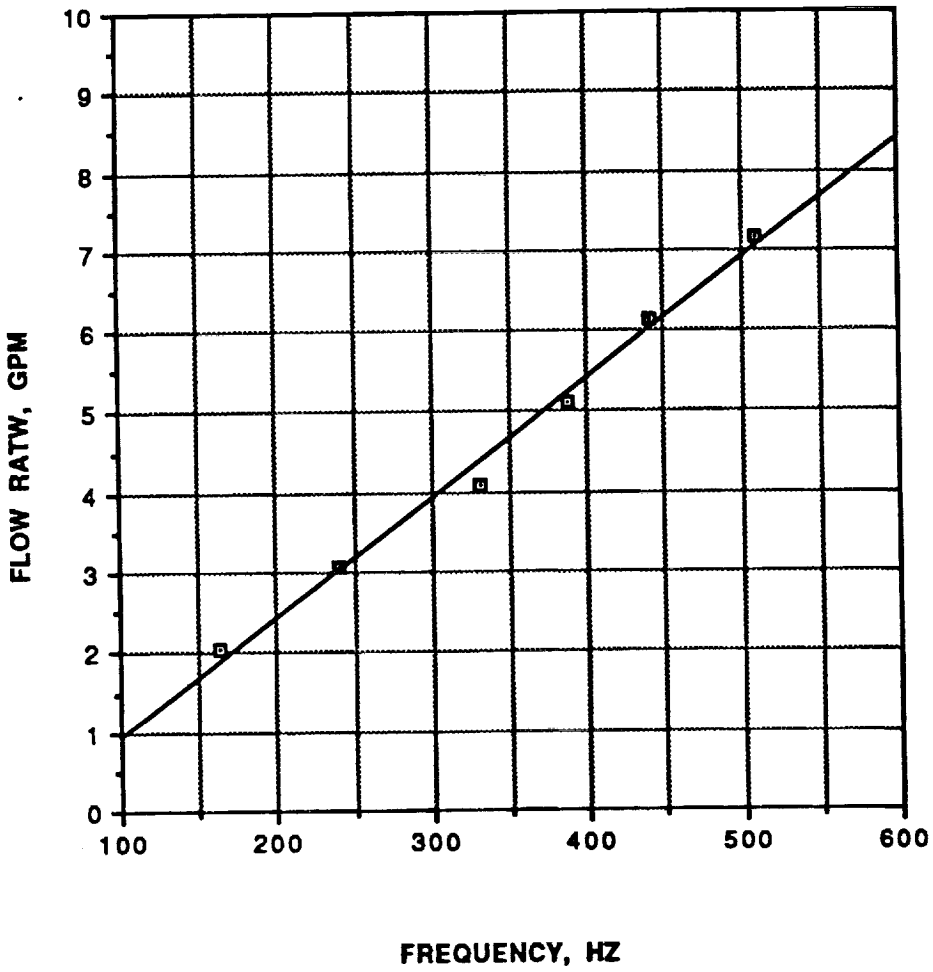

Figure 3.4 TEST RESULTS FOR THE 1/2" KSC MODEL

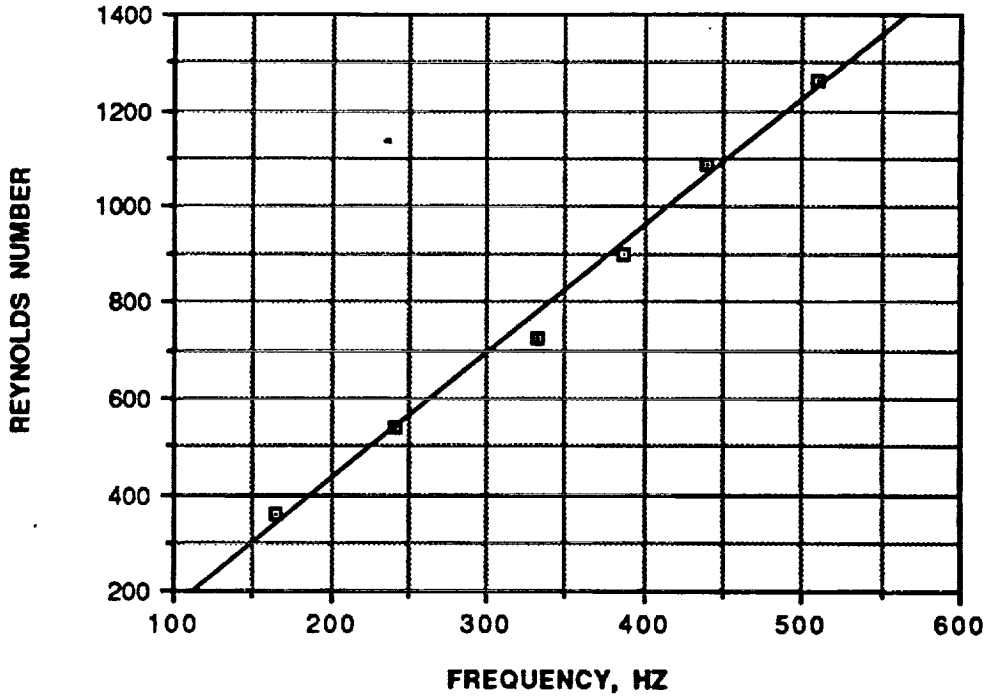

Figure 3.5 TEST RESULTS FOR THE 1/2" KSC MODEL RE vs FREQ.

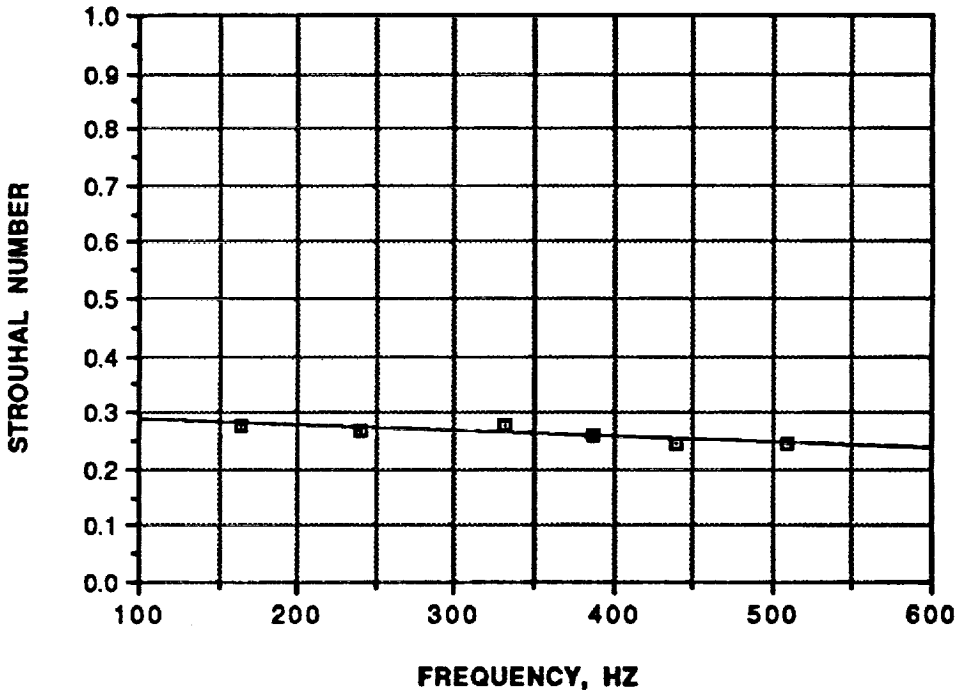

Figure 3.6 TEST RESULTS FOR THE 1/2" KSC MODEL ST vs FREQ.

IV. CONCLUSION AND RECOMMENDATION

Preliminary test results on the 1/2" model suggested that the vortex shedding flowmeter is a possible replacement for the turbine flowmeter which has been used to measure the loading of hypergols into the space shuttle. A family of vortex shedding flowmeters with various shedder bar shapes have been designed and fabricated. More experimental work have been scheduled for next summer.

The existing flow bench is adequate for the models with 1/2", 3/4" O.D.; however for the models with 1", 1 1/2" and 2" O.D. where more mass flow rate is needed, a new flow bench design will be required. It is suggested that a system which consists of a pump to circulate the Freon flow, be utilized for all models.

APPENDIX A

TURBINE FLOWMETER CALIBRATION

Nominal %F.S.	Flowrate GPM	Frequency Hz	K Factor Observed	Endpoint Line GPM
10	0.95	166.67	10571.036	0.95
20	1.95	340.48	10503.239	1.95
40	3.92	681.83	10436.173	3.92
60	5.90	1024.80	10430.534	5.90
80	7.84	1359.70	10412.508	7.84
100	9.82	1703.00	10402.117	9.82

APPENDIX B

MASS FLOW RATE MEASUREMENT

Turbine Flowmeter Voltage	2.0	3.0	3.8
#1 Pres. Gage	206.-167.	250.-190.	164.-145.
#2 Pres. Gage	198.-160.	238.-180.	154.-136.
#3 Pres. Gage	185.-151.	217.-166.	143.-127.
Time	120 sec.	120 sec.	30. sec.
Mass Flow Rate	.925 Lbm/s	1.409 lbm/s	1.767 lbm/s

APPENDIX C

TEST DATA FOR THE KSC 1/2" MODEL

TEST RUN 1

Turbine flowmeter as Reference Voltage (Volts)	Vortex Shedding flowmeter Voltage (Volts)	Frequency (Hz)
1.00	.55	184
1.50	.70	230
2.00	.91	318
2.50	1.13	372
3.00	1.35	439
3.50	1.56	539

TEST RUN 2

Turbine Flowmeter	Tank	Vortex Shedding Flowmeter		
Voltage (Volts)	Pressure (psi)	Voltage (Volts)	Freq. (Hz)	Inlet Pressure (psi)
1.00	60	.60	144	55.70
1.50	65	.70	211	58.50
2.00	75	.85	345	60.00
2.50	85	1.08	402	58.60
3.00	90	1.15	441	58.40
3.50	120	1.50	478	66.00

APPENDIX D

PRESSURE PULSES RECORDED

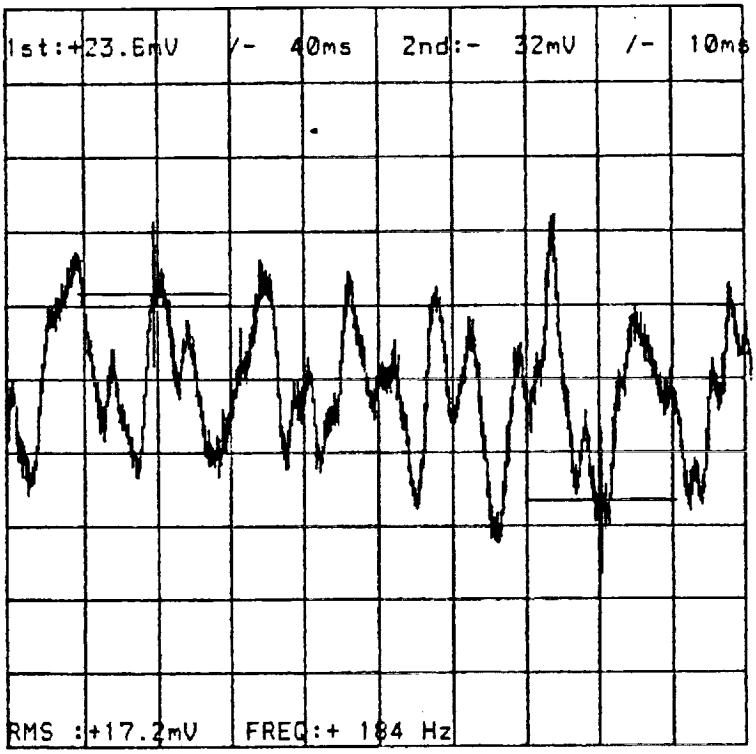

REG0 A: 20mV T: 5ms REC AUTO 90-07-18
B: 200mV D:- 10DIV / A 13:25:47

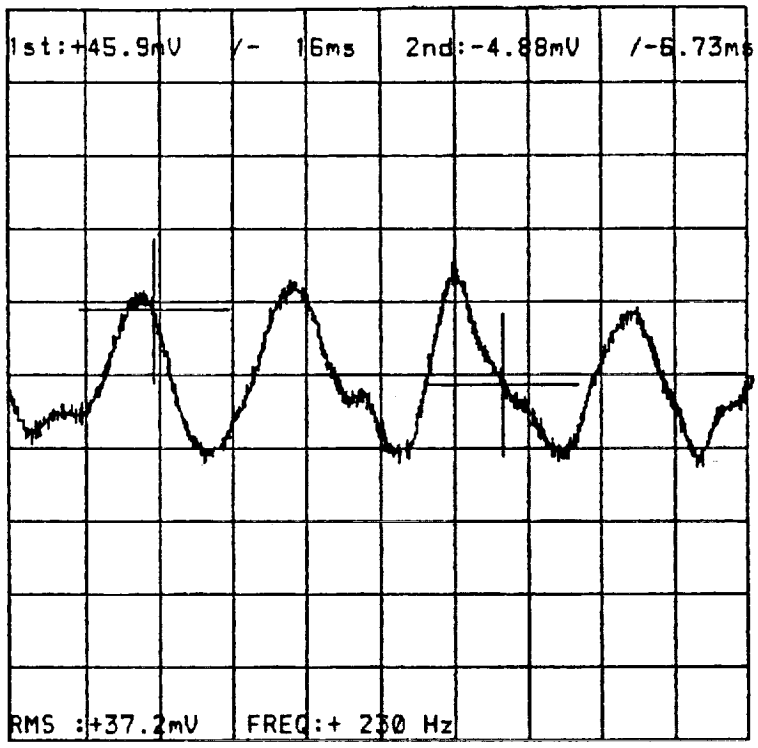

REG0 A: 50mV T: 2ms REC AUTO 90-07-18
B: 200mV D:- 10DIV / A 13:49:26

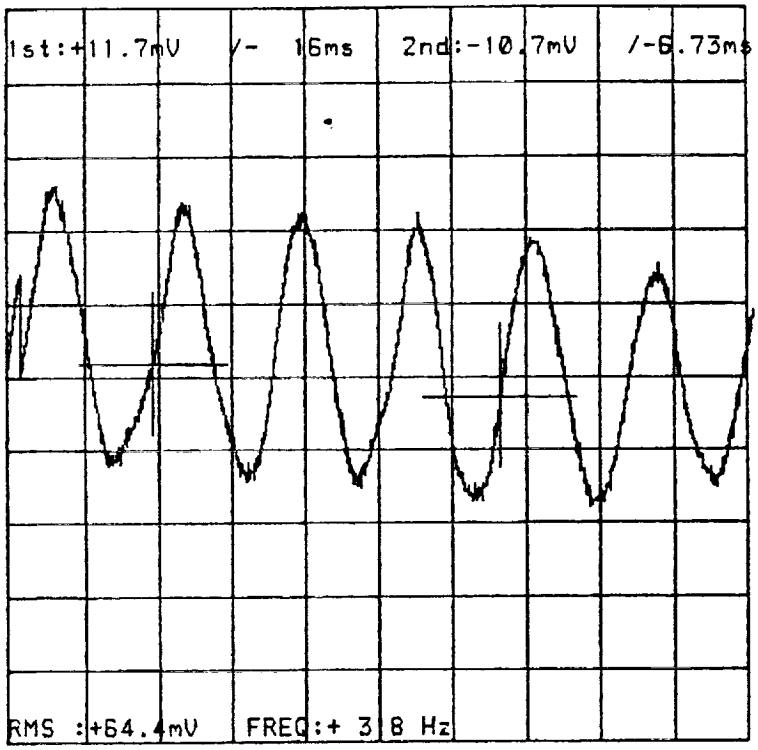

REG0 A: 50mV T
B: 200mV D:- 10DIV / A 13:54:07

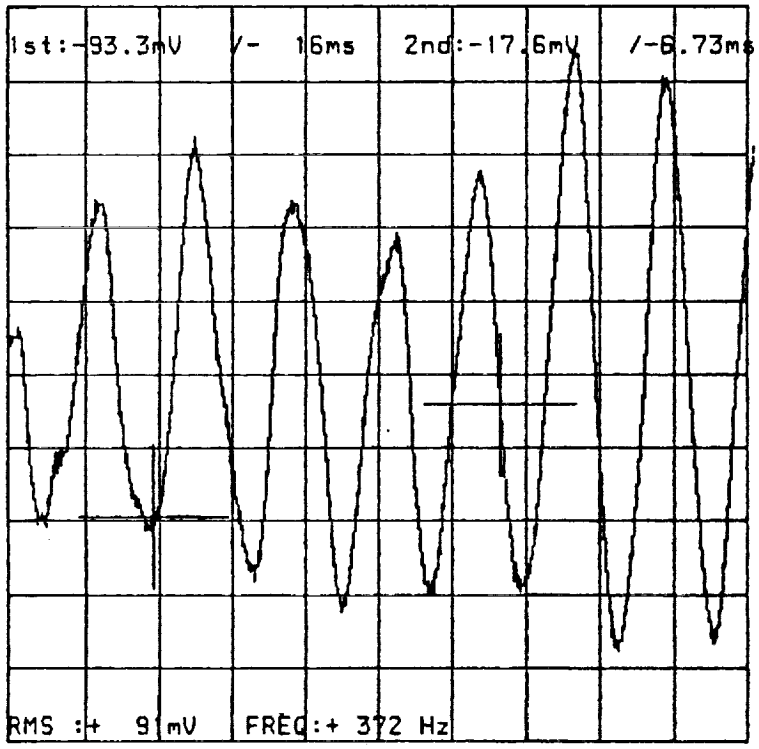

REG0 A: 50mV T: 2ms REC AUTO 90-07-18
B: 200mV D:- 10DIV / A 14:00:33

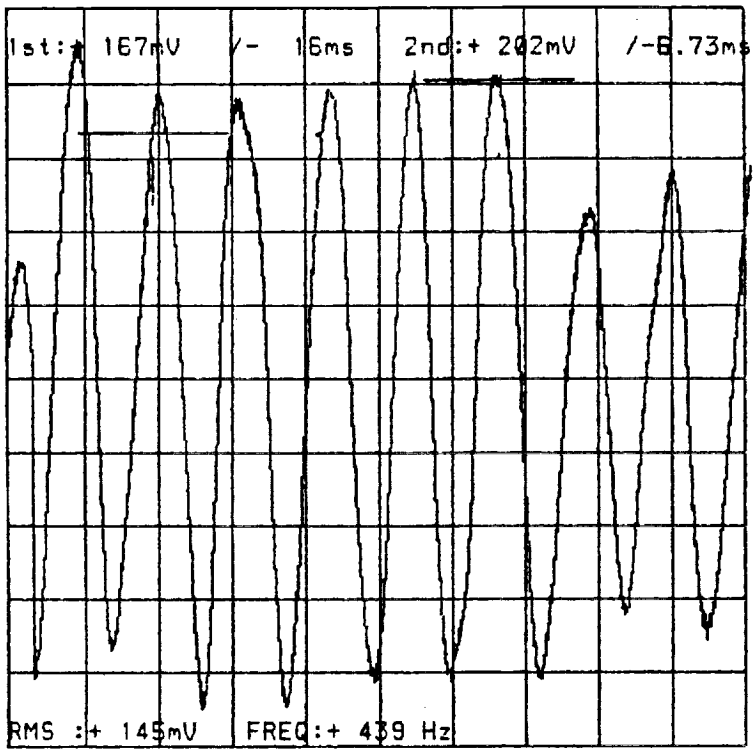

REG0 A: 50mV T: 2ms REC AUTO 90-07-18
B: 200mV D:- 10DIV / A 14:06:33

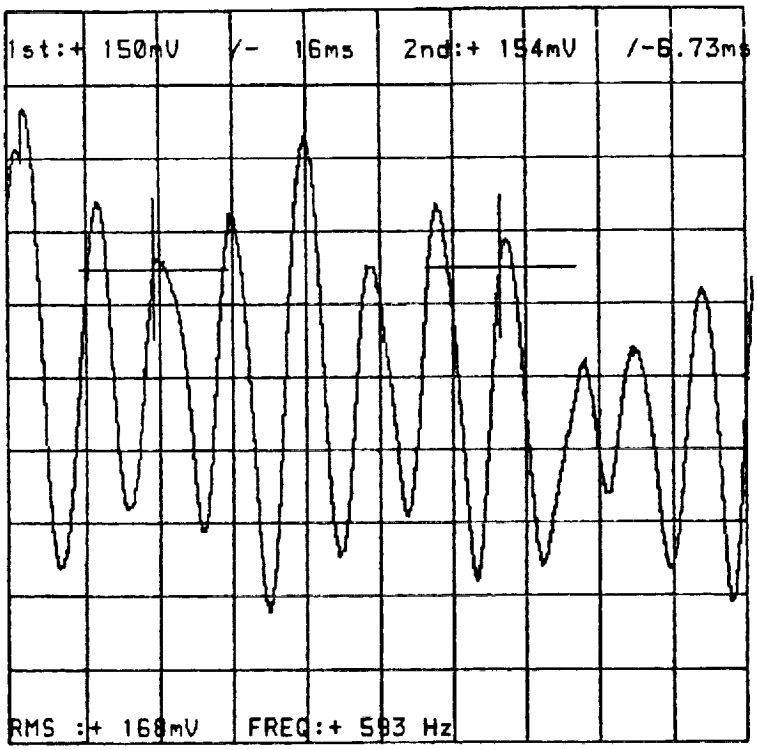

REG0 A: 100mV T
B: 200mV D:- 10DIV / A 14:15:13

07:45:55 90 Jul 21

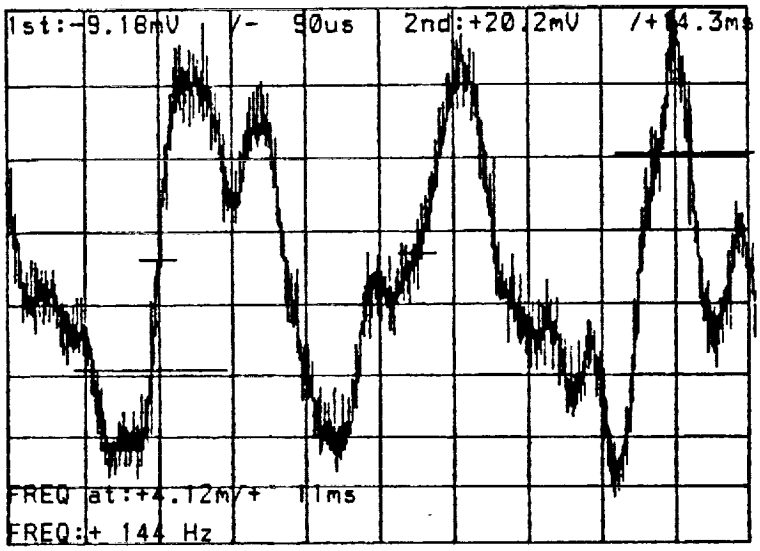

07:51:29 90 Jul 21

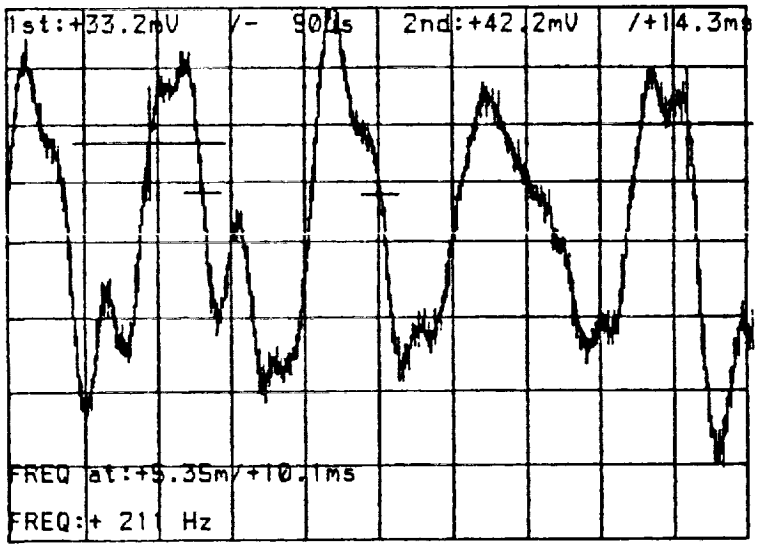

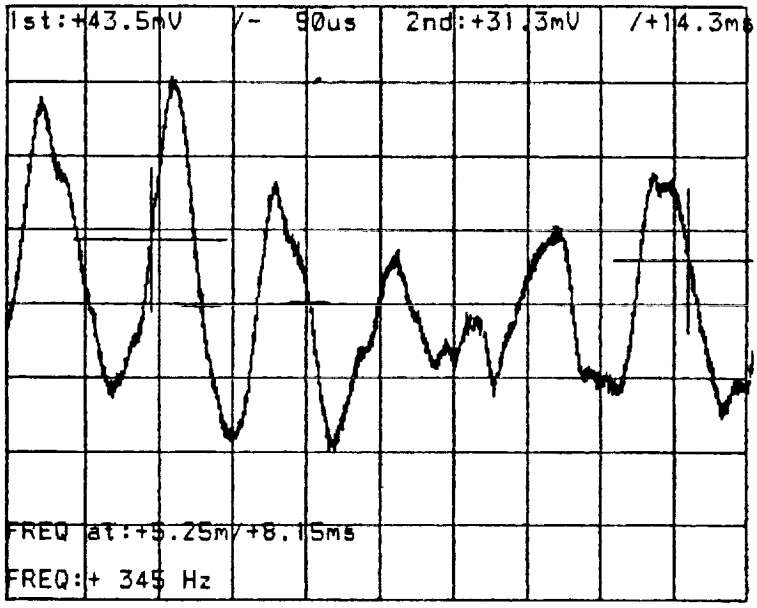

07:59:32 90 Jul 21

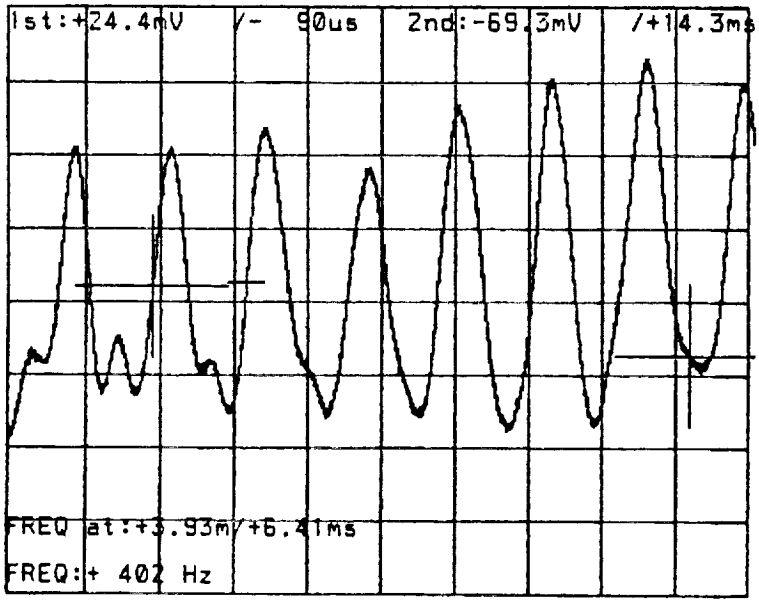

08:44:39 90 Jul 21

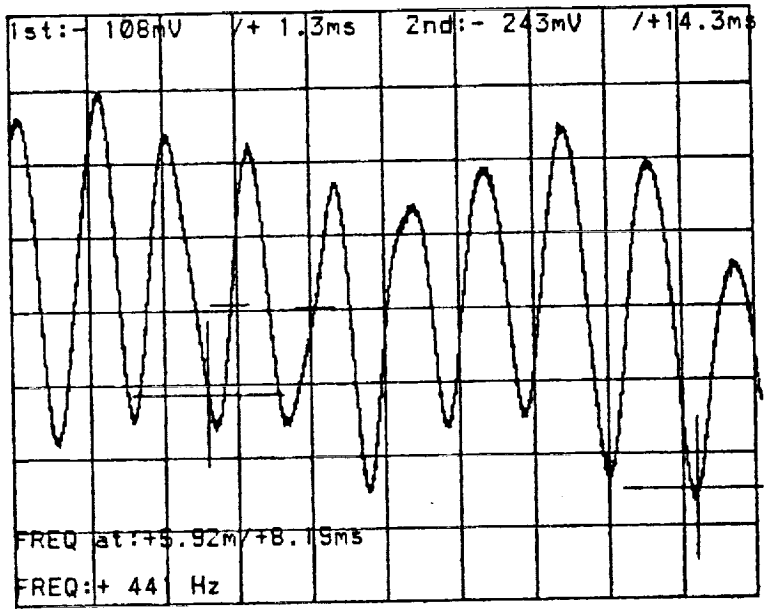

09:00:08 90 Jul 21

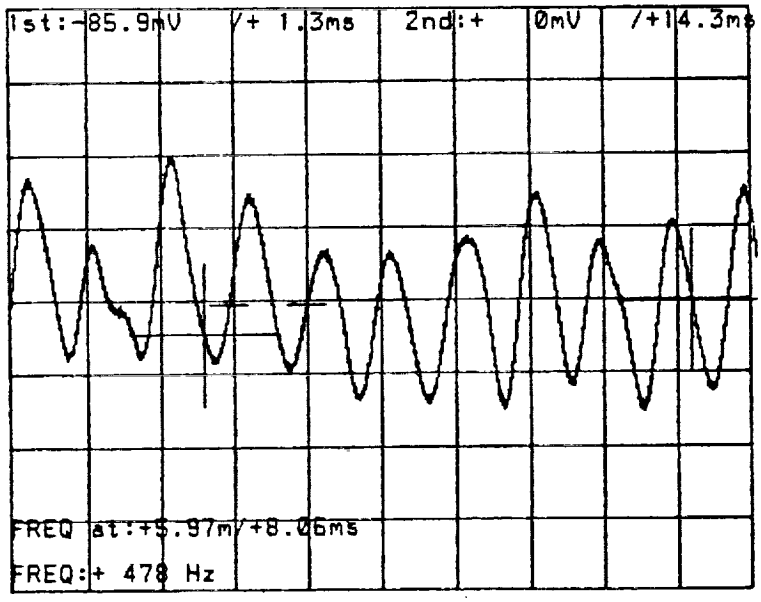

LIST OF REFERENCES

1. Birkhoff, G. and Zarantonello, E.H. , Jets, Wakes, and Cavities, Academic Press Inc., New York, 1957.

2. Pao, R. , Fluid Dynamics, Charles E. Merrill, Inc., Columbus, Ohio, 1967.

3. Siegwarth, J.D. , "Vortex Shedding Flowmeters for Space Shuttle Main Engines", National Bureau of Standards Tech. No. X89-10227, Boulder, Colorado.

4. Faber, E.A. and Hansen, E.C. , "Vortex Shedder Flowmeter", Final Report for NASA Contract Number NAS 10-11230, December 31, 1986.

5. Hansen, E.C. and Restrepo, J.A. , "Development of a Small Vortex Shedding Flowmeter for Hypergolic Propellants", AIAA, ASME, SIAM, and APS First National Fluid Dynamics Congress, Cincinnati, OH, July 25-28, 1988, AIAA Paper 88-3602, p. 1500-1504.

6. Baird, R.S. , "Flowmeter Evaluation for On-Orbit Operations. NASA Technical Memorandum 100465, August 1988.

1990 NASA/ASEE SUMMER FACULTY FELLOWSHIP PROGRAM

JOHN F. KENNEDY SPACE CENTER
UNIVERSITY OF CENTRAL FLORIDA

ROBOT TRACKING SYSTEM IMPROVEMENTS AND VISUAL CALIBRATION OF ORBITER POSITION FOR RADIATOR INSPECTION

PREPARED BY:	Dr. Gregory Tonkay
ACADEMIC RANK:	Assistant Professor
UNIVERSITY AND DEPARTMENT:	Lehigh University Department of Industrial Engineering
NASA/KSC	
DIVISION:	Mechanical Engineering
BRANCH:	Special Projects (RADL)
NASA COLLEAGUE:	Mr. V. Leon Davis
DATE:	July 31, 1990
CONTRACT NUMBER:	University of Central Florida NASA-NGT-60002 Supplement: 4

ACKNOWLEDGEMENTS

I would like to thank NASA and ASEE for the chance to participate in this program for a second year. My professional knowledge of launch operations, shuttle support, and robot applications, has increased greatly based on my interactions with the robotics group at NASA and the employees of Boeing Aerospace Organization, the engineering services contractor for the RADL. A special thanks to Leon Davis, my NASA colleague for giving me the freedom to change my emphasis as new and more interesting problems appeared.

ABSTRACT

This report dealt with two separate topics: (1) improving a robotic tracking system and (2) providing insights into orbiter position calibration for radiator inspection. The objective of the tracking system project was to provide the capability to track moving targets more accurately by adjusting parameters in the control system and implementing a predictive algorithm. A computer model was developed to emulate the tracking system. Using this model as a test bed, a self-tuning algorithm was developed to tune the system gains. The model yielded important findings concerning factors that affect the gains. The self-tuning algorithm will provide the concepts to write a program to automatically tune the gains in the real system.

The section concerning orbiter position calibration provided a comparison to previous work that had been performed for plant growth. It provided the conceptualized routines required to visually determine the orbiter position and orientation. Furthermore it identified the types of information which are required to flow between the robot controller and the vision system.

SUMMARY

The RADL (Robotics Application Development Laboratory) has been working on the robotic tracking for several years. The application of tracking is based on using a robot to mate and de-de-mate an umbilical connection on the shuttle launch pad as it is swaying in the breeze. The tracking system has many parameters which must be set. Unfortunately, there are so many parameters that it has been impossible to manually tune them. This project developed a model of the tracking system and then implemented a self-tuning algorithm to tune the variables in the model. With the success of the program there is now incentive to apply the self-tuning algorithm to the real tracking system. This paper describes the model and self-tuning algorithm in detail.

The paper discusses types of error criteria and supports the use of a combination of minimizing maximum deviation and mean absolute deviation.

By observing the model self-tuning the control system, several important discoveries were made or verified:

Target velocity affects the gains

Optimal gains could be negative for short trials

Length of tracking trials significantly changes the optimal gains

Start up biases exist which affect gains

Error criteria affects gains

Next, the concepts required for the implementation of a predictive algorithm are discussed. Several important issues are raised with recommendations of how to proceed initially. Although no experimental analysis was performed, it would be feasible to modify the tracking model to give some insights into the questions.

Finally, a discussion is presented about the requirements for a vision system attached to a robot to determine the position of the orbiter. Two methods of location determination are discussed: triangulation and analysis of known features. The issues involved in an interface protocol are also explored. Finally, a proposed scenario is given for the orbiter orientation determination task.

TABLE OF CONTENTS

LIST OF ILLUSTRATIONS

I INTRODUCTION

1.1 ROBOTICS AT KENNEDY SPACE CENTER

The mission of Kennedy Space Center is to provide manpower and support for fast, efficient and safe preparation of launch vehicles. Robotics can be a key ingredient to satisfy this mission. Many of the operations performed at Kennedy Space Center are dangerous or repetitive which make them ideal candidates for robots. The design and servicing procedures of present space vehicles and launch procedures make it difficult to implement robotics. However, the next generation spacecraft will most assuredly be designed with robots in mind. This requires KSC personnel to have familiarity with robots and related hardware such as sensors and control systems. The RADL (Robotics Applications Development Laboratory) provides this experience to NASA and its contractors.

1.2 OBJECTIVE OF THIS RESEARCH PROJECT

The objective of this research project was to assist NASA personnel in two separate areas: 1) target tracking and 2) radiator inspection. The body of this report will be divided into two parts, each describing the background and results of one project.

The objective of the target tracking project was to provide the capability to track moving targets more accurately. The physical tracking problem is a robot tracking the movements of the external tank of a shuttle on the pad so that an umbilical connection can be mated. Success has been achieved at tracking targets and mating umbilical connections when moving several inches per second. The recommendations in this report should provide the capability to track faster targets with greater accuracy using two separate methods. The first method was to write a computer program to self-tune the software PID loop found in the computer generating the system moves. This PID loop will be described in more detail later. The second method was to recommend implementation procedures for a predictive algorithm to predict the position of the target.

The radiator inspection project involves a robot being designed to inspect the radiators on the inside of the cargo bay doors of each orbiter. This robot will travel on a 67 foot track to provide coverage for all the radiator panels. Since the orbiter is parked in a slightly different position each time it enters the OPF, a calibration must be performed to determine the position of the orbiter and the radiator panels prior to inspection. This report describes the procedure which should be used to determine the orientation of the radiator panels.

II IMPROVEMENT IN TARGET TRACKING PERFORMANCE

2.1 DESCRIPTION OF TRACKING SYSTEM

A block diagram of the target tracking system is shown in Figure 2-1. The major components in this system are an ASEA IRB-90 robot, a MicroVax computer, and a DataCube vision system. The camera for the vision system is mounted on the end effector of the robot. The entire system can be thought of as a control loop. The vision system takes a picture of the target. From this picture it can calculate the relative error in inches (units used by vision system) between the camera and the target. This error is converted to millimeters (units used by the robot) and fed to the MicroVax computer at the approximate rate of 30 error vectors per second. Two buffers are maintained in the vision system. One always contains a completed picture ready for transfer, while the other is processing a picture [1].

In the MicroVax computer, the error vector is fed into a software PID loop. The purpose of this loop is to allow fine-tuning of the system moves. The PID loop outputs the coordinates for a relative move to be executed by the robot. After the relative move coordinates are determined from the PID loop, the absolute move coordinates are calculated by summing the relative coordinates with the previous absolute coordinates. Next the absolute coordinates are converted to quaternions, the orientation notation system used by the robot. Finally, the move command is sent to the robot for execution. Because the communication link between the robot and the MicroVax is slow (9600 baud), a new command is always calculated and waiting in the robot controller for execution. This leads to a problem of sending the robot to a position that is based on data which is one move old and thus introduces a lag into the system. This is an area for improvement and will be discussed in more detail later in this report.

When the robot finishes executing a command, it sends an acknowledgement to the MicroVax and immediately starts executing the next instruction which is already in its buffer. When the MicroVax receives the acknowledgment of the previous move command, it calculates the next move command and sends it to the robot communications buffer. In this way, the next command will already be available for execution and the tracking system will not experience delays due to communications.

2.2 SOFTWARE PID CONTROL LOOP

As stated previously, the purpose of the software PID loop is to transform an error into relative move coordinates for the robot to execute. By properly setting the gains in the PID loop, the

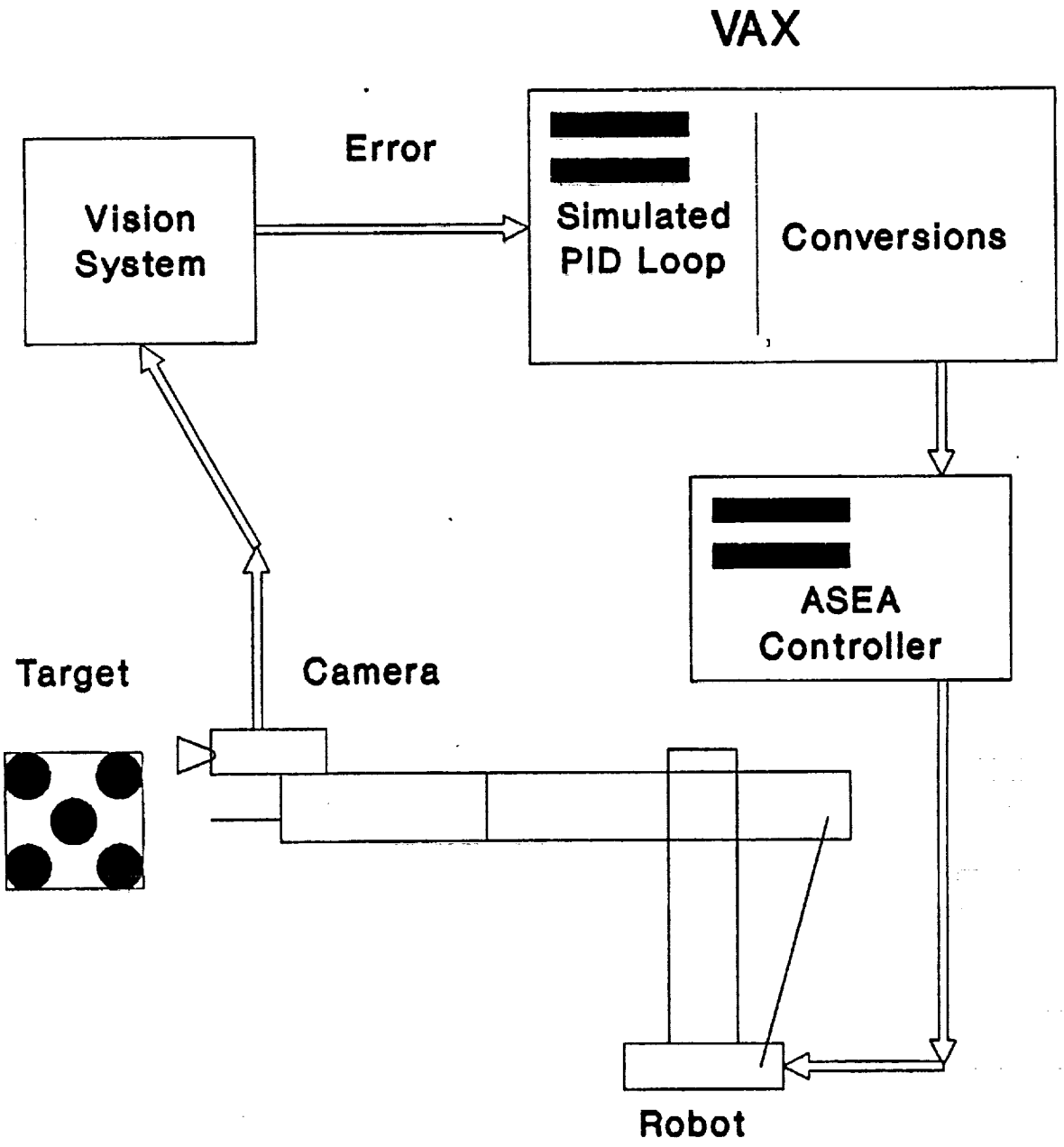

Figure 2-1. Tracking System Hardware

response of the plant (robot) can be substantially increased. There are two equations which represent the integral and derivative aspects of the PID controller, Equations (1) and (2) respectively. A third equation, Equation (3), provides the output of the PID loop.

$$I_i = I_{i-1} + e_i * T_v \tag{1}$$

$$D_i = \frac{D_{i-1} + K_d (e_i - e_{i-1})}{1 + K_d + T_v} \tag{2}$$

$$\Delta P = T_r * (K_p * e_i + K_i * I_i + K_d * D_i) \tag{3}$$

where:

I_i = integral error at time i
D_i = derivative error at time i
e_i = most recent calculated error by vision system at time i
K_p = proportional gain
K_i = integral gain
K_d = derivative gain
K_f = exponential weighting factor in the derivative equation
ΔP = delta move coordinates for the robot from PID loop

The equations above represent a single axis of the system. There are actually 6 sets of equations as represented above corresponding to X, Y, Z, Roll, Pitch, and Yaw. The 18 equations have a total of 24 gain constants.

2.3 PROBLEMS TUNING THE PID LOOP

Tuning the software PID loop presents several problems. First, the optimal gain values depend on the operating parameters of the system, such as target velocity, pattern of target motion, time between vision updates, time between robot moves, maximum robot velocity, and robot acceleration. These parameters are subject to constant change as the system is upgraded. It would take a long time to optimally tune the PID loop manually, at least one man-week. Even if the PID loop were tuned, changing a single operating parameter would require the loop to be re-tuned. These problems necessitate an automatic method to tune the loop.

2.4 MODEL OF TRACKING SYSTEM

To develop an automatic method to tune the loop, valuable system time and manpower would be required during development, debugging, and testing. Therefore, a computerized model was developed to

approximate the tracking system. By writing a program to self-tune the PID loop in this model before implementing it on the actual system, time and money would be saved. Furthermore, the tracking model could provide a graphical platform to explain the system and test hypotheses.

Several assumptions/limitations were made in order to reduce the complexity of the model. However, the operating principles of the actual system were used wherever possible. The first and greatest limitation is that of only modeling one axis of motion. Since the real-life target to be tracked is a shuttle on the pad blowing in the breeze, it is assumed that the major motion will be along one axis. Specifically, past research projects have dealt with a motion of 10 inches in the X direction, and 3/4 inch in the Y and Z directions. The same principles used to tune the single axis in this model could be used to tune all of the axes in the actual controller.

The second assumption is that the motion will be sinusoidal with time. The velocity will be at a minimum at the extremes of motion and a maximum through the mid-point. It should be noted that any pattern of motion could be simulated just by changing the motion generating function for the target.

The third assumption is that the robot controller is assumed to be perfect. No overshoot or instabilities result from the controller. While this may sound like a major limitation, it is believed that the time lags in the other systems cause instabilities which are orders of magnitude greater than those caused by the robot controller. The robot controller was modelled to ramp up to its required velocity at a given rate of acceleration. Furthermore, a variable was included to provide a delay between execution of robot commands. This would simulate the robot controller reading and setting up for the next move. The controller was also modeled to have an internal move buffer.

The fourth assumption is that there is no error in the vision system calculations. A possible way to model this error is to add a small random error to each calculation. The vision system was modeled with two buffers. When a robot move must be generated, the completed buffer is used even though the data in the buffer is already old.

Some thought was given to selecting a criteria for judging one set of gains against another. In the final program, the user must select one of the following three criteria:

> Mean Absolute Error - This measure treats all errors as equal and attempts to minimize the mean. Arguments could be made against this measure because one extremely large error could

be enough to shutdown the tracking system. However the effect of one large error on the overall mean would be insignificant.

Root Mean Square Error - This measure tends to magnify the larger errors (squares the error) and hence solves some of the problems of Mean Absolute Error. However, the effect on the mean of a single large error might still be insignificant.

Maximum Absolute Error - This measure records the largest error in the trial but disregards the other errors. Statistically, it is better to use a measure that uses more of the data. However, for the tracking problem, this is a reasonable criteria. Note that in reality a user might be willing to sacrifice a little maximum error in exchange for better mean square error.

Another possible criteria would be a weighted function including terms for the maximum absolute error and the mean absolute error (or root mean square error). This would allow the user to use both measures to choose the optimal gains. Yet another possibility would be to minimize the mean absolute error subject to maintaining the maximum absolute error below some value. For example, if the system could track as long as the error was less than 3 inches, the optimizing routine could minimize the mean absolute error in trials which keep the absolute error less than 3 inches. These last two optimization criteria were not included in the tracking system model. They are mentioned as possible candidates for further work.

There are many variables which the user can change in the model. The most typically changed variables are the 4 gain parameters from Equations (1), (2), and (3), the speed of the target, the maximum velocity and acceleration of the robot, and the amplitude of target motion. Other variables can be changed to perform what-if scenarios. For example, "what would happen if the robot position could be updated 20 times per second instead of 7" or "what would happen if the buffer in the robot were eliminated and the robot had to wait to receive the move command before execution could start?" There are many possible configuration changes that can be quickly and easily tested.

2.5 OUTPUT FROM THE TRACKING SYSTEM MODEL

The model is programmed to graphically show the motion of the target and the robot in time. Figure 2-2 is an example of the tracking system with no PID loop to speed up the robot controller (proportional gain equal to 1 with no derivative or integral gain). Time is shown on the horizontal axis and position is shown on the vertical axis. The error components, e_i, I_i, and D_i from the PID loop, are shown on a second graph at the bottom.

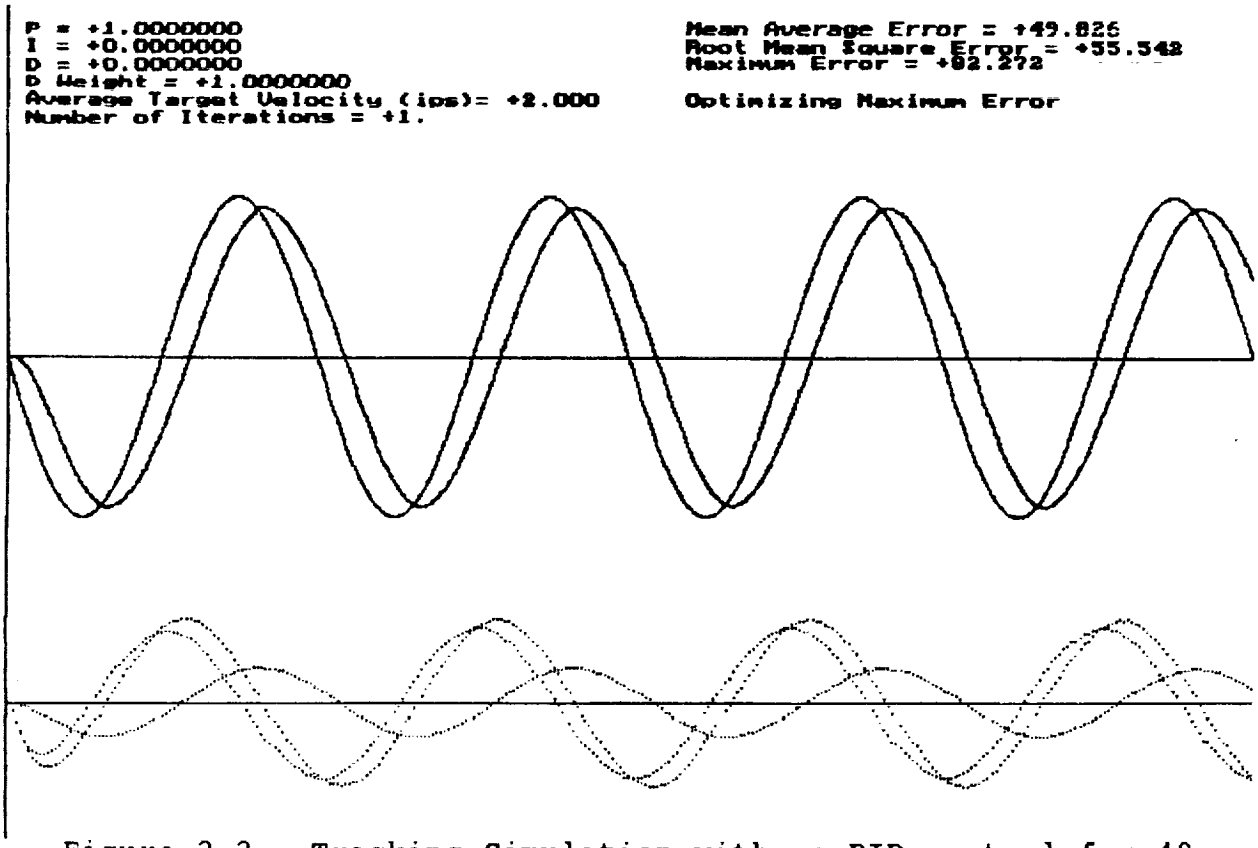

Figure 2-2. Tracking Simulation with no PID control for 48 seconds

As expected from experience, the robot lags the target because of the buffers, delays, and inaccuracies in the system. As the gains are increased, the robot lags less. As the gains continue to increase, eventually the robot will overshoot when the target slows down and reverses direction. Some overshoot is acceptable, but increasing the gains further can cause oscillation as shown in Figure 2-3 and eventually system instability.

2.6 SELF-TUNING ALGORITHM

The system model as described above could be used to determine which projects should be attempted first in order to receive maximum payback in the form of increased tracking capability. However, a major goal of this project was to write a computer program to self-tune the gains in the PID loop. This was accomplished faster by first modeling the tracking system as described previously and then writing a self-tuning algorithm to alter the gains in the model to optimize one of the measures of performance. It also proved the concept before tying up expensive robot and technician time. Now that the self-tuning concept has been demonstrated, it can be implemented on the system hardware.

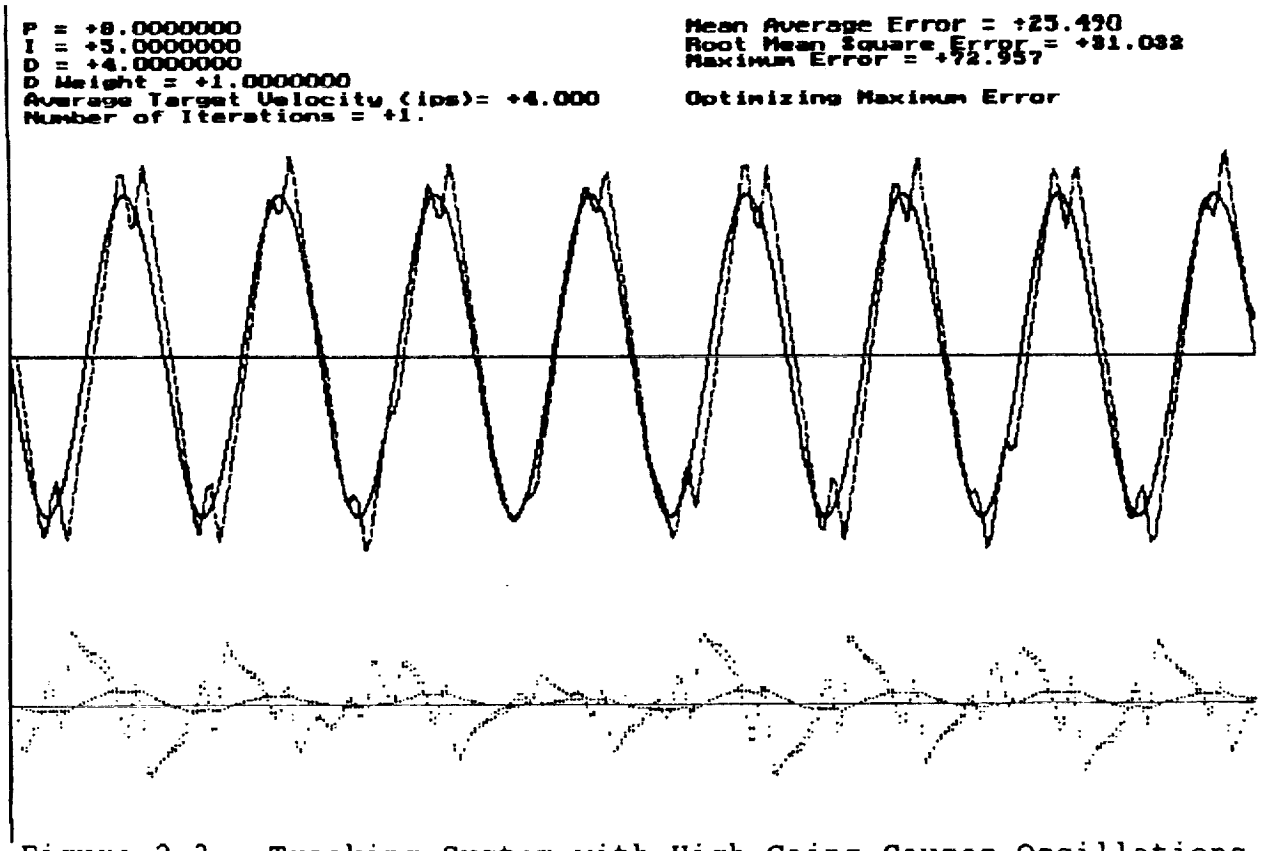

Figure 2-3. Tracking System with High Gains Causes Oscillations

The approach used to self-tune the PID loop was a response surface, hill-climbing technique. If there were only two gains, the response surface would look like a mountain. The elevation, or Z axis, would be analogous to the optimization criteria. The two gains would be analogous to longitude and latitude coordinates, or X and Y axes. As the gains, or X and Y coordinates, are changed, the mountain climber will either ascend, descend, or stay at the same altitude. There are several hill climbing techniques that could be used to reach the top of the mountain. In the coded algorithm there are actually 4 gains to be changed rather than 2, but the concept is still the same.

The method implemented in the model is the "method of steepest ascent." The tracking error is known for the gains set at their current values. Then one at a time, each gain is incremented a certain amount while the other gains remain at their original values. If for any gain the error gets worse, the gain is decremented instead of incremented and another error calculation is performed. Thus with 4 gains, a minimum of 4 trials and a maximum of 8 trials are performed before the new gain values are selected. The new gain values will be the ones used in the trial which produced the greatest reduction in error.

One further refinement added to the algorithm was to adjust the increments added to the gains so that a course search was conducted. Once the gains were tuned with the large increments, smaller increments were used to refine the gains. Finally, even smaller increments were used to attempt to reach the pinnacle of the summit. Trials have shown that depending on the increments that are specified for the trials, it could take several hundred iterations to achieve a final solution.

In order for this coded algorithm to work with the tracking system instead of the simulation, a function must be defined which takes as its inputs the four gain values, runs the tracking system, and returns a value representing the measure of error. In addition, other modifications might be required in the tracking system for automatic operation.

Because the hill climbing technique is a heuristic, it may find a local optimal solution instead of a global optimal solution. To reduce this possibility, the algorithm could be run several times, each with different starting gains. While this will not guarantee a global optimal solution, it will increase the chances of finding a global optimal.

2.7 RESULTS OF SAMPLE TRIALS

After running several trials and comparing the results, several conclusions can be drawn.

Target Velocity is Significant. Changing the speed of target motion will change the resulting optimal gains. Figures 2-4 and 2-5 show the self-tuning results for average target speeds of 2 and 4 ips, respectively. Note also that the tracking errors are significantly worse with the target moving at 4 ips, almost twice as bad.

Length of Tracking Trials is Significant. The length of the tracking trials could significantly affect the selected gains. For short tracking trials the gains could be set such that the system is slightly unstable. This would not be noticeable unless longer trials were performed with the same gains. Figure 2-6 shows the solution when the gains were tuned using 48 second trials. If these same gains were specified in a trial that is 200 second as shown in Figure 2-7, the system became unstable after about 70 seconds.

Optimal Gains Could Be Negative. Figure 2-5 shows that the integral gain could be negative, depending on the tracking conditions. The parameter most affecting the negative gains is the time that the system tracks in each trial. For a system tracking for long periods of time, the gains should never be negative.

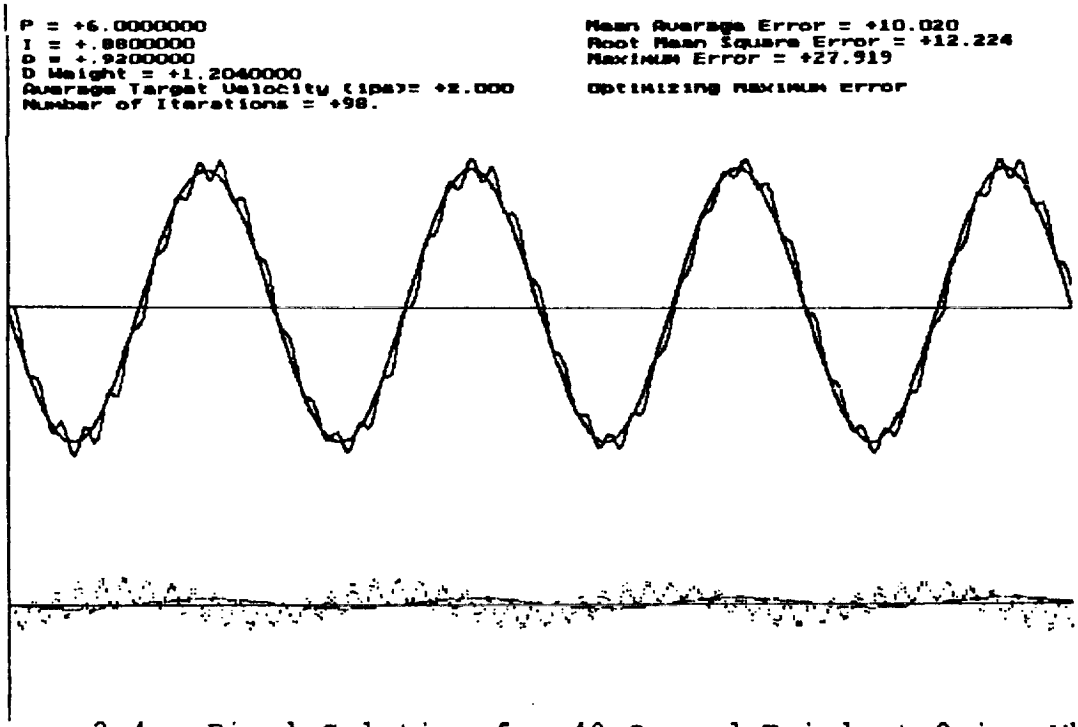

Figure 2-4. Final Solution for 48 Second Trial at 2 ips When Optimizing Maximum Error with Start Up Bias

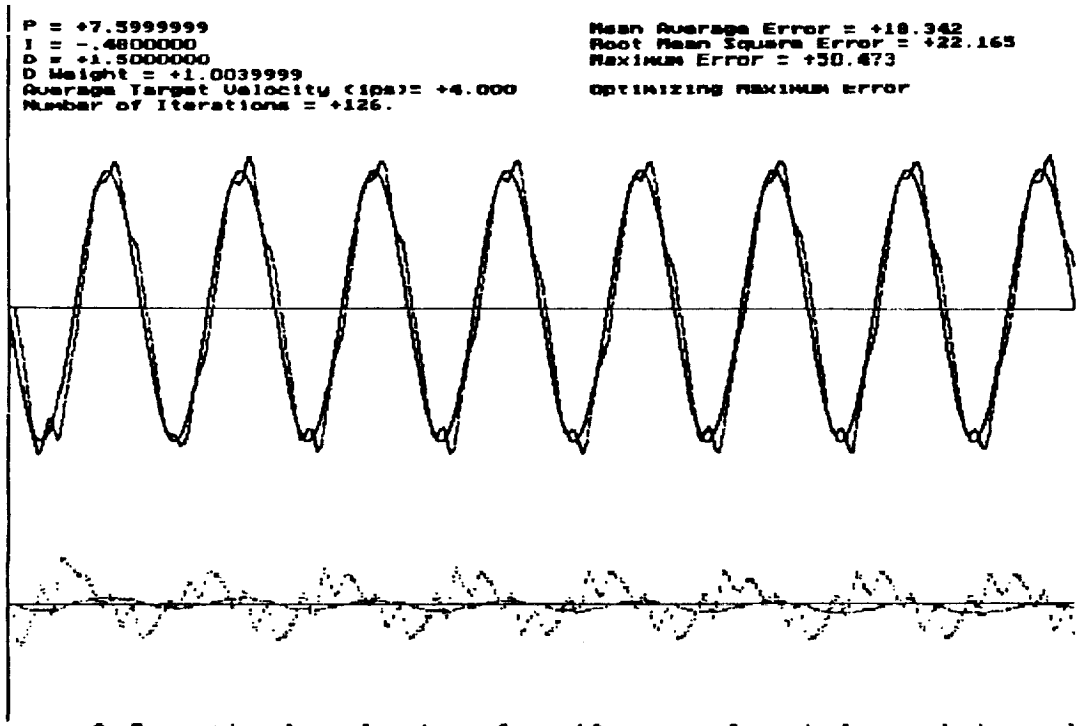

Figure 2-5. Final Solution for 48 Second Trial at 4 ips When Optimizing Maximum Error with Start Up Bias

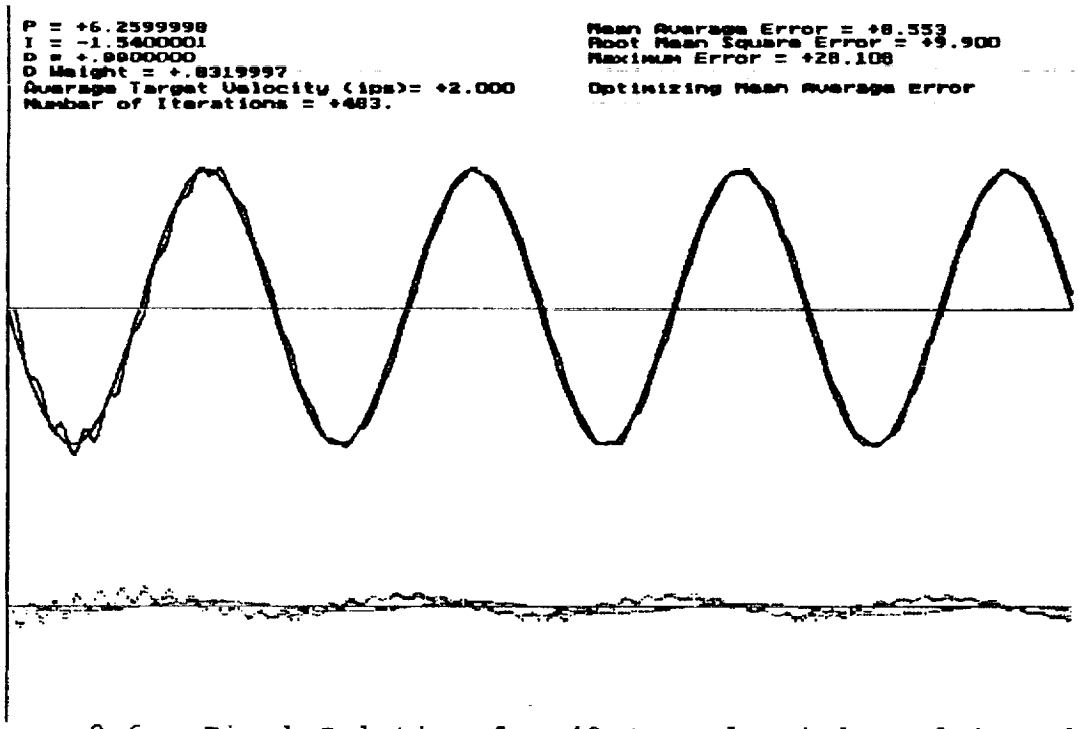

Figure 2-6. Final Solution for 48 Second Trial at 2 ips When Optimizing Mean Average Error with Start Up Bias

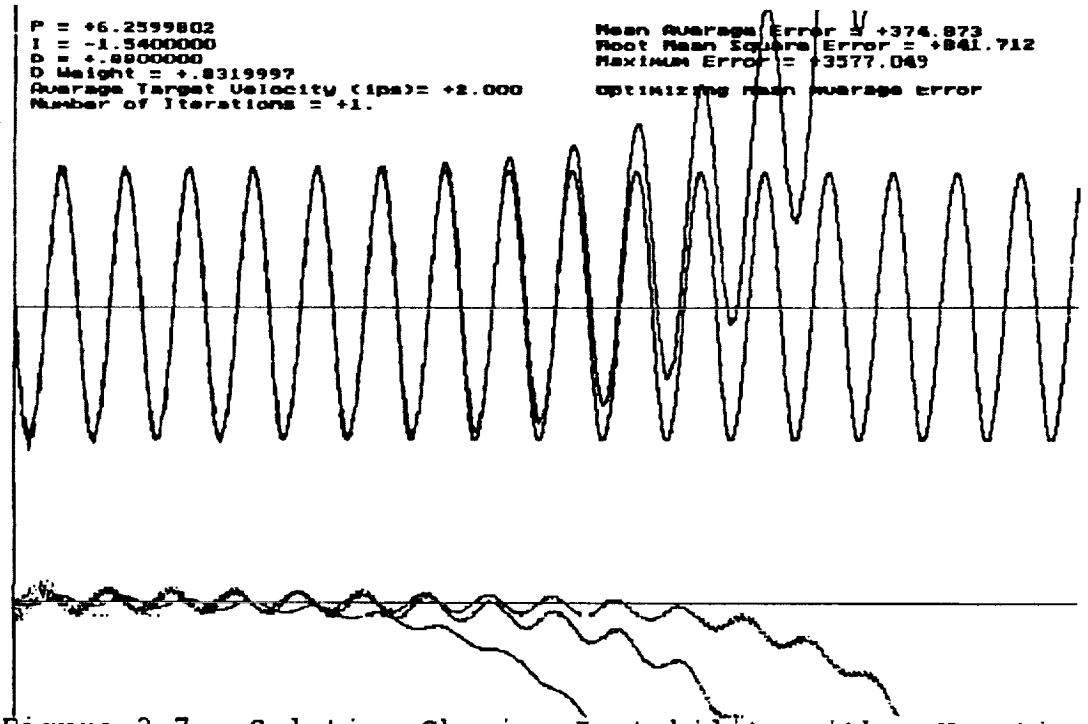

Figure 2-7. Solution Showing Instability with a Negative Integral Gain Tracking for 248 Seconds

Start up Bias Exists. A start up bias exists which can significantly affect the gains. It is most apparent in trials which attempt to minimize maximum error. A large error occurs at the beginning of the trial while the system overcomes the lags. This single source of error quickly becomes the maximum error. In order to minimize maximum error, gains will be selected that reduce the start up bias at the expense of the rest of the tracking cycle. Figure 2-4 shows a trial with start up bias that tracks for 48 seconds. Figure 2-8 shows the same conditions except that tracking

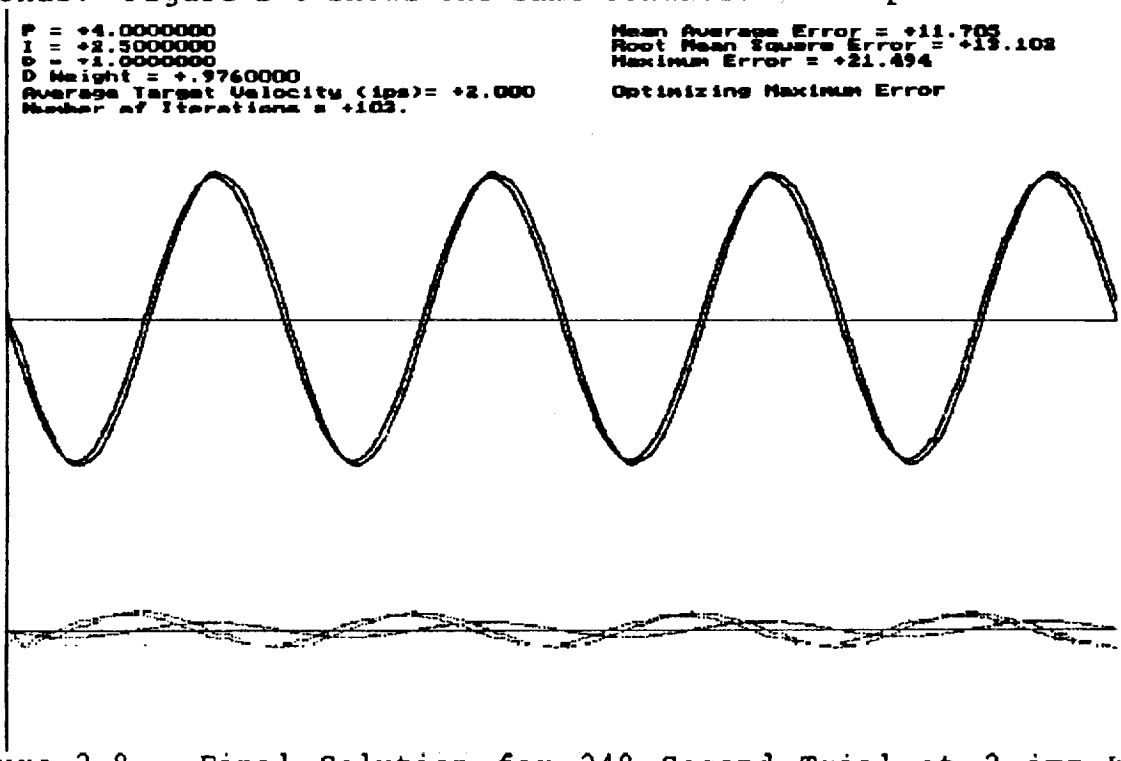

Figure 2-8. Final Solution for 248 Second Trial at 2 ips When Optimizing Maximum Error with No Start Up Bias

occurs for 248 seconds. The initial 200 seconds are not shown in the figure and errors are disregarded during this period. The results show a more stable system as the result of eliminating the start up bias. Measures using mean error are not affected as much by start up bias.

Optimization Criteria is Significant. The error criteria can play a significant part in the selection of gains. Figures 2-4 and 2-6 show the same trials except for a difference in error criteria. The difference will be more significant when the start up bias is not eliminated.

III PREDICTIVE ALGORITHM

The use of a predictive algorithm is another attempt to track more accurately. If a certain type of motion is assumed, an algorithm can be formulated to predict where the target will be at the next robot move. However, if the motion significantly deviates from the assumption, the system will track poorly.

3.1 PREDICTIVE EQUATIONS

The equations used to predict the target position should be based on an assumed type of motion. This could include polynomial, exponential, or sinusoidal. Polynomials offer an added advantage of being quicker to calculate on the computer. In the case of polynomials, the predicted value is based on previous values. The number of previous values and the coefficients assigned to them can vary depending on the type of motion. However, unless there is a specific reason for doing otherwise, the coefficients should sum to 1. Examples of two equations derived by NASA and Boeing Aerospace Organization (BAO) are:

$$X_{n+1}=2X_n-X_{n-1} \tag{4}$$

$$X_{n+1}=\frac{5}{2}X_n-2X_{n-1}+\frac{1}{2}X_{n-2} \tag{5}$$

where:

X_{n+1} is the predicted value 1 period in the future
X_n is the value at the present time
X_{n-1} is the value 1 period in the past

Equations (4) and (5) should provide better response if the motion is linear and quadratic, respectively. Further derivations could be conducted for cubic motion. However, the increasing complexity of the calculations often does not provide proportional increases in prediction accuracy.

3.2 PREVIOUS ATTEMPT AT A PREDICTIVE ALGORITHM

A previous attempt was made to implement a predictive algorithm in the vision system. This approach did not use information about the robot or target position, velocity, and acceleration. Instead, it only used the error information contained in the vision system. Since the error information is dependent on both the target and robot trajectories, it is impossible to predict target motion without knowing something about the robot motion that produced the previous errors.

Furthermore, the problem is compounded because the error reference frame is continually shifting with the target and not constant with respect to the world or the robot. By choosing to implement the algorithms in a reference frame which is continually shifting, an important implicit assumption was made:

> If an error of "zero" occurs, the proper control strategy is being used and tracking should continue at the same velocity/acceleration to keep the robot on track. In more general terms it could be stated that any prediction about error that is made assumes that the current trajectory of the robot will continue. The predicted error is with respect to the current change in the position of the reference frame.

This can be illustrated with an example. Suppose the target is moving at a rate of 5 ips and the robot is tracking right on target with a velocity of 5 ips (highly unlikely because of lags in the system but okay for the purposes of illustration). Furthermore, it has been correctly tracking for the last several points so all of the past vision system errors are also "zero." With the current implementation of the predictive algorithm, the next predicted error would be "zero" and a command would be issued to the robot not to move during the next time frame. However, the target would continue to move and the robot would be left behind.

Based on the assumption listed above, what the robot should be doing when the error is "zero" is to continue moving in the same direction at the same velocity and acceleration. The reference frame must continue to move as it was moved when the previous errors were calculated. When the predicted error is "zero," it means it will be zero if the current trajectory is maintained. Therefore, a command should be issued to continue moving for the next segment at the same velocity in the same direction. In this example, the robot would be instructed to move at 5 ips and thus stay exactly on target.

In the more general case, the robot should move to a point which is the sum of the absolute position at the end of the current move plus the previous incremental move (to maintain the moving reference frame) plus the predicted error. A similar example could be presented for the general case where the predicted error is not "zero." However, to maintain brevity, it will be skipped at this time.

From this discussion it should be clear that there is a problem with the present implementation of the predictive algorithm. It could probably be modified to make it workable. However, it probably is not the best method of implementation.

3.3 PROPOSED IMPLEMENTATION OF THE PREDICTIVE ALGORITHM

There are several methods which could be used to properly implement a predictive algorithm. However, it is not clear which is the correct path to take for predictive algorithm implementation. It is not clear whether the prediction should be made in the MicroVax or in the vision system. Another important issue is where the results should be applied. Should an additional move component be calculated to sum to the robot position, or should the results of the predictive algorithm be fed into the PID loop for processing? Also, should the PID loop still remain in the tracking system? Since the PID loop is, in a manner of speaking, also doing some predictions, there is the possibility that the two will conflict. There are many questions which need to be answered. To gain some insight into these issues, the tracking model developed and presented in the previous sections could be altered. This would give the user some indication of the relative benefits of different methods.

Parallel to the implementation issues is the issue of calculating the prediction. The most straight forward approach is to determine the target path by combining the robot position with the vision system error. Thus, the predictive equations could be applied to positions as opposed to errors. If errors are still required as inputs to the PID loop, the calculated robot position at the end of the current move could be subtracted from the predicted target position to yield the predicted error. This should be the first attempt at implementation. With the PID loop intact, the controller will have the capability to speed up the response of the robot. However, the gains will probably require tuning because the error input will contain more information. If the system works properly, the gains should be able to increase, which will result in better response.

The predictive algorithm offers an opportunity for more accurate tracking. However, it must be reiterated that the predictions are based on an assumed type of target motion. If the target behaves in a random manner or a manner significantly different from the assumption, severely degraded performance could occur.

IV VISUAL CALIBRATION OF ORBITER POSITION FOR RADIATOR INSPECTION

4.1 RADIATOR INSPECTION ROBOT

NASA is currently in the process of design and construction of a robot to inspect the radiator panels on the orbiter. These panels are located on the inside of the cargo bay doors. They are inspected when the orbiter is pulled into the OPF and resting in the horizontal position. The cargo bay doors are opened to expose the radiator panels. Presently, the inspection occurs by workers in a bucket moving over the surface. The surface is divided into grids and defects are cataloged by location in the grid. Not all defects are repaired. Many are noted for future inspection to see if they are growing worse.

This is an ideal application for automated inspection. A robot is being constructed to move lengthwise beside the orbiter on a long track. It will be capable of inspecting the entire surface of the radiator panels. The system will be able to divide the radiator panels into smaller grids and thus provide better cataloging of defects.

The visual inspection system requires 1/8 inch accuracy in the X, Y, and Z direction. Therefore, the orientation of the orbiter will have to be determined with an accuracy better than 1/8 inch. For this part of the report, the task was to conceptually determine how the orientation could be performed visually, whether the Perceptics vision system in the RADL could perform the task, and what types of communication would be required between the robot controller and the vision processor.

4.2 PERCEPTICS VISION SYSTEM ROUTINES

The Perceptics vision system is a powerful high-level vision processor that runs in parallel with a MacIntosh computer. It can act as a color system if the appropriate hardware is included. Functions are available to snap pictures, perform thresholding, blob analysis, and other complex vision calculations [2].

The system was used in a project that identified wheat heads and moved the robot to point to them. While at first glance this seems much different than the project at hand, it really is very similar. A calculation must be performed to determine the position of the wheat head with respect to the robot. This is exactly the same task which must be used to determine the position of the orbiter.

Many routines were written in C to perform the vision tasks and robot move tasks. Of particular interest are the routines to

determine the position of an object. There were two approaches to this problem. The first and most accurate was to use 4 fiducial points or dots arranged in a rectangle. By looking at these 4 points and using the vision system to measure the distance between them, the system could determine the orientation of the 4 points with 6 degrees of freedom. The accuracy achieved was about 1 mm which is well within the accuracy requirements. However, this method requires four dots to be laid out in a known rectangular pattern [3].

The second method used to locate objects was one of triangulation. Instead of a single picture as in the previous method, this method required two pictures to be taken a known distance apart. The same features must be located in each picture to determine the relative motion in the picture compare to the actual motion of the camera. This method provided accuracy that was barely acceptable in the axes of the vision system. In the third axis, the distance from the camera, the error exceeded that allowed for the system (5/32 inch error, 1/8 inch required accuracy). Better accuracy could be achieved by spreading the views apart. However, the previously described method would be preferred if implementable.

4.3 FEATURES TO USE FOR ORIENTATION

In order to determine the orientation of the orbiter, the position of 3 points on the surface must be known. In order to achieve maximum accuracy, the three points should be at the extreme ends of the object. On the orbiter, this might be three corners at the far extremes of the radiator panels. However, to achieve maximum accuracy the method using fiducial points is preferred. The corners of the panels do not offer this opportunity.

Another nearby feature is the set of bolts attaching the radiator panels to the cargo bay doors. In two of the corners, this is a 3 bolt pattern. In the other two corners, this is a 4 bolt pattern. By using these bolt holes and modified Perceptics vision system routines, the orbiter position could be calculated. A 3 bolt pattern will not provide a full 6 degree-of-freedom orientation like a 4 bolt pattern. However, it is not required in this case. By knowing the (X,Y,Z) position of 3 separate and known points on the orbiter, orientation of the orbiter can be calculated in 6 degrees-of-freedom.

4.4 PROPOSED SCENARIO

The proposed scenario to determine the orientation is:

1) Move to the first location. This could be either automatic or manual. The robot should be able to get close enough to perform the task automatically, although

initially manually controlled joystick motion might be preferred.

2) Take a picture and have the vision system send the appropriate coordinates with respect to the robot TCP.

3) The robot controller should calculate the location of the feature in OPF coordinates using the joint angles and kinematic transformations for the robot.

4) Perform tasks 1 to 3 for each of the remaining two features.

5) Determine the orientation of the orbiter using the robot controller. Pass any required information to the vision system performing the inspection.

4.5 INFORMATION EXCHANGE BETWEEN COMPUTERS

The communication link between the robot controller and the vision calibration system should require little information transfer. Since there are no processing speed requirements for the orientation task, a serial link should prove satisfactory. The robot controller should act as the master, issuing commands to the vision processor and waiting for responses.

The robot controller should be able to issue commands to the vision system to take pictures, process the pictures for specific features, and return the coordinates of the feature. The robot controller should also know the exact instant a picture is taken so that it can record its joint values. This will eliminate the problem of drift between the time the vision system takes the picture and the robot controller processes the data. However, it also requires that a single parallel signal be input to the robot controller to identify when a picture is taken. The vision system has no need to issue commands in this system.

V CONCLUSIONS

There were two distinctly different topics approached in this research project. The purpose of the first part of this research was to increase the tracking accuracy of a robotic tracking system. Two methods were explored: tuning the parameters in the system and implementing a predictive algorithm. A program was developed to self-tune the gains in the system by a heuristic "hill climbing" approach. The method implemented was the method of steepest ascent. Each of 4 gains in the system was incremented or decremented and the resulting reduction in error noted. The gain providing the best reduction in error was changed and the entire process was repeated until no further gain could be achieved.

To test this algorithm, a model of the tracking system was developed. This model included the lags inherent in the system due to buffering. It also modeled the acceleration rates of the robot controller. The model was used by itself and in conjunction with the self-tuning algorithm to better understand the tracking system. Several important conclusions were reported. The optimal gain values were found to be dependent on many factors in the system including the velocity of the target, the error criteria employed, the length of a tracking trial, and start up biases. The model was found to agree with most of the system responses observed by technicians and engineers over several years of trials.

Criteria for errors were discussed and although no trials have been performed, a measure was recommended for further study which included both the maximum absolute error and the mean absolute error. A possible implementation would be to use the maximum error as a constraint while minimizing the mean error.

Issues were raised and discussed in the implementation of a predictive algorithm. A previous attempt was discussed and the error was pointed out. It was proposed that the target position should be determined by summing the robot TCP position with the vision system error recorded at the same time. Questions were raised about where the predictive algorithm should be located and whether the PID loop would still be required. A recommendation was made to add these capabilities to the model to obtain some knowledge about the decisions which are required.

In the second topic of this report, the use of a vision system to determine the orientation of the orbiter in the OPF was discussed. The task of radiator inspection was defined. Next, the use of the Perceptics vision system located in the RADL was explored. Next, a scenario was proposed to determine the orientation. Finally, the communication between the robot controller and the vision system was discussed.

VI REFERENCES

[1] Davis, Virgil Leon, "Systems Integration for the Kennedy Space Center Robotics Applications Development Laboratory," MS87-482 SME Technical Report, 1987.

[2] User's Manual for the NuVision Image Processing Workstation, Perceptics Corporation, Knoxville, TN, 1989.

[3] Myjak, Michael; Sklar, Mike; Tharpe, Roy; Thomas, Mark; and Wegerif, Dan, Automated Plant Growth Development Project: FY89 Final Report, Advanced Technologies Branch of McDonnell Douglas Space Systems Company, Kennedy Space Center, 1990.

N91-20038

1990 NASA/ASEE SUMMER FACULTY FELLOWSHIP PROGRAM

JOHN F. KENNEDY SPACE CENTER
UNIVERSITY OF CENTRAL FLORIDA

p20

MODELING OF FLOW SYSTEMS FOR IMPLEMENTATION UNDER KATE

PREPARED BY:	Dr. Jonathan E. Whitlow
ACADEMIC RANK:	Assistant Professor
UNIVERSITY AND DEPARTMENT:	Florida Institute of Technology Department of Chemical Engineering
NASA/KSC	
DIVISION:	Data Systems
BRANCH:	Technical and Information Systems
NASA COLLEAGUE:	Ms. Carrie Belton
DATE:	August 30, 1990
CONTRACT NUMBER:	University of Central Florida NASA-NGT-60002 Supplement: 4

ABSTRACT

The modeling of flow systems is a task currently being investigated at Kennedy Space Center in parallel with the development of the KATE artificial intelligence system used for monitoring diagnosis and control. This report focuses on various aspects of the modeling issues with particular emphasis on a water system scheduled for demonstration within the KATE environment in September of this year. LISP procedures were written to solve the continuity equations for three internal pressure nodes using Newton's method for simultaneous nonlinear equations.

SUMMARY

KATE is a model-based expert system being developed at Kennedy Space Center for the monitoring, diagnosis and control of launch operations. This work focused primarily on modeling issues associated with the construction of the knowledge-base for a water tanking demonstration system.

In order to accurately predict expected values of various sensor readings in the water system for various flow configurations, the model used for simulation by KATE had to be modified. The original model of the flow network used a single mass continuity equation which required an iterative solution for an internal pressure node at each increment of time. In order to sufficiently model the process for certain combinations of valve positions, three mass continuity equations were needed. As a consequence, the values of three unknown internal pressure nodes were then required for solution of the resulting nonlinear equations at each time step.

Various methods were examined for the solution of the three simultaneous nonlinear equations. Newton's method was ultimately chosen for implementation in the KATE knowledge-base due to its speed of convergence. In general, Newton's method requires an initial starting value for the solution vector which is sufficiently close to the actual solution. Testing of the method indicated that initial guesses provided within physical constraints of the system, converged. The concern over guaranteed convergence resulted in the more stable Steepest Descent minimization method to also be examined. The time required for convergence of this method however was more than an order of magnitude greater than Newton's method. Both algorithms were encoded in LISP for use by KATE.

Additional LISP code had to be included in the procedure written to perform Newton's method in order to prevent the generation of error messages. The source of the error messages came from discontinuity in the modeling equations which would result from various valve positions. The discontinuities resulted in a singular matrix being formed in the program and hence the resulting errors. The method used to avoid the error generation in effect looked at all possible valve combinations and flow conditions and dealt with each as necessary.

Although the model complexity was increased in this work over previous work, there are still various simplifications included in the model which may cause severe inaccuracies during simulation under certain conditions. A discussion of these issues, as well as a discussion on modeling of more complex cryogenic systems is also included in this report.

TABLE OF CONTENTS

I. INTRODUCTION

Investigations in the use of Artificial Intelligence to aid in launch operations began at Kennedy Space Center in the early 1980's. The first implementation of AI at KSC was an expert system developed for the monitoring of liquid oxygen. LES or Liquid oxygen Expert System was the predecessor to the present system being developed at KSC (KATE). KATE or Knowledge-based Autonomous Test Engineer has been under development since 1985. KATE is a frame-based expert system which has been developed within the Common LISP programming environment.

Present work at KSC is focused on the continued development of the KATE system to ultimately achieve autonomous launching capabilities. This development effort, which is being supported by Boeing, requires a series of demonstrations on various hardware systems. In 1989, a demonstration of KATE's ability to monitor, diagnose and control was given on a scaled down version of the shuttle environmental control system. This year, a similar demonstration will be given on a water tanking system which is modeled after the liquid oxygen loading system. For 1991 another demonstration will be given this time on a liquid nitrogen loading system.

With each successive demonstration, the complexity of the task increases. For KATE to operate on any process, a knowledge-base must be created from which a simulation can be run. It is through the running of this simulation, that allows KATE to perform monitoring, diagnosis and control tasks. Hence the model of the process becomes a critical component of the overall system.

The objective of this work was to address various modeling issues which are of concern in the knowledge-base construction. In particular, the ALO water model was the primary focus of the effort. This report however, also includes observations and recommendations with respect to other models which are under development within the KATE environment.

II. PROCESS MODELING

All of the demonstrations for KATE under the ALO project will be based on flow processes. For the systems under consideration a single component is being transported without chemical reaction, hence, individual component mass continuity equations are not required. A general mass continuity equation for a given can be written for any pure, non-reacting flow system as follows:

(2-1) Mass In - Mass Out = Mass Accumulation

2.1 The ALO-H_2O Model

For the conditions in which the ALO - water demonstration will be operated, water can be considered an incompressible fluid. In addition, the assumption of isothermal operation can be made, since ambient temperatures are present throughout the system. As a consequence, the density is constant in time and space and the general balance can be written in terms of flow rates since the mass flow rate is the product of density and volumetric flow rate. Furthermore if we write the continuity equation around a section of pipe filled with liquid we can consider the process to be effectively at steady state at any given instant of time. Hence the continuity equation can be simplified to:

(2-2) Flow In = Flow Out

The process flow diagram for this system, which can be generated by KATE, is shown in Figure 1. Indicated on the Figure, are three distinct sections in which the equation for continuity of mass is applied. The three modeling equations around these points are:

Section 1:
(2-3A) Pump Flow = Recycle Flow + Platform Flow

Section 2:
(2-3B) Platform Flow = Drain Flow + Vehicle Flow

Section 3:
(2-3C) Vehicle Flow = V-Tank Flow + Engine Flow

where:
Pump Flow = The total flow from both pumps.
Recycle Flow = The flow recirculated to the storage tank.
Platform Flow = The flow lifted to the elevated platform.
Drain Flow = The flow out the drain valve.
Vehicle Flow = The total flow going to the vehicle.
V-Tank Flow = The flow to the vehicle tank.

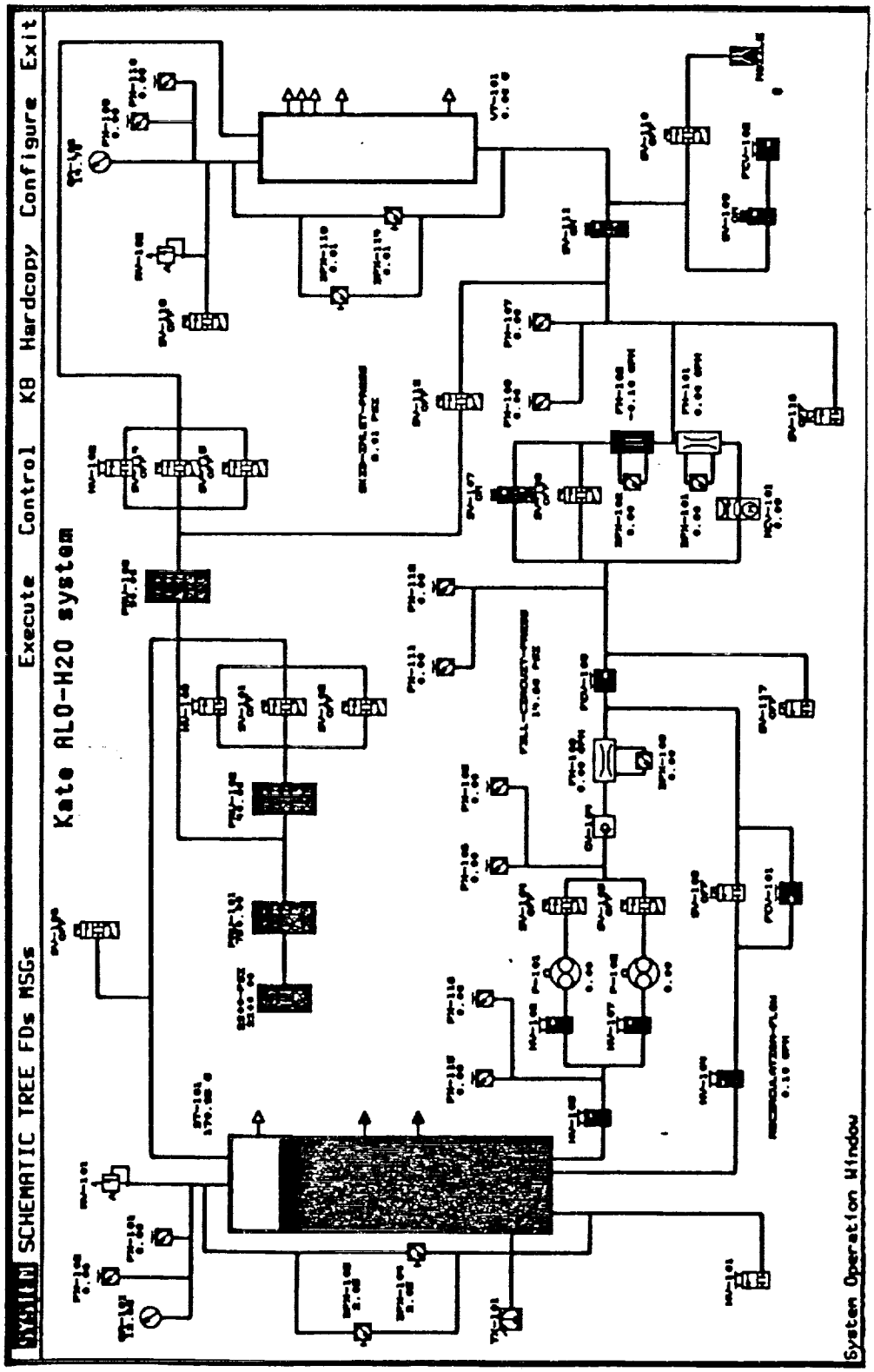

FIGURE 1. Process Diagram for ALO-H_2O Model

Engine Flow = The flow to the engine nozzle and drain.

The flow rate of water through a pipe, valve or fitting can be determined from the equation:

(2-4) $$Q = C_V(\Delta P)^{1/2}$$

where:
Q = the volumetric flow rate.
ΔP = the pressure drop over the hardware.
C_V = the flow coefficient for the hardware.

For a valve the flow coefficient is typically determined from manufacturer's data. The value of C_V is defined as the flow of water at 60 degrees Fahrenheit in gallons per minute at a pressure drop of 1 pound per square inch across the valve. For a pipe or fitting the value of C_V can be determined from the equation:

(2-5) $$C_V = \frac{29.9\ d^2}{(K)^{1/2}}$$

where:
d = the inside diameter of the pipe or fitting in inches.
K = the coefficient for resistance.

Fluid velocity through a pipe, valve or fitting is obtained at the expense of static head. The coefficient for resistance K is the proportionality constant which relates head loss to velocity through the relationship:

(2-6) $$h_L = \frac{Kv^2}{2g}$$

where:
h_L = the head loss through the hardware.
v = the fluid velocity.
g = acceleration of gravity.

Values of K for fittings and hence C_V through the use of equation 2-5 are given in various handbooks. For a given fitting or valve of fixed size, K is constant. For flow through a straight pipe the value of K can be determined from the equation:

(2-7) $$K = f(L/D)$$

where:
f = the friction factor
L/D = the length to diameter ratio for the pipe.

The friction factor is a function of the Reynolds number

which can be obtained from published nomographs or iteratively through equations such as the von Karman-Nikuradse formula:[1]

$$(2\text{-}8) \qquad [f]^{-1/2} = 4.0 \log (Re[f]^{1/2}) - 0.4 \quad (Re > 4000)$$

For a given section of the process a single flow coefficient (or admittance) can be obtained by considering the individual flow coefficients for the valves, fittings and sections of pipe which make up the section as a series of resistances to flow. The admittance is in effect a reciprocal resistance. The effective admittance for n resistances in series can be obtained from the relationship:

$$(2\text{-}9) \qquad A = \frac{1}{[(1/C_{V1})^2 + (1/C_{V2})^2 + \ldots\ldots + (1/C_{Vn})^2]^{1/2}}$$

Rewriting equations 3-3A through 3-3C in terms of differential pressures and effective admittances leads to:

$$(2\text{-}10A) \quad A1[PP - p1]^{1/2} = A2[p1 - STP]^{1/2} + A3[p1 - (HP + p2)]^{1/2}$$

$$(2\text{-}10B) \quad A3[p1 - (HP + p2)]^{1/2} = A4[(p2 + EP) - ATM]^{1/2} + A5[p2 - p3]^{1/2}$$

$$(2\text{-}10C) \quad A5[p2 - p3]^{1/2} = A6[p3 - VTP]^{1/2} + A7[p3 - ATM]^{1/2}$$

where:

PP = the pump discharge pressure
STP = the storage tank pressure
VTP = the vehicle tank pressure
HP = the head pressure loss from the elevation change
EP = the head pressure gain from the elevation change
ATM = the barometric pressure
p1 = pressure at point 1
p2 = pressure at point 2
p3 = pressure at point 3
A1 - A7 = admittance values for each branch

At each of the three points, the flow branches into two streams and an unknown pressure node is developed. For a given instant of time all of the parameters except the internal pressures can either be calculated directly (e.g. STP) or assumed constant (e.g. A1). Hence we are faced with the simultaneous solution of three nonlinear equations.

2.2 Modeling of Cryogenic Fluids

The modeling of flow systems involving cryogenic fluids, involves much more complexity. If it could be assured that the fluid was only in the liquid phase, the physical properties and

flow characteristics are less understood then those of water. In reality however, some vaporization of the fluid will occur. This gives rise for the need to model the heat transfer in the system as well as mass continuity. The degree of heat transfer will effect the stream quality and hence the thermodynamics of phase equilibrium will also need to be accounted for.

To sufficiently model this process will require a large effort. Equation 2-1 can no longer be simplified to get equation 2-2 as we are now dealing with a two phase compressible fluid. There have been two approaches taken to model the two phase flow problem: (1) a homogeneous approach in which the two phases are treated as a single phase with averaged fluid properties, and (2) a separated-flow model, in which the two phases are considered artificially segregated.[2] Lockhart and Martinelli [3] developed a semiempirical correlation segregated flow model for flow in horizontal tubes. A modification of this correlation has been shown to give good accuracy for cryogenic nitrogen. [4]

The Lockhart and Martinelli correlation calculates a two phase pressure drop by determining a correction factor ϕ^2_L which is applied to the liquid phase pressure drop. The correlation for adiabatic two phase pressure drop data is:

$$(2\text{-}11) \qquad (\Delta p / \Delta L)_{TP} = \phi^2_L \ (\Delta p / \Delta L)_L$$

where:

$(\Delta p / \Delta L)_{TP}$ = pressure drop per length for two phase flow
$(\Delta p / \Delta L)_L$ = pressure drop per length for liquid flow

The correction factor ϕ_L is determined from the relationship:

$$(2\text{-}12) \qquad \phi_L = (X^2 + CX + 1)^{1/2} / X$$

where C is an empirical constant ranging from 5 (when both phases are in laminar flow) to 20 when both phases are turbulent. The parameter X is given by:

$$(2\text{-}13) \qquad X^2 = \frac{C_L \ (Re_G)^m}{C_G \ (Re_L)^n} \ \frac{\rho_G}{\rho_L} \left(\frac{1 - x}{x}\right)^2$$

where:

C_L and n are empirical constants for the liquid phase
C_G and m are empirical constants for the gas phase
Re_G = gas phase Reynolds number
Re_L = liquid phase Reynolds number
x = the vapor mass fraction (quality)
ρ_L = the liquid phase density
ρ_G = the gas phase density

Since in reality, heat transfer will be occurring in the

system, a modified differential version of equation 2-11 must be coupled with an energy balance and numerically integrated along the length of the tube to get the total frictional pressure drop. This process is complicated by the fact that the physical properties and hence Reynolds numbers will be changing along the tube length. Also the change in the state variables will result in variations in the fluid quality.

The change in fluid quality results in a change in the bulk fluid velocity and consequently a change in fluid momentum. Hence a momentum pressure drop must be added to the contribution from the frictional pressure drop to calculate a total pressure drop. The equation to calculate the momentum pressure drop is:

$$(2\text{-}14) \qquad p_m = \phi_m \, (M_L + M_G)^2 \, / \, g_c \, \rho_L \, A^2$$

where the correction factor O_m for the momentum pressure drop is given by:

$$(2\text{-}15) \qquad \frac{(1 - x_2)^2}{R_{L,2}} - \frac{(1 - x_1)^2}{R_{L,1}} + \left(\frac{x_2^2}{1 - R_{L,2}} - \frac{x_1^2}{1 - R_{L,1}} \right) \left(\frac{\rho_L}{\rho_G} \right)$$

R_L is the volume fraction of liquid phase where the subscript 1 indicates inlet conditions and the subscript 2 indicates outlet conditions. R_L is a function of the Lockhart-Martinelli parameter X:

$$(2\text{-}16) \qquad R_L = X \, / \, (X^2 + CX + 1)^{1/2}$$

III. SOLUTIONS FOR SYSTEMS OF NONLINEAR EQUATIONS

As discussed above, improved modeling of the ALO- H_2O system requires the numerical solution of simultaneous nonlinear equations. Two distinct groups of methods are the most commonly employed for this task: functional iteration and minimizing methods. Both of the aforementioned methods were considered for this study and LISP functions were written for implementation in the KATE knowledge-base. A brief description of the rational behind these schemes is presented here.

3.1 Newton's Method

The specific technique used under the functional iteration category is known as Newton's method. It has the advantage over minimization methods in the speed of convergence of the algorithm. This method is an n dimensional extension of the 1 dimensional Newton-Raphson algorithm. Hence to help illustrate the method, the 1 dimensional case will be considered first.

Consider a function f which is twice continuously differentiable in an interval of interest. Let x^0 be an approximation to the root p (i.e. $f(p) = 0$) of the function such that the first derivative $f'(x^0)$ is not equal to 0. The function $f(x)$ can then be approximated with a Taylor series expansion about the point x^0 as follows:

$$f(x) = f(x^0) + (x - x^0)\, f'(x^0) \tag{3-1}$$

Since $f(p) = 0$ the above equation can be rewritten with $x = p$ as:

$$0 = f(x^0) + (p - x^0)\, f'(x^0) \tag{3-2}$$

Solving for p gives:

$$p = x^0 - f(x^0) \,/\, f'(x^0) \tag{3-3}$$

This gives rise to the Newton-Raphson algorithm which involves generating the sequence p_n defined by:

$$p_n = p_{n-1} - f(p_{n-1}) \,/\, f'(p_{n-1}), \quad (n > 1) \tag{3-4}$$

This sequence is generated in the algorithm until successive values of p_n and p_{n-1} are within a specified tolerance. This method is illustrated graphically in Figure 2. It is seen that at each iteration a new approximation of the root p_n is obtained from the slope of the tangent to the function evaluated at the previous approximation p_{n-1} (i.e. the first derivative).

The extension of this method to n dimensions is relatively straight forward. For n dimensions, there are n functions of the

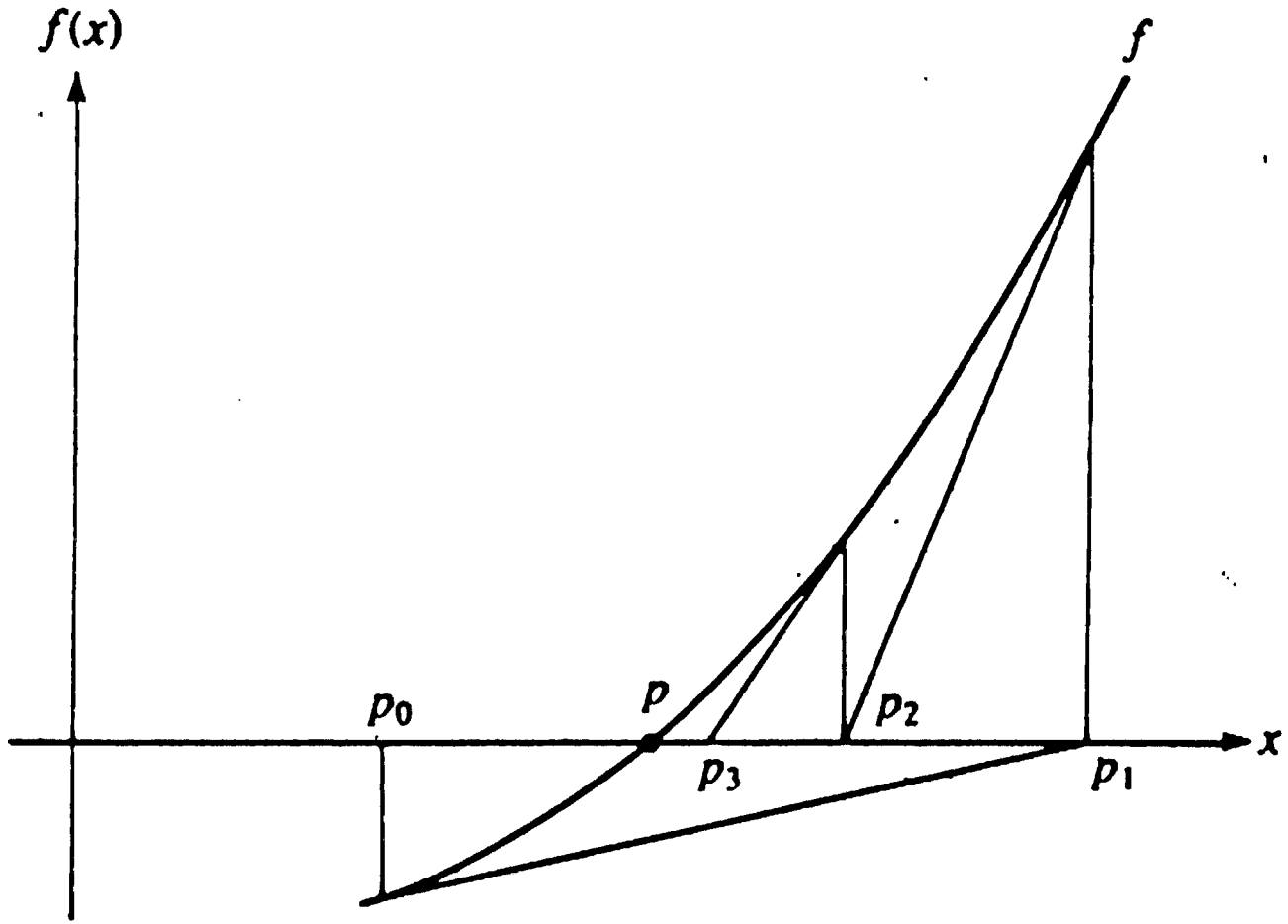

FIGURE 2. Graphical Interpretation of Newton's Method

n independent variables. Analogous to equation 3-1 for the 1 dimensional case, a Taylor's expansion about an approximate solution vector $\mathbf{x}^0 = (x_1^0, x_2^0, \ldots\ldots, x_n^0)^t$ can be truncated after the first degree terms for each of the n functions.

To illustrate this, we can consider the two dimensional case. The results of the Taylor approximations leads to:

$$(3\text{-}5A) \qquad f_1(x_1,x_2) = f_1(x_1^0,x_2^0) + \frac{\partial f_1}{\partial x_1}_0(x_1^0,x_2^0)\,[x_1 - x_1^0] + \frac{\partial f_1}{\partial x_2}_0(x_1^0,x_2^0)\,[x_2 - x_2^0]$$

$$(3\text{-}5B) \qquad f_2(x_1,x_2) = f_2(x_1^0,x_2^0) + \frac{\partial f_2}{\partial x_1}_0(x_1^0,x_2^0)\,[x_1 - x_1^0] + \frac{\partial f_2}{\partial x_2}_0(x_1^0,x_2^0)\,[x_2 - x_2^0]$$

As with equation 3-2 the value of the functions f_1 and f_2 is zero at the roots p_1 and p_2. Rearranging equations 3-5A and 3-5B, replacing x_1 and x_2 with p_1 and p_2 respectively and putting into matrix notation gives:

$$(3\text{-}6) \qquad \mathbf{J}(x_1^0,x_2^0)\ \mathbf{y} = -\mathbf{b}$$

where:

$$\mathbf{J} = \begin{vmatrix} \frac{\partial f_1}{\partial x_1}_0(x_1^0,x_2^0) & \frac{\partial f_1}{\partial x_2}_0(x_1^0,x_2^0) \\ \frac{\partial f_2}{\partial x_1}_0(x_1^0,x_2^0) & \frac{\partial f_2}{\partial x_2}_0(x_1^0,x_2^0) \end{vmatrix}$$

$$\mathbf{y} = \begin{vmatrix} (p_1 - x_1^0) \\ (p_2 - x_1^0) \end{vmatrix}$$

$$\mathbf{b} = \begin{vmatrix} f_1(x_1^0,x_2^0) \\ f_2(x_1^0,x_2^0) \end{vmatrix}$$

The matrix can be solved for $\mathbf{y}$ by multiplying both sides of equation 3-6 by $\mathbf{J}^{-1}$. Then in a manner analogous to equation 3-4 new guesses are generated for the roots repeatedly until convergence within the desired tolerance is obtained.

Hence for the n dimensional case, the n functions require n partial derivatives to be evaluated. The result of this differentiation is placed in an n x n matrix known as the

Jacobian matrix. The n elements in the first row of this matrix contains the results of differentiating the first function with respect to each of the n variables. Similarly the nth row elements contain the differentiation of the nth function with respect to the n variables. Although the n equations can be solved by inverting the Jacobian matrix, in practice an iterative technique would be used [3].

3.2 Steepest Descent Method

The specific method investigated under the category of minimization techniques is known as the method od steepest descent. Although the minimization methods will generally converge slower than the iterative methods they will generally converge with any initial approximation. The method of steepest descent determines a local minimum for a multivariable function $G(\mathbf{x})$ defined by:

$$(3\text{-}7) \qquad G(x_1, x_2, \ldots, x_n) = [f_i(x_1, x_2, \ldots, x_n)]^2$$

where each function $f_i(x_1, x_2, \ldots, x_n) = 0$. An exact solution at $\mathbf{x} = (x_1, x_2, \ldots, x_n)^t$ is determined when the function G is zero.

The algorithm for finding the solution can be summarized as follows:

1. Evaluate G at an initial approximation $\mathbf{x}^0 = (x_1^0, x_2^0, \ldots, x_n^0)^t$

2. Determine a direction from $\mathbf{x}^0$ that results in a decrease in the value of G.

3. Decide the amount which should be moved in this direction and call the new value $\mathbf{x}^1$.

4. Repeat steps 1 through 3 with $\mathbf{x}^0$ replaced by $\mathbf{x}^1$.

From calculus, the Extreme Value Theorem implies that a single variable differentiable function has a minimum when the derivative is zero. This can be extended to a multivariable function in that a minimum exists at $\mathbf{x}$ when the gradient is zero. Hence the solution vector $\mathbf{x}$ occurs where:

$$(3\text{-}8) \qquad G(\mathbf{x}) = \left[\frac{\partial G(\mathbf{x})}{\partial x_1}, \frac{\partial G(\mathbf{x})}{\partial x_2}, \ldots\ldots \frac{\partial G(\mathbf{x})}{\partial x_n}\right]^t = 0$$

Explanation of the logic involved in the determination of steps 2 and 3 above is detailed and of little value to this report since this method was not actually implemented. Further details of this method are given by Burden and Faires [3].

IV. RESULTS AND DISCUSSION

The source code for the solution of the modeling equations is given in the Appendix. Comments have been included in the code to aid in any future modifications. The LISP routine had to be capable of handling not only the normal situation of forward flow (i.e when the pump is on) but the back flow condition when the pump is off. In addition various valve configurations leading to zero admittance values had to be addressed. As a consequence, much of the code written was aimed at dealing with these "abnormal" situations can occur.

A example of the problem encountered with particular values of zero admittance can be shown if say both A4 and A5 in equation 2-10b are equal to zero. This indicates there is no flow in either the fourth or fifth legs in the second section of pipe. Hence the flow in the third leg must also be zero and either A3 must be zero or the differential pressure in the leg must be zero. In either case the original treatment will cause problems in the Jacobian matrix. Having A3 also zero would cause **J** to become singular, while a zero differential pressure would cause the element $J_{2,2}$ to go to infinity. Comments within the code try and address the logic for each of the cases encountered and hence no further discussion will be given on them.

The program developed to solve the three internal pressure nodes by Newton's method was loaded into the KATE system and a simulation run. Although all possible combinations of events which could occur were not tested, the system worked well on those that were tested. Figure 3 shows a plot of the values for p1, p2 and p3 during a simulation run. Six distinct changes were made in the system in order to observe the response by the program. These changes are labeled A through F on Figure 3.

When the system was first started p1 was at approximately 52 psi as a single pump was operating. As the vehicle tank was filled a slight decrease in p1 was observed while p2 and p3 showed increases. This behavior is expected as p1 drops some since the pressure in the storage tank decreases, while p2 and p3 increase due to the filling, and subsequent head pressure, of the vehicle tank. At point A the drain valve is opened. This is equivalent of changing A4 to a non-zero value. Again, the results are expected as little effect is observed on p1 and p3, however p2 has an immediate drop in pressure.

At point B the valve is shut again and the system responds accordingly. At point C the second pump is turned, resulting in pressure increases throughout the system. Point D signifies the start of back flow as the pumps were stopped. As expected p1 has an immediate drop in pressure, while p2 and p3 slowly decline. As shown on the plot, p3 is greater than p2, which is greater than

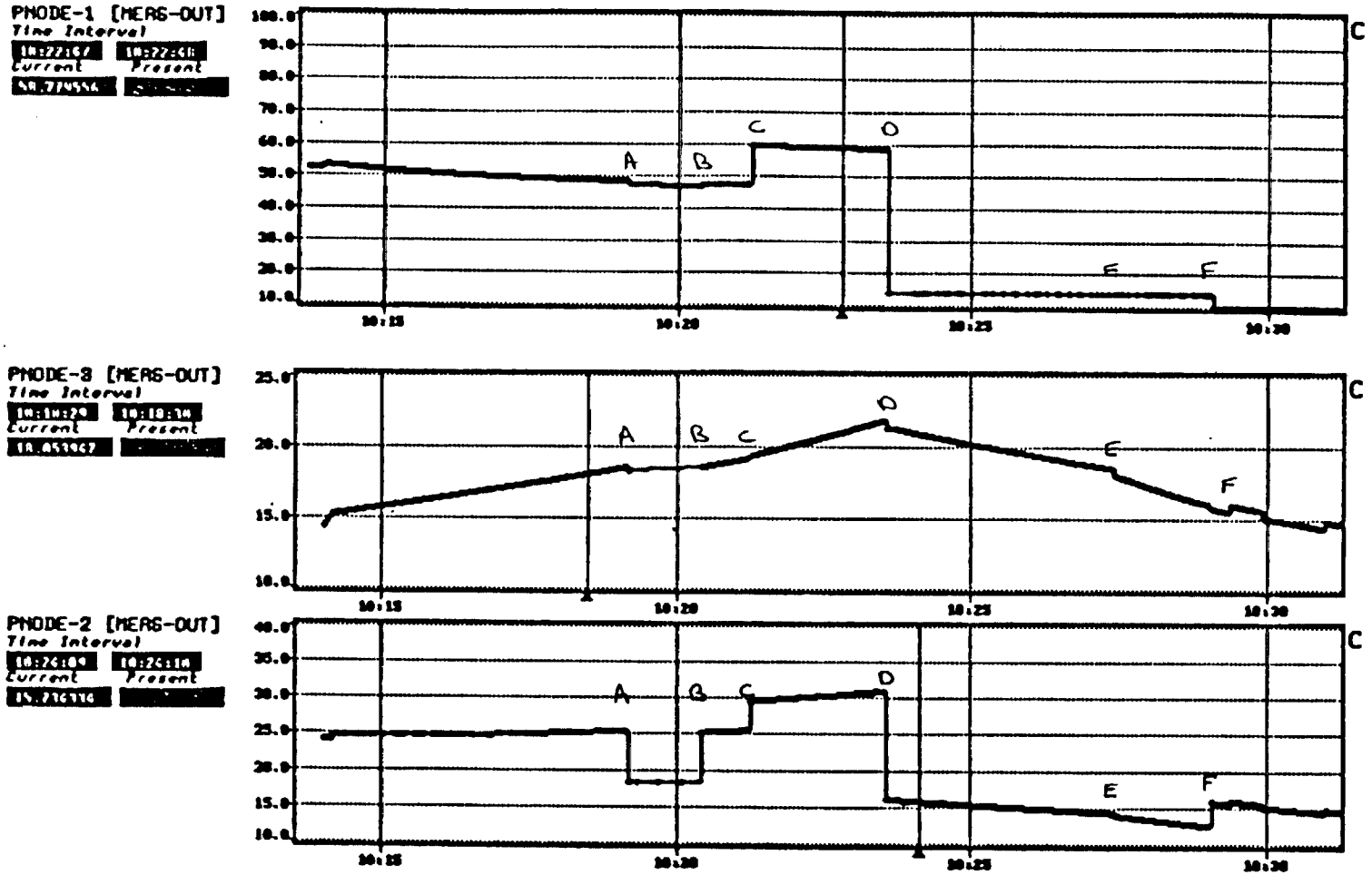

FIGURE 3. Data Plots for P1, P2 & P3 During the Simulation Run

p1 as required for back flow. At point E, the valves to the engine section (i.e. A7) were opened. Since flow is now draining through the engine as well as the transfer lines, the rate of pressure decrease in p2 and p3 should become greater as is observed.

The last change made to the system (point F) was to set A3 to zero. At this point, p1 equalizes to the storage tank pressure as expected, while a sudden increase is observed in p2 and p3. Again this is expected since less area is available for flow.

V. CONCLUDING REMARKS

Although a liquid water transfer system is a relatively easy system to model, various assumptions are being used to allow for real-time implementation. For example, the use of an effective flow coefficient for each section of the transfer hardware was used in the model. Although the values used can be readily determined for a given set of conditions they will change as conditions change since the resistance coefficient depends on the Reynolds number which in turn depends on the flow.

The initial values being used in the knowledge-base are approximated assuming highly turbulent flow. In the highly turbulent regime the friction factor does in fact become constant and hence fairly accurate simulation values could be obtained. When the pumps are turned off however and the water drains back into the storage tank the flow regime will not be highly turbulent and I anticipate substantial error to be present if the flow coefficients are not adjusted.

As an example of the magnitude of the error which could be expected let's consider water flowing through a 10 foot section of 1 inch smooth pipe in highly turbulent flow. The lowest Reynolds number for highly turbulent flow in this size pipe is 8×10^5. This corresponds to a friction factor of 0.023. Using equation 3-7 with a L/D ratio of 120 gives a resistance coefficient of 2.76 and a flow coefficient of 18.00. If the flow is reduced to by one tenth during say a pump failure, the Reynolds number will be dropped proportionately. The new value of the friction factor will be .025 resulting in a new resistance coefficient of 3.0 and a new flow coefficient of 17.26. The increase in the resistance translates into an 8.8% error in the calculation of pressure drop from the model if a correction is not made.

As the complexity of the systems to be modeled increases, more simplifications will be required in order to allow real-time simulations to be carried out. With cryogenic systems, the simplifications may prove to cause substantial error in the predictive ability of the model. It is my belief that before the KATE system can adequately deal with systems of increased complexity, a methodology for verifying and updating model parameters needs to be developed. In some instances, this could be done by comparing predicted values from the simulation to sensor data within tolerance limits. If drift in the predictive abilities is observed over time, the model parameters could be modified to correct for it. Monitoring of the model base would probably require the use of a distributed processor to analyze trends in the data.

In addition to updating model parameters, it may also be necessary to have separate modeling equations under different conditions. For example, the modeling of line chill down requires a much higher degree of model sophistication due to the unsteady state heat transfer involved than the modeling after a thermal steady state has been reached.

VI. APPENDIX

```
;;;;;;;;;;;;;;;;;;;;;;;;;;;;;;;;;;;;;;;;;;;;;;;;;;;;;;;;;;;;;;;;;;;;;;;;;;;;;;;;;;;;;;;;;;;;;;;;;;;;;;
;; This variable is used to account for the elevation head above the nozzle bleed and drain
;; A 1.5 foot elevation was assumed
;;;;;;;;;;;;;;;;;;;;;;;;;;;;;;;;;;;;;;;;;;;;;;;;;;;;;;;;;;;;;;;;;;;;;;;;;;;;;;;;;;;;;;;;;;;;;;;;;;;;;;

(defvar nozzle-head 0.65)


;;;;;;;;;;;;;;;;;;;;;;;;;;;;;;;;;;;;;;;;;;;;;;;;;;;;;;;;;;;;;;;;;;;;;;;;;;;;;;;;;;;;;;;;;;;;;;;;;;;;;;
;; Function to check if two numbers are essentially equal.
;;;;;;;;;;;;;;;;;;;;;;;;;;;;;;;;;;;;;;;;;;;;;;;;;;;;;;;;;;;;;;;;;;;;;;;;;;;;;;;;;;;;;;;;;;;;;;;;;;;;;;

(defun almost-equal (x y)
  (< (abs (- x y)) .000001))


;;;;;;;;;;;;;;;;;;;;;;;;;;;;;;;;;;;;;;;;;;;;;;;;;;;;;;;;;;;;;;;;;;;;;;;;;;;;;;;;;;;;;;;;;;;;;;;;;;;;;;
;; Function to count the number of zero admittances.
;;;;;;;;;;;;;;;;;;;;;;;;;;;;;;;;;;;;;;;;;;;;;;;;;;;;;;;;;;;;;;;;;;;;;;;;;;;;;;;;;;;;;;;;;;;;;;;;;;;;;;

(defun count-zeros (list)
  (do* ((cnt 0)
        (mlist list (cdr mlist)))
       ((null mlist) cnt)
    (when (zerop (car mlist))(incf cnt))))


;;;;;;;;;;;;;;;;;;;;;;;;;;;;;;;;;;;;;;;;;;;;;;;;;;;;;;;;;;;;;;;;;;;;;;;;;;;;;;;;;;;;;;;;;;;;;;;;;;;;;;
;; Function to determine if any complex numbers were encountered in
;;   which case the solve routine will exit with an error message.
;;;;;;;;;;;;;;;;;;;;;;;;;;;;;;;;;;;;;;;;;;;;;;;;;;;;;;;;;;;;;;;;;;;;;;;;;;;;;;;;;;;;;;;;;;;;;;;;;;;;;;

(defun cmplx-chk (list)
  (do* ((cnt 0)
        (mlist list (cdr mlist)))
       ((null mlist) cnt)
    (when (complexp (car mlist))(incf cnt))))


;;;;;;;;;;;;;;;;;;;;;;;;;;;;;;;;;;;;;;;;;;;;;;;;;;;;;;;;;;;;;;;;;;;;;;;;;;;;;;;;;;;;;;;;;;;;;;;;;;;;;;
;; Function to compute the square root of the pressure difference in the first leg.
;; Logic is included to avoid dividing by zero in the Jacobian matrix by returning the symbol DELP0
;;   when the differential pressure is zero.
;; Logic is also included to avoid the return of complex numbers.
;;;;;;;;;;;;;;;;;;;;;;;;;;;;;;;;;;;;;;;;;;;;;;;;;;;;;;;;;;;;;;;;;;;;;;;;;;;;;;;;;;;;;;;;;;;;;;;;;;;;;;

(defun pvar1 (p1 ppump)
  (cond ((> ppump p1)
         (sqrt (- ppump p1)))
        ((almost-equal p1 ppump)
         'delp0)
        (t (- (sqrt (abs (- ppump p1)))))))


;;;;;;;;;;;;;;;;;;;;;;;;;;;;;;;;;;;;;;;;;;;;;;;;;;;;;;;;;;;;;;;;;;;;;;;;;;;;;;;;;;;;;;;;;;;;;;;;;;;;;;
;; Function to compute the square root of the pressure difference in the second leg.
;; Logic is included to avoid dividing by zero in the Jacobian matrix by returning the symbol DELP0
;;   when the differential pressure is zero.
;; Logic is also included to avoid the return of complex numbers.
;;;;;;;;;;;;;;;;;;;;;;;;;;;;;;;;;;;;;;;;;;;;;;;;;;;;;;;;;;;;;;;;;;;;;;;;;;;;;;;;;;;;;;;;;;;;;;;;;;;;;;

(defun pvar2 (p1 st-press)
  (cond ((> p1 st-press)
         (sqrt (- p1 st-press)))
        ((almost-equal p1 st-press)
         'delp0)
        (t (- (sqrt (abs (- p1 st-press)))))))
```

```
;;;;;;;;;;;;;;;;;;;;;;;;;;;;;;;;;;;;;;;;;;;;;;;;;;;;;;;;;;;;;;;;;;;;;;;;;;;;;;;;;;;;;;;;;;;;;;;;;;;;
;; Function to compute the square root of the pressure difference in the third leg.
;; Logic is included to avoid dividing by zero in the Jacobian matrix by returning the symbol DELP0
;;   when the differential pressure is zero.
;; Logic is also included to avoid the return of complex numbers.
;;;;;;;;;;;;;;;;;;;;;;;;;;;;;;;;;;;;;;;;;;;;;;;;;;;;;;;;;;;;;;;;;;;;;;;;;;;;;;;;;;;;;;;;;;;;;;;;;;;;

(defun pvar3 (p1 p2 head-press)
  (cond ((> p1 (+ head-press p2))
         (sqrt (- p1 head-press p2)))
        ((almost-equal p1 (+ head-press p2))
         'delp0)
        (t (- (sqrt (abs (- (+ p2 head-press) p1)))))))


;;;;;;;;;;;;;;;;;;;;;;;;;;;;;;;;;;;;;;;;;;;;;;;;;;;;;;;;;;;;;;;;;;;;;;;;;;;;;;;;;;;;;;;;;;;;;;;;;;;;
;; Function to compute the square root of the pressure difference in the fourth leg.
;; Logic is included to avoid dividing by zero in the Jacobian matrix by returning the symbol DELP0
;;   when the differential pressure is zero.
;; Also if p2 is less than atmospheric pressure or the lines are not filled the symbol delp0
;;   is returned to indicate no true flow.
;;;;;;;;;;;;;;;;;;;;;;;;;;;;;;;;;;;;;;;;;;;;;;;;;;;;;;;;;;;;;;;;;;;;;;;;;;;;;;;;;;;;;;;;;;;;;;;;;;;;

(defun pvar4 (p2 in-sys)
  (cond
    ((not (> in-sys drain-capacity)) 'delp0)
    ((> (+ p2 elevation-press) ambient-atm)
     (sqrt (- (+ p2 elevation-press)  ambient-atm)))
    ((almost-equal p2 ambient-atm)
     'delp0)
    (t 'delp0)))


;;;;;;;;;;;;;;;;;;;;;;;;;;;;;;;;;;;;;;;;;;;;;;;;;;;;;;;;;;;;;;;;;;;;;;;;;;;;;;;;;;;;;;;;;;;;;;;;;;;;
;; Function to compute the square root of the pressure difference in the fifth leg.
;; Logic is included to avoid dividing by zero in the Jacobian matrix by returning the symbol DELP0
;;   when the differential pressure is zero.
;; Logic is also included to avoid the return of complex numbers.
;;;;;;;;;;;;;;;;;;;;;;;;;;;;;;;;;;;;;;;;;;;;;;;;;;;;;;;;;;;;;;;;;;;;;;;;;;;;;;;;;;;;;;;;;;;;;;;;;;;;

(defun pvar5 (p2 p3)
  (cond
    ((> p2 p3)
     (sqrt (- p2 p3)))
    ((almost-equal p3 p2)
     'delp0)
    (t (- (sqrt (abs (- p2 p3)))))))


;;;;;;;;;;;;;;;;;;;;;;;;;;;;;;;;;;;;;;;;;;;;;;;;;;;;;;;;;;;;;;;;;;;;;;;;;;;;;;;;;;;;;;;;;;;;;;;;;;;;
;; Function to compute the square root of the pressure difference in the sixth leg.
;; Logic is included to avoid dividing by zero in the Jacobian matrix by returning the symbol DELP0
;;   when the differential pressure is zero.
;; Logic is also included to avoid the return of complex numbers.
;; Also if the lines are not filled the symbol delp0 is returned to indicate no true flow.
;;;;;;;;;;;;;;;;;;;;;;;;;;;;;;;;;;;;;;;;;;;;;;;;;;;;;;;;;;;;;;;;;;;;;;;;;;;;;;;;;;;;;;;;;;;;;;;;;;;;

(defun pvar6 (p3 vt-press in-sys)
  (cond
    ((not (> in-sys line-capacity)) 'delp0)
    ((>  p3 vt-press)
    (sqrt (- p3 vt-press)))
    ((almost-equal p3 vt-press)
     'delp0)
    (t (- (sqrt (abs (- p3 vt-press)))))))
```

ORIGINAL PAGE
OF POOR QUALITY

```
;;;;;;;;;;;;;;;;;;;;;;;;;;;;;;;;;;;;;;;;;;;;;;;;;;;;;;;;;;;;;;;;;;;;;;;;;;;;;;;;;;;;;;;;;;;;;;;;;;
;; Function to compute the square root of the pressure difference in the seventh leg.
;; Logic is included to avoid dividing by zero in the Jacobian matrix by returning the symbol DELP0
;;   when the differential pressure is zero.
;; Also if p3 is less than atmospheric pressure or the lines are not filled the symbol delp0
;;   is returned to indicate no true flow.
;;;;;;;;;;;;;;;;;;;;;;;;;;;;;;;;;;;;;;;;;;;;;;;;;;;;;;;;;;;;;;;;;;;;;;;;;;;;;;;;;;;;;;;;;;;;;;;;;;;

(defun pvar7 (p3 in-sys)
  (cond
    ((not (> in-sys line-capacity)) 'delp0)
    ((> (+ p3 nozzle-head) ambient-atm)
     (sqrt (- (+ p3 nozzle-head) ambient-atm)))
    ((almost-equal p3 ambient-atm)
     'delp0)
    (t 'delp0)))



;;;;;;;;;;;;;;;;;;;;;;;;;;;;;;;;;;;;;;;;;;;;;;;;;;;;;;;;;;;;;;;;;;;;;;;;;;;;;;;;;;;;;;;;;;;;;;;;;;;
;; Function for the material balance around section 1.
;;   [Flow from pump - Recirculation Flow - Flow to the elevated platform = 0]
;; Logic is included to check to make sure the functions PVAR1, PVAR2 & PVAR3 return a number.
;;   Return of the symbol DELP0 from these functions occurs when a pressure differential of zero is
;;   encountered. If DELP0 is returned the contribution from the leg is set equal to zero.
;; Logic is also included to have the function F1 return zero if any two admittances passed to the
;;   function are zero. This avoids discontinuity in the material balance.
;;;;;;;;;;;;;;;;;;;;;;;;;;;;;;;;;;;;;;;;;;;;;;;;;;;;;;;;;;;;;;;;;;;;;;;;;;;;;;;;;;;;;;;;;;;;;;;;;;;

(defun f1 (p1 p2 ppump st-press head-press a1 a2 a3)
  (cond
    ((or (and (zerop a1)(zerop a2))
         (and (zerop a1)(zerop a3))
         (and (zerop a2)(zerop a3)))0)
    (t
     (- (cond ((numberp (pvar1 p1 ppump))
               (* a1 (pvar1 p1 ppump)))
              (t 0))
        (+ (cond ((numberp (pvar2 p1 st-press))
                  (* a2 (pvar2 p1 st-press)))
                 (t 0))
           (cond ((numberp (pvar3 p1 p2 head-press))
                  (* a3 (pvar3 p1 p2 head-press)))
                 (t 0)))))))


;;;;;;;;;;;;;;;;;;;;;;;;;;;;;;;;;;;;;;;;;;;;;;;;;;;;;;;;;;;;;;;;;;;;;;;;;;;;;;;;;;;;;;;;;;;;;;;;;;;
;; Function for the material balance around section 2.
;;   [Flow to the elevated platform - Flow toward the vehicle - Flow out the drain = 0]
;; Logic is included to check to make sure the functions PVAR3, PVAR4 & PVAR5 return a number.
;;   Return of the symbol DELP0 from these functions occurs when a pressure differential of zero is
;;   encountered. If DELP0 is returned the contribution from the leg is set equal to zero.
;; Logic is also included to have the function F2 return zero if any two admittances passed to the
;;   function are zero or the functions PVAR4 and PVAR5 return DELP0. This avoids discontinuity in
;;   the material balance.
;;;;;;;;;;;;;;;;;;;;;;;;;;;;;;;;;;;;;;;;;;;;;;;;;;;;;;;;;;;;;;;;;;;;;;;;;;;;;;;;;;;;;;;;;;;;;;;;;;;

(defun f2 (p1 p2 p3 head-press a3 a4 a5 in-sys)
  (cond
    ((or (and (zerop a3)(zerop a4))
         (and (zerop a3)(zerop a5))
         (and (zerop a4)(zerop a5))
         (and (not (numberp (pvar4 p2 in-sys)))(not (numberp (pvar5 p2 p3)))))0)
    (t
     (- (cond ((numberp (pvar3 p1 p2 head-press))
               (* a3 (pvar3 p1 p2 head-press)))
              (t 0))
        (+ (cond ((numberp (pvar4 p2 in-sys))
                  (* a4 (pvar4 p2 in-sys)))
                 (t 0))
           (cond ((numberp (pvar5 p2 p3))
                  (* a5 (pvar5 p2 p3)))
                 (t 0)))))))
```

```
;;;;;;;;;;;;;;;;;;;;;;;;;;;;;;;;;;;;;;;;;;;;;;;;;;;;;;;;;;;;;;;;;;;;;;;;;;;;;;;;;;;;;;;;;;;;;;;;;;;;;;;;;
;; Function for the material balance around section 3.
;;   [Flow toward the vehicle - Flow to the vehicle tank - Flow to the engine nozzle and bleed = 0]
;; Logic is included to check to make sure the functions PVAR5, PVAR6 & PVAR7 return a number.
;;   Return of the symbol DELPO from these functions occurs when a pressure differential of zero is
;;   encountered. If DELPO is returned the contribution from the leg is set equal to zero.
;; Logic is also included to have the the function F3 return zero if admittances a5 and a7 are passed
;;   to the function as zero or the functions PVAR6 and PVAR7 return DELPO. This avoids discontinuity
;;   in the material balance.
;;;;;;;;;;;;;;;;;;;;;;;;;;;;;;;;;;;;;;;;;;;;;;;;;;;;;;;;;;;;;;;;;;;;;;;;;;;;;;;;;;;;;;;;;;;;;;;;;;;;;;;;;;

(defun f3 (p2 p3 vt-press a5 a6 a7 in-sys)
  (cond
    ((or (and (zerop a5)(zerop a7))
         (and (not (numberp (pvar6 p3 vt-press in-sys)))(not (numberp (pvar7 p3 in-sys)))))0)
    (t
     (- (cond ((numberp (pvar5 p2 p3))
               (* a5 (pvar5 p2 p3)))
              (t 0))
        (+ (cond ((numberp (pvar6 p3 vt-press in-sys))
                  (* a6 (pvar6 p3 vt-press in-sys)))
                 (t 0))
           (cond ((numberp (pvar7 p3 in-sys))
                  (* a7 (pvar7 p3 in-sys)))
                 (t 0)))))))


;;;;;;;;;;;;;;;;;;;;;;;;;;;;;;;;;;;;;;;;;;;;;;;;;;;;;;;;;;;;;;;;;;;;;;;;;;;;;;;;;;;;;;;;;;;;;;;;;;;;;;;;;;
;; Function to compute the element in row 1 and column 1 of the Jacobian matrix. This function
;;   represents the partial derivative of the function F1 with respect to the variable P1.
;; Logic is included to check to make sure the functions PVAR1, PVAR2 & PVAR3 return a number.
;;   Return of the symbol DELPO from these functions occurs when a pressure differential of zero is
;;   encountered. If DELPO is returned the contribution from the leg is set equal to zero.
;; Logic is also included to have the the function J11 return one if any two admittances are passed to
;;   the function as zero or the flow in the leg is zero. This prevents the Jacobian matrix from
;;   becoming singular.
;;;;;;;;;;;;;;;;;;;;;;;;;;;;;;;;;;;;;;;;;;;;;;;;;;;;;;;;;;;;;;;;;;;;;;;;;;;;;;;;;;;;;;;;;;;;;;;;;;;;;;;;;;

(defun j11 (p1 p2 ppump st-press head-press a1 a2 a3)
  (cond
    ((or
       (and (zerop a1)(zerop a2))
       (and (zerop a2)(zerop a3))
       (and (zerop a1)(zerop a3)))1)
    (t
     (let* ((result
              (+ (cond ((numberp (pvar1 p1 ppump))
                        (/ (* -.5 a1)
                           (abs(pvar1 p1 ppump))))
                       (t 0))
                 (cond ((numberp (pvar2 p1 st-press))
                        (/ (* -.5 a2)
                           (abs(pvar2 p1 st-press))))
                       (t 0))
                 (cond ((numberp (pvar3 p1 p2 head-press))
                        (/ (* -.5 a3)
                           (abs(pvar3 p1 p2 head-press))))
                       (t 0)))))
       (cond ((zerop result) 1)
             (t result))))))
```

```
;;;;;;;;;;;;;;;;;;;;;;;;;;;;;;;;;;;;;;;;;;;;;;;;;;;;;;;;;;;;;;;;;;;;;;;;;;;;;;;;;;;;;;;;;;;;;;;;;;;;;;;;
;; Function to compute the element in row 1 and column 2 of the Jacobian matrix. This function
;;   represents the partial derivative of the function F1 with respect to the variable P2.
;; This function is also used for the element in row 2 and column 1 of the Jacobian matrix and hence
;;   also represents the partial derivative of function F2 with respect to the variable P1.
;; Logic is included to check to make sure the function PVAR3 returns a number.
;;   Return of the symbol DELP0 from this function occurs when a pressure differential of zero is
;;   encountered. If DELP0 is returned the function is set equal to zero.
;;;;;;;;;;;;;;;;;;;;;;;;;;;;;;;;;;;;;;;;;;;;;;;;;;;;;;;;;;;;;;;;;;;;;;;;;;;;;;;;;;;;;;;;;;;;;;;;;;;;;;;;

(defun j12 (p1 p2 head-press a3)
  (cond ((numberp (pvar3 p1 p2 head-press))
         (/ (* .5 a3)(abs(pvar3 p1 p2 head-press))))
        (t 0)))


;;;;;;;;;;;;;;;;;;;;;;;;;;;;;;;;;;;;;;;;;;;;;;;;;;;;;;;;;;;;;;;;;;;;;;;;;;;;;;;;;;;;;;;;;;;;;;;;;;;;;;;;
;; Function to compute the element in row 2 and column 2 of the Jacobian matrix. This function
;;   represents the partial derivative of the function F2 with respect to the variable P2.
;; Logic is included to check to make sure the functions PVAR3, PVAR4 & PVAR5 return a number.
;;   Return of the symbol DELP0 from these functions occurs when a pressure differential of zero is
;;   encountered. If DELP0 is returned the contribution from the leg is set equal to zero.
;; Logic is also included to have the the function J22 return one if any two admittances are passed to
;;   the function as zero or there is no flow in the leg. This prevents the Jacobian matrix from
;;   becoming singular.
;;;;;;;;;;;;;;;;;;;;;;;;;;;;;;;;;;;;;;;;;;;;;;;;;;;;;;;;;;;;;;;;;;;;;;;;;;;;;;;;;;;;;;;;;;;;;;;;;;;;;;;;

(defun j22 (p1 p2 p3 head-press a3 a4 a5 in-sys)
  (cond
    ((or
       (and (zerop a3)(zerop a4))
       (and (zerop a4)(zerop a5))
       (and (zerop a3)(zerop a5))
       (and (not (numberp (pvar4 p2 in-sys)))(not (numberp (pvar5 p2 p3)))))1)
    (t
     (let* ((result
              (+  (cond ((numberp (pvar3 p1 p2 head-press))
                         (/ (* -.5 a3)
                            (abs(pvar3 p1 p2 head-press))))
                        (t 0))
                  (cond ((numberp (pvar4 p2 in-sys))
                         (/ (* -.5 a4)
                            (abs(pvar4 p2 in-sys))))
                        (t 0))
                  (cond ((numberp (pvar5 p2 p3))
                         (/ (* -.5 a5)
                            (abs(pvar5 p2 p3))))
                        (t 0)))))
       (cond ((zerop result) 1)
             (t result))))))


;;;;;;;;;;;;;;;;;;;;;;;;;;;;;;;;;;;;;;;;;;;;;;;;;;;;;;;;;;;;;;;;;;;;;;;;;;;;;;;;;;;;;;;;;;;;;;;;;;;;;;;;
;; Function to compute the element in row 2 and column 3 of the Jacobian matrix. This function
;;   represents the partial derivative of the function F2 with respect to the variable P3.
;; This function is also used for the element in row 3 and column 2 of the Jacobian matrix and hence
;;   also represents the partial derivative of function F3 with respect to the variable P2.
;; Logic is included to check to make sure the function PVAR5 returns a number.
;;   Return of the symbol DELP0 from this function occurs when a pressure differential of zero is
;;   encountered. If DELP0 is returned the function is set equal to zero.
;;;;;;;;;;;;;;;;;;;;;;;;;;;;;;;;;;;;;;;;;;;;;;;;;;;;;;;;;;;;;;;;;;;;;;;;;;;;;;;;;;;;;;;;;;;;;;;;;;;;;;;;

(defun j23 (p2 p3 a5)
  (cond ((numberp (pvar5 p2 p3))
         (/ (* .5 a5)(abs(pvar5 p2 p3))))
        (t 0)))
```

```
;;;;;;;;;;;;;;;;;;;;;;;;;;;;;;;;;;;;;;;;;;;;;;;;;;;;;;;;;;;;;;;;;;;;;;;;;;;;;;;;;;;;;;;;;;;;;;;;;;;;;;;;;;
;; Function to compute the element in row 3 and column 3 of the Jacobian matrix. This function
;;   represents the partial derivative of the function F3 with respect to the variable P3.
;; Logic is included to check to make sure the functions PVAR5, PVAR6 & PVAR7 return a number.
;;   Return of the symbol DELPO from these functions occurs when a pressure differential of zero is
;;   encountered. If DELPO is returned, the contribution from the appropriate leg is set equal to zero.
;; Logic is also included to have the the function J33 return one if admittances a5 & a7 are passed to
;;   the function as zero or there is no flow in the leg. This prevents the Jacobian matrix from
;;   becoming singular.
;;;;;;;;;;;;;;;;;;;;;;;;;;;;;;;;;;;;;;;;;;;;;;;;;;;;;;;;;;;;;;;;;;;;;;;;;;;;;;;;;;;;;;;;;;;;;;;;;;;;;;;;;;

(defun j33 (p2 p3 vt-press a5 a6 a7 in-sys)
  (cond
    ((or (and (zerop a5)(zerop a7))
         (and (not (numberp (pvar6 p3 vt-press in-sys)))(not (numberp (pvar7 p3 in-sys)))))1)
    (t
     (let* ((result
             (+  (cond ((numberp (pvar5 p2 p3))
                        (/ (* -.5 a5)
                           (abs(pvar5 p2 p3))))
                       (t 0))
                 (cond ((numberp (pvar6 p3 vt-press in-sys))
                        (/ (* -.5 a6)
                           (abs(pvar6 p3 vt-press in-sys))))
                       (t 0))
                 (cond ((numberp (pvar7 p3 in-sys))
                        (/ (* -.5 a7)
                           (abs(pvar7 p3 in-sys))))
                       (t 0)))))
    (cond ((zerop result) 1)
          (t result))))))


;;;;;;;;;;;;;;;;;;;;;;;;;;;;;;;;;;;;;;;;;;;;;;;;;;;;;;;;;;;;;;;;;;;;;;;;;;;;;;;;;;;;;;;;;;;;;;;;;;;;;;;;;;
;; Function which is called by the solve function if any 5 admittance values are equal to zero.
;; The values returned depend on the exact configuration of valves being open and closed (0 admittance)
;;;;;;;;;;;;;;;;;;;;;;;;;;;;;;;;;;;;;;;;;;;;;;;;;;;;;;;;;;;;;;;;;;;;;;;;;;;;;;;;;;;;;;;;;;;;;;;;;;;;;;;;;;

(defun get-vals->4 (p1 p2 p3 ppump st-press vt-press head-press a1 a2 a3 a4 a5 a6 a7)
  (setq p3 vt-press)
  (cond
    ((not (zerop a1))
     (setq p1 ppump))
    ((not (zerop a2))
     (setq p1 st-press))
    ((not (zerop a3))
     (setq p1 + head-press (/ (+ p1 p2 - head-press) 2))
     (setq p2 (- p1 head-press)))
    ((not (zerop a4))
     (setq p2 ambient-atm))
    ((not (zerop a5))
     (setq p2 vt-press))
    ((not (zerop a7))
     (setq p3 (/ (* vt-press (square (/ a6 a7)))
                 (+ 1 (square (/ a6 a7)))))))
  (values p1 p2 p3))
```

ORIGINAL PAGE IS
OF POOR QUALITY

```
;;;;;;;;;;;;;;;;;;;;;;;;;;;;;;;;;;;;;;;;;;;;;;;;;;;;;;;;;;;;;;;;;;;;;;;;;;;;;;;;;;;;;;;;;;;;;;;;;;;;;;;;;;;;;;;
;; Function which is called by the solve function if any 4 admittance values are equal to zero provided
;;   that one of the zero values for admittance is a4 or a5.
;; The values returned depend on the exact configuration of valves being open and closed (0 admittance)
;;;;;;;;;;;;;;;;;;;;;;;;;;;;;;;;;;;;;;;;;;;;;;;;;;;;;;;;;;;;;;;;;;;;;;;;;;;;;;;;;;;;;;;;;;;;;;;;;;;;;;;;;;;;;;;;

(defun get-vals->3 (p1 p2 p3 ppump st-press vt-press head-press a1 a2 a3 a4 a5 a6 a7)
  (cond
    ((zerop a7)
     (setq p3 vt-press))
    (t
     (setq p3 (/ (* vt-press (square (/ a6 a7)))
                 (+ 1 (square (/ a6 a7)))))))
  (cond
    ((and (not (zerop a1))(not (zerop a2)))
     (setq p1 (/ (+ st-press (* ppump (square (/ a1 a2))))
                 (+ 1 (square (/ a1 a2))))))
     ((and (not (zerop a1))(not (zerop a3)))
      (setq p1 ppump)
      (setq p2 (- ppump head-press)))
     ((and (not (zerop a1))(not (zerop a4)))
      (setq p1 ppump)
      (setq p2 ambient-atm))
     ((and (not (zerop a1))(not (zerop a5)))
      (setq p1 ppump)
      (setq p2 vt-press))
     ((and (not (zerop a1))(not (zerop a7)))
      (setq p1 ppump))
     ((and (not (zerop a2))(not (zerop a3)))
      (setq p1 st-press)
      (setq p2 (- st-press head-press)))
     ((and (not (zerop a2))(not (zerop a4)))
      (setq p1 st-press)
      (setq p2 ambient-atm))
     ((and (not (zerop a2))(not (zerop a5)))
      (setq p1 st-press)
      (setq p2 vt-press))
     ((and (not (zerop a2))(not (zerop a7)))
      (setq p1 st-press))
     ((and (not (zerop a3))(not (zerop a4)))
      (setq p1 head-press)
      (setq p2 ambient-atm))
     ((and (not (zerop a3))(not (zerop a5)))
      (setq p1 (+ vt-press head-press))
      (setq p2 vt-press))
     ((and (not (zerop a3))(not (zerop a7)))
      (setq p2 (- p1 head-press)))
     ((and (not (zerop a4))(not (zerop a7)))
      (setq p2 ambient-atm))
     ((and (not (zerop a5))(not (zerop a7)))
      (setq p2 p3)))
    (values p1 p2 p3))
```

```
;;;;;;;;;;;;;;;;;;;;;;;;;;;;;;;;;;;;;;;;;;;;;;;;;;;;;;;;;;;;;;;;;;;;;;;;;;;;;;;;;;;;;;;;;;;;;;;;;;;;;;;;;;
;; Function which is called by the solve function if any 3 admittance values are equal to zero provided
;;   that one of the zero values for admittance is a4 or a5. In addition, none of the following
;;   conditions can exist for this function to be called:
;;                                                        a1, a4 & a7 can not all be zero
;;                                                        a2, a4 & a7 can not all be zero
;;                                                        a2, a5 & a7 can not all be zero
;; The values returned depend on the exact configuration of valves being open and closed (0 admittance)
;;;;;;;;;;;;;;;;;;;;;;;;;;;;;;;;;;;;;;;;;;;;;;;;;;;;;;;;;;;;;;;;;;;;;;;;;;;;;;;;;;;;;;;;;;;;;;;;;;;;;;;;;;;

(defun get-vals->2 (p1 p2 p3 ppump st-press vt-press head-press a1 a2 a3 a4 a5 a6 a7)
  (cond
    ((zerop a7)
     (setq p3 vt-press))
    (t
     (setq p3 (/ (* vt-press (square (/ a6 a7)))
                 (+ 1 (square (/ a6 a7)))))))
  (cond
    ((and (zerop a1)(zerop a2)(zerop a4))
     (setq p2 p3)
     (setq p1 (+ p2 head-press)))
    ((and (zerop a1)(zerop a2)(zerop a5))
     (setq p1 head-press)
     (setq p2 ambient-atm))
    ((and (zerop a1)(zerop a3)(zerop a4))
     (setq p1 st-press)
     (setq p2 p3))
    ((and (zerop a1)(zerop a3)(zerop a5))
     (setq p1 st-press)
     (setq p2 ambient-atm))
    ((and (zerop a1)(zerop a4)(zerop a5))
     (setq p1 st-press)
     (setq p2 (- st-press head-press)))
    ((and (zerop a1)(zerop a5)(zerop a7))
     (setq p1 st-press)
     (setq p2 (- st-press head-press)))
    ((and (zerop a2)(zerop a3)(zerop a4))
     (setq p1 ppump)
     (setq p2 p3))
    ((and (zerop a2)(zerop a3)(zerop a5))
     (setq p1 st-press)
     (setq p2 ambient-atm))
    ((and (zerop a2)(zerop a4)(zerop a5))
     (setq p1 ppump)
     (setq p2 (- ppump head-press)))
    ((and (zerop a3)(zerop a4)(zerop a5))
     (setq p1 (/ (+ st-press (* ppump (square (/ a1 a2))))
                 (+ 1 (square (/ a1 a2))))))
     ((and (zerop a3)(zerop a4)(zerop a7))
      (setq p1 (/ (* vt-press (square (/ a6 a7)))
                  (+ 1 (square (/ a6 a7)))))
      (setq p2 vt-press))
     ((and (zerop a3)(zerop a5)(zerop a7))
      (setq p1 (/ (+ st-press (* ppump (square (/ a1 a2))))
                  (+ 1 (square (/ a1 a2)))))
      (setq p2 ambient-atm))
     ((and (zerop a4)(zerop a5)(zerop a7))
      (setq p1 ppump)
      (setq p2 (- ppump head-press))))
    (values p1 p2 p3))
```

ORIGINAL PAGE IS
OF POOR QUALITY

```
;;;;;;;;;;;;;;;;;;;;;;;;;;;;;;;;;;;;;;;;;;;;;;;;;;;;;;;;;;;;;;;;;;;;;;;;;;;;;;;;;;;;;;;;;;;;;;;;
;; Function which solves the nonlinear flow equations using Newton's method. This involves iterating
;;   on the unknown internal pressures p1, p2 & p3 until convergence within a tolerance of .01 is
;;   achieved. The solution procedure involves solving for the vector x, where each element of x
;;   represents the difference in the guessed values for p1, p2 & p3 and the next approximation for
;;   each. The equation which is solved is:
;;                                          J x = F
;; The elements of the Jacobian matrix J and the vector F have been defined above. Solution of the
;;   system of equations is accomplished by using the LISP functions from the mathematics package
;;   MATH:DECOMPOSE and MATH:SOLVE.
;; Logic is included to check for conditions which can not be solved directly by these functions and
;;   therefore need special attention. Explanation of these special conditions is included within
;;   the body of the code.
;;;;;;;;;;;;;;;;;;;;;;;;;;;;;;;;;;;;;;;;;;;;;;;;;;;;;;;;;;;;;;;;;;;;;;;;;;;;;;;;;;;;;;;;;;;;;;;;

(defun solve (p1 p2 p3 ppump st-press vt-press head-press a1 a2 a3 a4 a5 a6 a7 it in-sys)
  (cond
    ((and (almost-equal vt-press p2) (almost-equal vt-press p3)       ;; stagnant system
          (almost-equal p1 st-press) (almost-equal ppump st-press)) ;; just return the
     (values p1 p2 p3))                                               ;; previous values

    ((and (almost-equal vt-press ambient-atm) (< p1 (- st-press 1))) ;; initialize system when the
     (setq p1 st-press)                                               ;; function is first called
     (setq p2 ambient-atm)
     (setq p3 ambient-atm)
     (values p1 p2 p3))
    (t
     (cond
       ((and (almost-equal vt-press ambient-atm) (almost-equal p1 st-press) ;; initialize the
             (not (almost-equal ppump st-press)) (zerop it))                ;; recirculating
        (setq p1 (- ppump .1))                                              ;; system after
        (setq p2 ambient-atm)                                               ;; pump is first
        (setq p3 ambient-atm)))                                             ;; turned on
     (cond
       ((and (zerop a1) (almost-equal vt-press ambient-atm)      ;; when backflow occurs
             (not (almost-equal head-press elevation-press))) ;; and the vt-press = atmospheric pressure
        (setq p3 ambient-atm))                                  ;; set p3 to atmospheric pressure

       ((and (zerop a1) (almost-equal vt-press ambient-atm))   ;; when backflow occurs
        (setq p2 ambient-atm)                                   ;; and the upper level piping has drained
        (setq p3 ambient-atm))                                  ;; set p2 to atmospheric pressure

       ((and (not (zerop a1)) (almost-equal vt-press ambient-atm) ;; if the 20 foot riser is just filled
             (almost-equal head-press elevation-press))           ;; p3 is still equal to atmospheric
        (setq p3 ambient-atm))                                    ;; pressure

       ((and (not (zerop a1)) (almost-equal vt-press ambient-atm)) ;; before the 20 foot riser is filled
        (setq p2 ambient-atm)                                       ;; p2 and p3 are equal to atmospheric
        (setq p3 ambient-atm)))                                     ;; pressure

     (cond
       ((almost-equal ppump st-press) ;; if the pump is off set the a1 admittance to zero
        (setq a1 0)))

     (let*
       ((zero-ads (count-zeros (list a1 a2 a3 a4 a5 a7)))) ;; count how many admittances are zero
       (cond
         ((> it 800) ;; Too many iterations exit the solve routine
          (values p1 p2 p3))

         ((> zero-ads 5) ;; if all 6 admittances are zero set p3 to vt-press and return
          (setq p3 vt-press)
          (values p1 p2 p3))
```

```
((> zero-ads 4)                    ;; if 5 admittances are zero determine what to return from
 (multiple-value-setq (p1 p2 p3)   ;; solve by calling the function get-vals->4
   (get-vals->4 p1 p2 p3 ppump st-press vt-press head-press a1 a2 a3 a4 a5 a6 a7))
 (values p1 p2 p3))

((and (> zero-ads 3) (or (zerop a4) (zerop a5))) ;; if 4 admittances are zero and a4 or a5
 (multiple-value-setq (p1 p2 p3)                 ;; are zero, call the function get-vals->3
   (get-vals->3 p1 p2 p3 ppump st-press vt-press head-press a1 a2 a3 a4 a5 a6 a7))
 (values p1 p2 p3))

((and (equalp vt-press ambient-atm) (zerop a3))
 (setq p1 (/ (+ st-press (* ppump (square (/ a1 a2))))
             (+ 1 (square (/ a1 a2)))))
 (values p1 p2 p3))

((and (> zero-ads 2) (or (zerop a4) (zerop a5))                ;; if 3 admittances are zero and
      (and (not (zerop a1)) (not (zerop a4)) (not (zerop a7))) ;; a4 or a5 are zero and in
      (and (not (zerop a2)) (not (zerop a4)) (not (zerop a7))) ;; addition (a1, a4 & a7),
      (and (not (zerop a2)) (not (zerop a5)) (not (zerop a7))));; (a2, a4 &a7) & (a2, a5 & a7)
 (multiple-value-setq (p1 p2 p3)                               ;; are not all zero, call the
   (get-vals->2 p1 p2 p3 ppump st-press vt-press head-press a1 a2 a3 a4 a5 a6 a7)) ;; function
 (values p1 p2 p3))                                                               ;; get-vals->2

((and (zerop a1) (zerop a5))                ;; if this point is reached and both a1 & a5 are
 (setq p1 (+ st-press))                     ;; zero return the appropriate values
 (setq p2 (+ ambient-atm))
 (setq p3 (/ (* vt-press (square (/ a6 a7)))
             (+ 1 (square (/ a6 a7)))))
 (values p1 p2 p3))

(t
 (cond                                                          ;; if this is first iteration &
   ((and (zerop a1)(zerop a2)(zerop a3)(zerop a7)(zerop it))    ;; a1, a2, a3, & a7 are all zero,
    (setq p3 (- vt-press 1))                                    ;; adjust the initial guess of p2
    (setq p2 (- p3 1))                                          ;; and p3 to avoid divergence
    (setq it 1))

   ((zerop a1)
    (cond                               ;; if this is the first iteration and a1 is
      ((zerop it)                       ;; zero adjust the initial guesses for the
       (setq p3 (- vt-press .1))        ;; pressures to avoid divergence
       (setq p2 (- p3 .1))
       (setq p1 (- (+ p2 head-press) .1))
       (setq it 1)))
    (cond                               ;; if both a1 & a2 are zero also set a3 to zero
      ((zerop a2)                       ;; in order to avoid discontinuity and adjust
       (setq a3 0)                      ;; the value of p1
       (setq p1 (+ p2 head-press)))
      ((zerop a3)                       ;; if both a1 & a3 are zero also set a2 to zero
       (setq a2 0)                      ;; in order to avoid discontinuity and adjust
       (setq p1 st-press))))            ;; the value of p1

   ((zerop a3)
    (cond
      ((zerop it)                       ;; if this is the first iteration and a3 is
       (setq p1 (- ppump 1))            ;; zero adjust the initial guesses for the
       (setq p3 (- vt-press 1))         ;; pressures to avoid divergence
       (setq p2 (- p3 1))
       (setq it 1)))
    (cond                               ;; if both a2 & a3 are zero also set a1 to zero
      ((zerop a2)                       ;; in order to avoid discontinuity and adjust
       (setq a1 0)                      ;; the value of p1
       (setq p1 ppump))
      ((zerop a4)                       ;; if both a3 & a4 are zero also set a5 to zero
       (setq a5 0)                      ;; in order to avoid discontinuity and adjust p2
       (setq p2 p3))
      ((zerop a5)                       ;; if both a3 & a5 are zero also set a4 to zero
       (setq a4 0)                      ;; in order to avoid discontinuity and adjust p2
       (setq p2 ambient-atm))))
```

```
            ((zerop a5)
             (cond                                 ;; if a5 is zero and this is the first iteration
               ((zerop it)                         ;; adjust the initial guesses for the pressures
                (setq p1 (- ppump 1))              ;; to avoid divergence
                (setq p2 (- p1 1 head-press))
                (setq p3 (- vt-press 1))
                (setq it 1)))
             (cond
               ((zerop a4)                         ;; if both a5 & a4 are zero also set a3 to zero
                (setq a3 0)                        ;; in order to avoid discontinuity and adjust
                (setq p2 (- p1 head-press))))))     ;; the value of p2

          (let*  ;; set up the vector b and matrix a to solve for x in the equation A x = b
            ((b (make-array 3 :initial-contents
                             `(,(f1 p1 p2 ppump st-press head-press a1 a2 a3)
                              ,(f2 p1 p2 p3 head-press a3 a4 a5 in-sys)
                              ,(f3 p2 p3 vt-press a5 a6 a7 in-sys))))

             (a (make-array '(3 3) :initial-contents
                             `((,(j11 p1 p2 ppump st-press head-press a1 a2 a3)
                                ,(j12 p1 p2 head-press a3) 0)
                               (,(j12 p1 p2 head-press a3) ,(j22 p1 p2 p3 head-press a3 a4 a5 in-sys)
                                ,(j23 p2 p3 a5))
                               (0 ,(j23 p2 p3 a5) ,(j33 p2 p3 vt-press a5 a6 a7 in-sys)))))

             (x (multiple-value-bind (c d)(math:decompose a)(math:solve c d b)))

;;      (x (iterate a b x))) ;; This routine only needs to be used for ill-conditioned matrices
             )                ;; & has been commented out.

            (cond
              ((< (max (abs (aref x 0))(abs (aref x 1))(abs (aref x 2))) .01)
               (values p1 p2 p3))
              (t
               (setq it (+ it 1))             ;; update the iteration number and obtain the next
               (setq p1 (- p1 (aref x 0)))    ;; value for the unknown pressures and then recursively
               (setq p2 (- p2 (aref x 1)))    ;; call solve until the tolerance is reached.
               (setq p3 (- p3 (aref x 2)))
               (solve  p1 p2 p3 ppump st-press vt-press head-press a1 a2 a3 a4 a5 a6 a7 it in-sys)
               )))))))))


;;;;;;;;;;;;;;;;;;;;;;;;;;;;;;;;;;;;;;;;;;;;;;;;;;;;;;;;;;;;;;;;;;;;;;;;;;;;;;;;;;;;;;;;;;;;;;;;;;;;;;;;;;;;;;
;; This functon could be used if ill-conditioned matrices were being encountered. This does not seem
;;   to be the case, however the code has been left for future reference.
;;;;;;;;;;;;;;;;;;;;;;;;;;;;;;;;;;;;;;;;;;;;;;;;;;;;;;;;;;;;;;;;;;;;;;;;;;;;;;;;;;;;;;;;;;;;;;;;;;;;;;;;;;;;;;

(defun iterate (a b x)
  (let* ((ax (math:multiply-matrices a x))

         (r (make-array 3 :element-type 'double-float
                        :initial-contents
                        `(,(- (aref b 0)(aref ax 0))
                          ,(- (aref b 1)(aref ax 1))
                          ,(- (aref b 2)(aref ax 2)))))

         (y (multiple-value-bind (e f)(math:decompose a)(math:solve e f r)))


         (xx (make-array 3 :initial-contents
                         `(,(+ (aref x 0)(aref y 0))
                           ,(+ (aref x 1)(aref y 1))
                           ,(+ (aref x 2)(aref y 2))))))
    (cond
      ((< (abs (max (- (aref x 0)(aref xx 0))(- (aref x 1)(aref xx 1))(- (aref x 2)(aref xx 2)))) .0001)
       x)
      (t
       (setf (aref x 0)(aref xx 0))
       (setf (aref x 1)(aref xx 1))
       (setf (aref x 2)(aref xx 2))
       (iterate a b x)))))
```

VII. REFERENCES

1. Denn, M. M., Process Fluid Mechanics, Prentice-Hall, Englewood Cliffs, NJ, 1980.

2. Barron, R. F., Cryogenic Systems, Second Edition, Oxford University Press, New York, 1985.

3. Martinelli, R. C., and R. W. Lockhart, "Proposed Correlation of Data for Isothermal Two-Phase Flow in Pipes", Chemical Engineering Progress, 45, 1, 39, 1949.

4. Shen, P. S., and Y. W. Jao, "Pressure Drop of Two-Phase Flow in a Pipeline with Longitudinal Variations in Heat Flux, Advances in Cryogenic Engineering, 15, Plenum Press, New York, 1970.

3. Burden, R. L. and J. D. Faires, Numerical Analysis, Third Edition, Prindle, Weber & Schmidt, Boston, 1985.

NASA
National Aeronautics and Space Administration

Report Documentation Page

1. Report No.	2. Government Accession No.	3. Recipient's Catalog No.
CR-187638		

4. Title and Subtitle

1990 Research Reports
NASA/ASEE Summer Faculty Fellowship Program

5. Report Date

September 1990

6. Performing Organization Code

7. Author(s)

Dr. Loren A. Anderson, Editor
Dr. Mark A. Beymer, Editor

8. Performing Organization Report No.

10. Work Unit No.

9. Performing Organization Name and Address

NASA - Kennedy Space Center
Systems Training and Employee Development Branch
Kennedy Space Center, Florida

11. Contract or Grant No.

NASA Grant NGT-60002
Supplement 4

13. Type of Report and Period Covered

Final Contractor Report
6/90 - 8/90

12. Sponsoring Agency Name and Address

NASA Headquarters
University Programs Branch
Washington, D.C.

14. Sponsoring Agency Code

15. Supplementary Notes

16. Abstract

This contractor's report contains all seventeen final reports prepared by the participants in the 1990 Summer Faculty Fellowship Program. Reports describe research projects on a number of different topics.

17. Key Words (Suggested by Author(s))

human-computer interface software, multimode fiber optic communication links, electrochemical impedance spectroscopy, rocket-triggered lightning, robotics, flowmeter

18. Distribution Statement

Unclassified - Unlimited

19. Security Classif. (of this report)	20. Security Classif. (of this page)	21. No. of pages	22. Price
Unclassified	Unclassified	526	

NASA FORM 1626 OCT 86